Imperial College London,
Department of Materials

The micromechanical testing of Ni-based superalloys

Suki Adande

I declare that this work is original and my own.

Submitted in full requirements for the degree of

Doctor of Philosophy (PhD), June 2018

Supervised by Dr Ben Britton

I. Abstract

Ni superalloys are engineered material systems, where each microstructural feature conveys specific strengthening mechanisms. This project establishes experimental techniques which focus on understanding deformation in Ni superalloys; building upwards from single crystal CMSX-4, to polycrystalline FGH96, to carburised CMSX-4 & 10. The project combines micromechanical testing and material characterisation with the aim of extracting engineering properties, to help further advance the micromechanics field and aid in the development of new alloys.

Micropillar compression experiments were used in this study and enable the analysis of deformation at characteristic strain(s) on the same length scale as the deformation processes.

The critical resolved shear stress of pillars fabricated in {001}{011}{111} on single crystal CMSX-4 varied by 380 ± 10 MPa, 420 ± 15 MPa, 460 ± 16 MPa respectively, the resolved shear stress of pillars fabricated on individual grains on a polycrystal0

line sample, with nearly identical areas in the same orientation varies by less than 5% and these results were found to be consistent with literature.

The critical resolved shear stress of pillars fabricated on single crystal CMSX-4, with carbide type phases captured on the top surface of the pillars varied by 400 ± 3.4 MPa, 420 ± 6 MPa 450 ± 23 MPa respectively, despite being the same crystal orientation and in similar locations ± 20 µm. The area fraction of the pillars mentioned above were; 5% 17% and 27% respectively. The variation in τ_{crss} was found to be a consequence of the leeching of alloying elements, via the formation of carbide type phases which disrupted the ϒ/ϒ' microstructure and disrupted the propagation of dislocations. The carbide size, area fraction, number density and shape abnormality were theorised to be proportional to the extent of ϒ/ϒ' disruption. Transmission electron microscope (TEM), based analysis shows that the carbide type phases orientate themselves at junctions and dislocations tend to agglomerate around the phases at these points.

Declaration

‘The copyright of this thesis rests with the author and is made available under a Creative Commons Attribution Non-Commercial No Derivatives licence. Researchers are free to copy, distribute or transmit the thesis on the condition that they attribute it, that they do not use it for commercial purposes and that they do not alter, transform or build upon it. For any reuse or redistribution, researchers must make clear to others the licence terms of this work’

Statement of originality

This work is my own and is original, I thank all collaborating parties who contributed towards the completion of this degree. I have referenced all text and figures accordingly as meets the requirements for the degree of Doctor of Philosophy (PhD), awarded by Imperial College London.

Acknowledgements

I would like to dedicate this thesis to my grandad Dominic Ogunbiyi Adande, who passed away on the 26th of September 2017. He was a true inspiration and it was through his experiences that I decided to dedicate my 20's to studying, mastering and finally contributing towards the engineering discipline. I would like to thank the Materials department at Imperial College London for nurturing and educating me. In particular I would like to thank Dr Ben Britton and the micromechanics group for giving me a chance and helping me excel and grow as a scientist and an individual. It has been a pleasure to see the young group grow and become a strong force within the department. I would like to thank Dr Vassili Vronotsov for his patience in training me in advance microscopy techniques and giving me a unique perspective. Finally I would like to thank my friends and family, in particular my mother Joanna Adande, who pushed me and never gave up on me. I am eternally thankful.

"If at first you don't succeed, take a step back, pick yourself up and try again; it always seems impossible until you get it done."

"When you combine a strong imagination with scientific knowledge, the word impossible ceases to exist"

Suki Adande 2018

Table of Contents

1. Abstract 2

Declaration 3

Acknowledgements 4

2. Glossary 9

3. Introduction 10

4. Literature review 13

4.1. Mechanics of dislocations 13

4.1.1. Dislocation mechanics of Ni at the large scale 13

4.2. The stress / strain response 17

4.2.1. Stage 1: Low hardening rates 18

4.2.2. Stage 2: High constant hardening rate 19

4.2.3. Stage 3: Decreasing work hardening 19

4.3. Introduction to dislocations 19

4.3.1. The Dislocation Line 19

4.3.2. Frank Read partial 21

4.3.3. Dislocation multiplication – Frank Read source 22

4.3.4. Work hardening / barriers to dislocation motion 24

4.3.5. Kinks & Jogs 25

4.4. Strengthening effects in Ni superalloys 26

4.4.1. The yield point 28

4.4.2. Dislocations in γ' 29

4.4.3. Dislocations in γ 33

4.4.4. Altering the γ' affecting the γ'/γ interface at high temperature 36

4.4.5. Weak and strong coupling in Ni-based superalloys 41

4.5. Diffusion mechanics in Ni-based superalloy bond coat system 41

4.5.1. A brief introduction to the alloying of component parts in Ni alloys 41

4.5.2. The bond coat system in Ni alloys 42

4.5.3. Diffusion mechanics in pure Ni 45

4.5.4. Diffusion mechanics in Ni-based superalloys 47

4.5.5. Carbides / diffusion precipitates 52

4.6. Micromechanical testing 58

4.6.1. Ni specific 58

4.6.2. Dislocation modelling 63

4.6.3. Size effects 64

4.7. Supporting size effect theories 66
4.7.1. Starvation of mobile dislocations 66
4.7.2. Exhaustion hardening 67
4.7.3. Statistical models 67
4.8. Pillar manufacture – Focused Ion Beam 68
4.8.1. The basics 68
4.8.2. The liquid metal ion source 69
4.8.3. Imaging 70
4.8.4. Damage / Controllable features 70
5. Materials and Methodology 73
5.1. Introduction 73
5.1.1. Pillar fabrication 74
5.1.2. Pillar analysis 76
5.2. Electron microscopy imaging with scanning electron microscopy: secondary electron, backscatter electrons and electron backscatter diffraction 87
5.2.1. Focused Ion Beam 90
5.2.2. Aligning the dual FIB/SEM 92
5.3. Pillar manufacture 94
5.3.1. Method 94
5.3.2. Fabrication 96
5.3.3. Pillar fabrication for Transmission Electron Microscopy (TEM) 98
5.3.4. TEM 99
5.4. In-situ set up – Alemnis 104
5.4.1. Software 106
5.5. Materials preparation 107
5.5.1. Pillar design 108
5.5.2. TEM Pillar sample preparation 110
5.5.3. Slip trace analysis 114
5.5.4. Shape descriptors 120
5.5.5. The composition and origin of each alloy used in this study 123
6. Results - Single crystal Ni super alloy testing 124
6.2. Motivation 124
6.3. Introduction 124
6.4. Pillar scaling / size effect 126
6.4.1. Load, Displacement, Time 126
6.4.2. Engineering stress strain 127

6.4.3. Yield point determination 131
6.4.4. Hardening and modulus 133
6.4.5. Compression testing – Pillar geometries 134
6.5. Mechanical effects 136
6.6. Mechanical effects with respect to orientation 143
6.7. Dislocation effects 152
6.7.1. Crumple slip 155
6.7.2. Localised shear slip 160
6.8. Summary – Results chapter 1 176
7. Results – Polycrystalline Ni-based superalloy & orientation testing 180
7.2. Objectives – Results chapter 2 180
7.3. Motivation 180
7.4. Introduction 180
7.5. Polycrystalline FGH-96 188
6.4.1. FGH-96 method and testing 190
6.4.2. Deformation modes and mechanical properties in FGH-96 197
7.6. Single crystal CMSX-4 204
7.6.1. Deformation in the CMSX-4 <001> <011> <111> 205
7.6.1.1. Slip systems CMSX-4 206
7.6.1.2. Slip traces and deformation CMSX-4 210
7.6.1.3. Mechanical properties CMSX-4 214
7.7. Comparison of FGH-96 and CMSX-4 215
7.8. Summary – Results chapter 2 217
8. Results - Carburised Ni-based superalloy: CMSX-4 219
8.2. Objectives 219
8.3. Motivation 219
8.4. Introduction 219
8.5. Characterisation of carburised CMSX-4 222
8.5.1. Energy Dispersive X-ray Spectroscopy (EDS) – Bulk carbide rich region 222
8.5.2. Microstructure 228
8.5.3. Carbide zones 231
8.5.4. Summary – Characterisation of carbides 242
8.6. Carbide zones & energy dispersive spectroscopy 243
8.6.1. Carbide rich region 245
8.6.2. Segregates zones 1-3, within the carbide rich region 247
8.6.3. Carbide type 248

8.6.4. Summary – Carbide zones & chemical analysis 249
8.7. Mechanical properties of carburised CMSX-4 249
8.7.1. Micropillar testing 250
8.7.2. Microindentation testing 258
8.7.3. Summary – Mechanical properties 265
8.8. Tranmission electron microscopy of carbides 266
8.9. Summary – Results chapter 3 273
9. Results - Carburised Ni superalloy: CMSX-10 275
9.2. Objectives 275
9.3. Motivation 275
9.4. Introduction 275
9.5. Characterisation of Carburised CMSX-10 278
9.5.1. EDS 279
9.5.2. Carbide character 280
9.6. Mechanical properties of CMSX-10 281
9.7. Summary – Results chapter 4 289
10. Discussion 290
10.1. Introduction 290
10.2. Discussion overview 294
10.3. Characterisation 295
10.3.1. Υ/ Υ’ structure 295
10.3.2. Chemical analysis 297
10.4. Mechanical behaviour 298
10.4.1. Overview 298
10.4.2. Stress strain analysis / phenomena 299
10.4.3. Orientation / slip trace phenomena 304
10.4.4. EDS + Mechanical properties 309
10.4.5. Microindents 310
11. Problems and advantages of methodology 320
11.1. The elastic modulus 320
11.2. Yield Point evaluation 321
11.3. The effect of carbides on the yield point 322
11.4. Plasticity and hardening 328
11.5. The effect of carbides on dislocations 330
12. Conclusion 332
13. References 337

2. Glossary

SX	Single crystal
PX	Poly crystal
TEM	Transition Electron Microscopy
HV	Vickers hardness
TBC	Thermal Barrier Coating
EDS	Energy-dispersive X-ray spectroscopy
fcc	face centered cubic
APB	Anti phase boundary
SISF	Super Intrinsic Stacking Fault
CSF	Complex Stacking Fault
LC	Lomer Cotrell
KW	Kear-Wilsdorf
HCP	Hexagonal Close Packed
SEM	Scanning Electron Microscope
FIB	Focused Ion Beam
LMIS	Liquid Metal Ion Source
SBE	Surface Binding Energy
EBSD	Electron Backscatterd Diffraction
TCP	Topologically Close Packed
BSD	Back Scattered Detector
FEG	Field Emission Gun
ESEM	Environmental Scanning Electron Microscope
CAD	Computer Aided Design
µm	Micrometer
µA	Microampere
ev	Electron Volts
τ_c	Resolved Shear Stress
τ_{crss}	Critical Resolved Shear Stress
MPa	Mega Pascals
GPa	Giga Pascals
nm	Nano Meter
kN	Kilo Newton
G	Shear Modulus
B	Burgers vector
V	Poissons constant
p	Dislocation density

3. Introduction

This project aims to use micro mechanical testing to examine the performance of Ni-based superalloys used in bespoke jet engine components. The micro mechanical technique was developed initially by Dimiduk[1] and Uchich[2] the technique can provide high fidelity mechanical data that can be used in tandem with micromechanical models to quantify the performance of individual microstructural features[3] and orientations[4]. The tests can apply to many types of in service behaviour[5,6,7].

The benefit of the flat punch compression technique, used in this study, is that it can obtain ~uniaxial stress vs strain behaviour of individual microstructural units[8,9], such as precipitate rich alloys. It can also be used in tandem with microscopy techniques to give a broader understanding of deformation[10].

Ni superalloys are exposed to in service temperature ranging from room temperature - 1000°C[11], at 20000 rpm which constitutes to a constant stress of ~ 100 MPa[12]. The deformation behaviour of these materials at room temperature is equally important as high temperature[11] and should first be understood thoroughly before moving onto higher temperature systems.

Understanding the deformation behaviour of materials requires knowledge of the local stress-strain behaviour of individual microstructural phases and constituents[13]. These can include specific orientations[14], dual phases[6] and precipitates.

The size and geometry of the pillars being tested is very important, as strain localisation can occur at the top and bottom of the pillar as shear accumulates[15], and furthermore large and sudden shape changes of the pillar can also result in an unstable friction zone between the pillar and the compression tool[13]. The effects of all of the above are outlined in this thesis.

This thesis is separated into four results chapters, followed by a discussion, each section in the thesis has its own focused introduction. Examining the project globally; it can be separated into three parts:

(1) Single crystal (SX) CMSX-4 compression tests and companion TEM observations of the associated slip mechanisms. TEM of deformed pillars will reveal how glissile dislocations move through the ϒ/ϒ’ matrix on associated slip systems. The representative slip systems are found by tilting to a zone axis, moving through to reveal which dislocation systems are present. The technique also indicates which modes contribute to changes in the load-displacement response. This is done by loading to a high strain, providing an outline to how a micropillar deforms in compression and at what % strain the elastic to plastic transformation takes place. When testing a pure CMSX-4 micropillar in displacement control yield takes place at approximately 3-5% strain, as outlined by the inflection point in the stress strain curve. The ϒ/ϒ’ volume fraction of un altered SX-CMSX-4 is 70%, the average ϒ’ particle length is 544 nm, the

average yield point was found to be 850 ± 60 MPa which corresponds to a hardness of approximately 4 GPa (410 HV) these values are consistent with the literature[11].

SX-Ni superalloys undergo a costly and time expensive heat treatment to promote the formation of a stable and evenly distributed microstructure[16]. It is common for SX-alloys to undergo a 3-stage homogenization process with controlled rapid cooling[16], followed by a 2-stage aging treatment enabling a fine dispersion of secondary and tertiary precipitates[17]. The ability to isolate unique regions of these homogenised microstructures especially when used in tandem with a thermal barrier coating (TBC) is crucial to the development of these alloys. The top layer of a TBC is made of ceramic materials and so a gradient layer is grown to accommodate for the thermal mismatch between metal and ceramic[18].

(2) Polycrystaline (PX) Ni superalloy FGH-96 in-situ compression in which preliminary tests have been performed on three isolated grains, with surfaces of {001}, {011} & {111} parallel to the loading axis. The results are as follows; two micropillars orientated with the {111} plane parallel to the flat punch (i.e. perpendicular to the loading axis) had yield points - 1200MPa / 1206MPa respectively, the same test performed with the flat punch parallel to {011} planes gave compressive yield points – 1023 MPa & 1058 MPa respectively (note that size effects and pillar testing geometry considerations need to be addressed in more detail before a full comparison with macroscopic yield and modulus responses of these alloys can be performed). When compared to SX-CMSX-4 pillars, cut via a goniometer stage the yield points of the pillars orientated {001} / {111} / {011} || loading axis were 750 MPa 1140 MPa and 1000 MPa respectively.

The crystal structure of Ni superalloys results in an anisotropic material response from grain to grain in PX-materials, and it is therefore important to understand how they behave mechanically in different crystallographic orientations. It has been found that orientation anisotropy is more significant at low temperatures[19]. SX-turbine blades commonly come fabricated in the <001> direction.

(3) Carburised Ni superalloy testing, where two ~9 mm diameter samples containing a colony of carbide type phases, located around the outer circumference were examined and tested. One sample is second generation SX-CMSX-4, the other is third generation SX-CMSX-10. The alloying elements vary slightly between the second and third generation alloys. The variation in alloying chemistry influences the precipitation of carbides[20]. Carburised alloys are used for a range of applications, such as strengthening and wear resistance[21] and in the case of this study, are a by-product of a coating process[22] Initial EDS analysis which provides a resolution of up to ~1 μm[23] indicates the carbide type phases are primarily derived from a combination of alloying elements with preferential segregation involving regions based on C content and carbide type phase. EDS experiments reveal Ta, Ti, Hf, Ti, Re segregate to carbide phase rich zones, whereas Ni, Co and Cr are depleted.

5 µm pillars were fabricated in carbide phase rich areas through to the bulk microstructure, this was characterised through a distance of 0-800 µm. The experiments were designed to test the plastic response at various regions (diffusion zones, matrix and different carbide type phases) to extract information concerning the influence of carbide type phases on plastic deformation.

Testing indicated that the carbide type phase in CMSX-4 which penetrate roughly 120 µm from the edge of the sample to the bulk, cause a decrease in the resolved shear stress but increase the hardening response. It was also found that the yield point of the alloy begins to increase a certain distance away from the carbide type phase, rich region. In the CMSX-10 alloy the carbide type phase rich region is only 30 µm from the edge of the sample and acts to improve the yield strength slightly. The carbide type phase in CMSX-10 are small in nature and appear faceted, they range in size from 5-600 nm. The carbide type phase in CMSX-4 is larger, varies in size and distribution from 60nm – 2 µm.

Alloys containing precipitates which act as obstacles preventing the glissle flow of dislocations in the form of Orowan strengthening[24], stacking fault energy[25], interfacial energy[11] and differences in modulus[26] have been considered in the literature[27],[28]. However the effect of carbides in Ni superalloys, using localised mechanical testing has not, and is thus examined and discussed in this thesis. The carbide type phase in this study were formed during the pack aluminzation diffusion process. C from the parent Ni is dissolved into solution and precipitated out in the form of an intermetallic phase[21]. When comparing PX and SX alloys the PX alloys contain less C[21].

The aluminizing process is diffusion controlled[29] whereby the concentrations of refectory metals significantly influence the type of stable carbide phases[21].

The carburised alloys in this study, were the direct result of a maskant layer being used to protect the alloy substrate from aluminium deposition, the maskant consists of polymer based binders, ceramic filler and a powdered nickel chromium aluminium alloy. During the process the maskant can interact detrimentally with the alloy and form the carbide type phases examined in this study.

When carbides form via C diffusing from a PVA binder put on the surface of material to the substrate of the material / substrate interface[30] they are heavily influenced by processing temperatures[21]. Higher rates result in a finer dispersion of carbides and lower rates result in blocky low surface energy structures[30].

The type of carbide type phase, found in the carburised alloys would need further TEM based analysis to deduce; thus only the on the shape, size and (possibly) composition of the carbide type phases is analysed in this thesis.

4. Literature review

This literature review is introduced with a brief introduction to dislocations and their importance in the plastic slip in FCC metals. It is then developed further with specific aspects of the Ni-based superalloys. In order to understand the strengthening in Ni superalloys the individual strengthening effects of the disordered and ordered gamma must first be understood. The APB and SFE energies are phenomena that occur in the ϒ'/ ϒ respectively as dislocations travel through the phases and impart and energy penalty on the microstructure. The phases can be tailored accordingly with alloying elements to finely tune these values. The disruption of the phases by the precipitation of carbide like phases can disrupt these values and thus alter the mechanical properties of the alloy. Carbide and precipitate types will be discussed in section.

4.1. Mechanics of dislocations

4.1.1. Dislocation mechanics of Ni at the large scale

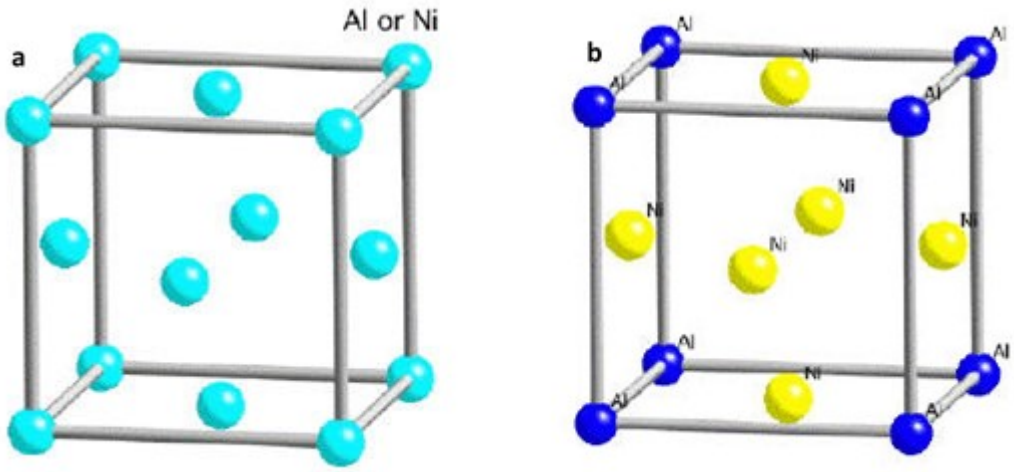


Figure 1: Crystal structure of (a) dis ordered fcc γ and (b) ordered L_{12} γ'[11]

Ni-based superalloys contain two phases (Figure 1): γ which is a disordered FCC cell where Ni and Al can be on any lattice site and these are mixed; and the γ' ordered structure which is a L_{12} ordered intermetallic. The L_{12} is formerly cubic but is often thought of as the FCC unit cell with Al atoms on the corners and Ni in the face centres. The two structures are cubic and have a [100]{100} cube orientation relationship, and so the discussion of dislocations will focus on the progress of dislocations in a cubic cell.

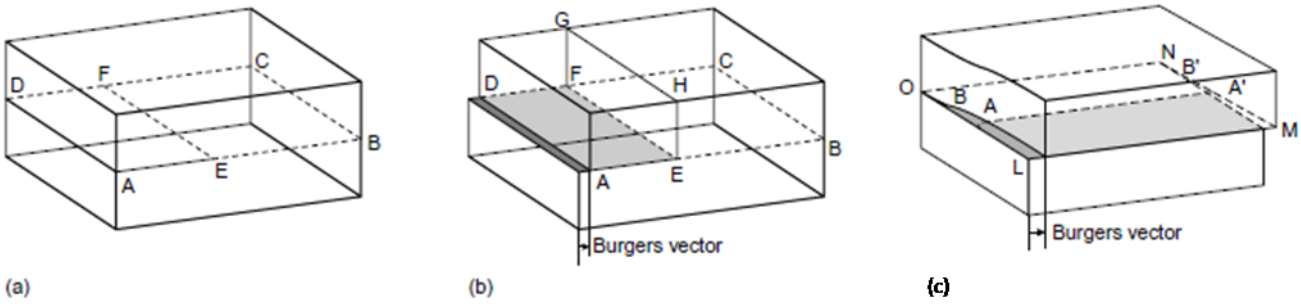


Figure 2: Formation of a pure edge dislocation FE a-b, c: The formation and movement of a pure screw dislocation AA' To BB' by slip. Hull et al [31].

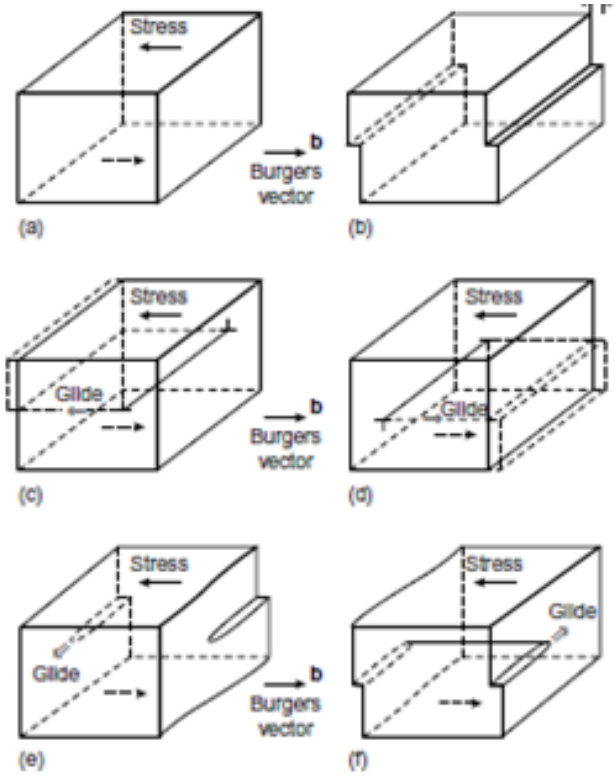


Figure 3: Plastic deformation by glide of edge and screw dislocations. Hull et al[31]

The glide mechanism requires the breaking and reforming of atomic bonds and is the dominant mechanism of deformation at low temperatures as dislocations propagate through the material, figure 2 and figure 3 show the formation of edge and screw dislocations via glide..

The climb of a dislocation is dictated by a motion out of the glide plane by the addition or subtraction of atoms or vacancies along the dislocation line. The principal role of climb is to provide a mechanism for dislocations to bypass microstructural barriers by changing slip plane. A line of atoms must be added for downwards climb and a line of vacancies introduced for upwards climb, and this process is usually thermally activated.

Plastic deformation is controlled by dislocations that are driven by shear[32] To move a dislocation and shear an fcc crystal the critical resolved shear stress (τ_c). must be overcome. τ_c is a material property related to the local chemistry and bonding in the system. It can be related to either the migration of existing dislocations or the activation of sources to enable the crystal to slip. This is seen at the macroscale where yield in a stress strain-curve is related to the microstructure and crystal orientations in a large scale testing object.

Typically the yield strength varies with orientation of the crystal[33]. The yield strength as a function of orientation can be quantified by understanding the dominant and subsequent activation of slip systems in the crystal. The activity of individual slip systems that contribute towards yield and plastic strain can be predicted using Schmid's law.

Schmid's law defines the relationship between the orientation of the slip system, the shear stress and the applied stress. The law enables one to determine the stress in a slip plane which is being deformed as well as the angle of the slip plane. This law can help quantify the differences in behaviour of different metal / alloy systems when subjected to a force[31]. Crystallographic slip and its relation to Schmid's law can be explained diagrammatically as follows, figure 4:

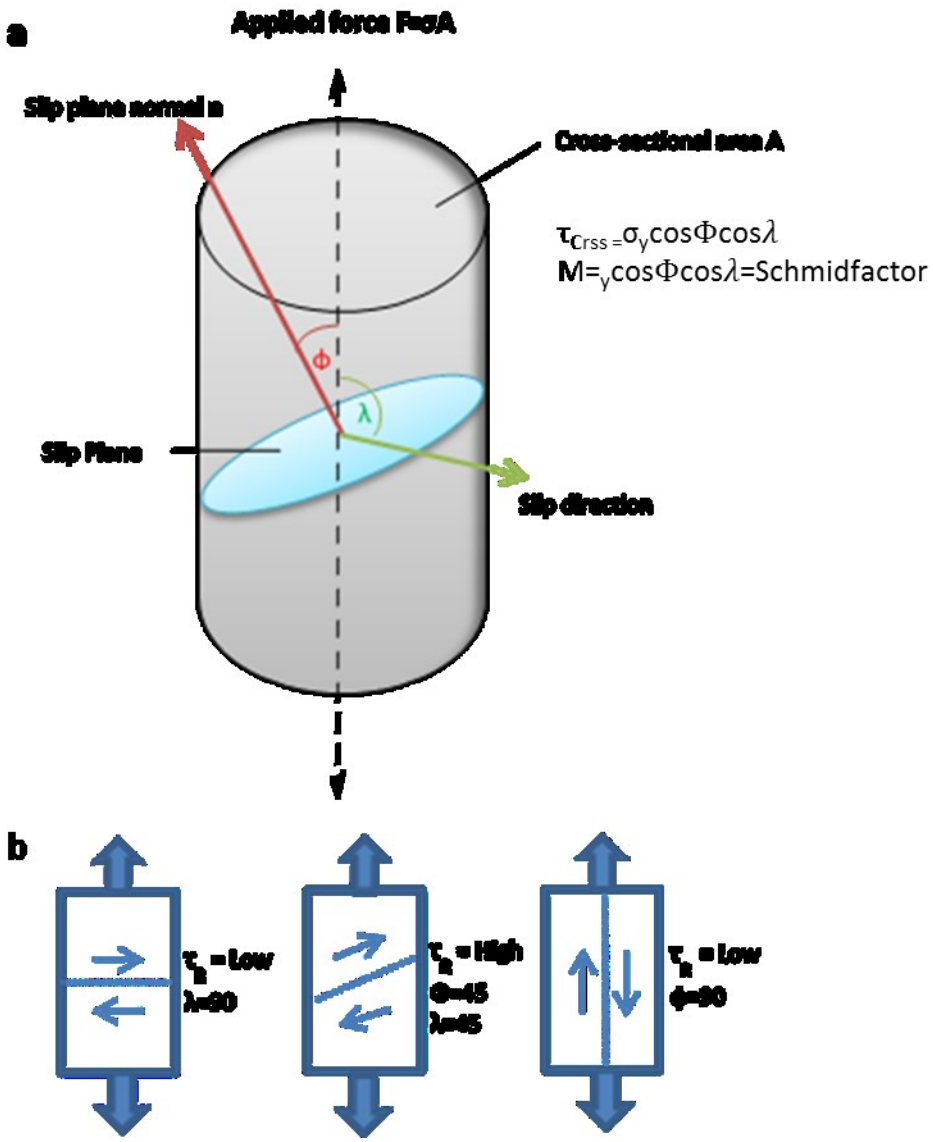


Figure 4: (a) Schematic illustrating the influence of angle orientation φ/λ on the Schmid factor M (b) Illustrating Schmid law in single crystal (modified from [11])

The yield point and subsequent hardening and softening mechanisms of a material can be quantified by the stress strain behaviour measured during a tensile or compression test. Yielding begins when the applied compressive stress reaches a value whereby dislocations are free to move and/or sources activate. The energy that has to be provided for dislocations to overcome barriers they come into contact with during plastic flow, determines the dependence of the flow stress on temperature and applied strain rate[28,34,35]. These effects can be quantified at a fixed temperature and strain rate via a stress v strain graph.

4.2. The stress / strain response

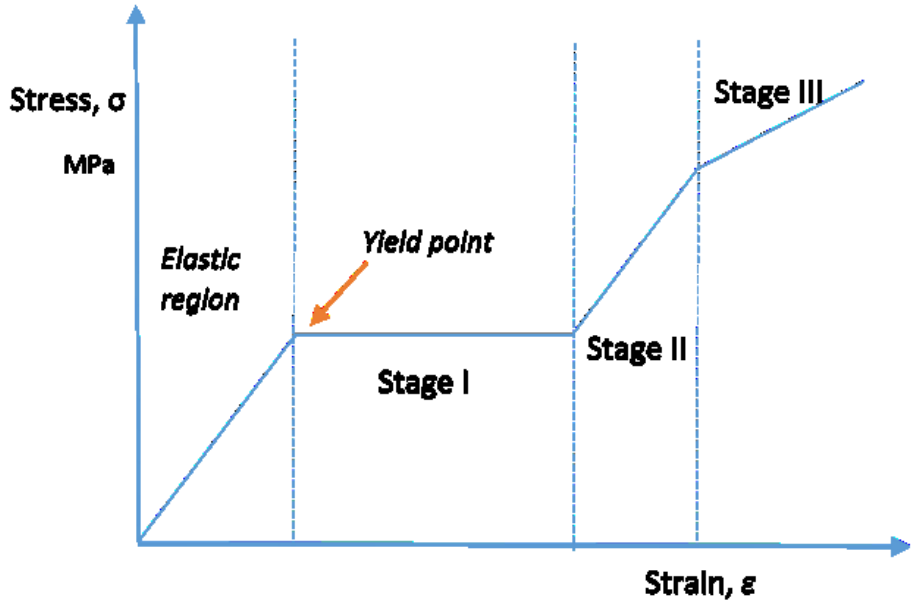


Figure 5: Schematic of the three stage stress strain response of a single crystal exhibiting the easy glide regime.

Figure 5, shows the three-stage stress, strain response typically found in fcc metals with an easy glide regime. The stress, strain response will vary according to crystal orientation and of course will greatly differ from single to poly crystal samples[36],this is shown schematically in Figure 6.

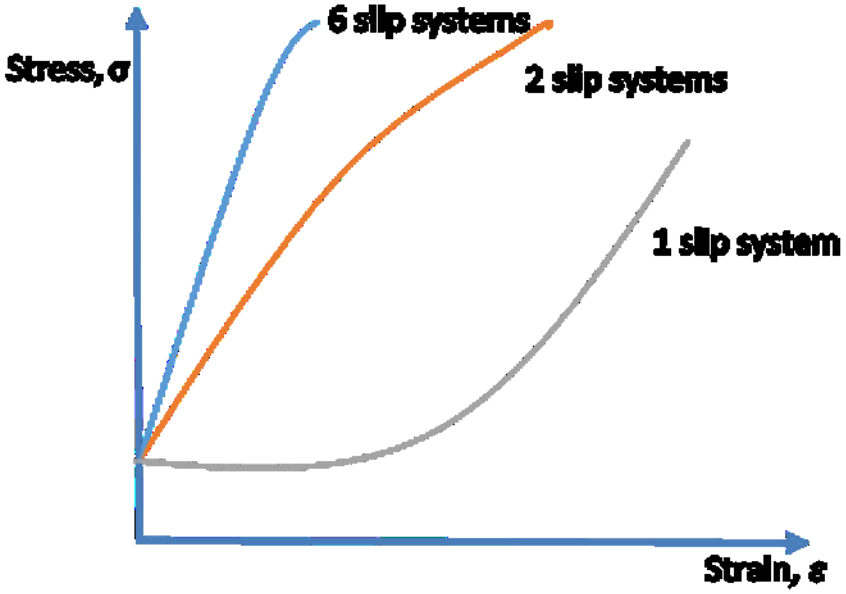


Figure 6: Schematic of the stress axis orientation and relation to the number of active slip systems

When testing single crystals it is common to resolve the stress and strain onto the plane and direction for which slip occurs first[37,38,39]. Polycrystalline materials do not show a stage one, but deform via stage II and III[40] due to no easy glide regime in these materials.

The extent of the three stages depends on the material, alloy composition, dislocation arrangement, grain size and crystal orientation of the compression axis. In the linear elastic region, the stress is proportional to strain, following Hooke's law. The elastic region as the name dictates is elastic and represents bonds stretching and returning back to equilibrium positions when the load is removed, and the gradient for a uniaxial test is the Young's modulus. When bonds are stretched too far, Hooke's law breaks down and plasticity begins at the yield stress. The orientation of the stress axis plays a major role in the mechanical behaviour of a single crystal, as it is indicative of the number of active slip systems. The more slip systems a material has, the harder the material is[41]. This is important due to geometrical hardening whereby the slip plane surface rotates away from the compressive axis figure 1.

The stage 1 regime known as the easy glide regime[11] is more predominant in crystal orientations where the resolved shear stress on other slip systems is low. Stage 1 easy glide should rarely occur in fcc crystals, as most grains are orientated in such a way that slip occurs simultaneously on many systems[11,13,42,43]. However it is possible to select an orientation such that this does not happen within a microscale single crystal[44].

4.2.1. Stage 1: Low hardening rates

In this stage the shear stress needed for plastic deformation remains constant. A single slip system is active. Dislocations do not interact much with each other and there is little or no work hardening. Therefore plastic deformation gives rise to slip but remains constant. In a constrained test, the crystal gradually rotates as it slips. This rotation brings a second slip system into a favourable orientation which begins stage II. There is a considerable increase in the interaction and multiplication of dislocations in this stage and it can be said that it is the onset of this secondary activity that brings stage 1 to an end and stage 2 to an onset[45].

The dislocation sources operate at the critical resolved shear stress and very few secondary slip systems are formed in stage 1[46]. This stage is greater in orientations for which the resolved shear stress on other potential systems is low.

The extent of stage 1 depends entirely on crystal orientation[11]. In polycrystalline materials stage 1 is normally absent.

4.2.2. Stage 2: High constant hardening rate

The transition from stage 1 to stage 2 in which the stress required for plastic flow to continue is increasing, can be defined by the onset of work hardening. In this stage the flow stress required to maintain plastic deformation increases with increasing strain. Stage 2 is the consequence of the applied load and crystal orientation such that the critical resolved shear stress on two different slip systems are high enough for them to activate.

The barriers to slip which inhibit plastic flow are the key contributor to work hardening. This can be observed by the linear increase in gradient in the stage 2 regime. The work hardening in this regime is due to the interactions between dislocations moving on intersecting slip planes[31,46]. This begins when slip is initiated on multiple slip systems whereby the shear stress needed to continue plastic deformation begins to increase[46]. When forest dislocations intersect the slip plane they provide obstacles to glide and although new primary slip lines appear as strain increases it can be shown experimentally that the slip line length decreases with increasing strain[34].

4.2.3. Stage 3: Decreasing work hardening

The decrease in work hardening rate can be attributed to many factors such as the materials sensitivity to temperature and strain rate. Effects such as cross slip may also play a role in the decrease[47]. Stress is also very high in this region, so dislocations can rip through existing 'soft' barriers. Formerly, the rate of hardening must be lower than the rate of softening for the material to be in stage 3. Typically this is due the rate of dislocations overcoming obstacles, and annihilating, being greater than the rate of new dislocation creation. This typically occurs due to very high local stresses which enables dislocation cross slip and mobile dislocations to free themselves from dislocation locks and jogs.

To summarise, In stage 1 the strain rate is relatively small and only one slip system is active with very few barriers to plastic flow and the stress field from dislocations in dipole pairs is weak. In stage 2 the onset of secondary slip leads to strong barriers to plastic flow accompanied with dislocation pile ups. Stage 3 begins when dislocations leave their original slip planes and relaxation occurs whereby the strain rate begins to decrease due to dislocation interactions such as annihilation. This can occur at high temperatures (at high temperatures dislocation motion can be assisted due to lattice vibrations[48]).

4.3. Introduction to dislocations

4.3.1. The Dislocation Line

Perfect dislocations can be modelled as a flexible extensible string with a force of:

$$T = \frac{Gb^2}{2} \qquad \textit{Equation 1}$$

Dislocation mobility is difficult in a system or material in which line tension is high or mobility is restricted.

The line tension of a dislocation relates to the energy per unit length (with a modification depending on the dislocation type)[1]. This line energy of a dislocation is the elastic energy stored by the distortion of interatomic bonds around the defect. The above equation assumes that edge, screw and mixed segments have the same energy per unit length[31] and negates contribution of the dislocation core (which is ~10% contribution but can control the relative activation and motion of dislocations on different slip planes).

If we recall that plastic flow occurs via the movement of interatomic bonds at low temperatures. The dislocations that are most likely to occur are the ones with the minimum energy or minimum magnitude of **b**, where **b** can be defined as a surface step equal to the glide of one dislocation across a slip plane[31]. The fact that **b** is the surface slip step associated with the dislocation as a line defect means that we can also consider separation (or combination) of one or more dislocations together in a dislocation reaction, such that the total **b** is conserved.

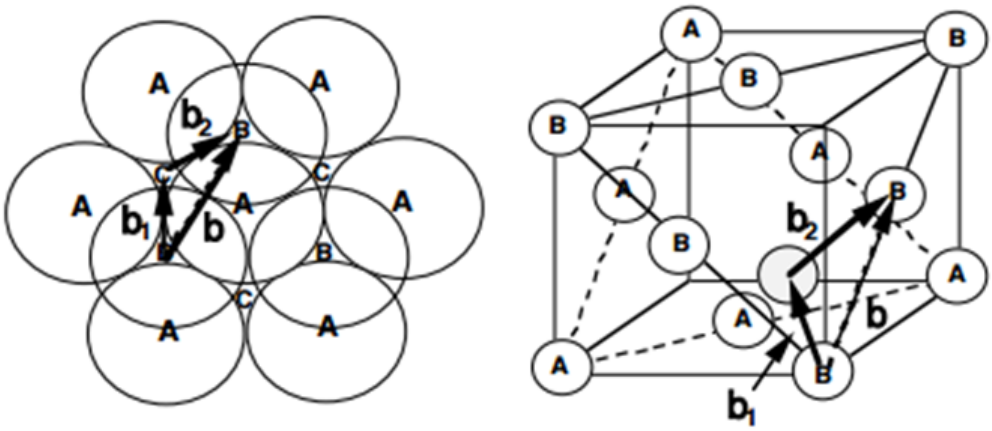


Figure 7: The slip of close packed planes in fcc lattice: (a) in the stacking of closed packed {111} planes (b) a unit cell. The dashed arrows represent slip by a total dislocation (b=1/2[101]). The solid arrows show successive slip by partial dislocations (b=1/6[211]). Morris et al[32].

Figure 7, shows a schematic representation of the slip of closed packed in an fcc lattice, in both a 2d and 3d model. A finite stress is needed to move a dislocation from one energy well to another. This is governed by the spacing and bond energies of the atoms. These wells are effected by temperature (lattice vibrations). At low temperatures the dislocation can minimise its core energy by aligning itself along a close – packed direction. The shear stress needed to move a dislocation from one well to another is known as the Peirels – Nabarro stress (τ_p).

$$\tau_p \approx \frac{2G}{1-v}\exp[-\frac{4\tau}{b}] \approx \frac{2G}{1-v}\exp[-\frac{2\pi h}{b(1-v)}]$$ *Equation 2*

Equation 2 as shown above, represents a pure edge dislocation, a screw dislocation can be represented by τ_p without the (1-v). τ_p Increases with shear modulus G and decreases with interatomic spacing h/b.

The most common form of slip in the fcc structure is the dislocation that causes close-packed {111} planes to slip over each other by a complete lattice vector translation. The Burgers vectors that accomplish unit slip are the $\frac{1}{2} < 110 >$ vectors that connect atoms to their nearest neighbours in the {111} planes.

Partial dislocations are not lattice vectors; Instead of moving from B site to B site, they move (slip) from B to C then back to B. This movement is accomplished by the sequential passage of two partials.

i.e.

$$b1 = (\frac{1}{6}[\bar{1}\bar{1}2] \text{ and } b2 = (\frac{1}{6}[\bar{2}11])$$ *Equation 3*

Equation 3, above represents the burgers vectors of two Shockley partials, as shown diagrammatically below in figure 8. Partials act to lower the energy of the system and their separation alters the energy of the system per unit. The separation of partials by a ribbon of stacking fault or anti phase boundary normally ~ 5-500 Å depending on configuration[11].

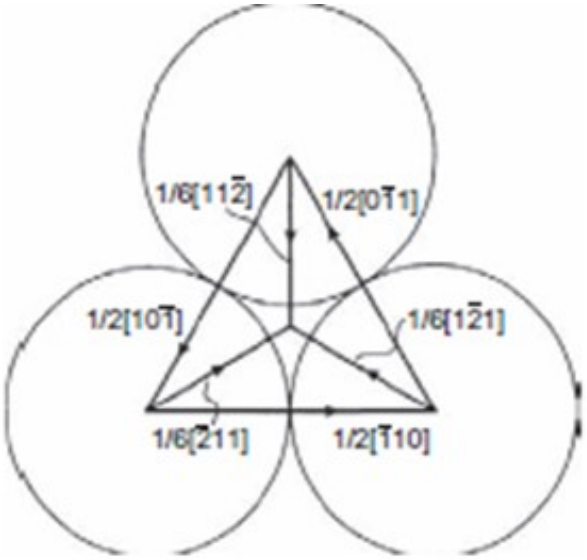


Figure 8: Burgers vectors of perfect and Shockley partial dislocations in the {111} planes. Hull et al.[31].

4.3.2. Frank Read partial

A Frank partial dislocation is formed as the boundary line of a fault and is a way a stacking fault can end in the crystal, this is shown in figure 9. A Frank partial has a Burgers vector normal to the {111} plane of

its associated fault and the magnitude of the vector is equal to the change in spacing by a closed packed layer I.e. b = $\frac{1}{3} < 111 >$.

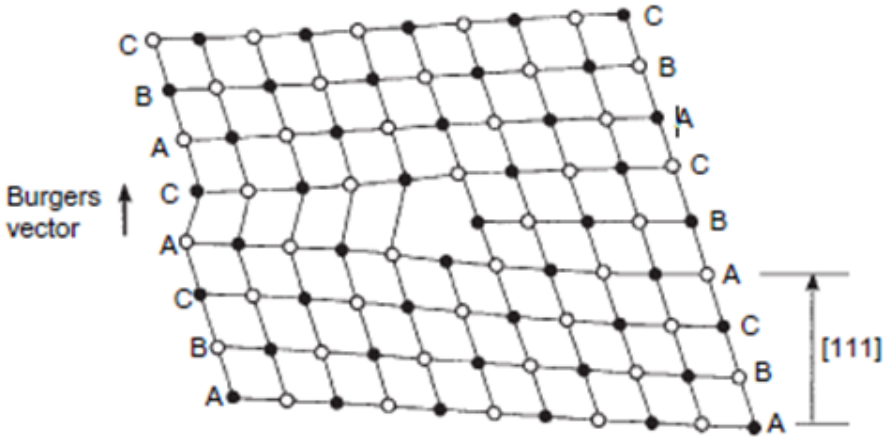


Figure 9: The formation of a Frank partial by the removal of one layer of closed packed atoms. Hull et al[31].

The Burgers vector in this case is not contained in any of the {111} planes it cannot glide or move conservatively under the applied stress. The Frank partial dislocation is therefore sessile. It can however move by climb, where both (+) and (-) ve contain stacking faults. The stacking fault created by a Frank partial can be removed by a Shockley partial at $\frac{1}{6} < 112 >$

$\frac{1}{6}[112] + \frac{1}{3}[111] = \frac{1}{2}[110]$

4.3.3. Dislocation multiplication – Frank Read source

The density of a dislocation can be defined as the line length per unit volume and increases rapidly during plastic deformation. Dislocations become larger as they extend to avoid microstructural barriers and forms loops which expand. Dislocations can also be created by mechanisms such as the Frank Read sources, in which a dislocation is pinned firmly between two points, as shown in figure 9.

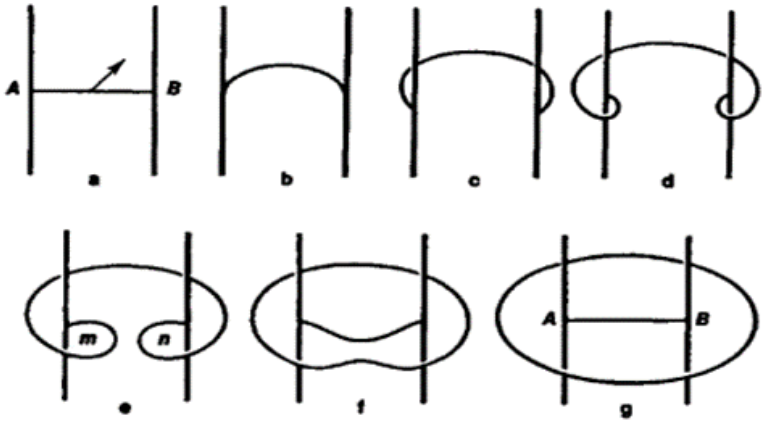


Figure 10: Diagram of Frank - Read dislocation source. A section of the dislocation is fixed between points A and B. The section is bent under the influence of an external force and subsequently assumes the configurations a-g until the closed dislocation loop is separated forming the generation of another section A-B Reed et al. Reed[11].

When a dislocation encounters an array of obstacles it can bow out between them in a circular arc of dimensionless radius. The force that dislocations exert on obstacles are due to the line tension, If the shear stress on the dislocation and line can be considered constant. There are other types of dislocation sources which involve irregularities at free surfaces, grain boundaries or mis fitting inclusion particles. In the bulk material the yield strength of a material increases with dislocation density, p , according to the relation:

$$\sigma = \sigma_o + \sigma_d . Gb\sqrt{\rho} \qquad \textit{Equation 3}$$

The above is known as the Taylor hardening relationship, with σ_d lying in the range of 0.3-0.9

Dislocation pile ups result when like dislocations attempt to glide on a plane that is blocked by an obstacle and this impedes their motion. The lead dislocation becomes blocked and the trailing dislocations pile up behind it. The pile up of dislocations acts to magnify and concentrate the shear stress acting on the obstacle.

The expected number of edge dislocations in a pile up of length L under stress τ can be formulated[32]:

$$n = \pi(1 - v)(\frac{L}{b})(\frac{\tau}{G}) \qquad \textit{Equation 4}$$

Where **b** is the Burgers vector, G is the shear modulus and v is Poissons constant.

Crystallographic interactions can also arise when dislocations interact, as dislocations on different planes meet they can pass through another creating jogs. The jogs exert a dragging force on the dislocation impeding motion.

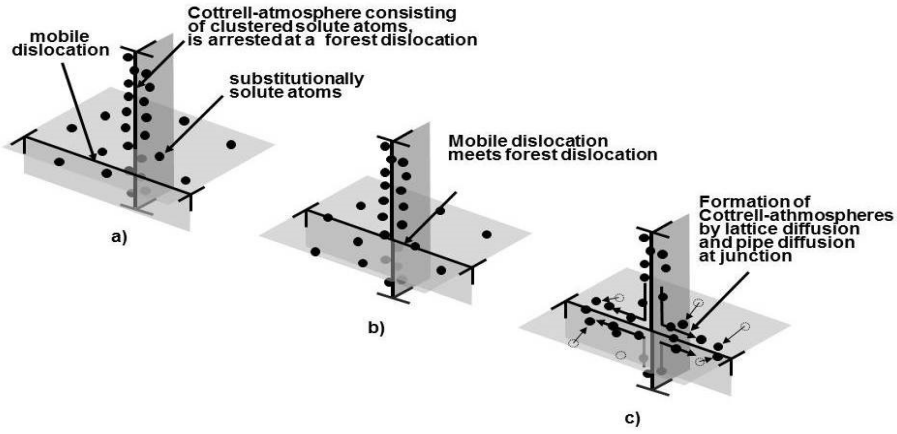


Figure 11: Schematic of stationary forest dislocations which generate Cottrell atmospheres. Schneider et al[49]*.*

Microstructural obstacles that inhibit slip can come in the form of solute atoms, forest dislocations that thread through the slip plane or small second phase precipitates, this is shown in figure 11. When obstacles are widely spaced such that their elastic fields do not overlap they can be modelled as independent barriers.

4.3.4. Work hardening / barriers to dislocation motion

The basic mechanism of work hardening are dislocations interacting to reduce dislocation mobility. As strain builds up inside the material, dislocation sources operate, dislocations slip, intersect and interact with each other. The interactions can cause an increase in dislocation density which increases if the material hardens with strain.

In a polycrystalline material dislocation densities increase for two reasons (1) The multiplication of dislocations within grains and (2) the necessary development of dislocation density along grain boundaries to match plastic strain across the boundaries and keep grains together.

There are $3\,\frac{1}{2}(110)$ vectors plus reverses on each of the four (111) glide planes. This makes 18 possible reactions that can occur between dislocations on one slip system and dislocations on the three other planes. Pure edge dislocations can react to form a Lomer dislocation. This reaction results in a 50% reduction in dislocation energy per unit length and therefore minimises the energy of the system.

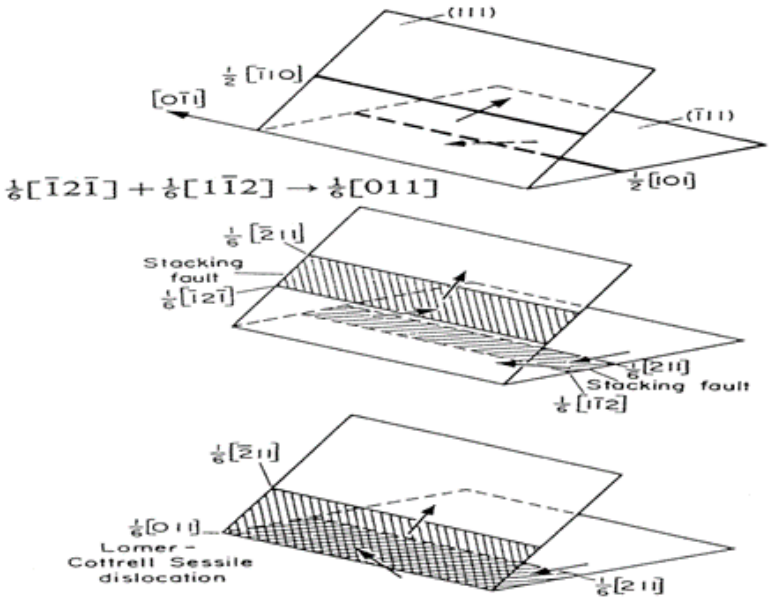


Figure 12: Formation of a Lomer Cottrell sessile dislocation[50]

Figure 12, shows the formation of a Lomer Cotrell sessile dislocation. When two perfect dislocations lying in differing {111} planes are both parallel to the zone axis of the <111> plane a Lomer – Cortrell barrier is formed[43]. This barrier impedes dislocation flow and is a source of strain hardening within the material. Glide for a Lomer dislocation is [100] it is sessile it cannot glide on any of the four other planes and impedes the further glide of dislocations. This is important because it increases the effective hardness of the system by impeding plastic flow. In essence the Lomer dislocation acts as a barrier and this work hardens the material.

4.3.5. Kinks & Jogs

Two characteristic features of dislocations are that: (1) a dislocation will tend to lie in a position of minimum energy (2) a dislocation will tend to reduce its energy by being as short as possible. Jogs and kinks are short elements of the dislocation line with the same Burgers vector as the line on which they lie. They are fundamentally different in character.

Jogs are steps on the dislocation line that move it from one atomic slip plane to another. A jog is edge in character and impedes the glide of a pure screw dislocation. It has a height of approximately 1 lattice spacing and characteristic energy of 1ev due to the increase of length of the dislocation line.

A kink acts on the same slip plane as the dislocation line and does not impede glide. The stress required to move a dislocation line from one energy minimum to the next is less than the stress which is required to move the line as a whole. If a dislocation is unable to lie completely in one energy minimum it will contain kinks where it moves from one minimum to the next.

Screw dislocations unlike edge dislocations in principle have no extra half plane and cannot climb. A small edge component or jog on a screw dislocation can provide a site to start climb which is a very important high temperature process. A schematic representation of kinks and jogs in edge and screw dislocations is shown schematically below in figure 13.

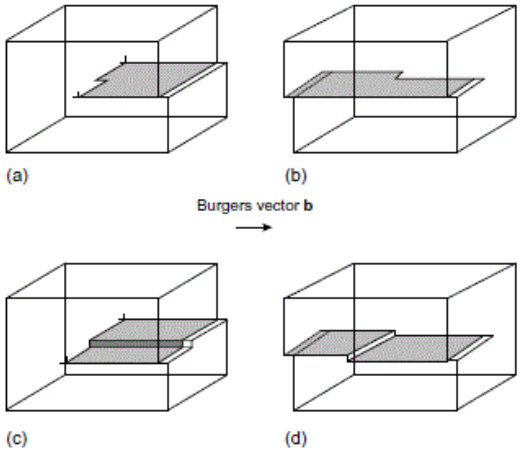


Figure 13: (a), (b) Kinks in edge and screw dislocations. (c), (d) Jogs in edge and screw dislocations. The slip planes are shaded. Hull et al[31].

4.4. Strengthening effects in Ni superalloys

In the Ni-based super alloy system with γ and γ' phases, dislocations form with differing values of **b** according to the energy required for plastic flow to occur. One of the key characteristics of this system is the formation of a super dislocation which can dissociate into partials (each with an associated value of **b**). This enables the system to minimise its energy as dislocations travel through the γ/γ' ordered/disordered system.

In the γ' phase the atoms have an ideal coordination, as this is an ordered lattice. This means that the progress of a dislocation on the {111} can change the local ordering and affect how the Ni and Al atoms are coordinated. Thus progress of one $\frac{1}{2} < 1\bar{1}0 >${111} dislocation will create local disorder, and so the lattice requires dislocations to travel in pairs, with the leading dislocation creating local disorder and the trailing dislocation correcting this disorder. The two dislocations are separated by an anti phase boundary (APB) and this is shown in figure 15 & figure 16.

The disorder associated with the APB has an associated energy attached to its formation due to the destruction of the coordination in the crystal. $\frac{1}{2} < 110 >$ Is the lattice translation through the L_{12} lattice. A super dislocation with this unique Burgers vector can separate into super partials and partials in order to travel through the γ' lattice. The leading (super)partial penetrates through the γ/γ' interface leaving behind a region of disorder and the trailing (super)partial acts as a closure vector to restore the γ' lattice

to its perfect state as shown in figure 25, page 39. This pair of dislocations is called the super dislocation and their separation with an APB is shown figure 14

As with FCC materials, the two perfect . $\frac{1}{2} < 110 > \{111\}$ type dislocations can be each split into partial dislocations, each with . $\frac{1}{6} < 211 > \{111\}$ character which eanbles the energy of these two dislocation to be reduced figure 17.

The total progress of this system can be explored in terms of the local change in atomic order within the γ' phase see figure 15 & figure 16.

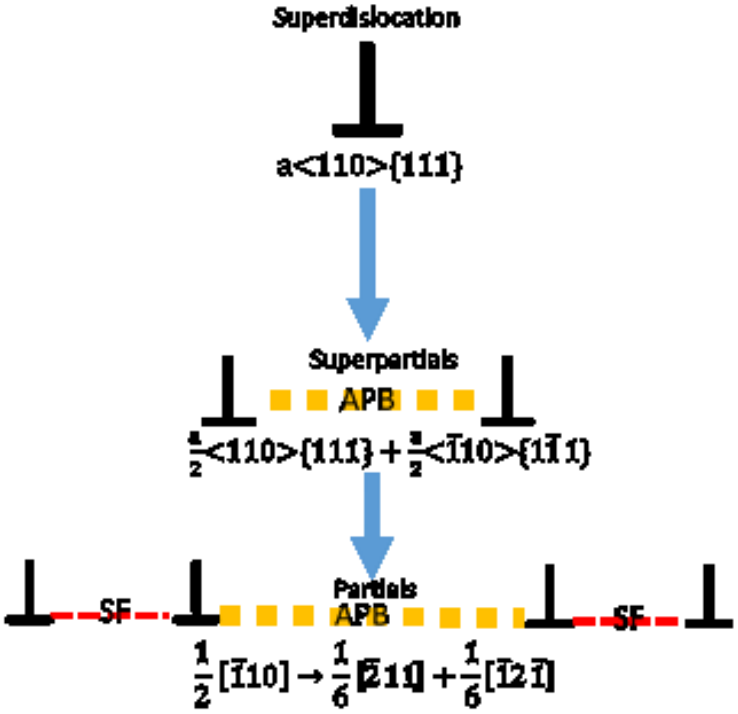


Figure 14: Formation of super partials and partials from a super dislocation in an L_{12} structure

The breaking down of a super dislocation and super partials results in an associated APB and stacking faults (SF) as shown in figure 7. An APB is a planar default which commonly lies on the {111} and in NI_3Al alloys these arise as a direct consequence of mechanical deformation[11]. Different SFs can form due to partials re orientating themselves to minimise energy.

A superlattice intrinsic stacking fault (SISF) with a Burgers vector of $\frac{1}{3} < \bar{2}11 >$ involves altering the stacking sequence of the {111} planes equivalent to a single {111} layer being removed. It produces no neighbour violations **Error! Reference source not found.** & figure 4, page16 and therefore the energy associated with the fault is small approximately 10 mJ/m^2.

A complex stacking fault (CSF) has a Burgers vector of $\frac{1}{6} < \bar{1}\bar{1}2 >$ and results in atomic neighbour violations thereby resulting in a large associated energy approx 250 mJ/m^2 ± 50 mj/m^{211}. A superlattice extrinsic stacking fault can also be formed in which shearing of the {111} planes is equivalent to the addition of an extra {111} layer, it forms no neighbour violations and has a similar energy to a SISF[51]. Complex extended kinks and constrictions can also form when these configurations join and the conversion processes can relate to the formation of KW and Lomer Cotrell (LC) type locks, figure 11, figure 12.

4.4.1. The yield point

At yield a material transforms from elastic to plastic, characterised by a permanent shape deformation which i initiated by the propagation of a dislocation and its characteristic Burgers vector **b**.

In Ni superalloys the dual phase ϒ/ϒ' microstructure has been engineered to optimise the mechanical properties of the alloy once yielded. It has been theorised[52,5354] that dislocations first start to form in the dis ordered fcc phase and then travel into the ordered ϒ' phase .

As noted previously on page 34,when a full screw dislocation travels in the fcc phase post yield, with a Burgers vector $b = {}^{a}/_{2}\langle 110\rangle$ it disassociates into two 30° mixed partials[55,56]; forming a stacking fault in a [111] plane via the following reaction ${}^{a}/_{2}\langle 110\rangle \rightarrow {}^{a}/_{6}[121] + {}^{a}/_{6}[21\bar{1}]$, in which a higher SFE leads to a lower spacing between the dislocations pairs based on their relative attraction / repulsion being mixed in character[57,32].

It has been found in several studies[57,58,59], [60] that Co, Cr, Mo and W all act to lower the SFE energy and thus the spacing between the partials that can be seen in figure 319 and figure 320, based on the stacking fault probability, whereby the SFE probability is inversely proportional to the SFE energy.

Dislocations can only enter the harder ϒ' phase by passage of a full dislocation as expounded upon on page. As a standalone phase, the ϒ' phase is known to be brittle and have low ductility at low temperatures[61,62] however when combined within the more ductile disordered Ni solid solution ϒ phase, the mechanical properties become enhanced.

The burgers vector of a dislocation in the ϒ phase is a lattice vector and so slip does not alter the crystal structure. However when a ϒ dislocation with Burgers vector $½a\langle 110\rangle$ enters the ordered ϒ' phase it disrupts the crystal structure resulting in an APB. The order is restored by an equivalent dislocation trailing behind it, forming a super pair of dislocations. It is the phenomena of the dislocations breaking into pairs that carries plastic flow through the system at the point of yield[53,63]. In short the requirement

of the ϒ ‘ double Burgers vector means it is more difficult for he dislocations to penetrate the ϒ’ thus, the majority of dislocation pairs will first be formed in the ϒ phase at the point of yield.

The high ϒ’ volume fraction of the modern Ni superalloys means that the majority of the dislocations are trapped in the ϒ channels at the early stages of deformation and this has been shown experimentally by TEM[53,64] whereby the dislocations grow out from dendrite cores in the ϒ/ϒ’ phase[63] and when significant enough stress is applied, the dislocations are able to penetrate into the ϒ’[65] where they shear through the ϒ’ as closely spaced dislocation partial pairs[63].

ϒ solute strengthening is dependent on the atomic diameter and electron valency of alloying elements[63], whereas the solution strengthening in the ϒ’ can be largely be attributed to Al and also Cr, V Mo followed by Tu and V[60]. A high Ti/Al ratio also acts to increase the APB energy[66].

To summarise; post yield the dislocations can perform a number of operations whilst travelling through the γ and or γ’, such as glide, cross slip climb and the formation of dislocation pairs. These operations are influenced by the properties of γ and γ’, which are influenced by the alloying elements, the temperature, existence and size of precipitates and the γ’ volume fraction. Where dislocations are mobilised by the multiplication from old sources and activation of fresh ones[63].

4.4.2. Dislocations in γ’

γ’ phase is an ordered face centred cubic (fcc) crystal structure (L_{12} superlattice) which resides in the disordered γ matrix. An anti phase boundary (APB) forms during deformation and switches to a sessile configuration blocking dislocation motion through γ’. The effects of which become more predominant at high temperatures. The effect is commonly referred to as the yield stress anomaly in which, at low temperatures L_{12} alloys behave like fcc metals however when the temperature is increased the critical resolved shear stress (CRSS) is found to increase with temperature. The key to conceptualising the yield stress anomaly lies in understanding the structure and break down of dislocations responsible for slip. Thus knowledge of APB energies in L_{12} ordered alloys is essential to the understanding of their high temperature deformation mechanisms[67]. Figure 18, shows a 2d schematic illustration of the formation of an APB on the {111} plane in the γ’ phase.

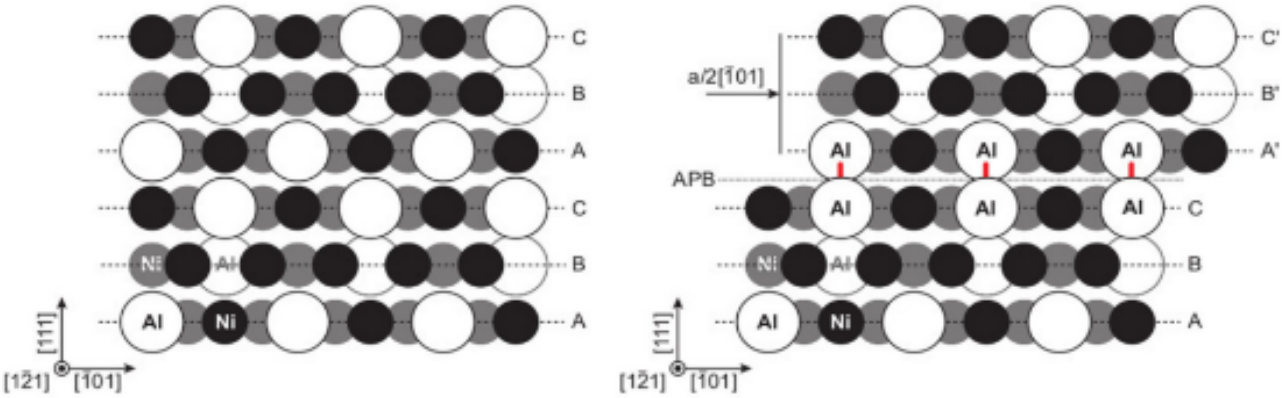


Figure 15: Two Dimensional schematic illustration of the formation of the APB on the {111} plane, In the γ' phase. Crudden et al[28]

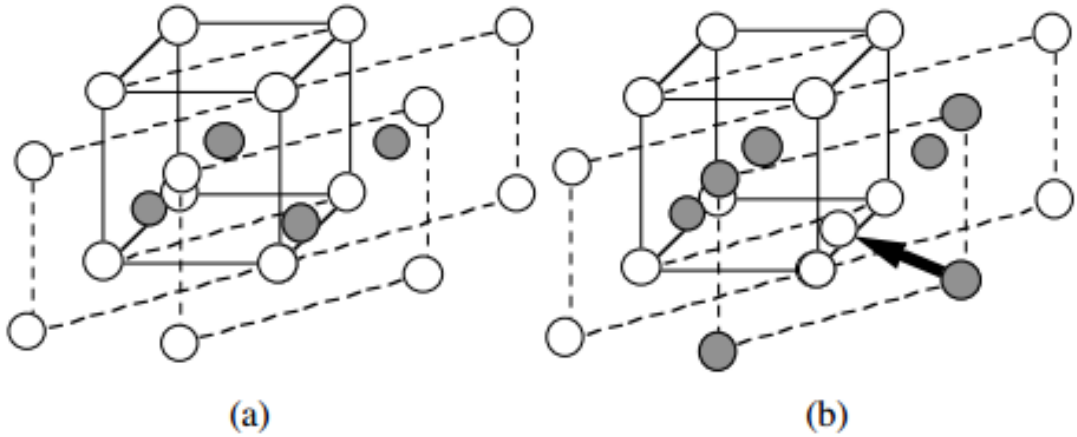


Figure 16: Three dimensional schematic of a L_{12} structure as a stacking of {110} planes (b) An APB in the L_{12} structure made by a displacement type ½<110> in the third plane – The white atoms representing Al the dark Ni. Morris et al[32].

Figure 16, shows a 3d schematic of the L_{12} phase, with and without the formation of an APB. In the vicinity of the APB, the number of NI-Al bonds are reduced and replaced by NI-Ni and Al-Al bonds. The energy of which is related to a number of factors such as the size of the γ' precipitates, the length of the dislocation line and the level of disorder created by the planar faults. There has been dispute into the exact formulation of this quantity. However the scientific community agree that the fundamentals of the APB can be determined experimentally by using bright and dark field transmission electron microscopy (TEM) to measure the distance between super partials and partial dislocation pairs in the γ' phase[67-68]. The growth in the size of APB domains occurs very rapidly above 750°C in the bulk material[67] this coincides with the peak flow stress observed in Ni super alloys at around 800°C[11] figure 25 and figure 27 on pages 39 and 40.

The energy of the APB is closely linked to the yield stress and can be quantified by the following equations dependant on whether the dislocations are strongly (1a) or weakly (1b) coupled. When the

volume fraction of γ' (f) is high the super dislocations are strongly coupled and this depends on ppt size, alternatively when f is low the super dislocations are weakly coupled:

$$\tau_y = \frac{\Delta E_{APB}}{2b}\left[\left(\frac{6\Delta E_{APB} f r}{\pi T_L}\right)^{1/2} - f\right] \quad (1a) \qquad \textit{Equation 5}$$

$$\tau_y = \sqrt{\frac{3}{2}}\left(\frac{Gb}{r}\right) f^{1/2} \frac{w}{\pi^{3/2}} \left(\frac{2\pi\Delta E_{APB} r}{wGb^2} - 1\right)^{1/2} \quad (1b) \qquad \textit{Equation 6}$$

Equation 5 refers to the case when dislocations are strongly coupled and Equation 6 for the weak case. E_{APB} is the APB energy, **b** is the Burgers vector, r is the mean precipitate radius, T_L is the line tension, G is the shear modulus of the γ phase and w is a dimensionless constant to account for uncertainties. In general terms this equation illustrates that as the energy of the APB is increased the shear yield stress follows suit.

Another approximation that links f to the resistance to deformation provided by the APB energy τ_{APB} can be expressed by[27]:

$$\tau_{APB} = \frac{KS^3}{b^2 a^3}\sqrt{\left(\frac{T_c^3 f_{r_s}}{G}\right)} \qquad \textit{Equation 7}$$

S is the long range order degree in γ', Tc is the transition temperature from order to disorder, r_s is the radius of the γ', **b** is the Burgers vector, a is the lattice constant, G is the shear modulus and K is the proportionality constant. In both of the above equations it is clear that the proportional and inversely proportional relationship between f and b in relation to the shear stress remains constant.

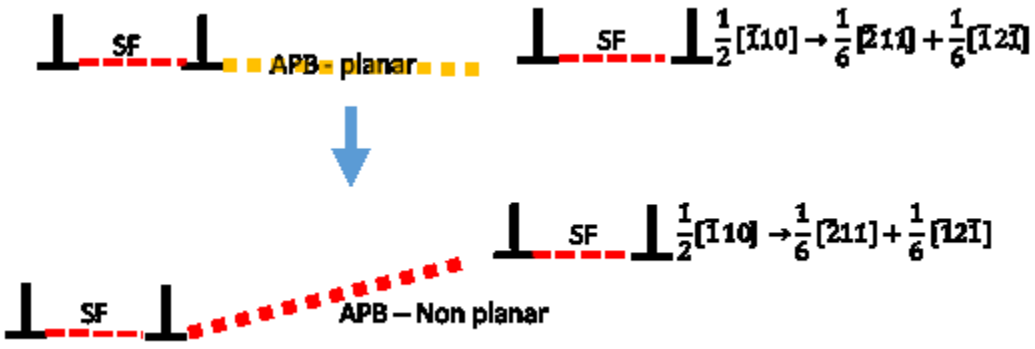


Figure 17: Switch of a planar APB to a non-planar APB. Forming a barrier to dislocation motion

Figure 17, shows the switch of a planar APB to a non planar APB, which subsequently forms a barrier to dislocation motion. As the temperature rises the APB switches from glissile (planar) to sessile (non planar) as the ~~stacking~~ Anti-Phase Boundary fault is lower energy when it sits on a {100} in the ordered

structure. The sessile boundary blocks dislocation motion and this mechanism is known as a Kear-Wilsdorf lock. The thermally activated locking of screw super dislocations by cross slip onto the cube plane are known to form the Kear-Wilsdorf (KW) configuration illustrated in figure 6.

Segments of the γ' superpartial are promoted to cross slip from the glissile octahedral plane (111) onto the sessile cubic (001) plane as the temperature is increased. In general terms the APB energy in Ni superalloys is anisotropic, with the lowest energy lying on the {100} cube plane[67-69]. The Peierls stress resisting glide on the cube plane is much higher than on the octahedral.

Slip is promoted on the cube plane as the system acts to minimise its energy which allows a closer to equilibrium structure to develop at high temperatures[67]. Complete KW locks have the right configuration to glide in the cube plane. The cube slip is theorised to be controlled by a Peirels mechanism resulting from non planar superpartial cores induced[68]. The cube slip occurs via glide and therefore in the non screw segments of the KW lock the resistance to plastic deformation is higher. As the resistance to slip increases so does the level of strain hardening. The formation of KW locks exhausts the mobile dislocation density which must be compensated for by the activation of new sources[70]. The strain hardening coefficient is said to be proportional to the exhaustion rate, which increases with temperature and decreases with stress as more locks are able to unlock. As a result the strain hardening coefficient goes through a maximum when the rate of exhaustion is the highest[68,71]

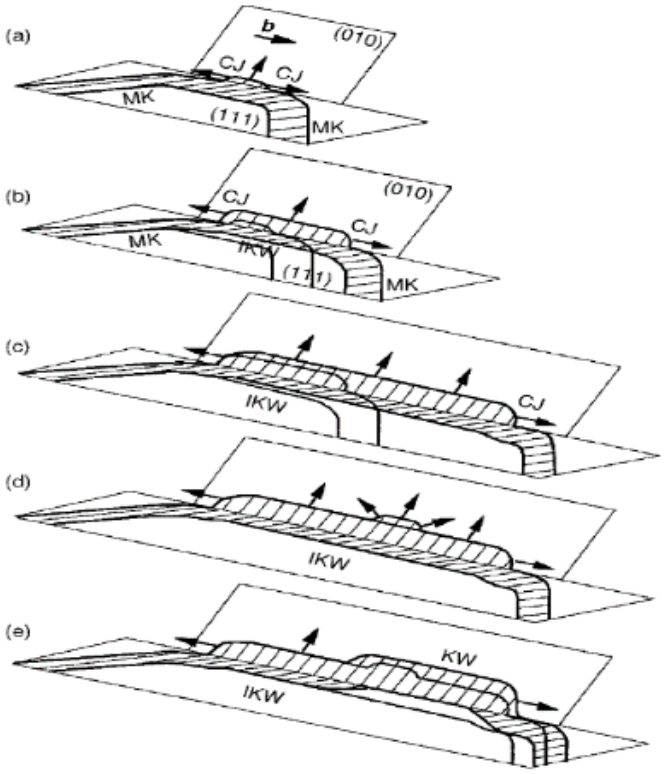


Figure 18: Steps in the transformation of a screw superdislocation by cross-slip onto the glissile (010) cube plane. CJ stands for complex jog and MK stands for macrokink; these lie on the cube and actahedral planes respectively [11].

Figure 18, shows the steps in the transformation of a screw super dislocation to the cube plane. The rate of creation of KW locks increases both with temperature and with force acting on the cube plane[72]. When a stress is applied, examining the dislocations at the micro level the super partials are subjected to a shear stress in the primary octahedral {111} plane and in the cube cross-slip plane[70]. The micro stresses that can act on the super partials include the elastic interaction in the anisotropic media and the surface tension of the APB. The stability and locking mechanisms of the KW locks are the dominant cause for the positive temperature dependence of the yield stress In γ/γ' Ni superalloys[11,71]. It can therefore be said that the intrinsic unlocking and destruction of the KW locks is what emanates the drop in the peak of the yield stress at high temperatures[72], figure 18.

4.4.3. Dislocations in γ

The γ phase is a disordered fcc solid solution in which the ordered γ' precipitates reside. In modern day commercial polycrystalline alloys the γ occupies a 30-55% volume fraction. As the temperature increases dislocations become more mobile which increases cross slip & climb as more point defects are created. At high temperatures the volume fraction, distribution and shape of γ' changes affecting the mechanics of dislocations through the γ channels. At low temperatures dislocations can cut through or loop around γ' precipitates. The ability to do so depends largely on the size of the precipitate. The general trend is that the smaller the precipitates are, the easier they are to shear, this is generally the case for γ'' precipitates that are of the length scale of approx 10 nm[11]

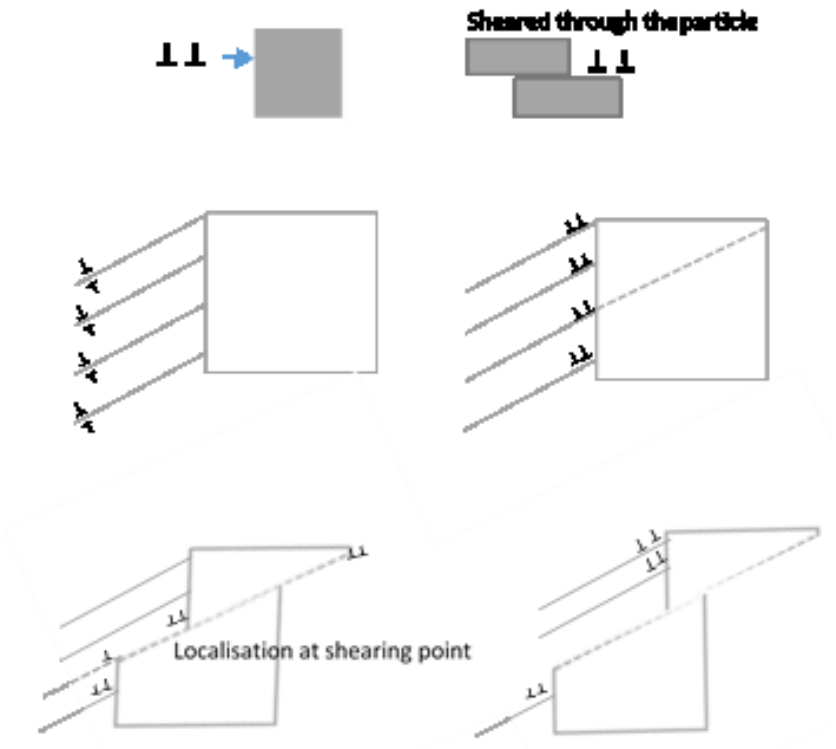


Figure 19: Dislocations moving through a precipitate at room temperature by shearing

Figure 19 shows dislocations moving through a precipitate at room temperature by shearing. figure 20 shows a force distance profile of a dislocation cutting through a γ' precipitate . At room temperature where diffusion is difficult in the absence of a non equilibrium concentration of point defects, the movement of dislocations is restricted almost entirely. γ' planar slip on glide planes minimises the need for cross slip and encourages the localisation of dislocations at obstacle interfaces due to low dislocation mobility.. Glide is a conservative motion as it involves the volume of the system being conserved, climb which involves dislocations moving out of their slip planes involves point defects being created and mass transport of material via thermal activation and is therefore non conservative.

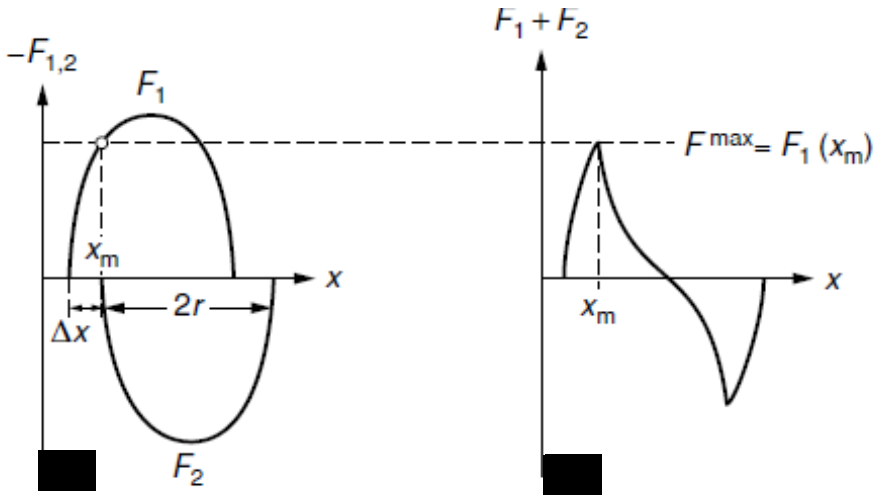


Figure 20: Force- distance profile of a dislocation cutting a γ' precipitate. (a) variation of the forces acting on the first and second dislocations with distance x measured from the point of penetration; (b) net force on the pair, with their spacing assumed to be constant. Reed[11]

Increasing the temperature will increase the amplitude of atomic thermal vibrations creating an effective vibration of the dislocation line. This results in penetration through obstacles that could not be bypassed by stress alone. It can be said that low temperature strengthening mechanisms become ineffective at temperatures above 1/4 to 1/3 of the melting point of Ni super alloys[11].

At high temperatures dislocations also become more mobile due to increased diffusivity. However the free path of the dislocation can become impeded due to a strong γ' interface. This can be overcome by the cross slip and or climb whereby the dislocation changes its slip plane. Both positive and negative climb proceeds by the nucleation and motion of jogs as jogs act a sources and sinks for vacancies.



Figure 21: Two dimensional schematic of a dislocation moving around a precipitate at high temperature

Figure 21 shows a 2d schematic of a dislocation moving around a precipitate at high temperature. There is a relation between the APB energy γ_{APB} and the ability of a dislocation to shear or loop around a γ' precipitate that was developed from the earlier models of dislocation line tension Γ_{loop} put forward by Glazer and Morris[73] adapted by Bacon et al[31] and improved upon by Ardel et al[69]:

$$d_{loop} \cdot \gamma^* = 2\Gamma$$ *Equation 8*

Where Γ is the line tension, d_{loop} is the planar diameter of the γ' precipitates at which the transition from particle shearing to bypassing by the Orowan mechanism (lopping) occurs. γ^* is the value of γ_{APB} obtained when the mutual attraction of the bowing arms is neglected.

The above is important as it helps quantify the strengthening mechanisms occurring as the dislocations move though γ channels and interact with γ' precipitates through the various mechanism that occur at high temperatures.

4.4.4. Altering the γ' affecting the γ'/γ interface at high temperature

In a superalloy the γ and γ' phases deform together due to the small lattice misfit. The hard γ' phase constrains dislocation motion in the soft γ phase, which means the strengthening of the γ' phase is ∝ to the γ phase. Figure 22 below shows how increasing the volume fraction of the γ' precipitates reduces the width of the γ channels.

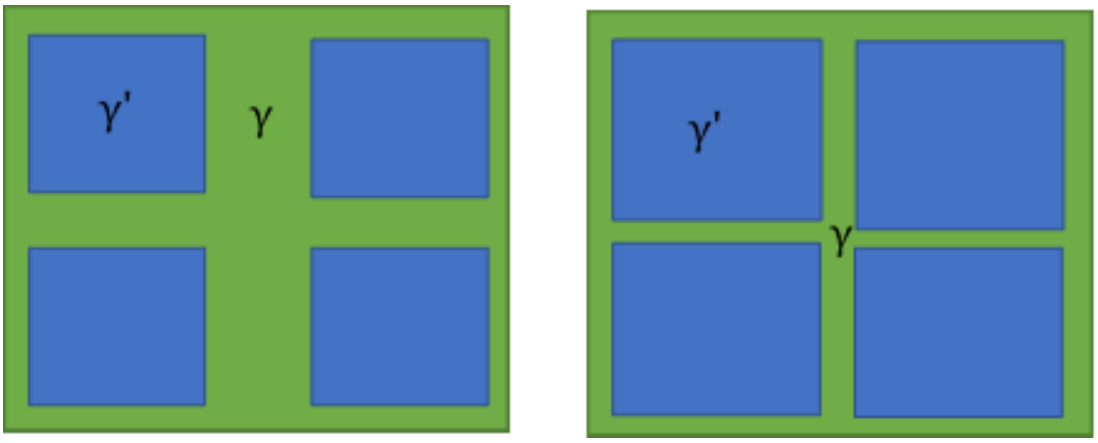


Figure 22: Increasing the volume fraction of the γ' precipitates affects the width of the γ channels

Tailoring the heat treatment accompanied with carefully selected alloying elements alters the volume fraction of the γ' volume fraction f. This decreases the γ channel width which affects the climb/cross slip of ribbon dislocations. f can also be altered slightly at high temperatures >800C°, however coarsening effects are dominant.

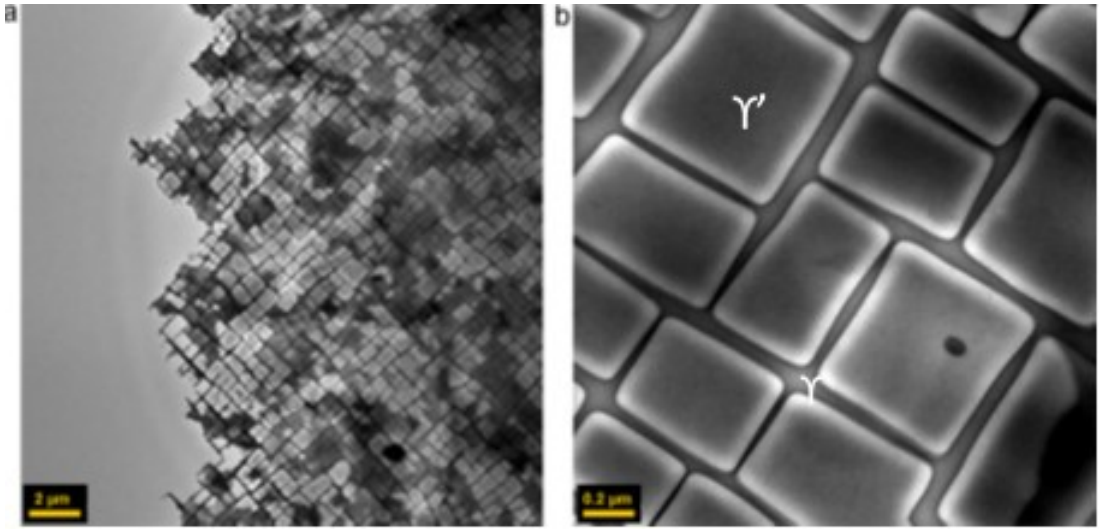


Figure 23: Microstructure of MC2 single-crystal Ni superalloy observed by TEM (brightfield). Brunetti[74].

Figure 23 shows a MC2 single crystal second generation alloy that has been solution treated at 1300°C for 3 hours to reduce solidification segregation. Followed by ageing at 1080°C for 6 hours, then 870°C for 20 hours to promote a high volume fraction of cuboidal γ' precipitates. The γ' precipitates are aligned along the [001] directions. Their mean size is ~400-500 nm, while the γ matrix channel width reaches a maximum of 50-75 nm[74].

The work done for a dislocation to move down a channel is given by :

$$(\tau.b.h)ds=E_l\ ds. \qquad \textit{Equation 13}$$

Thus the required stress τ can be calculated via:

$$\tau = E_l/bh \sim Gb/h \qquad \textit{Equation 14}$$



Figure 24: A dislocation travelling through a channel of width h

Figure 24, shows a dislocation travelling through a channel of width h. Equation 14 illustrates that decreasing the channel width h by altering the microstructure at high temperatures results in a stronger superalloy. There is a small degree of lattice misfit between the γ/γ' phases. This is evident on an EBSD map of a Ni superalloy as the individual phases cannot be seen, unlike in steel for example in which

phases such as ferrite and cementite are clearly evident. As the temperature is increased the lattice mismatch between the γ'/γ phases increases and in turn has an effect on the mechanics of the system. The lattice parameter of γ' at room temperature is 0.359nm which is very close to γ, 0.358 nm. The relation of atomic misfit can be given by[11]:

$$\delta = 2 \times \left[\frac{a_{\gamma'} - a_{\gamma}}{a_{\gamma'} + a_{\gamma}}\right] \qquad \textit{Equation 15}$$

Where a_{γ} is the lattice parameter of the gamma phase and $a_{\gamma'}$ is the lattice parameter of the gamma prime phase. The result of the room temperature misfit is that γ' precipitates are under triaxial tension and the γ' channels are under biaxial compression. There is asymmetry between the horizontal and vertical channels which leads to an elastic energy gradient[11]. Therefore for deformation along the [100] axis, in compression the vertical channels deform first and in tension the horizontal channels deform first.

As the temperature is increased the misfit between the two phases increases according to the following law[75]:

$$a_{\gamma'} = a_{Ni_3Al} + \sum_i t_i' c_i'$$
$$a_{\gamma} = a_{Ni} + \sum t_i c_i \qquad \textit{Equation 16}$$

Where a_{Ni3Al} and a_{Ni} are the lattice parameters of Ni_3Al and Ni, ti' and ti are the experimental coefficients, $C_{i'}$ and C_i are the chemical compositions of γ' and γ respectively. The increase in misfit makes the material more anisotropic as it alters the interface coherency between γ'/γ. However the strengthening effect of the change in misfit is negligible and the dominant factor of the high temperature strengthening has been found experimentally and theoretically to be dependent on the APB energy[27].

Figure 25, shows a dislocation pair passing through a γ' particle separated by an APB, as the misfit between the two phases is altered the spacing as thus APB energy changes as a result.

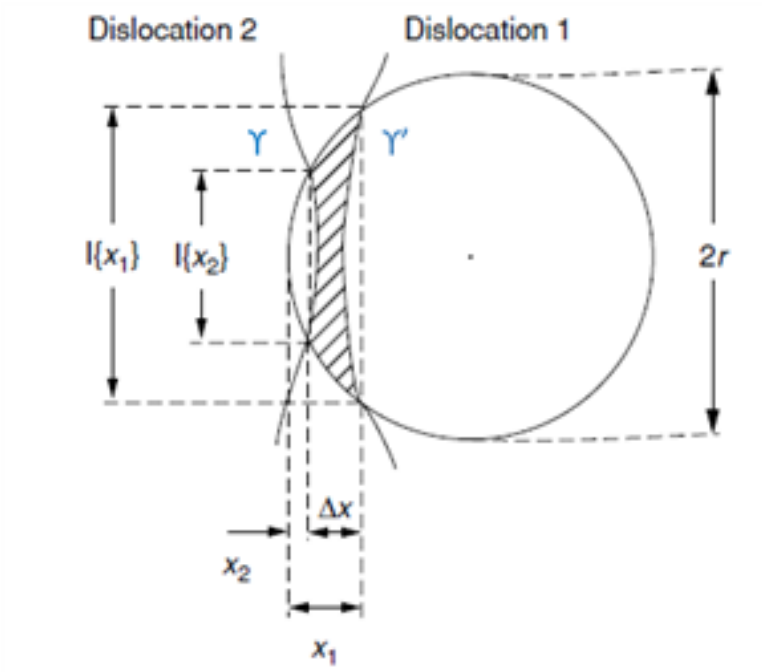


Figure 25: Representation of the strong interaction between a pair of dislocations and a γ' particle. The hatched area represents an APB. Reed et al[11].

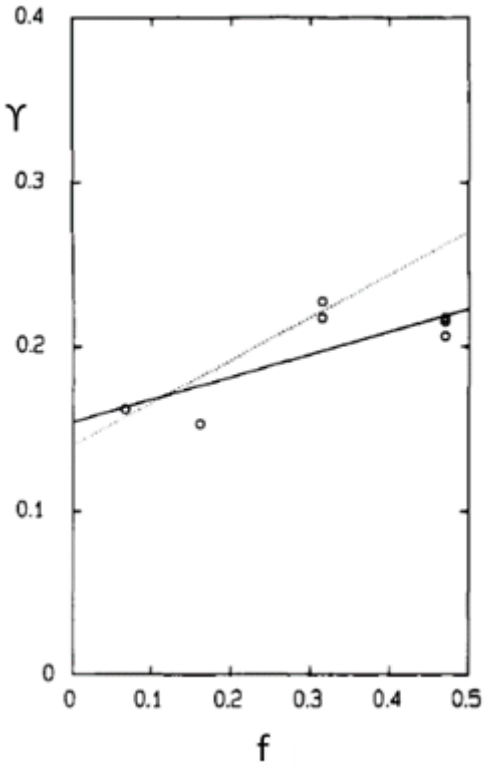


Figure 26: Experimental results for the antiphase boundary energy γ_{APB} (J m^{-2}) are plotted against the γ' volume fraction. The solid line represents peak aged specimens and the dotted line represents under aged specimens. Nembach et al[71].

Figure 26 shows the experimental results for the APB energy plotted against the γ' volume fraction, where the solid line represents a peak aged specimen and the dotted line an under aged specimen. The data shows that the APB energy increase as a function of γ' volume fraction.

Studies such as the above, have shown that the volume fraction of γ' (f) is proportional to the APB energy and the APB energy of under aged specimens are more sensitive to the increase in f[71]. This makes sense as the under aged γ' will have a larger volume to expand (Ostwald ripening). The shear stress of a peak aged single crystals can be related to the APBE, γ_{APB}, and the volume fraction of γ', f[71]:

$$\tau_p = \frac{\gamma}{2b} N f^{1/2} \qquad \textit{Equation 17}$$

Where N is a numerical constant governed by the distribution function of the particle radii. It is assumed in the above equation that in the critical moment when the leading dislocation of a pair breaks free from a γ' precipitate, that the trailing dislocation lies outside all γ' precipitates[71] I .e in the case of weak coupling as shown in figure 25.

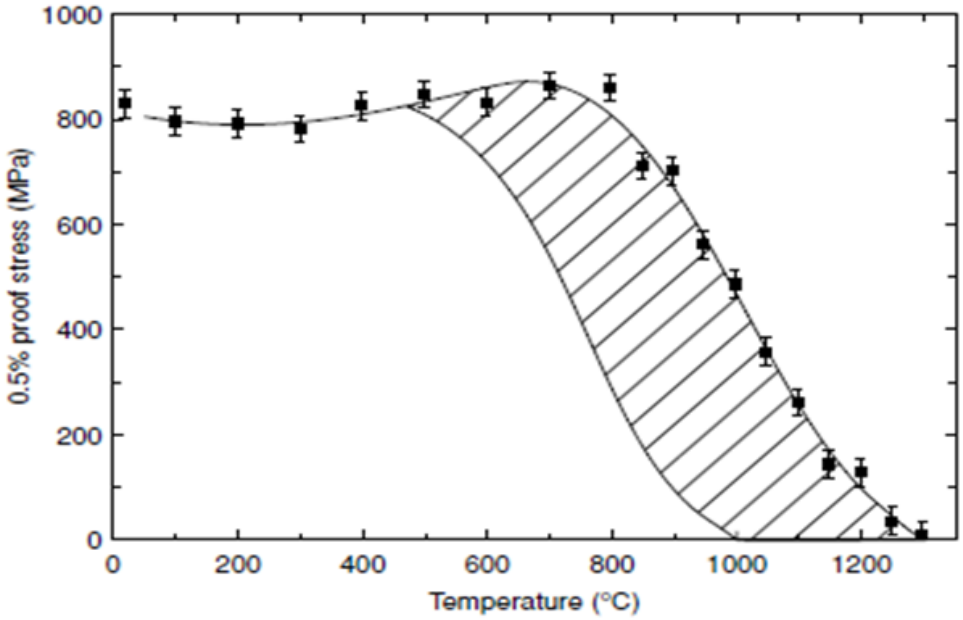


Figure 27: Variation of the uniaxial 0.5% yield stress with temperature of <001> orientated single-crystal superalloy CMSX-4. Reed et al[11]

It is the combination of all three points mentioned in this section; dislocations in γ, dislocations in γ' and the interface between the γ/γ' that lead the strengthening mechanics at high temperatures observed in figure 27. Diffusion and oxidation effects which occur at high temperatures can impact on the mechanical performance of the alloy. A bond coat system is established in which alloying elements are diffused in to the γ' /γ system to protect the alloy from thermal degradation. The study of the multi-layered phases which constitute bond coat systems is important both at high and low temperatures.

4.4.5. Weak and strong coupling in Ni-based superalloys

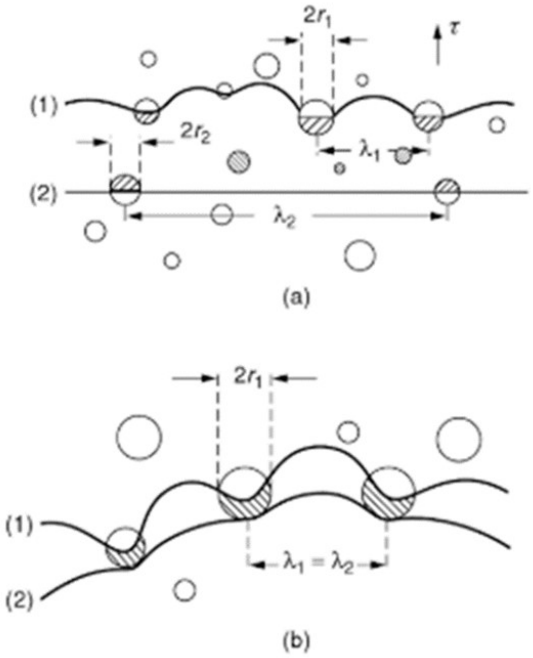


Figure 28: Particles of ordered γ' being sheared by dislocations(a) weakly and (b) Strongly paired dislocations

As dislocations interact with precipitates within the γ/γ' microstructure such as the ordered γ' it can choose to; bend, cut through, cross slip, or stop, whereby the interactions with said obstacles can be classified as strongly or weakly coupled as shown in figure 28. When the spacing between the dislocations is larger than the diameter of the obstacle the dislocations are known as weakly coupled. When the dislocations are both simultaneously within the same precipitated (a consequence of a larger precipitate size) the dislocations are termed as strongly coupled.

4.5. Diffusion mechanics in Ni-based superalloy bond coat system

4.5.1. A brief introduction to the alloying of component parts in Ni alloys

A gas turbine engine consists of the compressor, combustion chamber, turbine and exhaust nozzle. The combustion chamber is where the Ni blades and discs on which the blades are housed sit. The volume fraction of ϒ/ϒ' has increased through the generations of the turbine and disc alloys. The processing has evolved from wrought to vacuum casting which greatly improved the ability of alloying[76].

The alloying elements in Ni superalloys play a crucial role, as they constitute the main design strategy for stabilising compositions, microstructures and mechanical properties of the alloy[57].

The alloying elements can be categorised broadly into two groups[11,60]; The solid solution elements (Cr, Co, Mo, W, Re and Ru) which strengthen the γ phase and precipitation elements (Al,Ti) that strengthen the γ' phase.

The solid solution elements strengthen the alloy by increasing the solidus temperature and decreasing the stacking fault energy which increases the resistance to dislocation propagation[57]. The solid solution elements cause resistance to dislocation motion as they have higher atomic lattices than Ni[75] and thus distort the lattice causing an increase in the shear modulus[77].

The first derivatives on Ni superalloys, for example the Nimonic series in 1940s incorporated polycrystalline alloys with ϒ' in a ϒ matrix with metal carbides at the grain boundaries for additional strength[78]. The first generation of modern alloys were incorporated in the 80s and contained higher Al, Ti, and Ta content which acted to increase the ϒ' content[79]

The first cultivation of Ni superalloys used as blades, were wrought and polycrystalline alloys, developed to meet the need for better creep resistance and high temperatures[79,76]. Directionally solidified and then single crystal alloys were developed in the second generation of alloys.

The third and fourth generations of alloys had Re added to them to improve their resistance to creep[76]. The second and third generation alloys had higher amounts of Al, Ti, Ta, Nb added to them to improve fatigue deformation, corrosion and oxidation resistance, and resulted in improved microstructures as a direct by product of the alloying additions[76,60].

Another factor of the improved alloying conditions was that the ϒ' volume fraction increased substantially over the generations[76]. In which a higher ϒ' volume fraction leads to narrower ϒ channels (Figure 24), which has resulted in a shift from spherical to cuboidal precipitates. however, the change of shape can also be attributed to the additional alloying elements such as Re and Ru in third, fourth and fifth generation alloys, which have thus altered the misfit between the ϒ/ϒ' and thus the coherency strain[80]. All of these factors influence the propagation of dislocations through the microstructure and thus the mechanical performance of the alloy[57].

Re was added to 2nd and third generation alloys as it was said to enhance the creep properties, but was however later found to promote the formation of the embrittling TCP phase thus Ru was added in the fourth and fifth generation to increase phase stability and homogenise the distributions of Re between the ϒ' and ϒ phases[76,63,57].

4.5.2. The bond coat system in Ni alloys

The Pt – diffused γ'/γ bond coat is now an industrial standard for thermal barrier coatings (TBC's) used in aero-engines which protects the Ni parent metal from degradation. The TBC life is dependent on the interplay between substrate, bond coat and TBC. This becomes even more apparent at high temperatures when temperature gradients arise due to thermal cycling and the mechanical / thermal mismatch between the different systems[18,81]. Traditionally a pure β-NiAl intermetallic compound was

grown on the superalloy as the bondcoat[82]. This intermetallic phase provided good alumina formation combined with good oxidation and corrosion resistance[83]. However Al depletion at high temperatures would lead to the formation of brittle phases with low slip systems[84]. To counter this, MCrAlY was introduced via direct deposition where M=Ni,Co,Fe. Later on in the evolution process Pt was added to the NiAl system via diffusion and was found to provide even better properties resulting in service life increasing by a factor of 3 in some cases[85]. Diffusion is very important in understanding the many properties of the current bond coat systems such as microstructural stability and deformation mechanics[86],[87]. The phase layers in a bond coat are controlled by diffusion and are known as diffusion layers, this is shown as a cross section in figure 29., these layers grow and shrink during service creating internal stresses in the system thereby affecting the mechanical performance of the alloy[84,88,89].

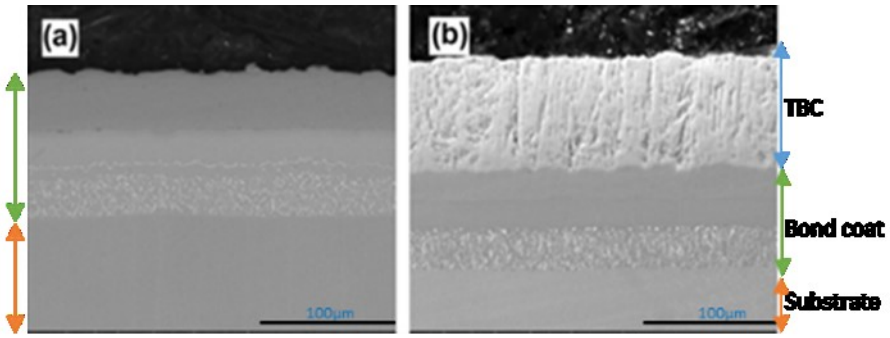


Figure 29: Cross sectional microstructures of the double layer bond coat without (a) and with TBC (b). Zhoue et al,[81]

The role of oxides in Ni superalloys is an important area, as the formation of oxides increase the mass of the Ni system and can form phases which degrade mechanical and thermal stability[90]. The ceramic bond coat is unable to prevent the ingress of oxygen and thus a thermally grown oxide (TGO) forms. The TGO forms due to oxidation at the interface with the underlying bondcoat. The thickness of the TGO increases parabolically with temperature[81]. The bond coat becomes depleted of Al over time due to the formation of the TGO. The TGO is predominantly α – alumina[11]. It has been found experimentally that the oxidation time of the graded alloy is inversely proportional to the volume fraction of γ'[91]

The stresses which the oxides impart on the system become apparent at low temperatures and the growth occurs at high temperatures. It is therefore very important to study the bond coat at ambient and high temperatures. Foreign object damage can also effect the engine performance[11] and so measuring the mechanical properties of the bond coat at various points is also useful. To create the bond coat layer typically a Pt layer is deposited onto the superalloy substrate followed by a diffusion treatment. During the treatment Pt destroys the initial crystal structure of the superalloy and precipitates into the γ and γ' phases, with Pt in solid solution.

The total length scale of the bond coat and TBC varies from alloy to alloy but on average they range approximately 100 µm[84] in the z direction from the substrate upwards in Ni superalloys[84]. This study will examine sections ~30-40 µm. The region of interest is the intermetallic bond coat which grows via inward diffusion into the substrate layer in which Ni and Al are consumed.

Micropillar testing could be performed on such an alloy structure and the resulting chemistry Vs micromechanical response can be examined. The results of which would be very interesting and compliant with industry and compliment the literature[91-18] see figure 30.

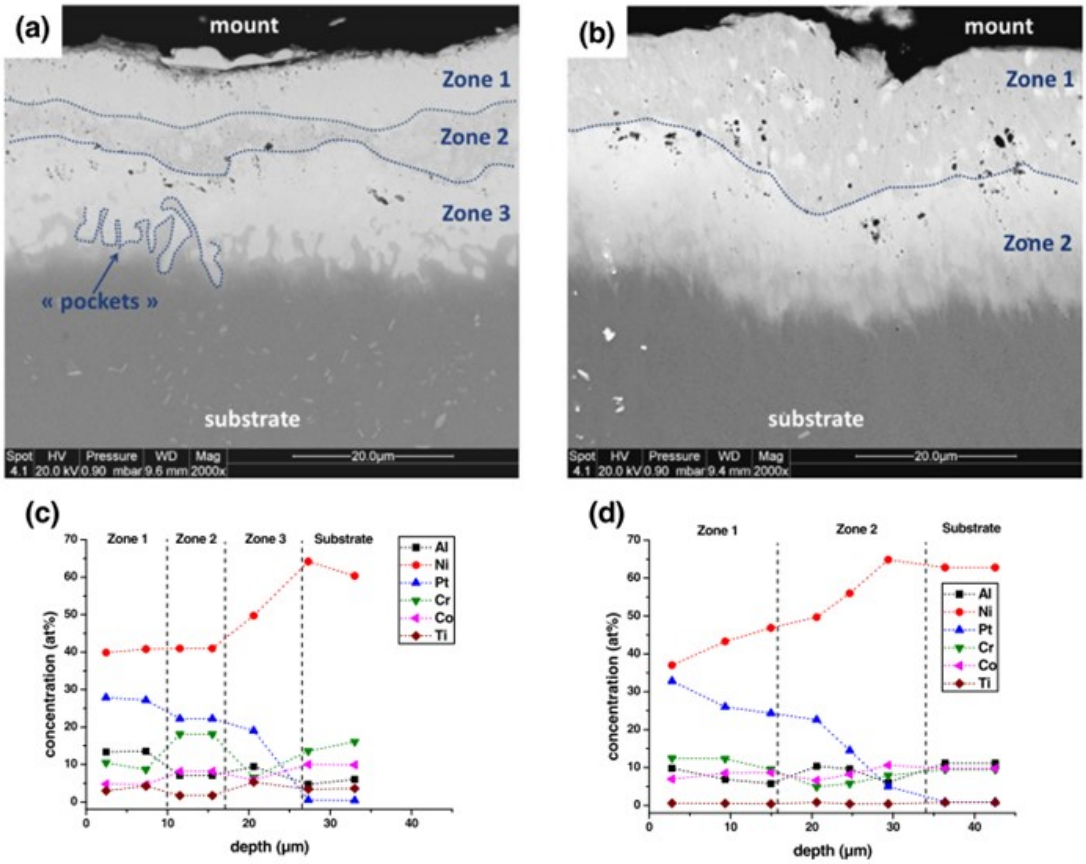


Figure 30: Backscattered electron images and EDS diffusion profiles across the layer platinum heat treatment of a) and c) the SX (PWA-1483) and b) and d) the DS (CM-247LC). The PWA – 1483 is a single crystal alloy, DS (CM-247LC) is a directionally solidified alloy. Mollard et al,[90].

Figure 30,shows BSE images and EDS diffusion profiles across a diffusion layer separated into zones. Zone 3 shows a sharp drop in (at.%) of Ni and subsequent increase in Pt. The drop in Ni and increase in Pt are proportional to each other, when Pt diffuses into the Ni substrate the γ' and γ lattice parameters both expand figure 30. It should also be noted that in the single crystal alloy figure 30c the Al at.% is highest in region 1. This makes sense as the formation of the Al_2O_3 protective scale is favourable in this region to protect the Ni substrate, in the literature this is commonly referred to as an Al reseviour[18].

Diffusion processes in a coating material[90,92] oxide scale[93], chemical reactions at interfaces[92,29], as well as equilibrium oxygen pressure at the alloy[94] / oxide interface as a function of alloy composition[94,81], and temperature[95] all play a crucial role in the high temperature / oxidation mechanisms in pure Ni[96] and alloyed Ni systems[84]. In certain circumstances oxidation can be the predominant mode of in service damage as the metal temperature can approach or exceed 1000°C. Thus the careful examination of the mechanisms and constituents involved in the processing, development and degradation of coated Ni superalloy systems are important. As the diffusion processes in alloys can be complicated by the presence of alloying elements a grasp of the diffusion mechanisms in pure Ni should first be understood.

4.5.3. Diffusion mechanics in pure Ni

The ingress of oxygen into pure Ni via diffusion helps to explain the various physical phenomena such as oxidation and or changes in mechanical properties that can effect performance[97]. Earlier studies of the solubility of oxygen in Ni supported the theory that the solubility decreases with temperature[98]. This contradicted other studies that examined the diffusion of oxygen in fcc metals[99]. This theory was later proved invalid by researchers who used electrochemical techniques such as secondary ion mass spectrometry (SIMS) [96,100] to study this effect. The recent studies of oxygen diffusion in Ni by SIMS[100] indicates that oxygen will not diffuse in bulk Ni without the presence of vacancies[97,101,102].

Considering interstitial transport first, it was found by authors Garruchet et al[97] that oxygen is most stable as an interstitial atom on an octahedral site within the Ni lattice and the diffusion proceeds via a vacancy mechanisms following an Arrhenius law:

$$D = D_0 \exp\left(-\frac{E_a}{k_b T}\right) \qquad \textit{Equation 18}$$

This theory is supported by the work of Nam et al[102] who studied the diffusion of atomic oxygen in Ni. They used first principles for their study that derived from the earlier research of Kim et al[103] who theorized that the diffusion of oxygen interstitials via octahedral sites has a metastable site between them. The theory was based on the activation energy for the diffusion of oxygen along an octahedral – octahedral site is higher than the octahedral-tetrahedral-octahedral method. Hyo On Nam et al[102] went on to further explain the transport mechanisms in interstitial oxygen diffusion based on the Arrhenius equation by quantifying that when a sufficiently deep tetrahedral interstitial site exists, a diffusing interstitial oxygen can be equilibrated at the metastable tetrahedral site temporarily. It can then jump forwards and backwards to an adjacent octahedral site[102,103]:

$$D = \frac{1}{6}.(ב.\Gamma_s).\gamma^2 = \frac{1}{6}.\Gamma.\gamma^2 \qquad \textit{Equation 19}$$

The equation above is based on the Wert and Zener[104,105] coefficients for interstitial and substitutional diffusion in primitive cubic lattices. Where ב is the nearest neighbour co-ordination number, $\Gamma = (ב.\Gamma_s)$ is the rate at which the diffusing particle jumps between adjacent sites and γ is the jump length.

$$D = \frac{1}{6}.(12.\Gamma_s).(\frac{\sqrt{2}}{2}a)^2 = \Gamma_s.a^2$$ *Equation 20*

The above is derived considering the interstitial diffusion of oxygen in fcc Ni having a lattice constant a with the octahedral site being the most stable state proceeded by the interstitial site.

Considering substitutional transport it is theorized that for all temperatures the oxygen moves very rapidly (a few ps) to a vacancy and then becomes trapped in the substitutional position during the rest of the diffusion process[97]. The transport of oxygen towards the substitutional position should always be considered as the substitutional site is the most stable defect position for oxygen which has been determined via modelling and experimental efforts[101,102,106]

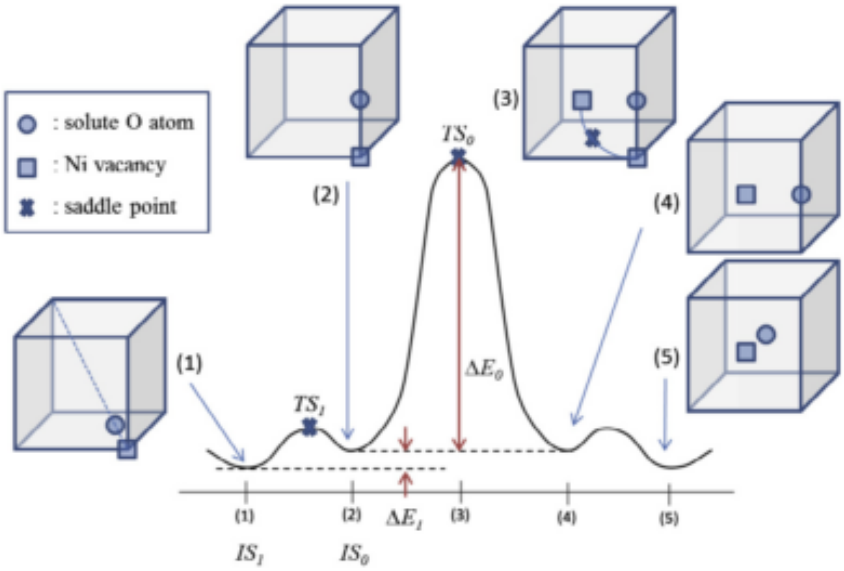


Figure 31: Schematic diagram showing the oxygen jumps possible in an fcc structure. Nam HO et al[102].

Figure 31 illustrates vacancy diffusion transport of oxygen in pure Ni where the oxygen atom can be paired with a mono vacancy. The oxygen atom can then jump to the nearest octahedral site leaving behind a vacancy such as in state 2. When the oxygen atom moves to a more stable site, it can create a full oxygen vacancy pair where the saddle point represents a position that a vacancy can switch locations with an atom of the solvent Ni i.e. points 3 and 4. The modelling of oxygen transport by vacancy diffusion can be translated to Ni alloy systems. In the case of Pt, the situation becomes a bit more complicated as Pt effects become interesting when Pt interacts with multiple phases and elements within the Ni alloy system and diffusion layer,[107,108].

4.5.4. Diffusion mechanics in Ni-based superalloys

The oxidation mechanics of Ni alloys is integral to ensuring the structural stability of gas turbine engines in the aviation and power transmission industries[93]. The underlying science of which is governed by anion and cation interactions at the metal/oxide and oxide/gas interfaces[29]. A complicating factor in understanding these mechanics lies in the chemical complexity of Ni alloys which can contain ten or more elements which each give rise to distinct oxidation products via the diffusion and subsequent oxidation within one hundred micrometres from the exposed surface[95].

Common alloying elements include – Cr, Al, Ti, Ta, W as well as some platinum group metals such as Re and W, giving rise to oxidation products – Cr_2O_3, Al_2O_3, TiO, Ta_2O_5, WO_3 as well as spinel phases such as $NiCr_2O_4$, $NiAl_2O_4$, $NiTa_2O_6$ among others. Co,Tc,Ru,Rh,Re,Os,Ir and Pt have a preference for the Ni sublattice whereas Ti,Zr,Nb and Ta have a preference for the Al sublattice and significant improvements in ductility of the NiAl phase can be improved when Mo and Cr occupy Al sites[109]. Al has the highest thermodynamic driving force for oxidation compared to the other alloying elements and gives rise to an oxide scale that provides the greatest resistance to oxidation[93]. Alloy designers have found that a concentration of ~5-6 wt.% of Al is often adequate to maintain Al_2O_3 scales[94], in the presence of Cr and the addition of Pt to Ni alloys can act to promote and further stabilise the scale[87].

The intermetallic B2 β–NiAl is used largely in high temperature applications due to its high melting temperature, good oxidation resistance, high thermal conductivity, low density and is stability over a wide temperature range[109]. β–NiAl is an ordered B2 structure that consists of two interpenetrating simple cubic sub lattices with each sub lattice having a number of lattice sites, where one sub lattice is entirely occupied by Ni atoms and the other Al atoms[109,83]. Deviations from ideal stoichiometry are accommodated by point defects (vacancies and antisites) in which Ni vacancies and Ni antisites are the most stable point defects in the Al rich and Ni rich system. The oxidation resistance of β–NiAl is very sensitive to impurities and the addition of Pt drastically improves the oxidation resistance of these aluminides[110]. The structural instability of the B2-NiAl phase coincides with the formation of martensitic transformations which occurs at high Ni concentrations[83]. Improvements in the oxidation resistance of Ni base superalloys warrants the study and further understanding of intermetallic multi-phase equilibrium between; the Ni-rich fcc A1-(Ni,Al,Pt) phase denoted ϒ and the ordered intermetallic L^{12} $(Ni,Pt)_3Al$ phase denoted as ϒ'[111] [86] . The two phase equilibrium of and β-B2-(Ni,Pt)Al is important as (Ni,Pt)Al is used as a bond coat for traditional Ni superalloys. The phase can be treated as a triple defect phase[112]. The constituent binaries of the current Ni-Al-Pt alloys formed in the intermetallic bond coat layer are; Ni-Al, Ni-Pt, Al-Pt[111,112].

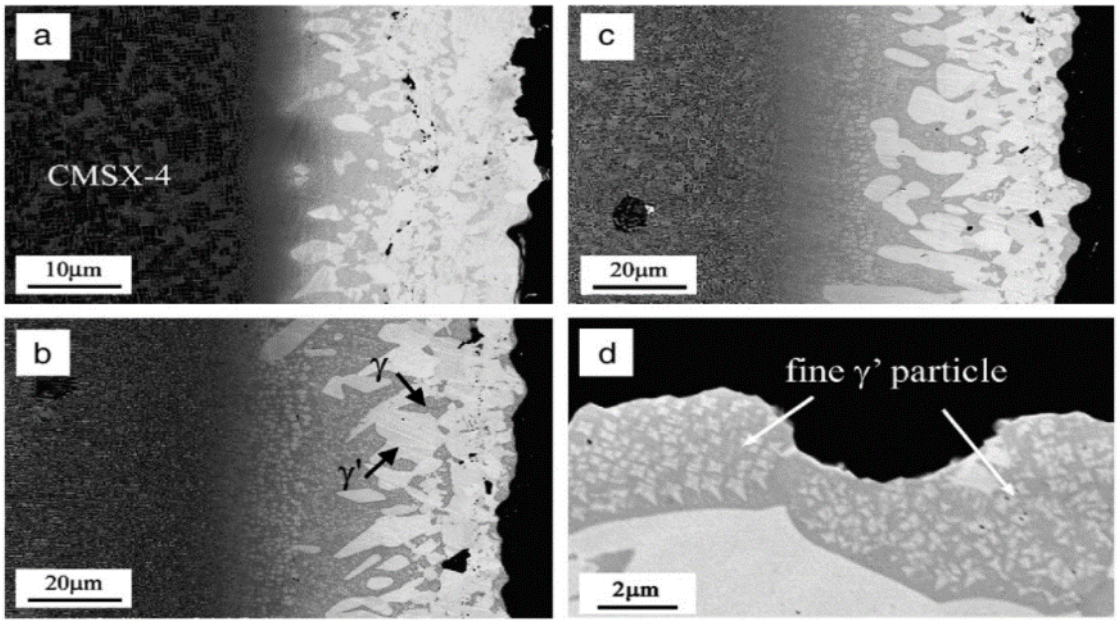


Figure 32: Cross sectional images of the bond coat on a CMSX-4 single crystal singlealloy (a) as processed; (b) after oxidation at 1150°C for 20 hours; (c) after oxidation at 1150°C for 40 h; and (d) the fine γ' precipitation near the surface region oxidation. The γ' phase exhibits a bright contrast under back-scattered electrons. Zhao X et al[91]

Figure 32, shows cross sectional images of the bond boat on a CMSX-4 single crystal superalloy as through an oxidation cycle. It was found experimentally by Danielewski et al[92] that at all temperatures and oxygen pressures, oxidation process in Ni-Pt intermetallic alloys follow a strictly parabolic rate law which is diffusion controlled and the same trend is found in pure Ni[102]. They concluded (In agreement with Wagner's theory) that the slowest step of the overall oxidation rate in high Ni regions (≥ 40 at.%) is determined by the outward diffusion of Ni cations in the growing oxide scale. Whereas in lower Ni content regions <40 at.%, the oxidation rate is governed by the solid state diffusion in the metallic phase. The NiO which is formed in the γ'/γ regions of Ni-Al-Pt alloys can be expected to gradually convert to $NiAl_2O_4$ through the solid state reaction between NiO and Al_2O_3 during further oxidation.

The formation of Ni oxide is important as its formation leads to the mechanical property degradation of Ni-based superalloys by metal loss[95]. Ni oxide can be modelled as a metal-deficit p-type semiconductor ($Ni_{1-\gamma}O$) with the predominant defects being doubly ionized cation vacancies and electron holes. In accordance with Wagner's theory that is based on the assumption that metal oxidation proceeds mainly via the diffusion of charged particles. The formation of the defects can be modelled as follows[95]:

$$\frac{1}{2}O_2 \leftrightarrow V''_{Ni} + 2h^{\cdot} + O_o \qquad \textit{Equation 21}$$

Applying the mass action to this defect equilibrium:

$$K = [V''_{Ni}][h^{\cdot}]^2 p_{o_2}^{-1/2} \qquad \textit{Equation 22}$$

And the electro neutrality condition:

$$2[V''_{Ni}] = [h^{\cdot}] \qquad \textit{Equation 23}$$

Yielding the relationship:

$$[V''_{Ni}] = \left(\frac{1}{4}K\right)^{\frac{1}{3}} p_{O_2}^{\frac{1}{6}} = 0.56 p_{O_2}^{1/6} \exp\left(\frac{\Delta S_f}{3R}\right) \exp\left(\frac{-\Delta H_f}{3RT}\right) \qquad \textit{Equation 24}$$

If the defect concentration is low and the mobility of defects is not dependant on concentration then the parabolic rate constant of Ni oxidation is directly proportional to the concentration of cation vacancies in the growing scale[29]. Therefore the parabolic rate constant of Ni oxidation must increase with increasing oxygen pressure. It can thus be said that the oxidation rate increases with oxygen pressure in the same way as it does in pure Ni. This agrees with the activation energy of pure Ni oxidation (232 kJ/mol) being virtually the same as the activation energy of oxidation in Ni – Pt alloys (228 kJ/mol)[92].

Another way to look at the ingress of oxygen into the Ni alloy system derived from Wagner's theory is to examine the impurities that can arise from the substrate in the form of metal cations. The metal cations can act to strongly influence the defect chemistry[94] and mechanical performance[84]:

Where the oxidation of an alloying element M from the super alloy can be represented by[93]:

$$\left(\frac{2x}{y}\right) M + O_2 \rightarrow \left(\frac{2}{Y}\right) M_x O_y \qquad \textit{Equation 25}$$

A parabolic oxidation constant can then be established based on Wagners theory:

$$k_t = -\frac{\sigma_t t_{ion} t_{el}}{z_c^2 z_a^2 e^2} \Delta G_f \qquad \textit{Equation 26}$$

Where σ_t is the conductivity of the M_xO_y oxide, and t_{ion} and t_{el} represent the transport numbers of ions and electrons, respectively. The valencies of the metal and oxygen ions are denoted z_c and z_a respectively and the elementary charge by e. ΔG_f is the Gibbs free energy of formation of the oxide and can be expanded via the Vant Hoff isotherm to give:

$$\Delta G_f = \Delta G_0 + RT\ln\left(\frac{a_{MxOy}^{2/y}}{a_m^{2x/y}.P_{O_2}}\right) \qquad \textit{Equation 27}$$

The above can be used to determine whether the Al_2O_3 scale will form based on the dominant defect. For example the authors Sato et al[94] theorise that alloys which readily form a continuous and stable

Al_2O_3 scale will have a large negative ΔG_f and the inverse relationship holds true based on an expansion of the above to incorporate defect concentrations and valences. This is based on assumptions and experimental results such as Al_2O_3 being the most stable oxide in the Ni alloy system deriving from an Ellingham diagram of Ni superalloy SCA425.. The second and third most stable oxides at 1000°C were Ta_2O_5 and Cr_2O_5 which was validated by both theoretical and experimental results[94].

Table 1: Nominal compositions (wt.% Ni-bal) of superalloy investigated Sato et al[94]

	Co	Cr	Mo	W	Al	Ta	Hf	Si
SCA425+	5.0	15.5	1.0	4.0	4.55	8.0	0.1	–

Table 1, shows the weight % of the SCA425+ alloy. SCA425+ is an interesting alloy as it is a weak alumina forming Ni superalloy when compared to a Rene5 for example[93]. The most important conclusion from the work of Sato et al[93] for use in this study is the expansion of the Wagner-Hauffe theory to apply to a multicomponent system such as the Ni superalloy type. The theory dictates that when the valence of an impurity ion is greater than the parent cation the growth of the oxide is reduced. So in the case of the Al^{3+} parent cation the formation can be decelerated in the presence of Ta^{5+} or W^{6+} as the dominant defect concentration (vacancies on the O^{2-} lattice) is reduced. However in the presence of Ni^{2+} the defect concentration is increased and so is the rate of formation of Al_2O_3.

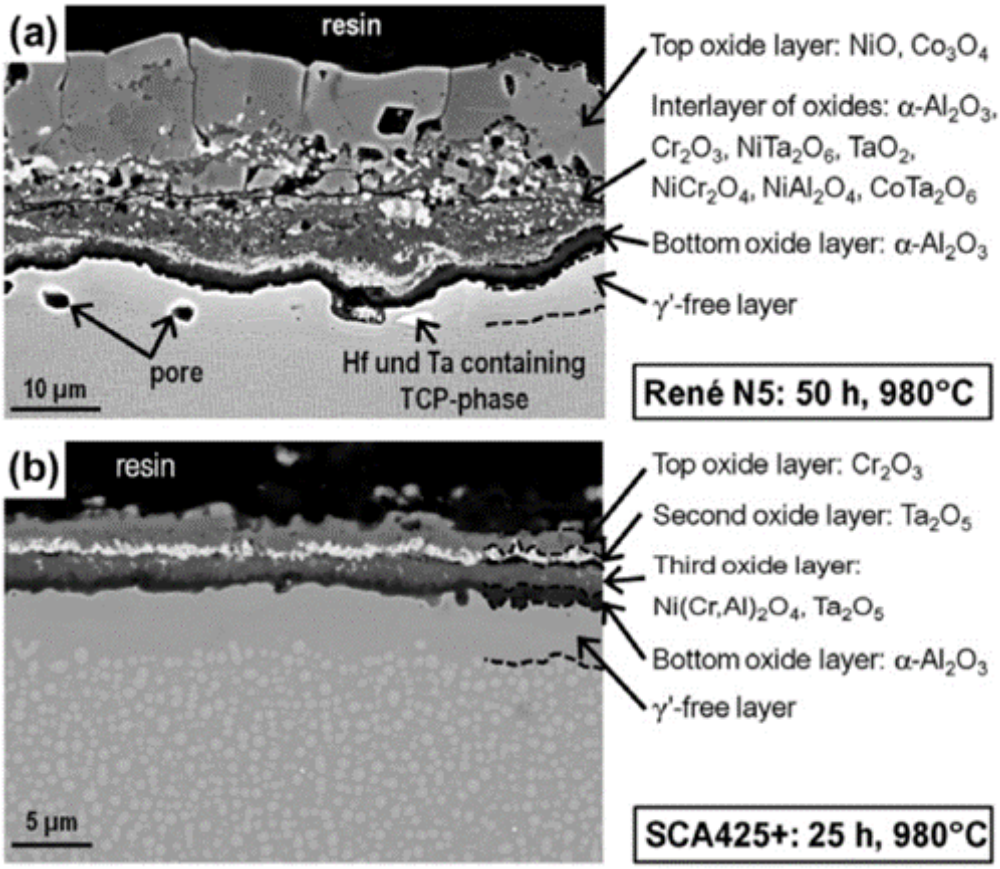


Figure 33: Formed oxide scales on Rene N5 oxidised for 50 h at 980C (a) and SCA425+ oxidised for 25 h at 980C (b). The difference in length scales should be noted. Bensch et al[93]

Figure 33 shows oxide scales that have formed on two Ni superalloys, Rene N5 and SCA425+ AT 980 C. The formation of Al_2O_3 is integral to the oxidation resistance of Ni alloys. It provides a strong stable scale at high temperatures that protects against most environments. One of the underlying scientific principles behind alumina's excellent protection is its associated high band gap energy. The high band gap energy creates a large energy barrier for ionic species which retards the diffusion of cations through the scale[95]. The Al concentrations in ternary Ni systems are high in order to produce this scale, however the increase in Al at.% in the alloy system can have detrimental effects[49], therefore elements such as Pt can be added to alleviate this issue and promote the formation of a stable and adherent Al_2O_3 scale[90,92,87].

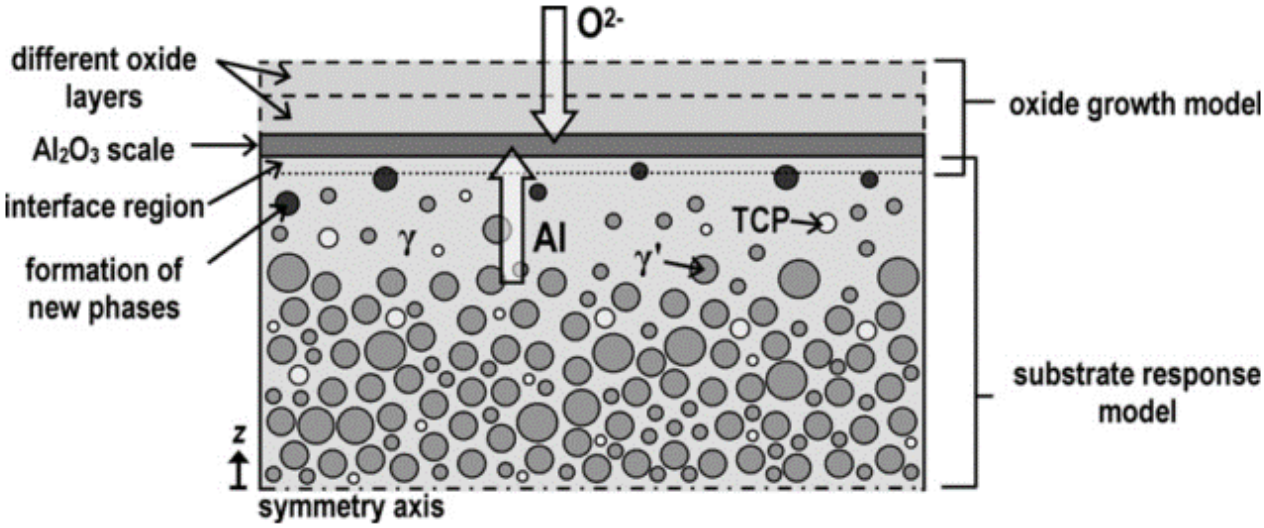


Figure 34: Schematic illustration of the oxide growth model in Ni alloys coupled with the substrate response model. Bensch et al[93]

4.5.5. Carbides / diffusion precipitates

Microstructural obstacles that inhibit slip can come in the form of solute atoms, forest dislocations that thread through the slip plane or small second phase precipitates. When obstacles are widely spaced enough that their elastic fields do not overlap they can be modelled as independent barriers.

C addition to Ni superalloys can have a host of applications[11], from the reduction in the frequency of solidification defects to the reduction in scale formation during casting, to the formation of carbides [30113 21].

Carbides in single crystal Ni super alloys can often be formed from C that has diffused into the alloy through processes such as pack aluminziation[16],[21] that is used to prepare the alloy for TBC coating[18], as seen in figure 30, page 44. The process that forms carbides, in Ni superalloys is diffusion controlled[29]. Whereby the concentrations of refractory metals significantly influence the type of stable carbide phases[21] formed during the precipitation process. Studies have shown that certain carbide types favour particular elements[114,115,116] such as Ti,[117]This can cause significant disruption to the carefully tailored microstructures. For example a study by Amrite Basak et al in 2016, showed that both regular and nodular type carbides favour Ti[117]. The susceptibility to strain age cracking and the alloy weldability is often linked to the Ti/Al[118], thus disrupting the ratio would alter the carefully designed criteria of the alloys microstructure and thus effect the mechanical properties in the carbide rich regions. The effect of carbides on the mechanical properties of Ni based alloys is complex and dependant on the morphology and distribution of carbides[117].

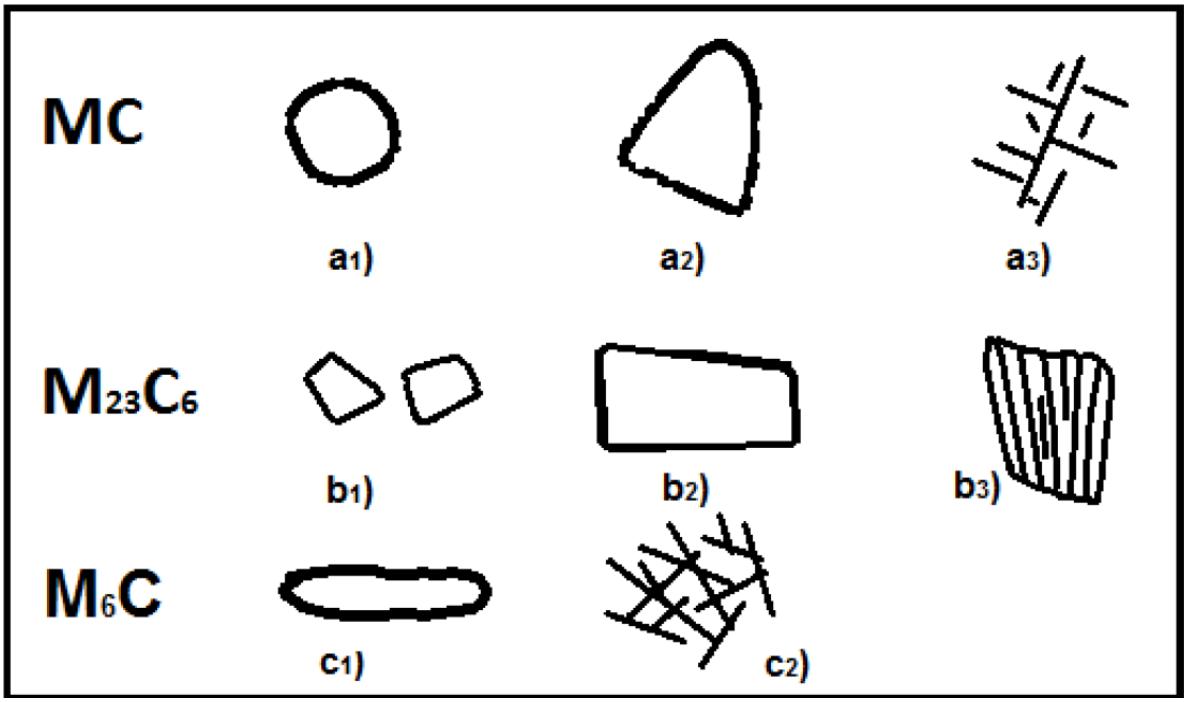


Figure 35: Image a1) shows a typical MC carbide, a2) and a3) respectively, blocky and script morphologies. B1) represents discontinuous blocky particles, b2) plate and b3) cellular type carbides. Image c1) represents a blocky form M6C and c2) represents Widmanstatten morphology[20]

Figure 35, shows schematic illustrations of the different forms that MC, $M_{23}C_6$ and M_6C carbides can take following their precipitation from the matrix. The carbide type phases shown in figure 35 precipitate due to differences in solutioning windows and partitioning of alloying elements. shown in Other studies have shown that during carbide formation C diffuses from the substrate of the material to the new interface[30] and is heavily influenced by processing temperatures. Higher cooling rates have been found to result in a finer dispersion of carbides and lower rates result in more blocky low surface energy structures[30]. High solidification and small thermal gradients result in more faceted nodular MC type carbides[30]. Hf has also been found to increase the carbide precipitation temperature and can thus change the morphology from a fine distribution to more nodular type[113].

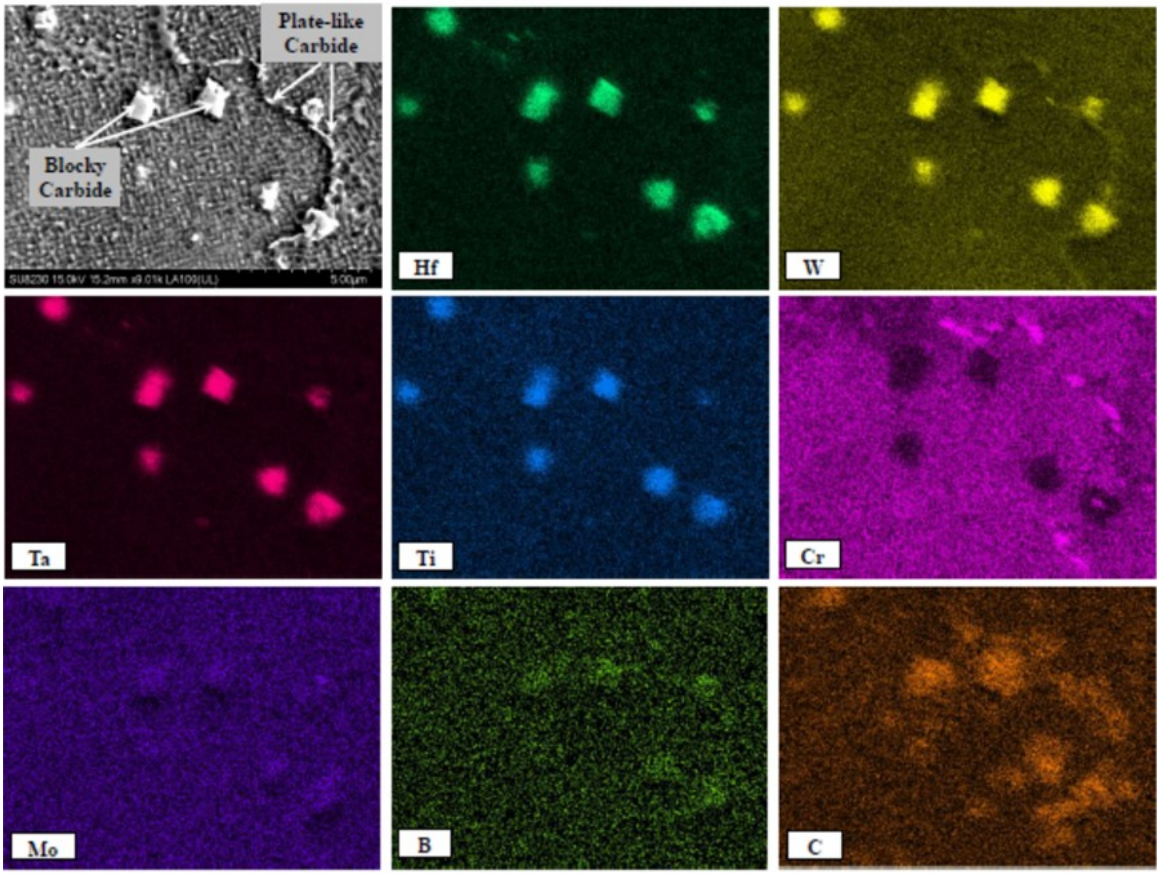


Figure 36: SEM-EDS profile of regular type carbides in the deposit region of a heat treated ,Mar-M247 alloy[117]

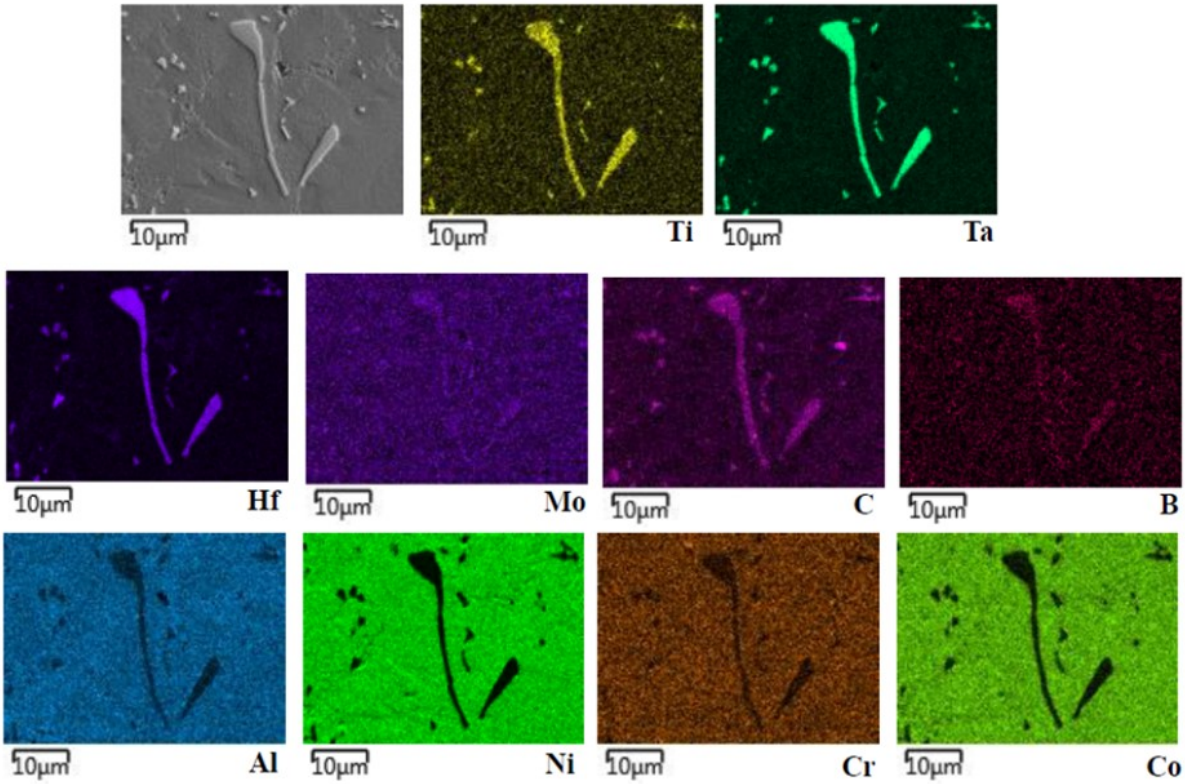


Figure 37: SEM-EDS element maps for TCP phases, in the deposit region of a heat treated ,Mar-M247 alloy[117]

Figure 36 and **Error! Reference source not found.** show SEM-EDS profiles of regular type carbides and T CP phases in the diffusion region of a Mar-M247 alloy. When examining a second generation single crystal Ni superalloy (SC2000) researchers[21] found that the finer carbides of the form M_6C correspond to the ϒ phase, whereas the larger more blocky carbides are linked to the intermetallic TCP phases and have a rhombohedral structure[113]. This is shown schematically in figure 35 and with SEM-EDS profiles in figure 36 and Figure 37.

TCP type precipitates can take many phases and crystal structures based on formation temperature and the size of atoms that sit on the kasper polyhedral, figure 38[119]. TCP phases have a high degree of coherency with the {111} planes of ϒ/ϒ' and form plate like morphologies parallel to {111} planes[17], which is what gives rise to the needle like appearance when sectioned in the {001} plane.

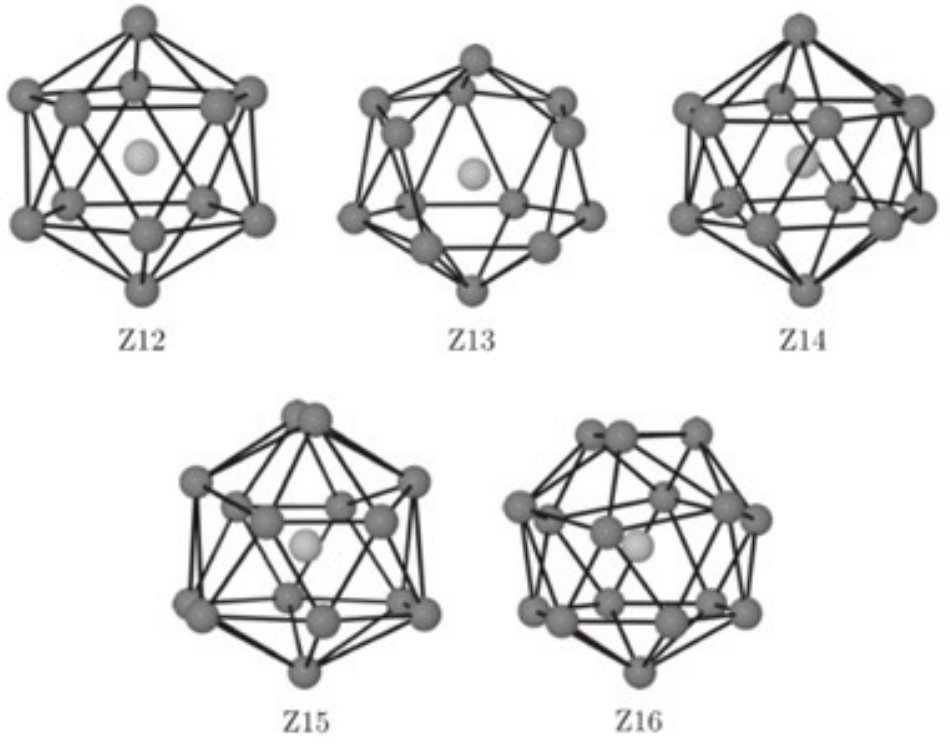


Figure 38: Frank-Kasper coordination polyhedral[120]

The difference between the phases in TCP structures is linked to the symmetry of the rhombohedral structure[121] as shown in figure 38. Studies of the TCP phases indicate that they are deleterious and reduce the mechanical performance of the alloy[17].

The typical response expected from precipitates is that they act to strengthen the material by acting as points which impede dislocation motion, thereby increasing both the yield point and hardening response[21,20,30].

Table 2: Common carbides phases in Ni single crystal alloys[57]

Phases	Structure	Parameter (Å)	A (°)	Constituent
MC	Cubic	a = 4.300	90.0	Ti, Ta, Hf
M_6C	Cubic	a = 1.085	90.0	Mo, W
$M_{23}C_6$	Cubic	a = 10.500	90.0	Cr, Mo, W
M_7C_3	Hexagonal	a = 13.980, c = 4.523	90.0	Cr
M_3B_2	Tetragonal	a = b = 5.600, c = 3.300	90.0	Ta, Mo, Cr

Table 3: Crystallography of the TCP phases,34

TCP Phase	System	Space Group	Space Group No.	Atoms per Unit Cell	Lattice Parameter	α
σ	Tetragonal	$P4_2/mnm$	136	30	a = b = 0.878nm, c = 0.454nm	90°
P	Orthorhombic	Pnma	62	56	a = 1.698nm, b = 0.475nm c = 0.907nm	90°
μ	Rhombohedral	R-3m	166	13 (hex. 39)	a = b = c = 0.904nm a = b = 0.4755nm, c = 2.583nm	30.5° 120°
R	Rhombohedral	R-3	148	53 (hex. 159)	a = b = 1.093nm, c = 1.934nm	120°

Table 2 shows the common carbide phases in Ni single crystal alloys, with their associated lattice parameters and segregation elements and table 3 shows the crystallography of the common TCP phases. Carbides can be formed as a by-product of a protective layer used during the pack aluminization process in which an intermetallic bond coat is grown from the Ni substrate to accommodate the ceramic TBC overlay coating which protects the Ni alloy from hard and corrosive environments[16]. These protective layers are most commonly Al or AlSi derivatives[122].

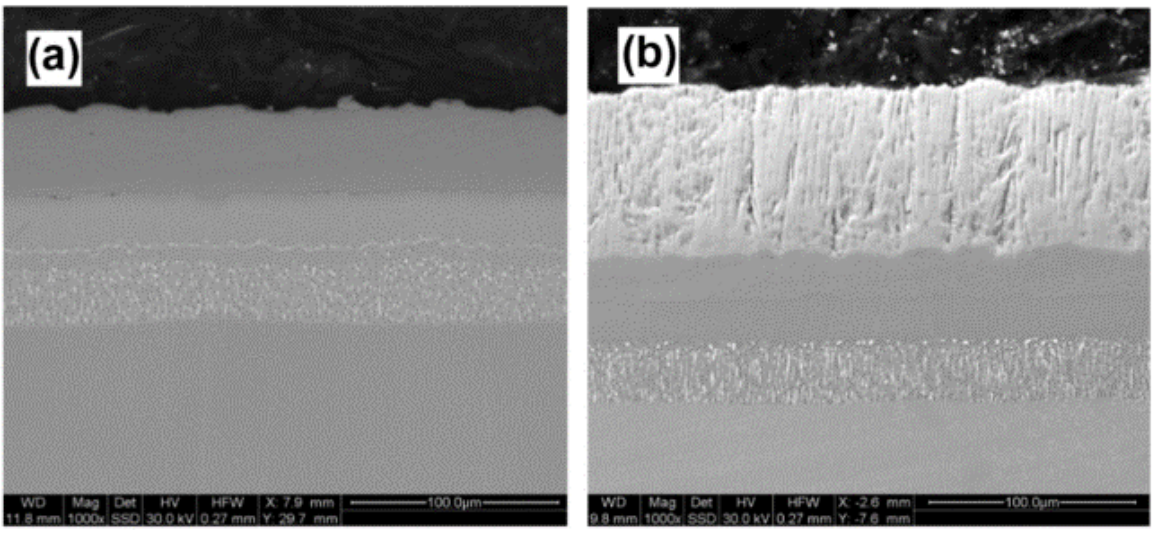


Figure 39: Cross - sectional microstructures of the double-layer bond coat (a) without (b) with a TBC[81]

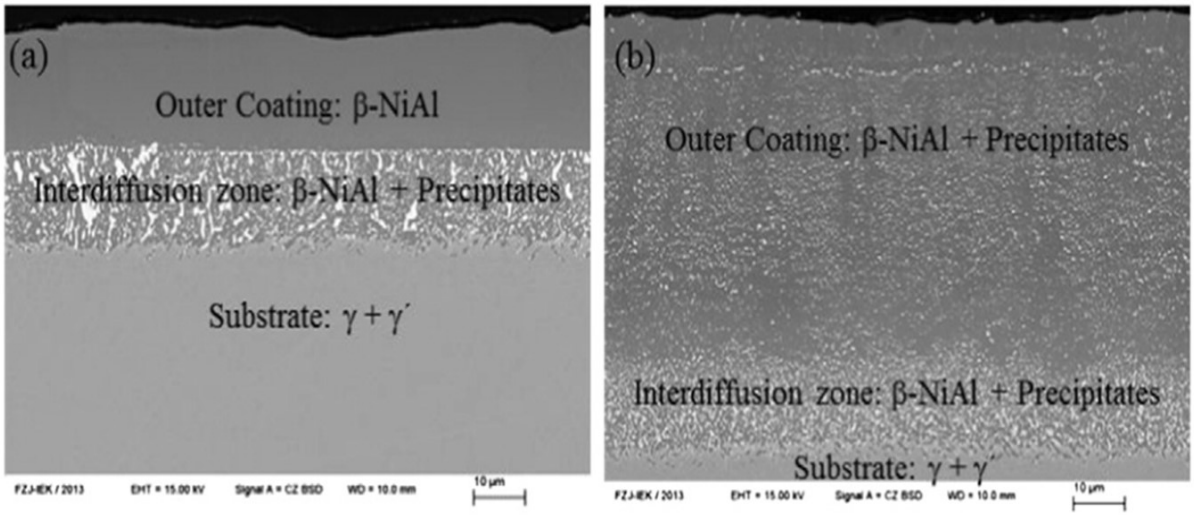


Figure 40: BSE-images of the cross sections of the as coated material with the (a) low-activity (b) high activity aluminde coatings on the single crystal SC2000[21]

Figure 39 and figure 40 show BSE cross sectional images of coated Ni superalloys under different conditions. When comparing a second generation Ni-based superalloy such as CMSX-4 to a third generation alloy, CMSX-10; CMSX-10 has an alloy composition that has been slightly redesigned to include 30°C maximum temperature improvements which includes a solutioning window that prevents the formation of the deleterious TCP phase, described in table 4 and shown in figure 41.

Table 4 shows the typical heat treatment cycles for single crystal superalloys. Two secondary heat treatments follow the main solutioning in both CMSX-4 and CMSX-10, table 4. These secondary heat treatments are used to promote the formation of finer ϒ' within the alloys matrix channels. It can be assumed that the formation of precipitates disrupts this, by changing the chemical stability and misfit of the carbides forming in the ϒ/ϒ' matrix.

Table 4: Typical solution heat treatment cycles for single crystal Ni-base superalloys[17]

Alloy	Refractory metal content W+Re+Mo+Ta (wt.%)	Solution heat treatment[a]
CMSX-2	14.6	1315°C for 3 h/GFQ
CMSX-4	16.4	1276°C for 2 h → 1287°C for 2 h → 1296°C for 3 h → 1304°C for 3 h → 1315°C for 2 h → 1321°C for 2 h → 1324°C for 2 h/GFQ
CMSX-10	20.7	1315°C for 1 h → 1329°C for 2 h → 1335°C for 2 h → 1340°C for 2 h → 1346°C for 2 h → 1352°C for 3 h → 1357°C for 3 h → 1360°C for 5 h → 1363°C for 10 h → 1365°C for 15 h/GFQ

[a] – GFQ – Gas (Argon or Helium) Furnace Quench.

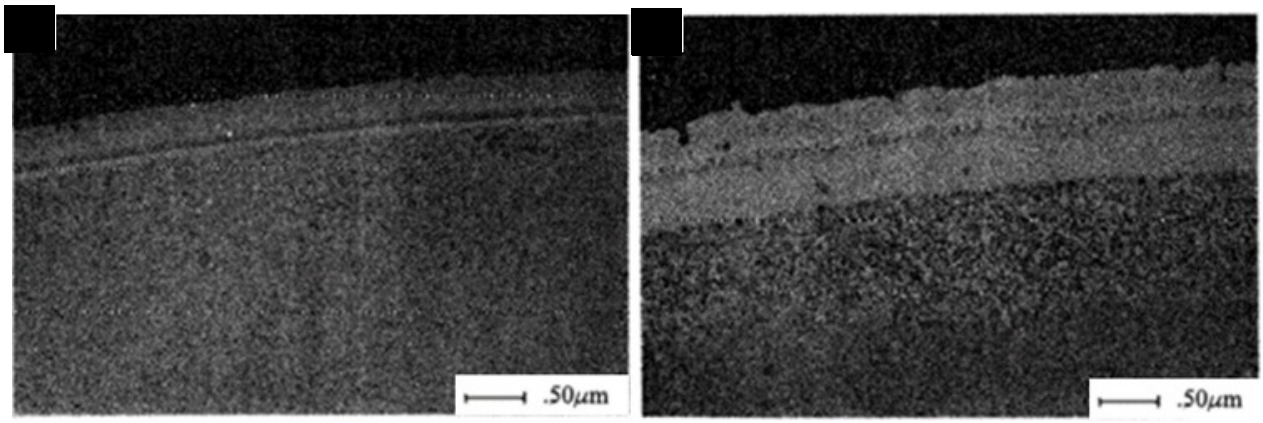


Figure 41: CMSX-10 alloy aluminide coated specimens with no TCP phase present following a 150 hour soak in static air at 1100° C (a) As coated (b) Soaked 150 hrs. At 1100° C [122]

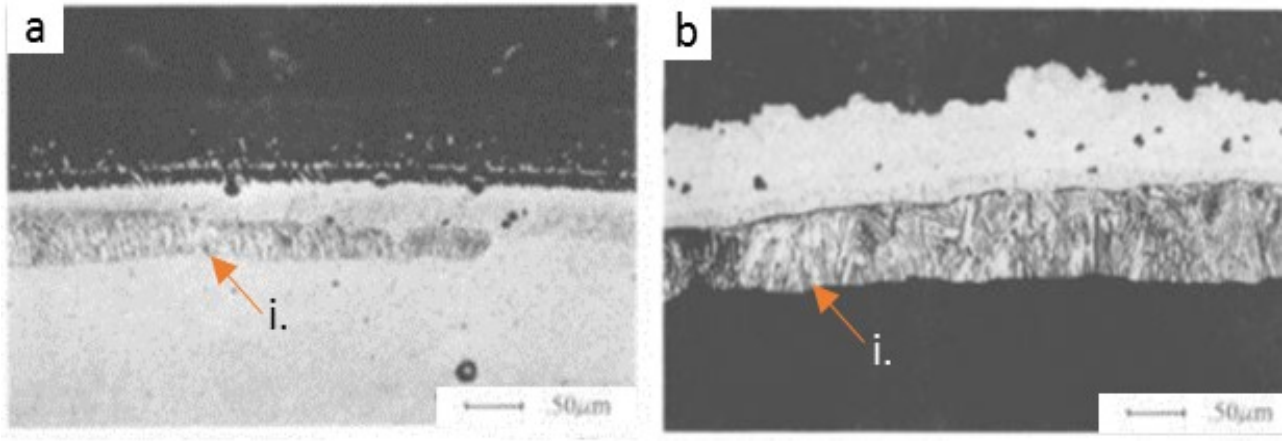


Figure 42: Standard Pt Aluminde overlay coatings on CMSX-10 (a) coating soaked for 100 hrs at 1080° C, the tcp phase is present in 10% of the specimen perimeter (b) CoNiCrAlY overlay coating soaked for 50 hrs. at 1100°C continuous TCP zone under the coating (i) TCP needle like phase [122]

4.6. Micromechanical testing

4.6.1. Ni specific

Ni micropillars can be fabricated and the local deformation mechanics can be studied at the micro level. Typically the pillars are machined using a focused ion beam in which the pillar is attached to the substrate material. At this level the dislocations interactions can be studied closely using micro pillar compression tests[123]. These tests can be performed using a flat ended nanoindenter punch at ambient and high temperatures. Attempts to understand and quantify the size effect can also be made using the micromechanical data extracted from these experiments[124].

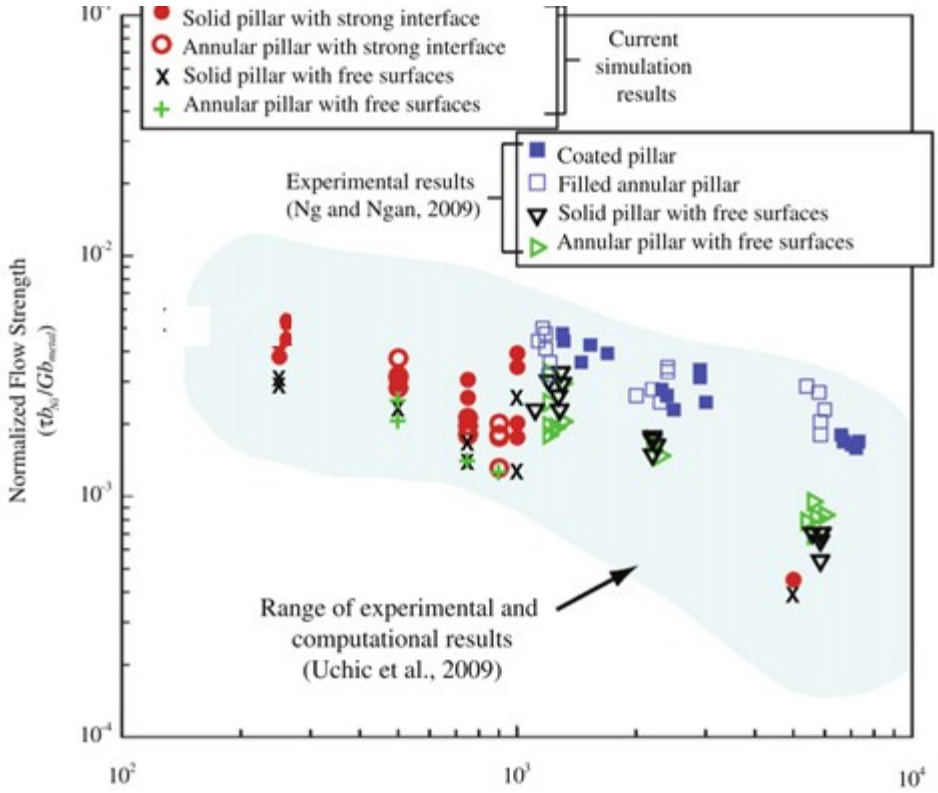


Figure 43: The flow strength versus micropillar size for the current simulations of solid and annular Ni micropillars, in addition to the experimental results of coated and center-filled Al pillars by Ng and Ngan (2009). Flow strength data are normalized by the shear modulus and the Burgers vector of each material.The shaded area represents the range of experimental and computational results as reported by Uchic et al. (2009). El-Awady[125].

The size effect is a phenomenon where the flow stress increases as the sample size is decreased. This effect has been heavily studied in Ni superalloys spearheaded by authors such as Uchic[126] and Raabe[127]. The micropillars exhibited this unique strengthening effect in samples with diameters ranging from 1 – 20 μm[128]. Two important conclusions extracted from the experimental research were that (1) post deformation the dislocation density ρ was higher than the expected size and (2) the density ρ increases with decreasing pillar size[129].

The data from figure 43 which was extracted from the study of Ng & Ngan[130] on tungsten coatings on Al micro pillars, revealed that a thin surface coating acts to trap dislocations within the pillar therefore raising the stored dislocation density by up to three orders of magnitude. The trapping of dislocations by the coating eliminates strain bursts which are a localised effect within the material[131] and increases the strain hardening rate. The study reveals that these effects are insensitive to the volume fraction of the tungsten phase and that the mechanical behaviour of microcrystals can be significantly improved when dislocations are trapped inside them. The work of Ng & Ngan paved the way for future studies which enabled theories such as 'the starvation of mobile dislocations' to be found to help explain microcrystal mechanical behaviour.

The ‘starvation of mobile dislocations’[129] is one theory that has been put forward to explain the size effect in Ni micro-pillar tests. In this case it is proposed that mobile dislocations leave the sample through the increased proximity of free surfaces and this clearly increases as the sample dimensions are reduced. When validating the size affect a large amount of scatter is observed in experimental results[41,132].

A study focused on the size effect in pure Ni microcrystals illustrates this clearly table 5. The samples used for this study were orientated for single slip deformation so that the surface normal orientation was near the <269>. After sectioning, the samples were electrolytically polished and annealed at 500°C for 1 hour in an argon atmosphere.

Table 5: Diameter size vs Critical resolved shear stress for pure Ni pillars orientated in the <269>. Dimiduk et al2

Diameter µm	τ_{Crss} MPa
18 - 39.7	15-25
10-11	10-58
4-6	25-65
1-2	5-250

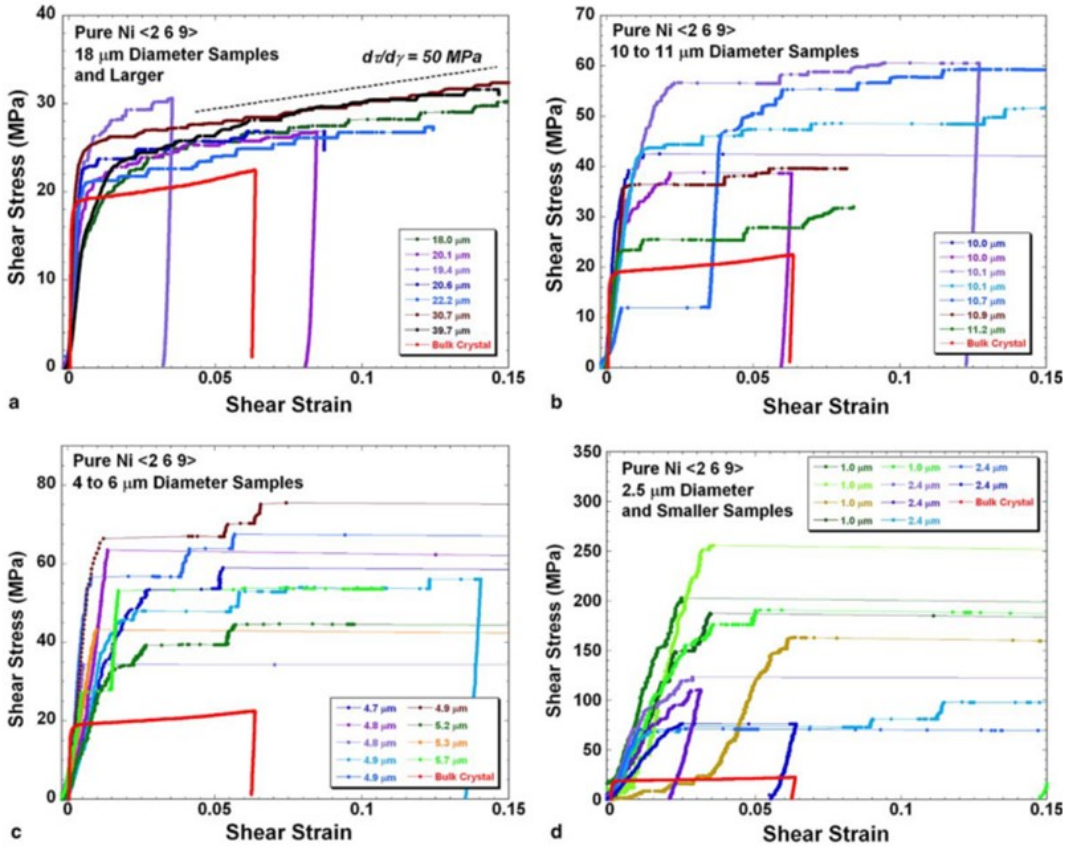


Figure 44: Shear stress versus shear strain plots grouped by sample diameter: (a) 18m and greater (b) 10-11 m (c) 4-6m and (d) 2.5 and smaller. The curves are truncated at 15% strain for clarity. Dimiduk et al82

Figure 44, shows the shear stress versus strain plots, grouped by sample diameter. Dimiduk et al theorise that the forest dislocations are the primary reason for both the size effect and scatter within the pure Ni[37,133, 55]. TEM experiments can be used to look at the dislocation structures post compression. To examine how dislocations, penetrate through free surfaces by measuring/modelling pre and post dislocation densities. Research by El Awady et al[125] that supports the "weakest-link activation mechanism" theory examines experiments which quantify the trapping (which results in hardening) and the escaping (softening effect) of dislocations in various sizes of Ni micropillars. It was found that for a pillar having a diameter of 1 µm the initial ρ was 3.7 x $10^{12}m^{-2}$ and activated dislocation length ~0.216 µm. The flow strength at 0.5% strain was 234.2 MPa, with samples taken from the same bulk sample with diameters of 0.1, 0.25 and 0.5 µm respectively the dislocation lengths were 0.21, 0.1637 and 0.1124 µm respectively.

The flow strength at 0.5% strain was found to be 239.94, 300.79 and 392.28 MPa respectively. This experimental evidence was used to justify "the weakest link" theory. There are two primary methods of measuring dislocation line length[51134] and dislocation density which complement each other and provide a good resources for checking the error associated with these measurements. (1) The line intercept method: A TEM section is cut parallel to the slip plane and five randomly placed lines of different orientations are added to the section, by a specified software that can manually place points at the intersection of each dislocation image with the lines.

Using the following relationship:

$$\rho = \frac{N}{Lt} \qquad \textit{Equation 25}$$

Where N is the number of points, L is the total line length of the random lines L and t is the thickness of the foil. The second technique (2): Is performed by manually tracing the total dislocation line length L using the designated software, the density is calculated via $= \frac{L}{A}$, where A is the foil area.

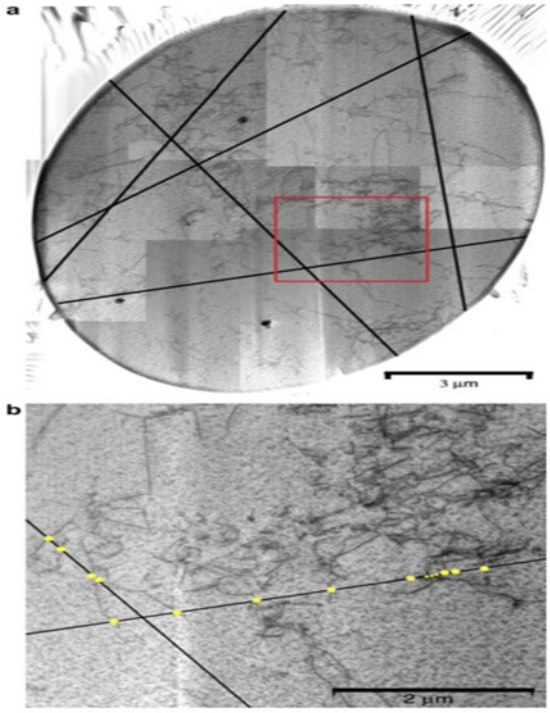


Figure 45: Example of the line intercept method or dislocation density measurements (a) random lines super imposed on the BF - STEM image taken from a deformed 10m sample (b) marks are placed at each point where a dislocation intersects a line. Norfleet et al[134]

Figure 45 gives an example of the line intercept method used for dislocation measurements. The length at which the size effect ceases to come into effect both as the size of the pillars is increased / decreased and what is the cause of this effect, is an interesting research area. Authors[34,135] have found that this occurs around 20-40 µm heading towards the macro scale and around 1-0.1 µm heading towards to the nanoscale. This will however vary from alloy to alloy, depending on the scope of my project this form of dislocation analysis could prove very useful. Shade and Uchic performed similar research on single crystal Ni superalloy Rene N5[132] and showed that pillars orientated for single slip gave rise to multiple slip and that the cut off between the bulk like and micro behaviour was around 350µm, which was near the dendrite spacing of the alloy. There was also a large amount of scatter observed in pillars with 5 µm diameters.

Figure 44 compares results from pillar tests and current findings from Uchic et al[34]. The results give further evidence to support the size effect and the weakest link theory[125] which can be explained and quantified by the joint efforts of modellers and experimentalists. The work of several authors including Gil Sevilano[44,136] and Parthasarathy[133], combined with others operating in the 3D dislocation dynamic modelling (DDD) community present data to support the activation of the weakest single ended source theory. They conclude that the small scale plastic response of Ni micropillars is largely dependent on the statistics of dislocation sources, number density per slip system and stress required to operate the resultant slip system(s)[137].

3D DDD enable the researcher to see important dislocation interactions based on theoretical assumptions in a 3 dimensional space. They are important because the models build upon assumptions made in 2D models, in which cross slip cannot occur and screw dislocations are not well represented. In 2D systems the crystal can only rotate in plane but in reality the z axis is also involved, so in certain instances 2D models cannot capture the fundamental types of dislocation interactions.

4.6.2. Dislocation modelling

Ni fcc crystals are mechanically anisotropic[138], this means that the deformation of crystals depends on the direction of loading and the orientation dependence of the activation of the crystallographic deformation mechanisms such as dislocations. systems and how they will activate, and this is the subject of crystal based approaches such as dislocation dynamics and crystal plasticity based finite element modelling.

2D discrete dislocation simulations prove greatly advantageous over the TEM method in which dislocation motion is tracked by representing dislocations as infinite line singularities figure 45. 2D models are constrained as a set of assumptions must be made in order to represent the 3D nature of dislocation mechanisms. These assumptions can greatly affect the results of the model[45].

3D modelling has significant advantages over 2D modelling in that the local interactions between dislocations can be accounted for (avoiding approximation's associated with the plane strain requirements of the 2D models) and the motion of dislocations, particularly those that interact with free surfaces and obstacles can be more accurately modelled[139,1,137]. The majority of all 3D discrete dislocation studies model the initial dislocation density as a Frank Read source(s), in which these sources can have a single fixed length with little to no variance or the complete opposite, the Frank Reed sources can be distributed evenly among all possible slip systems, randomly distributed or placed randomly on one[45,1].

The joint collaboration between both simulated and experimental results can be used to improve the quality of the next generation of Ni superalloys where the use of 2D and 3D dislocation modelling will play an important role in understanding the deformation mechanisms that are occurring on the micro level and can help scale the models to bulk size values[136].

Recent studies by Benzerga and colleagues[46, 140-79] have helped investigate the size effects that arise from compression testing using 2D modelling. The key attributes of these investigations are described as followed;

There was some evidence to support the size effect in that certain models displayed a size dependent increase in the proportional limit as the simulation cell size "modelled pillar dimension" is reduced. The

underlying theory supported the weakest link theory. Where the size effect was linked to the change in the activation stress for sources limited to the few largest sources in any given cell.

Other variances that can be taken from experimental results and tailored in computer models include; the effect and extent of cross slip, the magnitude of the applied strain rate, the influence of free surfaces and their associated boundary conditions, the loading mode, crystal orientation, aspect ratio and sizes and volumes of the simulation cells[141-79].

4.6.3. Size effects

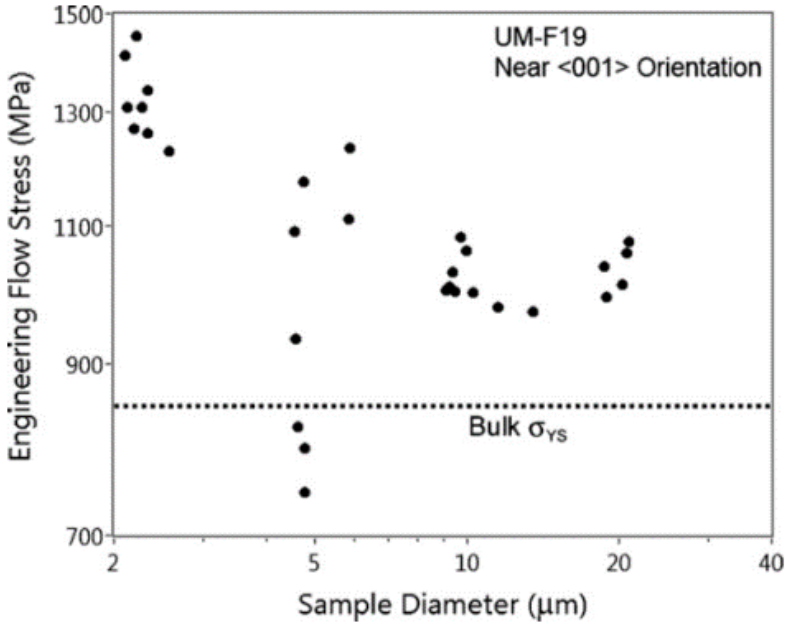


Figure 46: Flow scaling plot on log-log axes for the microcrystals prepared from the single crystal Ni base superalloy UM-F19. The orientation is near -<001> and the stress values have been measured at 1% engineering strain. The dashed line represents the bulk yield stress. Shade et al[132].

Figure 46, shows that the engineering flow stress of micropillars prepared from a single crystal Ni superalloy in the <001> orientation is inversely proportional to the diameter of the micropillar. The general trend in this regime is that smaller is stronger. Smaller specimens yield at higher stresses and exhibit higher strain hardening rates. Theories such as "dislocation starvation[138,129,139,135,125]" and "the weakest link[129,1-133]" have been put forward to explain the phenomenon.

The effect may be due to the smaller length scales once the microstructural units have been initiated and the pillar slips from the elastic to plastic region, the dislocation interactions are confined to a much smaller unit volume and therefore interact more closely with each other creating a larger strain effect rendering them stronger at these smaller length scales. These large congregation of dislocations are commonly referred to as forests[142] shown in figure 11.

Interest has been created around the area of micropillar tests fabricated from a bulk crystal via a focused ion beam (FIB) technique[54-72] results from the early tests showed a complete deviation from the bulk like behaviour of the macro scale tests and a clear size dependent strengthening.

It has been found experimentally[129,128,2] that there is a clear relationship between strength and microcrystal diameter, D that follows a power – law relationship with an exponent that is typically in the range of 0.2-1.0[143,144,1]. However, note that these power law relationships are limited in that they assume that an infinite macroscopic crystal has zero strength.

Studies have been conducted where parameters such as the pillar diameter or width[37], the crystal orientation[145] the dislocation density[129] (commonly known as pre straining) are altered and the resulting shear, stress / strain and critical resolved shear stress analysis are conducted[146].

Arguably the most important aspect to take into consideration when validating the size effect scaling law is the critical dimension depending on whether the pillar has been fabricated in the annular or lathe conformation[34].

The width / diameter play such an important aspect due to their derivative of the stress. Where $\sigma = F/A$, Force can be taken to be the load used to compress the pillar which is converted from MN to MPa & the area is calculated from the width or diameter.

The present work deals with the top width of micropillars, whereby due to the taper we are most concerned with the width in the middle of the pillar, the square of which is used to determine the area. Going back to the discussion of the Schmid factor and slip planes, the middle of the pillar would also most accurately represent the area of this plane.

Authors such as Uchic[126], Shade[131] and Dimidk[1] have concluded that in a regime where size- dependant strengthening is observed the relationship between flow stress and sample diameter (or in my case width) can be described by the following power law[147]:

$$\sigma_y = \sigma_0 + Ad^m \qquad \textit{Equation 26}$$

Where σ_0 is a scale dependent yield stress, and A and m are empirical constants[147] – this relationship is said to hold true for sample diameters that are a couple of hundred nanometers to tens of micrometers[1]. This model has been used in several studies[148,149,150,151] and so can be taken as reliable in this authors opinion where the power law exponent for fcc metals varies per study ranging from 0.61 to 0.97 and the strain at which the flow stress is determined varies as well. Therefore more analysis is needed to validate this model.

However these effects differ when taking into account poly and single crystal mechanics[28]. This is due to factors such as rotation gradients and multiple slip systems activating in tandem. When the micropillars are pre – strained more dislocations are introduced into the system. Experimental results show that the increase in dislocation density decreases the strength scaling component considerably[1]. Some authors[44,128] argue the inverse of this.

The size effect scaling law also holds true in other materials such as copper, gold and glass [152,3,145,153]. Although conclusions can be drawn from authors such as Uchic heading the research area in Ni superalloys that the rationale for the size effect behaviour is still under debate, with emerging theories all pertaining towards dislocation mechanics such as dislocation exhaustion and stochastic, scale- free dislocation mechanisms [1,154].

Results from dislocation dynamic simulations utilising Frank Read sources have reproduced the experimental observation that smaller is stronger[46] In both two dimensional and three dimensional simulations [28,45,155]. The next step lies in the ability to scale this up to the macroscale and quantify this process.

4.7. Supporting size effect theories

4.7.1. Starvation of mobile dislocations

"Starvation of mobile dislocations" – This theory was put forward by Greer and Nix. It is based upon the assumption that the proximity of free surfaces allows for the movement of mobile dislocations out of the sample before they have a chance to multiply[129,1].

These mobile dislocations are required for material to deform plastically[8], if the number density of these dislocations is reduced through penetration at the free surfaces of the micro pillar the flow stress increases to compensate.

Volkert and Lilleodden suggested that the loss of mobile dislocation density was due to free- surface image stresses and source limited behaviour.

Authors such as Senger et al[139,156] and Rao et al[55,157] have provided some excellent studies in this area. Senger et al propose that the size affected strengthening mechanisms are due to the size distribution and density of sources within the pillar.

In simulations they observed a decrease in flow stress as a result of the creation of new sources that were longer than the initial contributors from dislocation reactions.

Rao et al[157] put forward two new theories one commonly referred to as source truncation hardening[142] in which the strengthening due to sources is attributed to the proximity of free surfaces.

Therefore the length of the largest Frank source arm sets the precedent and flow stress for the rest of the operations within the simulated cell.

4.7.2. Exhaustion hardening

Another theory put forward by the studies of Rao et al[157], Senger et al[139] and Tange et al is commonly known as exhaustion hardening and is related to the flow behaviour in a source limited microcrystal proceeded by the sequential activation and obstruction of weakest link sources[1].

In this theory the basis is that there will be a larger function of stress each time a dislocation comes into contact with an obstacle or barrier i.e. the stress required to activate the next weakest source becomes higher due to the limited number of sources in the μ specimens.

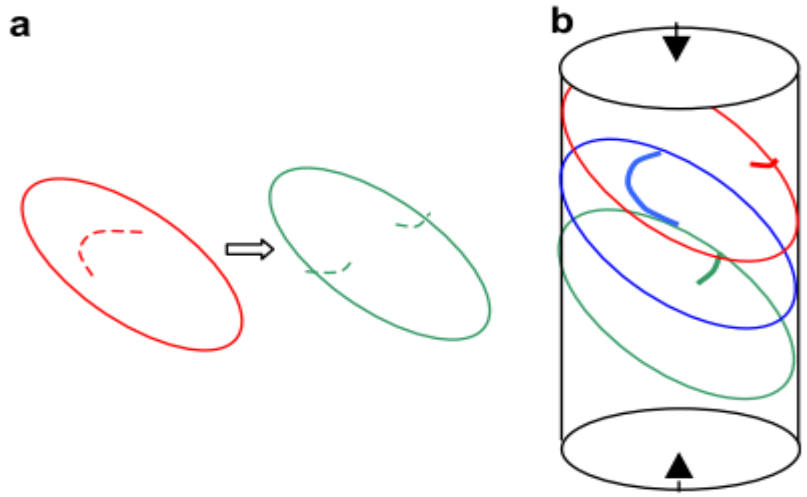


Figure 47: Schematic sketch of how double pinned Frank – Read sources quickly become single-ended sources in samples of finite dimensions. (b) Schematic sketch of single-ended sources in a finite cylindrical sample in critical configuration, which occur where the distance from the pin to the free surface is the shortest. The longest arm among the available sources (blue) determines the critical resolved shear stress. Thus the statistics of pins within a sample of finite size determines the yield strength of the sample. Parthasarathy et al[146].

Figure 47 shows a schematic sketch of how doubled pinned Frank – Read sources can become single ended sources in the finite dimensions of micropillars. In bulk material there are a huge number of mobile dislocation segments that can multiply, In microcrystals these sources are limited as evidenced by the strong strain hardening response when a source stops operating due to forest encounters[46,1,2]. In microcrystals the source truncation and exhaustion hardening process give evidence to support the stochastic flow commonly observed in small cell simulations and experiments[83-87].

4.7.3. Statistical models

Parthasarthy[146] et al and Gil Sevillano[44] have also provided further insight into the weakest link theory and dislocation process operating on these small scales.

The study by Parthasarathy et al[55] developed a statistical model for the flow stress in micropillar compression, in which the flow stress was heavily influenced by single ended dislocation source operation in the 3D models, giving evidence to this in that the source operation becomes a dominant factor in the determination of the critical resolved source stress[131]

Gong and Wilkinson have studied the size affect in micro cantilevers fabricated from Ti alloys, in which the cantilevers were made using a focused ion beam[158,9].

The slip system in Ti is based on a hcp crystal so the study cannot be directly reflected onto the Ni fcc system, however what is interesting is the scaling law

$$\tau = \tau_0 + \frac{A}{w} \qquad \textit{Equation 27}$$

Where τ_0 is the critical resolved shear stress for an infinite sample, A is a constant and w Is the sample width.

The equation takes into account the scaling of the critical resolved shear stress as the sample size is reduced. The results of these studies were produced by fitting a crystal plasticity finite element model to the experimental load-displacement data to find the τ_{crss} values. The size effect in these cantilever samples are modelled by examining the back stress from dislocations piling up at a neutral axis[158].

The exponent n was found to be -1.1 for the CP-Ti and fits in with a similar experiment undertaken on copper[159] in which the exponent was -1.14. An interesting point from this study are the authors taking data from three materials as a whole and fitting it into one equation. $\tau_y = \tau_{cp} + Aw^{-1} + \tau_{Al} + \tau_b - \tau_{cp}$ represents the basic CRSS of the bulk CP-Ti, τ_{Al} is the strengthening from the Al addition, τ_b is the additional strengthening from the beta phase and the Aw^{-1} incorporates the length scale effect by representing the back stress from the dislocation pile ups[158].

The scaling equation could prove very useful if it could be applied to Ni and the additional terms can represent different crystal orientations, or error functions to help prevent scatter and validate these effects.

4.8. Pillar manufacture – Focused Ion Beam

4.8.1. The basics

The primary features of a Focused Ion beam (FIB) machine are the vacuum system, liquid metal ion source, ion column stage, detectors and gas inlets. The distinguishing feature of a FIB is the liquid metal source, which produces a finely focused ion beam with high lateral resolution of material removal with rapid sputtering at various angles allowing complex geometries to be made. A vacuum is required for

the source (~1x10^{-8} torr) and the sample chamber (~1x10^{-6} torr) anything lower than 1x10^{-4} will cause the ion beam to interact with the gas molecules.

The dual beam FIB – scanning electron microscope (SEM) system has advantages over a single system in terms of sample preparation and microscopy applications for non-destructive imaging and site specific material removal. The two beams have a coincident point, in which they intersect with the sample. SEM can produce higher quality images but FIB can produce better contrast through differential primary and secondary ion emission. However care must be taken as ion implantation from initial imaging with the FIB can lead to deposition and can cause 20-30 nm[160] of damage through the surface layer.

4.8.2. The liquid metal ion source

The most commonly used liquid metal ion source LMIS used in FIB systems is gallium. A Ga reservoir wets a metallic tip (normally tungsten) which is extracted by an applied voltage. This can produce a source of ions of 5 nm in diameter. Ga is the most commonly used source material for the following reasons:

i. Low T_m – 29.8°C which reduces any high temperature interactions between Ga and the W needle.
ii. Low volatility at T_m, which conserves the material and produces a longer source life.
iii. Low vapour pressure – Ga can be used in pure form and will not evaporate. Therefore longer source life.
iv. Low surface energy – Viscous behaviour on the needle.
v. Emission characteristics – Which enable high angular intensity with a small energy spread.

The heated Ga flows and wets the W needle, an electric field of approximately 10^8 V/cm is applied to the tip producing a tip radius of ~2-5 µm. The Ga+ atom is pulled by an extraction voltage ionised by field evaporation. The typical lifetimes for Ga are ~400 A hours/mg

The voltage and emission current output characteristics for the FIB system are non linear thus the source tends to be operated at low emission currents (~1-3 µA) to reduce the energy spread and yield a stable beam and the lifetime of the LMIS is measured in terms of µA hours per mg of source material.

The condenser lens is the probe forming lens. The objective lens is used to focus the beam of ion at the sample surface. Beam currents from a few pA to as high as 20-30 nA are used for milling my pillars used in this study. A series of apertures of various diameters help to define the probe size and produce varying ion currents. Optimisation of the beam shape is also achieved through aperture alignment, estimators and column lenses. The FIB has a good working distance of around 20 mm or less and can be used with

samples having varying surface structures without worry of field variations. Space charge effects limit the source size and increases the width of energy distribution of the ions. Chromatic aberration is the limiting factor in the resolution. Eucentric motion is used to avoid having to realign the sample every time the stage is moved.

4.8.3. Imaging

Penetration of the ion beam into the sample varies with different materials and crystal orientations. The secondary electrons for images can be collected via a multi channel plate or electron multiplier. Secondary ion imaging provides a different type of contrast when compared to secondary electron imaging. A dirty metallic sample that contains some insular material can result in charging in which an excess positive charge is accumulated. Insulating regions appear dark, conductive light and the contrast is switched in the SEM. Pt can be deposited by ion beam assisted chemical vapour deposition of a precursor organometallic gas. The process works via the delicate balance of the sputtering and deposition. The gas molecules are adsorbed on the surface in the vicinity of the gas inlet, but decompose only where the ion beam strike. The deposition of Pt onto the surface of a sample is a chemical vapour deposition process. The advantage of having an SEM is that non-destructive imaging can be done. In a secondary electron image a lighter region is indicative of more secondary electrons and darker is less.

4.8.4. Damage / Controllable features

Milling takes place as a result of physical sputtering of the target. An atom is sputtered if it receives kinetic energy sufficient to overcome a characteristic activation energy known as the surface binding energy (SBE). Inelastic scattering in metals produces plasmons and SE electrons. The number of secondary electrons per incident ion is approximately 1 and is 10 – 1000x greater than the number of secondary ions per incident ion.

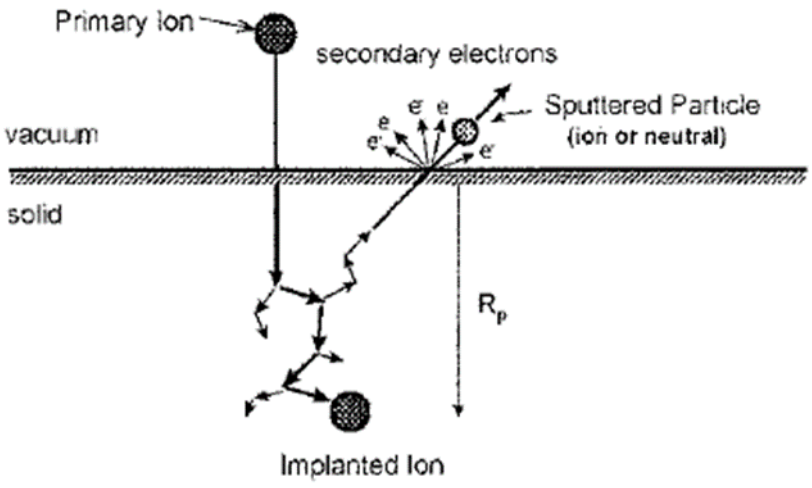


Figure 48: Schematic diagram of the sputtering process and ion-solid interactions. Lucille et al

Figure 48, shows a schematic diagram of the sputtering process and ion-solid interactions. Sputtering can be considered as physical erosion on the atomic scale. The mean number of atoms ejected per incident ion with an energy exceeding some arbitrary minimum energy E_0 which may be expressed by the equation below:

$$Y(E_0) = \frac{1}{4}\Gamma_M \frac{\propto NS(E)\Delta x_0}{E_0} \qquad \textit{Equation 28}$$

$\propto$ Is a dimensionless function incorporating the incident angle. M_2/M_1 the mass ratio, E is the ion energy, x_0 is the depth interval for which the atoms set in motion have an energy greater than E_0.

On average sputtered particles possess an energy ~2-5 eV where the emission follows a cosine distribution for normal incidence ion bombardment. Ions can be back sputtered using a FIB beam much like electrons are back sputtered in a SEM. The rate increases with angle of incidence and mass ratio M_2/M_1. When creating features such as deep and narrow trenches for pillars, sputtered material and back sputtered ions may redeposit onto the surface. Redepositon is a function of:

i. The kinetic energy of the atoms leaving the surface
ii. The sticking coefficient of the target material
iii. The geometry of the features being milled
iv. The sputtering yield Y of the target material

A sputtered particle can be considered a projectile and interfere with results. This can be alleviated by the rate of removal which is controlled by the vacuum. The sputtering rate increases steadily with an increase in accelerating voltage. Based on sputtering yields, range data and computer modelling, material dependant properties of a solid are governed by the forces that bind the constituent atoms together. The sputtering yield is inversely proportional to T_m, as T_m is a direct indicator of bond strength. The more tightly bound an atom is, the more difficult it is to eject it as a sputtered particle.

Channelling ions may penetrate greater distances along low index directions not a property of amorphous materials. Atoms that are displaced from their equilibrium positions by the onset of energetic ions to generate a cascade within the material and ionic species remain post cascade. One consequence of ion implementation is the development of a surface amorphous phase. The amorphous phase is metastable and depends on the unit cell size complexity of chemical ordering and the width of an intermetallic phase field. The more complex the material unit cell, the larger the amorphous layer will be. This could be particular apparent in the bond coat layer of a Ni superalloy. Materials with smaller unit cells are harder to amorphous. There is a difference between damage due to inherent ion-solid interactions and redepositon artefacts. It is stated by research[161] that Ga implantation is due to

redepositon artefacts and not inherent ion-solid interactions. The response of a given target material to the ion beam is strongly dependant on factors such as; beam current, Incident ion energy, trench / feature geometry, raster pattern, milling angle. Problems associated with redepositon include; sidewall sloping, undesired topography, Ga+ implantation.

5. Materials and Methodology

Three Ni-based super alloy samples have been examined throughout this study.

- The first sample studied was a single crystal CMSX-4, a second generation directionally solidified alloy grown in the <100> direction.
- The second sample a polycrystalline second generation FGH-96 alloy with grain sizes 5-20 µm.
- The third set of samples were carburised CMSX-4 and CMSX-10, in which the mechanical properties local to the carbide type phase rich regions and bulk microstructure were examined.

5.1. Introduction

This section will outline the techniques, equipment and materials used to examine the fundamentals of micromechanical deformation as explored in this thesis.

The single crystal alloy was used to develop and facilitate the fundamental testing criteria for micropillar compression *in-situ* testing. Using methodologies developed by Terry Jun[162] and Ben Britton[163] as well as external experimentalists such as Raabe[15] Uchihc[126] and Lilliedoden[38]. They, as well as others, innovated ideas such as the size effect[128] The fabrication of pillars via FIB[160] substrate effects[164], compliance issues[165] and pillar geometries with a viewpoint on taper angle, aspect ratio and friction[15].

All of the above methods were used and expounded upon to provide adequate, reliable and repeatable testing methods for micromechanical testing. The main micromechanical testing method involved the compression of micropillars, but micro indents were also used to validate mechanical results.

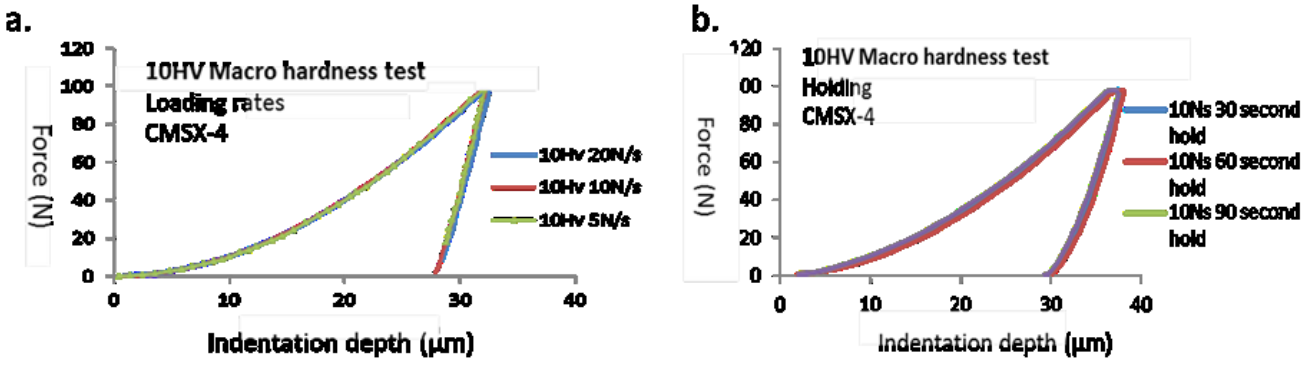


Figure 49: 10HV Macro indent traces (a) loading rates (b) Holding. Illustrating re traceable curves, indicating no strain rate sensitivity.

Figure 49, shows macro indent traces for CMSX-4. The first generation of indent experiments used a macro indenter on a single crystal alloy. This gave a representative view of the mechanical behaviour of

the alloy and the results could be compared to literature along with an EDX analysis to ensure the alloy was true to the specification. Micro indents were later used along a carbide type phase, alloy microstructure.

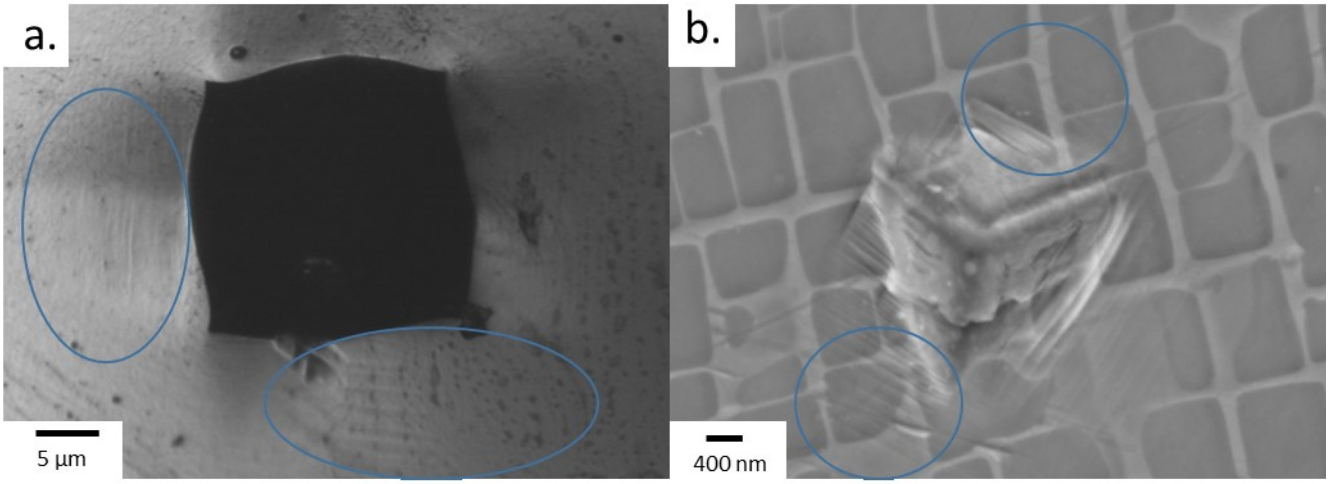


Figure 50: Indents on CMSX-4 alloy (a) Macro indent showing parallel slip (b) Micro indent showing diagonal slip.

Figure 50, shows macro and micro indent impressions made on CMSX-4. The orientation of the indent with respect to the region of interest is also important. One should ensure all orientations are consistent within the specified testing region. In the case of the above figure, the orientation of the macro indent is set up such that the slip propagates parallel to the load. Whereas in the case of the micro indent the orientation is such that the slip propagates at roughly 45° to the deformation through the ϒ/ϒ' microstructure. The effect of orientation and setting this up correctly for accurate testing criteria will be discussed thoroughly in later sections. The hardness value found was ~420 Gpa which is an accurate value for the CMSX-4 alloy in the <001> orientation[166]. The micro indents also mirrored this value within the bulk alloy and will be discussed in results - carburised ni-based superalloy: cmsx-4.

Micropillars were fabricated using a focused Ion beam (FIB) via the annular method with multiple geometries. This was done in favour, over the lathe method, which exposes the pillar to high ion doses[161].

5.1.1. Pillar fabrication

FIB milling is the typical method used to fabricate micropillars to study small-scale plasticity and size effects in uniaxial compression[167].

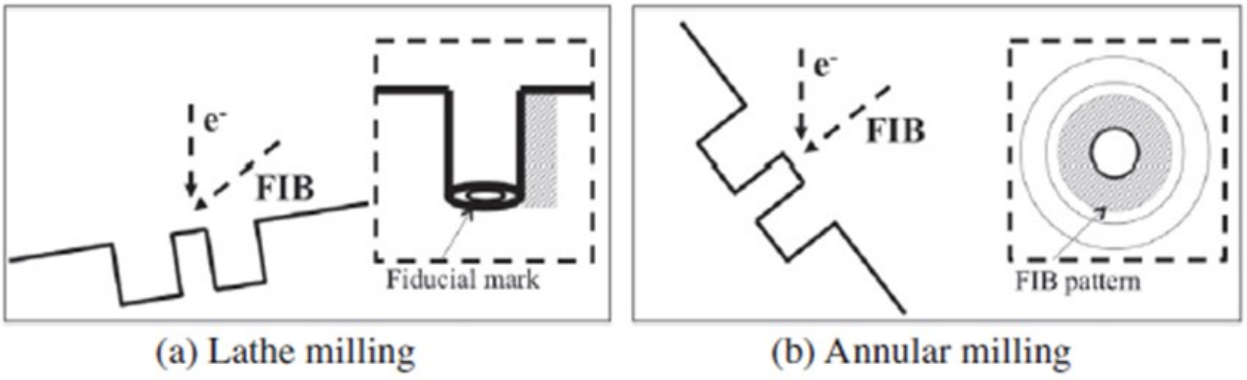


Figure 51: Schematics of the two approaches for FIB specimen preparation (a) Lathe milling and (b) Annular milling[161]

Figure 51, shows schematics of the lathe and annular milling methods. The two primary methods for milling pillars are the annular & lathe confirmations[161].

The lathe milling technique was favoured in earlier micro pillar experiments[168-34]. The manufacture of pillar by this method involves several steps in which large rings are milled into the surface of the material, each rotation step requires the sample to be imaged – this is what results in the high ion dosage.

The technique was favoured due to the relatively low tapering angles and good control over the samples dimensions (width / height) producing a uniform pillar. The best aspect ratio for milling is approximately 1:2/3[15] as it gives a good compromise between barrelling and buckling during testing.

However some concerns have been raised with this method, principally due to the effect of the high ion exposure which has been claimed to effect the stress-strain response and deformation morphology[161].

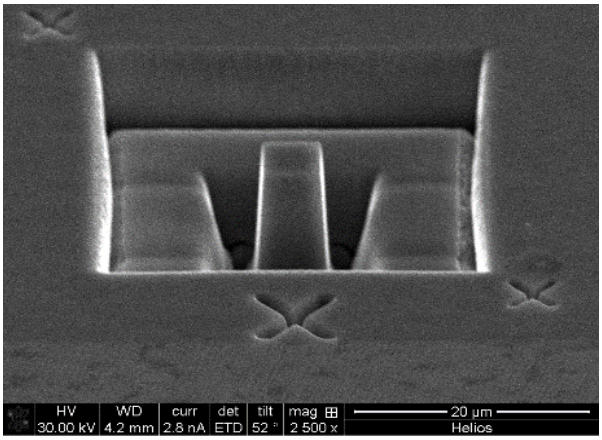


Figure 52: 4 µm pillar fabricated using the square cross section. Authors work.

Annular milling which is now used in the majority of micro compression studies[132], uses circular or square patterns such that the sample face remains perpendicular to the beam throughout the process.

The micropillars for this study are prepared with a square cross section milled in multiple steps and keeping the pillars within an aspect ratio of 1:2/3 width to height respectively.

Research conducted by Hutsch and Lilleodden (2014)[161] examined the effect of the high ion dose on the micro plastic response of the pillars in two different crystal orientations [001] and [111]. It was found that the surface layer in the lathe milled pillars is greatly affected by the ion beam damage and shows stresses approximately 4 times higher than in the annular pillars. It is theorised that this ion beam damage creates artefacts within the pillar and resists the emission of plastic slip through the surface and so effects the flow stress moving through the pillar. However due to the complexity of the problem one needs to fully understand the multiplicity of the defect types and their gradients to fully quantify the effects in a given material[167]. When comparing the effect of crystal orientation between the two milling techniques, the shape of the stress strain curves remain constant with the only difference being the magnitude of stress between the two orientations[161].In the case of the annular pillars the stress strain response has a strong dependence on orientation, which is to be expected and has been previously observed in similar *in-situ* experiments[161].

5.1.2. Pillar analysis

Following on from the FIB micropillar manufacture, the pillars can be compressed using a flat ended nanoindentor punch. The resultant time, displacement and load data is recorded with a live video feed. The load / displacement data is used to create a stress / strain plot for the compression test. Key mechanical parameters such as; the yield point, work hardening rate and Young's modulus can be extracted. Combining the engineering stress / strain data with the live video feed, features such as rotation gradients, τ_{crss} and plastic flow can be calculated.

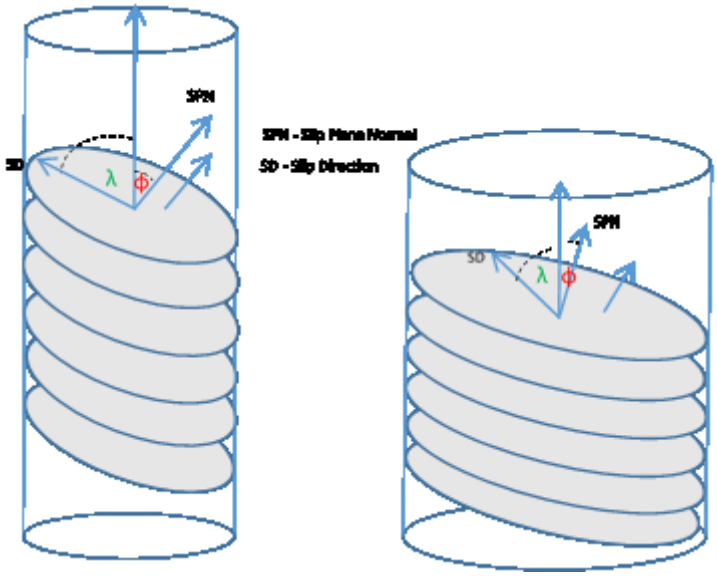


Figure 53: Micro pillar in compression (a) Schematic - non deformed (b) Schematic deformed ~30% deformation

Figure 53, shows a schematic of a compressed and non-compressed micropillar. After compression, microstructural features such as slip bands (slip trace analysis) can be observed using an SEM. As the pillar is compressed the slip plane rotates towards the compression axis[169]. Crystal rotation axis orientations can be calculated by comparison of the crystal orientations before and after deformation. Electron back scattered diffraction (EBSD) can be used to measure the crystal orientation of a specific area before and after deformation. The EBSD method provides the Euler angles which can be used to calculate crystal orientation. The crystal rotation axis orientation can be obtained from a rotation matrix;

$$G = SA_2A_1^{-1} = \begin{bmatrix} g_{11} & g_{12} & g_{13} \\ g_{21} & g_{22} & g_{23} \\ g_{31} & g_{32} & g_{33} \end{bmatrix} \qquad \textit{Equation 29}$$

Where S is the symmetry matrix which has 24 different patterns in cubic materials. A_1 and A_2 are the orientation matrices for crystal orientations before and after deformation respectively. The rotation angle θ between the orientations before and after deformation can be given by;

$$\theta = \cos^{-1}\left[\frac{g_{11} + g_{22} + g_{33} - 1}{2}\right] \qquad \textit{Equation 30}$$

Deformation of a single crystal sample involves simple shear and rigid body rotation – If rigid body rotation is taken out of the deformed sample the remainder is lattice rotation which results from the simple shear introduced by the operation of slip systems[170]. The active slip systems in the material that generate crystal rotation relative to the initial orientation can be estimated from slip bands, crystal rotation axis orientations and Schmid factors. The change in angle and rotation about the compressive axis as the pillar is compressed is important because work is being done on the crystal as the slip plane rotates. The compression therefore alters the primary slip system / activates any alternative slip systems that are dependent on the Schmid factor.

In a given crystal there are multiple slip systems that can be activated. During a compression test as the compressive load is increased the resolved shear stress τ_R responds according to;

$$\tau_R = \frac{Resolved\ force\ acting\ on\ the\ slip\ plane}{Area\ of\ the\ slip\ plane} = \frac{F}{A}\cos\emptyset\cos\lambda \qquad \textit{Equation 31}$$

F/A (the yield stress) is the stress in the crystal at which slip begins. Slip will occur when τ_R reaches the critical resolved shear stress τ_{crss}.

The shear stress acting on the $(11\bar{1})$ plane in the [011] direction in a Ni superalloy micro pillar exposed to a compressive stress of 900MPa (which is near the yield point of the micro pillars fabricated from MarM002 Ni-Cr-Al superalloy) applied parallel to the {001} direction can be calculated as follows:

$$\cos\lambda = \frac{[001].[11\bar{1}]}{\sqrt{0+0+1^2}.\sqrt{1^2+1^2+1^2}} = -\frac{1}{\sqrt{3}}$$

$$\cos\theta = \frac{[001].[011]}{\sqrt{0+0+1^2}.\sqrt{1^2+1^2+0}} = \frac{1}{\sqrt{3}}$$

$M = \cos\theta\cos\lambda = -1/3$

$\tau_{crss} = (900MPa).(-1/3) = 300MPa$

Vattre et al[13] the author of a study which examines how the τ_{crss} changes with applied strain used dynamic casual modelling (DCM) simulations in favour of finite element (FE) / dynamic dislocation (DDD) models and has modelled the dislocation interactions occurring through the γ/γ' channels.

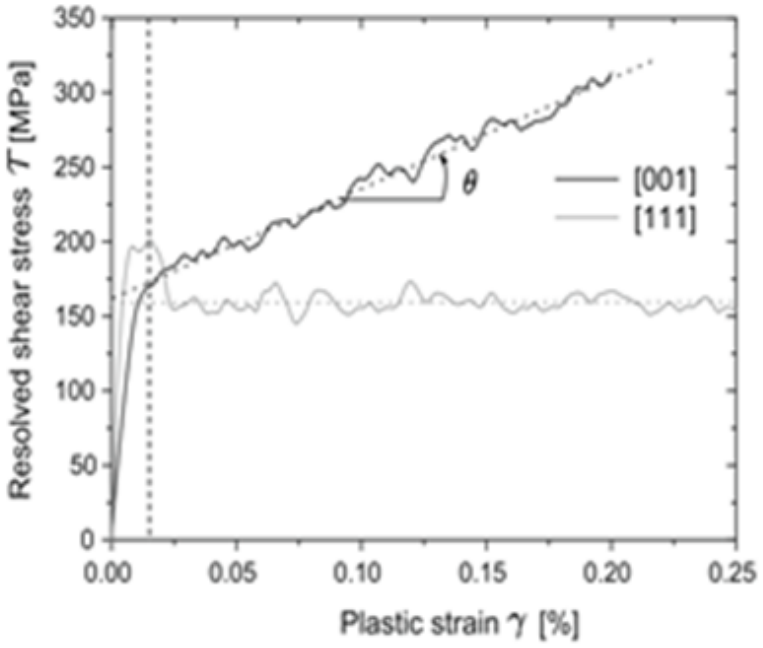


Figure 54: the evolution of resolved shear stress and dislocation density with increasing plastic strain, for the [001] and [111] crystal orientations in a single crystal Ni super alloy. Vattre et al,[13].

Figure 54, shows the evolution of resolved shear stress with plastic strain. The research was however taken on macro sized samples it can be used in direct accordance with studies undertaken on the microscale. If specific boundary conditions are altered.

High ion doses are unfavourable as the effects can influence the stress – strain response and deformation morphology of the micropillar[161]. High ion doses can influence the stress – strain response during deformation by introducing artefacts which disrupt dislocation flow. Earlier micropillar

compression studies[171,149] focused on the examination of the size effect. A phenomenon in which the resolved shear stress at yield increases with decreasing pillar size, quantified by the width of the pillar[123]. For this reason, the aspect ratio and areas of the pillars were not kept constant during preliminary testing, leading to results supporting the work of authors such as Raabe et al[15]. This will be discussed in more detail in the following chapter.

Two important theories supporting the size effect phenomenon help explain the importance of keeping the ion exposure of the micropillar low; source truncation[130] and exhaustion hardening[134]. With the importance lying in how the dislocations interact with each other in the presence of constricted volumes and foreign artefacts.

It is therefore very important to fabricate pillars with suitable geometries and minimal FIB damage. The FIB damage was minimised by using low ion currents and dwell times. The low ion currents were used at the final stages as the micropillar is “polished” establishing the final structure. Low dwell times were used for image correlation features pre-programmed into the milling scripts.

Once an ideal geometry has been achieved the fabricated micropillars can be compressed using a flat punch indenter mounted inside an SEM. To avoid contact with the side of the trench a 10 µm flat punch was used.

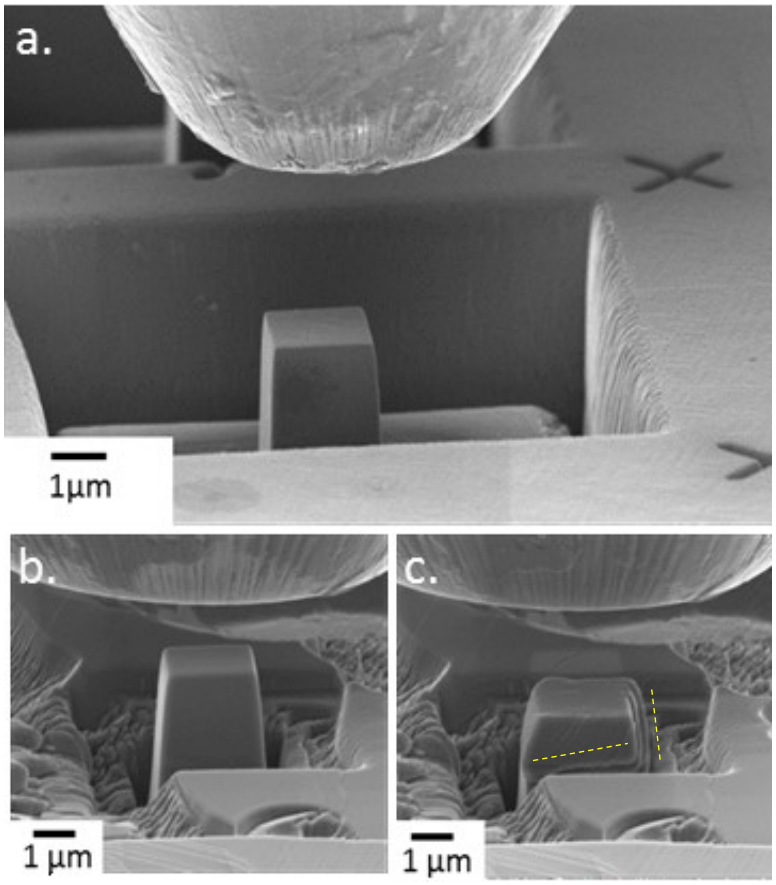


Figure 55: Flat punch interacting with micropillar (a) Aligning the flat punch to the top surface of the pillar, (b) Approaching the pillar - pre deformation (c) post deformation. The pillar dimensions change during compression based on the displacement used. The slip lines, which emerge as the pillar is taken past yield are highlighted in yellow.

Figure 55 shows the flat punch interacting with a micropillar and different stages of the pillar compression. It is important to align the flat punch with the pillar as traced by the shadow imprint of the compression tip on the top surface of the pillar. This is handled through careful control of the approach function. Lowering the speed of approach as the tip casts a shadow on the top of the pillar is important to avoid pre straining the pillar, thereby giving an accurate description of the stress- strain response and a repeatable testing criteria.

If the micropillar is deformed past the yield point, there is a clear shape change, as evidenced by figure 55c. The shape change is defined by the plastic flow carried by dislocations moving along set directions and planes. This was exemplified by figure 50a in which slip bands can be observed emanating from the edges of a macro indents and figure 50b, in which slip lines can be seen emanating ~45° through the cuboids in a sample orientated <100>.

The shape change combined by slip characteristics of the micropillars figure 55c (highlighted in yellow) can be used to quantify the deformation of the tested specimen. It is therefore important to take clear pre and post deformation images.

The level of strain can be controlled to examine the characteristics of the test specimen in the elastic, plastic or near yield conditions and be subsequently analysed using TEM and SEM based techniques.

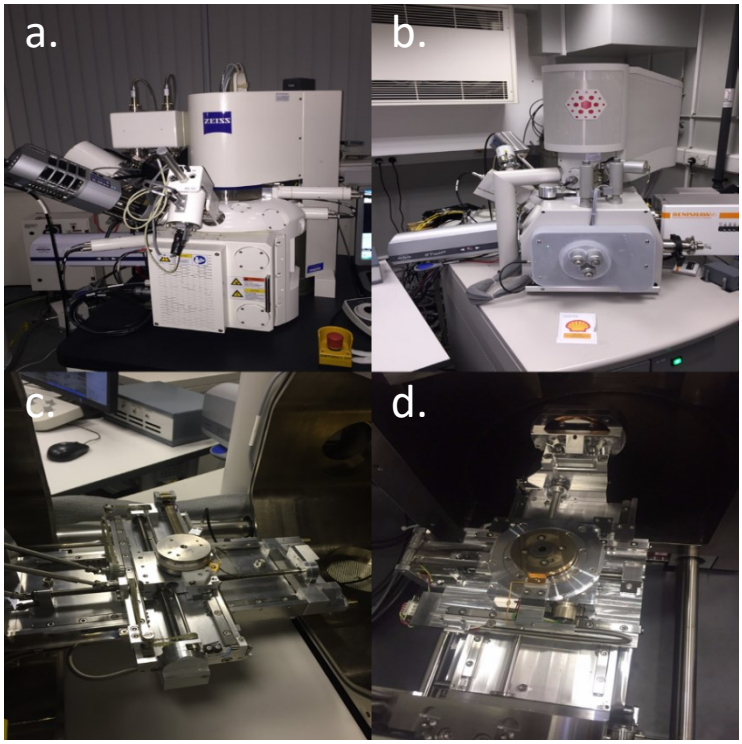


Figure 56: SEM machines used for in-situ testing (a) Auriga (b) Quanta (c-d) Inside of the SEM for the compression stage mount Auriga & Quanta respectively.

Figure 56, shows SEM machines used for in-situ compression experiments. The Zeiss Auriga was the first SEM used, followed by the Quanta environmental SEM. The Quanta has a larger chamber more suitable for *in-situ* testing. If a visual description is the most important testing criteria, for example for DIC, (at the time of testing) the Auriga would be recommended as it can achieve a higher spatial resolution. When examining for a visual description, a crisp image with good contrast is key. If the main testing parameter is mechanical data then a machine such as the Quanta, with a larger chamber is better. An ideal machine would combine the electron optics from the Auriga with the chamber of the Quanta. The working distance between the sample and the pole piece is also important to achieving a good image and must be taken into account. Achieving a good working distance becomes difficult when the *in-situ* testing frame is loaded into the SEM, due to the proximity of the frame with the pole piece. Therefore the orientation of the frame and the angle of the indenter must be taken into consideration when setting up the experiment.

The flat punch indenter is controlled via a displacement control and tests were typically performed at a constant displacement rate (5 nm/s). Tests in which the strain rate was varied, indicated that CMSX-4 in the <001> direction does not show strain rate sensitivity in accordance with the macro indentation

preliminary experiments. Different orientations were examined and the samples were prepared accordingly.

No heat treatments were performed on the alloys used in this study, at the risk of altering the microstructure and thus changing the mechanical properties. Changing the microstructure of the alloy can affect the coherency between the ϒ/ϒ' phases. Figure 57, shows the ϒ/ϒ' microstructure across CMSX-4 alloys exposed to different conditions.

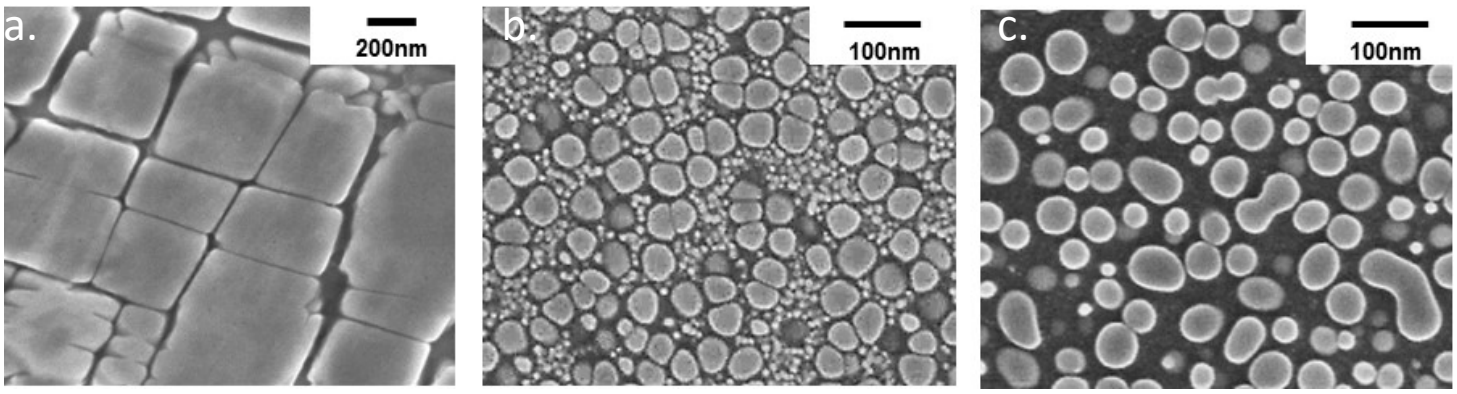


Figure 57:ϒ/ϒ' microstructure in (a) industrially prepared CMSX-4 illustrating square precipitates (b) FGH aged 700°C for 100h - spherical precipitates (c) FGH aged 850°C for 100h – largely disordered spherical precipitates.

Samples orientated so that the {011} and {111} were parallel to the compression axis, were cut from a {001} sample using a precision saw figure 62 and crystal orientations were first observed using Oxford Instruments software on a JEOL 6400 SEM. Sample etching and high resolution SEM revealed that the surfaces were cut in the correct orientation. However, the top and the bottom of the samples were not parallel, due to the error introduced by the saw blade. The un-parallel surfaces, resulted in a non-uniform compression surface and so an alternative method was used. The CMSX-4 sample was subsequently sectioned into the respective orientations using a goniometer stage.

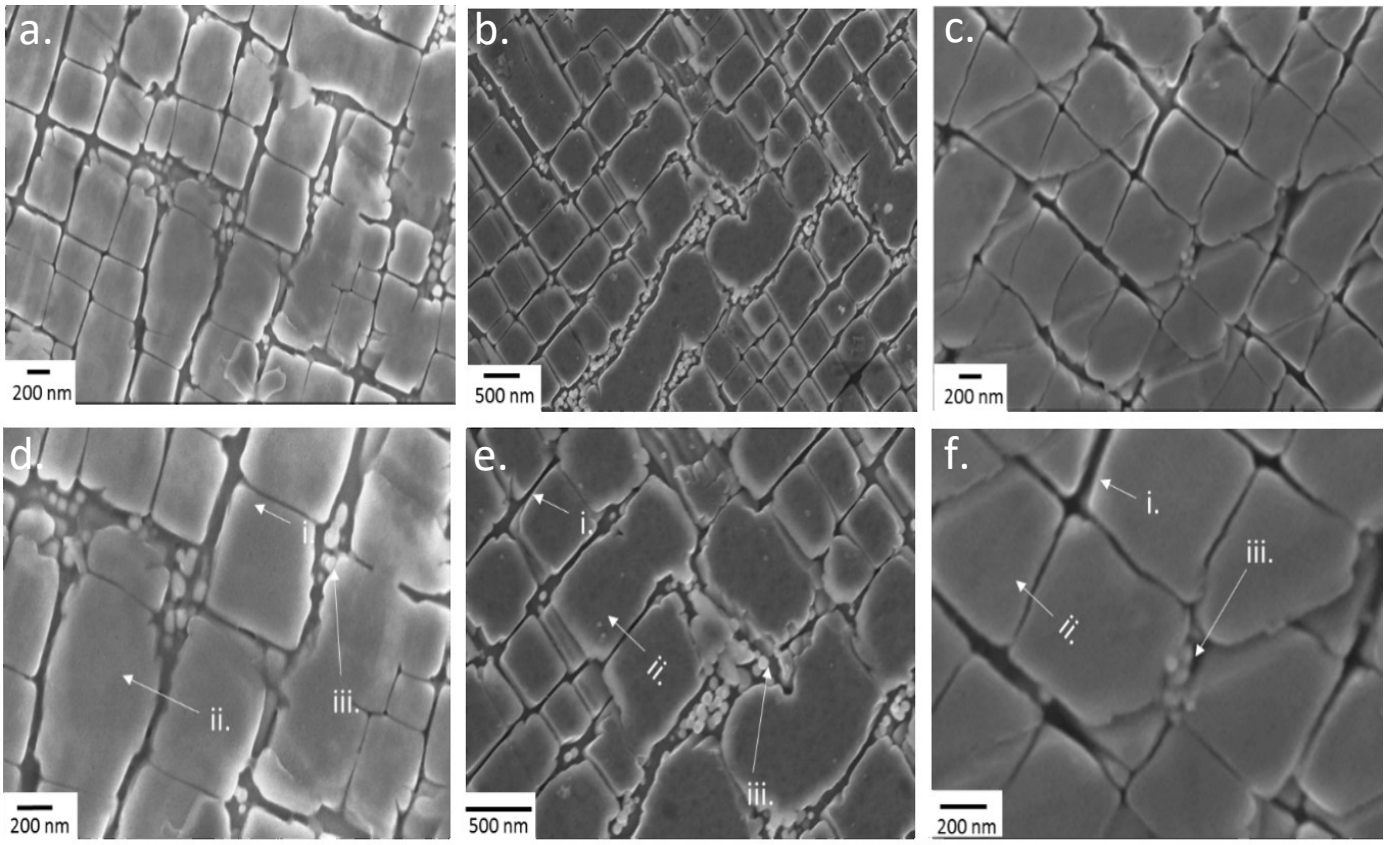


Figure 58: single crystal Ni superalloy (a&d) <001> (b&e) <011> (c&f) <111> (i) ϒ' phase (ii) ϒ phase (iii) ϒ'' phase.

Cutting with the goniometer stage provided two parallel surfaces; one, which was mounted to the stub, the other, pillars had been fabricated parallel to the flat punch. Two parallel surfaces are key to obtaining uniform compression and hence representative results via the *in-situ* compression.

Figure 58 illustrates the orientation of the disordered ϒ phase, the ordered ϒ' phase and the smaller ϒ'' phase, with the compression faces parallel to the <001>, <011> and <111> respectively. It can therefore be assumed that in a pillar with a top width of ~4 μm there would be ~4 ϒ' precipitates on the top surface of the pillar representing a volume fraction of ~70% of the total area. Alignment of the compression tool parallel to the top surface of the pillar is crucial to attaining uniform compression. Figure 59 indicates an ideal and non-ideal set up.

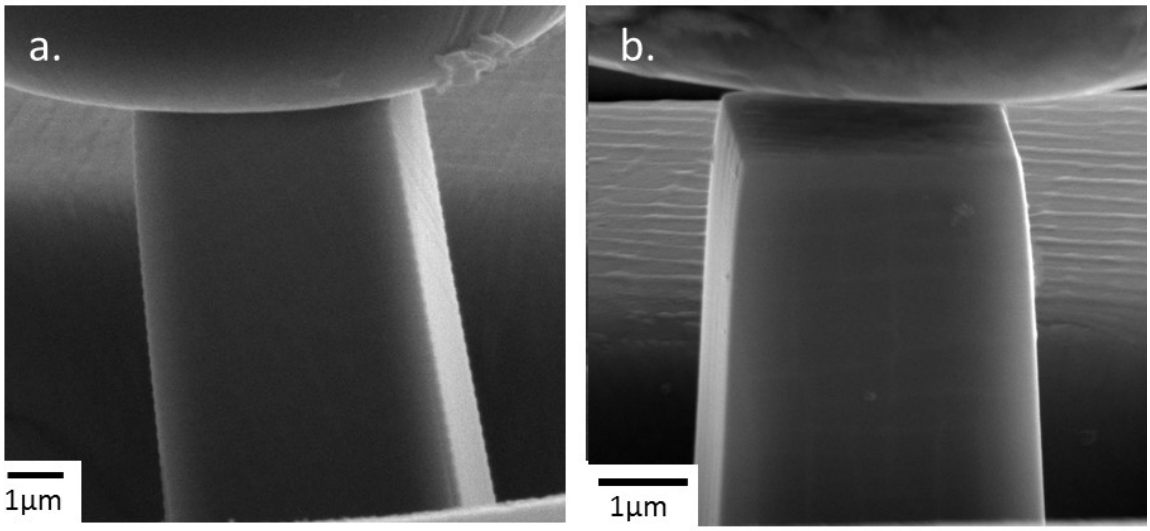


Figure 59: SEM images of single crystal micropillars taken on the Quanta environmental SEM AT 30° tilt (a) An un acceptable test set up, in which the pillar top surface is subtended to an angle with respect to the compression tip - non uniaxial compression (b) An acceptable flat punch set up, where the pillar top surface is parallel to the compression tip – uniaxial compression.

The second Ni super alloy sample under investigation was polycrystalline FGH-96 used for turbine discs. Micropillars with descriptions of width and height that enable the bottom and top surface to be viewed clearly, with no interference from milling features, were fabricated on select grains corresponding to the three principal axis of the fcc crystal structure {001},{011},{111} as quantified by EBSD and illustrated in figure 60.

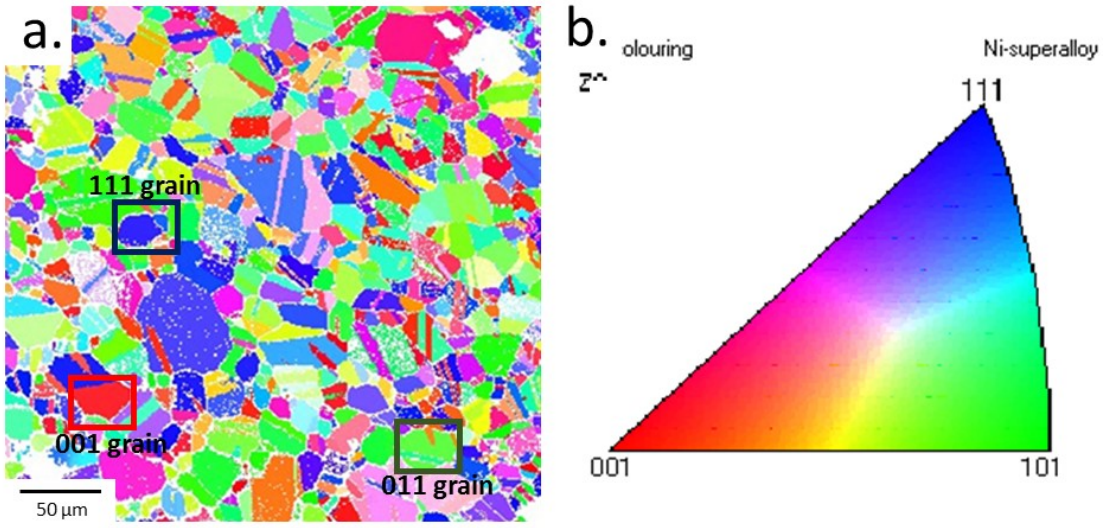


Figure 60: EBSD map of isolated region on FGH96 marked out by micro indents. The EBSD map was taken on the JEOL 6400. The red, blue and green grains are {001},{011},{111} grains orientated parallel to the compression axis. (a) EBSD map (b) Legend

The alignment of the orientation in figure 60 is in reference to the z axis. The geometrical In plane (x,y) rotation of these grains, as characterised by Euler angles, with respect to the compression axis were taken into account when examining orientation.

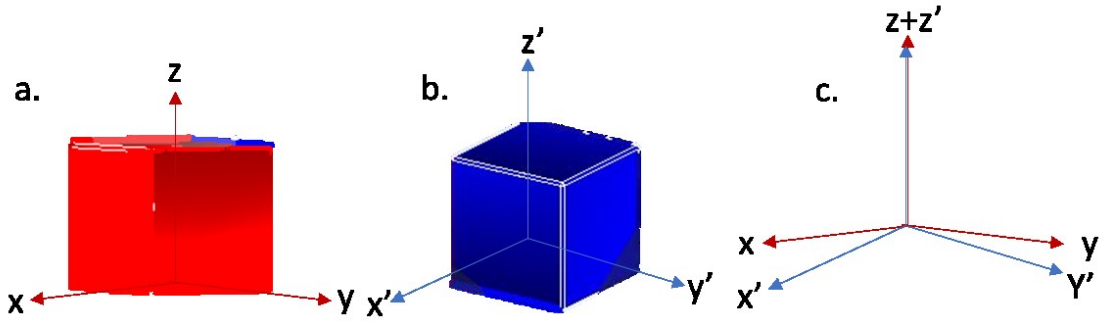


Figure 61: Crystal orientation of an fcc cube varied slightly by the x and y axis (a) orientation of near cube alignment i.e. x, y & z <001> (b) orientation slightly off cube alignment (c) representative axis denoted x,y,z, and x',y',z'

For example the Schmid factor, and thus the mechanical behaviour of an orientation in which all axis are aligned with the <001> directions would be slightly different than one in which the x and y axis are slightly off the (100) and (010) respectively.

The mechanical response and active slip systems were compared to the samples cut from single crystal CMSX-4 along the 45° degree angle (exposing the {011}) and 35.7° degrees (exposing the {111}) via a goniometer stage as shown in figure 62.

The crystal orientations of the pillars were measured from the top face of the pillars. This enables slip traces for deformed pillars to be characterised as the 3D geometry of the pillars is well described. The Schmid factor of the slip systems can also be evaluated considering a uniaxial compression of the pillar to assist in slip trace analysis as well as evaluation of the engineering yield stress of the pillar.

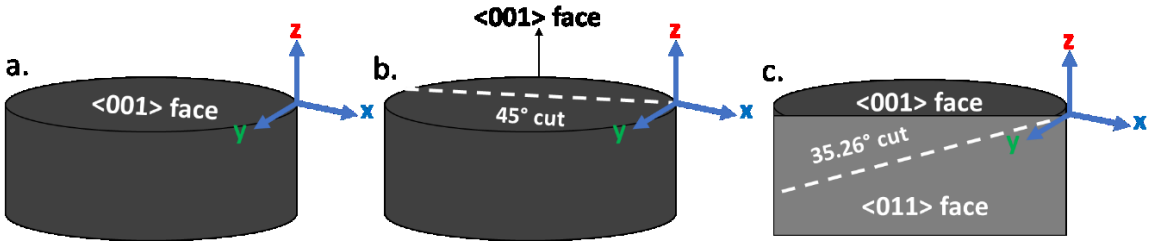


Figure 62: Schematic sample cuts <001> SX-CMSX-4 (a) as received (b) <011> (c) <111>

Ni is highly mechanically anisotropic with respect to orientation and microstructure, so the study of hardening, yield, elastic modulus and dislocation activity through different orientations and alloy types is an important development area for future alloys[172].

Understanding how the materials deform along these orientations and new microstructures can help programme the failure criteria of these alloys in commercial applications.

The third alloy system provided by a collaborating partner was carburised Ni CMSX-4 (second generation) and CMSX-10 (third generation). The carbide alloys under investigation currently have no commercial application. The carbide structures were formed as a by-product of pack aluminsation. The carbide types are different in character and orientation indicative of MC M_6C $M_{23}C_6$ carbide types with the deleterious TCP phases present also.

Micropillars have been placed along specific regions and consistent orientations within the carbide rich areas, on certain carbide phase clusters and in the bulk material. The results from micropillar experiments were validated by micro indent experiments Figure 50b, examined utilising the techniques developed from testing on virgin single crystal CMSX-4 and polycrystalline FGH96.

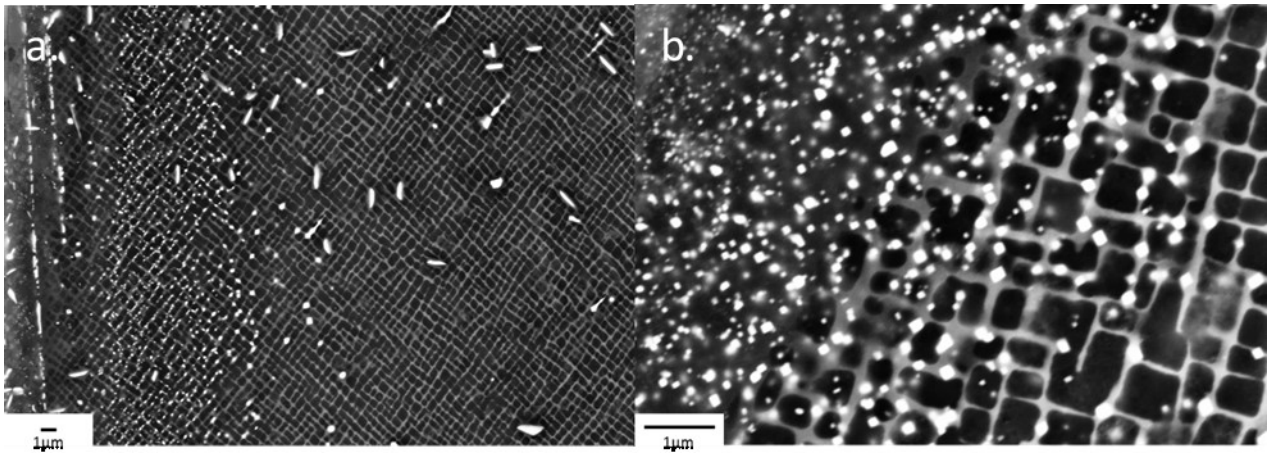


Figure 63: BSD images of carburised (a) CMSX-4 (b) CMSX-10 illustrating the different carbide types located within the ϒ/ϒ' microstructure. The carbide type phase in CMSX-4 extend ~120µm into the material from the outer edge. The carbide type phase in CMSX-10 extend ~30µm

The elemental information of the carbide alloys and the carbide type phases were measured predominately via SEM based EDS. EDS provides a resolution of up to 1 μm^2 and is useful for identifying elements local to the carbide alloy microstructure. EDS was also used on earlier alloys to identify alloying elements and compare the normalised mass % to literature.

Point scans at 20 kV were initially used on un carburised samples followed by area maps of roughly 2 μm^2 x 2 μm^2. On the carburised samples, point scans were initially used on carburised and un-carburised regions to first identify the key elemental differences. Line scans were then used to track the % increases and decreases of elements through carbide rich regions. Area maps of different sizes were used to measure the elemental information of individual carbide type phases and areas within the carbide rich regions and bulk regions.

Ni-based superalloys can be thoroughly characterised via SEM based techniques before mechanical testing. These microscopy techniques include SEM/BSD to examine the microstructure, SEM/EDS to identify the constitution of alloying elements present and EBSD to determine the crystal orientation

amongst other things. Crystal orientation, alloying elements, and microstructure all play a crucial role in the mechanical performance of Ni based alloys and thus a full analysis is necessary prior to testing.

Once characterised prior to deformation, the sample can have micropillars fabricated along regions of interest and or in distinct orientations. For example, pillars fabricated on a pure un carburised CMSX-4 sample in the <001> at slightly different angles, will result in different deformation behaviour due to the differences in crystal orientation. It is therefore important that a comprehensive characterisation of the sample is done prior to deformation.

5.2. Electron microscopy imaging with scanning electron microscopy: secondary electron, backscatter electrons and electron backscatter diffraction

An SEM was used for visual inspection of the surface place prior to testing, examination of the deformation as it happens *in-situ* and for high resolution imaging of the deformed sample.

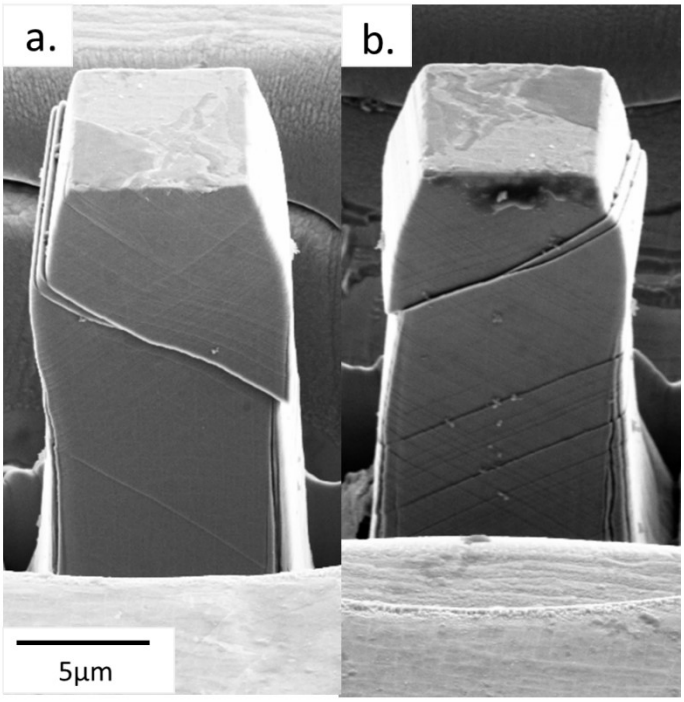


Figure 64: A CMSX-4 pillar deformed to 20% strain set up in the <011> orientation imaged on the Sigma SEM at 52° tilt (a) front face of the micropillar (b) back face of the micropillar

One of the main signal carriers in an SEM are secondary electrons, which are low energy particles with an average energy of 5 eV. A 5 kV operating voltage with a working distance of 8-10 mm was sufficient to give a good visual description of the features to be examined during this study. Four SEM machines were used throughout this study for different purposes; JEOL JSM 6400, Zeiss Auriga, FEI Quanta FEG Zeiss ESEM, Sigma 300. With focus being placed on the Sigma and the Quanta.

The SEM in the Sigma uses a Gemini optics system that reduces field influences (due to the electron optics) to a minimum and enhances focus of the electron beam, increasing spatial resolution and reducing signal noise. The magnification on the Sigma ranges from 10-1,000,000 x and has a resolution of 1-1.5 nm. It was used to image samples to a high-resolution utilising both SEM and BSD modes.

The mounted Alemnis stage in the Quanta tilts the surface plane to 30 ° during *in-situ* tests, whereas in the Sigma, the stage was tilted to 52° for image analysis as this gives the best description of height for visual inspection as illustrated in figure 64. The tilt angle is considered when measuring height, width, and angles of test specimens.

The SEM in the Quanta was used to examine the deformed pillars *in-situ*. BSE on the Sigma was used to examine the ϒ/ϒ' volume fraction across alloys and the carbide phase morphology in the carburised samples.



Figure 65: Image correlation using image j to determine the size of the ϒ/ϒ' particles (a) Unaltered image (b) Edited / altered image required for effective analysis (c) Resultant image illustrating 76 distinct particles.

Figure 65, shows the image correlation used via image J, to determine the size of the ϒ/ϒ' particles. When taking BSE images, the brightness and contrast, working distance and scan speed are crucial to obtaining good images. I use a scan speed of 7 a medium brightness and high contrast. It best to focus the area well in SEM mode after inserting the detector. The contrast and brightness will need to be adjusted accordingly when switched to BSE mode. The most crucial feature in obtaining a crisp image with good compositional contrast is the scan speed. Figure 66, shows BSE images of ϒ/ϒ' taken with different scan speeds.

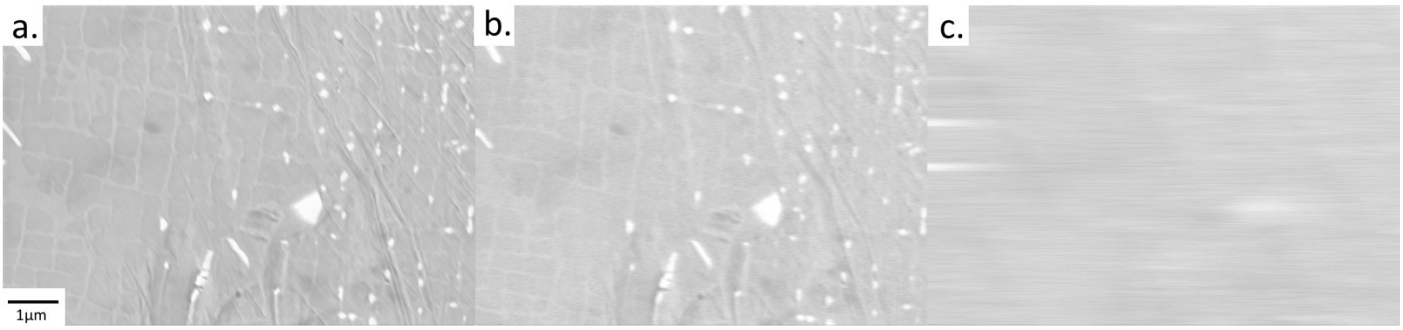


Figure 66: BSE images with different scan speeds (a) 10 (b) 6 (c) 3

BSE are high energy electrons, where typically> 15 kV are used to image in this mode. BSE give images that vary in compositional contrast. The strong compositional contrast comes from the proportional relationship between the BSE η coefficient and atomic number. Areas with a high atomic number will appear bright, whereas areas with a low atomic number will appear dark. In this study for BSE imaging a high voltage 20 kV and low working distance 5-8 mm worked best.

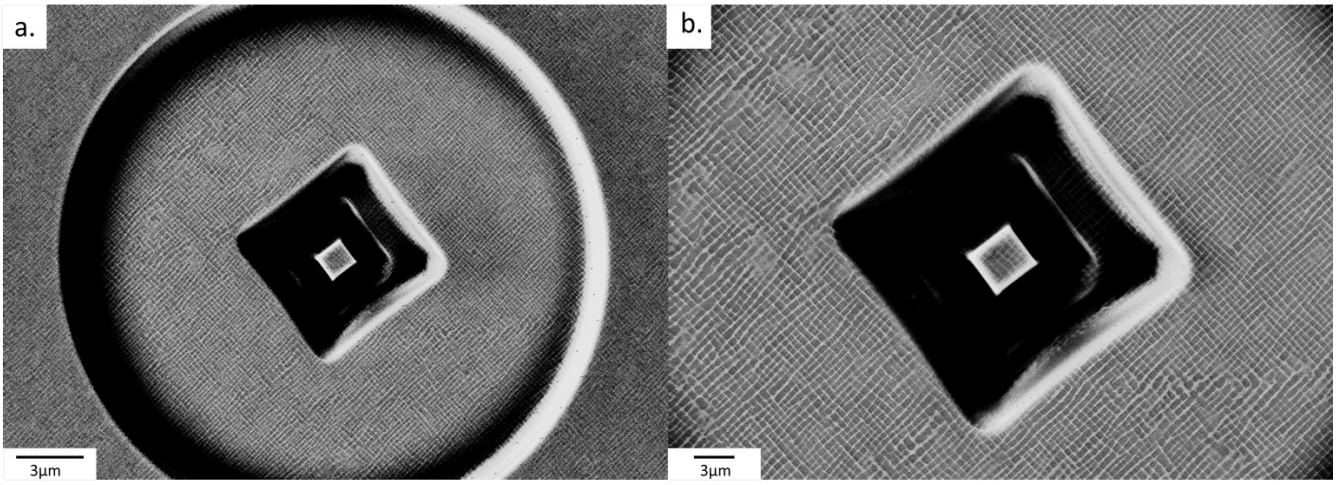


Figure 67: Birdseye view BSD image of a <001> CMSX-4 micropillar (a) Far (b) Close. Illustrating the clear distinction between γ/γ'

Figure 67, shows a 'birds eye' view BSD image of a <001> CMSX-4 micropillar. In the case of the carburised samples, BSD was used extensively. The images were analysed using ImageJ and the carbide phases, characterised through shape descriptors, which describe, the solidity, roundness, aspect ratio and area of the different carbide type phases.

EBSD is an SEM based technique that provides quantitative information about a materials microstructure, namely the crystallography, grain size, grain boundary character, texture, grain orientation and phase identity[173]. The angular resolution is roughly 0.5° and generally for modern SEM's like the Quanta or Sigma, 10-20 nm grains can be measured with good accuracy[173].

EBSD works by orientating a sample with an excellent surface finish 70° to the incident electron beam. The sample must be smooth and free of any sectioning damage as the EBSD pattern is generated from a very thin surface layer (~40 nm)[173]. The accelerating voltage is high usually 20 kV. When the electron probe hits the surface of the sample under investigation an EBSD pattern emanates spherically from the incident point. As the beam interacts with the samples crystal lattice, low energy backscattered electrons are produced. They emanate from the sample spherically causing constructive and destructive interference. If a phosphor screen is placed incident to this beam a diffraction pattern is produced, in the form of Kikuchi lines. Analysis of the Kikuchi lines can provide a detailed description of the materials crystallography and grain structure.

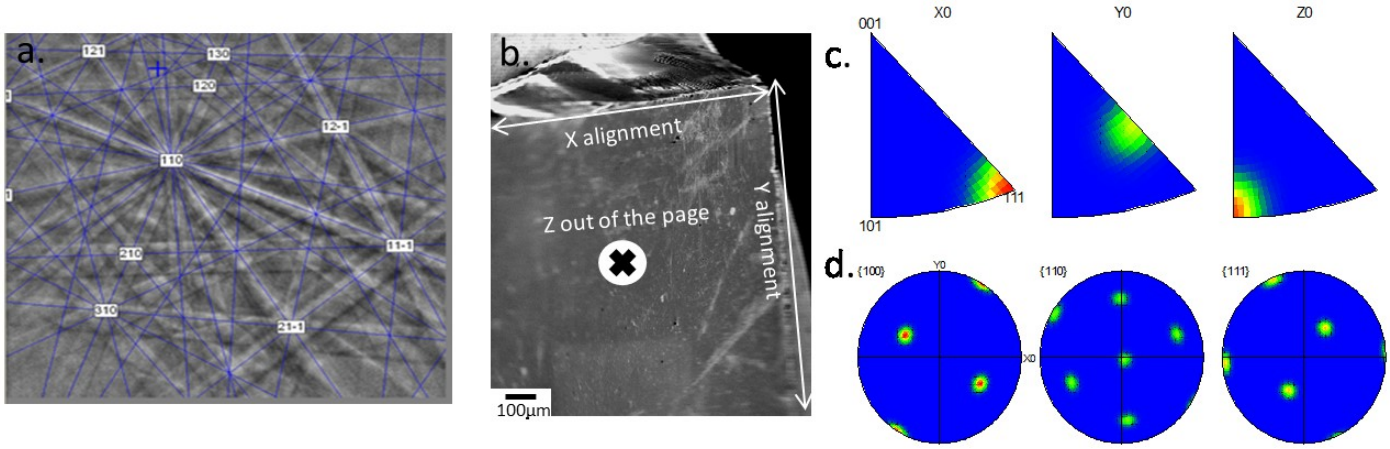


Figure 68: SEM/EBSD data from a Si sample(a) Kikuchi pattern illustrating the band centres aligned with the 110 direction (b) SEM image of Si edge aligned with the x & y axis (c-d) Inverse / pole figure respectively.

Figure 68, shows the SEM/EBSD orientation data from a Si sample. The samples were aligned in the x and y direction along set axes or a fiducial marker in the case of circular samples. This technique was used on a consistent basis to ensure the orientations were correct for each test. A working distance of 19 mm was used for the Ni super alloy samples, with an aperture size of 3000 µm and a probe current of 20 kV the samples were focused and aligned for astigmation accordingly.

5.2.1. Focused Ion Beam

A Helios Nanolab 600, with dual beam SEM / FIB capability was used to fabricate the micropillars in this study. The machine is equipped with an Elstar electron column with a FEG electron source that is capable of 1-2 nm resolution and the Ga+ ion source can image and machine down to 5 nm resolution levels[174]. The machine is also equipped with an OmniProbe, which is an in-situ tool for sample lift out that allows the preparation of site specific TEM samples.

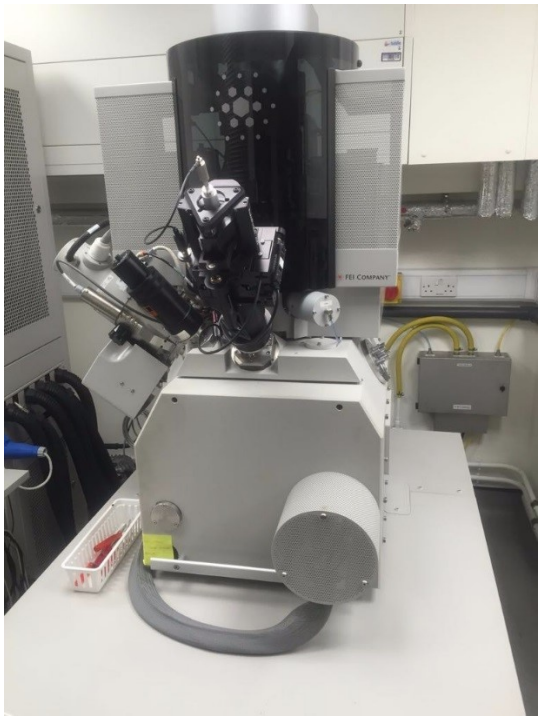


Figure 69: Helios nanolab

Figure 69, shows the Helios Nanolab used to fabricate pillars during this study. Penetration of the ion beam into the sample varies with different materials and crystal orientations. The secondary electrons for images can be collected via a multi-channel plate or electron multiplier. Secondary ion imaging provides a different type of contrast when compared to secondary electron imaging. A dirty metallic sample that contains some insular material can result in charging in which an excess positive charge is accumulated. Insulating regions appear dark, conductive light and the contrast is switched in the SEM. Platinum can be deposited by ion beam via assisted chemical vapour deposition of a precursor organometallic gas.

The process works via the delicate balance of the sputtering and deposition. The gas molecules are absorbed on the surface near the gas inlet, but decompose only where the ion beam strike. The deposition of platinum onto the surface of a sample is a chemical vapour deposition process. Platinum deposition was used to shield the micropillar from FIB damage when preparing samples for TEM.

The advantage of having an SEM is that non-destructive imaging can be done where the more complex the material unit cell, the larger the amorphous layer will be. Materials with smaller unit cells are harder to amorphize. To counter this in specimens prepared in this study both for TEM and micro compression the ion current density is reduced incrementally at each fabrication stage to minimize damage to the pillar[175].

There is a difference between damage due to inherent ion-solid interactions and redepositon artefacts. It is stated by research[161] that Ga implantation is due to redepositon artefacts and not inherent ion-solid interactions. Problems associated with redepositon include; sidewall sloping, undesired topography, Ga+ implantation. The response of a given target material to the ion beam is strongly dependant on factors such as; beam current, Incident ion energy, trench / feature geometry, raster pattern and milling angle. In order to fabricate a pillar the microscope must be aligned accordingly.

5.2.2. Aligning the dual FIB/SEM

Aligning the dual FIB/SEM and adjusting for the eucentric motion is crucial. A focal point should always be used when aligning the FIB and SEM, with the eucentric height between the SEM and FIB being 4 mm. The eucentric height is controlled by the z stage and is the height at which the FIB and SEM come into mutual view point.

In this instance an array of micropillars manufactured via the Nanobuilder software will be used as the reference point figure 71. Use of the Nanobuilder software will be outlined later.

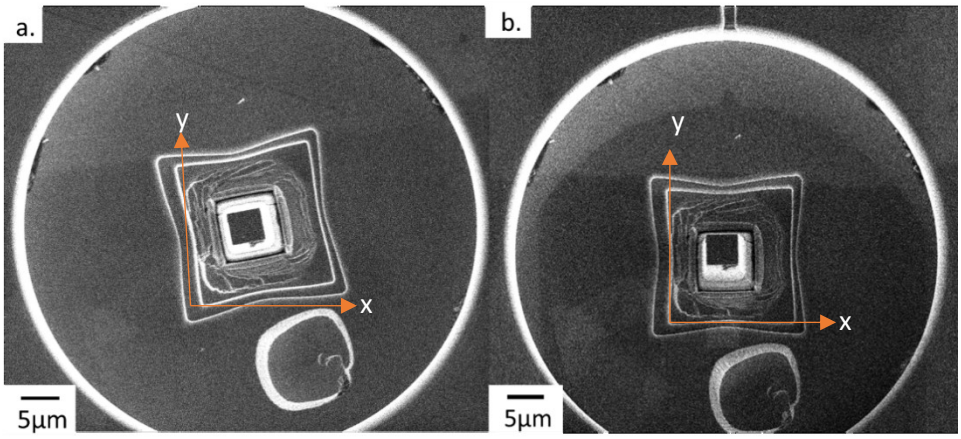


Figure 70: SEM screen image of micropillar (a) misalignment (b) aligned correctly

In the first instance regarding the SEM screen, the alignment should be specified. The pillar in figure 70a is not aligned correctly, whereas the pillar in figure 70b is. Whereby the x and y axis of the trench correspond to the x and y axis of the microscope. Any other fiducial marker with an x and y axis can be used.

The view in the SEM screen is 52° off the viewpoint in the FIB screen. Therefore for milling, the stage must be tilted to 52° and the viewpoint of the SEM and FIB are switched.

In tilting from 0-52° the drift in the eucentric height must be taken into account and is corrected for by adjusting the z height at various degrees of tilt. For example aligning the mouse cursor to a focal point as shown in figure 71 a i and figure 71 b ii and adjusting to realign to the focal point (middle of the pillar)

by adjusting the z stage. This will ensure the focal point remains constant in light of drift and aperture adjustments.

The aperture adjustment can be adjusted in the ion beam column section of the software, in which the focal point is centred by pre-programmed axis in the software at the different currents used for milling. For example at 21 nA, 9 nA, 0.92 nA.

Imaging with the FIB should be minimised at all times to avoid introducing defects into the top surface of the pillar as discussed above and therefore eucentric adjustments should always be done using the SEM screen. Alignments for the FIB apertures should always be done on non-important regions or on the sample stub.

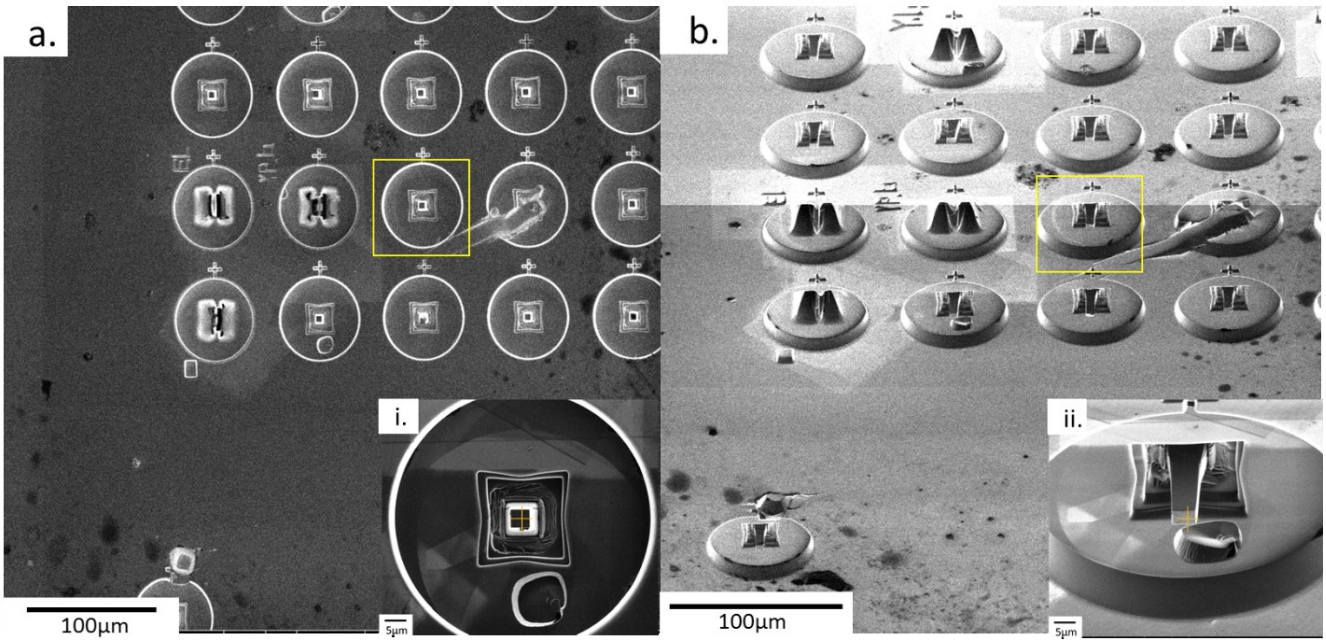


Figure 71: Dual SEM/FIB image screen at 0° tilt on the Helios Nanolab (a) SEM screen (i) micropillar with focal point for eucentric height adjustments (b) FIB screen (i) tilted micropillar.

5.3. Pillar manufacture

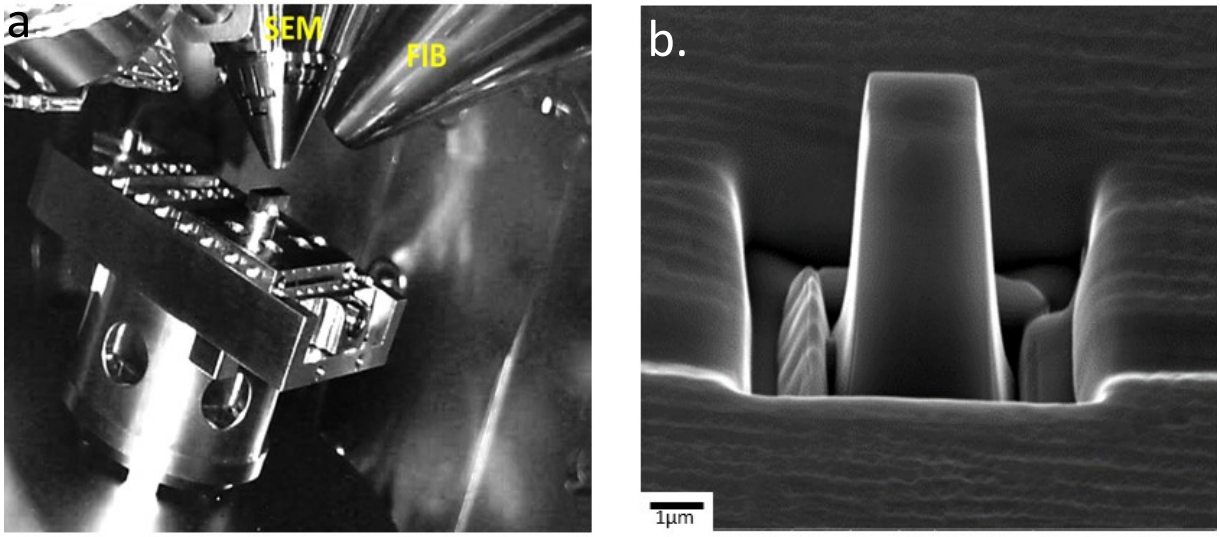


Figure 72: (a) Helios stage set up for fabrication of micropillars 52° tilt (b) First generation micropillar

5.3.1. Method

An automated script was used to create rectangular pillars, with a low taper angle and a good description of height. A taper angle can be defined as the angle between the tangent of the pillar wall and the axis of the pillar[176]. Pillars were fabricated with probe currents of 21 nA, 9 nA, 6.5 nA and 0.92 nA for trenching, rough cutting, and final polishing steps respectively. A low probe current allows more intricate shapes to be fabricated but requires longer processing times. A high probe current minimises time constrains but reduces resolution. A compromise between several currents is therefore needed. Low currents were used at later stages to minimise redepositon and enable a finer rectangular geometrical shape as mentioned above.

The Nanobuilder software was used to fabricate the second generation of pillars. It works in a CAD like process where a series of layers that correspond to process variables; layer thickness / sample depth, beam voltage / current and scan directions, all of which can be built to form a desired shape on the micro scale.

Fiducial markers are placed at strategic points to ensure beam stability / drift do not compromise the fabrication process. The use of the fiducial markers is important, as every time the probe current is changed there is an aperture misalignment. The aperture misalignment requires the system to re-focus and find the equilibrium position, which is found via the fiducial marker.

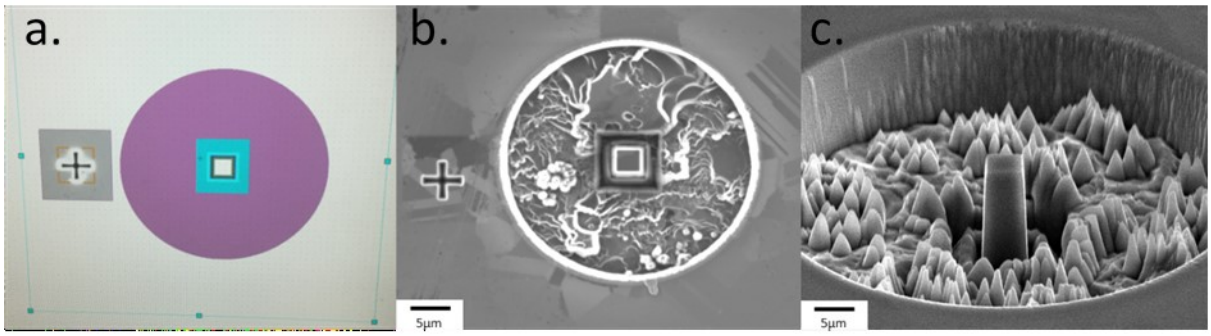


Figure 73: Pillar fabrication (a) Nanobuilder scripting screen (b) Birdseye view of fabricated pillar via FIB (c) Planar view of pillar from SEM

The new version of the Nanobuilder software offers several features over its predecessor and the old scripting system used for the first generation of pillars in this study. Features such as; reduced area correlation alignment, in which only the area around the fidicual marker is scanned, therby protecting other areas of the sample from ion beam exposure. Alignments which provide a corrective step to align the miscroscope scan field to the substrate, such as drift alignment in which drift can be accounteed for at fixed intervals during patterning by realigneing. After the alignment is defined and programmed it must be assigned to a layer. A layer corresponds to a series of shapes that can be programmed to create the desired 3 dimensional geometry. The software gives an option for a series of layers, in which within each layer there are specifications such as scan direction and depth.



Figure 74: Fabrication parameters

Shapes can be ascribed to each layer, to build up the desired pattern. The dimesions of the shape, the ion flux, depth and the milling (scanning) direction can be changed accordingly to give the desired 3 dimensional shape. The scanning direction is important to give a smooth finish and avoid redeposition. The nanobuilder offers 6 different scan directions see figure 75.

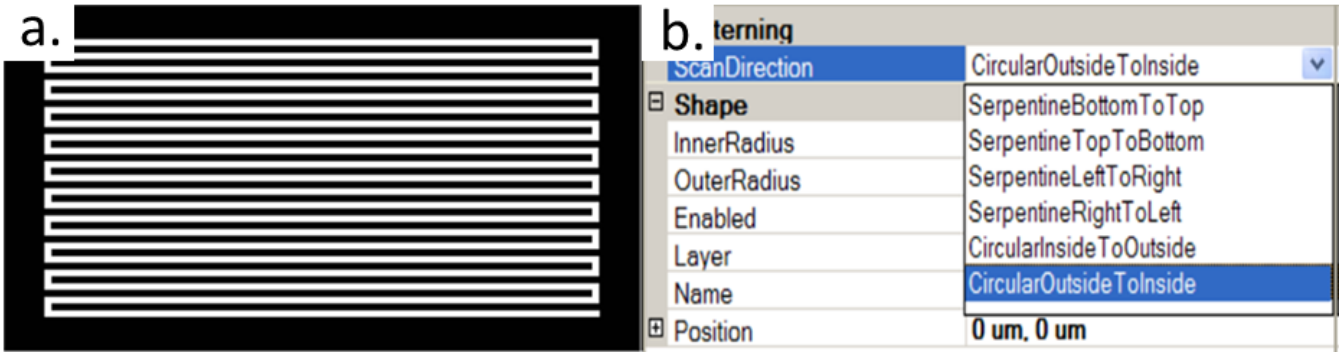


Figure 75: (a) Mathematical serpentine image (b) Scan direction parameters

Serpentine scanning was used for the majority of the fabrication process' used in this study.

5.3.2. Fabrication

To specify the depth of the milled region (which changes depending on orientation and sample type) the thickness was used. The fluences, passes and time were then calculated accordingly.

A typical thickness setting on an single crystal Ni superalloy aligned <001> to attain a height of 13 µm would be 2.4 µm and would take ~40 minutes on a 21 nA current. This value varies across alloys and orientations.

$$Fluence = \frac{Thickness}{VolumePerDose} \qquad \textit{Equation 32}$$

$$FluencePerPass = Current\,.\,Pitch^2\,.\,DwellTime \qquad \textit{Equation 33}$$

$$Passes = INT\left[\frac{Fluence}{FluencePerPass}\right] \qquad \textit{Equation 34}$$

$$Time = Passes\,.\,TimePerPass \qquad \textit{Equation 35}$$

Equations 32-5: Depth parameters in Nanobuilder software appended by the thickness

The pillars for this study were prepared using the Nanobuilder software after the initial size effect study. Pillars were fabricated in a series of 5 layers from rough to final polishing. This gave rise to an ideal

geometry and the taper / undesirable material was removed manually by tilting the stage ± 2° and cleaning.

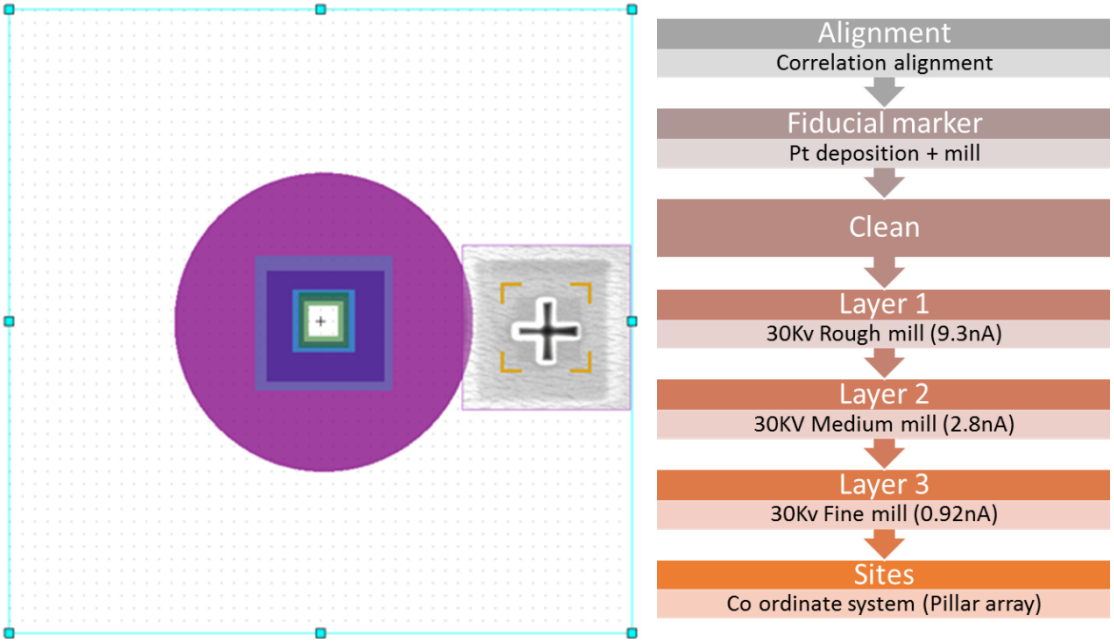


Figure 76: Nanobuilder command screen 2d micropillar blueprint

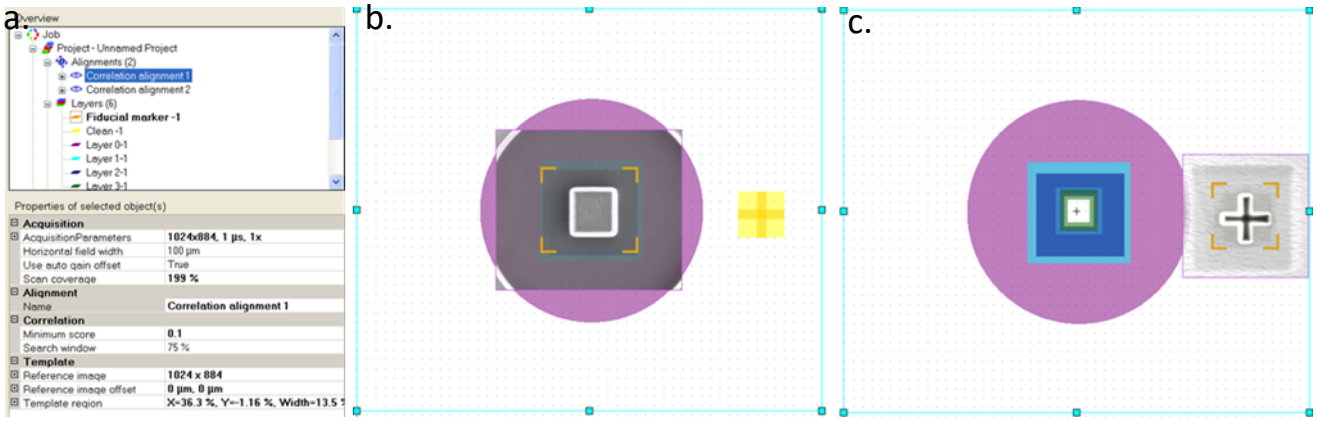


Figure 77: Correlation alignment (a) Command screen (b) Top surface of the pillar (c) Fiducial marker

The initial structure formed in the rough milling at 21 nA has a width of 30 µm which is slowly taken down to 5 µm through a series of steps as illustrated in figure 78. Correlation alignment and line scans are used to ensure a stable shape at each aperture stage and to correct for drift in the microscope. Two correlation alignments were used, one across the fiducial marker and one with a lower dwell time and ion flux on the top surface of the pillar.

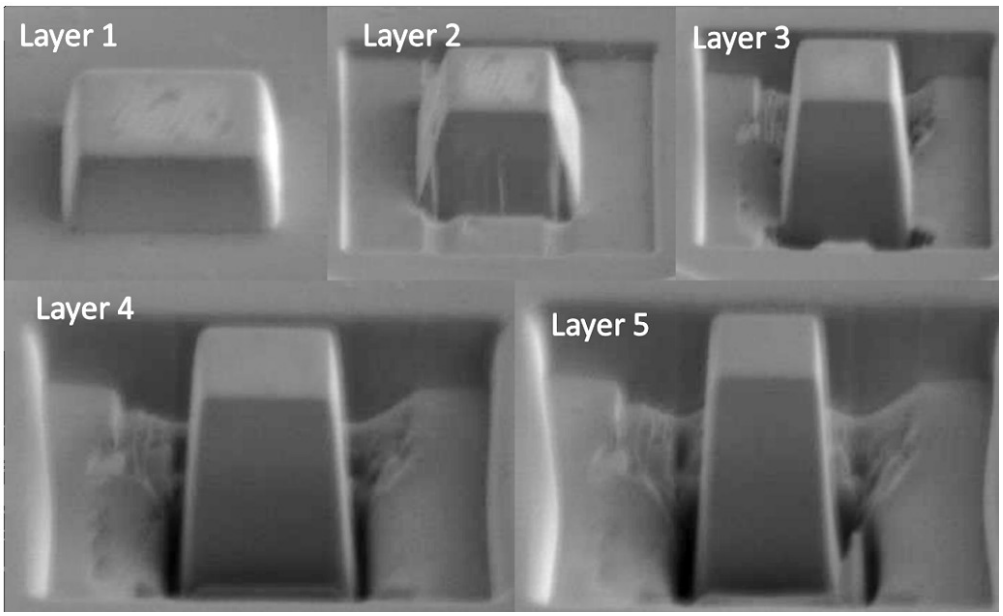


Figure 78: The FIB fabrication of 5 µm micropillar in 5 layers

5.3.3. Pillar fabrication for Transmission Electron Microscopy (TEM)

The FIB can also be used to prepare TEM samples in which selected areas are deposited in an organo platinum compound and sectioned at different currents to produce a "slice" ≤ 10 µm. The slice is then transferred onto a foil via an omniprobe and thinned / polished similar to a grinding / polishing regime for an alloy but instead using a variety of beam voltages and currents until an ideal thickness ~ 400 nm is achieved. Once the sample is ready it can then be carefully transferred to the TEM.

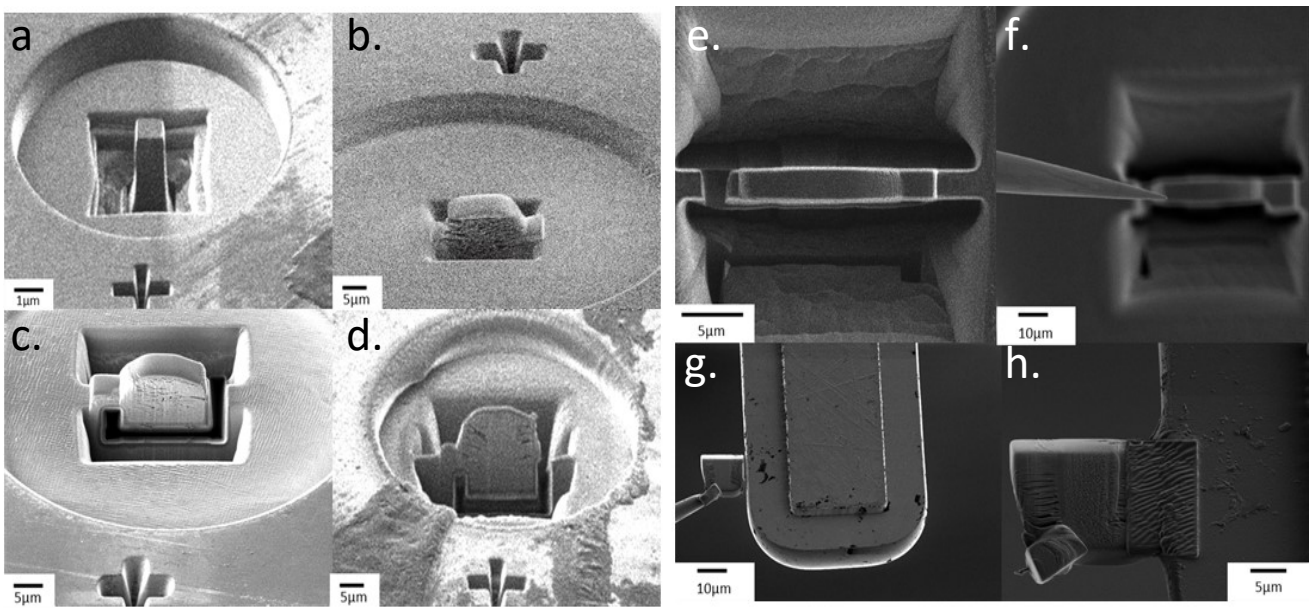


Figure 79: Pillar sectioning for TEM. SEM screen (a) un touched pillar (b) Pt deposition over pillar (c) sectioned pillar (d) Thinned pillar section, showing the pillar outline FIB screen (e) pillar section (f) Insertion of omni probe to remove pillar (g) grid alignment with pillar section (h) pillar section attached to foil ready for thinning

5.3.4. TEM

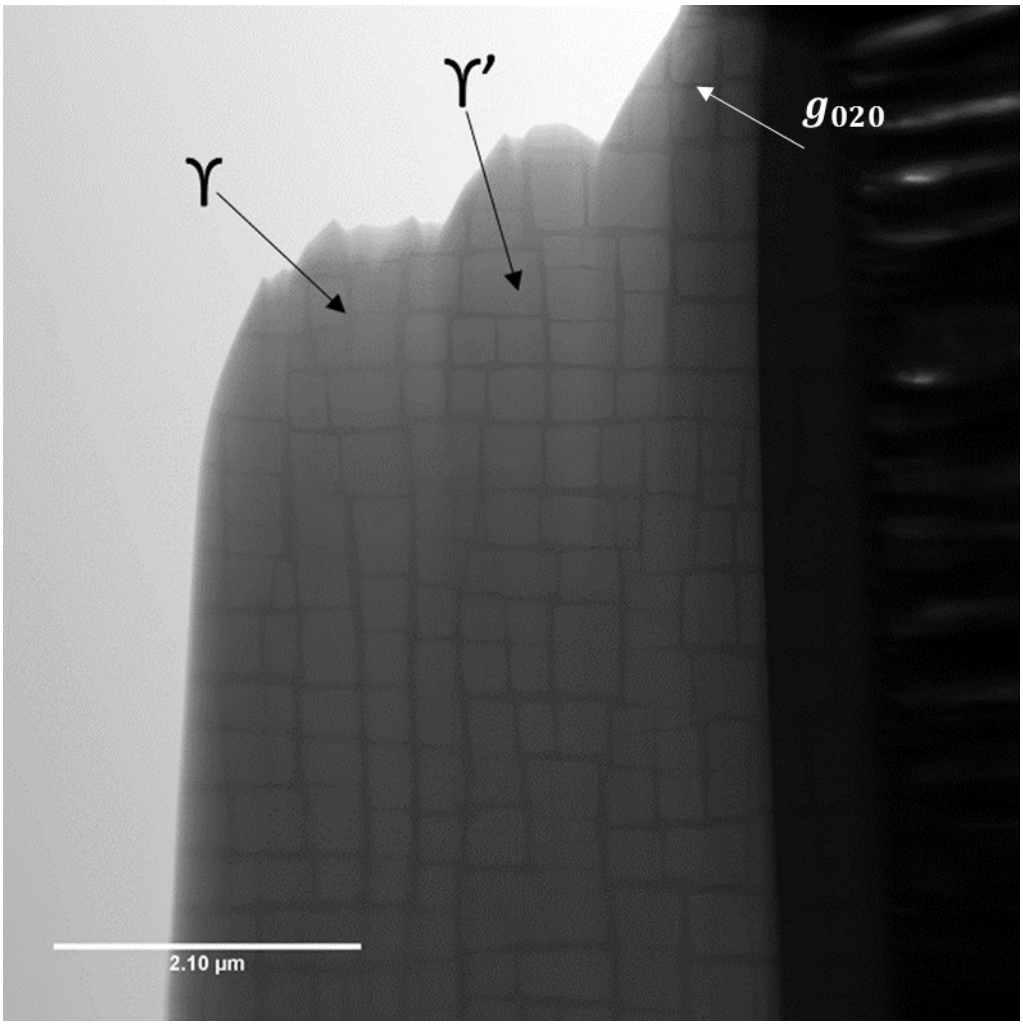


Figure 80: 3% Dark field TEM image of strained single crystal CMSX-4 micropilar in the <001> orientation, the diffraction spots can be seen below in figure 82.

The TEM works by shining a beam of electrons through an electron transparent (~400 nm) sample in which the viewing modes can be adjusted by aligning the subsequent beams which penetrate through the sample.

A stationary image, a scanned image and a diffraction pattern amongst other modes can be used to examine the internal structures in the micropillar. The imaging modes, dark and bright field are useful for different reasons.

The transmission electrons are used to form either an image or a diffraction pattern and this is due to the alignment of the beam. When using the microscope in conventional imaging mode, the objective aperture is used to select only one electron beam from which to form the image.

A bright field image is formed if the directly transmitted beam is selected and a dark field image if a diffracted beam is selected.

A diffraction pattern is formed in the back focal plane of the objective lens. If this condition is met and the objective aperture removed, the diffraction pattern will be visible on the final screen.

Figure 80 shows a bright field image of a lightly deformed pillar, showing minimal dislocation activity. The ϒ/ϒ' structure can also be viewed clearly due to the differences in crystallography as illustrated in figure 83. A diffraction pattern is useful as it can be used to quantify strain introduced by deformation and or precipitates such as carbide type phases.

The most important and time consuming aspect of TEM imaging is the alignment which needs to be done carefully before an image can be produced. The contrast of the sample can be altered according to the thickness of the foil. It is therefore imperative to try and keep the thickness constant when comparing patterns in the same data set.

This is done in the FIB thinning mode as explained above. When preparing a heavily deformed pillar, it is best to leave a thick section across 25% of the pillar to ensure stability of the localised slipped region. Ensuring structural stability of the foil is very important.

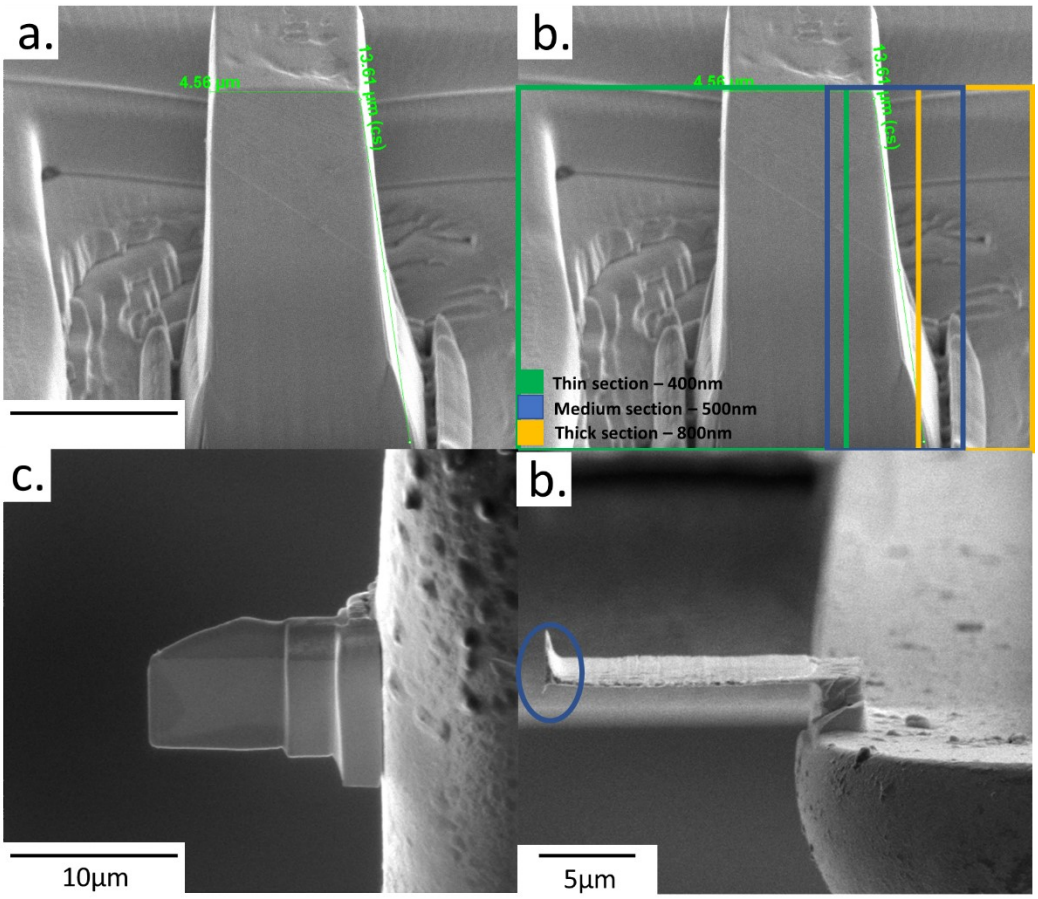


Figure 81: Micropillar preparation for a TEM foil (a) deformed micropillar showing a clear slip line (b) schematic over the micropillar indicating how the thickness of the foil can be graded to ensure structural stability (c) TEM foil attached to grid showing graded structure (d) an un ideal geometry with a thick section highlighted that should always be removed.

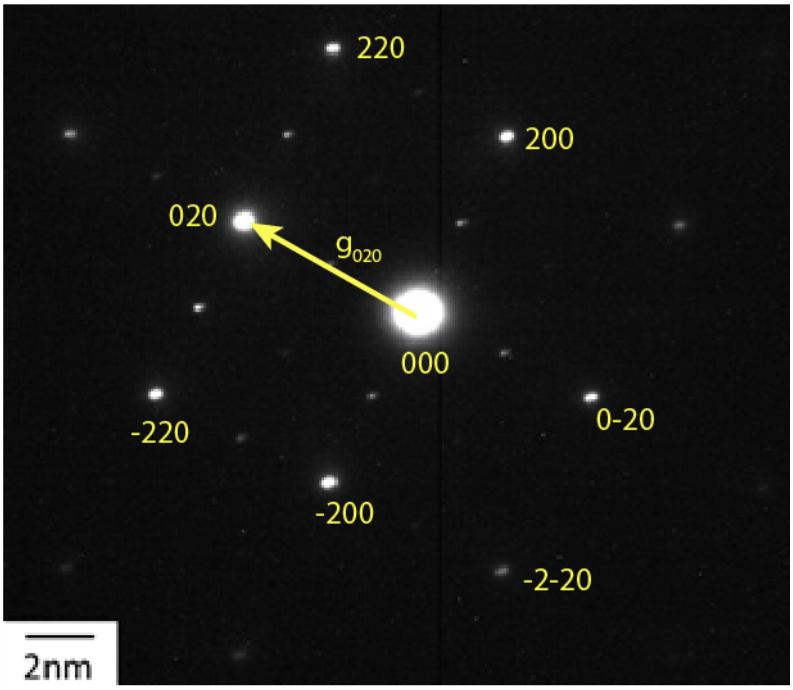


Figure 82: single crystal CMSX-4 <001> transmission mode diffraction pattern of ϒ/ϒ' microstructure

Figure 82 shows the diffraction pattern of both the disordered and the ordered ϒ / ϒ' phases. Using an undeformed foil as reference, one can map the level of deformation in transmission mode by comparing the TEM image of a deformed sample to a reference pattern as shown above in figure 82 . Transmission mode accounts for a large area and any bending in the foil as a consequence of the deformation should not interfere with results. However scanning pixel by pixel in scanning mode in a similar method to EBSD map straining would become more difficult. The large white spot in figure 82 is indicative of the 001 axis the smaller spots surrounding the large central spot are diffraction spots from ϒ'. Figure 83 shows this with greater clarity.

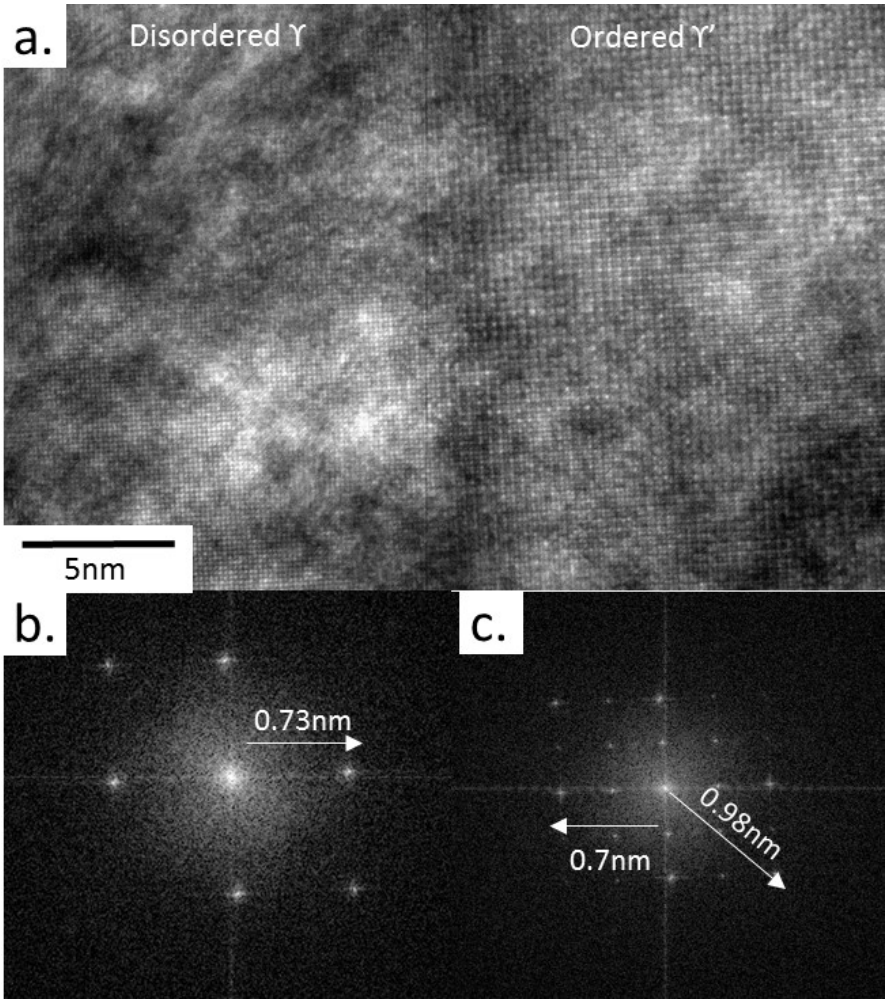


Figure 83: lattice image of ϒ/ϒ' with diffraction patterns of (b) ϒ (c) ϒ' analysed via FFT

The characterisation of microstructure and crystallography can be viewed via the TEM. The ordered and disordered structures of the ϒ/ϒ' microstructure can be viewed above, and the dislocation substructure can be identified through alignment of the incoming electron beam direction with respect to specific crystallographic directions and the relative contrast of the dislocations present.

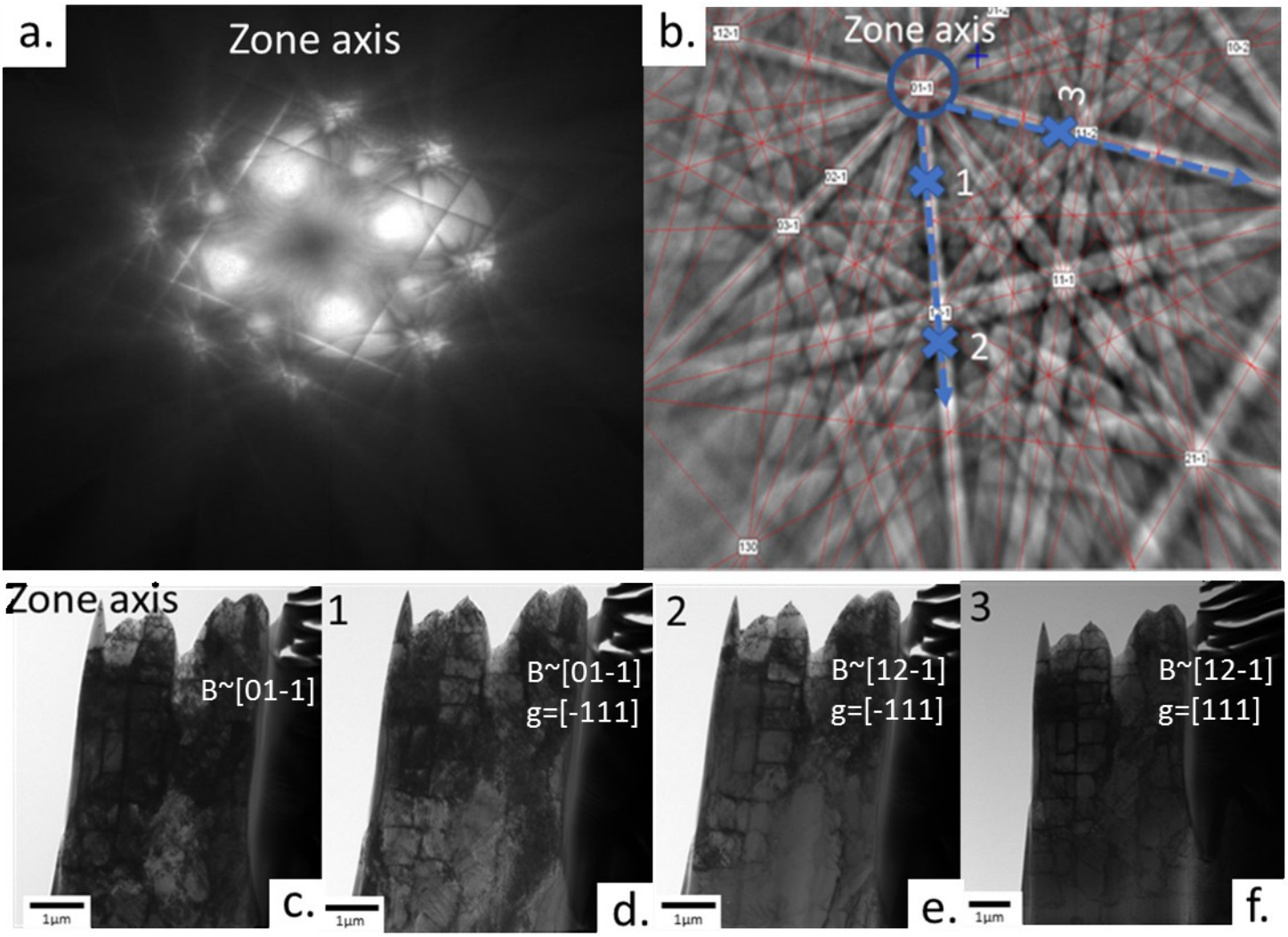


Figure 84: Movement along the zone axis to different diffracting conditions. Kikuchi lines in a Ni superalloy (a) TEM configuration (b) EBSD configuration showing shift along a plane to different conditons. Transmission image of micropillar (c) Zone axis (d) condition 1 (e) condition 2 (f) condition 3.

Figure 84 a-b shows the <001> zone axis as viewed in the TEM and in EBSD. Dislocation mapping through **g.b.** analysis is undertaken by aligning a zone axis; (In which the zone axis contains the most information as shown in, figure 84c) then subsequently moving along a Kikuchi line to a different condition along a plane, to examine which dislocations are and are not present on which planes. figure 84 c-f shows 4 conditions including the zone axis, in which different features can be observed in each condition. Figure 85 shows the dislocation species present in the deformed micropillar, as viewed from the zone axis condition in greater detail.

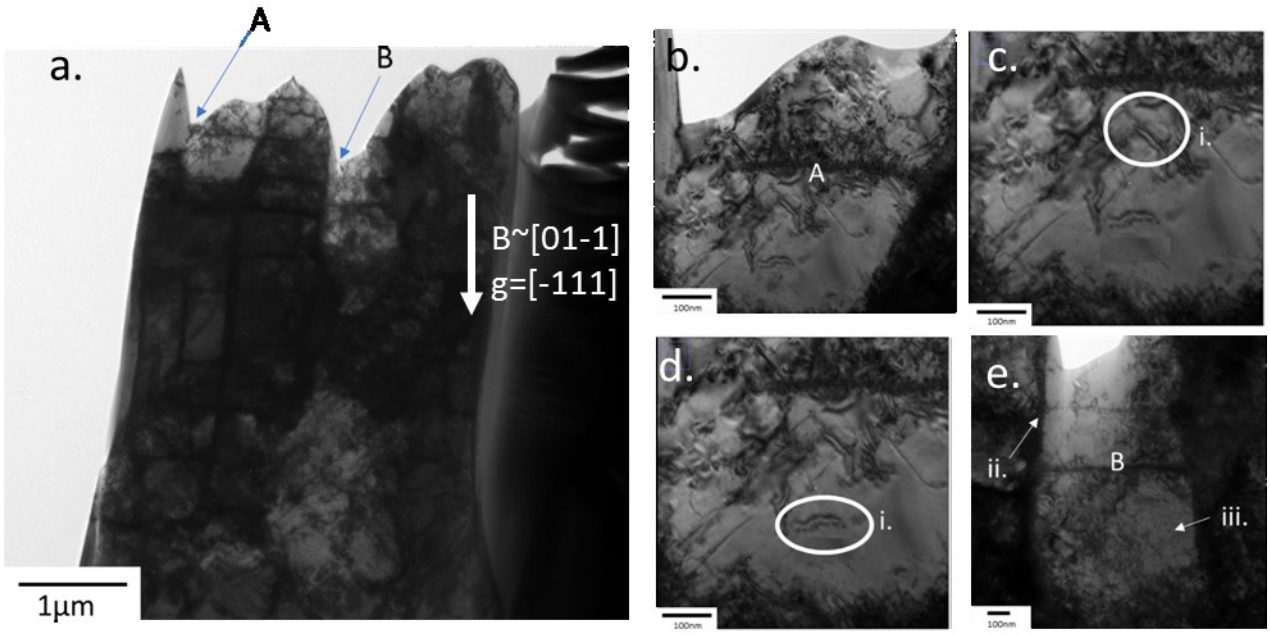


Figure 85: Close inspection of zone axis condition (a) full pillar zone axis (b) Area A (c-d) i. dislocation partials that have penetrated through into separated by an anti-phase boundary (e) Area B ii ϒ. iii.ϒ'

Figure 85 exemplifies the dislocations species that can be observed in a TEM, comparing figure 80 to figure 85, figure 85 is a micropillar that has been heavily deformed to 25% strain, compared to figure 80 at 6% strain and hence the image in figure 85 is heavily contrasted with dislocations that have penetrated through the ϒ into the ϒ' in a series of mechanisms, that will be discussed later.

The micropillars can be deformed to set strains through control of the Alemnis and AMCIS software, then taken to the TEM to be thoroughly characterised. However careful set up of the instrument should be exercised as the length scales of these tests are small and the difference between 3 & 20 % strain can be 1.5 µm displacement.

5.4. In-situ set up – Alemnis

The Alemnis SEM indenter is a compact machine enabling *in-situ* mechanical testing on the micro and nano scale. It has a two-axis positioning stage to align the sample with the compression / indenter tip and provides nanometre resolution. The distance between the sample and the tip (z axis) can also be controlled to nanometre resolution. The compression / indentation is done with a piezo stack actuator and the applied force is measured with a high precision load cell.

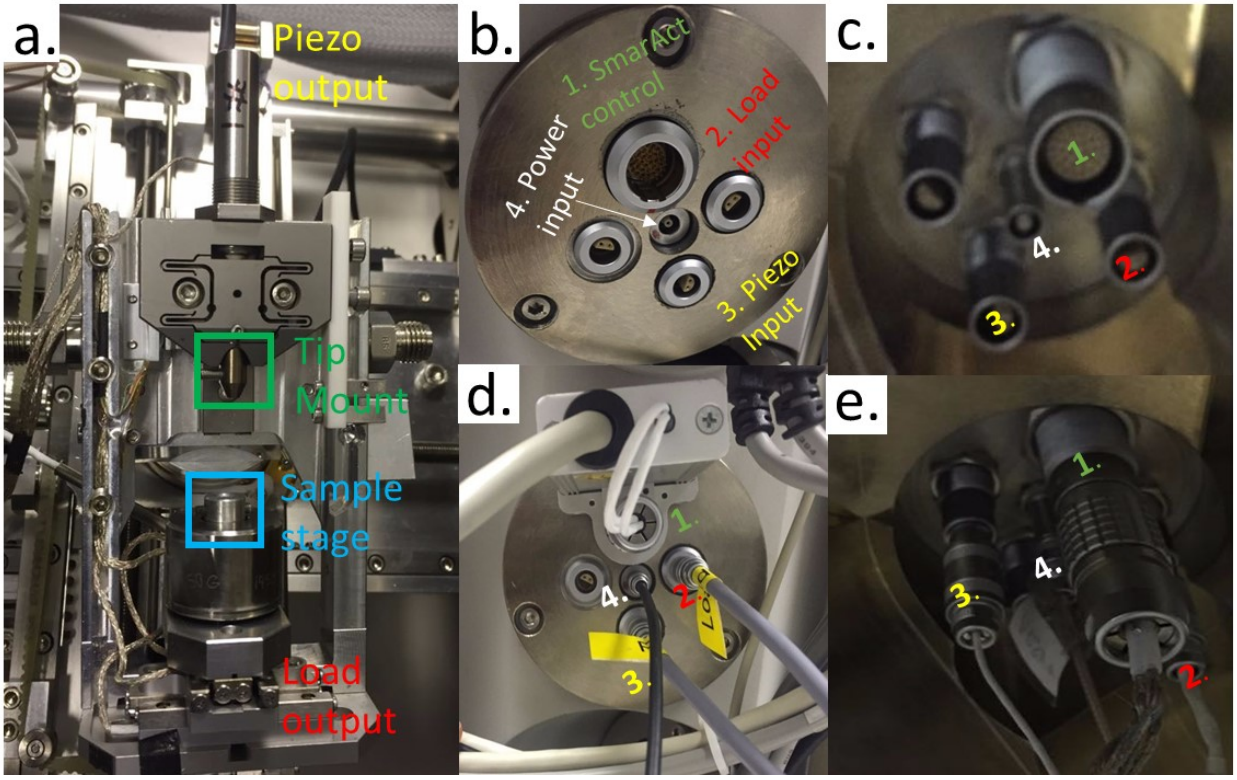


Figure 86: Alemnis in-situ indenter Quanta set up (a) Alemnis stage mounted inside the SEM (b) Outside flange (b) Inside flange (c-d) outside & inside flange with SmarAct controller, Load connectors, Piezo connector, Power connector inserted respectively

Figure 86, shows the set up of the in-situ indenter inside the Quanta The piezo ceramic is controlled by an output voltage that expands a ceramic crystal stack. A spring is placed between the tip and the ceramic to ensure linear displacement. The spring avoids the step wise expansion of the crystal and moves linearly with the output voltage, thus ensuring uniaxial displacement in z. The piezo is controlled by the Noliac high voltage amplifier.

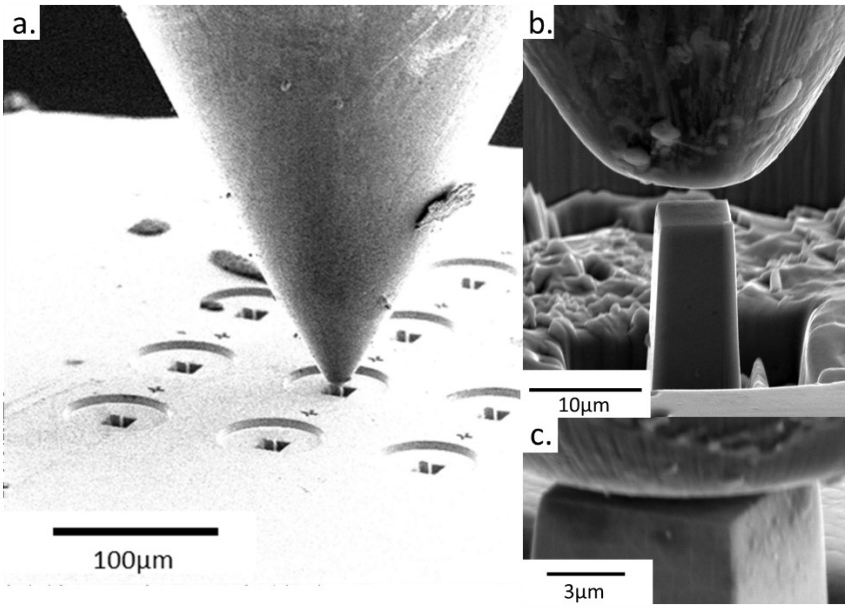


Figure 87: Alemnis flat punch approaching pillar (a) Far view (b) shadow on top surface (c) tip near touch of the top surface

As the tip approaches the pillar care needs to be taken not to cause any prior strain. It becomes clear the tip is directly above the pillar when a shadow can be seen on the top surface of the pillar figure 87. The manipulation of the tip is then controlled using the Amcis software which provides a more delicate control.

5.4.1. Software

All the tests were run in displacement control, in which the maximum displacement was set according to desired % strain or indentation size.

On approach to the pillar, the tip is controlled by the approach button which is controlled by the voltage and provides nm level displacement. Once the tip touches the surface of the pillar a small jump in the load is recorded. The tip is then slightly retracted and the system is tared. The tare feature corrects the load and displacement traces to correct for drift and noise. Thus ensuring no preliminary deformation to the pillar and the correct displacement is recorded.

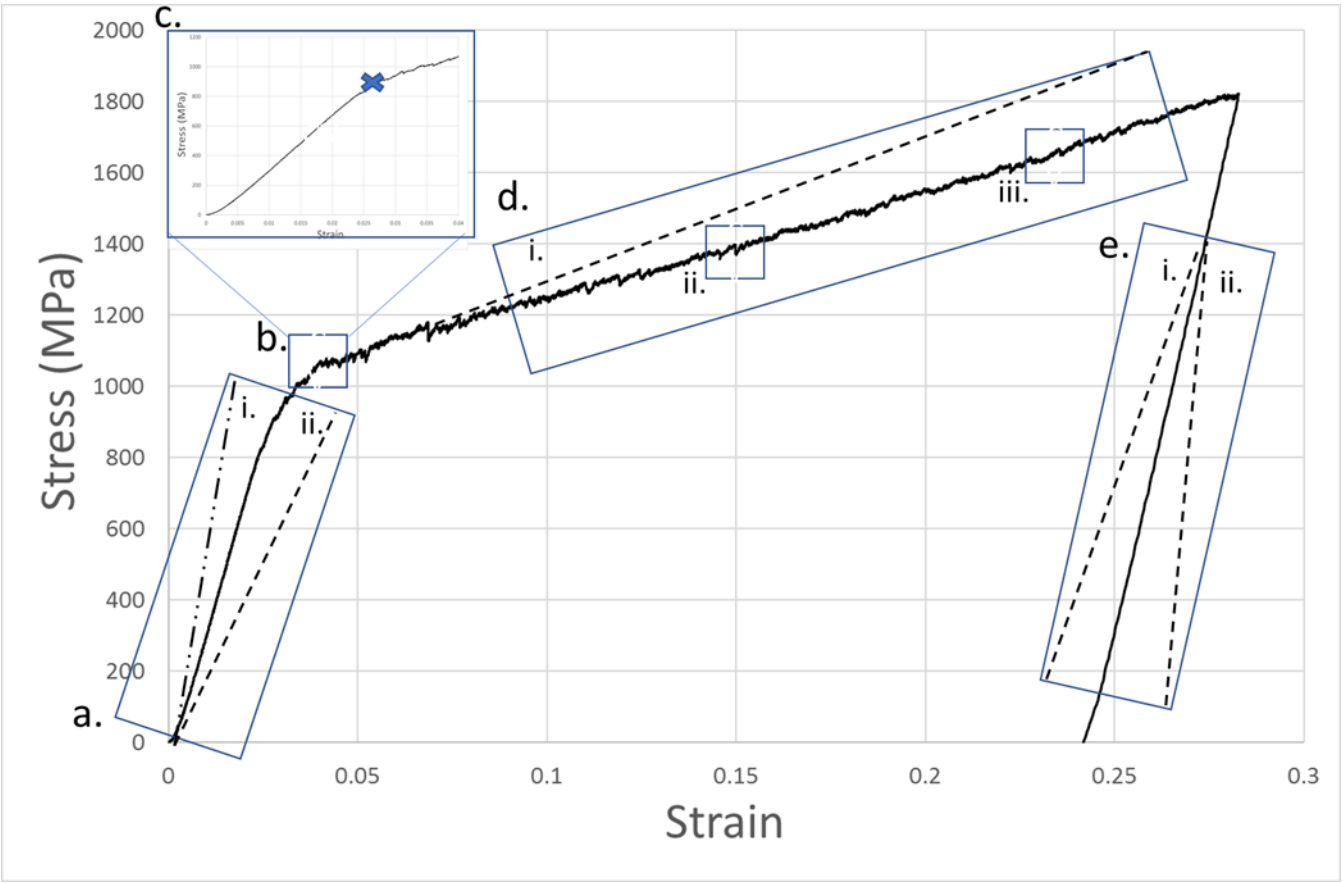


Figure 88: Stress - Strain curve adapted from load x displacement x time data illustrating regions of interest. (a) Elastic compression regime. Care should be taken to note the gradient (b) Area of inflection (yield point) (c) Localised point of inflection taken as the yield point (d) Hardening plastic regime (i-ii) strain bursts (e) Unloading regime.

Each region in figure 88 is important and gives different deformation information. In the case of figure 89, the loading and unloading regimes (a) and (e) are in agreement. This is rare and is indicative of an excellent pillar geometry and good instrumentation.

Care should be taken to note the primary features of each region when testing multiple samples in the same alloy. A full description if the stress – strain curve derived from the load x displacement x time data extracted from the Amcis software through the *in-situ* micro compression of pillars will be examined in the next chapter.

5.5. Materials preparation

The as received Ni based super alloys were prepared in three stages using the following regime:

Cutting was performed at 2000RPM at a 0.01 mm/s feed rate. Grinding involves 5 steps at 10N and 300rpm; 1. 500 Grit – 2 minutes 2. 800 Grit – 2 minutes 3. 1200 Grit – 3 minutes 4. 2000 Grit – 5 minutes 5. 5000 Grit – 8 minutes. Polishing requires - 15 minutes (OPS) (5 parts Water 1 Part Ops). 15 minutes

(Water polishing). 15-20 minutes (Ultrasonic). This provided a finish that was suitable for SEM/BSD and EBSD.

Depending on the alloy, an extra step involving an acetone or ethanol rinse with and extra 40 minutes in the ultrasonic bath was used to remove any excess ops staining.

5.5.1. Pillar design

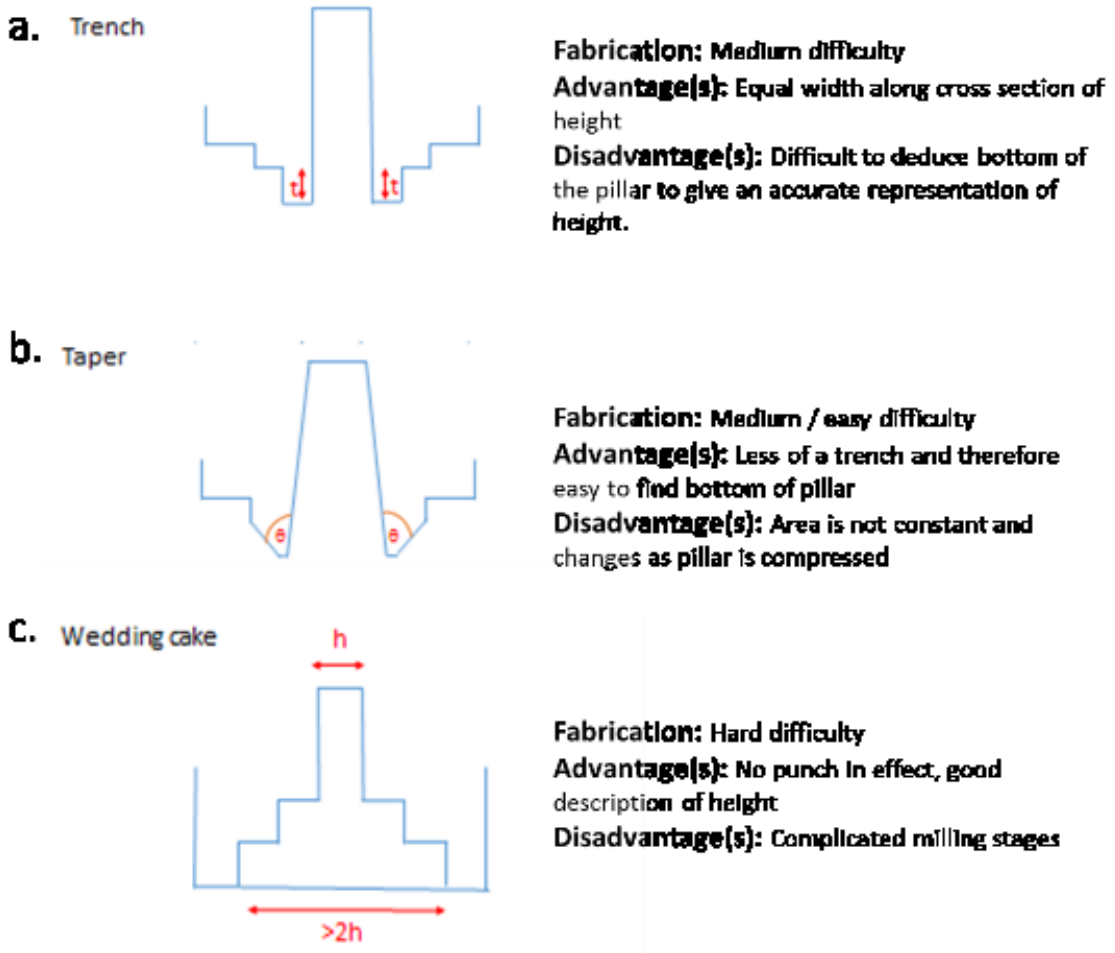


Figure 89: Schematic representation of three pillar designs (a) Trench (b) Taper (c) Wedding cake. Each design has its own associated advantage and disadvantage.

Figure 89 shows the schematic of three pillar designs that were found to be the most suitable for subsequent analysis. For the work done in this experimental study, tapered pillars were chosen. Tapered pillars were chosen as they combine the most effective combination of time and mechanical stability.

The wedding cake structure would, in theory, be the most suitable. This is in accordance to criticisms by other authors[176] of punch in substrate effects and non-uniform height measurements via both the taper and trench designs.

However, my investigations have led me to conclude that the wedding cake design takes the longest time to fabricate, is the most complicated to script and wastes the most material. Another issue is the

time the ion beam spends on the pillar. The more complicated the design the more ion damage the pillar is exposed to and this is not desirable[160]. Figure 90 shows the live designs of the pillars in figure 89. One of the key issues when designing a pillar, is a clear description of the width and height, as these variables are used to calculate, stress and strain.

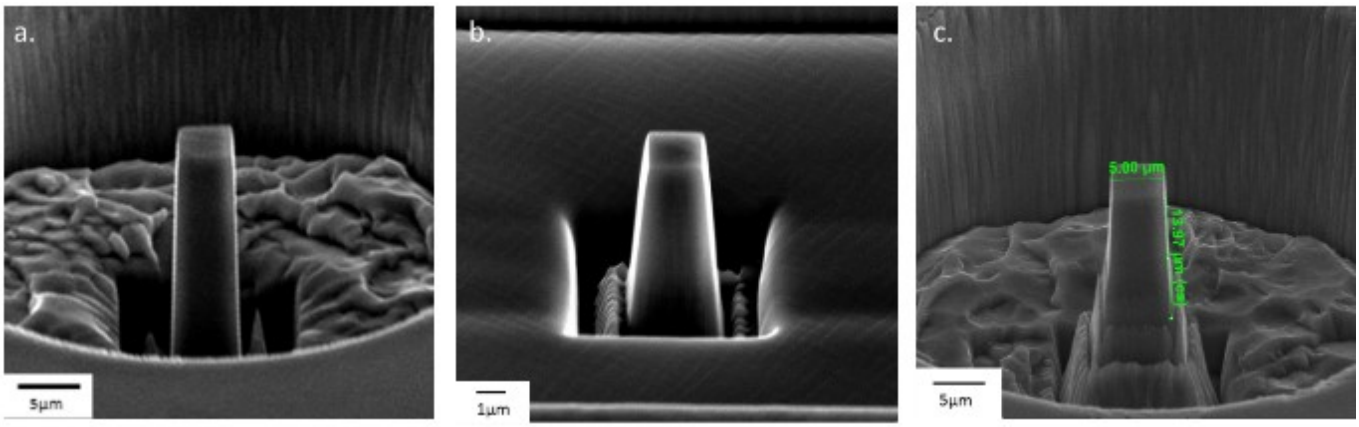


Figure 90 FIB milled pillars CMSX-4 <001> (a) Trench (b) Taper (c) Wedding cake

If fabricated well, the bottom of the pillar can be observed providing a wide enough rough trench / sufficient tilt for the viewing angle. The rough trench is the first and most time intensive part of the pillar fabrication process. The viewing angle is changed when the sample is mounted onto the in-situ testing frame. It is important for the pillar taper to be kept small and consistent when testing. A taper of roughly 5° is acceptable and can act to reduce any sink in effects[176]. A low taper angle can ensure mechanical stability of the pillar and avoid mechanical buckling. A large taper can be reduced as as shown in figure 91.

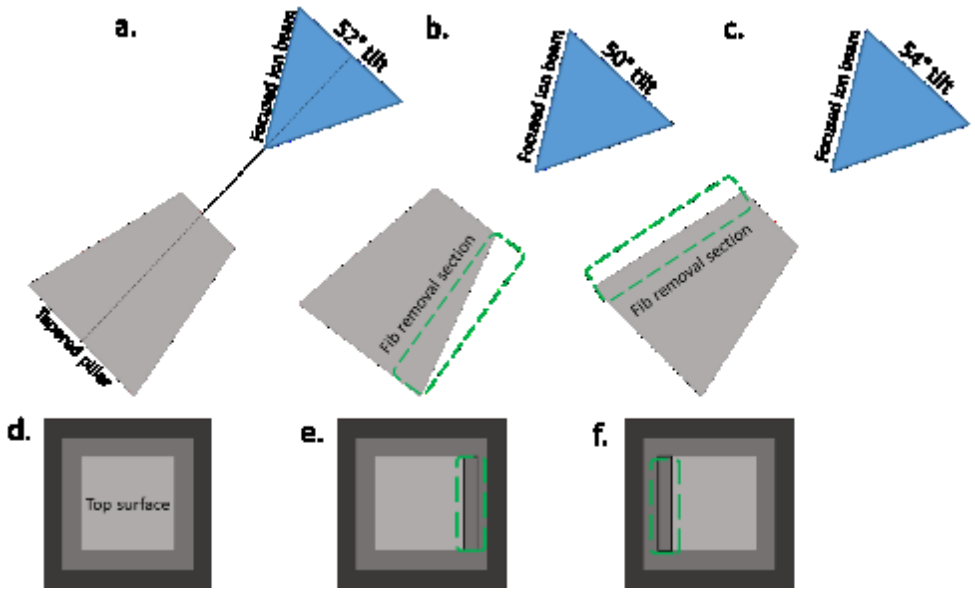


Figure 91: Schematic representation of taper removal (a-c) SEM view (d-f) FIB view

Figure 91 shows the birds eye of view of a micropillar (d-f) being tilted ± 2° from the resting position of 52°. As the pillar is tilted ± 2° the side section (highlighted in green) are removed, thus reducing the size of the taper. Ensuring a good description of pillar width and height is key to translating the load, displacement, time data to engineering stress and strain, figure 90 and figure 105.

5.5.2. TEM Pillar sample preparation

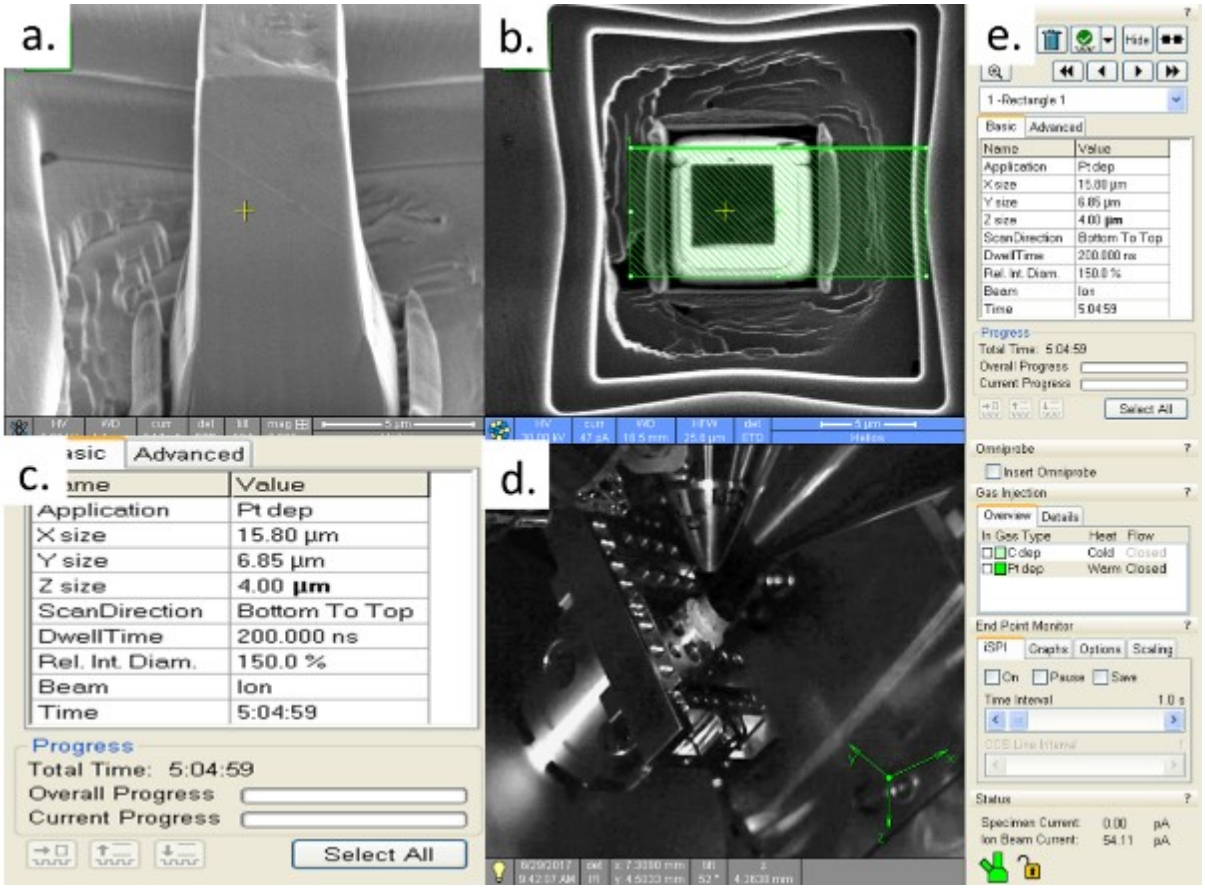


Figure 92: Software screen with a 52° tilt showing (a) SEM - deformed micropillar (b) FIB -section ready for pt deposition (c) milling acquisition screen – pt deposition (d) sample tilited to 52°, ready for milling and pt deposition

As briefly outlined in the methodology sectioned micropillars can be examined in the TEM. However, they first need to be prepared in a series of steps:

1. Align the pillar, as outlined in the methodology section
2. Tilt stage to 52° correcting for eucentric motion
3. Warm up Pt source
4. Insert Pt needle
5. Place a rectangular box over the pillar ~ the width of the pillar and length enough to cover 75% of the trench. **(30 Kv – 0.92 Na) –** Figure 92b
6. Deposit roughly 3 µm of Pt (This step is important, if you need to observe the top surface of the pillar deposit 5 µm) – Figure 93 c
7. Remove two rectangular trenches 25 µm x 10 µm **(30Kv - 21 nA)** in parallel milling using this option should take 9 minutes 28 seconds
8. Clean the trench with the cleaning cross section. – Figure 93a
    a. In this step, If cleaned enough an imprint of the pillar can be observed, Figure 93 b

9. Tilt the stage to 7° and remove an L shaped cross section – Figure 93c & d

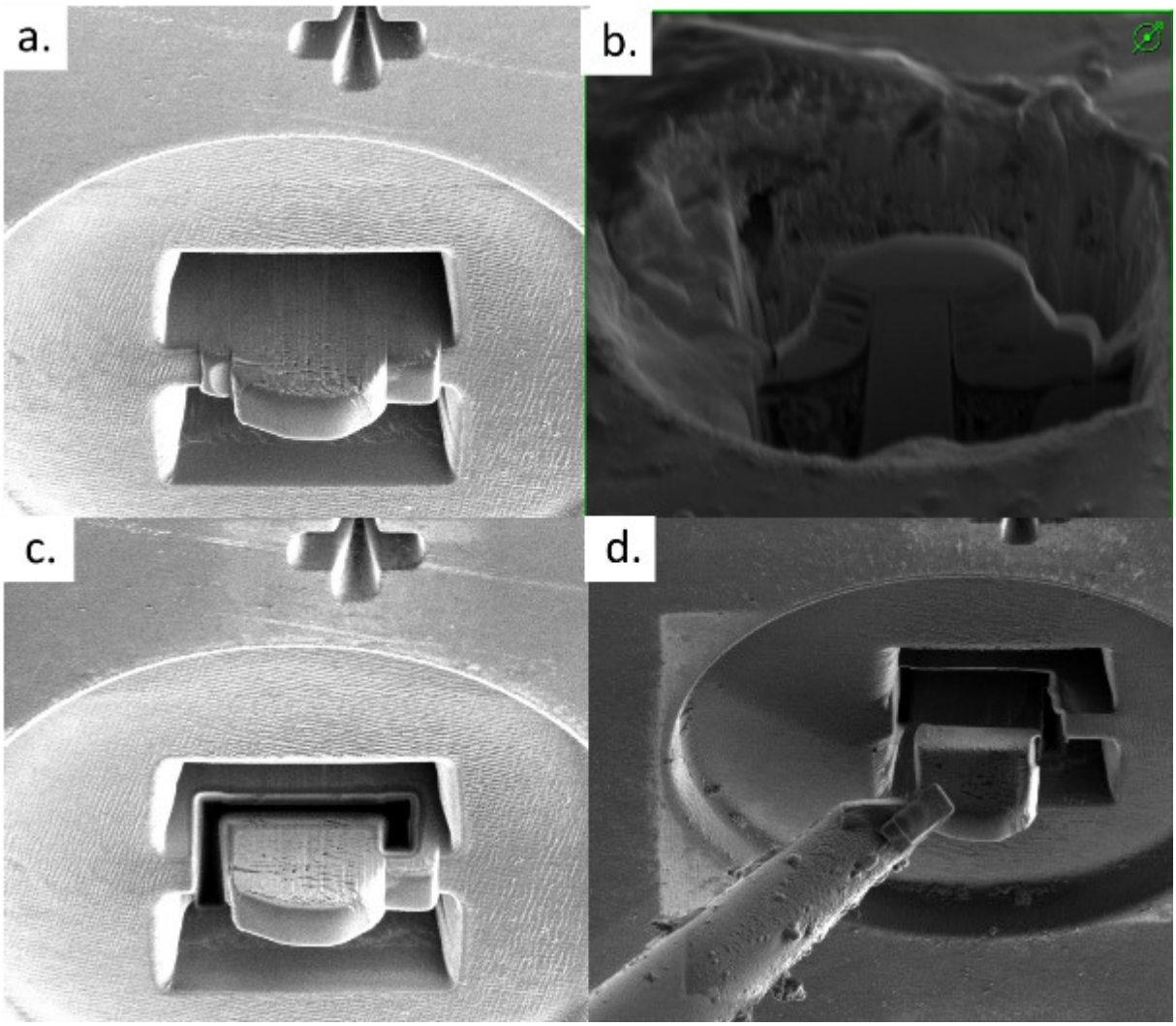


Figure 93: Cross section and removal of the pillar section at 7° tilt, by the omni probe to be placed onto the foil for thinning of the pillar to become electron transparent (a) Pillar section + trench (b) Cleaned trench cross section in which the pillar outline can be viewed (c) pillar section with L shaped cross section removed (d) removal of pillar section via omniprobe

Figure 93, shows the sectioning of a micropillar, ready to be transferred to the TEM and this completes the pillar section preparation.

The next section involves use of the omniprobe to transfer the sample onto the foil, figure 94. It is important to note that the stage should not be moved and only beam shift to be used to view a different region of the image.

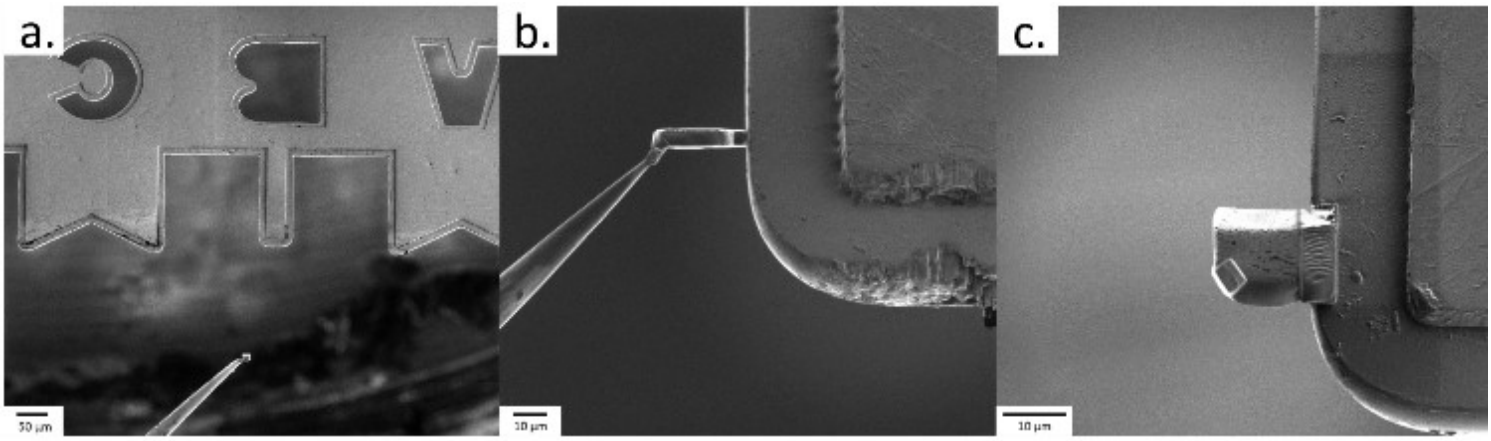


Figure 94: TEM foil attachment to the grid (a) Positioning adjacent to the grid stage (b) Attachment of the section onto the grid with pt (c) removal of the omniprobe + attachment of the section to the grid

Transfer of the pillar onto to the omniprobe should proceed as follows;

1. Insert the omniprobe
2. Position near the side of the pillar with no material
3. Deposit a thin section of Pt attaching the omniprobe to the pillar
4. Remove the corner section of material
5. Raise the pillar from the trench – Figure 93d
6. Park omniprobe
7. Transfer omniprobe with attached pillar to the grid – Figure 94a
8. Deposit Pt attaching the pillar to the grid – Figure 94b
9. Remove pillar from omniprobe
10. Secure pillar safely onto the grid – Figure 94d

This completes transferring the pillar onto the grid. The next steps involve thinning the pillar down to ~400 nm. This happens in 4 stages. In which the stage is tilted up and down accordingly. The line in the cleaning cross section should be pointing down for a negative tilt and upwards for a positive tilt.

1. Tilt stage to 52° ± 1.5° **(30 kV – 0.92 Na**) the z depth is 3 µm, however this can be altered depending on what you want to view.
2. Tilt stage to 52° ± 1.2° **(30 kV – 93 Pa)** the z depth is 3 µm, however this can be altered depending on what you want to view.
3. Tilt stage to 52° ± 1.5° **(5 kV – 47 Pa)** the z depth is 3 µm, however this can be altered depending on what you want to view.
4. Tilt stage to 52° ± 7° **(2 kV – 28 Pa)** the z depth is 20 nm and the mode is changed from cleaning to a rectangle covering the whole sample.

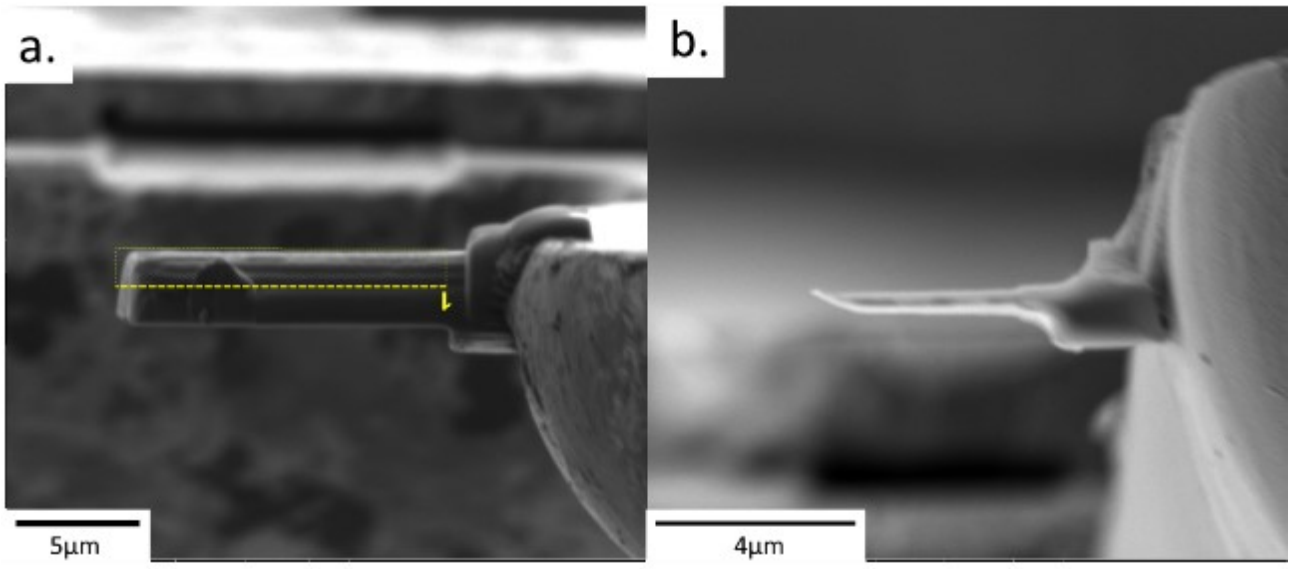


Figure 95: FIB view at 52° tilt of the pillar cross section mounted onto the grid (a) Thick section 2 µm ready to be thinned (b) Thinned section ~400 nm ready to be transferred to the TEM

Figure 94, shows the thinning of a micropillar section attached to a TEM grid, from the viewpoint of the FIB screen at 52° tilt. Figure 96, shows the viewpoint of the SEM screen at 52°. The orientations of the SEM and FIB screens are changed at 0° tilt.

Care must be taken as platinum is removed from the top section of the coated pillar during milling. Depending on the orientation, if there is a low level of strain, most of the dislocation mechanics happen at the top of the pillar so thinning to much will ruin the sample in the view of examining the dislocations, as shown later in figure 145.

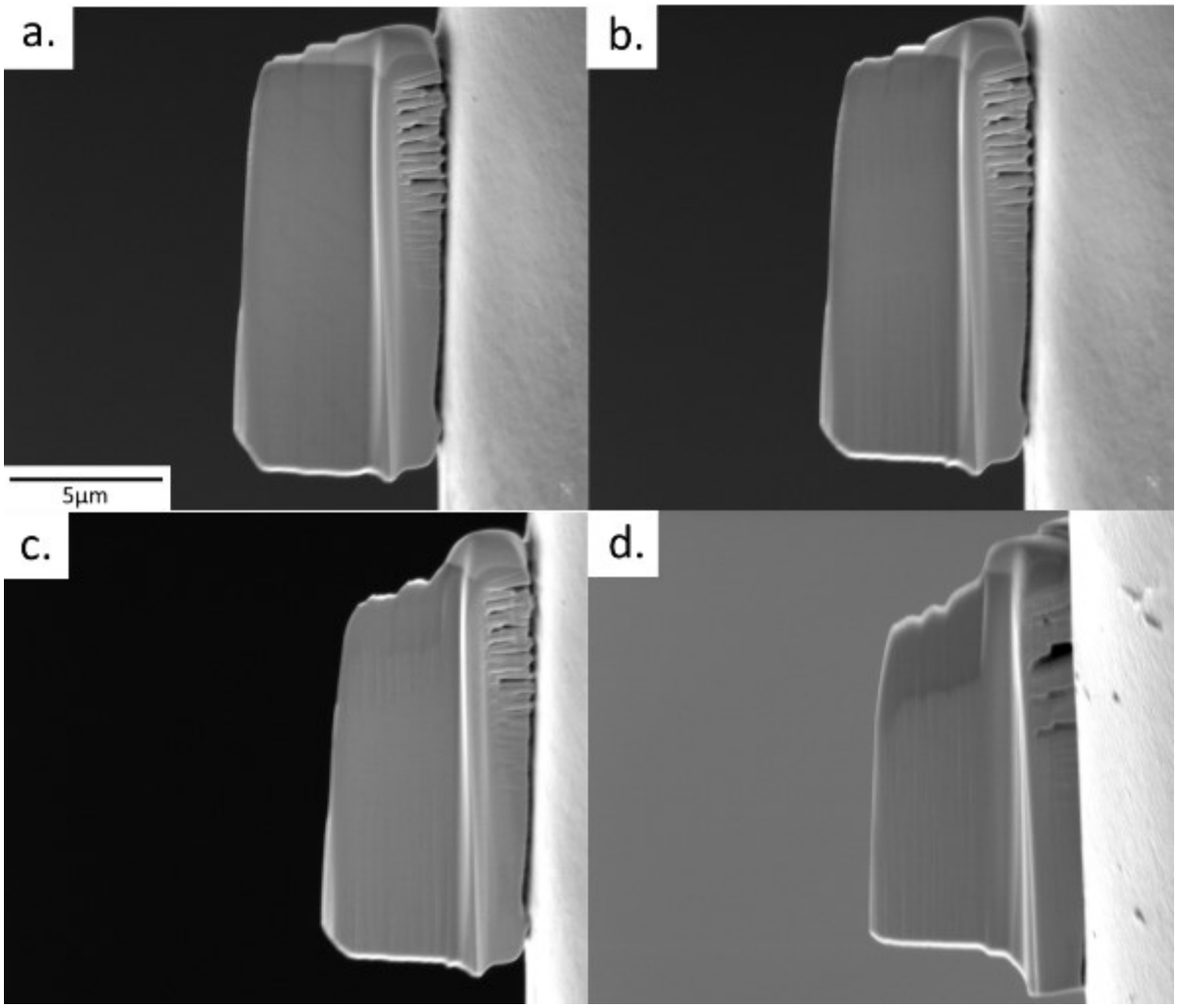


Figure 96: SEM view of thinned micropillar at different times (a) Beginning stage, reasonable amount of pt remaining (b) Pt level beginning to thin and eat into the sample (c) Sufficient pt removal with small degradation of the top surface (d) A high level of thinning with 6-7% of the top surface removed, this should be avoided.

Figure 96, shows a sectioned micropillar attached to a grid, being thinned, slowly removing the pt from the top section of the pillar. Pillar 5e which was deformed to 20% strain was the first sample to be successfully prepared for TEM analysis, as shown in, figure 138 & figure 141. Pillar 5e showed no clear shear localisation unlike pillar 5f. The preparation of Pillar 5f failed, due to the residual stresses caused by the shear band. When examining a heavily deformed pillar (≥ 15% strain), the contrast on the zone axis is heavy as the pillar has been strongly influenced by plastic flow as evidenced by the dark smokey regions figure 142a (i).

5.5.3. Slip trace analysis

Figure 97 illustrates that the orientation of any test fcc crystal can be taken from the top surface of the micropillar. This orientation denoted “test” can then be rotated about the z plane (α orientation along the <001> stacking line), and in plane (β orientation, with respect to the x and y faces of the pillar). Thus, the crystal orientation on each side of the pillar face, north, south, east and west can be deduced by rotating and tilting 52° toward the camera. Where 52° is the viewing angle of the micropillar taken on

the SEM, figure 98. This enables a 3d representation of the fcc crystal geometry enabling the crystal geometry to be matched with the slip trace on each side of the cuboidal pillar. The taper angle is also taken into account during analysis.

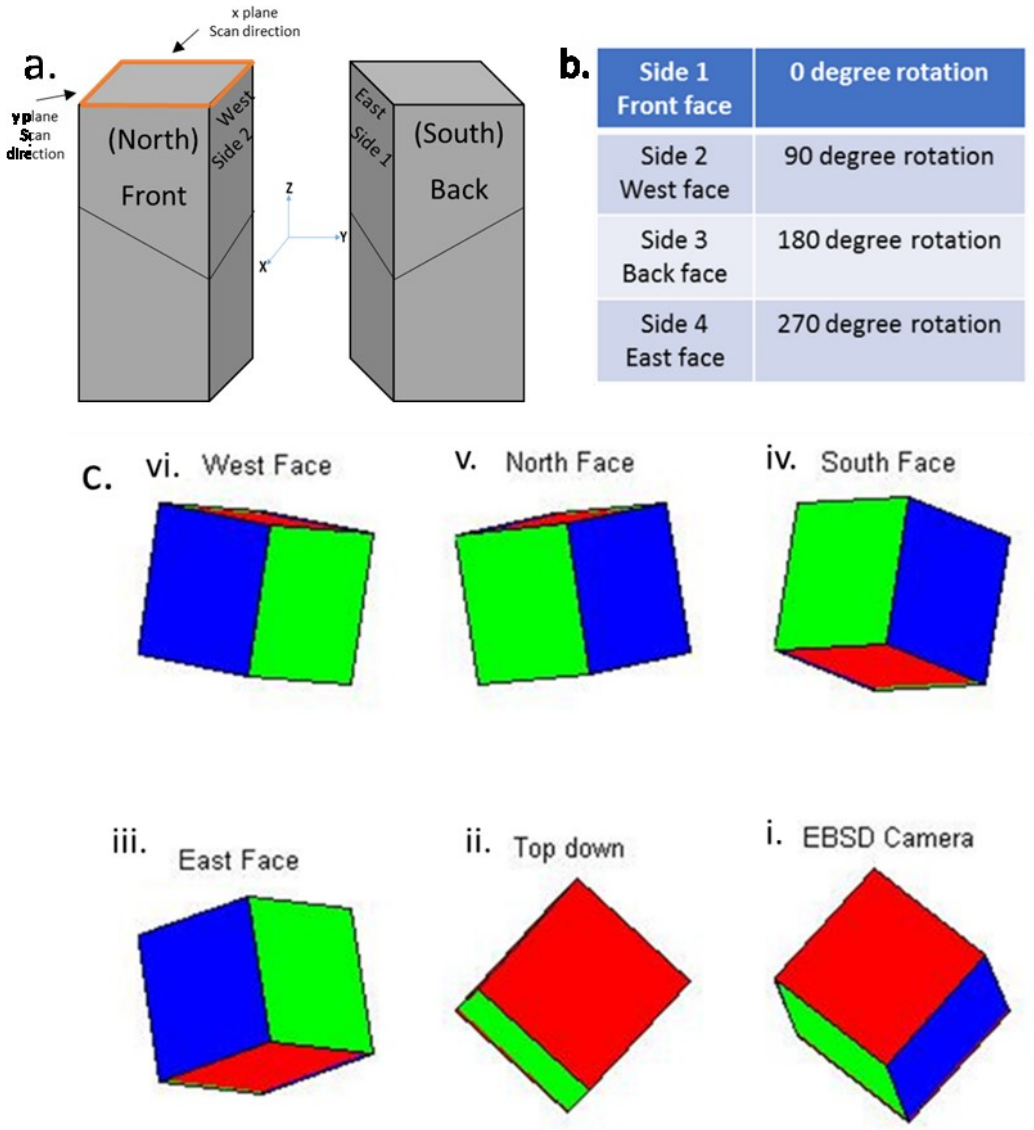


Figure 97: Slip trace schematic of a <011> pillar orientated with fcc crystal orientation rotated 0, 90°, 180°, 270°. (a) Schematic of pillar faces, north - 0° rotation, west – 90° rotation, south 180° rotation, east face 270° rotation (b) geometric rotation of each face (c) rotation of fcc crystal from test position (i) EBSD camera (ii) Top down orientation (iii) east face (iv) south face (v) north face (vi) west face.

Figure 97 provides a schematic representation of how each face of the micropillar; north, west, south, and east (0, 90°, 180°, 270° rotation about the origin, respectively) can be imaged and the orientation of the fcc crystal taken from EBSD, figure 166 c i, can be rotated about a reference axis and appended onto the representative face of the micropillar, figure 98 shows this in more detail.

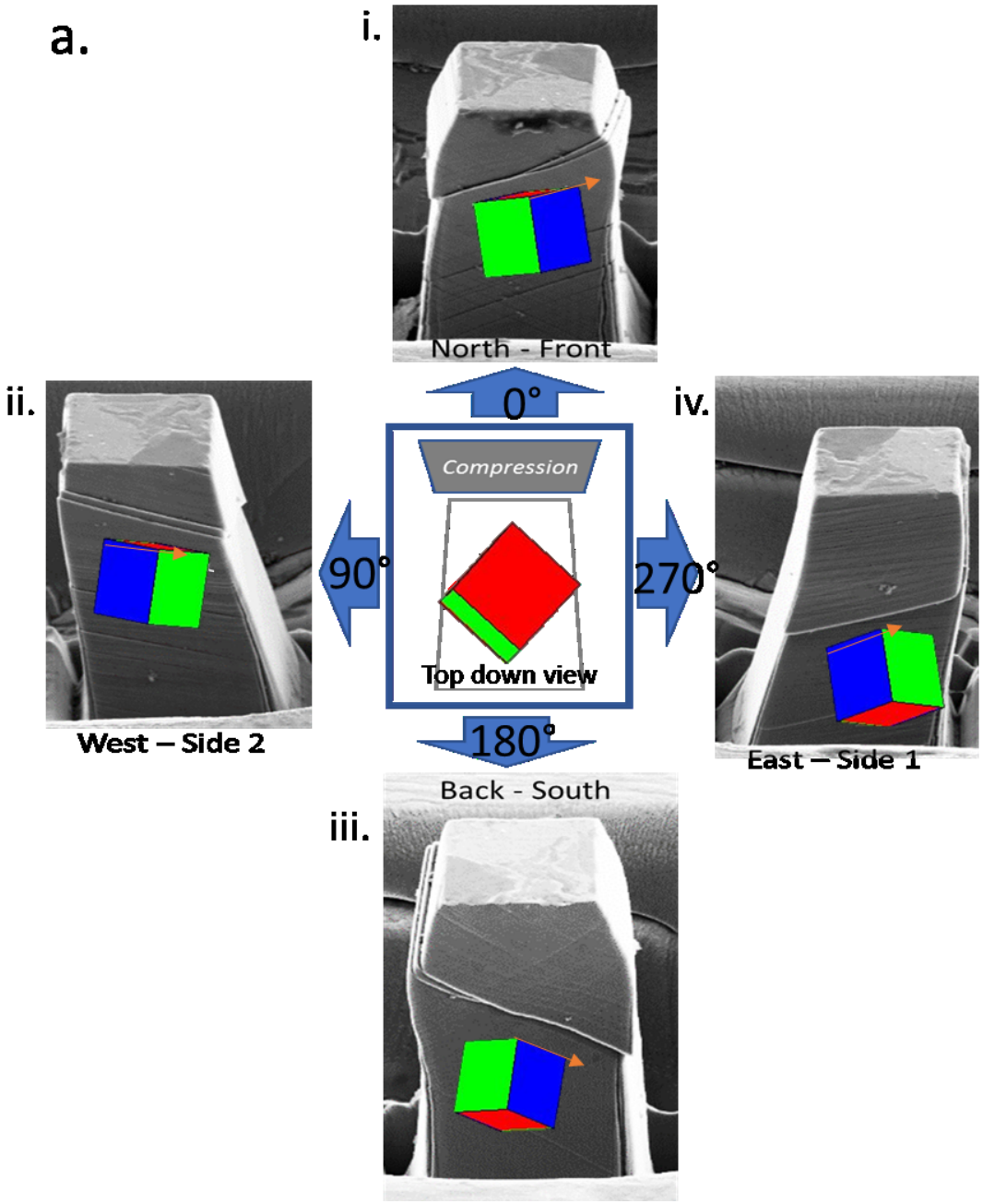


Figure 98: Slip trace analysis, using 4 faces of the pillar rotated at 90° intervals, enabling a full analysis of the slip trace with respect to the slip plane and direction as exemplified by Figure 190-4.

Figure 98 shows the post deformation images of a <011> orientated pillar deformed to 15% strain. The slip traces on each of the four faces of the pillar can be matched with the orientation of the fcc crystal. The slip trace can then be appended to the edge of the cube representing the plane and direction in which the slip system is orientated as shown in figure 164 and table 13.

Matching of the slip trace with the pillar can be performed, through comparison with the trace of the slip plane expected from the EBSD measurements and the slip traces on the surface of the pillar. Formerly, the slip trace can be calculated as the cross product of the expected slip plane normal and the

viewed surface of the crystal. This has to be presented in the frame of reference of the image (e.g. accounting for tilts of the pillar in the SEM).

Figure 99 illustrates how the theoretical value of a slip trace $\hat{r}$ can be deduced, adapting the orientation of the fcc crystal.

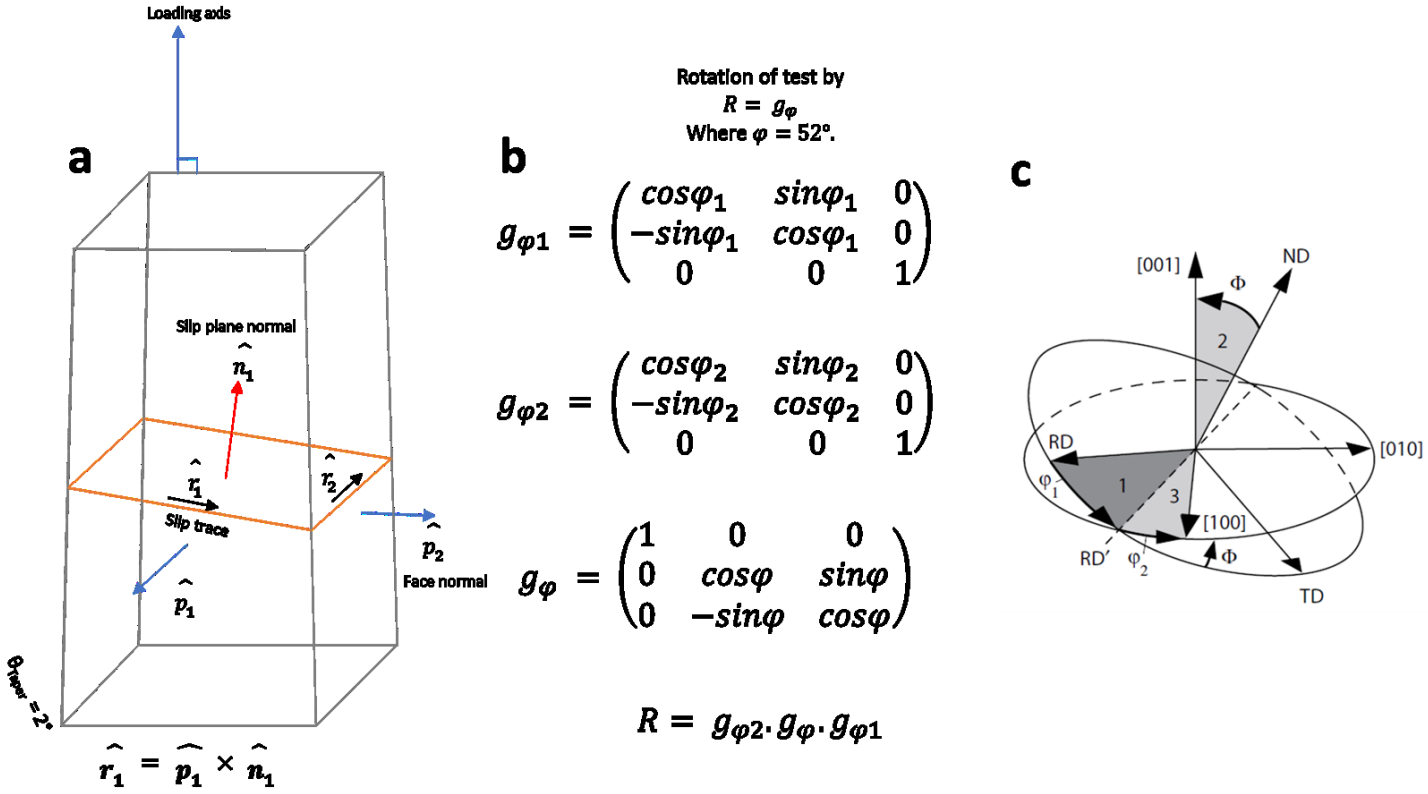


Figure 99: Schematic representation of slip trace $\hat{r}$ determination (a) Schematic of the cross product of $\hat{n}$ & $\hat{p}$ giving rise to the theoretical slip trace $\hat{r}$.[177] (b) Rotation of the test orientation $\hat{n}$, through R and cross of the product of $\hat{p}$ giving rise to the slip trace $\hat{r}$ (c) Schematic representation of how rotation through Euler angles, in order 1,2,3 as shown, describes the rotation between the specimen and crystal axes

Figure 99 provides a shcematic represenation of the slip trace determinaion. To get an output of the theoretical slip trace $\hat{r}$, first the plane normal of the active {111} plane, needs to be set up into a unit vector in the <001> position $\hat{n}$. The plane normal is then rotated through to test position using Euler

angles / Bunge notation $\hat{p}$. Then the cross of the normal of the {111} plane of the top surface of the pillar with the test position, as taken from EBSD is deduced to give to a slip trace $\hat{r}$.

The rotation of the pillar 52° towards the camera needs to be taken into consideration. As the SEM image has been orientated this way. Resulting in a 3 dimensional line vector.

The line vector is normalised and the axis scaled to be equivalent. The x-y position is locked and the final resultant slip trace $\hat{r}$ can be deduced, as shown in figure 100b.

A component of slip in this direction can be deduced from the post deformation experimental SEM images, via the Tan method, figure 100 c. Where the slip trace on any pillar face can be calculated after tilting, where θs = angle on any pillar face after tilting, Φ = the tilt angle and θ' = angle of slip trace from SEM screen, this is known as the Tan method.

This enables the part designer to tailor and programme failure criteria more effectively across any orientation and within polycrystalline materials. It must be noted that in order to perform the full slip trace analysis, each face of the pillar must be imaged post deformation. This was unfortunately not possible whilst testing on the polycrystalline FGH96 alloy.

Some pillars as in the case of CMSX-4 <011> have been deformed heavily, causing the pillar and slip trace to become displaced to an angle that cannot be deduced accuractely, caused by rotation of the

pillar body and slip of the shear plane, as shown in figure 98 ii and iv, with the bent and twisted side faces of the micripillar.

Figure 100, shows the theoretical determination of slip trace $\hat{r}$ compared to the experimental analysis through the Tan method, of <001>, <011> and <111> orientated pillars. In general the techniques agree with each other.

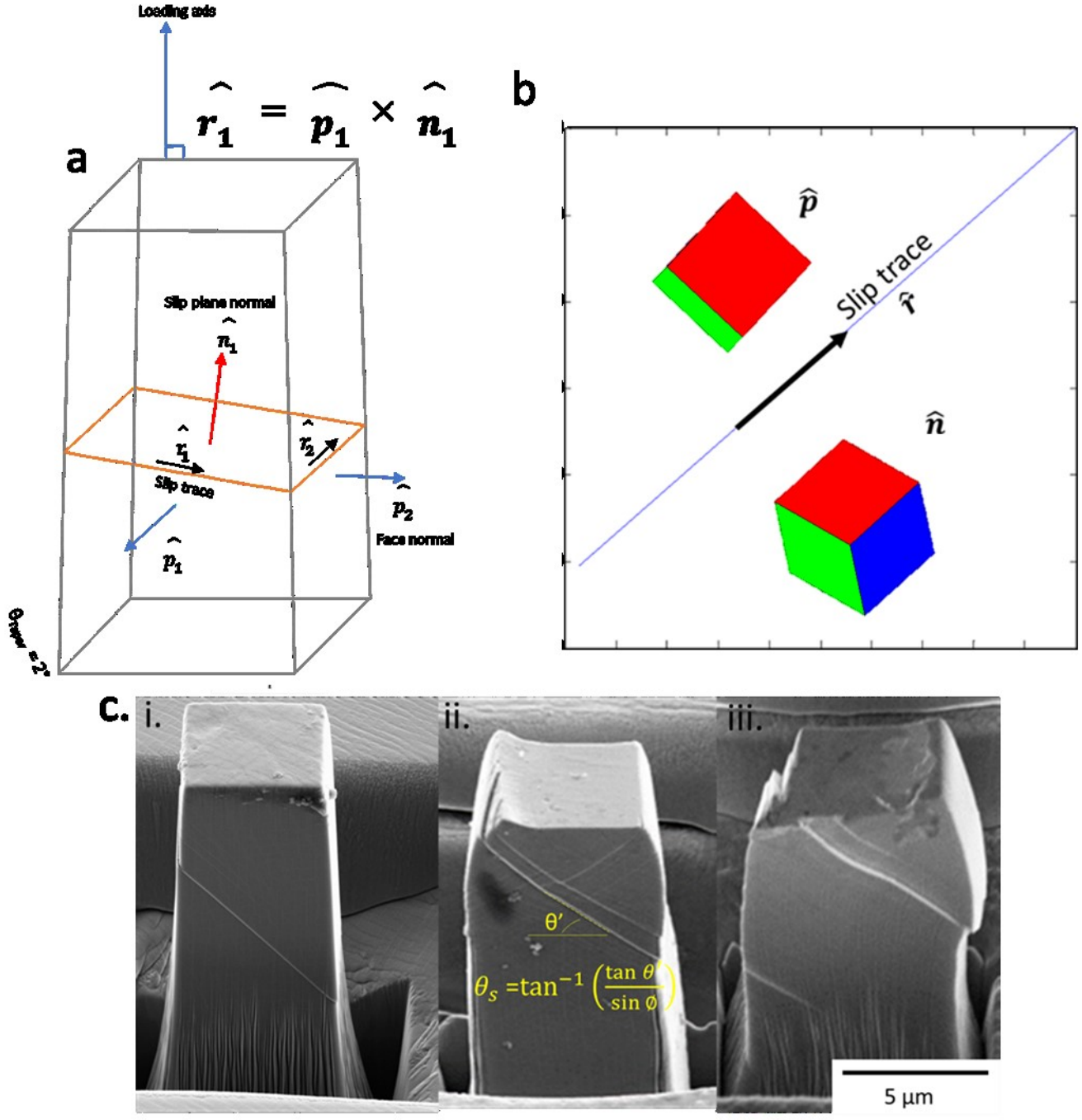


Figure 100: Theoretical slip trace analysis vs experimental slip trace determination through the Tan method (a) Schematic of theoretical slip trace analysis (b) Output of slip trace $\hat{r}$ (c) Experimental slip traces, calculated via the Tan method where ϑs = angle on any pillar face after tilting, Φ = the tilt angle and ϑ′ = angle of slip trace from SEM screen, from i. <001> orientation ii. <011> orientation and iii. <111> orientation, where the experimental slip trace is measured.

Figure 100 a and b, show the schematic of the slip trace determination and the result respectively. $\hat{p}$ is the normal of the slip trace, $\hat{n}$ is the normal of the slip plane. Figure 100 c (i-iii) shows the SEM post deformation images of the north face of pillars orientated <001> <011> and <111> respectively with active slip systems $(\bar{1}11) < \bar{1}0\bar{1} >$, $(\bar{1}11) < \bar{1}0\bar{1} >$,$(\bar{1}11) < \bar{1}01 >$ respectively.

5.5.4. Shape descriptors

The characteristic trends of the carbide type phases found in CMSX-4 and CMSX-10 can be examined using shape descriptors unique to each zone. The shape descriptors used in this study: circularity, aspect ratio, roundness, solidity, calculate and display the following:

Equation 40

$$\text{Circularity: } 4\pi \times \frac{[Area]}{[Perimeter]^2}$$

Circularity: A value of 1.0 indicates a perfect circle. As the value approaches 0.0, the feature becomes a more elongated elipse.

Equation 41

$$\text{Aspect ratio: } \frac{[Major\ axis]}{[Minor\ axis]}$$

Aspect ratio: The aspect ratio of the particle's fitted ellipse, i.e., [Major Axis] / [Minor Axis].

Equation 42

$$\text{Roundness: } \frac{4 \times [Area]}{\pi \times [Major\ axis]}$$

Roundness: 4 × [Area]π × [Major axis]^2 or the inverse of Aspect ratio

Equation 43

$$\text{Solidity: } \frac{[Area]}{[Convex\ Area]}$$

The BSD images, of the carbide phase and microstructure must first be altered using image software, to enable better analysis of the carbide phase. The analysis can give greater insight to the character of individual carbide phases, carbide phase zones, shape descriptors and the number / percentage volume of carbide phases in a local area, figure 213-figure 235, provide insight into this.

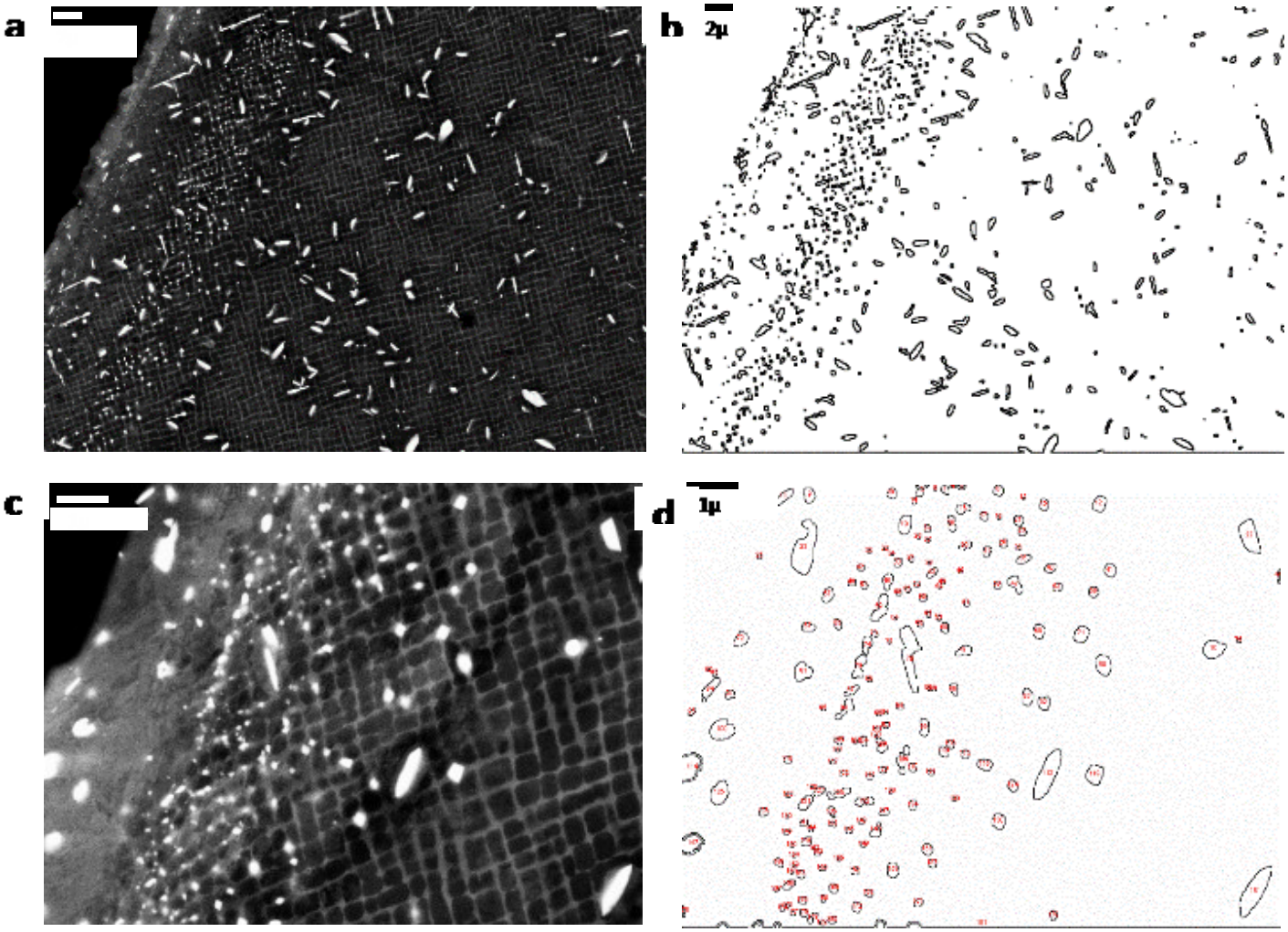


Figure 101: Micrographs of carburised CMSX-4 microstructure in two different regions. (a) Zones 1-3 BSD image at 40 k magnification (b) Threshold image of BSD image in (a) with particles clearly defined for analysis. (c) 50 µm^2 area BSD image from perimeter edge of sample to zone 3. (d) Threshold image of BSD image in (c) with particles analysed for shape descriptors.

The image analysis of the carbide type phase was done using Image J. The resolution and threshold of the original image was altered enabling the carbide phase to be modelled as individual solid particles, figure 101. Taking a sub sample of the microstructure from the outer edge through to zone 3, a global picture of the ϒ/ϒ' + carbide phase microstructure can be established, figure 214 figure 218 and figure 222.

Using figure 101 c and d, as reference, 180 particles were identified in a 200 µm^2 area. The average shape descriptors, circularity, aspect ratio, roundness and solidity across zones 1-3 were, 0.685, 2.05, 0.75 and 0.69 respectively. The relationship between the four shape descriptors in the 200 µm^2 area is shown graphically in figure 102. The aspect ratio, is the shape descriptor that varies the most.

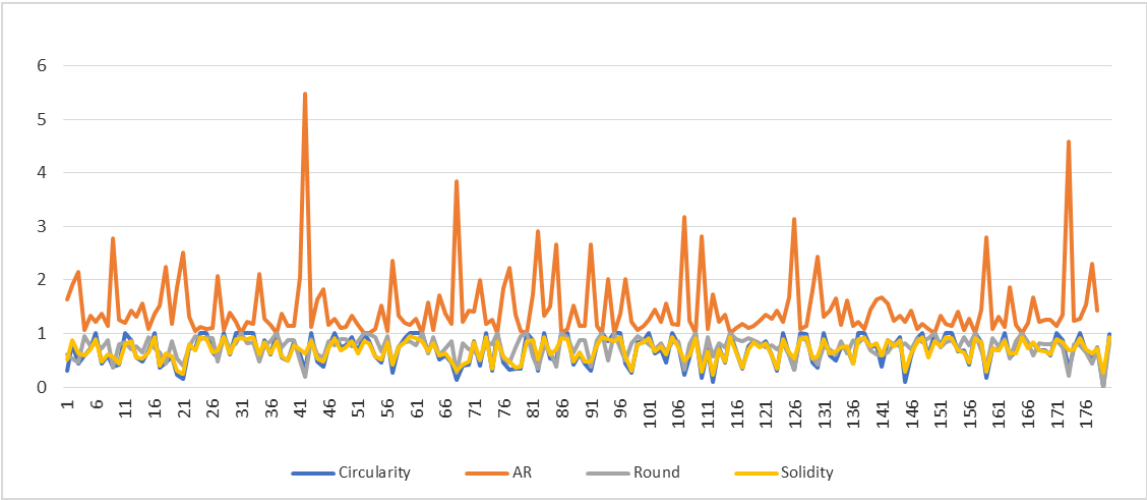


Figure 102: Shape descriptor trends in the 200 µm² area, shown in figure 101d, spanning zones 1-3 ~0-25 µm from edge, as shown in figure 101.

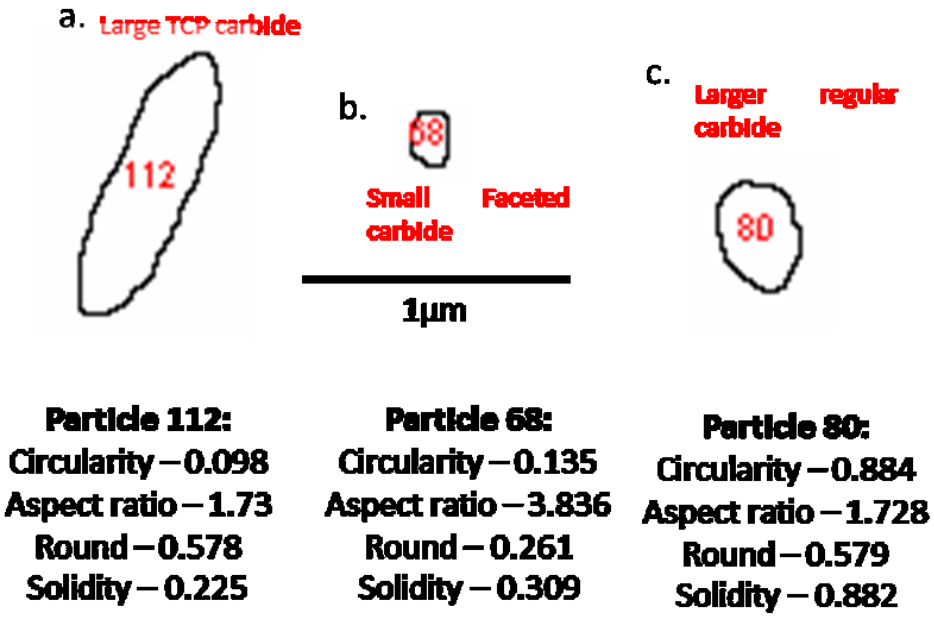


Figure 103: Three isolated carbide type phases within the carbide rich region. Particles unique to each zone analysed individually via shape descriptors

Figure 103, shows three characteristic carbide type particles located in the carbide rich region of the alloy; the large TCP phase (a), is generally local to zone 3, the small faceted carbide type phase that tends to populate the ϒ channels is local to zone 2 and 1 (b), and the large regular carbide type phase, which has the lowest number density, is local to zones 2 and 3 (c).

Figure 213, illustrates the BSD image from figure 212, segmented into zones and altered for image analysis allowing; the shape descriptors, area and volume fraction of the carbide type phase to be deduced.

5.5.5. The composition and origin of each alloy used in this study

This study examines several alloy types as listed below in, table 6. The alloys are used in different parts of the aeroengine due to their differences in microstructure and chemical composition[76]. Single crystal alloys such as CMSX-4 and CMSX-10 are used as turbine blades, whereas polycrystalline alloys such as FGH 96 are used as the disc material to house the blades.

Table 6: Chemical composition of alloy types, CMSX-4, CMSX-10, FGH-96 and carburised CMSX-4 & CMSX-10

	Al	Ti	Cr	Co	Ni	Mo	Hf	Ta	W	Re	C	Total
CMSX-4	4.29 ± 0.2	1.1 ± 0.1	6.17 ± 0.1	8.28 ± 0.2	55.03 ± 1.1	0.4 + 0	1.31 + 0	7.95 ± 0.2	6.15 ± 0.1	4.38 ± 0.1	4.29 ± 0.8	99.35
FGH-96	1.41 ± 0.03	5.39 ± 0.03	19.63 ± 0.12	12.92 ± 0.12	54.32 ± 0.17	4.3 ± 0.15	-	-	2.03 ± 0.06	-	-	100
C_CMSX-4	5.24 ± 0.21	1.70 ± 0.05	5.94 ± 0.15	8.55 ± 0.19	61.70 ± 1.14	0.27 ± 0.04	0.017 ± 0.0	7.59 ± 0.16	1.37 ± 0.12	1.37 ± 0.08	5.9 ± 0.80	99.6464
C-CMSX-10	1.72 ± 0.12	1.31 ± 0.08	8.63 ± 0.21	11.12 ± 0.17	64.13 ± 0.8	0.45 ± 0.06	0.00	6.36 ± 0.14	2.27 ± 0.11	0.59 ± 0.01	3.4 ± 0.07	100

6. Results - Single crystal Ni super alloy testing

6.2. Motivation

The motivation of this chapter is to set a robust testing regime to study the deformation mechanics, on the micro scale, of engineering alloys used in aero engines. Mechanical variables such as; the critical resolved shear stress (τ_{crss}), the rate of hardening (H_r) and elastic modulus (E) of the material can be extracted from these testing regimes. It was found that changes in the planar (x&y) axes of the micro specimens would result in deformation behaviour characterised by a crumple like effect, un characteristic slip, or a localisation of shear ~45° along a slip plane. The deformation behaviour can be characterised visually (to confirm slip activity) and the critical resolved shear stress for each slip system, as well as the hardening due to multiple slip, can be extracted. Changes in deformation behaviour through deviations in orientation can be used to pre-programme failure criteria for the future design of new alloys. This chapter focusses on a 'simple' single crystal example to develop the approach and provide understanding of the limitations of micropillar based testing.

The alloy under investigation is single crystal CMSX-4, which is used to drive power to the aero engine, as a consequence of this these alloys experience a high level of stress during in service operation[178].

The CMSX-4 alloy is grown in a preferential <001> orientation via the use of a grain selector and an acceptable misorientation, with respect to the growth axis is 10°[11]. Thus, understanding how changes in orientation affect the deformation mechanics is a noteworthy point. The hypothesis being that tailoring the orientation, can enable failure criteria to be pre-programmed through the evolution of heterogeneous dislocation networks that move along designated planes and directions as dictated by the change in orientation.

The TEM enables the evolution of the dislocation networks to be viewed as they interact with the ϒ/ϒ' microstructure. Thus, sectioning micropillars to examine how dislocations behave at specific points during deformation is useful in the engineering of the next generation of alloys[179].

6.3. Introduction

This chapter starts with the examination of the size effect[4]. The size effect is a phenomenon In which, as the width of the micropillars are decreased a strengthening effect is observed[146]. It was found that slightly tapered, square faced pillars with a top width of 3-4 µm and an aspect ratio within 1:3 (width to

height) were the most stable, with respect to deformation. This design of pillar was subsequently used for future tests.

A stable pillar geometry is important to ensure a reliable and repeatable micro mechanical testing regime[175]. Pillars that are too tall can result in buckling through being mechanically unstable. Pillars that have aspect ratios that are too large undergo an excessive shape change as they are deformed and can compromise interpretation of mechanical data with respect to Schmid's law. Pillars that have areas that are too small harden at a dramatic rate, due to the interactions of dislocations in small volumes.

During the size effect study, it was observed that small changes in the orientation altered the mechanical response. The mechanical response can be characterised by the slip characteristics of the micropillar, which occur as the deformation mode changes from elastic to plastic. As the orientation of the pillar changes, the stress tensor with respect to the compressive load changes and this can be viewed visually, post yield, in the form of slip bands as plastic strain localises on the predicted slip systems.

Orientation 1, in which the cartesian coordinates x, y and z are aligned orthogonal to the (100), (010) and (001) directions deformed in a crumple, step like fashion. In Orientation 2, the x and y axis are aligned orthogonal to the (110) and (101), and deformed with a diagonal localised shear band, resembling a triangular slice. Orientation 3, in which the x and y axes were aligned to points near the (120) and (102), deformed in an unstable fashion. All the orientations had the same z direction, orientated as received in the <001> direction. With the $\{111\}\langle 1\overline{1}0\rangle$ slip system.

Sectioning deformed micropillars to a few 100 nm's enabling them to become electron transparent can enable examination via TEM to further characterise the dislocation processes that give rise to deformation in the commercially grown <001> CMSX-4 single crystal Ni alloy.

I found that the dislocation networks first form and interact in the softer ϒ fcc phase, local to the point of contact with the flat punch. As the level of strain is increased the dislocations spread rapidly throughout the microstructure, penetrating into the harder $L1_2$ ϒ' phase and concentrate at points relating to slip or an extensive shape change.

Section 6.4 will be examining micropillar design, instrumentation and micromechanical analysis ensuring the testing criteria and extraction of mechanical variables is as efficient as possible. Section 6.5, will be examining the deformation response and mechanical results from the 16 micropillar compression tests used to study the size effect. Section 6.6, will be examining the deformation response and mechanical variables with respect to changes in orientation. Section 6.7, Will detail the sample preparation and examination of micropillars deformed to designated points and viewed on the TEM.

6.4. Pillar scaling / size effect

Square pillars were used in this study as this makes post mortem examination of the slip systems of Ni superalloys more effective, figure 89. This is due to the flat surface on each face. Concerns are raised over the localisation of stress at the corners of the square pillars however these concerns are more apparent in brittle materials such as bone[26] and ceramics, rather than ductile materials such as metals.

6.4.1. Load, Displacement, Time

As the pillar is compressed the load, displacement, time data is recorded and can be appended to the live video of the pillar being deformed, as shown in figure 104.

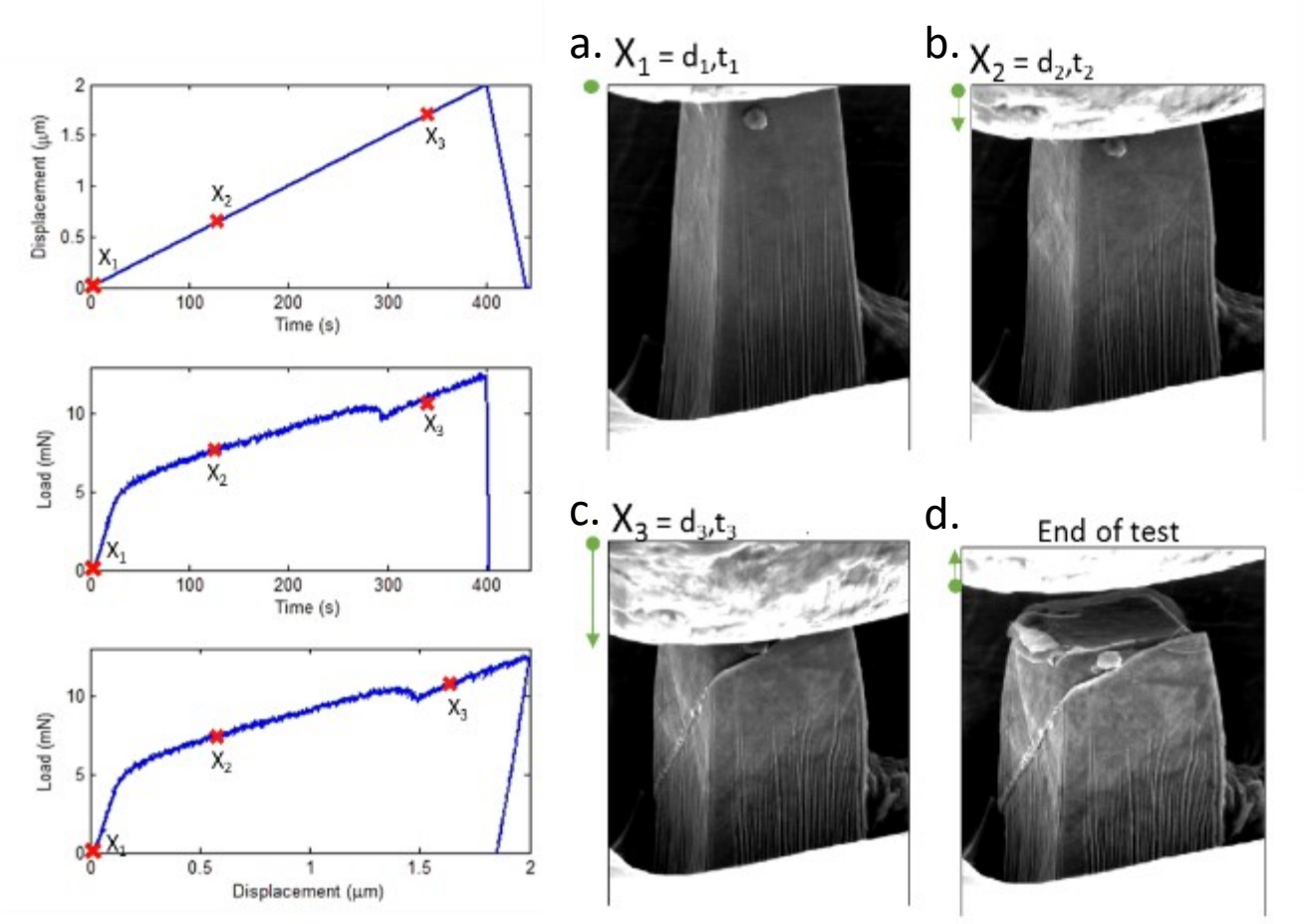


Figure 104: Load displacement time data at four points in the test (a) X_1 beginning of test (b) X_2 post yield (c) X_2 formation of shear slip (d) End of test – removal of flat punch

The load displacement time data is corrected to consider the load drift, adjusting the load and displacement values by a set amount accordingly, keeping this correction consistent through all tests.

The stress is calculated by dividing the load at any given time by the area of the pillar, calculated by squaring the half sum of the top and bottom widths of the pillar. The strain is calculated by the displacement at any given time divided by the original height of the pillar. This is shown schematically in figure 105. A height correction is applied to the taper and tilt angle of the SEM image. Error associated

with pillar area and height analysis can be minimised accordingly; The pillar widths (w_t and w_b) and the side length (l_s), taken as the distance from the bottom to the top of the pillar are measured, where the taper angle (θ_t) and a height (h) are then defined by the following equations:

$$\theta_t = \sin^{-1}\left(\frac{w_b - w_t}{2l_s}\right) \qquad \textit{Equation 36}^6$$

and

$$h = l_s \cos\theta_t \qquad \textit{Equation 37}$$

To ensure consistency between different compression tests, the area, width and aspect ratio must be kept constant.

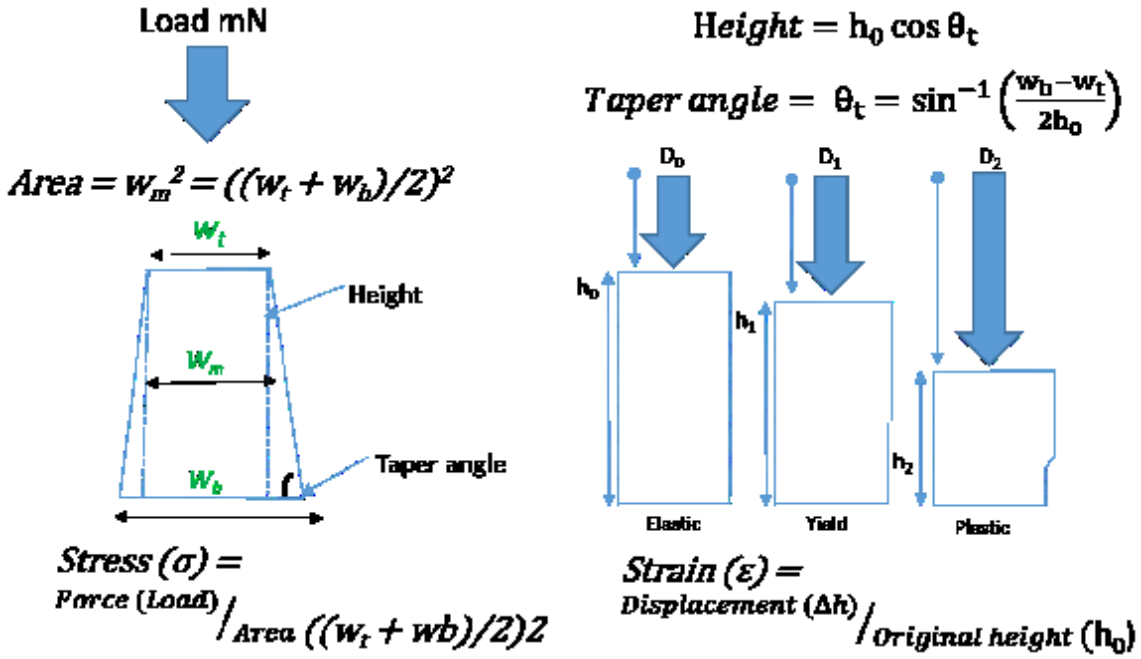


Figure 105: Pillar geometry for mechanical analysis (a) Stress. The stress determination is important as it is used to gauge the mechanical ability of the alloy and is used for the comparative study of strength through the yield point. (b) Strain. The strain gives a respective viewpoint of the level deformation as the tests are run in displacement control.

The engineering stress strain curve, given sufficient deformation quantified by % strain provides a finger print to the mechanical behaviour of the microstructure of the tested region as exemplified in figure 106.

6.4.2. Engineering stress strain

If a Ni super alloy micropillar is heavily strained it becomes very clear as to where the yield point occurs, and the level of hardening to be expected. This can be used as a statistical tool to ensure the testing methodology is reproducible and coherent.

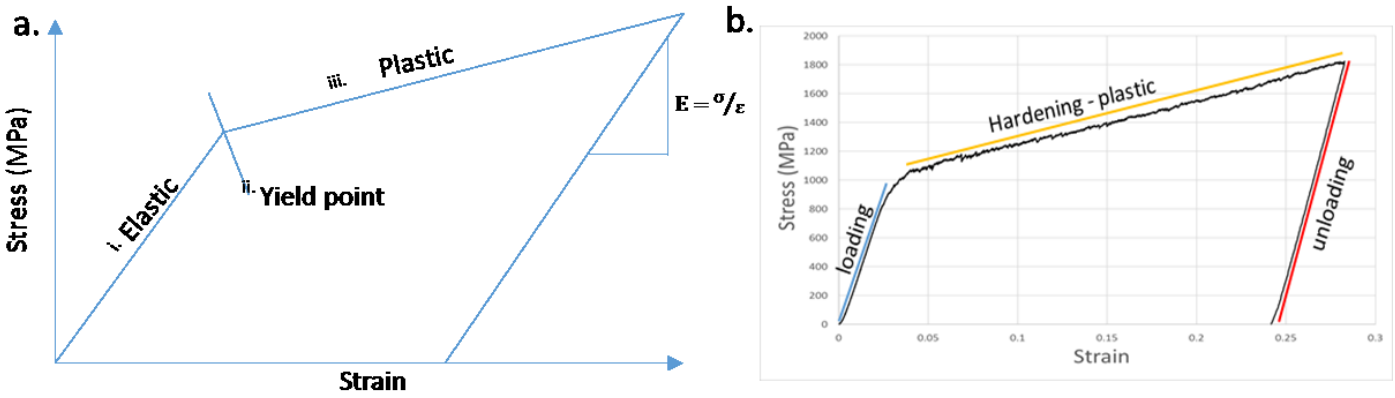


Figure 106: Engineering stress strain curve of a single crystal Ni superalloy <001> orientation ~30% strain

The deformation of the single crystal Ni super alloy CMSX-4 can be represented by the three regimes as shown in figure 106. The loading regime, figure 106 a (i) represents the elastic region of the deformation, in which the change in the gradient is indicative of the yield point. In this study, the proportional limit was used, to determine the yield point in favour of the 0.2 % offset method, figure 106a (ii). The plastic regime, figure 106a (iii) is indicative of the material hardening and is the gradient from which the hardening rate (H_r) is extracted, see figure 107.

The unloading regime, in which the flat punch is removed from the pillar is illustrated in figure 104d. The modulus is taken from the unloading regime and not the loading as there is an element of error, introduced when the flat punch comes into contact with the pillar. In short, the gradient in the loading regime cannot be trusted, figure 107.

As the flat punch comes into contact with the pillar there is a time delay between when the pillar fully conforms to uniaxial compression and or all the microstructural units align. The unloading regime is therefore taken to be representative of the modulus for the test.

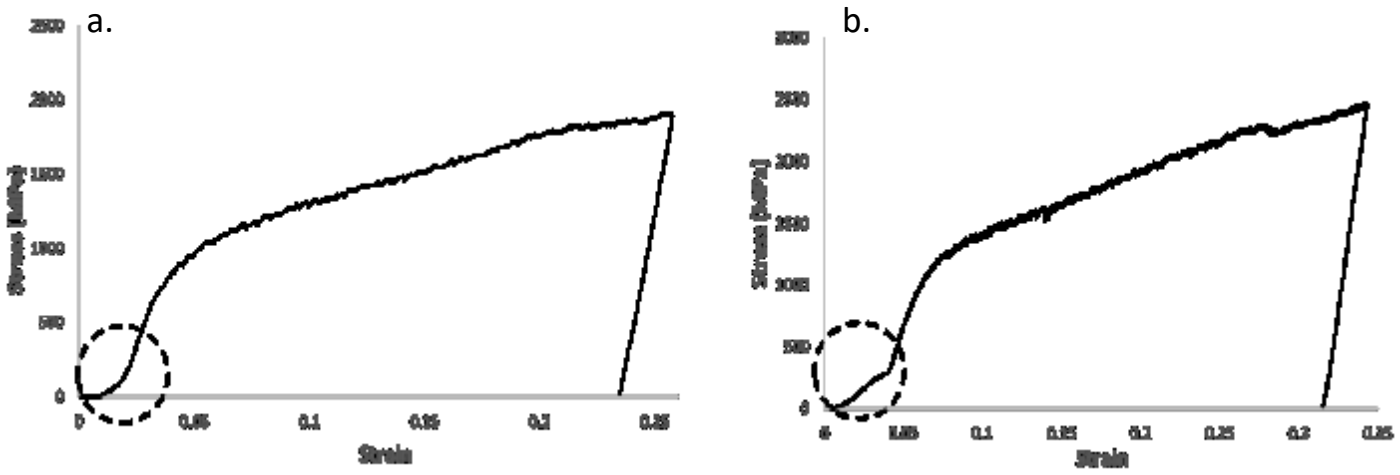


Figure 107: Stress strain curves from two separate micropillar compression tests, illustrating instability in the loading regimes. (a) Instability due to thermal drift / misalignment (b) instability due to structural / pillar geometry effects.

Figure 107 shows two conditions in which the loading regime has become displaced due to thermal drift and system error, which is normally corrected by the tare function. Figure 107 shows the elastic region experiencing drift / misalignment due to instrumentation and perhaps micro yielding in the case of figure 107b. Dramatic changes in the loading regime were also observed due to pillar instability as referenced by figure 107 and illustrated in figure 108. The extent of this error, in the form of micro yield is examined further in figure 108 in the form of the load displacement time trace paired with live *in-situ* video of the pillar deformation.

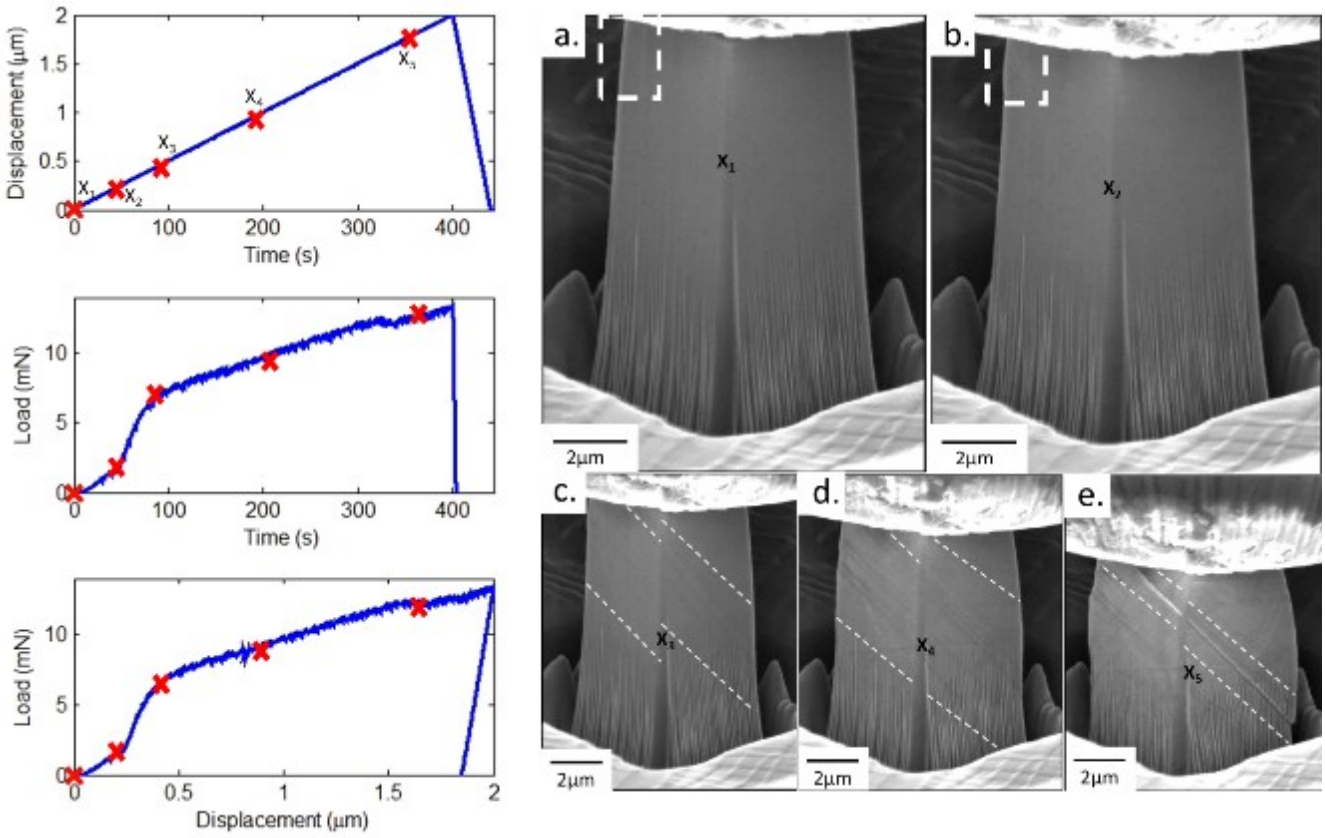


Figure 108: Appended load displacement time data for an unstable micropillar (figure 7b) (a) start of test (b) at 50 seconds change in the load response (c) at yield point (d) emergence of slip bands (d) competition between multiple slip systems (e) shear by localised slip band.

Figure 108 shows, pillar 8, from figure 107b, see table 1. Examining the load displacement time in-situ data from figure 108 b. The left side of the pillar begins to bulge and two changes in gradient are observed in the loading portion of the stress strain curve. One occurs at approximately 0.2 µm, X_2 displacement and the other 0.5 µm, X_3 displacement. This is indicative of non-uniform compression and or micro yield, figure 108 c and d show the emergence of slip bands competing with one another and a dominant localised shear band emerging at the dip in the load curve followed by shearing at point x_4 in figure 108e.

Despite trying, it was not possible to activate the easy glide regime in the CMSX-4 alloy and multiple active slip systems, as there is competition of multiple slip systems and strain bursts. The dips in the load displacement curves are known as strain bursts and both the completion of slip systems and strain bursts will be examined further, later in this section.

The correct interpretation of the three different regimes in the engineering stress strain curve is important when characterising the material, particularly when comparing different orientations and microstructures. For the size effect study, the key mechanical indicator was the yield point.

6.4.3. Yield point determination

To get an accurate representation of the strength, exhibited by the micropillars, the yield point was taken. The yield point is marked by the inflection in the stress strain curve as the deformation type changes from elastic to plastic. The yield point was measured using the proportional limit. The proportional limit was used in favour of the 0.2% offset method as in most instances the transition between elastic and plastic regimes is clear, as illustrated by figure 109.

The length scale of the micro compression tests is so small that substantial error can be introduced via the miscalculation of ± 0.5 µm in any dimension[126,134].

The determination of height has its own associated error via tilt and viewing angle[38]. The error from substrate / compliance effects also feeds into the determination of strain[45,150].

For these reasons amongst others, the use of the 0.2% offset method in this instance would not be wise. Figure 110 and figure 111 elaborate on this point in greater detail.

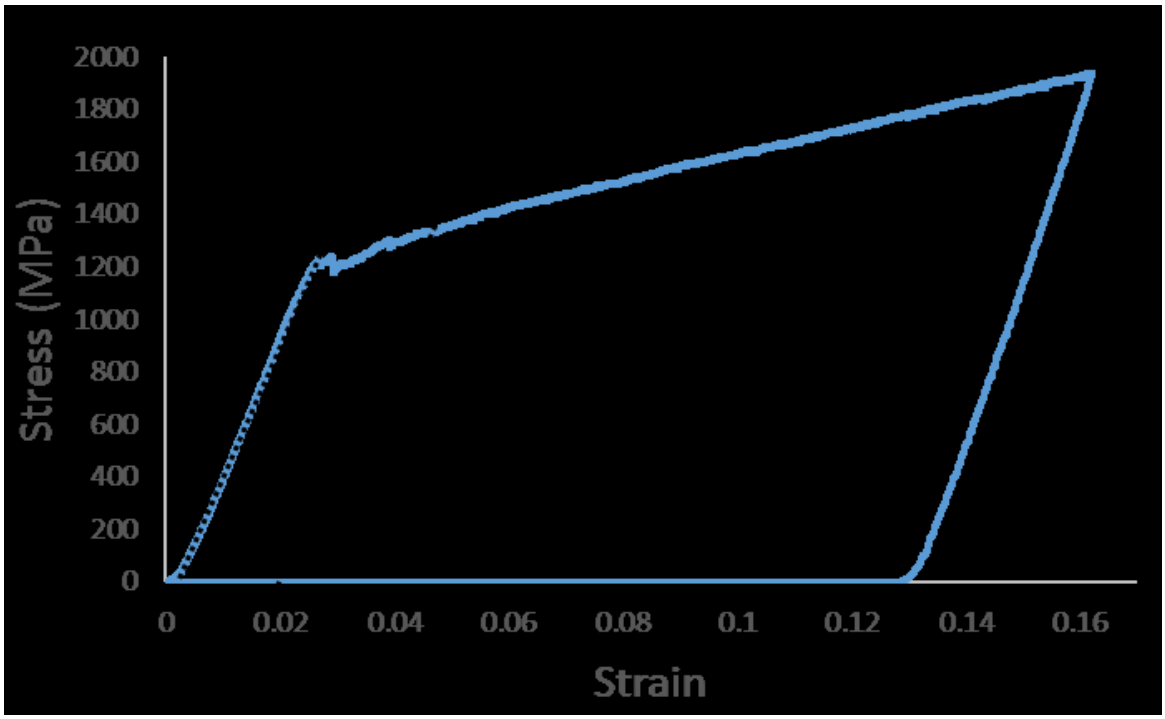


Figure 109: Stress strain curve from a CMSX-4 micropillar compression test, showing the difference between - The 0.2% offset method ($\sigma_{0.2\%}$) in which the yield point is extracted at a line tangential to 0.2% strain vs the proportional limit (σ_p) in which a line tangential to the 0 position is traced upwards until the gradient changes.

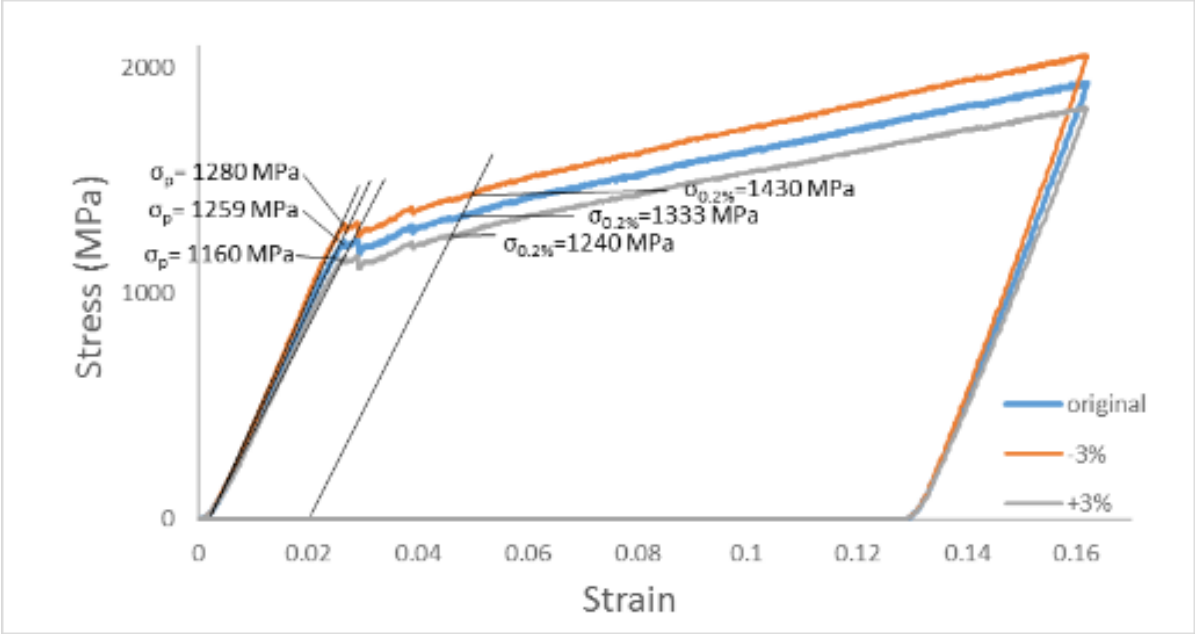


Figure 110: Stress strain curve from figure 9, with an additional ± 3% error added, illustrating the higher error margins incurred from the 0.2% method ($\sigma_{0.2\%}$) when compared to the proportional method (σ_p). Between 0-16 % strain

Figure 110 and figure 111 had ± 3% error added to the area, which is derived from the top and bottom width of the micropillar, this is seen in figure 105. The ± 3% error added to the area has been translated to the stress strain curve from figure 108.

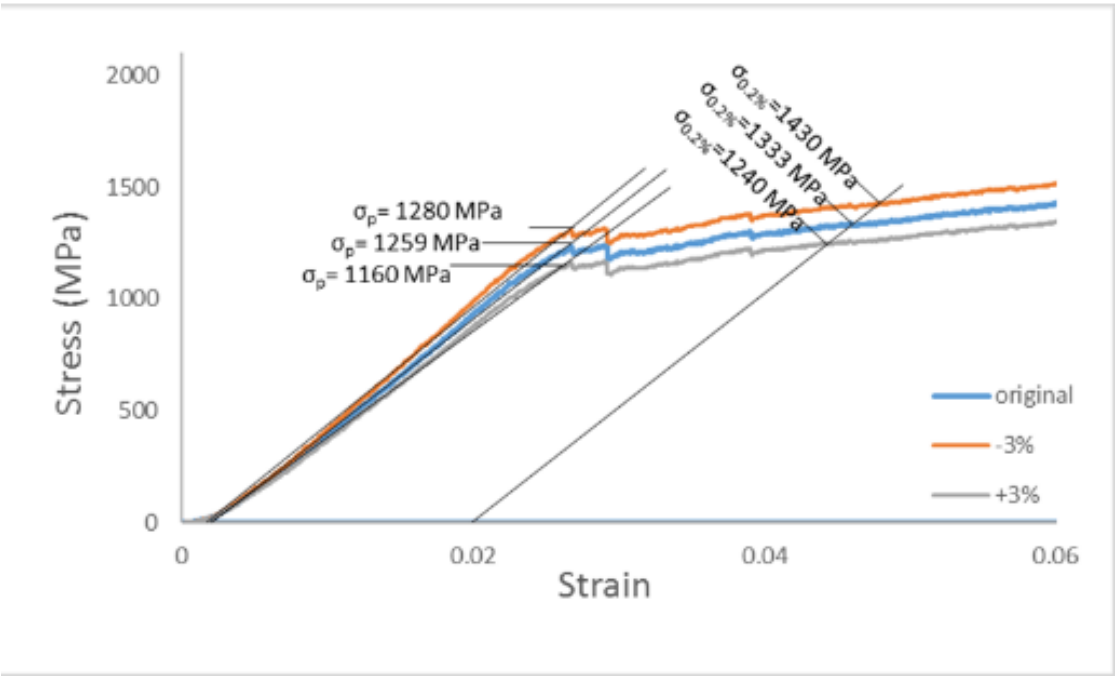


Figure 111: Stress strain curve from figure 9, with an additional ± 3% error added, illustrating the higher error margins incurred from the 0.2% method ($\sigma_{0.2\%}$) when compared to the proportional method (σ_p). Between 0-6% strain

Comparing the values of yield via the proportional limit vs the 0.2% offset method, it was found that the associated error when comparing the offset ($\sigma_{0.2\%}$) to the proportional (σ_p), was nearly double. The yield

point found via the offset ($\sigma_{0.2\%}$) is 1334 MPa ± 95 MPa whereas the yield point via the proportional (σ_p) method is 1233 MPa ± 50 MPa.

The 0.2% offset is affected by hardening which changes according to the orientation of the cubic lattice with respect to the loading direction. The hardening also varies according to the region in a precipitation alloys. This adds inconsistency / additional error to results. The effects of orientation and precipitates will be discussed in more detail in later sections.

6.4.4. Hardening and modulus

The determination of the hardening and the unloading modulus were kept consistent throughout this study. The hardening was calculated taking from the 10-15% strain region of the stress strain curve figure 112a. The unloading modulus gradient was taken from the peak of the curve down to ~850 MPa figure 112b.

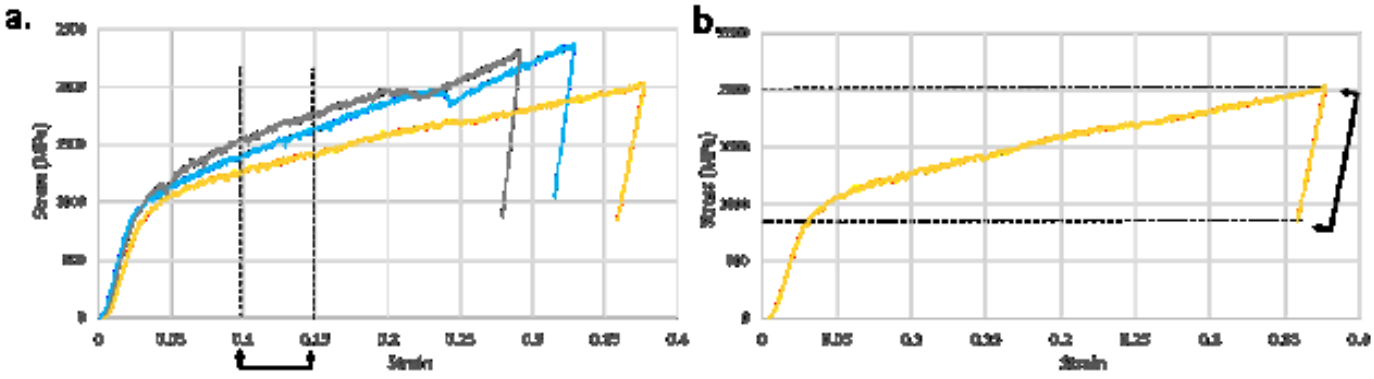


Figure 112: Stress strain curves illustrating the determination of (a) Hardening rate - taken from 10-15% strain (b) Unloading modulus - taken from the peak down to ~850 MPa

To conduct the size effect study, micropillars were fabricated with top widths ranging from 1 µm to 4 µm. This was done in three data sets each with a slightly different orientation. The orientation in the z direction remained consistent. However, the orientation of the x and y axis' varied slightly. When fabricating single crystal Ni super alloys the growth direction is always <001> with margins of 10°. It was found from this set of testing that changing the in plane orientation, could change the hardening and failure mode of the pillar. i.e. a crumple like deformation or a shear localisation in which a near 45° slip band would emerge figure 120.

6.4.5. Compression testing – Pillar geometries

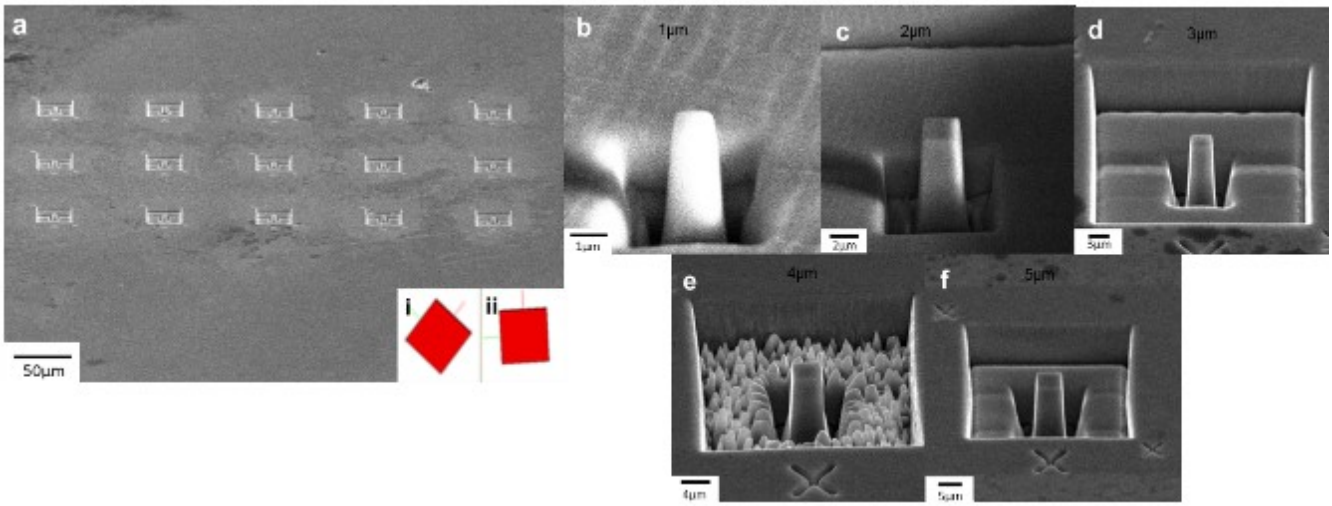


Figure 113: Fabricated pillars (a) an array of pillars ready for compression testing (b) 1µm (c) 2µm (d) 3µm (e) 4m (f) 5µm

The compression tip was aligned to the top surface of the pillar and the displacement was carefully controlled until a small peak in load was recorded. The compression tip was removed slightly, the system error tared and the test started. The representative stress strain curves for the compression of micropillars ranging from 1-4 µm are illustrated in figure 114.

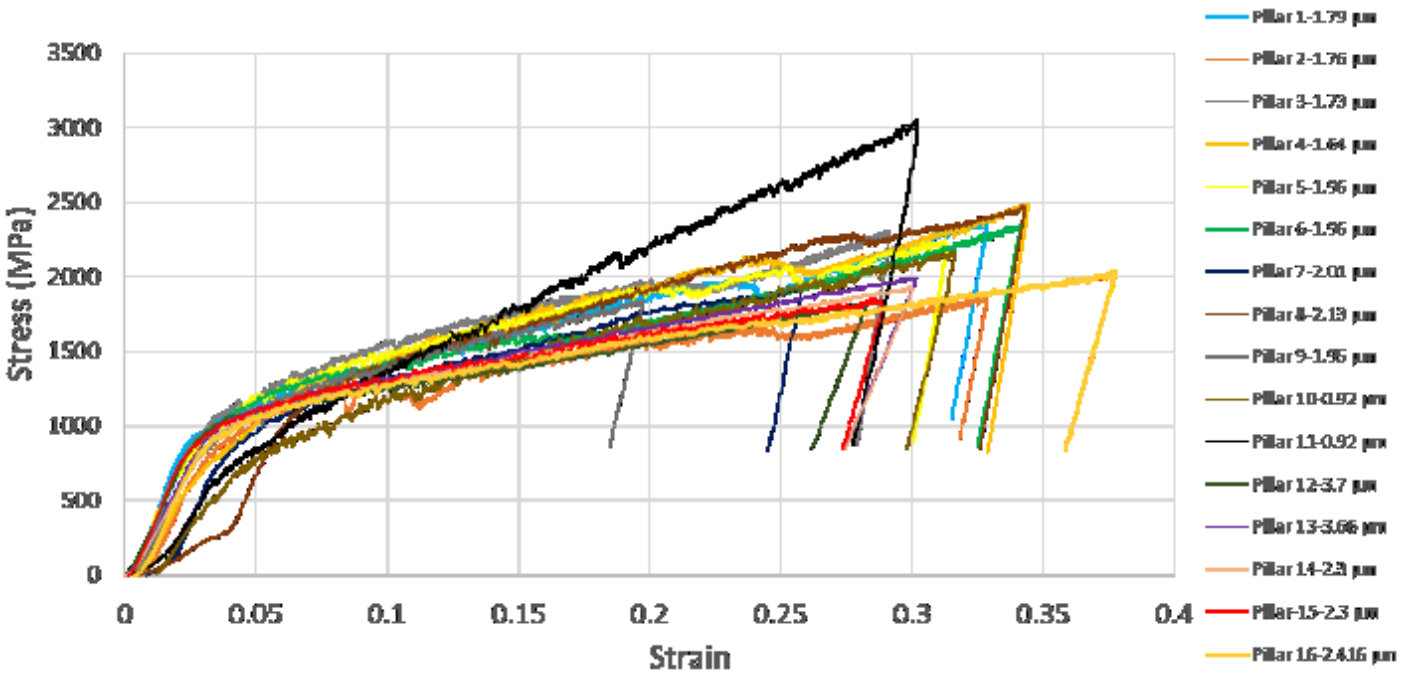


Figure 114: Stress strain curves for pillar tests 1-4 µm. illustrating the spread of data, due to the geometry and area of the micropillars. The variation in mechanical properties and deformation slip behaviour is discussed in more detail in section 1.4. Table 1 shows the numerical results of the 16 pillar tests illustrated in this figure.

Figure 114, shows the stress strain traces from the compression of the 16 pillars used in the size effect study. The numerical results are shown in table 7. The hardening and in some cases the elastic modulus

varied across the pillar sizes, as shown in figure 116 and figure 117. The general trend in yield point behaviour did not support the size effect theory. This could be attributed to the orientation effects, section 6.6 and or differences in aspect ratio and or geometry, figure 121-24.

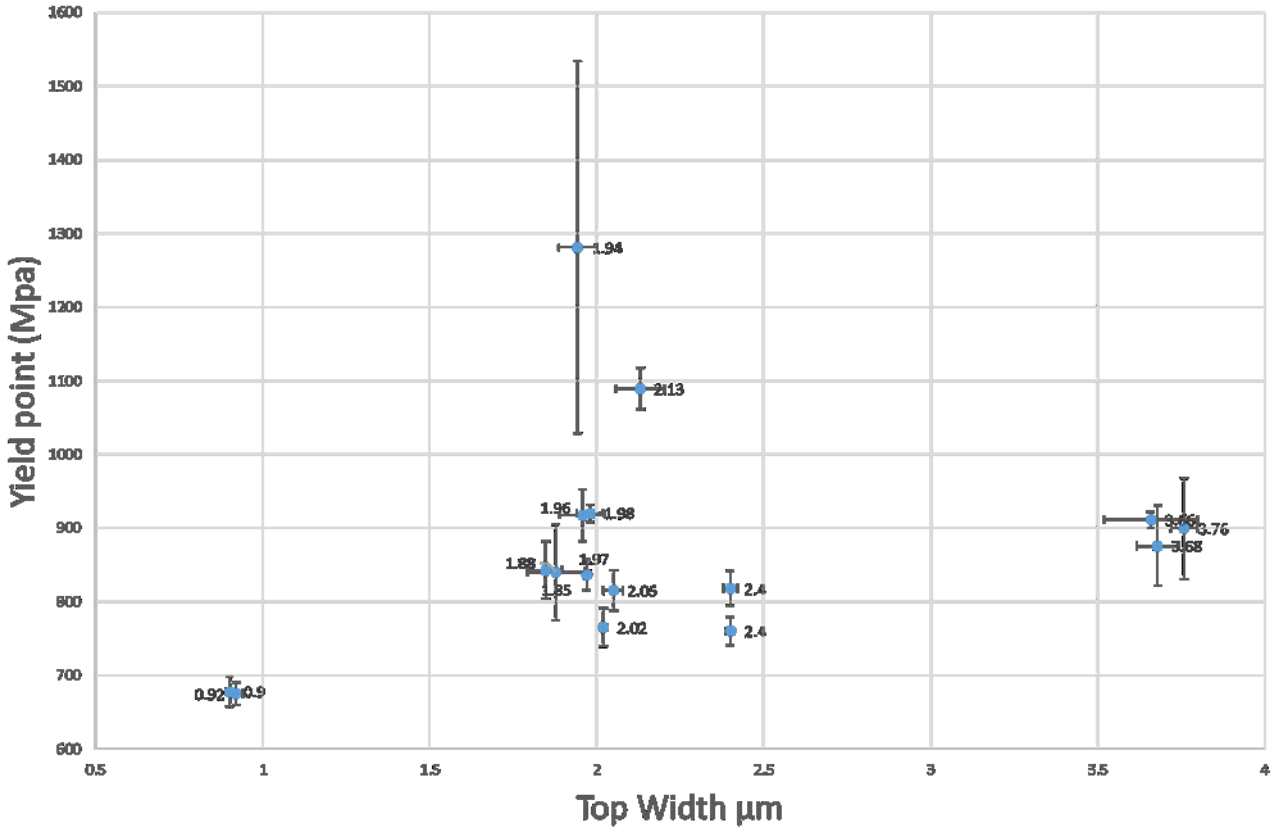


Figure 115: Top width vs Yield point σ_p method indicating the 3-4 µm is the most stable size

Figure 115, shows how the yield points (Y_p) from the 16 pillar compression tests correlate to the top width (W_t). The tests are from 3 different data sets with three different crystal orientations, with Schmidt factors lying near 0.41 indicative of a <001> compression axis. The misorientations of the planar axis x & y will be discussed further in section 1.4. The average yield point across the 16 pillars tested was found to be 870 MPa ± 148 MPa between the widths 1-4 µm. Which is consistent with literature[133]. One of the key trends observed from this series of testing indicated that pillars fabricated in the 3-4 µm region tend to be the most stable / have the least scatter and so for future studies this size was chosen, keeping the aspect ratio ≤ 1:3, top width to height. This study was important as the mechanical variables extracted from the micropillar tests can be used to feed models to predict the alloys performance on the macroscale.

Table 7: Table of results from 16 pillar compression tests used for the size effect study. W_t – top width, W_b – Bottom width, H_0 – Initial height, Y_p – Yield point, A_r – Aspect ratio, U_l – Unloading modulus, H_r – Hardening rate, W_t_sd – Top width standard deviation, Y_p_sd – Yield point standard deviation. The values for Wt, Wb, H_0 and area were taken in accordance to figure 5. The

yield point was extracted using the proportional limit, figures 9-11. The hardening rate and unloading modulus were extracted in accordance to Figure 112.

Pillar	W_t µm	W_{t_sd} MPa	W_b µm	H_0 µm	Y_p MPa	Y_{P_sd} MPa	Area µm^2	A_r	U_l MPa	H_r MPa
1	1.85	0.05	2.89	6.09	843	39.1	5.48	3.30	96185	4384
2	1.88	0.09	2.85	6.99	840	65	5.31	3.72	88671	2609
3	1.96	0.07	2.79	6.86	917.7	35	5.11	3.51	115413	4080
4	1.64	0.06	2.75	5.81	1281	253	4.82	2.99	105519	5619
5	1.97	0.01	2.97	6.39	837	21.1	5.43	3.24	102215	4387
6	1.98	0.04	2.77	5.86	920	11.53	5.73	2.96	90443	3168
7	2.05	0.03	2.81	5.82	815	27.84	6.08	2.84	85017	4513
8	2.13	0.07	2.97	5.82	1089	28.2	5.62	2.73	91754	5384
9	2.02	0.01	2.97	5.05	765	26.1	5.52	2.50	74450	4774
10	0.90	0.01	1.323	1.90	678	20	1.23	2.11	71881	4839
11	0.92	0.02	1.32	1.98	675	15	1.25	2.15	83705	9902
12	3.68	0.06	4.54	7.03	875.5	54.4	16.88	1.91	46711	2872
13	3.66	0.14	4.61	6.59	911	11.1	17.11	1.80	41744	3563
14	3.76	0.04	4.683	6.61	899.5	68.59	17.82	1.76	41530	3498
15	2.23	0.01	2.973	5.19	760	19.8	6.77	2.33	64671	3432
16	2.42	0.02	3.36	5.30	818	23.2	8.34	2.19	62409	2619

6.5. Mechanical effects

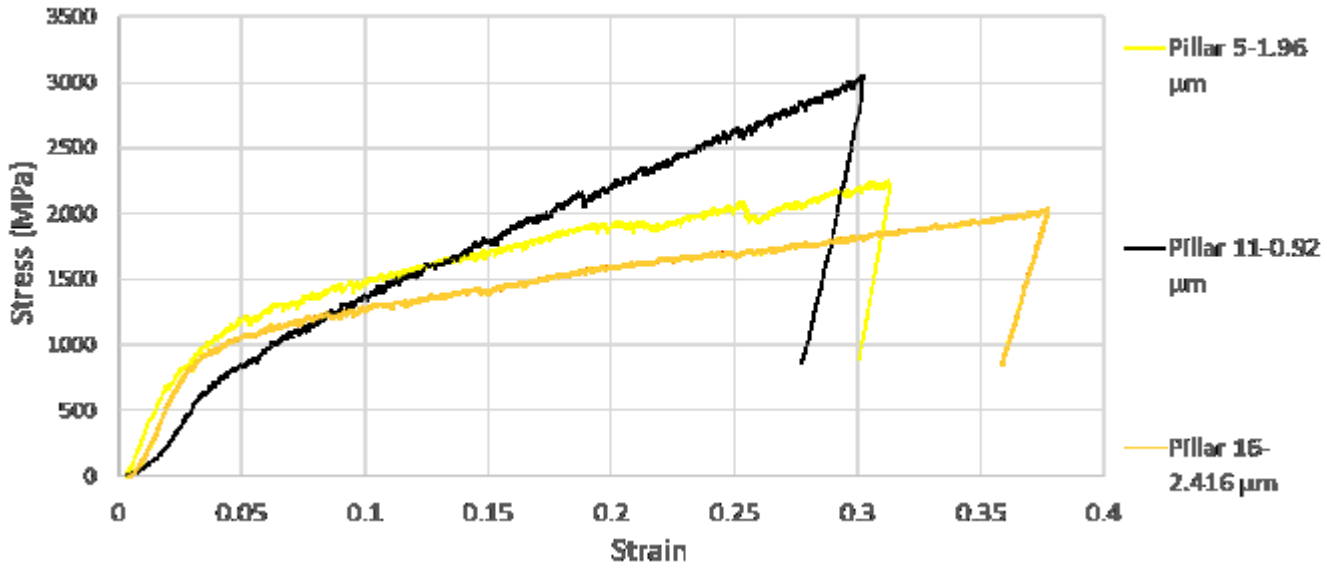


Figure 116: CMSX-4 stress strain curve showing the hardening response across three micropillars, 5,11,16, see Table 7, used in the size effect study. Illustrating the difference in hardening across pillars. The average hardening across the three micropillars was 5636 ± 3799 MPa. The difference between the lowest and highest value is 68%.

Figure 116 shows the hardening response across 3 pillars used in the size effect study, which represent the largest spread of hardening between pillars 5, 11 and 16. The hardening rate of pillars, respectively

are as follows; 4387, 9902, 2619 MPa. The average hardening rate across the 16 pillars tested being 4352 ± 1747 MPa.

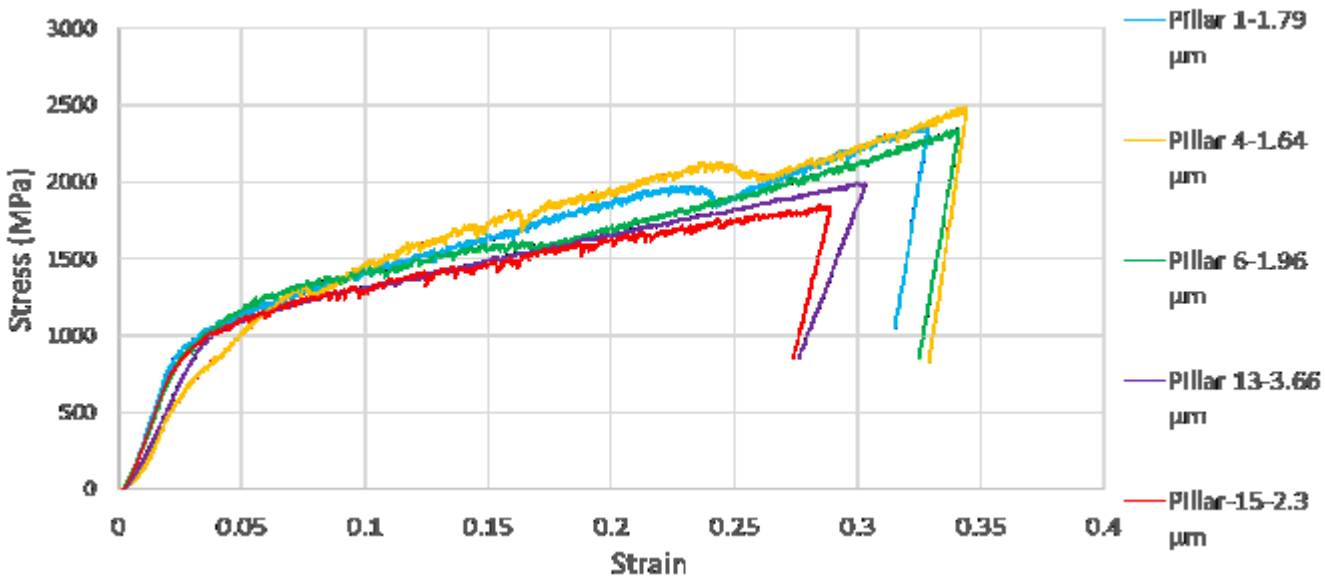


Figure 117: CMSX-4 stress strain curve showing the unloading modulus response across five micropillars used in the size effect study. Illustrating the differences in modulus response across pillars. The average hardening across the five micropillars was 81690 ± 28763 MPa. The difference between the lowest and highest value is 170%.

The unloading modulus of pillars; 1,4,6,13,15, in figure 117 are 96185, 115412, 90443, 41744, 64670 MPa. The average modulus across all 16 micropillars tested being 78895 ± 22650 MPa. Although the top width, size effect experiments examined in this study, did not agree with former studies, by other authors[171]. Figure 118 and table 7 indicate that as the width of the micropillar is decreased the hardening increases from below ~2 µm.

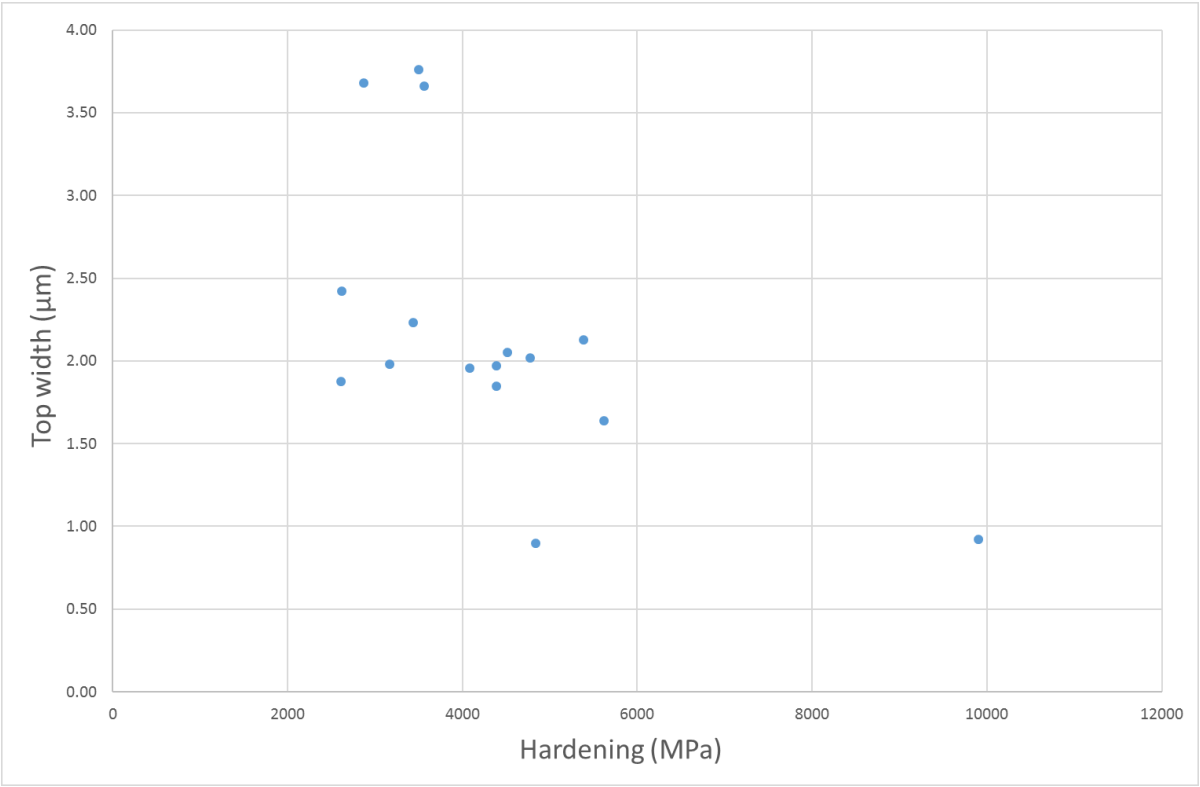


Figure 118: Top width of 16 tested micropillars vs their respective hardening rates. Illustrating an inversely proportional relationship between top width and hardening. Which seems to be more predominant below ~2µm.

The scatter in figure 118 is due to differences in aspect ratio and orientation, whereby the pillars are all taken from the same single crystal sample. It was found that as the aspect ratio is increased the pillars become stiffer, as shown in figure 121-22 and changes in orientation affect the hardening of the pillar through changes in area and shape, figure 127-28.

When the pillar yields, giving rise to the onset of plasticity, it forms slip bands, which appear as visible lines spanning the length of the pillar subtended at a certain angle depending on the Schmid factor.

A large number of dislocations are required to observe a slip step, whereby 1 dislocation equals 1 Burgers vector of displacement on the surface and therefore each slip trace is comprised of 100s of dislocations reaching the surface.

A distinction should be made between slip trace and slip system. Multiple slip traces can occur at different points on the pillar, characterised by a plane and a direction, whereas multiple slip traces can occur due the same slip system, it just depends where the shear localises to cause a band. Different slip systems can be characterised by a change in angle or direction of the slip trace. This can be seen in Figure 120 and is described in greater detail through figure 129-34.

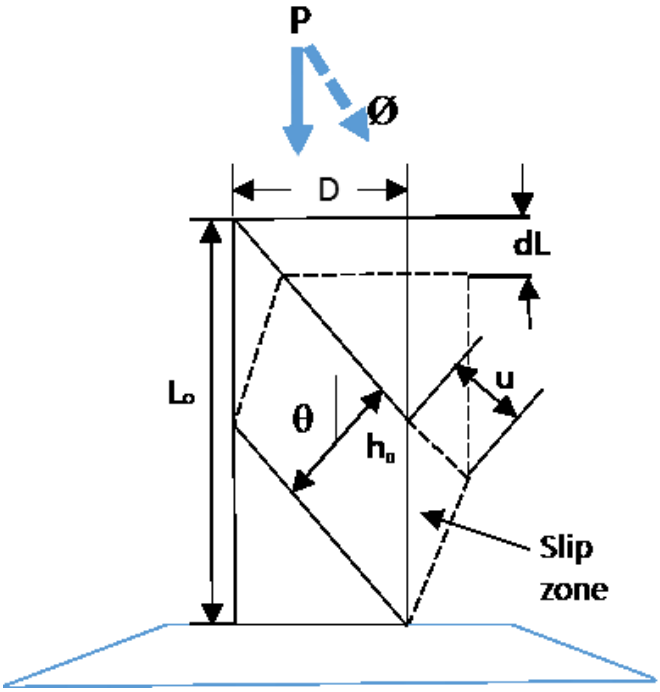


Figure 119: Schematic of slip plane traces adapted from a paper by Dimiduk & Uchic[41]

Figure 119 shows a two-dimensional schematic of a micropillar being compressed. The solid lines represent the initial arrangement where all microstructural units are aligned with the bulk of the crystal.

The dashed lines represent the sample after testing. θ is the angle between the slip plane normal and the load axis (needed for the τ_{crss} and Schmid factor calculation).

U is the projected off-set of the slip planes after the displacement dL. It is important to note that because of the load-point rotation Ø, about a distant point P (relative to L_o), the slip-zone height, h_0, remains constant with strain. The load point rotation Ø, changes depending on the orientation of the planar (x and y) axes and this affects the orientation and extent of the slip traces, that occur post yield as seen in figure 120.

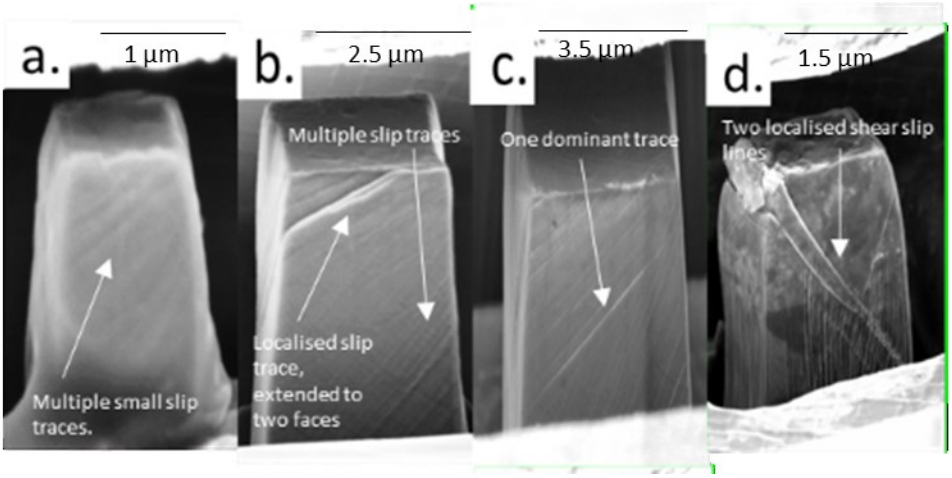


Figure 120: Deformed micropillars with top width 1-4 µm, illustrating the differences in slip traces, referenceing figure 19 (a) Pillar 10 w_t – 0.9 µm, area - 1.22 µm^2 (b) Pillar 16 w_t – 2.42 µm, area - 8.34 µm^2 (c) Pillar 14 w_t – 3.76, area – 17.8 µm^2 (d) Pillar 4 w_t – 1.64, area – 4.82 µm^2

Figure 120 shows pillars ranging from ~1-4 µm that have been deformed to over 15% strain. Slip lines are visible on each of the four pillars and the deformation in each pillar is slightly different, whereby dislocations have propagated leaving slip steps along the faces of the pillar. Each pillar has a different geometry and area, see table 1, based on the top width w_t, bottom width w_b and aspect ratio.

Figure 120 a, shows a pillar with a 0.9 µm top width, which has multiple slip traces emanating from one side of the pillar to the other in a diagonal orientation, with no clear shear localisation. Figure 120 b, shows a pillar, with a 2.42 µm top width, that has rotated and bulged at the lower edges slightly, with one dominant shear band localised at the top surface of the pillar. Figure 120 c, shows a pillar, with a 3.7 µm top width, again with multiple slip traces but with one local dominant band, that has formed in the middle of the pillar subtended to an angle ~45°. Figure 120 d, shows a 1.64 µm, with two very clear slip bands localised at ~45 subtending from one corner of the pillar to the other, with the x and y axis aligned to 110 and 011 respectively.

As evidenced in literature[15] the aspect ratio plays a role in the mechanical response of pillars during deformation. Pillars with large aspect ratios were found to be the most unstable, where is was found that an aspect ratio ≥ 1:3 (width to height) is deemed too large, ≥ 1:3 is ideal. Taking figure 119 as reference, this makes sense, as the schematic shows a pillar with no taper, as the pillar is compressed the cross-sectional area will change as a function of strain and thus in a pillar with a larger aspect ratio the area change is more significant giving rise to un characteristic slip activity.

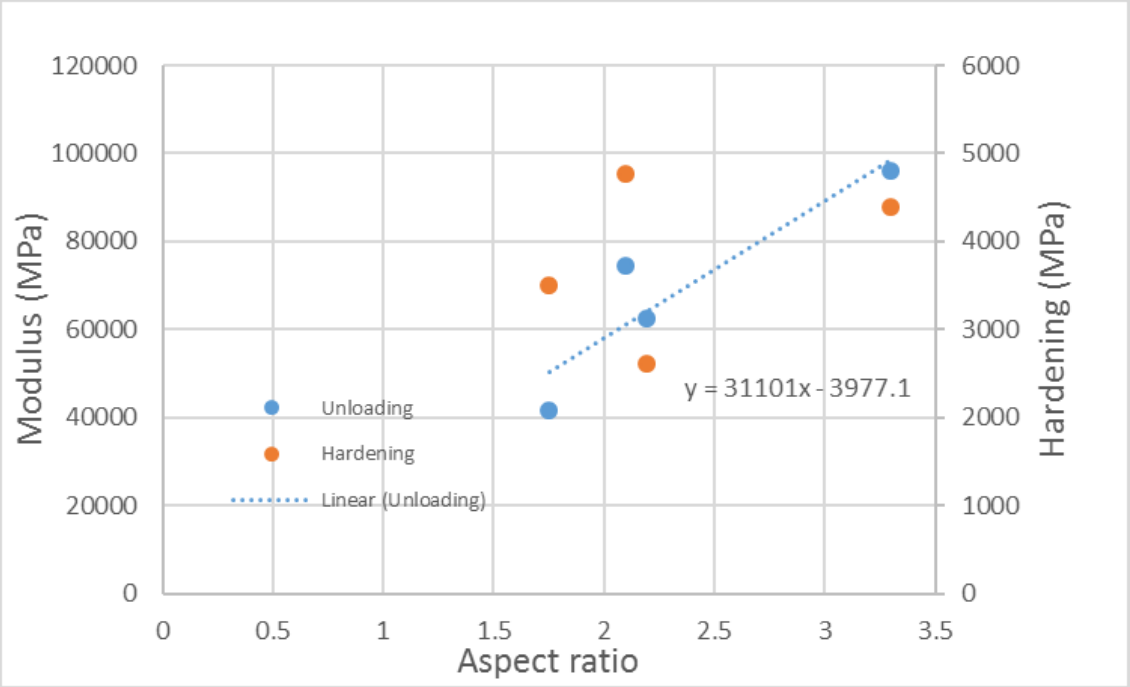


Figure 121: Modulus and hardening vs aspect ratio for the pillars ranging from 1-4 µm in figure 20. Representing the inverse proportionality between modulus and aspect ratio.

Figure 121 takes the representative data for the hardening and modulus' for pillars 10,16,14 & 1, from figure 120 representing the top widths 0.9, 1.85, 2.42, 3.76 µm. Examining figure 121 it is evident that the larger the aspect ratio, the apparent (engineering) elastic stiffness increase. The hardening seems to be in part agreement however as explained in figure 118, hardening appears to be inversely proportional to top width. Taking the whole data set of 16 pillars this trend becomes clearer, as can be seen in figure 122.

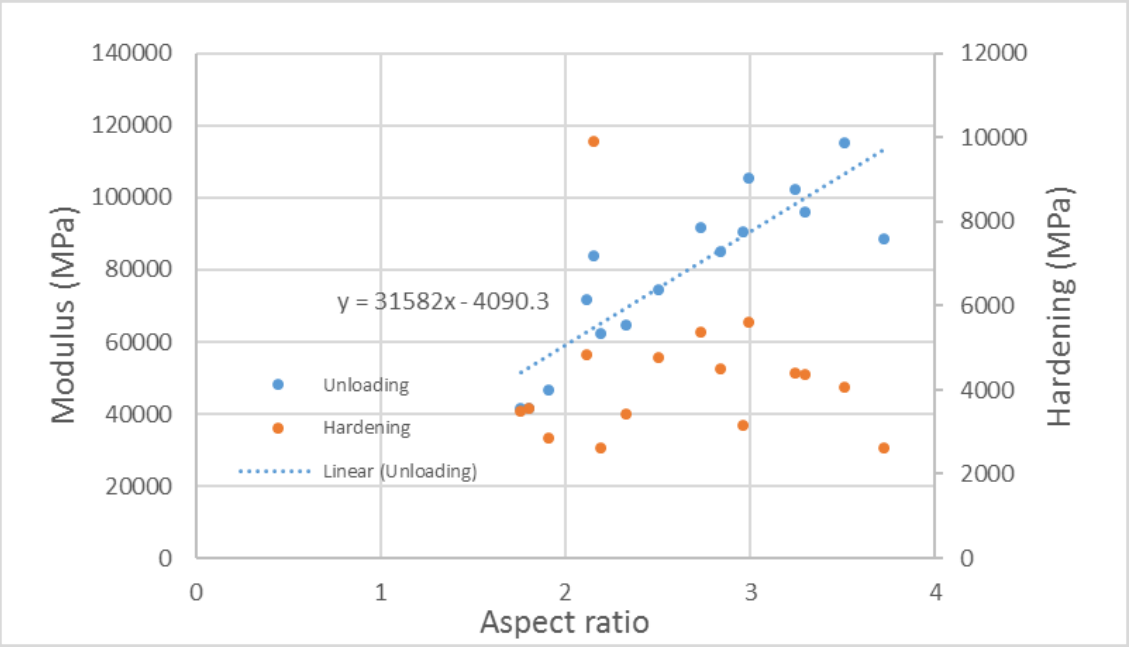


Figure 122: Modulus and hardening vs aspect ratio for all of the 16 tested pillars.

As the aspect ratio is increased the pillars become stiffer, however there is no correlation between aspect ratio and hardening. The gradient line in figure 122 has been fitted with a linear fit.

There were 3 pillars out of the 16 tested that had aspect ratios higher than 3 (3.3,3.5 & 3.7). One of these pillars is shown below in figure 123.

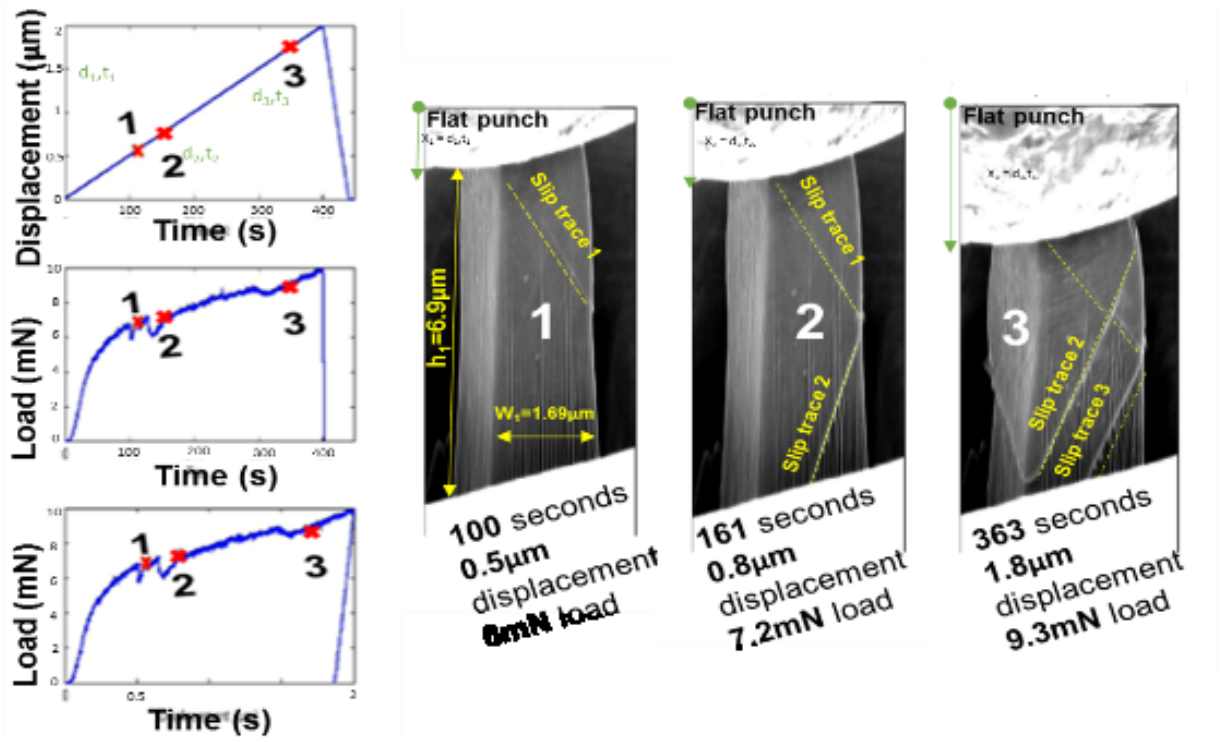


Figure 123: Pillar 2 which had the highest aspect ratio (3.7) of all the 16 pillars tested, shearing along 3 distinct slip traces which correspond to "blips" in the stress x strain response. The response is known as a strain burst.

The pillar shown in Figure 123 has the largest aspect ratio out of all the 16 pillars tested. It shows the emergence of three localised shear bands each one attributed to a slip event known as a strain burst[35].

Strain bursts can occur as independent shear localisation, or as a consequence of the competition of several slip systems and can be observed and traced back to events in the stress strain curve.

Whether the slip events occur because of several competing slip systems or as the emergence of one clear shear localisation, was found to ultimately be controlled by orientation and the deviation from ideal orientation whereby the x, y and z Cartesian axis are aligned along the 001, 010 and 001 [uvw] axis respectively.

Changing the orientation in this sense affects the mechanical properties. This was due to the orientation of the edge of the sample axis with respect to the pillar set up.

The orientation of the pillars was found to influence the mechanical behaviour also, namely in the form on slip behaviour, with slight deviations from <001>.

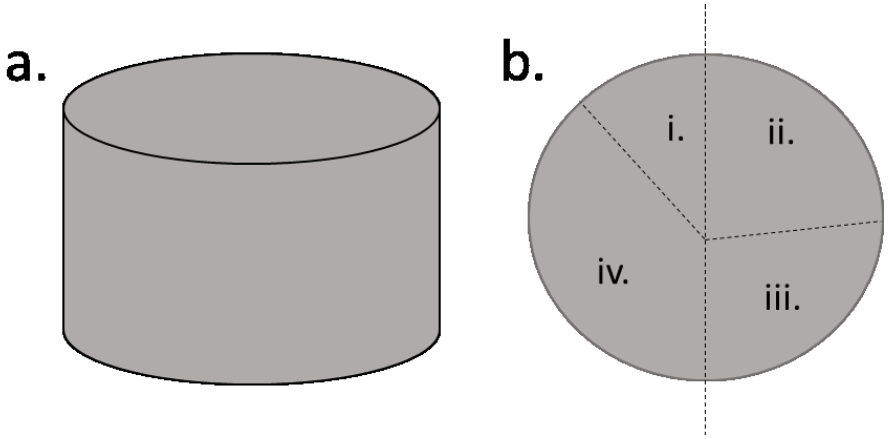


Figure 124: Sample preparation that lead to the slight deviations in orientation of the <001> single crystal CMSX-4 alloy (a) Original sample piece (b) section sample piece that was used for to align axis, however aligning along the acute and obtuse angles gave rise to small changes in orientation.

The main ingot was circular, cuts were taken to save material. Aligning along the respective edges of the samples, altered the planar axis and hence orientation. The three orientations were by products of sample preparation for the three orientations <001> <011> and <111> . All three orientations are aligned so that the compression axis is in the <001> direction.

6.6. Mechanical effects with respect to orientation

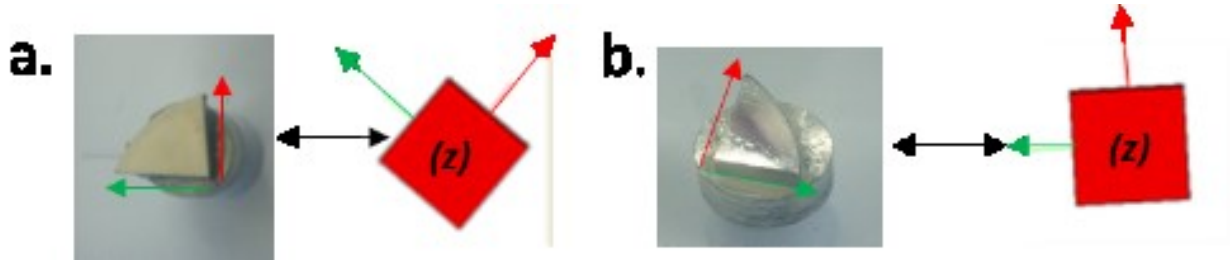


Figure 125: The two sample cuts (a) Figure 24bi – Sample 1, Orientation 1 (b) Figure 24bii – Sample 2, Orientation 2&3

Three orientations were used in the compression of the 16 pillars examined in the size effect study. In Orientation 1 (from sample 1), the sample was orientated in such a way that the edge is aligned with the crystal orientation in red figure 125 a. Whereby the green and red arrows represent the planar axis. The x pointing out of the page represents the (001) plane in the normal direction (pointing upwards). The reason for this being, It was taken from a sample being prepared to be cut in the (011) crystal orientation in the normal direction, figure 124.

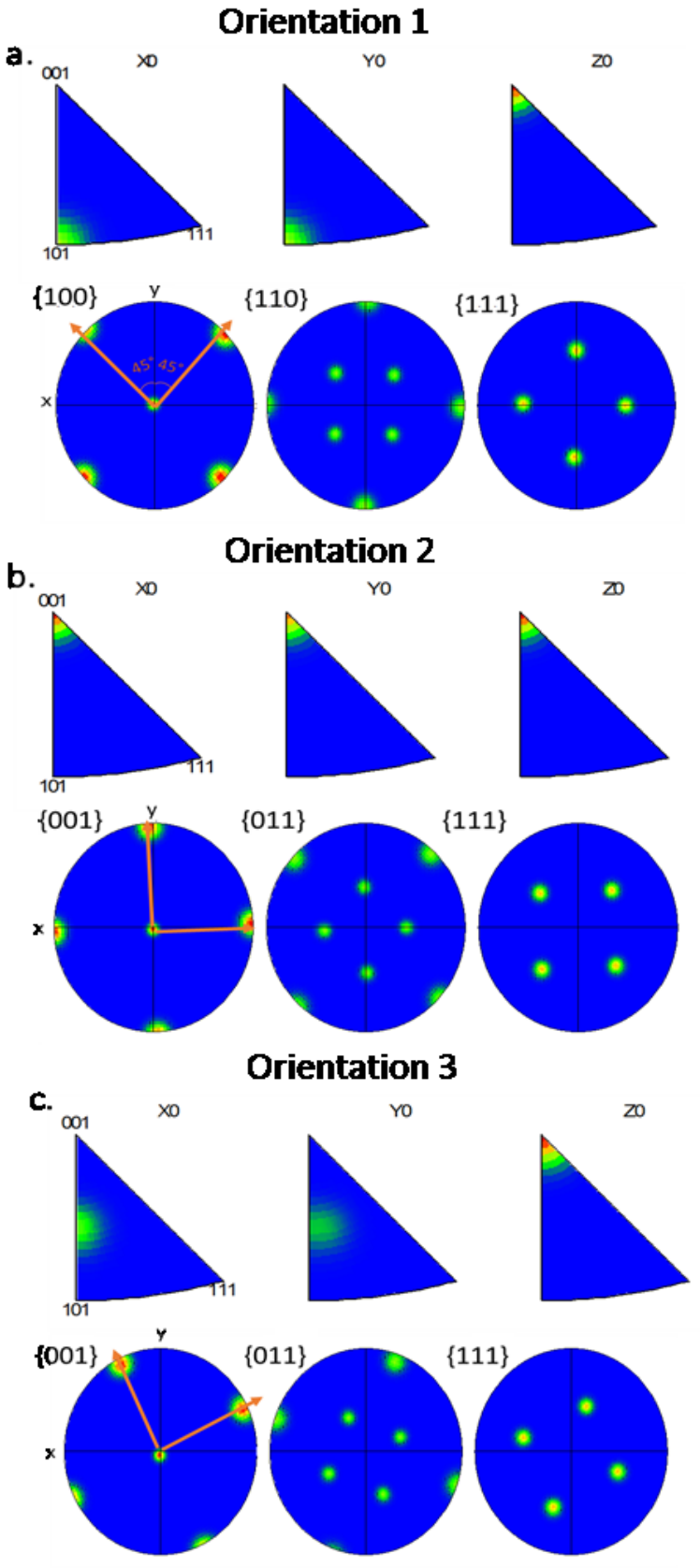


Figure 126: Inverse and pole figures, for the micropillar samples cut from the CMSX-4 superalloy, with the <001> loading direction, for orientations (a) 1 (b) 2 (c) 3

In Orientation 2, The sample is orientated in such a way that the edge is aligned with the <001> crystal orientation, figure 125b. Whereby the green and red arrows represent the planar axis. The x pointing out of the page represents the (001) plane in the normal direction (pointing upwards). There is a slight misorientation of approximately 2 degrees as measured from the pole figures taken via EBSD mapping on the JEOL 6400.

In Orientation 3, the planar axis were orientated 30° from the 100 and 001 respectively, see figure 120.

Error! Reference source not found., shows the inverse and pole figures of orientations 1-3. Figure 1 27, shows the stress strain curves for the pillars tested in orientations 1-3 respectively.

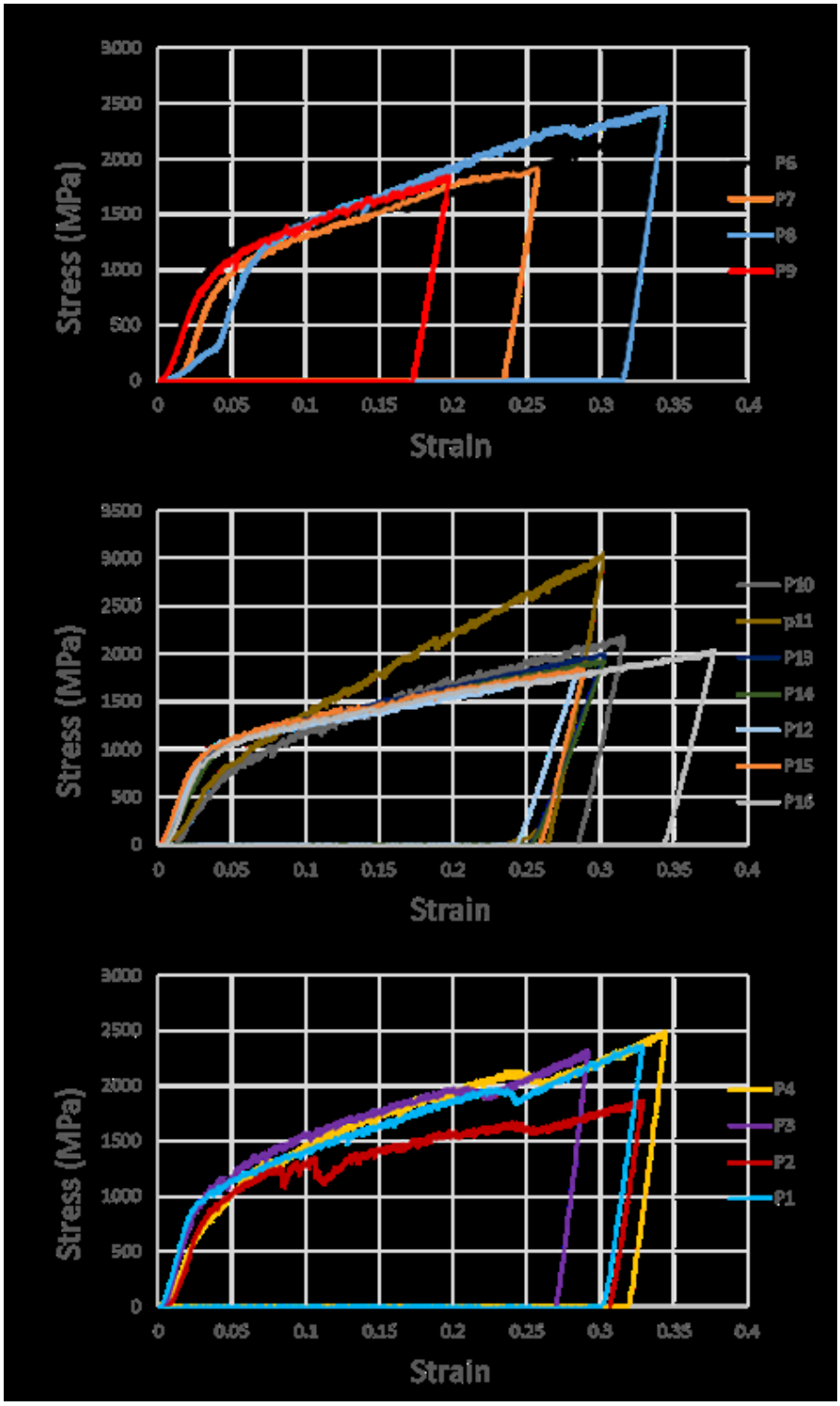


Figure 127: Stress x strain curves from the 16 micropillars tested for the size effect, separated into orientation. (a) Orientation 1 (b) Orientation 2 (c) Orientation 3. The favourable slip system is $(1\ \ \bar{1}\ \ 0)(1\ \ 1\ \ 1)$ *for all three orientations.*

Comparing figure 127 a-c, it can be seen that orientation 1 is the most stable of the three. The stress strain traces are retraceable with no major strain bursts and clear shear localisation of the near 45° slip line. Apart from pillar 8 in which there was micro yielding and or misalignment in the loading regime.

The stress strain traces for orientation 2 are not too dissimilar from those in orientation 1, with most traces in agreement except for one outlier. Orientation 3 however is the most unstable, with a very unstable hardening regime as evidenced by the large number of strain bursts, it is also the stiffest orientation.

The yield point, hardening rate and modulus for orientations 1 are, 898 ± 143 MPa, 4460 ± 850 MPa, 85416 ± 7870. For orientation 2, 803 ± 100 MPa, 4389 ± 2532 MPa, 58949.6 ± 16196.9. However, if the outlier pillar 11 is neglected the hardening rate becomes, 3471 ± 770. For orientation 3, 971 ± 210 MPa, 4173 ± 1237 MPa, 101447 ± 16197.

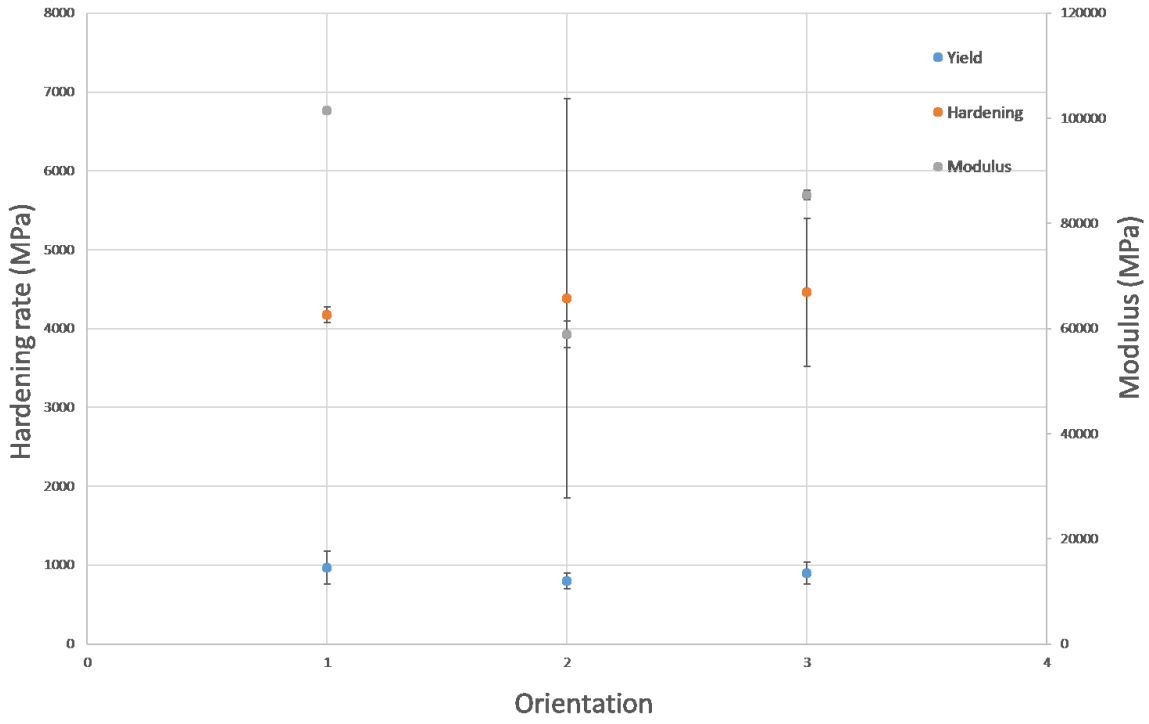


Figure 128: Hardening rate & modulus vs orientation. Indicating that orientation 1 is the most stable.

Figure 128, shows the average yield point, hardening rate and modulus of the three orientations. Orientation 2 has the largest margin of error, however as explained above this is because of the spurious result, in pillar 11 (The stress strain trace was not repeatable in respects to the other tests, particularly in regards to the hardening) If the spurious result is removed the standard deviation falls by 70%. The yield point across the three orientations shows the lowest level of scatter. Having a high yield point, low rate of hardening but being stiff, would typically result in catastrophic failure. As the dislocations which carry the plastic flow in these small micro volumes are not able to accommodate for the high level of strain. This is evidenced by the extensive strain bursts, that can be seen in figure 127 c. The extent to which the pillars deformed in their respective orientations is shown in figure 129-31.

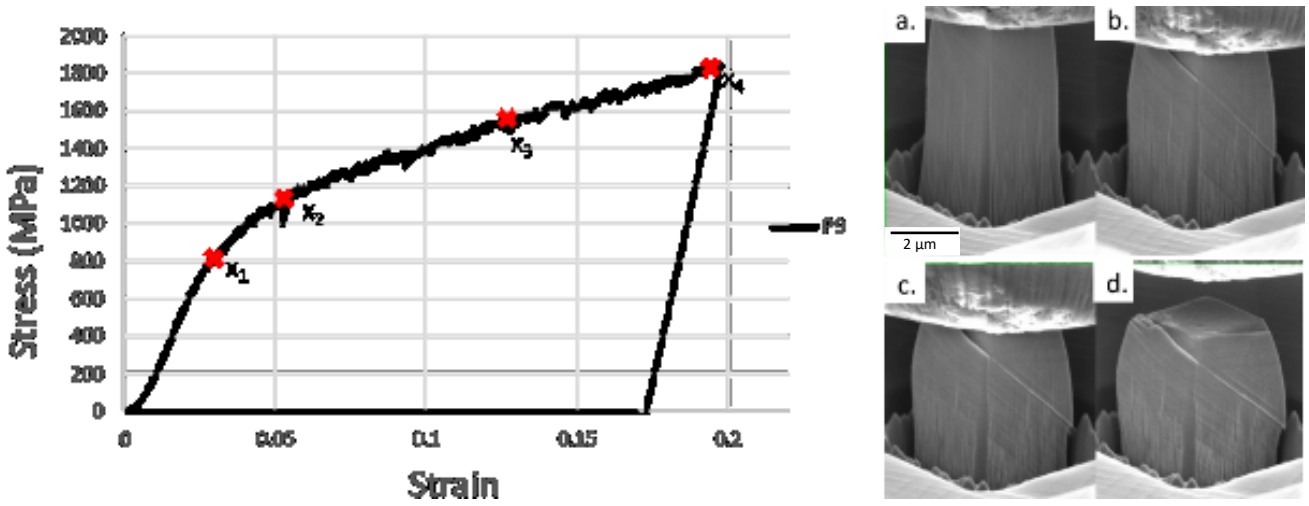


Figure 129: Stress x strain response from Orientation 1. (a) (X_1) compression to somewhere near the yield point (b) (X_2) strain burst in the hardening regime and the pillar is beginning to "bulge" out from the sides accommodating the deformation (c) (X_3) another smaller strain burst in the hardening regime (d) (X_4) End of test, removal, of flat punch.

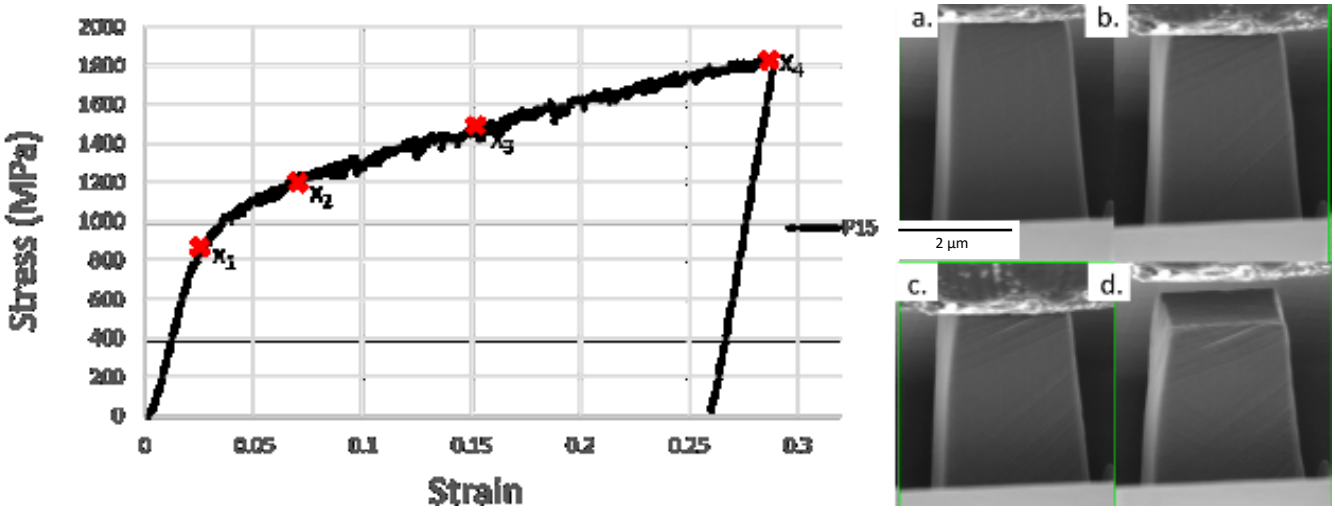


Figure 130: Stress x strain response from Orientation 2. (a) (X_1) compression to somewhere near the yield point (b) (X_2) emergence of multiple slip traces and what appears to be rotation of the pillar anti clockwise (c) (X_3) emergence of more slip traces with one dominant trace emerging (d) (X_4) End of test, removal, of flat punch.

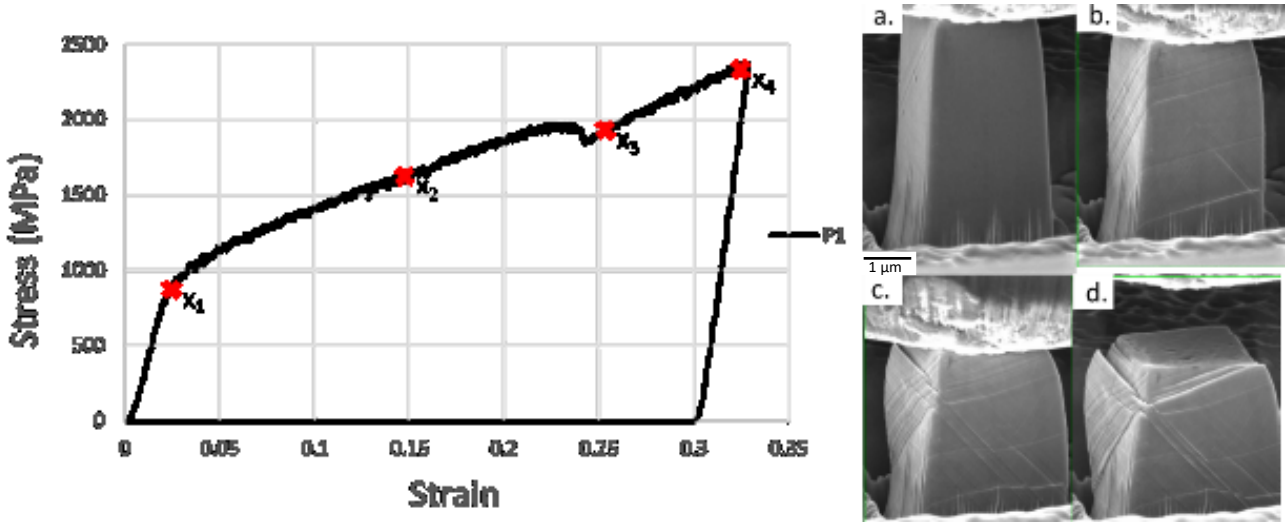


Figure 131: Stress x strain response from Orientation 3. (a) (X_1) compression to somewhere near the yield point, showing the emergence of one slip trace on the left-hand side of the pillar. (b) (X_2) emergence of multiple slip traces and what appears to be torsion of the pillar (c) (X_3) emergence of more slip traces with one dominant trace emerging (d) (X_4) End of test, removal, of flat punch.

Figure 131-figure 133, show that each orientation exhibits different deformation characteristics. In orientation 1, the shear stress is localised along one dominant slip trace and as a result the pillar bulges from the left and right faces of the pillar and continues to shear along the slip trace up to approximately 20% strain.

During the compression of orientation 2, several slight slip traces begin to appear at yield and become more apparent as the strain is increased. At ~ 10% strain, it becomes clear that two or more slip systems are competing. This is evidenced by the different angles of the slip traces located; at the top of the pillar, on the right-hand side and to some extent the left-hand face, see figure 133 c-d. As a consequence of this, the pillar appears to twist and rotate and this continues up to 25% strain with no clear trace that subtends from one side of the pillar to the other (shear localisation), as can be seen in orientation 1, figure 132b.

It appears the pillar, in orientation 2 has trouble accommodating for the shear strain however retains some of its shape and does not fail catastrophically even at this high strain. This type of deformation could be described as a “crumple” like deformation.

Orientation 3, appears to be the most unstable of the three. At yield several slip traces all aligned in the same direction appear on the left face of the pillar as shown in ss1 figure 134. The pillar appears to be twisting slightly. At 15% strain, well into the hardening regime and after the appearance of a strain burst at ~14% at point x_2 on figure 131, several slip traces begin to emerge on both visible faces of the pillar.

The traces on the front face, appear to be accommodating the traces that formed at yield on the left face of the pillar, plus the emergence of one or two additional slip systems. For example, the slip trace

which subtends from the right-hand side of the pillar upwards which can be seen in ss2, figure 134. However, at 25% strain after the emergence of a substantial strain burst, the pillar shears along a completely different system. This orientation seems unstable. The pillar also combines the deformation effects from orientation 1 and 2, in that it bulges and twists, with an almost buckling like effect, this can be seen in greater detail in figure 134.

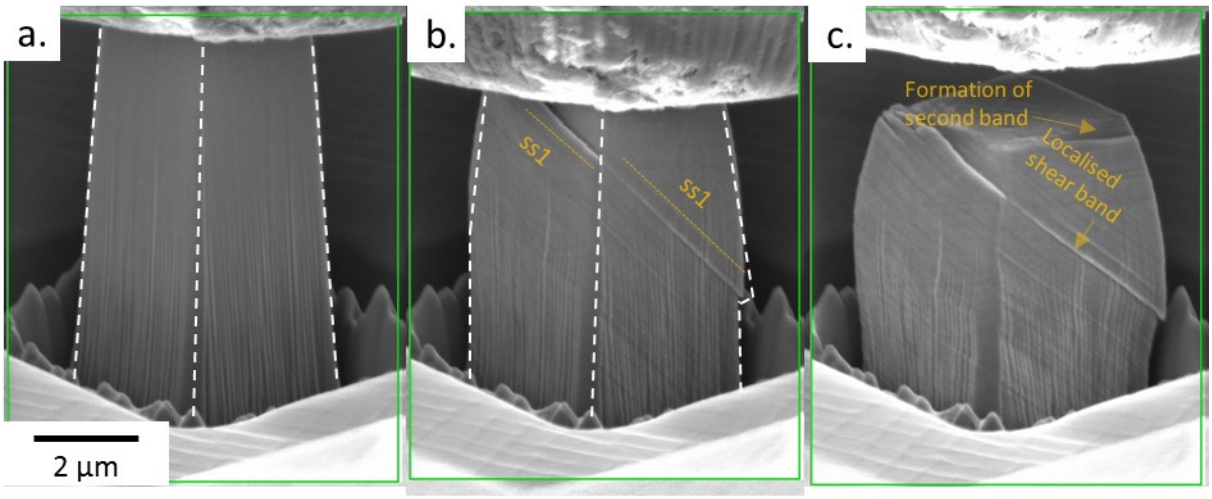


Figure 132: Pillar 9, Orientation 1. (a) Beginning of test, showing the initial arrangement of the pillar before any deformation has occurred (b) Middle of test, post yield showing the formation of one localised slip step and shape change of the pillar (c) End of test, shear along the localised slip band and a second band forming near the top of the pillar.

Figure 132, shows the side bulging of the pillar with a slip step and potential formation of a second slip step near the top of the pillar. This second slip step, resembles the localised shear band from orientation 2, figure 133c.

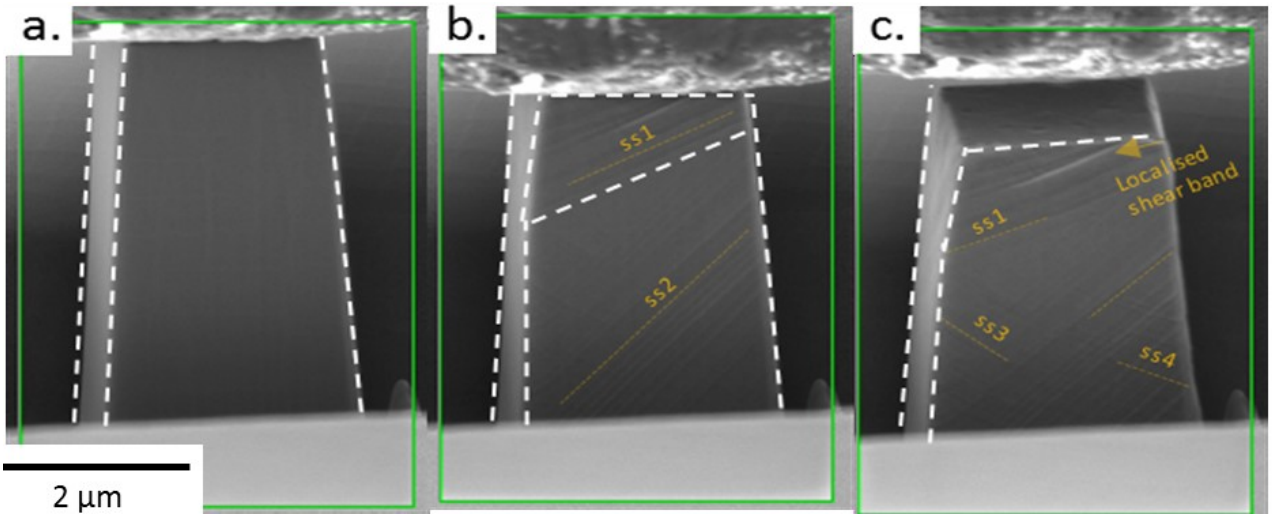


Figure 133: Pillar 15, Orientation 2. (a) Beginning of test, showing the initial arrangement of the pillar before any deformation has occurred (b) Middle of test, post yield showing the onset of one localised shear band, as well as the competition of many other shear bands (c) End of test, shear along the localised slip band and a second band forming near the top of the pillar. The dashed lines show the change in pillar shape as it rotates and bends inwards towards the camera.

Figure 133, shows the deformation in pillar 15. The deformation in pillar 15, shows rotation, multiple slip lines and no clear localisation of shear that extends from one side of the pillar to the other. The pillar appears to twist and even bend slightly as one slip system competes to accommodate the plastic strain due to the local resolved shear stress, source strength, and hardening.

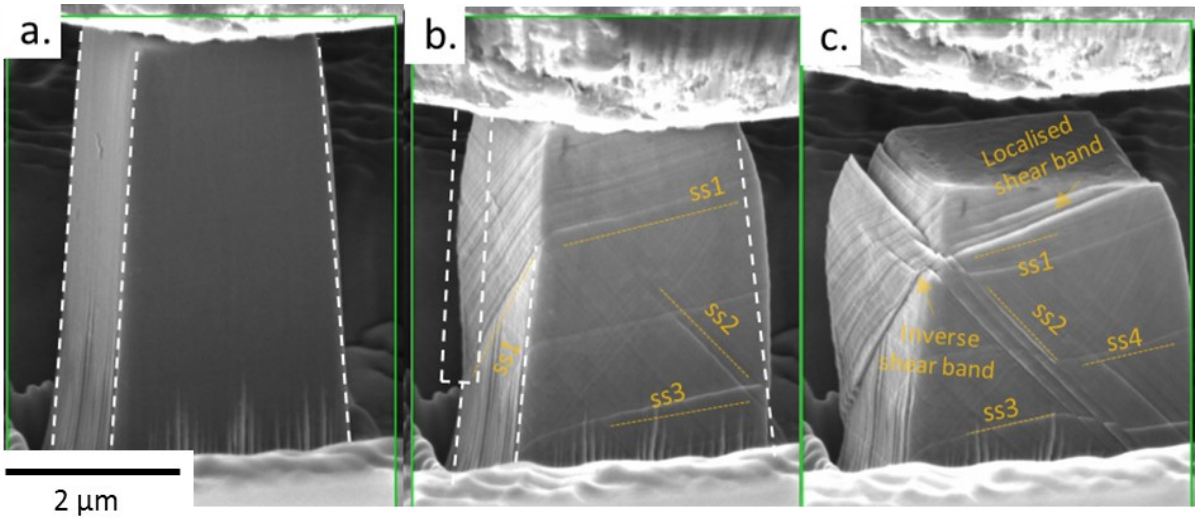


Figure 134: Pillar 1, Orientation 3 (a) Beginning of test, showing the initial arrangement of the pillar before any deformation has occurred (b) Middle of test, post yield showing the competition of multiple slip bands and systems (c) End of test, shear along two opposite slip systems. The deformation in this pillar has given multiple points of localised shear banding.

Figure 134, shows the deformation in pillar 1, shows twisting buckling and bulging of the side faces. Multiple slip traces begin to emerge at yield and extend through both visible faces of the pillar.

Table 8: Summary of top width W_t, Euler angles, τcrss and resultant deformation type of pillars 1,9,15 as extracted from figures 32-34

Orientation	Pillar	W_t	Euler angles Φ_1 ,Φ ,Φ_2	T_{crss}	Deformation type
1	9	2.02	[209.7,2.7,13.3]	313	One ~ 45° localised shear band
2	15	2.32	[21,2.3,70.9]	312	Crumple like deformation
3	1	1.85	[345.9,5.3,40.4]	346	Multiple, competing, uncharacteristic slip localisation

As the normal of the compression axis was <001> the Schmid factors of orientations 1-3 were all ~0.41, with the activated slip system being $\langle 1 \quad \bar{1} \quad 0 \rangle (1 \quad 1 \quad 1)$, determined by the highest Schmid factor. The extent of changing orientation with respect to the loading axis and the influence of slip systems, using the methodology outlined above will be discussed more in section 2.

The extent to which the dislocations carrying plastic flow move on the $(1 \quad 1 \quad 1)$ plane in the $\langle 1 \quad \bar{1} \quad 0 \rangle$ can be altered by changing the orientation of the planar axis, as described by the deformation characteristics, **Error! Reference source not found.**-34. The deformation in viewpoint of t he dislocations can be examined in the TEM at different points in the deformation process by loading to specific points in the stress strain cycle.

6.7. Dislocation effects

Pillars can be deformed to points in the elastic region, near the yield point and in the hardening regime as exemplified by the points X_1, X_2 and X_3 in Figure 129-31. The orientation and flow of dislocations at each of these regimes can be captured by preparing electron transparent samples and examining them in the TEM. This enables the characterisation of slip through the viewpoint of dislocation mechanics. For example, in the viewpoint of pillars 1,9 and 15 as shown in figure 129-34. The deformation would correspond to $\langle 0\bar{1}1 \rangle$ type dislocations moving along the (111) plane and disassociating into lower energy species as they move through the ϒ/ϒ' microstructure, see figure 142,figure 143,figure 145 and figure 146.

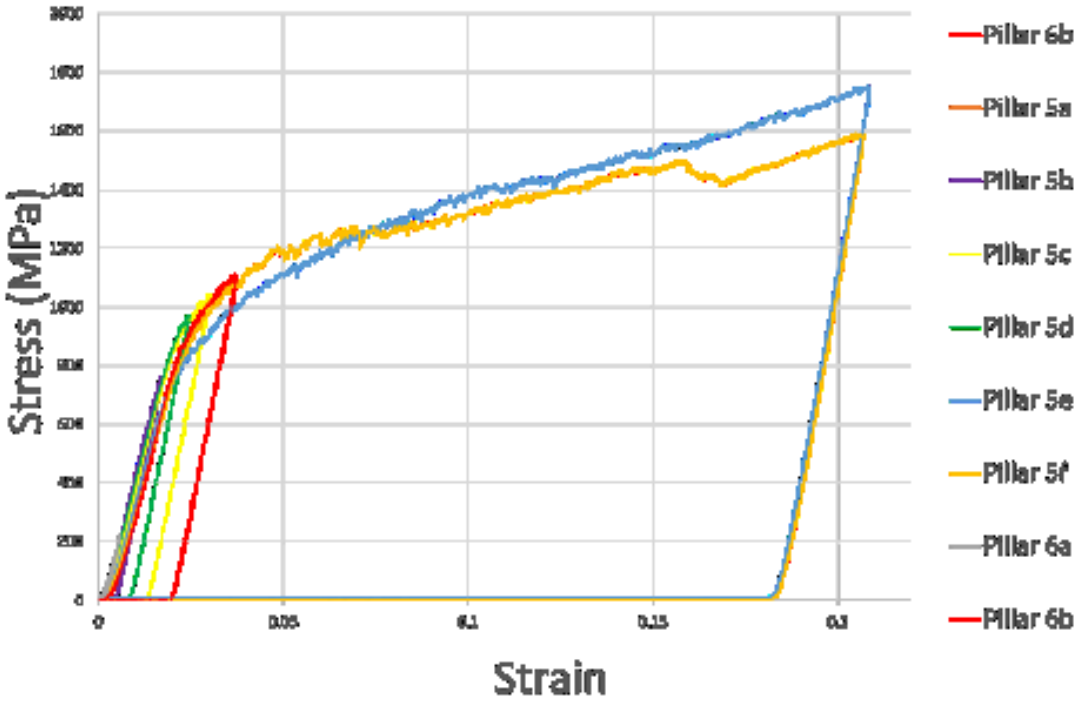


Figure 135: Stress strain traces for samples prepared for TEM, with micropillars having areas ~11 μm². Pillars 5c and 5e, deformed to 20% strain, were used as a blueprint to map the relative strain. Pillars, 5c and 5d were deformed to points somewhere near the yield point 2.5-3.5% strain. Pillar 5b, is in the elastic region at ~1% strain. Pillar 6b, is a pillar that has work hardened sufficiently to examine how the dislocations have penetrated through the ϒ/ϒ' microstructure.

Figure 135 shows a compound stress strain graph of 9 micropillars used for the TEM study where micropillars were deformed to the elastic regime, somewhere near yield and the hardening regime, figure 106. Examining the pillars from figure 135, pillars 5e and 5f were used as reference, to map the respective levels of % strain and hardening response. Pillars 5c and 5d at 2.5 and 3% strain respectively are just near the yield point, and pillar 5b lies in the elastic regime.

Figure 136 and figure 137 show pillars with similar geometries oriented for “crumble” slip vs shear localised ~45° slip, respectively, with the hopes of examining each via TEM. Pillars 5e and 5f also exemplify the effects described in the previous section 1.5, in which a micropillar can be orientated to initiate different deformation mechanisms in the joint fcc LI_2 system.

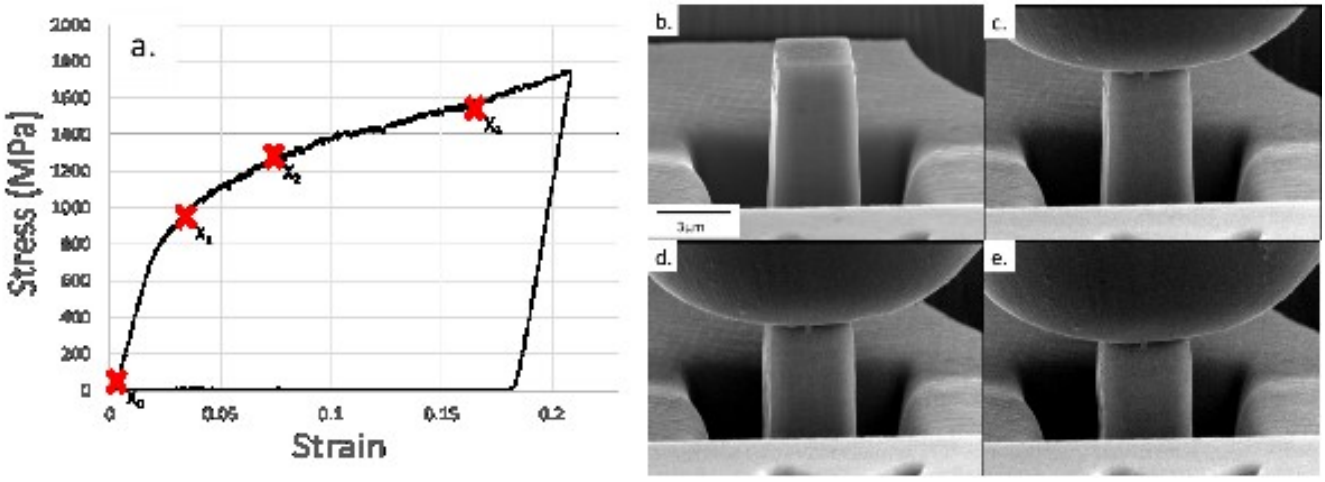


Figure 136: The deformation of pillar 5e to 20% strain, as illustrated by orientation 2, figure 26. Illustrating no strong dominant slip behaviour (a) Stress strain response (b) Undeformed pillar X_0 (c) Yielded pillar X_1 (d) Hardened pillar X_2 (e) Buckling and bulging of the pillar at ~16% strain X_3

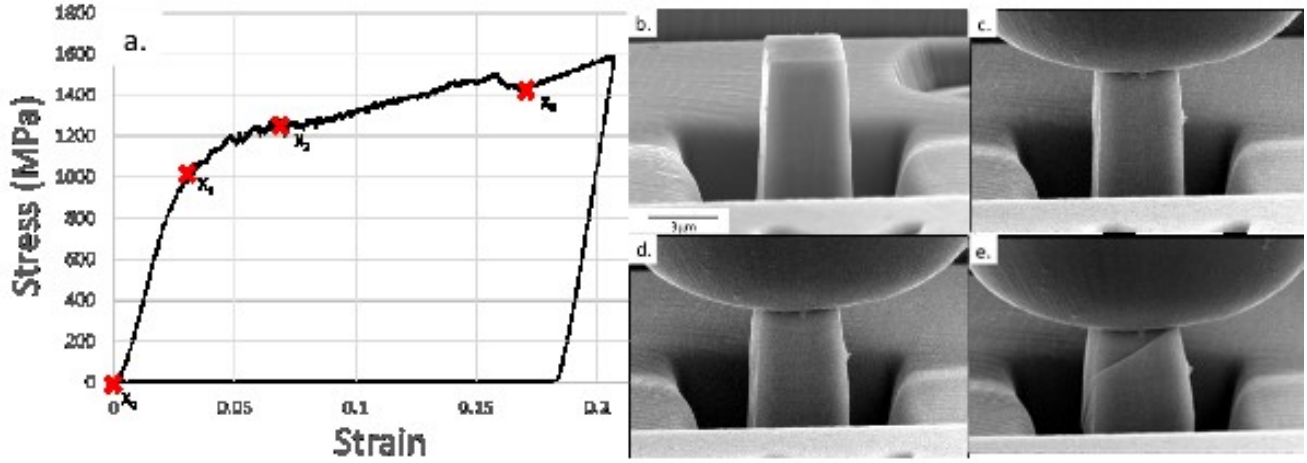


Figure 137: The deformation of pillar 5f to 20% strain, as illustrated by orientation 1, figure 26. Illustrating shear localisation and slip along a diagonal plane (a) Stress strain response (b) Undeformed pillar X_0 (c) Yielded pillar X_1 (d) Hardened pillar X_2 (e) Shear localisation 16% strain X_3

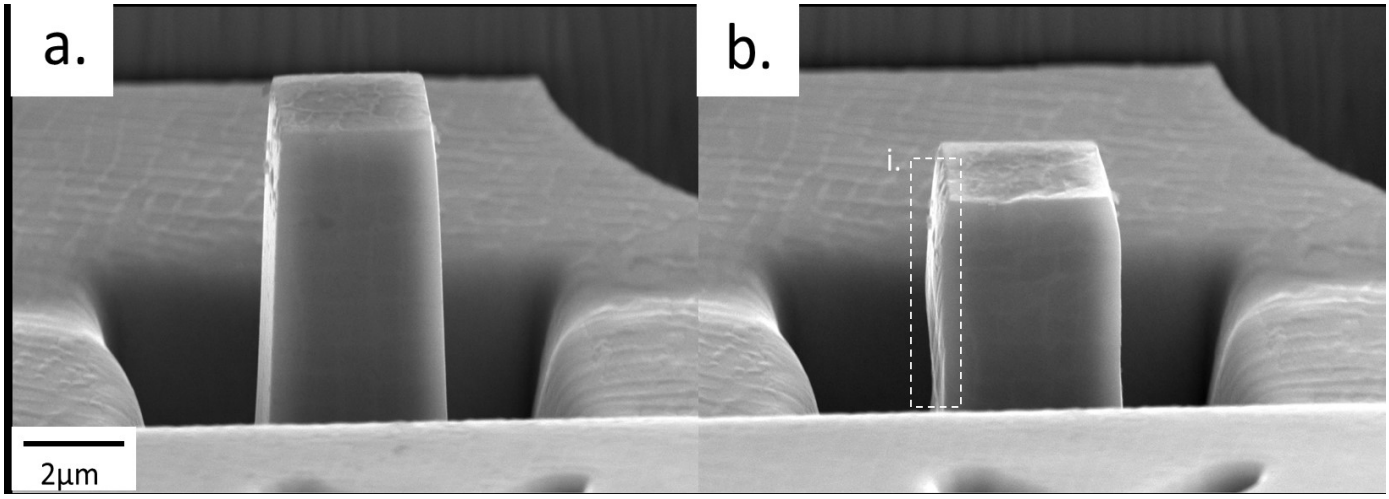


Figure 138: Pillar 5e, set up for crumple slip (a) before deformation, with the schematic from figure 19 appended over the pillar, illustrating theoretical deformation (b) after deformation (i) bulging of the sidewall to accommodate the deformation

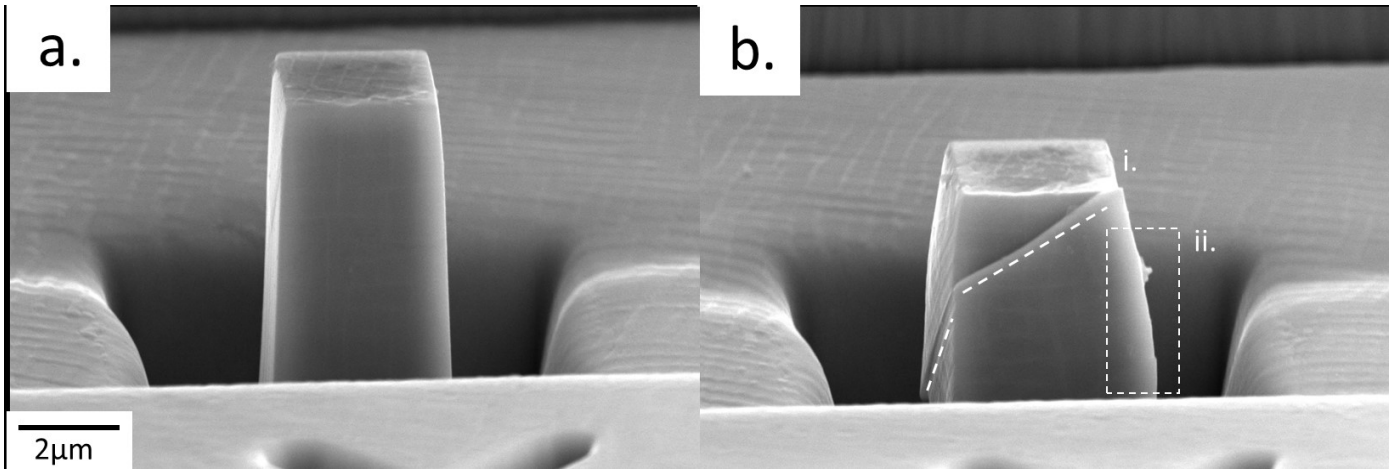


Figure 139: Pillar 5f, set up for shear localised slip (a) before deformation, with the schematic from figure 19 appended over the pillar, illustrating theoretical deformation (b) after deformation (i) Shear band, subtending a diagonal line across several faces (ii) bulging of the side due to large level of shear

Figure 138 & figure 139 show pillars 5e and 5f respectively before and after deformation. The two pillars have been set up (through changes in orientation) to deform in a “crumple slip” and “shear localised slip”, orientations 2 and 1, respectively **Error! Reference source not found.**.

For TEM analysis, careful preparation is needed to section the micropillars. Figure 136 & figure 138, exemplify a pillar, with a more ideal set up for TEM sample preparation. The pillar in figure 137 & figure 139, which has a localised shear band, will give rise to residual stresses once coated in platinum, which means the foil can be subject to failing, during preparation or examination. Care must be taken when preparing TEM foils on deformed pillars and a thicker section must be placed over the pillar to ensure the foil does not fail, as outlined in the methodology section.

6.7.1. Crumple slip

The TEM analysis of micropillars involves the examination of dislocation types and densities through tilting onto octahedral planes following the fcc kikuchi map, as shown in figure 140.

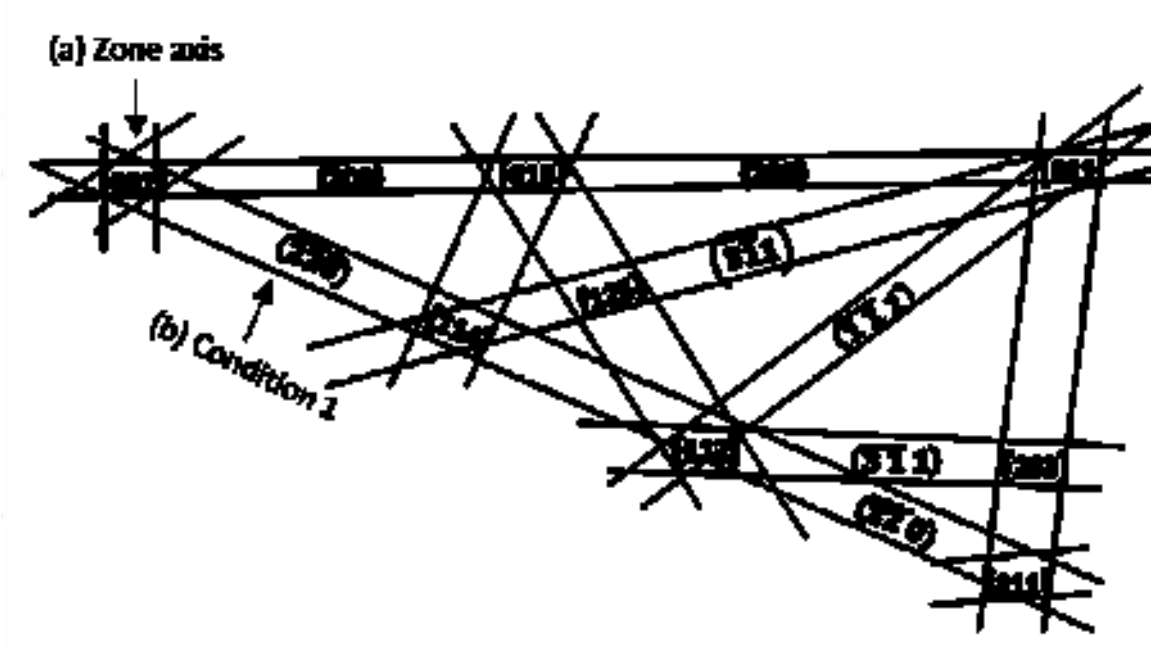


Figure 140: Schematic of one stereographic triangle representing the Kikuchi map for the fcc crystal system (a) The 001 zone axis (b) Condition 1 used to view dislocations at high strains.

Figure 140, shows a schematic of one stereographic triangle which represents the kikuchi map for the fcc system. The zone axis and condition 1 are marked at (a) and (b) respectively. The zone axis enables a large level of information to be observed and at high strains where dislocations cannot be observed clearly, so in the case of pillar 5e, figure 142 the sample was moved to a different condition, figure 140b.

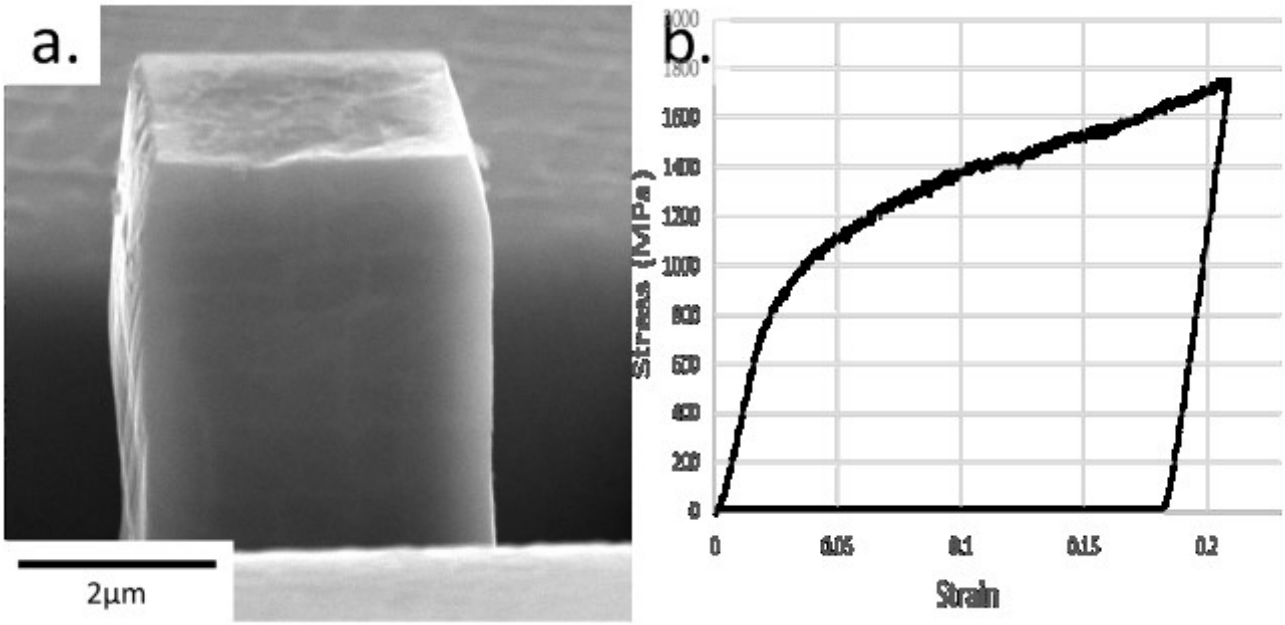


Figure 141: Pillar 5e that has been set up to deform in a "crumple" fashion and compressed to 20% strain (a) Deformed micropillar SEM image (b) Stress x strain graph

Figure 141, shows two faces of pillar 5e deformed to 20% strain, with the accompanying stress strain curve. The stress strain curve, shows a clear transition from elastic to plastic and a smooth hardening with minimal “strain burst” activity. The deformation in pillar 5e can be seen clearly at the left hand side of the pillar as illustrated in figure 141 and figure 138. The front face of the pillar figure 141 shows a few small slip traces, with no localisation and the displacement of the ϒ/ϒ’ cells. The deformation in the TEM sample can be seen in the form of heavy dislocation cells. Where the dislocations have travelled through the ϒ/ϒ’ microstructure and have left behind nucleation species such as antiphase boundaries and stacking faults in their wake as evidenced by the large dark smokey regions in figure 142 a(i) and the species in figure 48 b(iii).

In the area at the top of the pillar, where the strain has not localised as much, the individual dislocations can be viewed more clearly as shown in figure 142b and c**.**

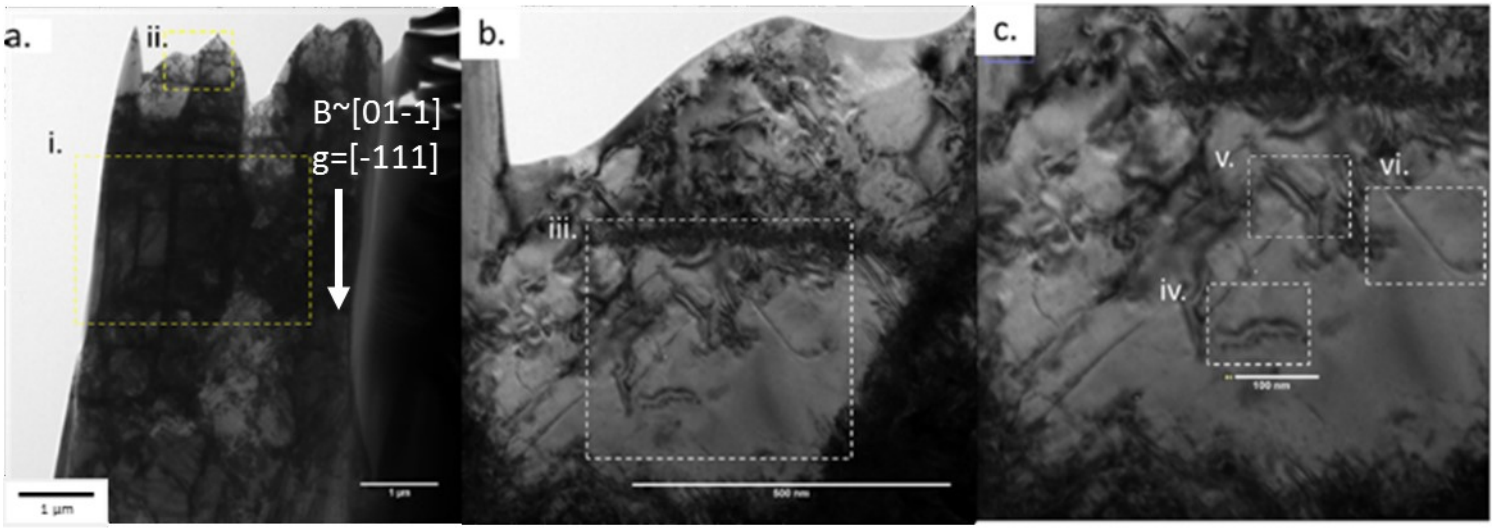


Figure 142: TEM section of pillar 5e deformed to 20% strain (a) Total view of pillar (i) Localised strain represented by the black smokey region, (ii) section highlighted in figure b, representing a large network of dislocations interacting with each other as they move through the ϒ into the ϒ' (b) two dislocation pairs and one super kink can be seen to have penetrated through the ϒ into the ϒ' (c) (iv) and (v) dislocation partials (vi) A super kink.

Figure 142, shows the completed electron transparent, TEM sample of pillar 5e, being viewed in bright mode in a TEM. The figure shows the pillar at the zone axis, and gives an indication to dislocation activity at 20% strain. Figure 142 a, shows the entire pillar and indicated point (i) in which the deformation has accumulated and (ii) in which individual dislocations can be observed.

The distance between the dislocation pairs in figure b is ~16 nm and the length of the dislocation pairs and the superkink figure 142(vi). is 100 nm. An approximation of the ϒ/ϒ' cell size can be taken from condition 1, tilted slightly away from the 001 zone axis. The active slip system in this instance is $\langle 1\bar{1}0\rangle(111)$.

The top section of pillar 5e has been thinned quite significantly and the darker regions are most likely indicative of areas in which the pillar has begun to bulge. Examining the ϒ/ϒ' microstructure shows 001 dislocations penetrating into the ϒ' and dissociating. The lower sections are too thick to examine and the dislocation structures cannot be viewed clearly.

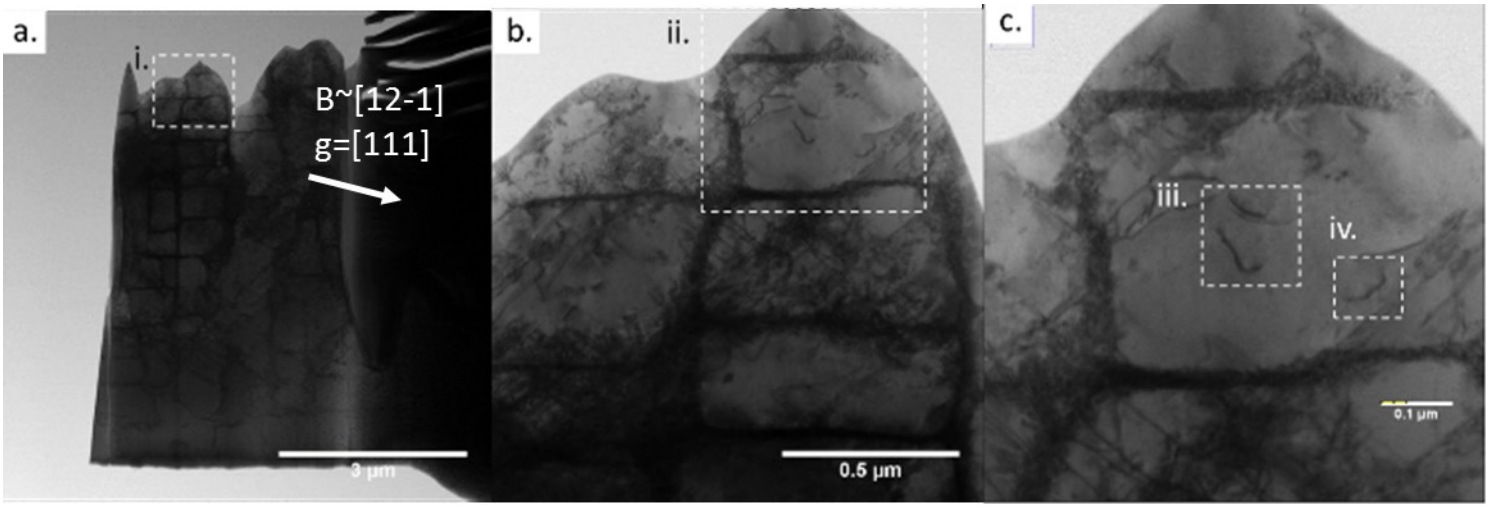


Figure 143: 20% strained pillar 5e at condition 3 as shown in figure 46 (a) Total view of pillar (i) Region with low level of localised strain showing dislocation reactions. (b) Clearer view of dislocation kinks inhabiting the ϒ'.

Figure 143, shows pillar 5e at condition 1. The dislocation reactions can be viewed more clearly in this plane (condition 1) kinks can be seen figure 143(c). The ϒ channels again are dark as they have been inhabited by dislocations accommodating the plastic flow driven by the compression. The separation of the two kinks in figure 143c is 68 nm, which is quite large suggesting they are not a pair set. In order to get a full representation of the deformation in the single crystal CMSX-4 alloy, examining a pillar that has just begun to experience plastic flow at a point somewhere near the yield is needed. This will give a viewpoint of how the dislocations begin to nucleate as they move through the softer ϒ phase into the stronger ϒ' phase.

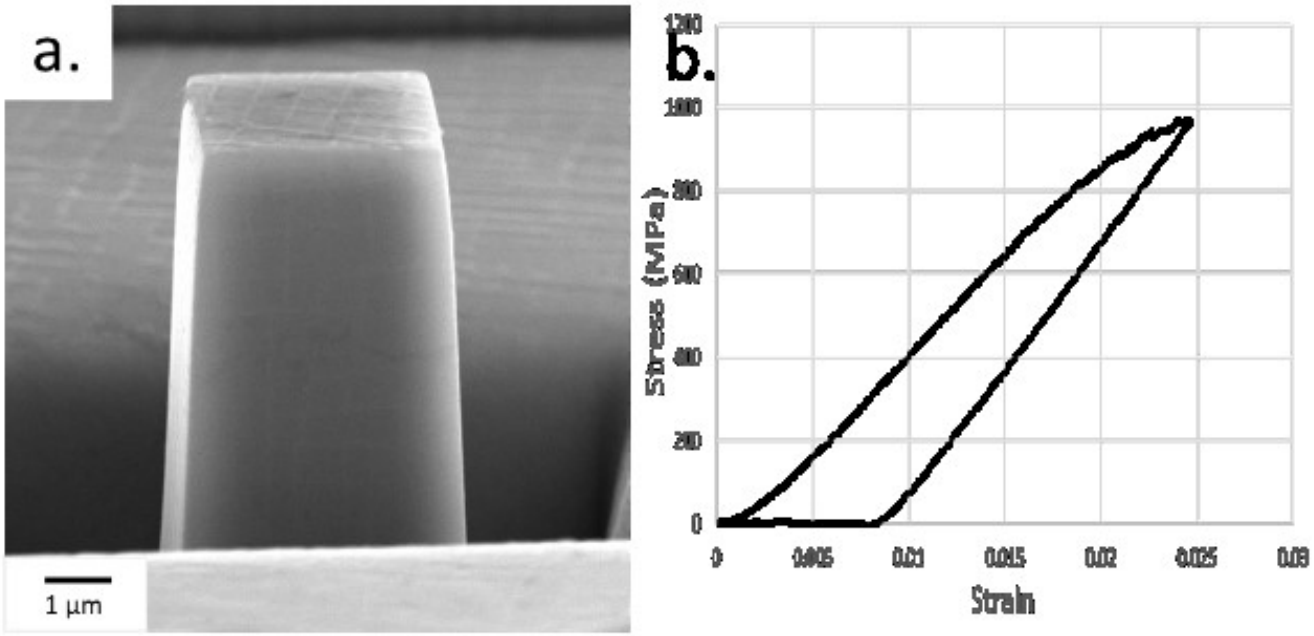


Figure 144: Pillar 5d deformed to 2.5% strain, near the yield point (a) SEM of deformed micropillar (b) Stress x strain response

Figure 144, shows Pillar 5d deformed to a point at the onset of yield, as seen in the small inflection and change in gradient at approximately 2.2% strain figure 144b. It has been deformed to this level of strain to observe how the dislocations nucleate as they originate in the ϒ and penetrate into the ϒ'. As can be seen from figure 145a, there is very little observable deformation in the body of micropillar, however closer inspection shows deformation in the top right hand corner figure 145a(i). The dislocations begin to nucleate and move through the microstructure driven by the compressive force acting downwards.

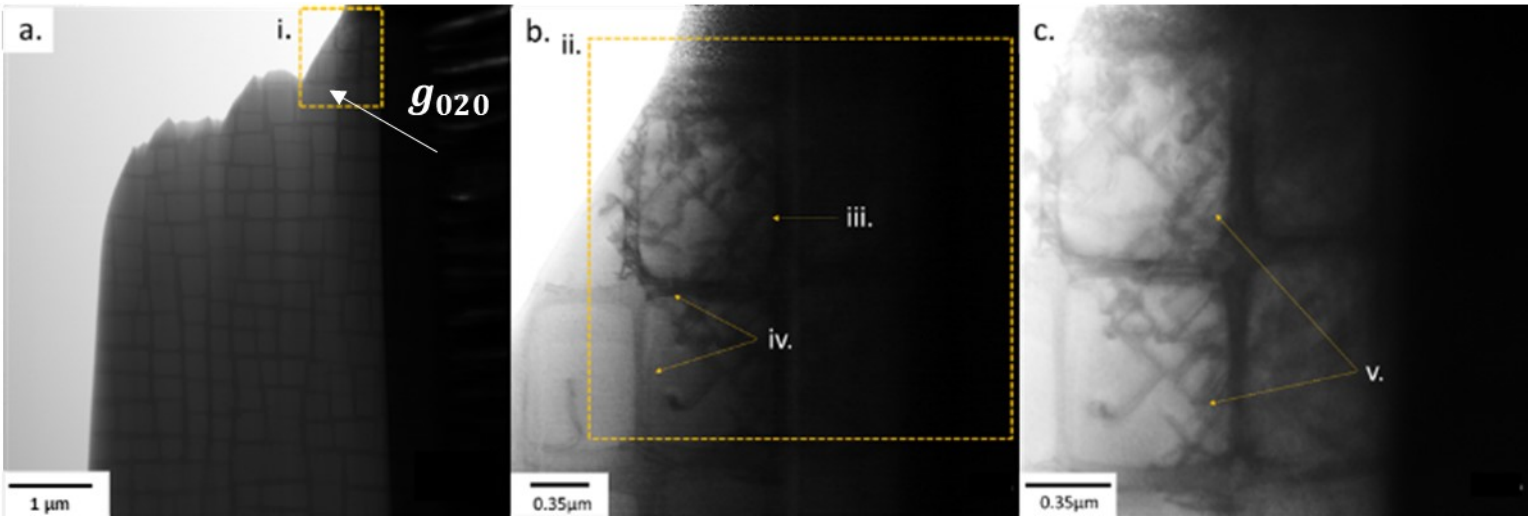


Figure 145: 2.5% strained pillar 5d at the 001 zone axis (a) whole viewpoint of the pillar showing some erosion of the top with a small level of deformation viewable at (i). Illustrated in b. (b) dislocation networks forming in the ϒ and penetrating to the ϒ' (iii), (iv) shows the difference in a ϒ channel inhabited by dislocations (the top arrow) and a channel with no dislocation networks (bottom arrow) (c) close up of figure 145b ii. Showing dislocation pairs and partials moving through the ϒ/ϒ'.

Figure 145 b and c, show the same curved kink that can be viewed in figure 142 c (vi) and 49 c (iii), can be seen in figure 145c (v) the length of the superkink is ~233 nm, the size of the ϒ' cell is 430 nm, the width of the ϒ channel is 60 nm and the average length is 650 nm.

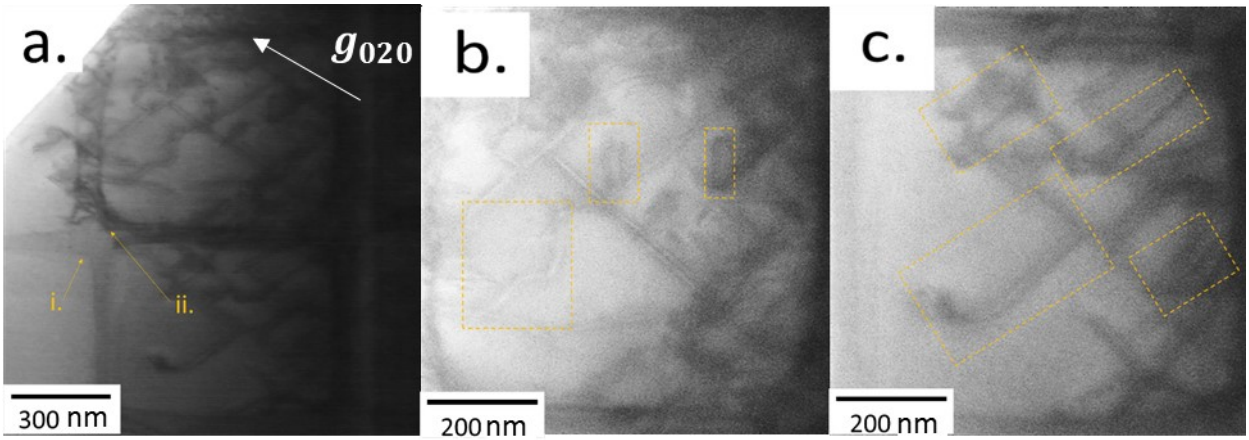


Figure 146: <001> zone axis TEM micrograph of dislocations inhabiting the ϒ/ϒ' channels in pillar 5d2 deformed to 2.5% strain (a) dislocation networks forming and moving through microstructure (b) dislocation species in the ϒ/ϒ'(c) superkinks and more extended dislocations within the ϒ'.

Figure 146 provides a clearer image of the dislocation nucleation process that occur as plastic flow begins to form in the micropillar. Figure 146a shows the ϒ in two conditions (i) a condition in which there is no deformation i.e. no dislocations inhabiting the channels, (ii) an array of dislocations interacting with each other within the ϒ channel as they begin to travel into the Y' phase. The average length of the extended dislocations in the ϒ' phase is 211 ± 123 nm. Extended dislocation pairs can be seen as highlighted in (b) and (c) the lengths vary as described above and the average separation is 23 nm.

The deformation mechanisms can be characterised well via TEM at the different levels of strain that give a representation snapshot of deformation at a point on the stress Strain curve. Both pillars 5d and 5e were set up in the same orientation with the slip system, as shown in figure 149 c, in the section below.

6.7.2. Localised shear slip

The pillar examined in this section for TEM analysis, was set up for localised shear slip as exemplified above and in figure 147-55. Pillar 6b, was deformed to a point just past the yield point ~ 4% strain, the pillar was sectioned and the section examined via TEM, figure 149 illustrates how the zone axis condition was changed from <001> to <011>.

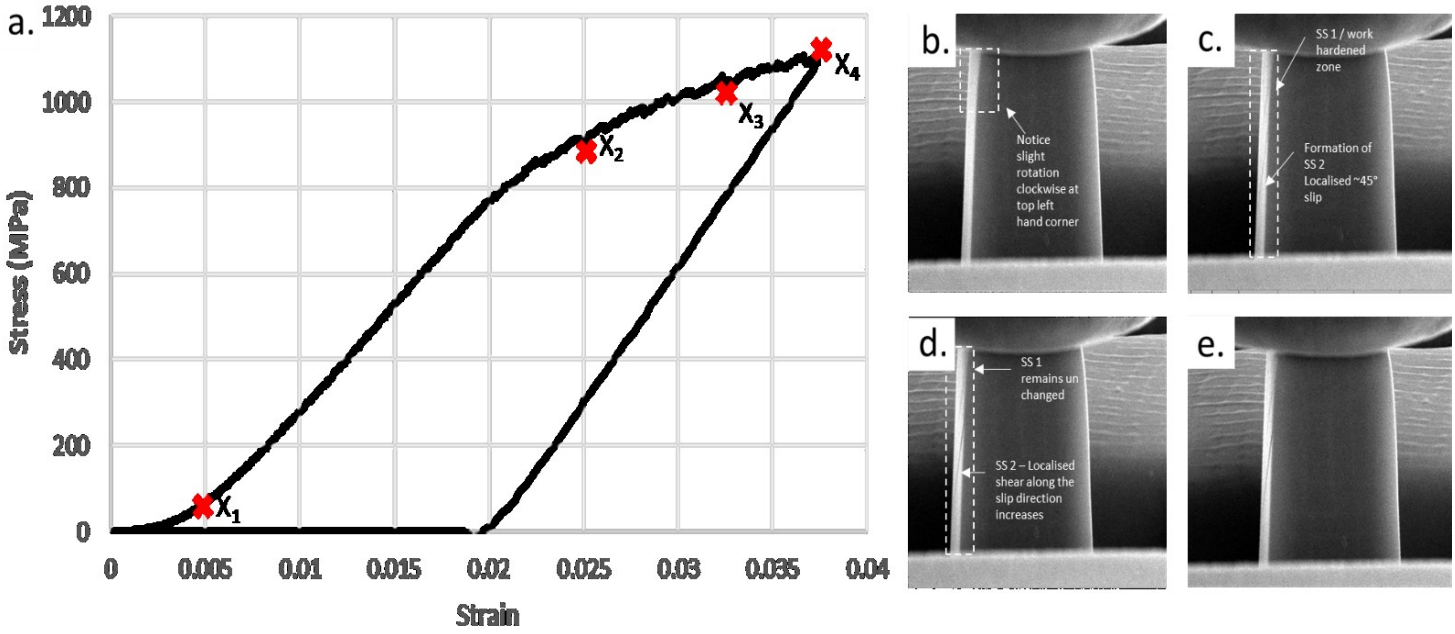


Figure 147: Stress strain curve for pillar 6b, w_t – 3 µm H_0 – 10.3 µm, with accompanying image stills at various points during deformation (x_1-x_4 / b-e), strained to 4% at a point ~1.5% strain post yield. (b) Beginning of the test – X_1 (c) Near the yield point ~2% strain – X_2, where a small strain burst is observed (d) Into the hardening regime, where the localised shear band, continues to shear X_3 (e) End of test X_4.

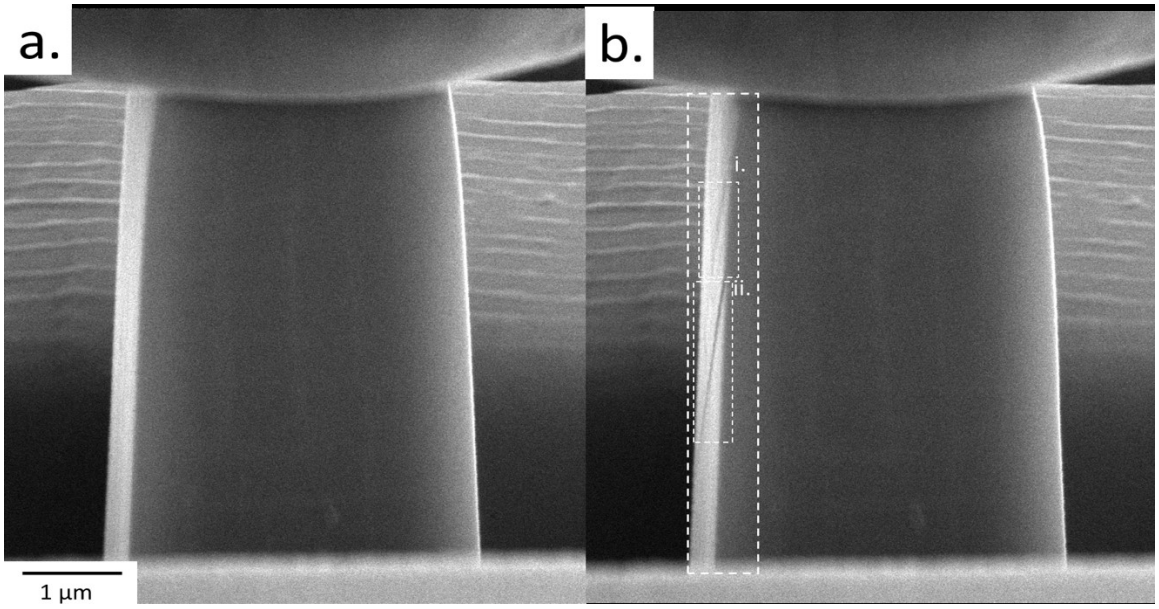


Figure 148: Pillar 6b deformed to 4% strain (a) before deformation (b) after deformation, indicating the deformed area, characterised by slip line 1 (i) and 2 (ii), slip line 2 can be described as a localised ~45° shear band. However due to the low level of strain it has not sheared onto the other faces of the pillar and so can only seen on the left hand face, unlike pillar 5f in Figure 139.

Figure 147 shows the stress strain trace and *in-situ* images from the deformation of pillar 6b. Pillar 6b was set up for localised 45° shear slip, however the level of deformation was so low that the shear band did not penetrate fully, however it can be seen on the left hand side of the pillar as shown in Figure 148 b. Figure 139, shows a pillar in the same orientation deformed to 20% strain. It was not until ~10% strain that the shear band localised across all the faces of the pillar. Capturing the deformation of the pillar at a point near the yield point enables clearer characterisation of dislocation types.

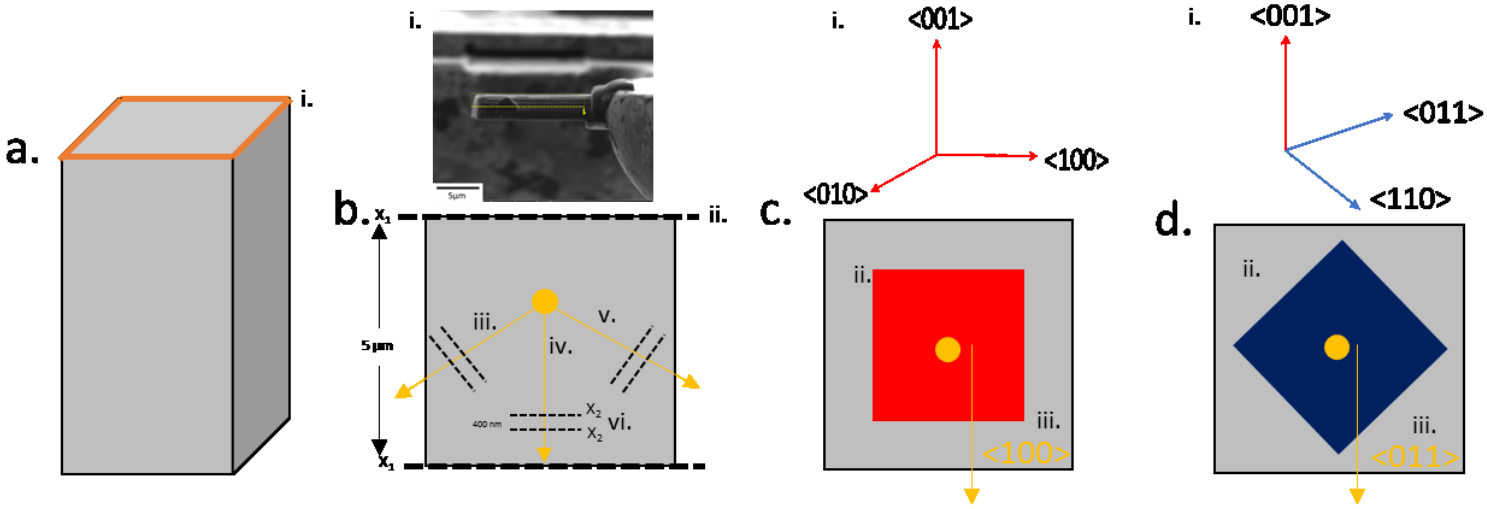


Figure 149: A schematic representation of the top surface of a pillar being sectioned and thinned for TEM analysis (a) Schematic of a micropillar, with the top surface (i) highlighted in orange, represented by figures (b-d). (b) Top surface of arbitrary micropillar, in three different orientations, represented by the yellow arrows (iii-v), where the foil normal is represented by the yellow circle. As the orientation of the pillar normal is changed, the zone axis is also changed accordingly (i) SEM image of a micropillar being thinned (ii) top surface of the pillar before being thinned (vi) top surface of the pillar after being thinned. (c) Pillar face orientated in the <100> direction, resulting in the pillar normal being parallel to the <100> zone axis (i) 3d orientation of the orientation in red (ii) whereby the <100> is aligned orthogonal to the x,y,z, axis (iii) orientation of the foil normal. (d) Pillar face orientated in the <011> direction, resulting in the pillar normal being parallel to the <011> zone axis, as represented by figure (i) 3d orientation of the orientation in blue (ii) whereby the <011> is aligned orthogonal to the x and y axis the z axis is in the <001> (iii) orientation of the foil normal.

Figure 149 illustrates how a micropillar is thinned with respect to the orientation of the fcc crystal with respect to the x and y axes. Figure 149 b shows an illustration of the top surface of a micropillar, highlighted in orange in figure 149a, in which the yellow arrows iii-v represent different foil normals, which in turn dictate where the zone axis will be viewed. Figure 55 b (i) shows the pillar foil from a 0 tilt angle, as viewed via the SEM. For the case of the pillars 5d and 5e, the zone axis was in the <100> direction, figure 149 c, for the case of pillar 6b the zone axis was in the <011> direction figure 149 d.

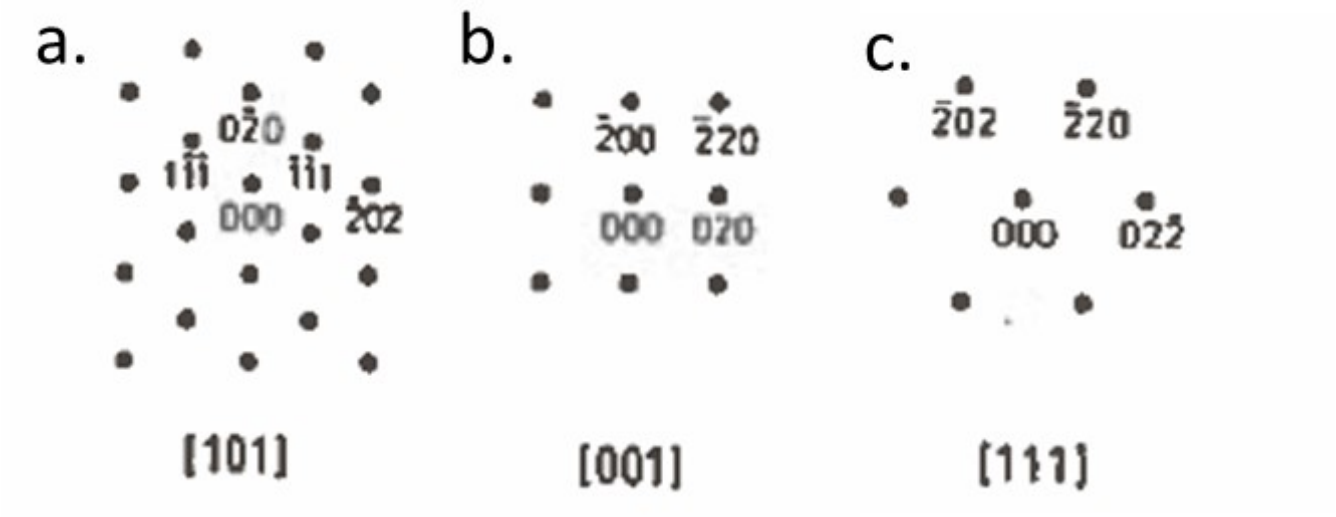


Figure 150: Schematic diffraction patterns for the [101], [001] and [111] directions in an fcc crystal. The electron bean direction is indicated underneath each respective diffraction pattern. Pillar 6b, is orientated so that the foil normal lies on the [101] zone axis, pillars 5e and 5d are orientated so that the foil normal lies on the [001] zone axis.

Figure 150 shows schematic diffraction patterns for the [101], [111] and the [001] zone axis, as seen in pillars 6b and pillars 5d-5e respectively. The [101] zone axis diffraction pattern taken from pillar 6b can be seen in figure 151 a.

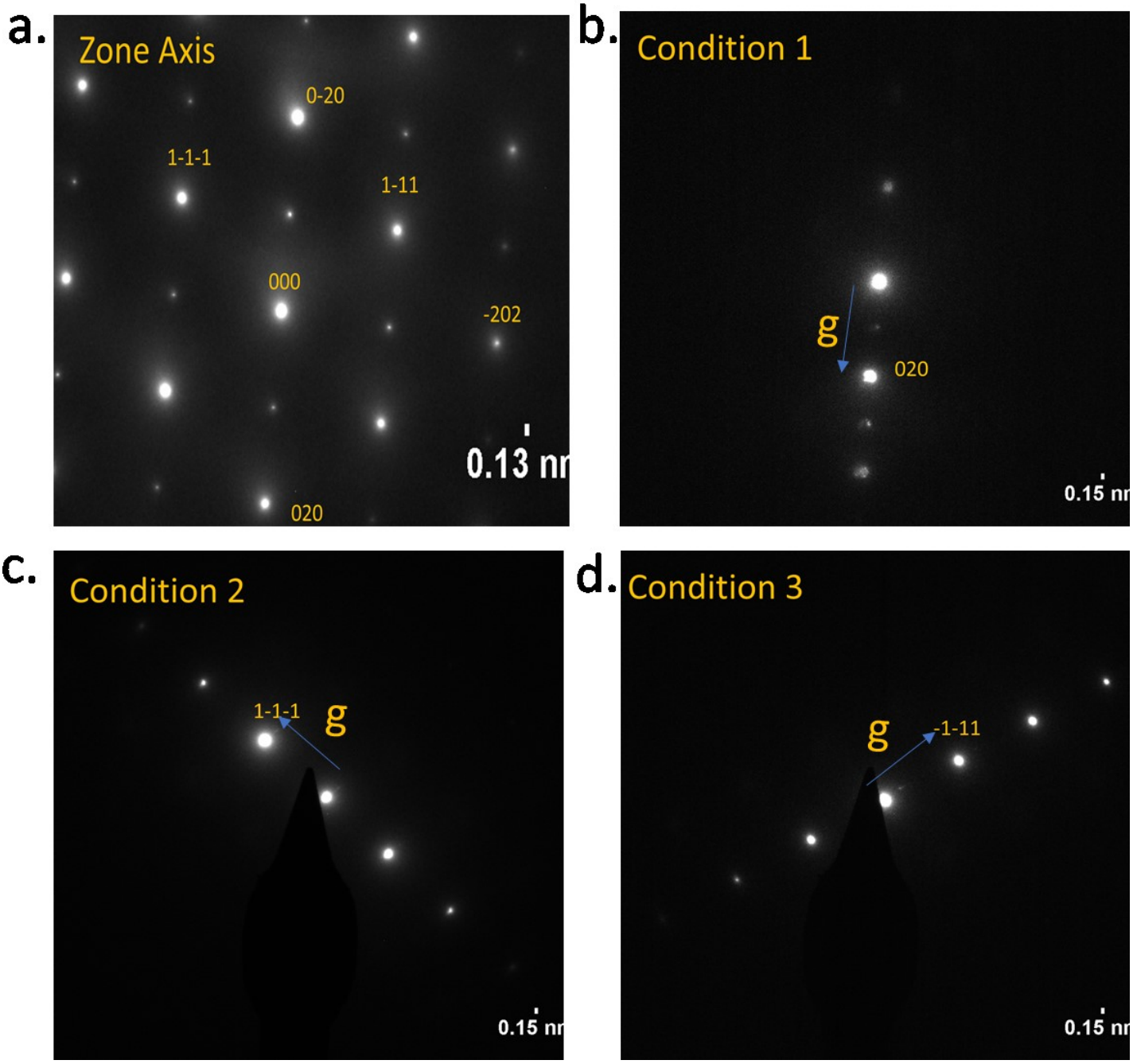


Figure 151: TEM diffraction patterns of the ϒ/ϒ' super lattice of pillar 6b, deformed to 4% strain (a) [101] Zone axis condition (b) Condition 1 with g vector 020. *(c) Condition 2 with g vector* $1\bar{1}\bar{1}$. *(d) Condition 3 with g vector* $\bar{1}\bar{1}1$

The orientation in pillar 6e had been set up for 45° shear localised slip and deformed to a point just past the yield point. This enabled the dislocations interacting with the slip bands to be visualised clearly through the TEM.

Figure 151, shows the different conditions, represented by diffraction patterns, used to image the dislocations with their respective g vectors. The g vectors for conditions 1-3 are as follows; 020. 1-1-1, -1-11.

Table 9: g.b analysis – pillar 6, indicating which screw dislocations are present

Slip plane	Slip direction	g vector		
		020	1-1-1	-1-11
(-111)	<0-11>	-2	0	2
(-111)	<10-1>	0	2	-2
(-111)	<-110>	2	-2	0
(-1-11)	<011>	2	-2	0
(-1-11)	<-101>	0	-2	2
(-1-11)	<1-10>	-2	2	0
(-111)	<0-11>	-2	0	2
(-111)	<-10-1>	0	2	0
(-111)	<110>	2	0	-2
(1-11)	<011>	2	-2	0
(1-11)	<10-1>	0	0	-2
(1-11)	<-1-10>	-2	0	2

Taking the dot product of g vector and the representative Burgers vectors from the 12 fcc slip systems, one can determine which dislocations inhabit the plane. If the dislocations fit the criteria where **g.b =** 0 then they are screw type dislocations, edge type dislocations incorporate **g.b x u** = 0, where u is the line direction of the dislocation, this is shown in table 9 and figure 152. In this chapter only screw type dislocations will be characterised.

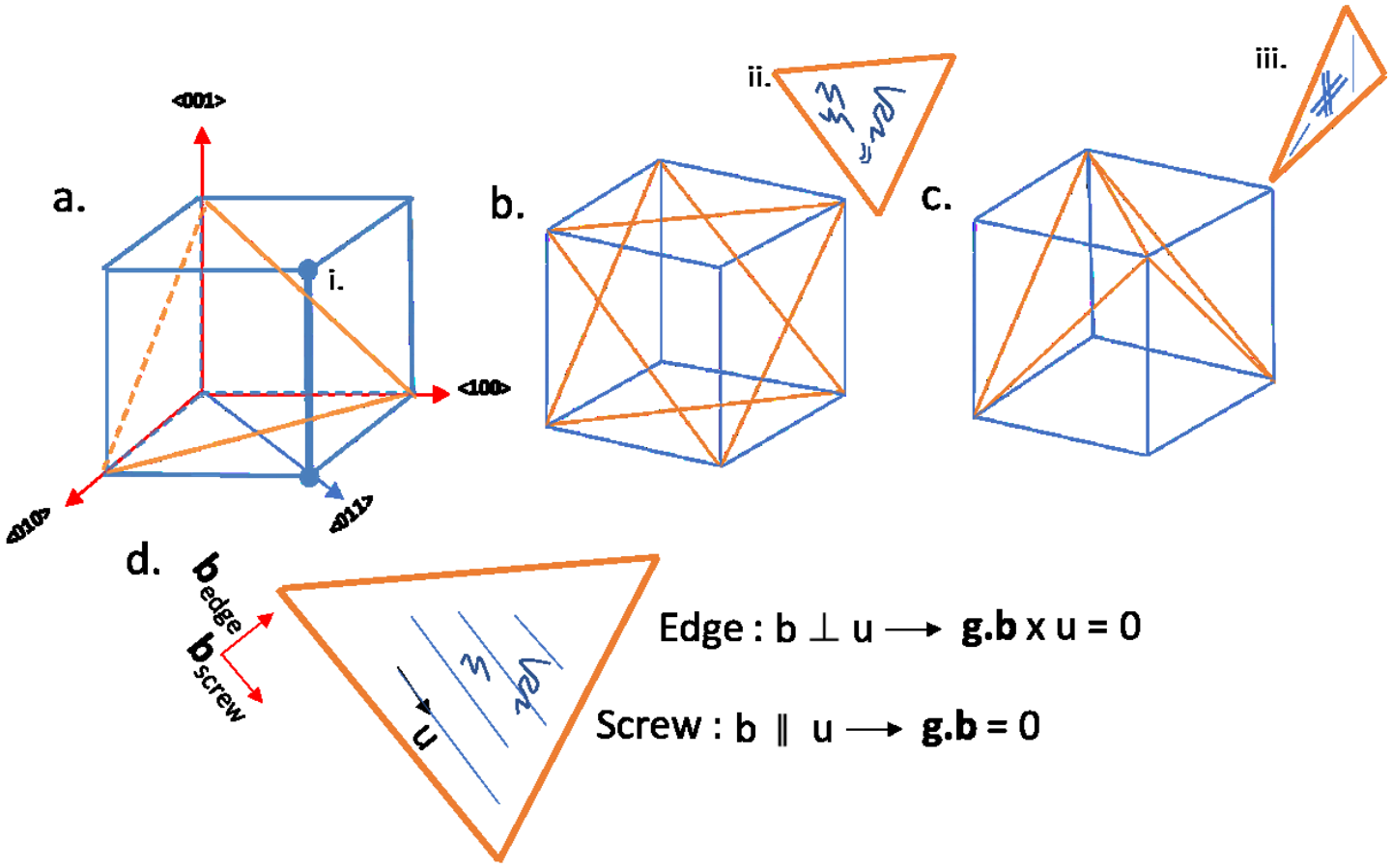


Figure 152: Schematic of the fcc crystal lattice illustrating different orientations of the {111} planes giving rise to different visible dislocation types, illustrating how dislocations can be viewed as straight lines or wavy depending on the orientation of the slip plane (a) fcc crystal lattice with the (111) plane visible in orange. In the case of the TEM examination of pillar 6e, figure 154-figure 160, the foil has been orientated so that the pillar normal is aligned in the <011> direction as shown in (i). This orientation results in the zone axis being aligned with the <011> and thus, the view of the dislocations on the {111} can be shown schematically by figures (b-c). (b) fcc cube orientation where the foil normal is parallel to the <011> showing wavy dislocations visible on the (-1-1-1) and (111) planes (ii). fcc cube orientation where the foil normal is parallel to the <011> showing criss cross dislocations visible on the (1-11) and (11-1) planes (iii) (d) The (in)visibility criteria for edge and screw type dislocations in standard dark field imaging.

Figure 152 shows a schematic illustration of the fcc crystal orientation as viewed down the <011> direction and a different set of {111} planes illustrating how dislocations can be viewed differently depending on the orientation of the slip plane. When wavy dislocations are viewed perpendicular to their respective slip plane, as shown in figure 152 ii, the wavy nature of the dislocations becomes obvious and appears distinct, however when viewed on or near to the slip plane, as shown in figure 152 iii, they appear as straight. With respect to figure 154-figure 160, four different dislocation types can be characterised; pairs, criss cross, straight extended type and Wavy. Figure 152 b (ii) shows wavy type dislocations and dislocation pairs, figure 152 c (iii) shows straight extended dislocations and criss cross dislocations. These will be discussed in more detail later. Figure 152 d illustrates how the Burgers vector for the screw and edge type dislocations differs and thus different analysis is needed, in this section only screw type dislocations will be analysed.

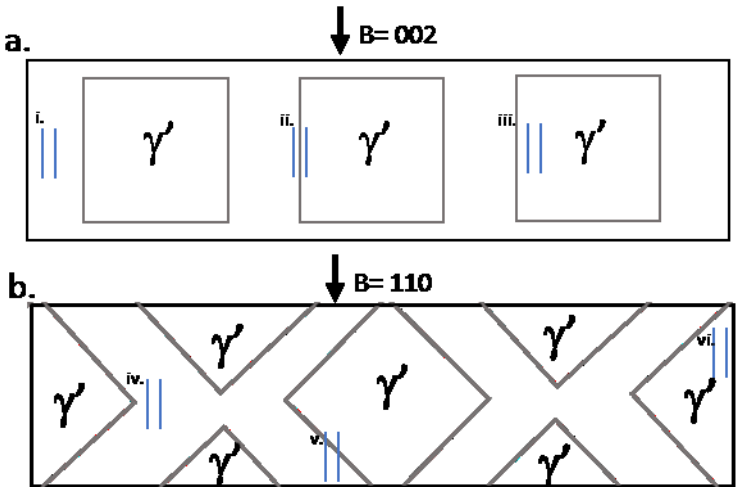


Figure 153: Schematic illustrating the different positions the dislocations pairs can take within the ϒ/ϒ' matrix and how the viewing angle effects the perspective. The dislocation pairs can exist within the ϒ matrix, partially within the ϒ and ϒ' or completely in the ϒ. This is shown at points i-iii and iv-vi.

Figure 153, shows a schematic illustration of the different positions the dislocations and dislocation pairs can take within the ϒ/ϒ' matrix and how the g vector and foil normal changes the perspective of their locations, this is exemplified by figure 152 and shown experimentally in figure 154-figure 160.

*Table 10: Slip systems characterised into **g** vectors with visible dislocation types and ledged*

Slip plane	Slip direction	g vector		
		020	1-1-1	-1-11
(-111)	<0-11>	-2	0	2
(-111)	<10-1>	0	2	-2
(-111)	<-110>	2	-2	0
(-1-11)	<011>	2	-2	0
(-1-11)	<-101>	0	-2	2
(-1-11)	<1-10>	-2	2	0
(-111)	<0-11>	-2	0	2
(-111)	<-10-1>	0	2	0
(-111)	<110>	2	0	-2
(1-11)	<011>	2	-2	0
(1-11)	<10-1>	0	0	-2
(1-11)	<-1-10>	-2	0	2

$g_{020} + g_{1\text{-}1\text{-}1}$

$g_{020} + g_{\text{-}1\text{-}11}$

$g_{1\text{-}1\text{-}1} + g_{\text{-}1\text{-}11}$

$g_{1\text{-}1\text{-}1}$

$g_{\text{-}1\text{-}11}$

Condition 1 has the most visible dislocation from the 12 slip systems with 8 visible dislocations, conditions 2 and 3 both have 7. Both conditions 1 and 3 with g vectors 020 and -1-11 respectively exhibit dislocation pairs and wavy type dislocations exclusively. Conditions 1 and 3 share the Burgers vectors <0-11>, <110> and <-1-10>. Conditions 1 and 2 with g vectors 020 1-1-1 respectively exhibit criss cross and straight extended type dislocations, with no wavy or dislocations pairs visible, with Burgers vectors <0-11>, <110>, <-1-10>. Conditions 2 and 3 exhibit criss cross dislocations with <10-1> and <-101> Burgers vectors.

Table 11: Visible dislocation types compared to g vectors conditions 1-3 respectively

Dislocation type	g_{020}	$g_{1\text{-}1\text{-}1}$	$g_{\text{-}1\text{-}11}$
Criss cross	✓	✓	×
Extended	×	✓	✓
Wavy	✓	×	×
Pairs	✓	×	✓

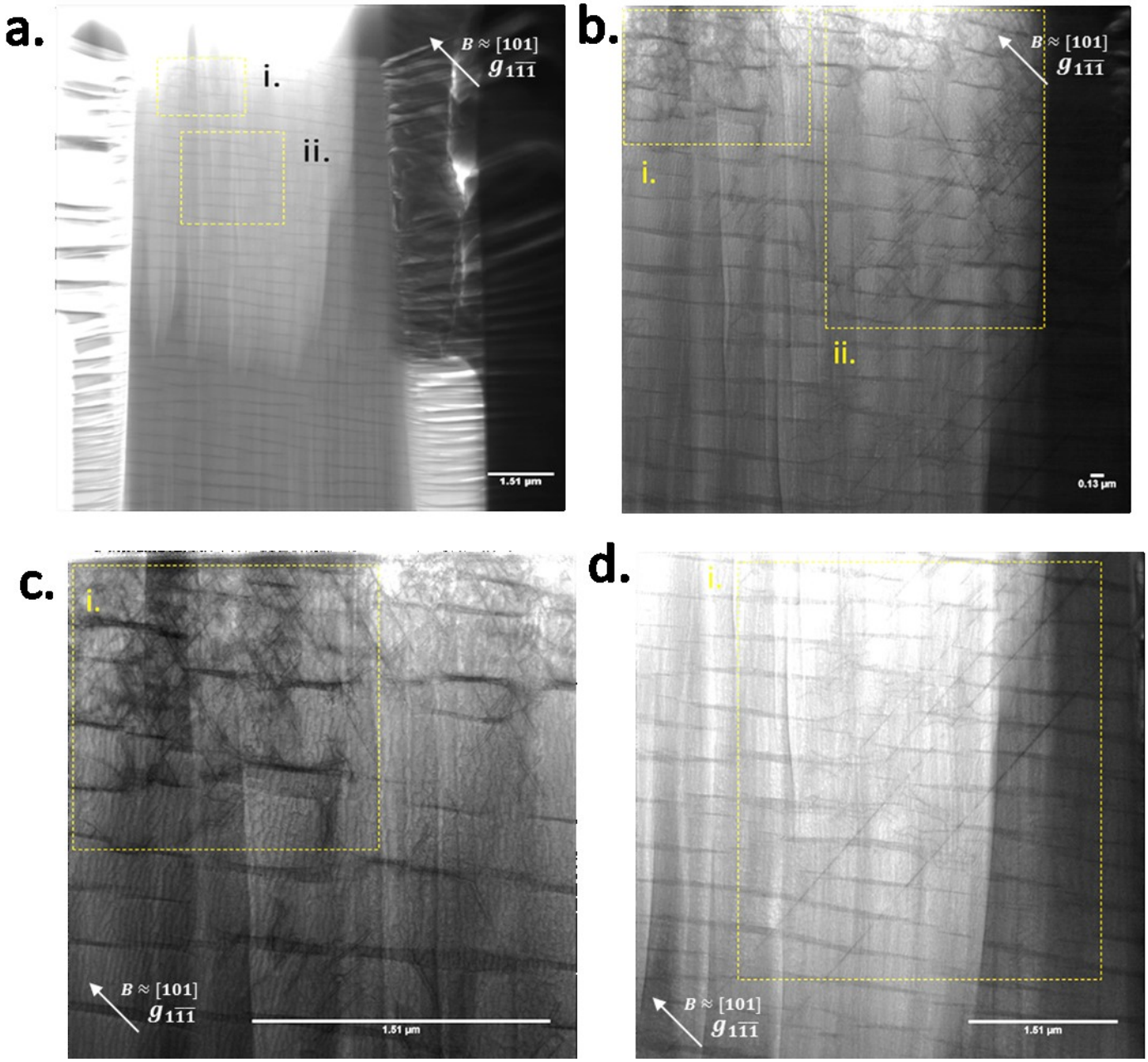


Figure 154: Zone axis condition of pillar 6e (a) Overview of pillar in the zone axis condition (i) localised deformation induced from the interaction of the flat punch with the top surface of the pillar as shown in (b-c) (ii) area shown in figure d. (b) top area of the pillar showing slip traces and localised deformation with forest dislocation represented as "wavy" and "criss cross" dislocations (d) slip traces interacting with dislocations exemplified in Figure 155.

The zone axis condition contains the most information and figure 154 illustrates various dislocation types, including pairs, wavy, extended and criss cross dislocations.

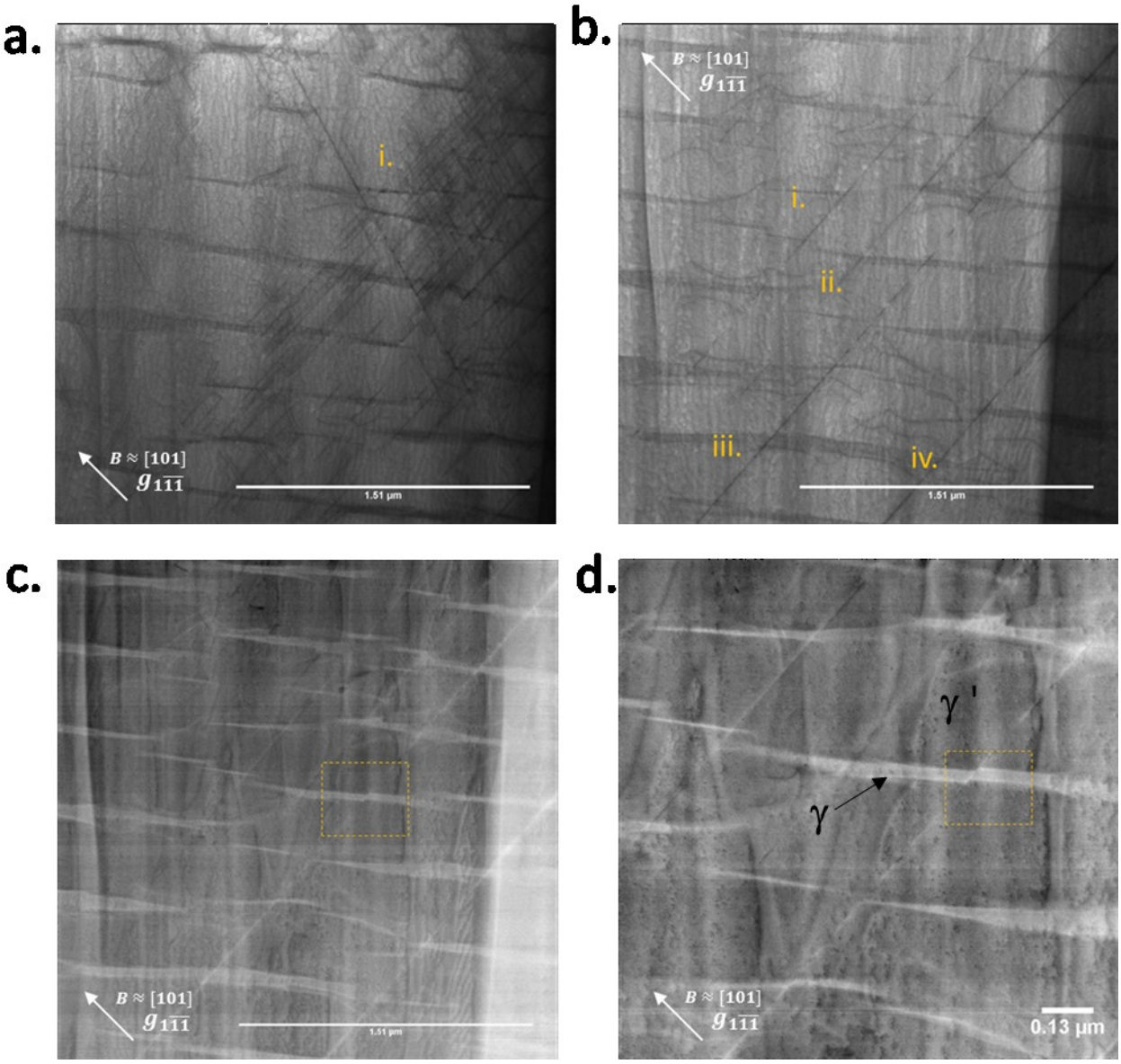


Figure 155: Zone axis condition of pillar 6e, illustrating dislocations interacting with slip traces and the shearing of the ϒ/ϒ' microstructure (a) "criss cross" dislocations interacting with a slip line, indicating work hardening, the dislocations are at ~45° angles with respect to the ϒ/ϒ' microstructure (b) Wavy type dislocations interacting with slip traces (ii-iv) (c) shearing of the ϒ/ϒ' microstructure by the slip traces HADF (d) Closer inspection of wavy type dislocations interacting with slip traces (ii-iv) (c) shearing of the ϒ/ϒ' microstructure by the slip traces HADF

Figure 155 (a&b) show dislocations interacting with slip bands, figure 155 a, shows criss cross dislocations, which are indicative of work hardening interacting with a slip band at point (i). Figure 155 b shows wavy type dislocations and dislocation pairs interacting with several small slip traces at points (i-iv). Figure 155 c, shows the shearing of a ϒ' precipitate and figure 155 d shows this at closer inspection. One can assume this is the predominant localised ~45° shear band.

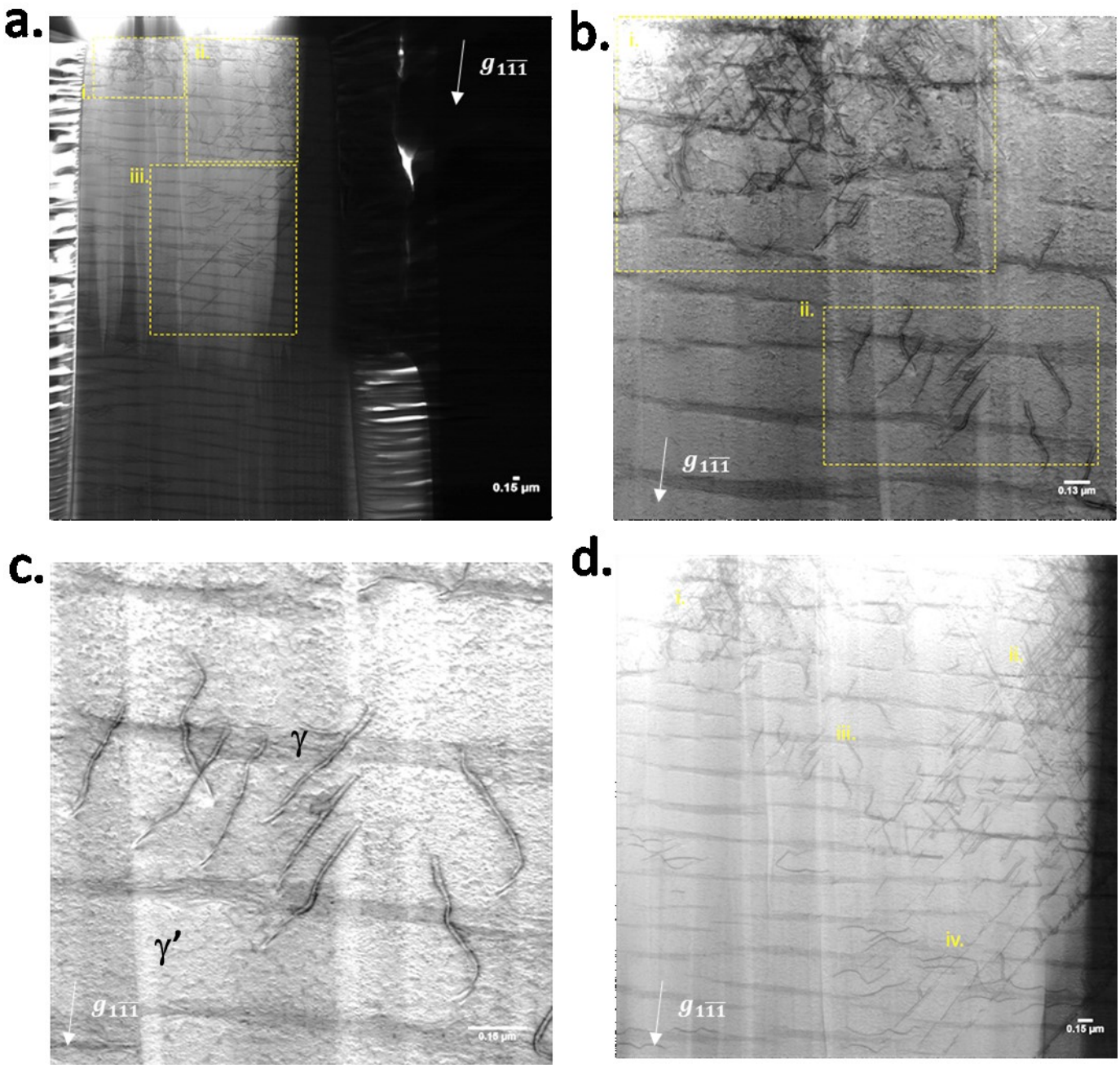


Figure 156: Condition 1 of pillar 6e, showing dislocation partials and "criss cross" dislocations interacting with the Y/Y' microstructure (a) Overview of the micropillar (i) localised deformation at the top of the pillar highlighted by figure b (ii) localised deformation moving downwards through the z cross section of the micropillar highlighted by figure (d) (b) dislocation types (ii) partial dislocations represented by figure c (c) multiple dislocation pairs (d) work hardened and deformed region, where several different dislocation types are interacting (iv) multiple wavy type jog dislocations.

Condition 1 shows criss cross, wavy and dislocation pair, type dislocations. The wavy type dislocations seem to interact heavily with the slip traces lower down the pillar, show in figure 156 d. The pairs and criss cross dislocations inhabit the work hardened / localised shear regions shown in figure 156 a i-ii and figure 156 b.

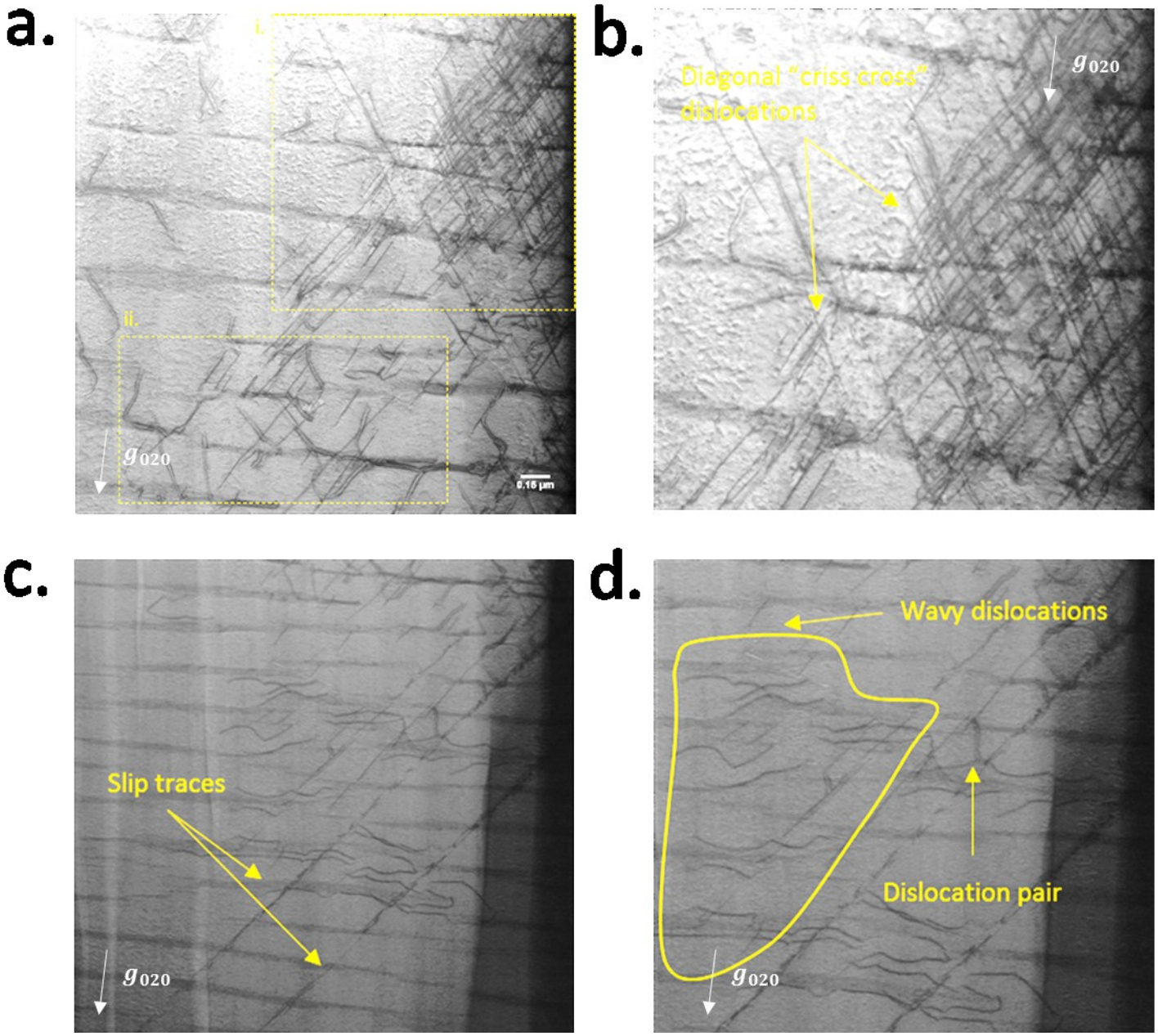


Figure 157: Condition 1 of pillar 6e, showing a closer inspection of dislocations interacting with the Ɣ/Ɣ' microstructure (a) "Criss cross" dislocations in a forest type orientation and wavy type dislocations interacting in a deformed region. (c) Wavy type dislocations interacting with slip lines (d) Closer inspection of wavy type dislocations interacting with slip lies.

Figure 157 a, shows dislocation interacting in the work hardened region, criss cross type dislocations dislocation pairs can be viewed at i and ii respectively. Figure 157 d shows a closer inspection of the wavy type dislocations interacting with the slip traces.

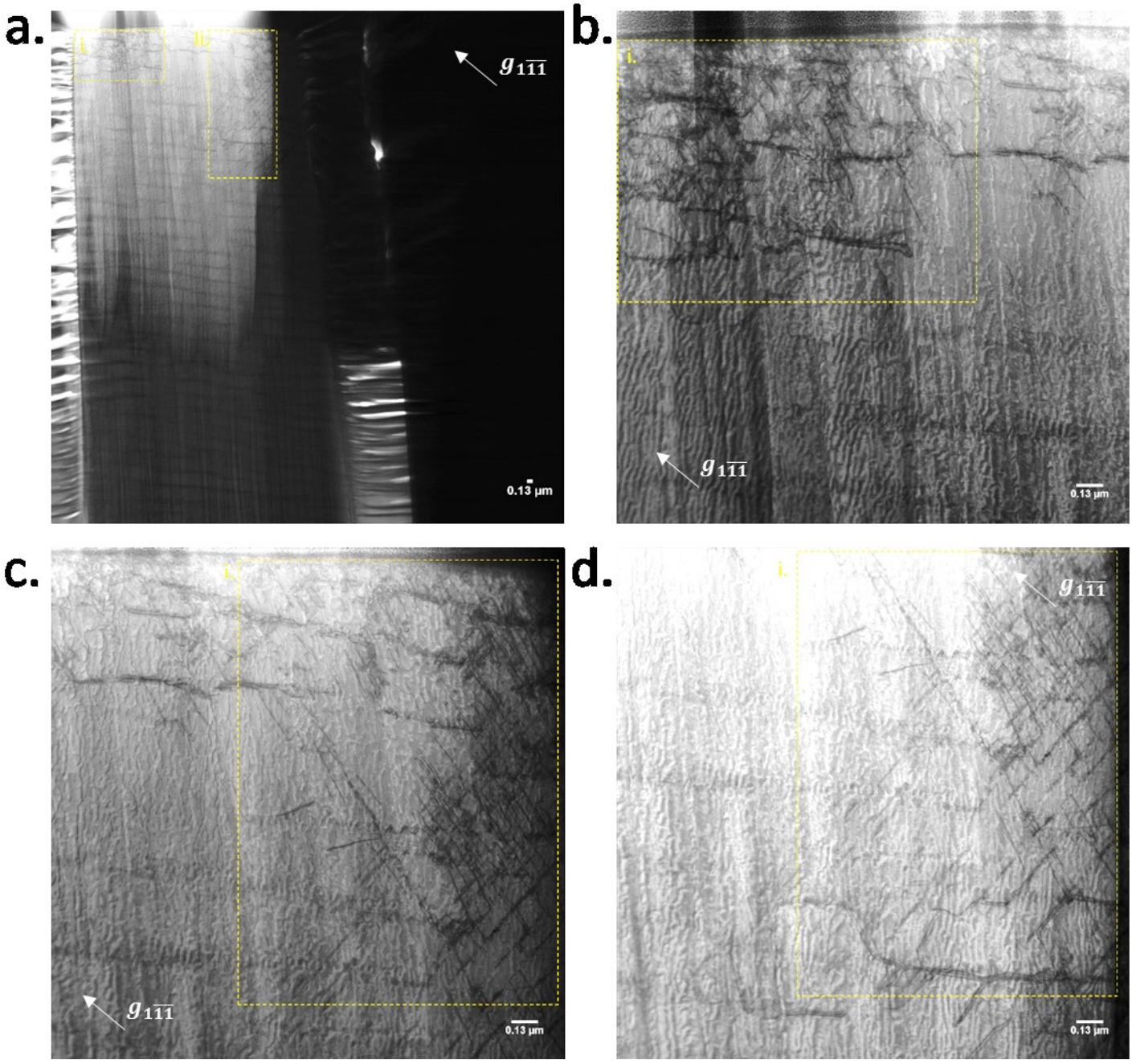


Figure 158: Condition 2 of pillar 6e, (a) Overview of the micropillar showing localised deformation at the top and right hand side of the pillar. (b) Extended dislocations in a 45 orientation at the top of the pillar (c) Extended dislocations in a 45° orientation at the right hand side of the pillar (work hardened region).(d) Closer inspection of extended dislocations.

Condition 2 shows several dislocation types, however extended straight type dislocations can be viewed clearly as shown in figure 158.

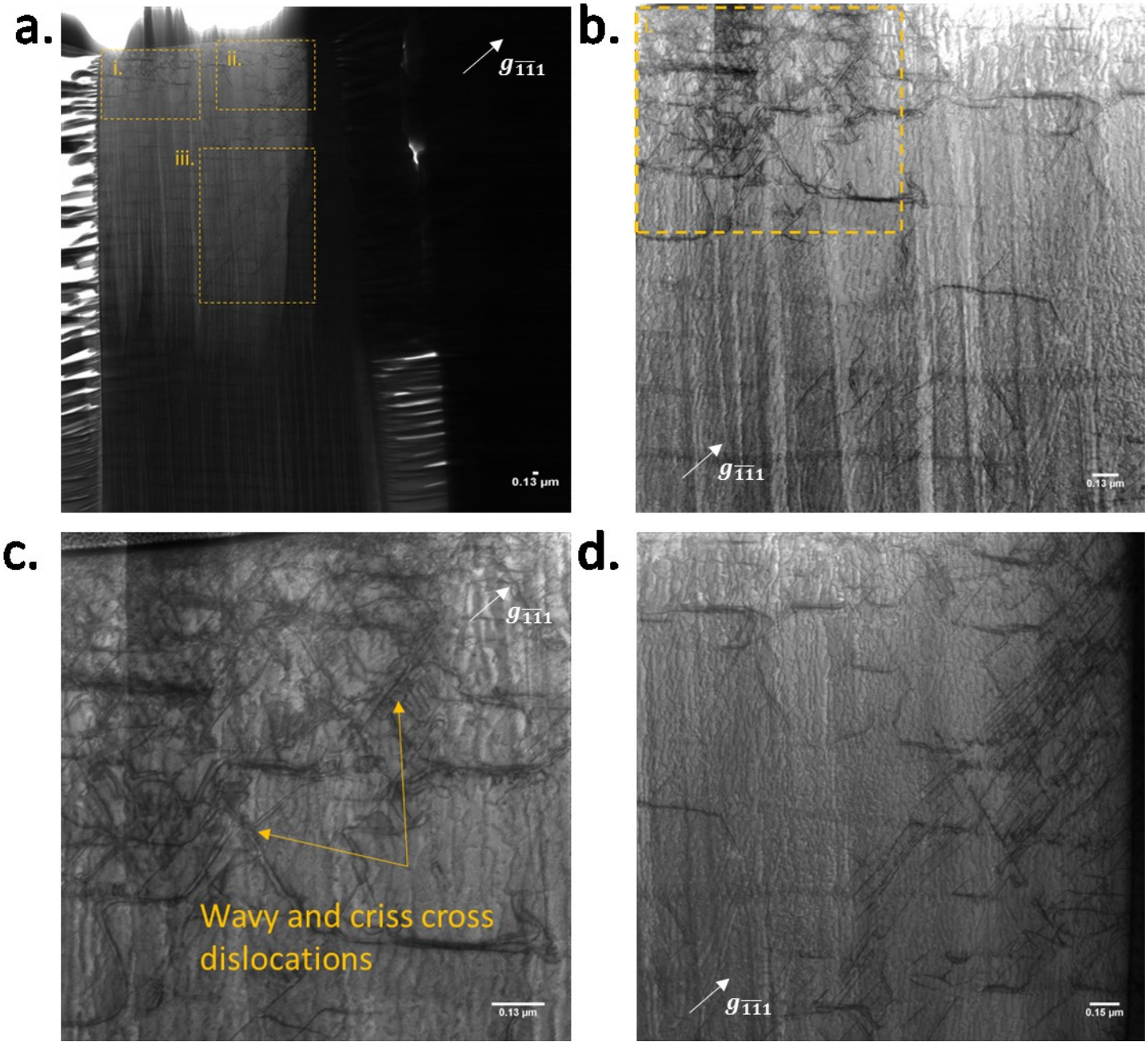


Figure 159: Condition 3, of pillar 6e, showing multiple dislocations pairs inhabiting the localised deformation region at the top of the pillar and more irregular wavy type dislocations interacting with the Ɣ/Ɣ' microstructure near the slip lines. (a) Overview of the micropillar with localised deformation regions at the top of the pillar (i&ii) representing figures b&c respectively, (iii) represents the area were the dislocations are interacting with the slip lines as shown in figure d. (b) Wavy, criss cross and paired dislocations in the localised deformation area at the top of the pillar. (c) Closer inspection of area (i) highlighted in figure b (d) Dislocations interacting with slip bands

Condition 3 shows dislocation pairs inhabiting the deformed region at the top the pillar, Figure 159 b&c, due to the interaction of the flat punch and the pillar surface, wavy type dislocations and extended dislocation types can also be viewed.

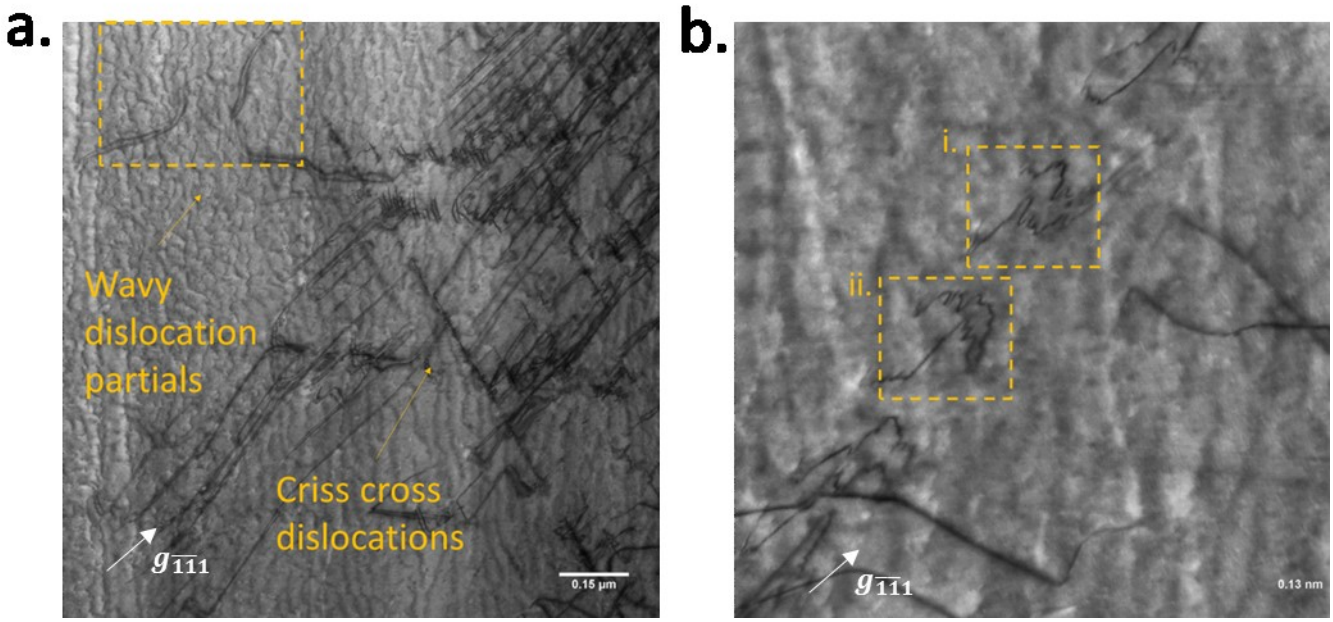


Figure 160: Condition 3, of pillar 6e, showing various dislocation types (a) dislocation pairs and criss cross dislocations (b) wavy irregular dislocations. (I&ii)

Figure 160, shows a closer inspection of the various dislocation in condition 3, such as wavy, extended and criss cross dislocations.

Table 12: Compound table of TEM information from figures 124-160. Listing the foil normal, G vector, image mode, pillar and pager number, taken from Carburised CMSX-4.

Fig No.	Foil normal	G vector	Image mode	Pillar	Page no.
142(a-c)	001	-111	BF	5e	157
143(a-c)	001	111	BF	5e	158
145(a-c)	001	020	BF	5d	159
146(a-c)	001	020	BF	5d	159
154(a-d)	110	1-1-1	BF	6e	169
155(a-b)	110	1-1-1	BF	6e	170
155(c-d)	110	1-1-1	HADF	6e	170
156(a-d)	110	020	BF	6e	171
157(a-d)	110	020	BF	6e	172
158(a-d)	110	1-1-1	BF	6e	173
159(a-d)	110	-1-11	BF	6e	174
160(a-b)	110	-1-11	BF	6e	175

6.8. Summary – Results chapter 1

Micropillars can be fabricated using a FIB, rectangular pillars were chosen as they mimic the slip characteristics of the fcc Ni based super alloy crystal structure and give a better description of slip lines for image analysis.

FIB damage will unfortunately always be introduced into the pillar. The key to minimising this is by patterning efficiently ensuring the bulk of the work is done in the rough stage. Depending on the size of the pillar, it may be advisable to pattern with a current no higher than 2 nA, post the first rough stage. This is to avoid redepositon

Also ensuring a good fiducial marker and fabrication stability is key, ensuring the milling does not drift to other areas of the pillar.

3-4 µm pillars take approximately 45 minutes to fabricate with 85% of the time arising from the rough mill which cuts a 3-dimensional square based pillar with a width of 9 µm and a depth of 5 µm. This rough mill provides a rough pillar shape which can be tailored to the desired dimensions, as well as a trench enabling the flat punch free motion and girth wide enough to provide a viewing angle sufficient to see the bottom of the pillar, provided sufficient tilt. The more layers the fabrication sequence has, the more polished the final pillar will be.

When calculating the engineering stress / strain from the load / displacement data, the area and height values will have a degree of error associated with them due to human and software error. As the micropillars are compressed the sample will deform but so will the tip (it is very rigid) as well as the load cell and other parts of the indenter system. There will therefore be some error associated with these results. However this is commonly referred to as load-train compliance and can be removed.

$$\theta_t = \sin^{-1}\left(\frac{w_b - w_t}{2l_s}\right) \qquad \textit{Equation 38}$$

A slight taper is ideal and aspect ratio 1:3 is ideal to ensuring pillar stability, anything larger 1:3 begins to show instability.

The size effect experiment could have been repeated with a new and improved testing methodology whereby the pillars were in exactly the same orientation and the aspect ratio kept constant. The results would then perhaps be more comparable to literature. However as stated in the motivation, the size effect experiment was first used as a set of *in-situ* micropillar compression tests, and led the way for the robust testing criteria which could further advance the study of micromechanical testing on new alloys and orientations.

The differences in orientation were due to aligning the pillars with the edge of the samples that were cut from a circular piece. The pieces were cut according to a set angle required to expose the faces of the 001, 001 and 111 orientations.

The orientation changes the mechanical response due to the competition of slip systems dictated by the similarity in Schmid factor

The failure response can thus be pre-engineered in single crystal alloys, according to deviations from ideal orientations <001> . It was found that in orientation 1, in which the x,y,z axes are aligned to the 001, 100 and 010 respectively deforms in a crumple like fashion. An orientation in which the x and y axis are aligned 45° away from the 100 and 001 respectively, which corresponds to the 011 and 110, deformed with a diagonal shear localised slip band. An orientation that is not aligned with respect to a corner of the fcc stereographic triangle, with a 30° misorientation from the x and y axis, failed with un characteristic deformation and what could be termed a catastrophic failure.

A more detailed study of orientation will be examined in the next chapter. Further analysis is needed whereby each of the four faces of the square micro pillar are analysed and appended to the designated slip system. This will be examined in section 6.

When examining the slip patterns, there is an error associated in the angle the slip line makes with the vertical boundary of the pillars as the sample is titled at an angle within the SEM chamber depending on the machine and operating stage.

It is therefore important to understand the errors that can arise to ensure results are as accurate as possible.

As the pillars are flat faced, slip trace analysis can be performed whereby the slip angle (θ_s) can be expressed as follows:

$$\theta_s = \tan^{-1}\left(\frac{\tan\theta'}{\sin\varphi}\right) \qquad \textit{Equation 39}$$

where θ' is an angle on any pillar faces after tilting and φ a tilting angle.

For bulk samples, there are many dislocation sources and these are activated when the resolved shear stress reaches a critical value. In small samples, the number of sources is likely to be limited and so the slip system with the highest Schmid factor may not contain the easiest operating source[180]. The compression tests are on the micro scale and as the sample size decreases, the dominance of the primary slip plane drops, and the secondary and even tertiary slip planes have a considerable probability of yielding. This stochastic phenomenon is more prominent[180]. This gives rise to interesting mechanical behaviour characterised by dislocations. If dislocations pre-exist, the mean length of half Frank Read

sources is expected to shorten in a smaller sample, and so the yield strength is expected to be higher[180]. This was not necessarily the case in this study, however the hardening was seen to increase with decreasing pillar size.

During the hardening regime, many slip traces can be observed on one pillar, however when the orientation geometry of the pillar is changed, several slip systems activating at once can be observed. In this instance, the easiest yielding source may not necessarily lie on the maximum Schmid factor.

The extent to which these phenomena occur can be examined through the study of dislocations. The nucleation of dislocations through the ϒ/ϒ' microstructure can be studied by preparing TEM specimens deformed to specific regions in the stress x strain response, at points before and during hardening.

The TEM micrographs show dislocations interacting with each in the softer ϒ phase before traveling into the harder ϒ' phase and separating into lower energy species consequently. In areas where shear has localised the entire ϒ/ϒ' microstructure is flushed with dislocation.

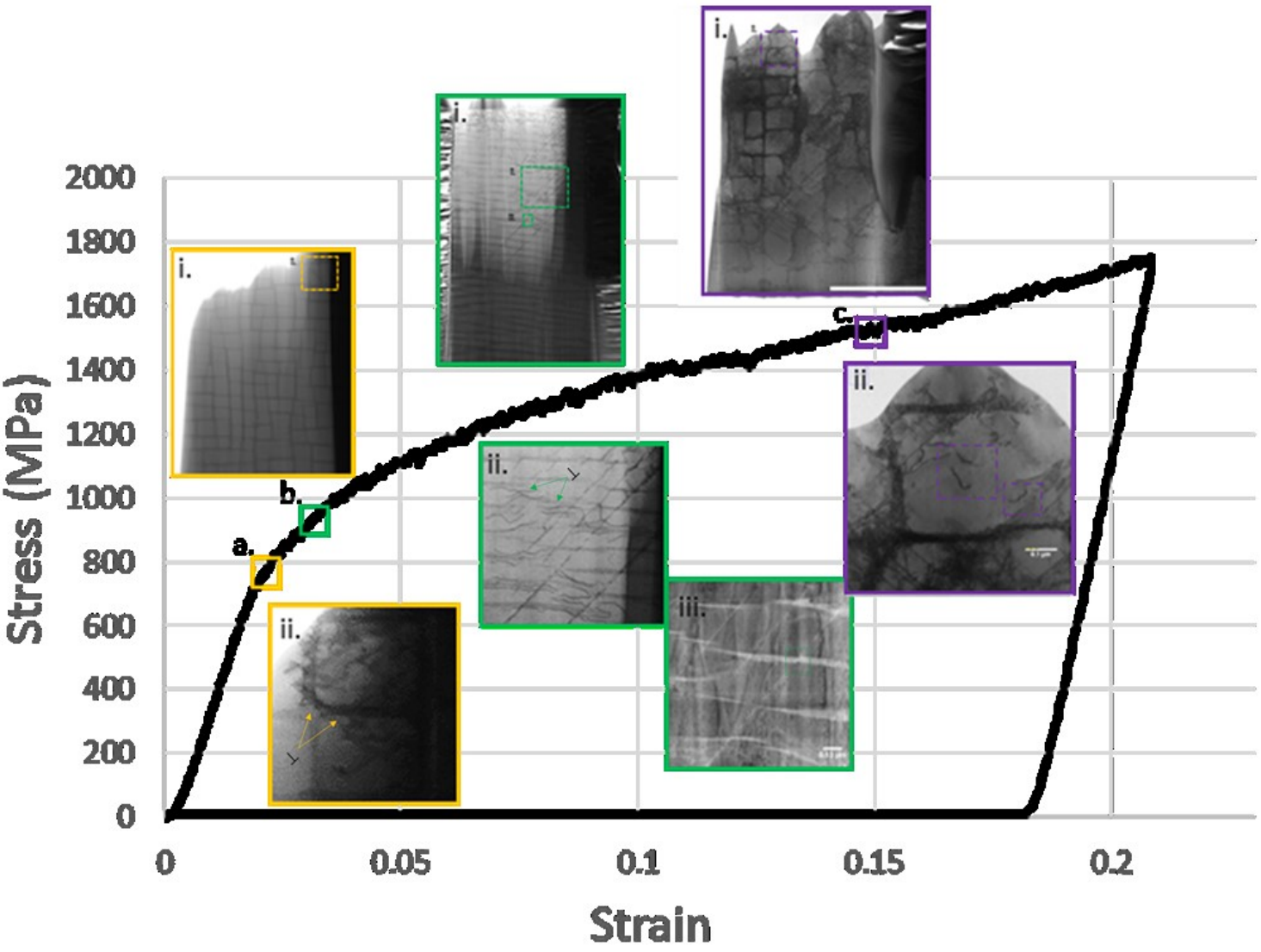


Figure 161: Compound stress strain trace with appended TEM micrographs showing the dislocation evolution through ϒ/ϒ' microstructure at different representative strains. (a) ~3% strain (near the yield point), illustrating dislocation networks forming forests in the ϒ channels and spreading into the ϒ' in pairs forming APB's. (b)~4% strain (plastic region / hardening effects), illustrating dislocations spreading through the microstructure on the (010) zone axis, separating into different dislocation types, the slip bands can clearly be seen in i&ii, (iii) shows the shearing of the ϒ/ ϒ' via a slip band. (c) ~15% strain (large levels of deformation), illustrating the ϒ channels flush with dislocations and partial kinks inhabiting the ϒ' cuboids, on the (101) zone axis.

Figure 161, shows a representative stress strain trace of an SX-CMSX-4 micropillar compressed to 17% strain with appended TEM micrographs showing the evolution of dislocation structures at points near the yield point (yellow), just after the yield point (green) and after significant deformation (purple). The figure shows how the dislocations structures first form forests in the ϒ channels before organising into slip bands causing shearing of the microstructure and subsequent evolution into the ϒ' cuboids in pairs giving rise to kinks and jogs.

7. Results – Polycrystalline Ni-based superalloy & orientation testing

7.2. Objectives – Results chapter 2

1. Establish a testing regime to examine the mechanical deformation of both single and polycrystalline Ni superalloys, along the <001> <011> <111> directions to assist in deformation and fatigue studies.
2. Analyse slip traces to correlate mechanical response to slip systems and crystal orientation.
3. Extract deformation information to assist in the optimization of the next generation of alloys.

7.3. Motivation

The motivation of this chapter is to extend the work undertaken in the first results chapter and apply it to examine the orientation, deformation and resultant active slip systems in two commercial alloys, in the hope of informing the improvement in the next generation of alloys. Fatigue cracks formed via cyclic fatigue are one of the predominant modes of failure of in service Ni superalloys[5,14]. Mechanical variables extracted from micromechanical testing can be fed into failure criteria and fatigue life evaluation procedures for Ni superalloy components[5]. Improving the lifetime of the Ni superalloys, will increase the lifetime of the engineered parts, which in turn decreases costs for the designer. The two main types of crack initiation in Ni superalloys occur via crystallographic and non-crystallographic failure. At low temperatures and stress conditions, crystallographic failure is the most prevalent mode[181]. An analysis and characterisation of the slip behaviour is therefore important, as the operative deformation mechanism has a strong influence on the nature of fracture[5,14,76,182].

7.4. Introduction

Metals are comprised of crystals, with different shapes and orientations. The Ni superalloys under examination in this thesis have an fcc + L_{12} structure. The microstructure contains a ~ 70% dispersion of precipitates with the L_{12} strengthening ϒ' phase[183] and the remainder, a solid solution of the softer, fcc ϒ phase. It is the interplay between the two phases that gives the alloy its exceptional properties at low and high temperatures. The Ni alloys are fabricated into parts that assemble to form the drive chain power transmission for the aero engine.

For this study, a new pillar design was scripted, using the Nanobuilder software. This new pillar design incorporated a larger rough trench, enabling a wider field of view when testing, whilst also minimising

the chance of the flat punch encountering the side of the trench. Prior to compression testing, it is important that the flat punch does not partially deform the pillar. During compression testing, a clear view of the top and bottom of the pillar aides in analysis.

Two Ni superalloys; a single crystal CMSX-4 and a polycrystalline FGH96 were examined and the results compared. Commercially, the single crystal alloy is used to fabricate compressor blades and the polycrystalline alloy is used to fabricate discs, which house the single crystal blades. Fatigue cracks, often start at areas of high stress concentration, such as the area in which the single crystal and polycrystalline alloys are friction welded together[181]. The chemistry between the two alloys varies slightly due to different heat treatments and the addition of grain boundary stabilisers in the polycrystalline alloy[183].

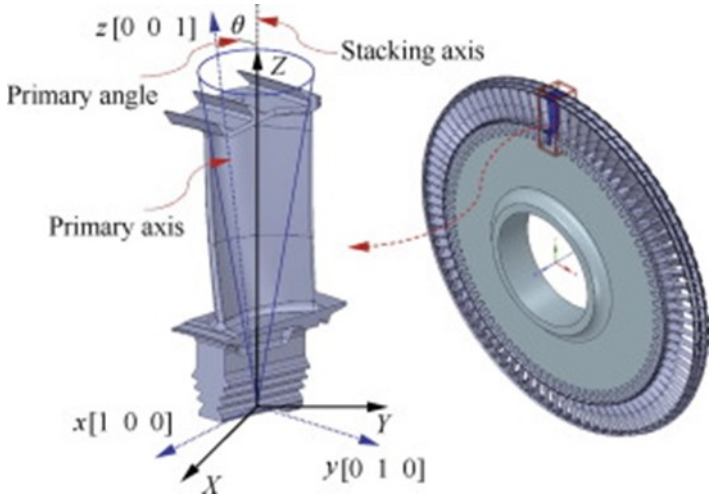


Figure 162: A Ni superalloy aerofoil blade, indicating the primary <001> growth direction and deviation ϑ, also known as α[184]:

Figure 162, shows a CAD image of a Ni superalloy aerofoil blade, indicating the primary <001> growth direction. The preferred orientation for the single crystal alloy is <001>[76], this is due to the growth direction of the macrostructures known as dendrites, which form as the liquid melt is cooled[19]. The crystallographic orientation of parts used in service can be quantified by α and β. α is the primary orientation, defined as the relative angle between the aerofoil stacking line and the <001> direction[181]. Current industry standards allow a misorientation of 5-15°[76].

β is the secondary orientation and can be defined as, the angle of the <001> orientation relative to the blade geometry, where the reference point of 0° is a line parallel to the blade attachment[145]. Altering either α or β will change how the dislocations move through the material as it is deformed[181].

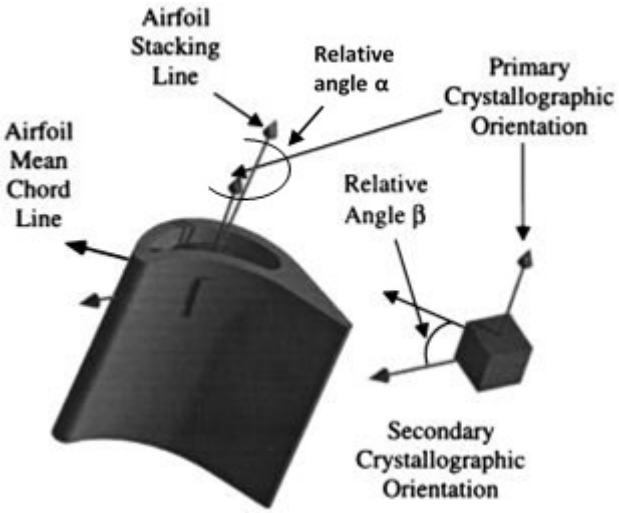


Figure 163: Convention for defining crystal orientation in turbine blades, illustrating the relative angles α and β[185,5]

Figure 163, shows a convention for defining crystal orientation in turbine blades, illustrating the relative angles α and β. The dislocation processes that carry the deformation in Ni superalloys occur on the same length scale as the micropillars. As a micropillar is deformed, the mechanical response, with respect to the loading direction, is dictated by the orientation of the cubic crystal. This is done by resolving the angle between the slip plane normal and the loading direction and the slip direction and the loading direction.

Dislocations, travel on planes with set directions, enabling calculation of the Schmid factor, which promotes understanding of the resolved shear stress on each active slip system. These planes and directions can typically be characterised via the use of microscopy techniques as illustrated in Chapter 6. These planes and directions are known as a slip systems and act in tandem, post yield to minimise the energy of the system. The four octahedral planes with the highest atomic density each have three primary slip directions, figure 165.

Slip in Ni superalloys occurs on one of the four {111} planes accompanied by one of the three $\langle 01\bar{1} \rangle$ directions. Taking into account the normal of the slip plane and the direction of the slip with respect to the loading the direction, one can predict the type of deformation behaviour and in turn calculate which slip systems are active during deformation.

The pillars examined in this chapter are cuboidal and have square faces, which is ideal for slip deformation analysis, as the intersection of the slip plane and the pillar face inscribes a line, which is the cross product of the slip plane normal and face normal.

Examining the slip trace on each face of the pillar, north, south, east and west, with respect to the equivalent rotation of the primary (top down) crystal orientation, can assist in quantifying the deformation behaviour of the given orientation in the microstructure and enables production engineers

to accurately predict and visualise the deformation mode of the alloy, at low temperatures, before the part is put into production.

This chapter will examine the deformation characteristics and mechanical properties, in the terms of slip systems, slip traces, mechanical properties and crystal orientations for two Ni superalloys, one single crystal CMSX-4 and one polycrystalline alloy FGH96.

The micropillars were compressed in displacement control with a flat punch in a Quanta SEM. The results were corrected for load / time drift and stress vs strain curves plotted. The yield point, hardening rate and respective moduli of the tested orientations were analysed.

Changing the alignment of the crystal orientation with respect to the loading direction alters the τ_{crss}. This in turn alters the slip behaviour and slip trace angle. Theoretical results will be tested against experimental to validate the testing criteria used in this chapter.

As FGH96 and CMSX-4 are different alloys the effects of the alloying elements will be considered briefly leading onto the more advanced carbide alloy system detailed in section 8.

As the orientation of the sample specimen changes so does the active slip system. The orientation of the micropillars were measured via EBSD by scanning along the x and y edge of the top surface of the micropillar calibrating the system. This is highlighted in orange and shown in figure 98 a. The active slip systems in the fcc system can be represented by the stereographic projection in an fcc crystal, figure 164.

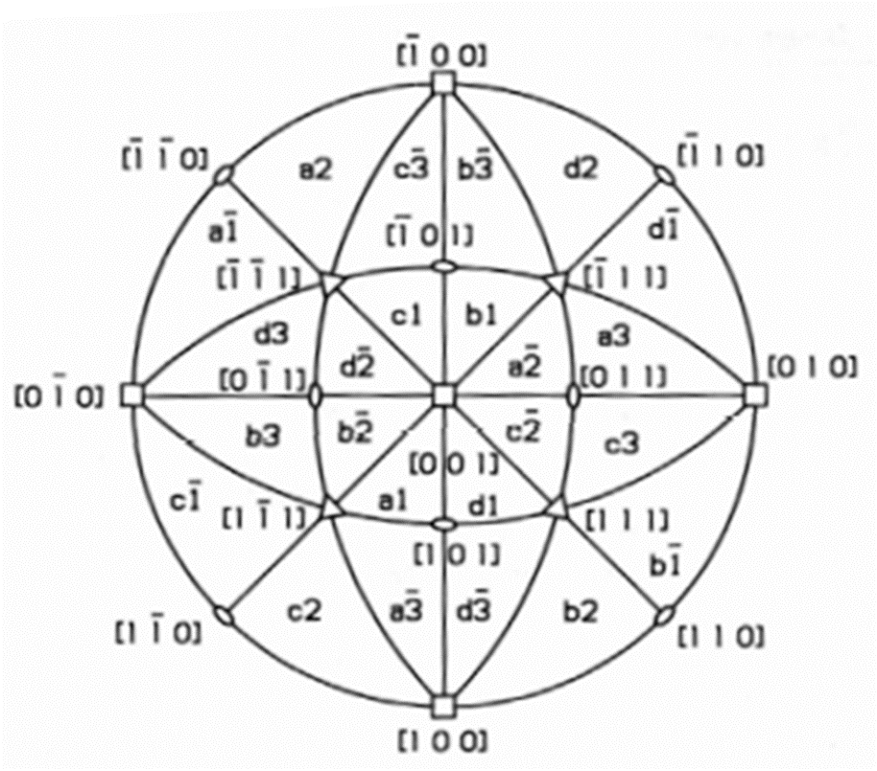


Figure 164: Slip systems in fcc materials – The Standard [001] stereographic projection of fcc crystals[170]

For fcc materials there are 12 slip systems with positive and negative shear directions[76]. The 12 slip systems correspond to the four {111} planes, each with three <0-11> directions, as shown in table 13.

Table 13: The fcc slip systems in fcc crystals

Plane		**(111)**			**(-1-11)**	
Direction	**[0-11]**	**[10-1]**	**[-110]**	**[011]**	**[-101]**	**[1-10]**
System	a_1	a_2	a_3	b_1	b_2	b_3
Plane		**(-111)**			**(1-11)**	
Direction	**[0-11]**	**[-10-1]**	**[110]**	**[011]**	**[10-1]**	**[-1-10]**
System	c_1	c_2	c_3	d_1	d_2	d_3

The combination of slip plane (a_v,b_v,c_v,d_v), and respective slip direction (1,2,3) that operates within each unit in the stereographic triangle is shown in table 13 and figure 164. For each plane there are four members of the <111> family which will give a dot product of zero with the {1-10} indices. This is important as it indicates that the direction lies on the plane and thus the slip system is a primary and not a secondary slip system, figure 166. The planes and directions listed in table 1, were chosen to represent the 12 fcc slip systems used in this chapter.

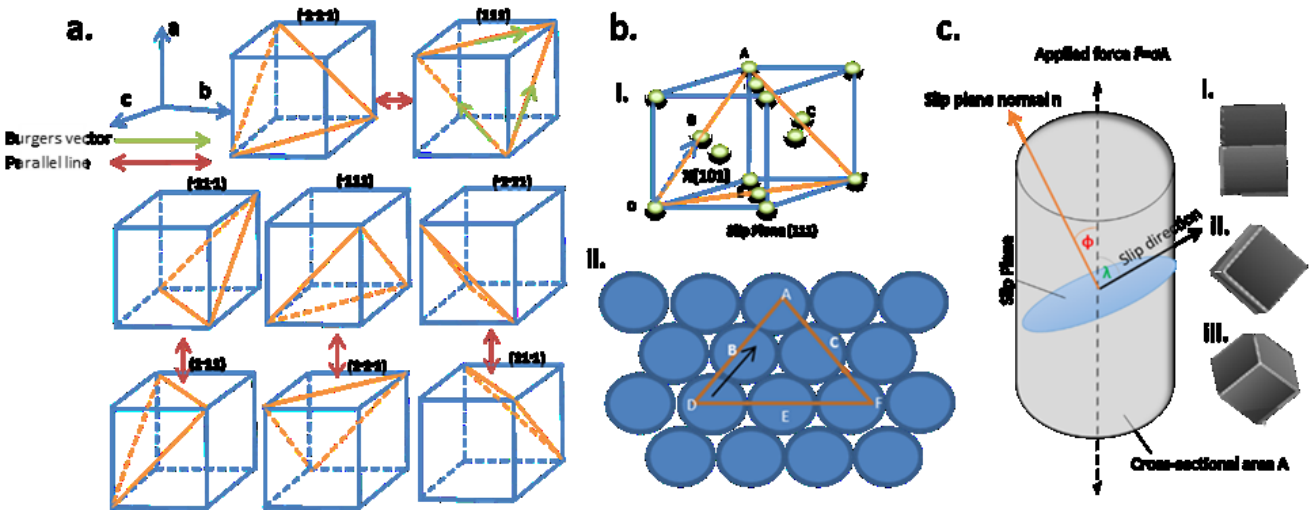


Figure 165: Slip systems in the fcc structure (a) fcc crystal lattice illustrating parallel planes, describing how the orientation of the slip plane changes. The orange triangle represents the various orientations the {111} planes can take, the bold orange lines correspond to the slip trace visible on the face of the pillar. (b) the fcc crystal lattice (i) 3d representation of (111) plane and <110> slip direction (ii) 2d representation illustrating the highest planar density and highest linear density (c) Schmid factor analysis, where, as the orientation of the normal of the slip plane with respect to the compression axis changes, so does the shear stress required to activate slip in said direction on said plane. The value of the Schmid factor M changes as the orientation of the fcc lattice is changes (i-iii).

Figure 165, shows different orientations of the {111} plane within the fcc crystal, illustrating the different planes and directions, dislocations can travel on, once a critical value of shear stress is reached. Slip occurs when this maximum value of shear stress is reached. This enables dislocations to move on the specified plane in a specified direction characterised by the plane of highest planar density and the direction of highest linear density, as shown in figure 2 b (i-ii). The orange triangles in figure 165 and figure 166 represent the various orientations the {111} planes can take, the bold orange lines correspond to the slip trace visible on the face of the pillar. An in depth slip trace analysis, of the single crystal CMSX-4 and polycrystalline FGH-96 alloy will be undertaken in this chapter.

The angle between the slip plane normal and the loading direction ϕ and the angle between the slip direction and the loading direction λ, change depending on the orientation of the fcc crystal as shown in figure 165 c. This is turn changes the resolved shear stress on the plane. As the load is increased and a critical value is reached, the material will deform.

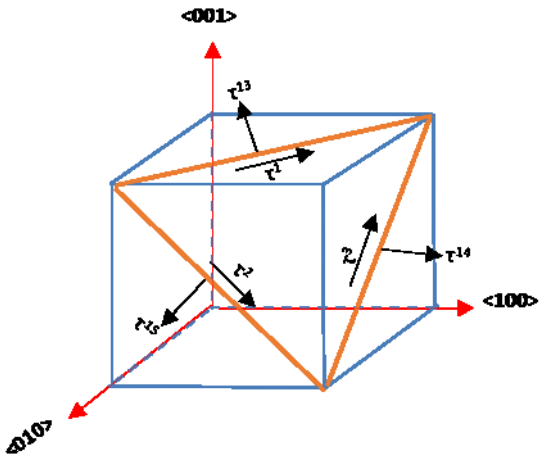


Figure 166: A cubic lattice, illustrating the [111] plane and respective primary (close packed) directions $\tau_{1,2,3}$ and secondary (non close pack) directions $\tau_{13,14,15}$[186]

Figure 166, illustrates the difference between primary and secondary slip directions. In this study, only primary slip directions will be considered. The slip systems 1,2,3 and 13,14,15 as are listed below in table 14.

Table 14: Slip number n and resultant slip plane and slip direction, drawing from Figure 166. n = 1-3, corresponds to primary (close packed) systems. n=13-15, corresponds to secondary (non close packed systems)

Slip number (n)	Slip Plane	Slip Direction
1	(111)	[10-1]
2	(111)	[0-11]
3	(111)	[1-10]
13	(111)	[-12-1]
14	(111)	[2-1-1]
15	(111)	[-1-12]

The relationship between slip systems and deformation mechanics can be quantified by the Schmid factor, whereby the highest Schmid factor corresponds to the activation of the first slip system. Table 15 lists the Schmid factors for a <011> orientated pillar. This is the same <001> pillar also shown in figure 97 and figure 98.

Table 15: slip systems for the <011> pillar shown in Figure 97 and Figure 98

	Slip system	Compression axis 011 – Schmid factor
1	(111)<0-11>	0.250
2	(111)<10-1>	0.483
3	(111)<-110>	0.233
4	(-1-11)<011>	0.226
5	(-1-11)<-101>	0.145
6	(-1-11)<1-10>	0.070
7	(-111)<0-11>	0.238
8	(-111)<-10-1>	**0.495**
9	(-111)<110>	0.257
10	(1-11)<011>	0.168
11	(1-11)<10-1>	0.168
12	(1-11)<-1-10>	0.081

Table 15 shows 12 fcc slip systems, for a <011> orientated single crystal CMSX-4 micropillar. The slip system with the highest Schmid factor is highlighted in bold. In this case it is the (-111) plane and the <-10-1> direction. Which corresponds to the c_2 inverse pole figure, figure 164 and table 13 respectively.

7.5. Polycrystalline FGH-96

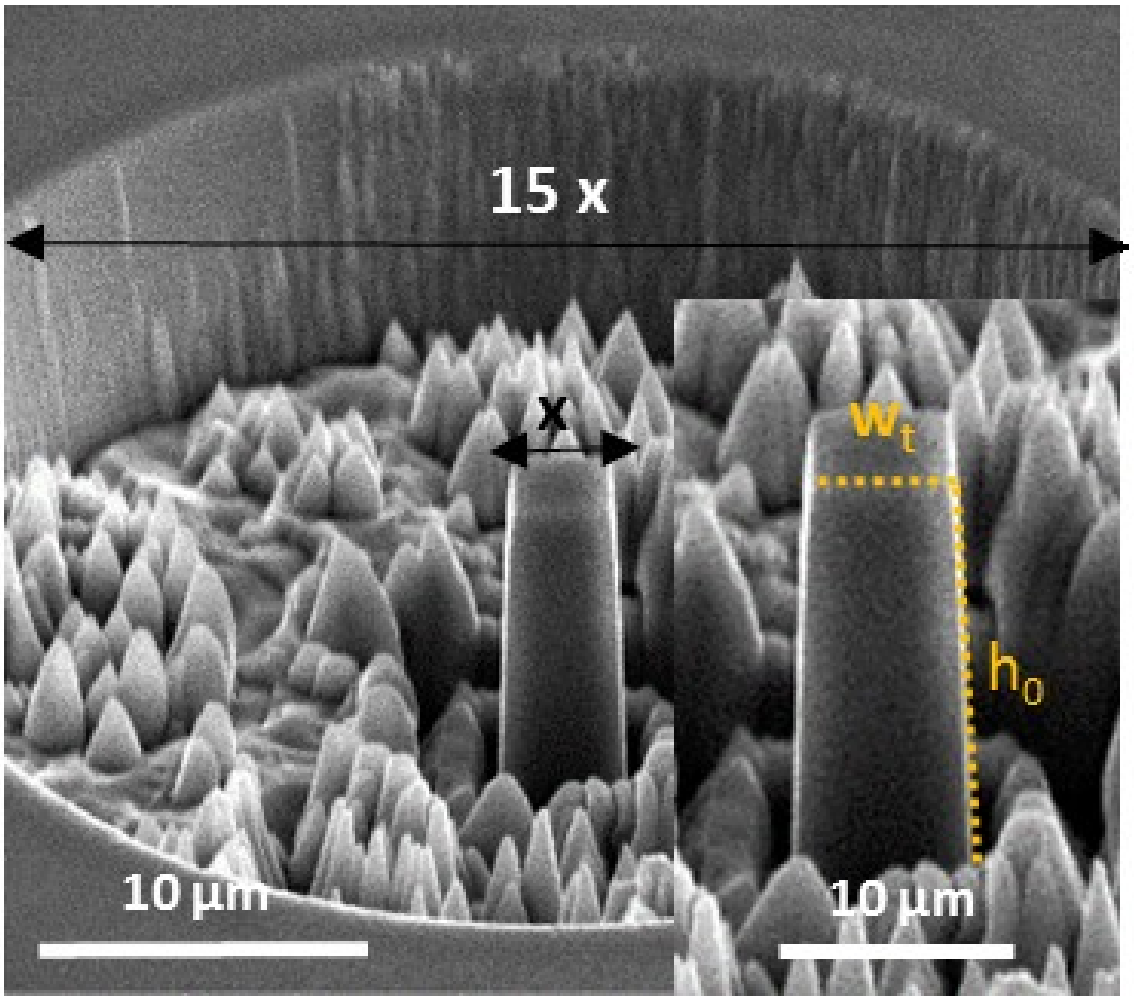


Figure 167: New version of micropillar designs fabricated using the Nanobuilder software. The rough trench has a wider girth allowing a large viewing angle. W_t, represents the top width and h_0 represents the height at 0% deformation

Figure 167 shows an updated micropillar design, fabricated using the Nanobuilder software. The rough trench has a wider girth allowing a large viewing angle. W_t, represents the top width and h_0 represents the height at 0% deformation. The pillars fabricated in this section are an improvement on those used in the last chapter. The area surrounding the pillar has changed from rectangular to circular and increased in size, allowing a larger field of view for both post and pre analysis of the pillar.

Table 16: Chemical composition at% of polycrystalline FGH96[187]

	FGH96										
	Ni	**Cr**	**Co**	**Mo**	**W**	**Ti**	**Al**	**Nb**	**Zr**	**B**	**N**
Literature	**Bal**	**16**	**13**	**4**	**4**	**3.7**	**2.2**	**0.8**	**0.036**	**0.03**	**0.011**
Material	**Bal**	**19.63**	**12.92**	**4.3**	**2.03**	**5.39**	**1.41**	-	-	-	-

Ni superalloy FGH96 is a polycrystalline material made up of a large distribution of grains orientated in different directions with respect to a principal load axis. The average size of the grains is ~25 µm.**Error! R eference source not found.**

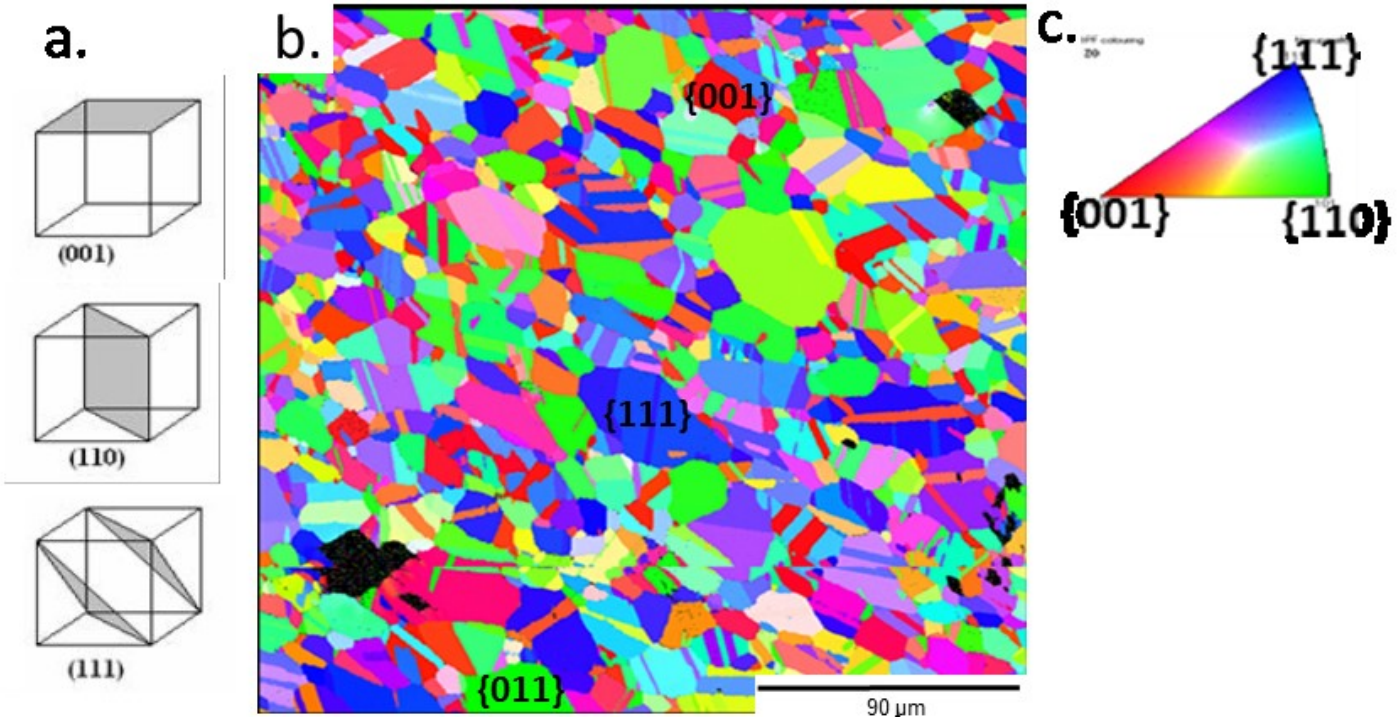


Figure 168: EBSD map of isolated region showing orientations with respect to the loading axis (a) Planes of the respective (001), (110), (111) grains (b) EBSD map of FGH96 alloy illustrating the distribution of the various grains (c) Inverse pole figure showing the colour distribution of the {001},{011},{111}.

Figure 168 shows a set area of the FGH-96 alloy, in which the texture of the alloy is illustrated. The red grains correspond to the <001>, the green <011> and the blue <111>. **Error! Reference source not f ound.** shows the size distribution of grains in the FGH-96 alloy, the scan was taken over a 350 x 250 µm area. The average grain size was found to be ~25 µm. The distribution of grains in the z direction favours the {110} orientation. Figure 169, shows the technique used to fabricate pillars on select grains. Figure 170, shows a fabricated micropillar that has no distinct orientation / Schmid factor and thus why it is so important to find large enough grains.

It is important to note that the pillars must be nearly identical in geometry to give a fair representation of the mechanical anisotropy of FGH-96 and predict in service behaviour.

Ideally, the average grain size in the FGH96 alloy would be larger than 25 µm, to avoid any overlap of different grains with different crystal orientation. However, heat treating the alloy, would alter the ϒ/ϒ’ microstructure and thus the mechanical properties.

An area suitable for fabricating micropillars in this study, contained a reasonable distribution of desirable grains >10 µm, no observable plastic strain in the surrounding diameter of the grain and was within 10° of the desired orientation in the z direction.

6.4.1. FGH-96 method and testing

Each region and pillar was carefully marked with a FIB milled indicator so that post compression the necessary data can be extracted, as shown in figure 169. Figure 170 shows a test pillar pre and post deformation, used as a fiducial marker that has no clear Schmid factor.

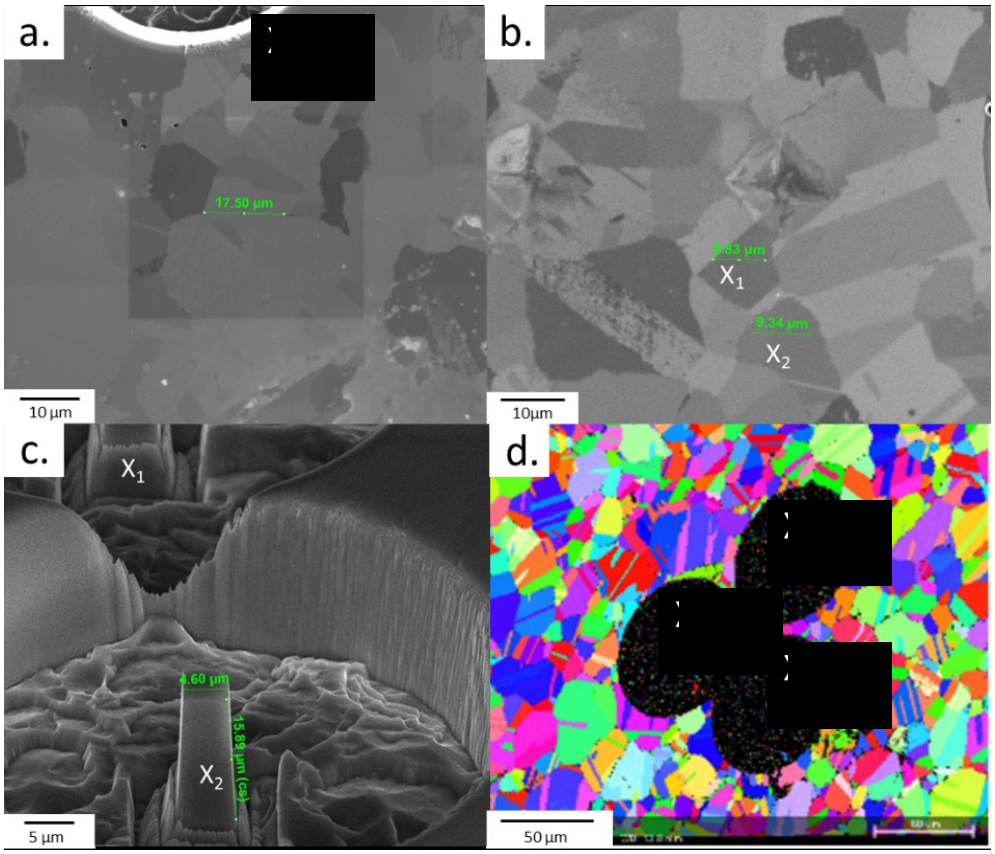


Figure 169: Preparation of micropillars on site specific grains, X_1 and X_2 (a) Identification of the region by removing the top surface of material with a low probe current on the FIB (b) Closer inspection of isolated grains for the fabrication of pillars X_1 & X_2 (c) Fabricated micropillars X_1 and X_2 (d) EBSD map over isolated micropillars X_1 and X_2 with fiducial marker X_3.

Grains within 10-20 µm, orientated <011> and <111>, out of plane were isolated following EBSD scans and pillars were fabricated and tested. Figure 169 shows the preparation of micropillars in specific orientations by removing the top surface of the material with the FIB beam at a low probe current and marking with a fiducial marker, which in the case of figure 169, was a micropillar, the pre and post deformation of this micropillar is shown in figure 170.

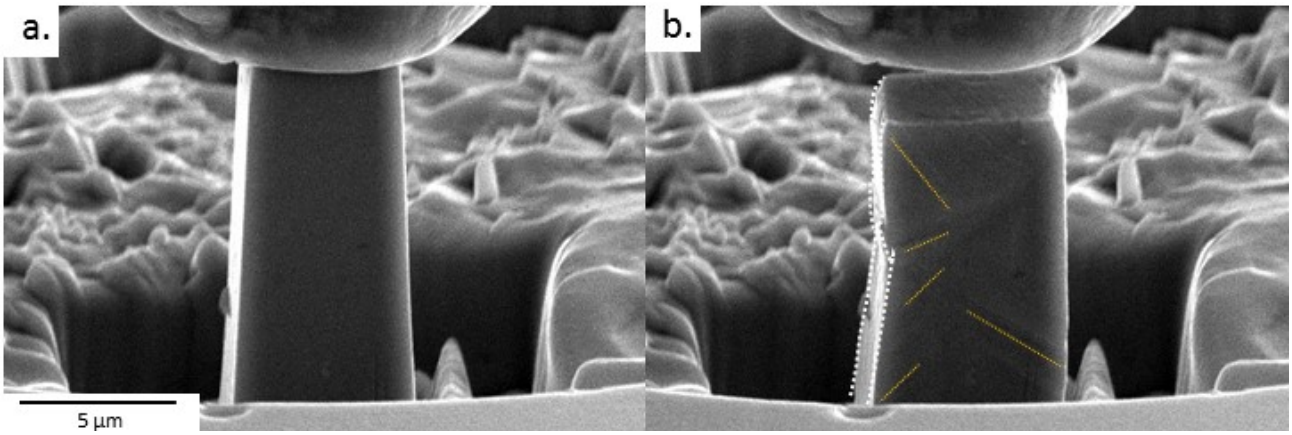


Figure 170: FGH96 pillar, with no clear orientation leading to a mixture of Schmid factors within the one pillar, resulting in a in an unstable deformation (a) Pre deformation (b) Post deformation, showing a twisted, deformation, with signs of buckling,

Figure 170 shows a pillar that has been fabricated on multiple grains with a mixed orientation. If the pillar is not aligned directly on one grain, with one orientation, then the Schmid factor is not a suitable analysis tool. The deformation of the pillar in figure 170, shows an extensive shape change, with no dominant slip trace. This is due to no dominant slip system being activated. A dominant slip system can be defined as the slip system with the highest Schmid factor.

Aligning grains with a fiducial marker and carefully removing the top surface of the area to be examined with a low FIB current ~46 pA enables the shape and size of the grains to be seen and so the centre of the pillar can be aligned ensuring the pillar is incident with only one orientation, as shown in figure 169.

Figure 171 shows the Schmid factor as a function of orientation in an EBSD map in the FGH96 alloy. The Schmid factor with the largest intensity is ~ 0.48, this corresponds to the <011> orientation.

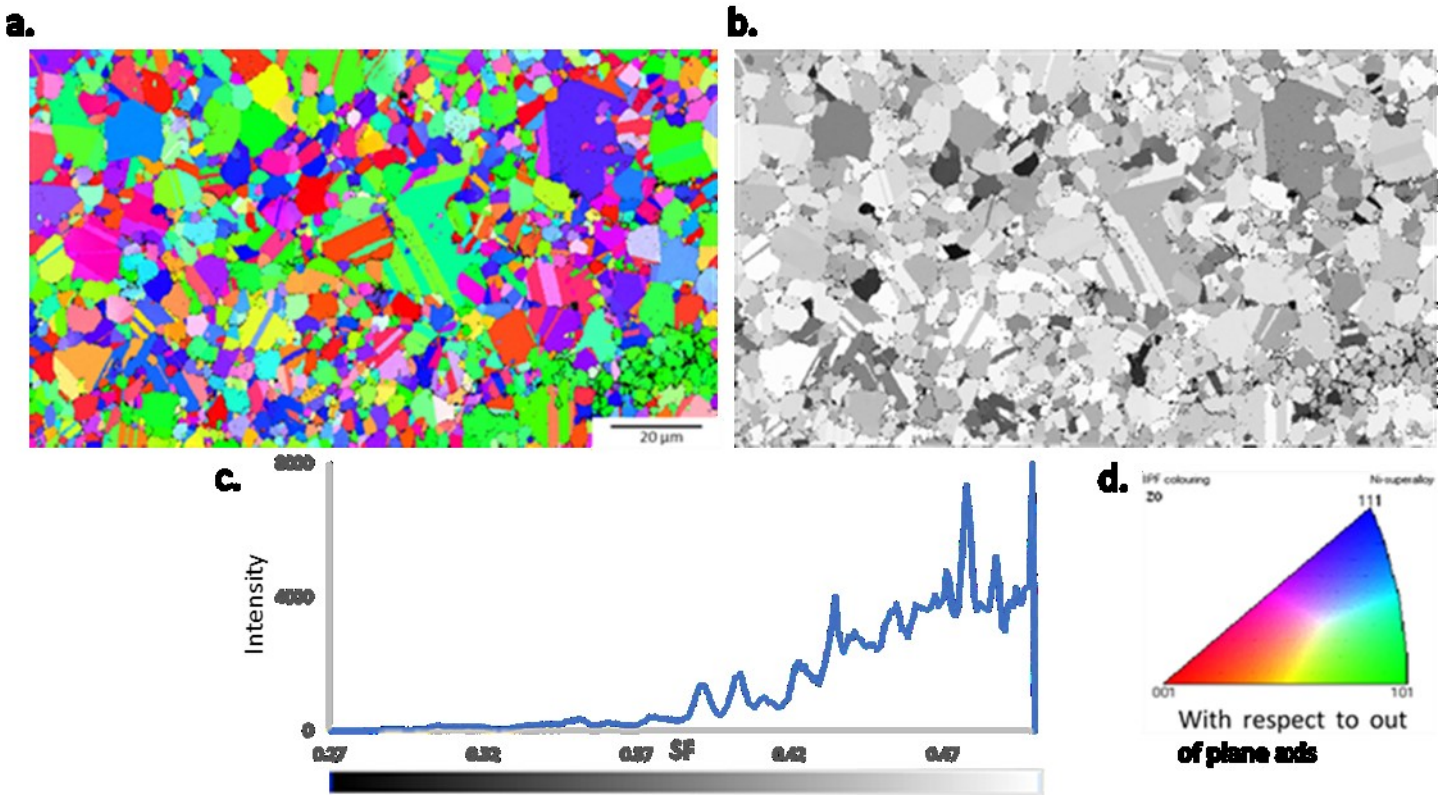


Figure 171: EBSD Map of a 150 x 90 µm area illustrating the variation in Schmid factors across grains. As each grain has a different orientation the Schmid factor varies accordingly, the Schmid factor with the highest intensity is ~0.47. (a) EBSD map showing the distribution of orientations (b) Schmid factor map showing the variation in Schmid factor (c) Schmid factor colour plot illustrating the highest the highest intensity of Schmid factor is 0.47 - 0.49 corresponding to the 011 grains. (d) Orientation of the grains with respect to out of plane axis.

Figure 171 shows the distribution of Schmid factors in a test area within the FGH96 polycrystalline alloy. The {111} grains have the lowest Schmid factors, illustrated by the darker grains in figure 171 b, the {001} and {011} share similar Schmid factors. The alloy favours the {011} grains in the z direction (α orientation).

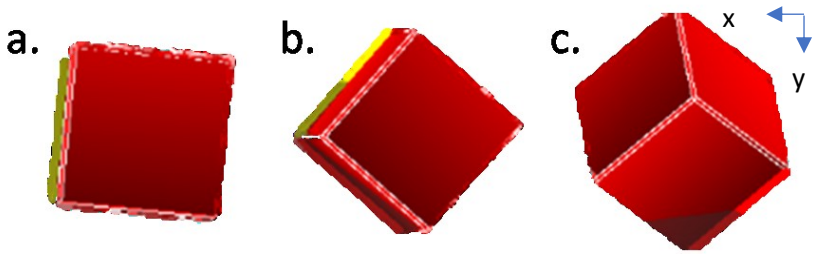


Figure 172: Top down crystal orientation of fcc structure in the, near (a) <001> (b) <011> (c) <111> orientations in the FGH96 alloy. The Euler angles of (a) (b) and (c) respectively are; Φ1=336.5 Φ=24.3 Φ2=25.0, $Φ_1$=179.8 Φ=39.7 $Φ_2$=145.9,$Φ_1$=227.3 Φ=42.3 $Φ_2$=93.8 (the pillar Is loaded along the Z axis, which forms a right handed set with respect to the x and y labelled axes)

Figure 172, shows the top down <001>,<011> and <111> crystal orientations in the FGH96 alloy. The primary slip systems for the three orientations respectively are (111)<0-11>, (-111)<-10-1>, (-1-11)<-101>, dictated by the highest Schmid factors, 0.4228, 0.4924 and 0.4169 respectively. Figure 173, figure

174 and figure 175 show the distribution of the slip systems and Schmid factors in relation to these three orientations, respectively.

The <001> orientated pillar has multiple slip systems with similar Schmid factors. In total the <001> orientation has 8 slip systems that can be considered to be competing with each other. The difference between the highest and lowest of these 8 slip systems is ± 0.0507. The resultant effect of these slip systems, competing with each other, as shown in figure 173, is a crumple like deformation of the micropillar, as shown in figure 177.

In “crumple” like deformation no predominant slip band is formed, even at high levels of deformation (20% strain). The average Schmid factor for the <001> orientation is 0.2715 ± 0.1916. The average Schmid factor between the 8 competing slip systems is 0.4009 ± 0.0157.

The <011> pillar can be considered to have two main slip systems that are competing, (111)<10-1>, (-111)<-10-1>. The difference between the Schmid factors of the two slip systems is ± 0.0045, as shown in Figure 174. The deformation in this orientation, gives rise to one clear shear band and one small slip trace that appears above the main shear band, as shown in figure 178. The deformation is stable and localised. The average Schmid factor for the <011> orientation is 0.2381 ± 0.1326. The average between the two main slip systems are 0.4901 ± 0.0032.

The <111> pillar can be considered to have four competing slip systems, (-1-11)<011>(-1-11)<-101>(-1-11)<1-10>(111)<10-1>, in which one is dominant, figure 179. The deformation is localised to three of the four slip traces, which begin to emerge at yield, figure 179. The three slip traces, that can be observed on the deformed micropillar, correspond to the (-1-11) family of planes. The difference between the lowest and highest of the four competing slip systems is ± 0.0965. The average Schmid factor for the <111> orientation is 0.2101 ± 0.1249. The average Schmid factor of the four competing slip systems are 0.3619 ± 0.0472.

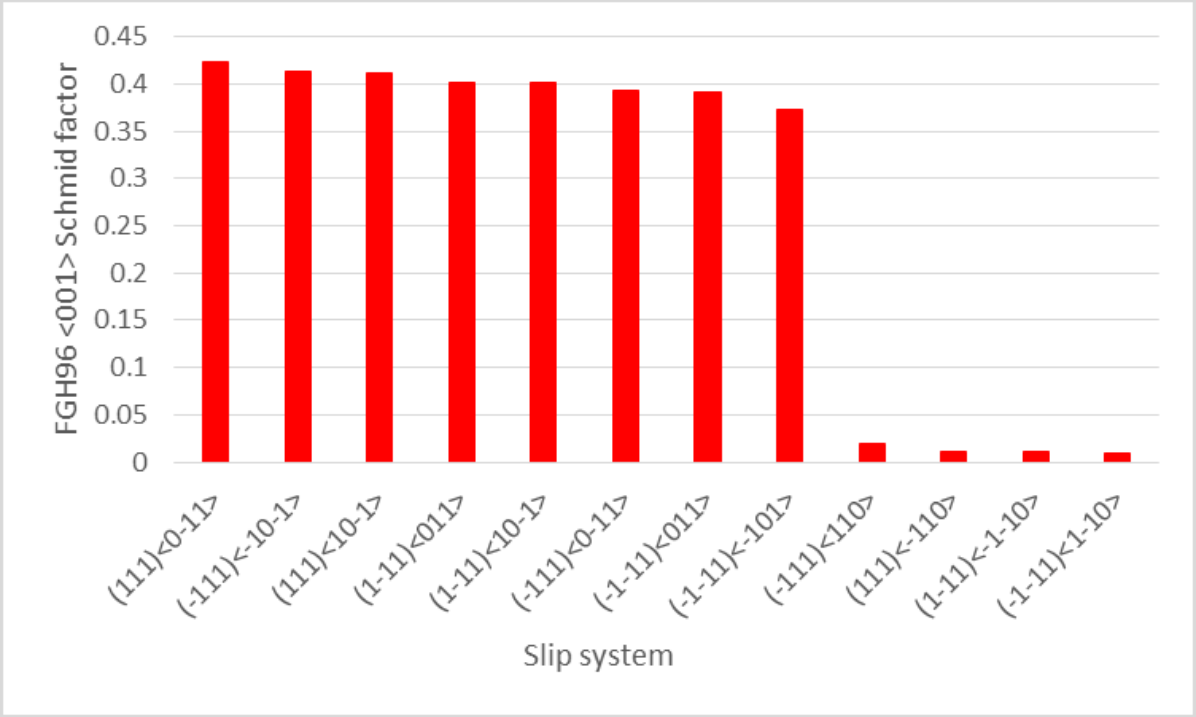


Figure 173: <001> Slip systems vs Schmid factor. There are several slip systems ~8 out of the 12 – 70% that share a similar Schmid factor ± 0.0507. Indicating that these slip systems are competing for dominance as the primary slip system.

Figure 173, shows the slip systems and resultant Schmid factors for the <001> orientated pillar in the FGH-96 alloy. Figure 173, shows that 8 slip systems ((111)<0-11>(111)<10-1>(-1-11)<011>(-1-11)<-101>(-111)<0-11>(-111)<-10-1>(1-11)<011>(1-11)<10-1>) with Schmid factors between 0.35 and 0.42 are competing with one another. 8 slip systems, in the same orientation, that have Schmid factors within 20% of the highest Schmid factor in the system are causing barriers to deformation in the form of dislocation forests and pinning points as the glide plane rotates towards the compression axis and the resolved shear stress on the plane changes. The competing slip gives rise to the crumple like deformation observed in results chapter 1 and again in figure 177.

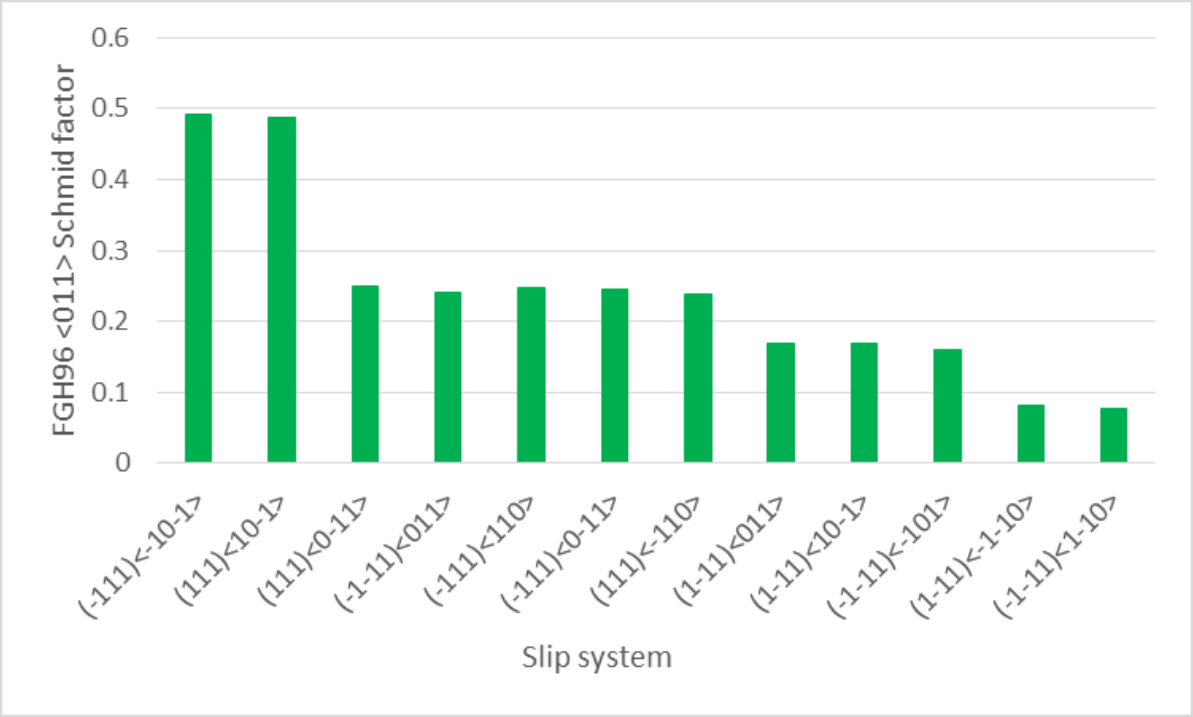


Figure 174: <011> Slip systems vs Schmid factor. The average Schmid factor is 0.23807 ± 0.13264. There are 2 dominant slip systems, (111)<10-1> (-111)<-10-1>. The minimal competition of slip systems gives a clear ~45° shear deformation as shown in Figure 178.

Dominant slip systems can be defined as slip systems that are within 20% of the highest Schmid factor of the given orientation. The two dominant slip systems in the <011> orientation are the $(111) < 10\bar{1} >$ and $(\bar{1}11) < \bar{1}0\bar{1} >$, this is shown in figure 174. The average of these two dominant slip systems is 0.49014 ± 0.00316. The difference between the average of the two dominant slip systems and the total average of the 12 slip systems is ± 0.25207, which is a 49% difference. Hence these two slip systems can clearly be called dominant, due to the low level of competition with the other 10 slip systems. This dynamic is what gives rise to the clear slip trace that can be observed in figure 178. A second fainter slip trace can be observed above the primary trace in the deformed <011> pillar, figure 178 and figure 182.

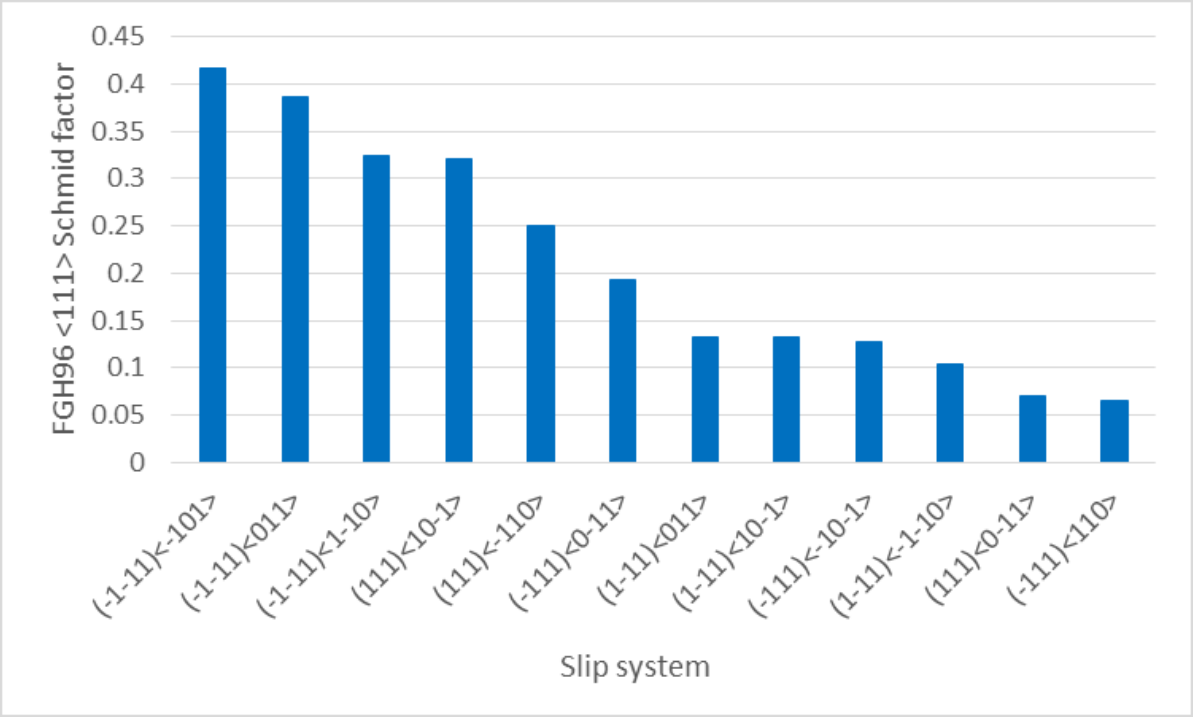


Figure 175: <111> Slip systems vs Schmid factor, the average Schmid factor is 0.40128 ± 0.02212 there are 3 dominant slip systems; (-1-11)<011>(-1-11)<-101>(-1-11)<1-10>. These slip systems correspond to the three clear slip traces that can be observed on the deformed pillar, Figure 179.

There are two dominant slip systems in the <111> system, $(\bar{1}\bar{1}1) < 011 >$ and $(\bar{1}\bar{1}1) < 1\bar{1}0 >$. The average Schmid factor of these two systems is 0.40128 ± 0.02212. The average of the 12 slip systems is 0.21007 ± 0.12488. The $(111) < 10\bar{1} >$ has a Schmid factor well above the average, however it is more than 20% less than the highest Schmid factor, so in this study, this slip system is not regarded as a dominant slip system. The traces of the two dominant slip systems, in the <011> orientates pillar can be seen in figure 179 and figure 183.

6.4.2. Deformation modes and mechanical properties in FGH-96

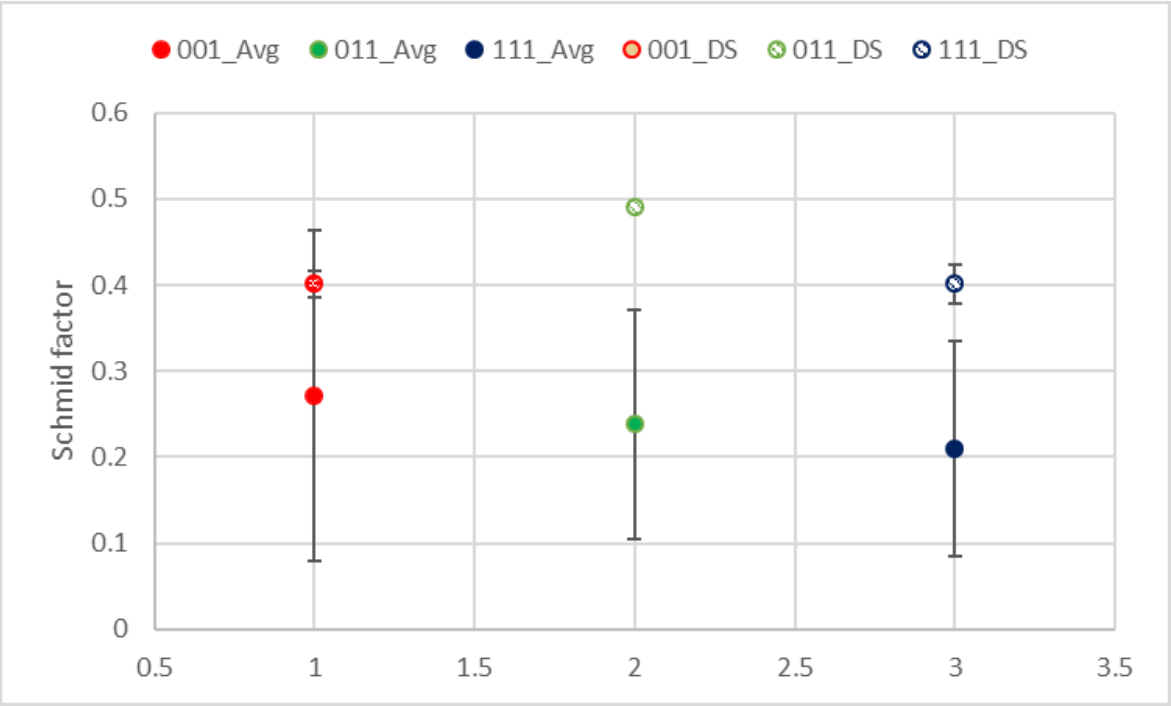


Figure 176: Schmid factor vs orientation where the x axis values correspond to; 1 - <001> 2- <011> 3- <111>. Avg – average, DS – dominant Schmid factor.

ΔS can be defined as the difference between the Schmid factor with the highest value and the average of all the Schmid factors in the orientation. In the case of Figure 176, ΔS is the difference between the average of the dominant slip systems in the given orientation and the average of all the slip systems in the given orientation. Figure 176 shows that the <011> orientation has the largest ΔS, 0.25 followed by the <111> orientation, 0.19 and the <001> orientation has the lowest value, 0.13. The larger the ΔS value, the more stable the deformation of the micropillar and the more defined the slip was found to be. This is reflected in the deformation behaviour shown in figure 177 and figure 181 for the <001> orientation, figure 178 and figure 182 for the <011> orientation and figure 179 and figure 183 for the <111> orientation.

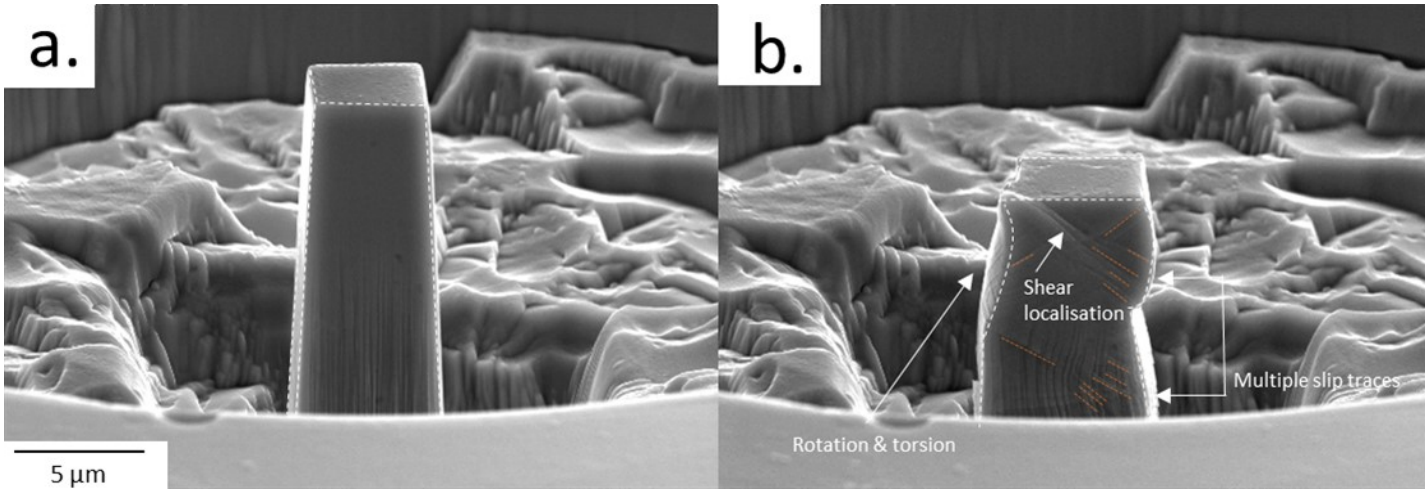


Figure 177: <001> FGH96 pillar deformed to 20% pre and post deformation (a) Undeformed pillar, W_t - 4.7 H_0 - 12.7 (b) Deformed pillar – 20% strain, showing local shear localisation, multiple slip traces and rotation / twisting of the pillar.

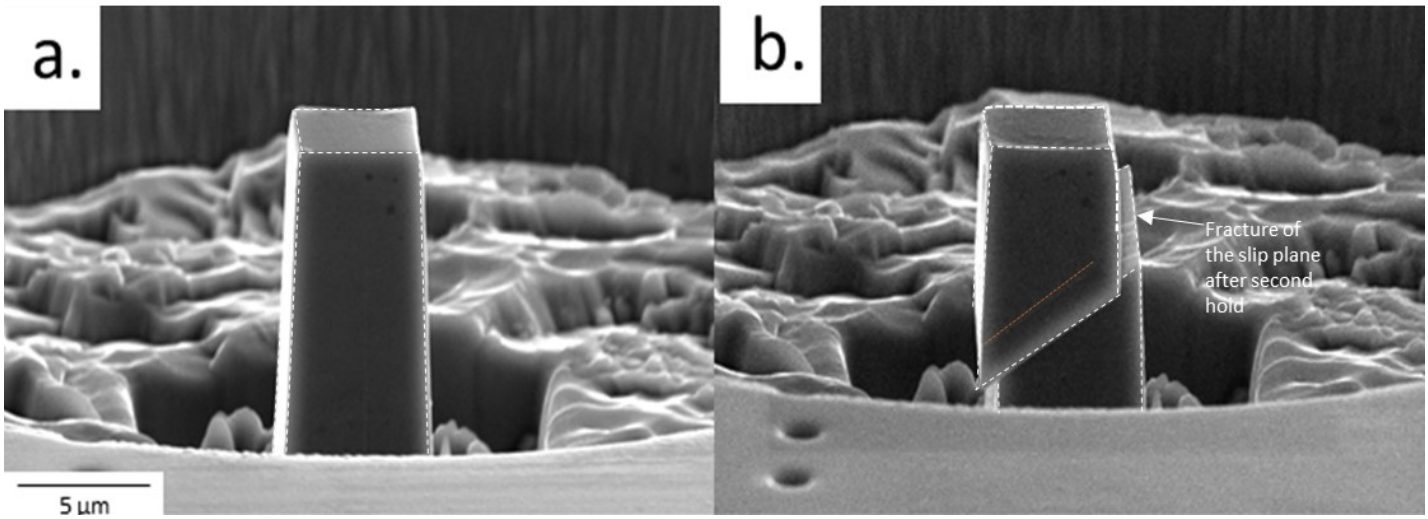


Figure 178: <011> pillar deformed to 15% strain with 2 withdrawal positions at 3% and 6% strain as shown in figure (a) Undeformed pillar W_t - 4.6 H_0 - 12.3 (b) Deformed pillar – 15% strain showing strong ~45 shear localisation and fracture of the shear plane as the pillar is compressed past 9% strain as shown in Figure 182.

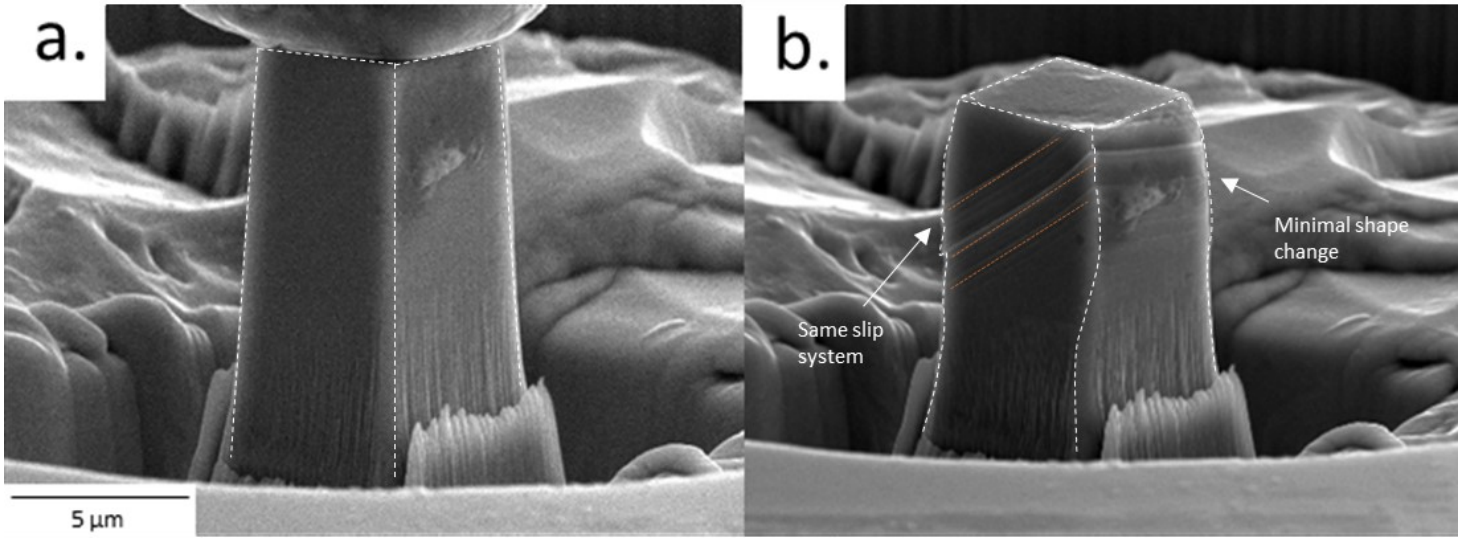


Figure 179: <111> pillar deformed to 16% strain, pre and post deformation (a) Undeformed pillar W_t - 4.6 H_0 - 12.6 (b) Deformed pillar - 16% showing minimal shape change and three clear localised shear bands, with one dominant band in the middle of the other two bands highlighted in orange, the emergence of the three slip bands can be seen clearer in Figure 183.

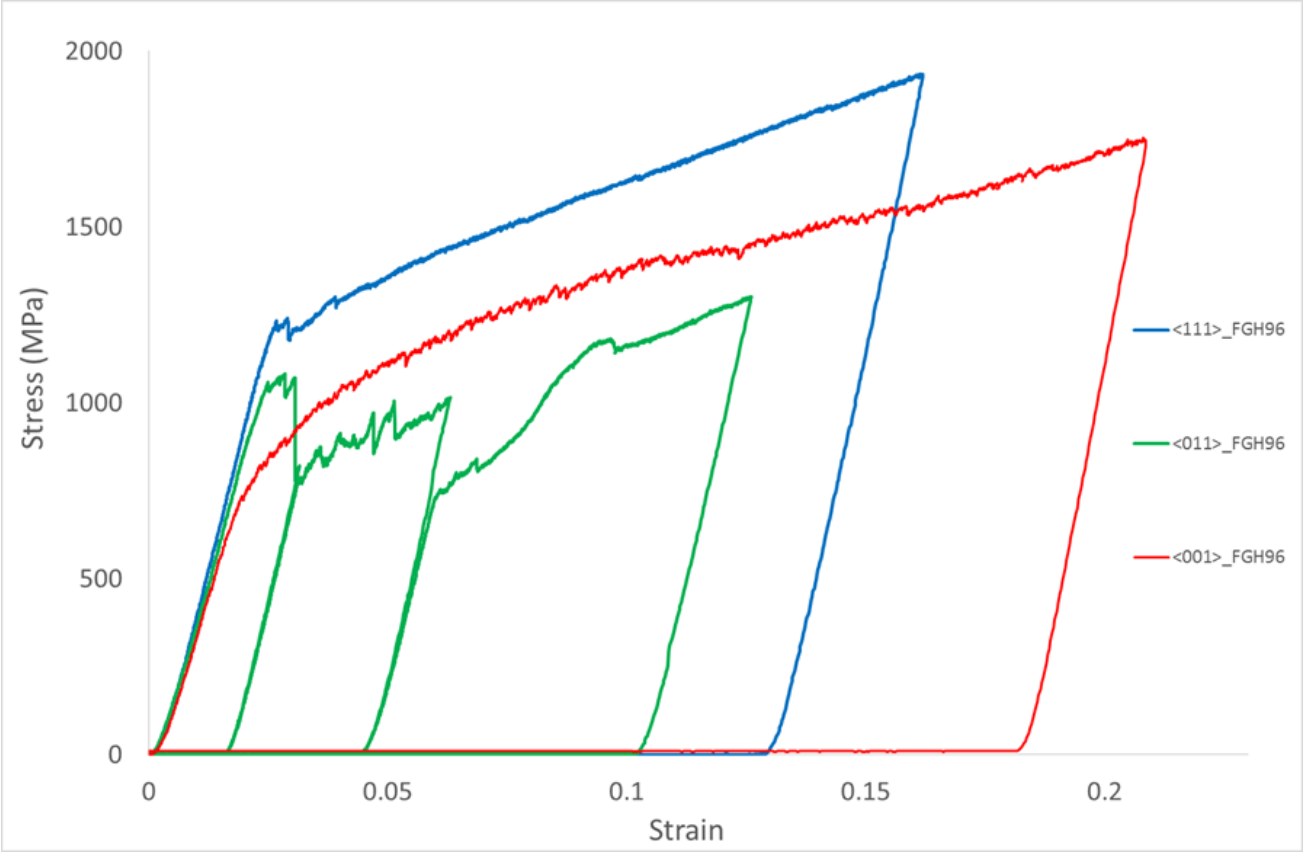


Figure 180: Resultant stress strain graph of pillars fabricated on <001>, <011> <111> grains. The <111> is the hardest with a yield point of 1200 MPa, followed by the <011>, with a yield point of 1050 MPa and the <001> with the lowest yield point 750 MPa. The modulus' varied accordingly. The variation and values of yield points are consistent with literature and theoretical calculations. The value of moduli of the three orientations' however varied when compared to theory.

Figure 180 shows the stress strain graphs for the micropillars tested in the <001>,<011> and <111> orientations in the FGH96 polycrystalline alloy. The <001> orientation is the weakest, with the lowest

yield point, hardening rate, and elastic modulus, 750 MPa, 3154 MPa and 60 GPa, respectively. The <011> orientation is in between the <001> and <111> in regards to the yield point and the hardening rate, however has the lowest average elastic modulus, 1050 MPa, 4263 MPa and 62 GPa. The elastic modulus in the <011> slip trace was taken from the 3 unloading segments at ~ 3%, 6% and 13% strain respectively and varied by ± 4718.18401. The <111> is the strongest orientation, with the highest yield point, hardening rate and modulus. The values for the <111> orientation are, 1200 MPa, 4959 MPa and 66 GPa respectively.

6.4.2.1. <001>

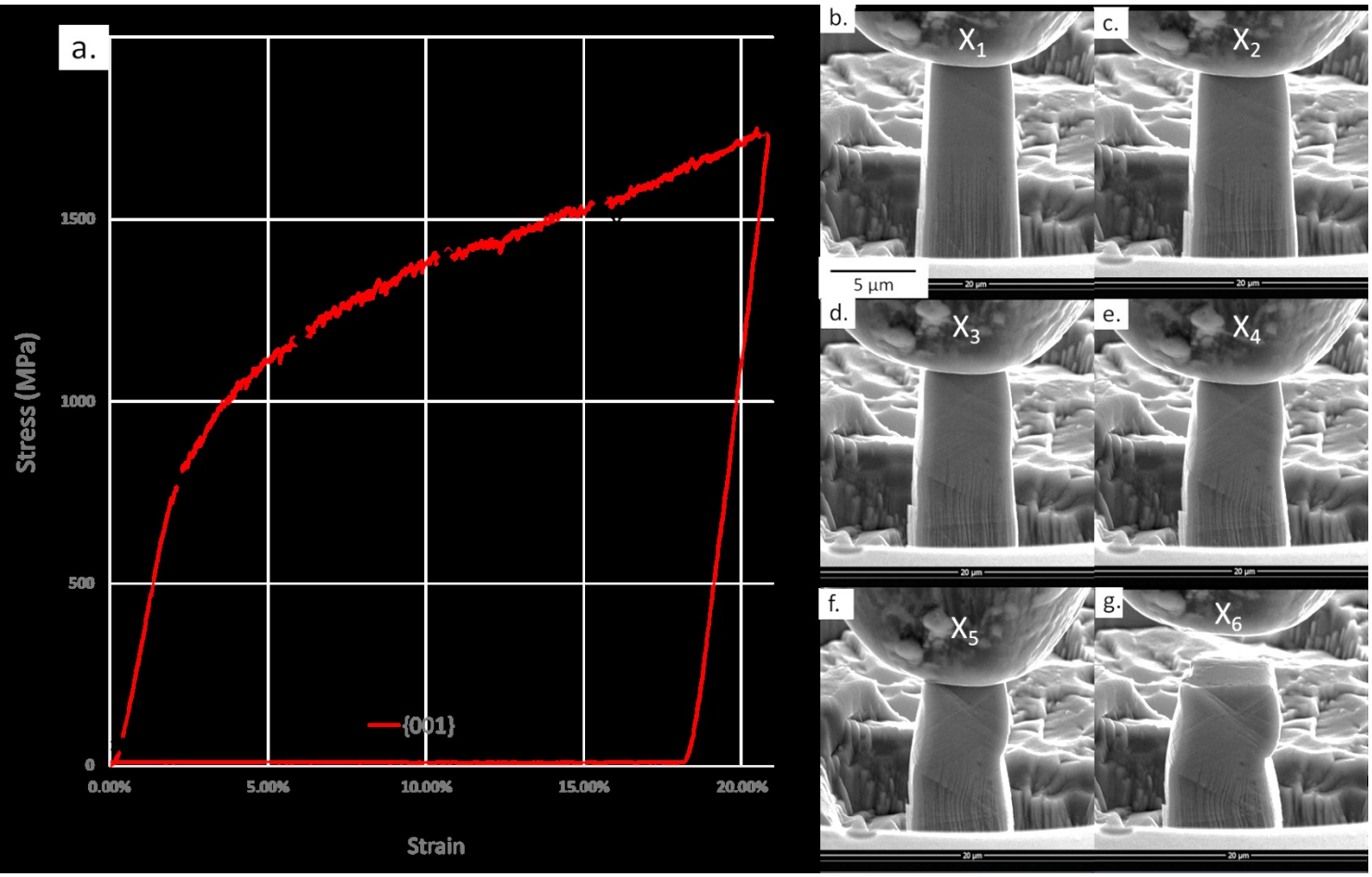


Figure 181: <001> orientated pillar, stress strain curve and compression images from in-situ testing (a) Stress strain trace with points X1-X5 corresponding to b-g respectively. (b) X_1 - beginning of the test ~0% strain (c) X_2 - Point near yield ~2.5% strain, showing a small level of deformation and a shear band localising at ~60% down the vertical length of H_0 (d-f) X_{3-5} slow rotation of the pillar as other slip systems engage with each other and the shape of the pillar changes, small strain bursts can be observed in the stress strain curve (g) End of test, multiple slip traces, shear localisation and shape change can be clearly observed, Figure 177.

Figure 181, shows the stress strain trace from the compression of the <001> pillar with still images taken from the SEM during the *in-situ* testing. Figure 182 and figure 183 illustrate this for the <011> and <111> orientated pillars respectively. Figure 181 a, shows a series of small strain bursts, which begin to emanate from ~2.5% strain, the yield point. The yield point in this orientation has a non-distinct

transition from elastic to plastic deformation. This effect could be attributed to the competition of several slip systems, Figure 173. The pillar bends and rotates, with one local slip band emerging at the top left hand corner of the pillar, figure 173 f. The slip band does not penetrate across the pillar even though the level of deformation is extremely high. Several smaller slip traces can be seen running parallel and at different orientations, figure 177 b. The strain bursts in the hardening regime of the stress strain trace, are high in frequency, with low amplitude. A large strain burst occurs at ~6% strain, this results in the formation of several small slip traces as shown in figure 179 c. As the strain increases the pillar changes shape and the traces adjust accordingly. The strain bursts increase in frequency after the emergence of the first large strain burst at ~6% strain. At ~12% strain, between points X4 and X5 in figure 181 another large strain burst occurs, this is followed by the emergence of a large shear band. This large shear band can clearly be seen in figure 179 g, at the top left hand corner of the pillar and is highlighted in figure 177 b.

6.4.2.2. <011>

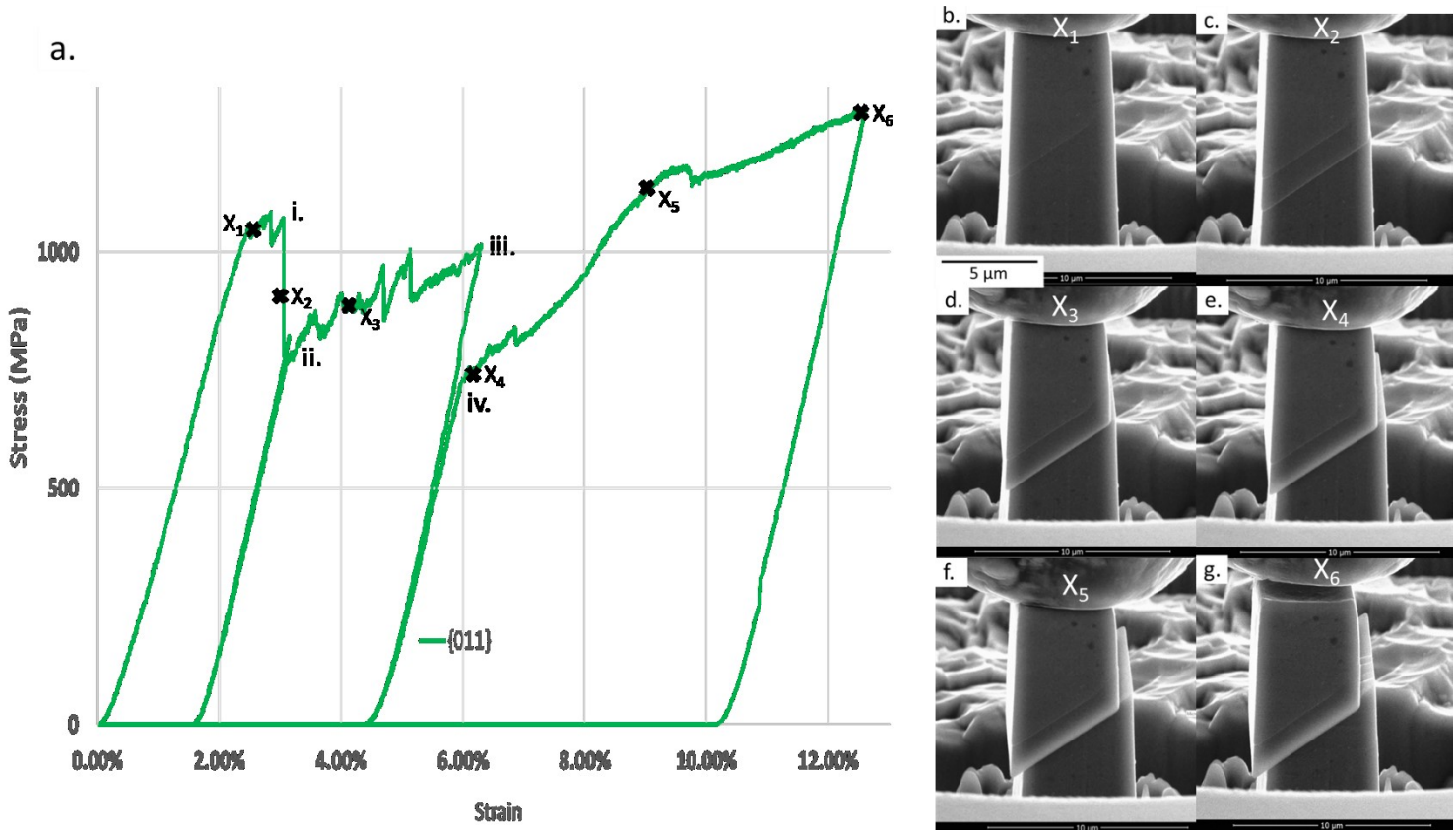


Figure 182: <011> orientated pillar, stress strain curve and compression images from in-situ testing (a) Stress strain trace with points X_1-X_5 corresponding to b-g respectively. (b) X_1 – Onset of the first yield point, before the flat punch is removed slightly, held for 1 second, returned to the top of the pillar and the test commences (the dips in the stress strain curve i-ii and iii-iv represent points where the flat punch was removed) (c) X_2 - Point near yield ~2.3% strain, small level of deformation and a shear band localising at ~60% down the H_0 of the pillar (d) X_3 - 6% strain within the second hardening regime between points ii and iii (e-f) $X_{4\text{-}5}$ shear of the shear surfaces, as the top and bottom surfaces rub against each other (e) X_6 - End of test, the fracture of the sheared surface, on the right hand side of the pillar can be seen, with minimal shape change and one significant shear band and accompanying slip trace.

Figure 182 shows the stress strain trace for the deformation of the <011> orientated pillar. For this test the flat punch was removed slightly, held for 1 second, returned to the top of the pillar and the test commences. The dips in the stress strain curve i-ii and iii-iv represent points where the flat punch was removed. The points i-ii and iii-iv represent the two hold points in which the flat punch was removed from the top surface of the pillar and then subsequently placed back into the start position and the test commenced X_4-X_5. The bursts observed between points ii-iii most likely represent frictional forces as the two shear faces of the slipped pillar glide against each other, at the subtended angle of ~45°. The fracture of the observable surface can be seen in figure 182 b and figure 182 g. The fractures emanated under the compressive load of the top shear surface. As the strain was increased, these fractures propagated to the observable face in the left hand corner. This can be seen in greater detail in figure 178 b. Despite the high level of deformation, the <011> orientation did not have an extensive shape change and deformed in a very stable fashion, with the strange hardening phenomenon linked to the shear of the two shear surfaces.

The slip system corresponding to the large shear band that penetrates through both sides of the pillar is the (-111)<-101>, this is the dominant slip system, the smaller slip trace that can be seen above this trace corresponds to the (111)<10-1>, they share similar Schmid factors, 0.4924 and 0.4879 respectively. However the slip system with the higher Schmid factor operates first and carries the extent of the deformation.

A consequence of the testing criteria resulted in the hardening response being affected. Between points X_5 and X_6, Figure 182 f-g, there is a strain burst at 9.8% strain which corresponds to a fracture of the shear plane surface. The <011> orientated pillar still retains its integral shape unlike the <001> pillar, Figure 181. The stable deformation, supports the texture of the FGH96 alloy as most of the grains are orientated in <011> with respect to loading direction, figure 171.

6.4.2.3. <111>

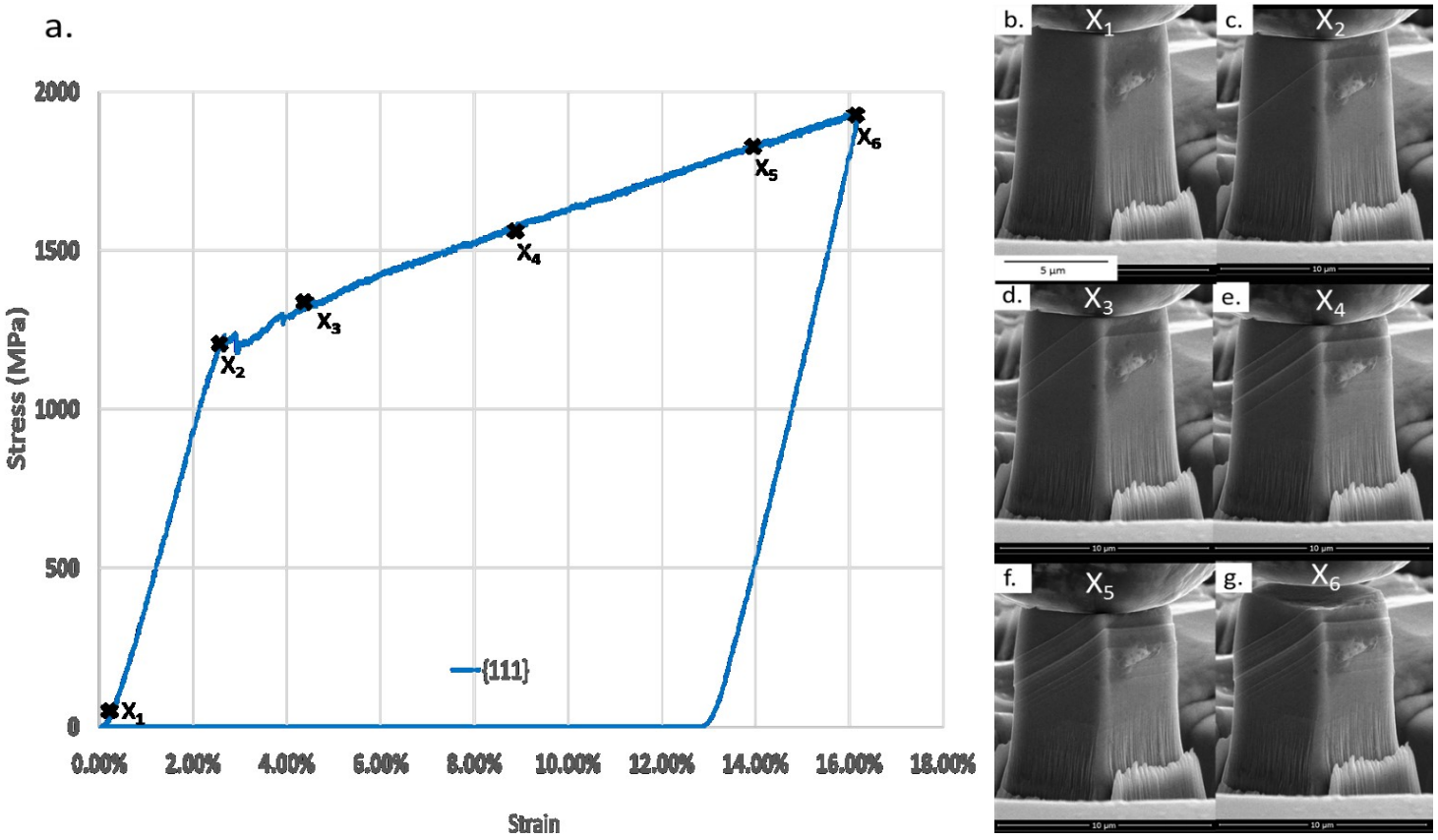


Figure 183: <111> orientated pillar, stress strain curve and compression images from in-situ testing (a) Stress strain trace with points X_1-X_5 corresponding to b-g respectively. (b) X_1 – beginning of the test ~0% strain (c) X_2 - Point near yield ~2.7% strain, one localised diagonal shear band localising towards the top of the pillar (d) X_3 second diagonal local shear band forming above the first shear band (e) smaller less local slip traces forming underneath the local shear bands, all slip traces have similar angles of deformation along the near front face of the pillar (g) End of test, multiple slip traces, with two local shear bands, minimal level of shape change visible.

Figure 183 shows the stress strain trace from the compression testing of the <111> orientated pillar, deformed to ~18% strain. The yield point and subsequent transition from elastic to plastic deformation is clear and occurs at ~2.7% strain. This is followed by the emergence of 2-3 strain bursts from 3-4% strain, which result in the emergence of three clear slip bands. The first slip trace that forms at yield can be seen in Figure 183 c, this slip band is the most prevalent of the three. The emergence of the other two slip traces can be seen in Figure 183 c-d, with the slip trace that forms in figure 183 c being more prominent than the lighter trace that can be seen in Figure 183 d. The emergence of three clear slip traces favours the Schmid factor analysis, Figure 175. The slip systems corresponding to the three slip traces occurring first to last are (-1-11)<011> , (-1-11)<1-10> and (111)<10-1>, respectively and are characterised by descending from the largest to the smallest Schmid factor respectively, 0.41692,0.38564,0.325.

The <111> pillar for the most part, retains its shape, there is no rotation and a small level of bulging occurs from 15% deformation. 15% deformation is quite large and so is to be expected. The <111> pillar

has the highest yield point and shows minimal strain bursts again referencing the relatively smooth deformation. In regards to slip bands, three dominant slip bands can be observed. The first occurs at yield, at point X_2, the second at point X_3 and third at point X_4, figure 183. Smaller slip traces can be observed underneath the two dominant bands corresponding to the similar Schmid factors, figure 175. The $(\bar{1}\bar{1}1) < 1\bar{1}0 >$ and $(111) < 10\bar{1} >$ slip systems share similar Schmid factors, 0.3248 and 0.3204 and so can be said to be competing. However the $(\bar{1}\bar{1}1) < 1\bar{1}0 >$ slip systems occurs first and can be seen in Figure 183 e. The first slip band that forms at point x2 figure 183 d, shears the pillar the most. There appears to be minimal rotation of the pillar.

Table 17: Mechanical properties of the FGH96 alloy in the <001>,<011>,<111> orientations. U_l – unloading modulus, Y_p – Yield point, H_r – Hardening rate, τ_{crss} – Critical resolved shear stress.

Orientation	U_l GPa	H_r MPa	Y_p MPa	τ_{crss} MPa
001_FGH96	57	3154	750	317
011_FGH96	62	4264	1050	517
111_FGH96	66	4959	1200	500

7.6. Single crystal CMSX-4

In this section the deformation mechanisms and mechanical properties of three orientations <001>, <011> and <111> are analysed from single crystal samples cut via a goniometer. The samples were deformed using the same methodology as the pillars in the FGH-96 alloy. The analysis for the single crystal, goniometer cut pillars involved a more in depth examination of the resultant slip traces, using slip trace analysis. In slip trace analysis, the Schmid factors for the 12 slip systems are deduced, as above. However, in slip trace analysis, the rotation of the pillar face, 90° from north, west, south, east, with respect to the slip trace, post deformation is examined. A theoretical value of the slip trace is deduced from the cross product of the normal of the {111} plane from the top surface of the pillar $\hat{p}$ with the normal of the {111} plane of the slip trace $\hat{n}$, to give the slip trace $\hat{r}$. $\hat{r}$ is compared to the experimental value of the slip trace deduced using the Tan method.

Sections were cut with a goniometer from a bulk CMSX-4 bar orientated in the <001> to reveal the <011> and <111> orientations with respect to the loading axis, the top surface of each face and the respective ϒ/ϒ’ microstructure can be seen in figure 184.

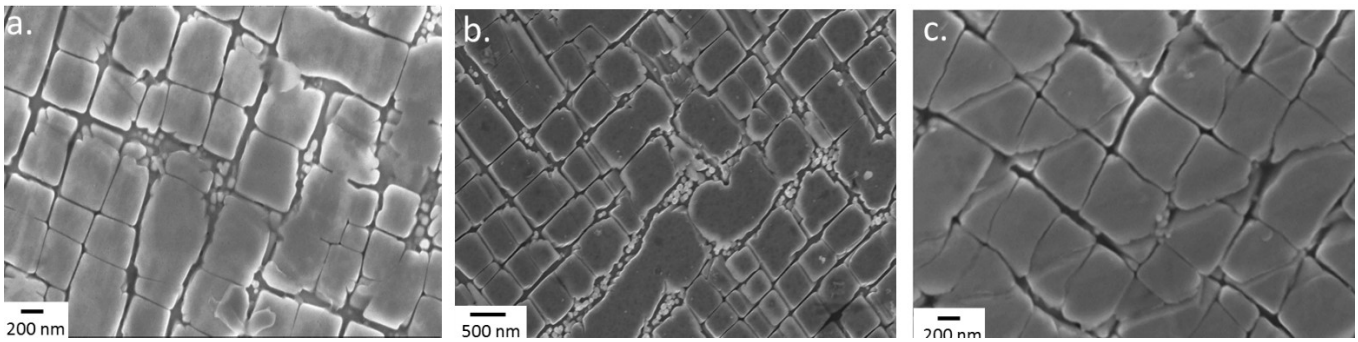


Figure 184: SEM images of the three orientations cut from the original <001> ingot (a) <001> original as received microstructure (b) <011> cut from 45° from the sample edge of the as received sample (c) <111> cut from 35.7° from the sample edge of <011>.

Table 18 shows the 12 fcc slip systems with their respective Schmid factors for the goniometer cut CMSX-4 micropillars as seen in Figure 190, figure 191 and figure 192.

7.6.1. Deformation in the CMSX-4 <001> <011> <111>

As shown in Table 18, the <011> orientation has the largest Schmid factor (0.4925) followed by the <001> (0.47386) and finally <111> with the lowest (0.41641). The accompanying slip systems are; $(\bar{1}11) < \bar{1}01>$, $(111) < \bar{1}10 >$ and $(\bar{1}11) < \bar{1}0\bar{1} >$ respectively. The <001> orientated pillar, with 45° in plane rotation and the <011> pillar share the same slip system.

Table 18: The 12 fcc slip systems and corresponding Schmid factors of the <001> <011> <111> orientated grains, in the CMSX-4 alloy. Where the x and y scans were taken from the representative side faces of the top surface of the micropillar, Figure 97

		Orientation of micropillar		
	Slip system	001	011	111
1	(111)<0-11>	0.379	0.247	0.046
2	(111)<10-1>	0.471	0.486	0.370
3	(111)<-110>	0.092	0.240	**0.416**
4	(-1-11)<011>	0.367	0.235	0.132
5	(-1-11)<-101>	0.299	0.153	0.097
6	(-1-11)<1-10>	0.058	0.076	0.109
7	(-111)<0-11>	0.369	0.241	0.082
8	(-111)<-10-1>	**0.474**	**0.493**	0.156
9	(-111)<110>	0.105	0.252	0.238
10	(1-11)<011>	0.382	0.253	0.261
11	(1-11)<10-1>	0.311	0.165	0.192
12	(1-11)<-1-10>	0.071	0.088	0.069

7.6.1.1. Slip systems CMSX-4

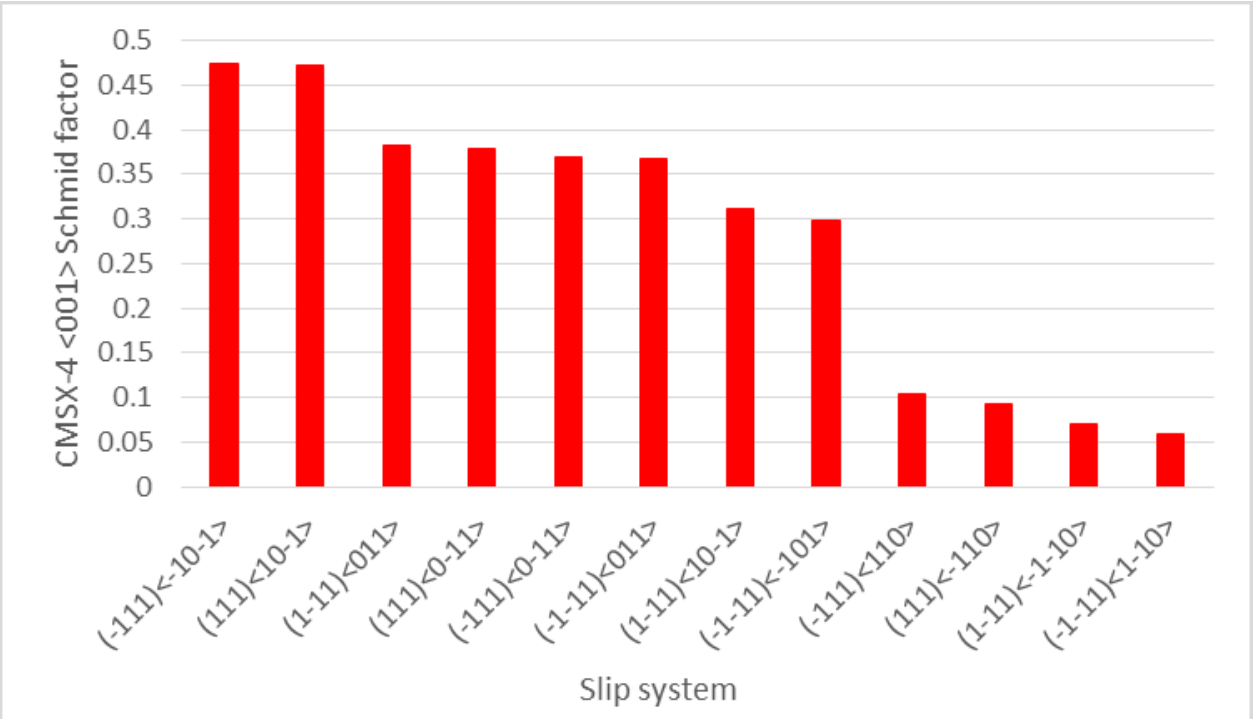


Figure 185: <001> Slip systems vs Schmid factor. There are two dominant slip systems; (111)<0-11> and (-111)<-10-1> with an average Schmid factor of 0.47256 ± 0.00185.

Figure 185 shows the slip systems and resultant Schmid factors for the <001> orientated pillar in the CMSX-4 alloy. Figure 186 and figure 187 illustrate this for the <011> and <111> orientated pillars respectively. For the <001> system, the two dominant slip systems are $(111) < 0\bar{\bar{1}}1 >$ and $(\bar{1}11) < \bar{1}0\bar{1} >$. The Schmid factors are 0.47386 and 0.47125 respectively. The two slip traces, corresponding to the $(111) < 0\bar{\bar{1}}1 >$ and $(\bar{1}11) < \bar{1}0\bar{1} >$ can be seen in figure 188a and figure 190a.

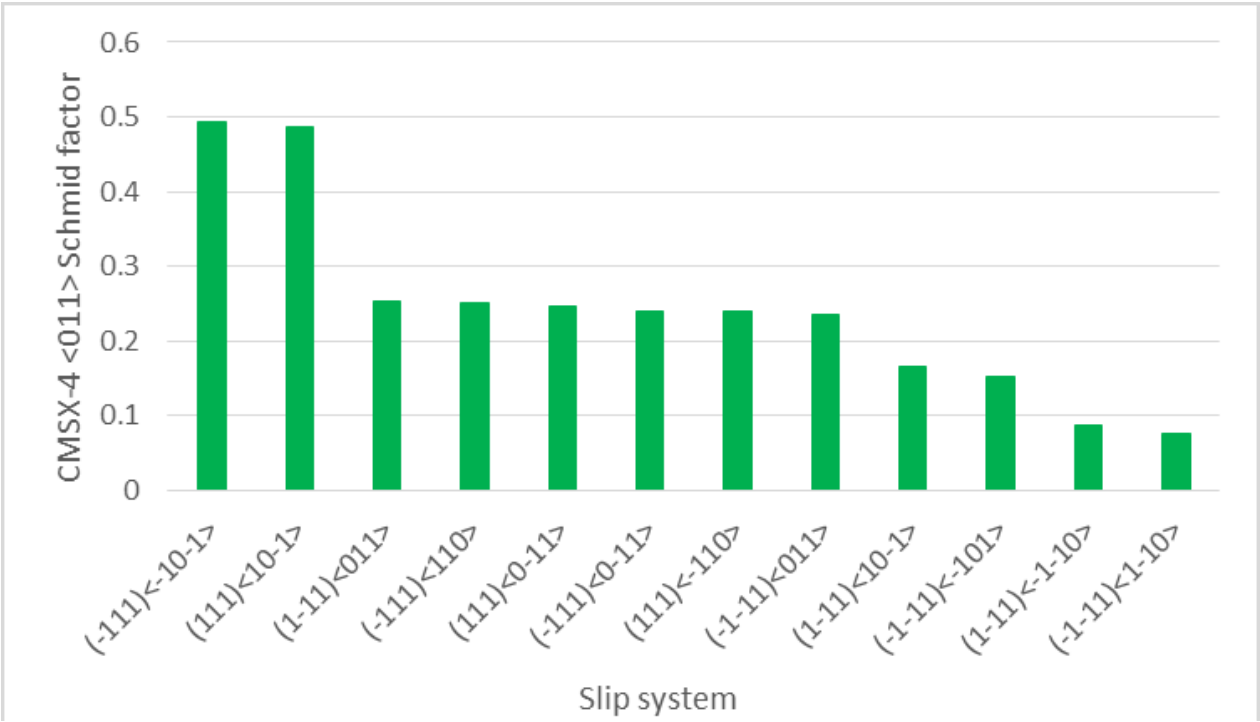


Figure 186: <011> Slip systems vs Schmid factor. The average Schmid factor is 0.24381 ± 0.13084. The slip system (-111)<-101> has the highest Schmid factor, 0.4925. There are 2 dominant slip systems, (111)<10-1> (-111)<-10-1>. The two dominant slip systems are ± 0.00427 in value and give rise to two prominent shear bands as shown in Figure 188 b.

Figure 186 shows the value of the Schmid factor vs the slip systems for the <011> orientated pillars. $(\bar{1}11) < \bar{1}01 >$, is the slip system that occurs first as it has the highest Schmid factor. The $(111) < 10\bar{1} >$ slip system has a Schmid factor similar to the $(\bar{1}11) < \bar{1}01 >$ slip system, with Schmid factors, 0.4925 and 0.48646 respectively. The combination of the two slip systems having different planes and directions as well as being close in value, has resulted in the shear of two planes in different directions, figure 188 a. The <011> pillar has maintained its shape, with minimal body rotation. The back (south) face of the pillar appears to have bulged slightly as the shear surfaces have slid across each other. The sides of the faces (east and west) have appeared to rotate slightly again accommodating the high level of strain and shear of the two opposing slip systems. This can be seen in figure 191 a i-iv.

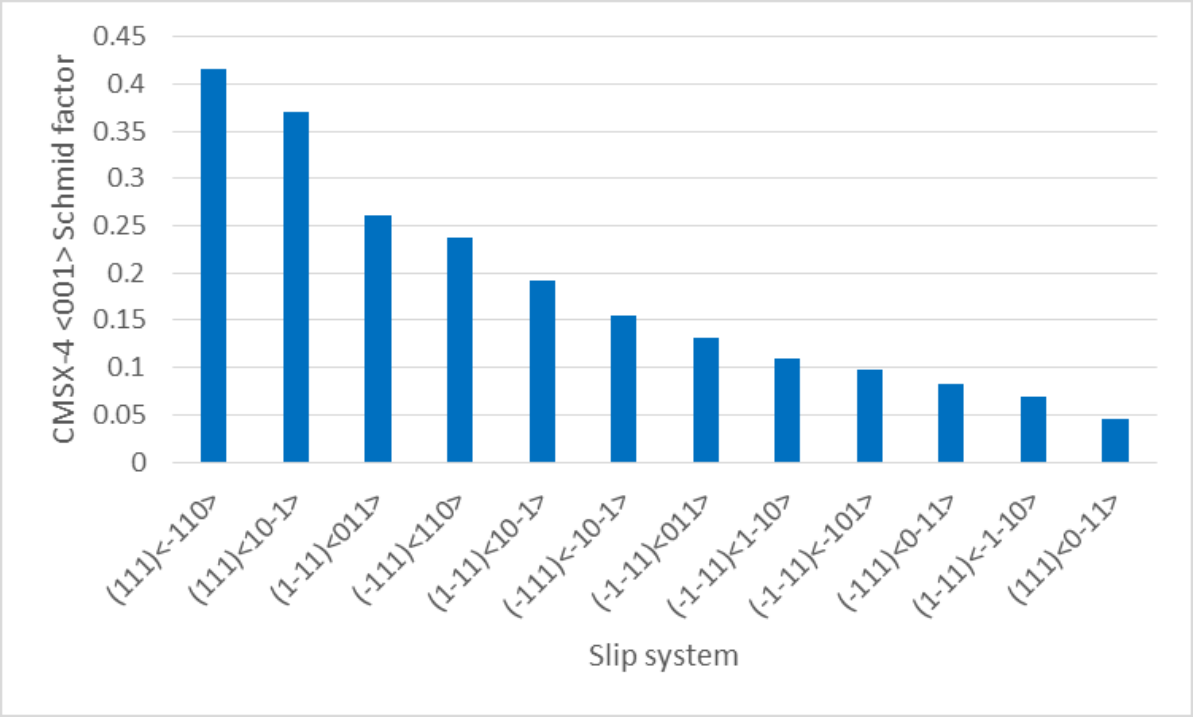


Figure 187: <111> Slip systems vs Schmid factor, (111)<10-1> is the slip system with the highest Schmid factor. The (111)<10-1> slip system has the second highest Schmid factor and can be considered a dominant slip system. The difference between the two dominant slip systems is ± 0.03268.

The average Schmid factor for the <111> orientated pillar is 0.18073 ± 0.11929 and the average Schmid factor between the two dominant Schmid factors is 0.3933 ± 0.03268. There are two dominant slip systems in this orientation; $(111) < 10\bar{1} >$ and $(111) < \bar{1}10 >$, with Schmid factors 0.4161 and 0.37019 respectively. Two slip traces can be observed on the <111> pillar, post deformation, figure 188 and figure 189. The dominant slip system, extends from the right hand side of the pillar to the left side. The slip trace appears to have propagated in a "wavy" fashion, the second slip trace can be seen lower down the face of the pillar. Examining the south, west and east faces of the <111> orientated pillar, Figure 192, shows that the trace of the dominant slip system is not necessarily wavy, the slip traces on the side and back faces of the pillar appear to be straight. The pillar has bulged slightly, indicating that the wavy slip trace is a consequence of the face shearing against each other and the pillar bulging. The wavy slip trace can be observed in both figure 188 and figure 189.

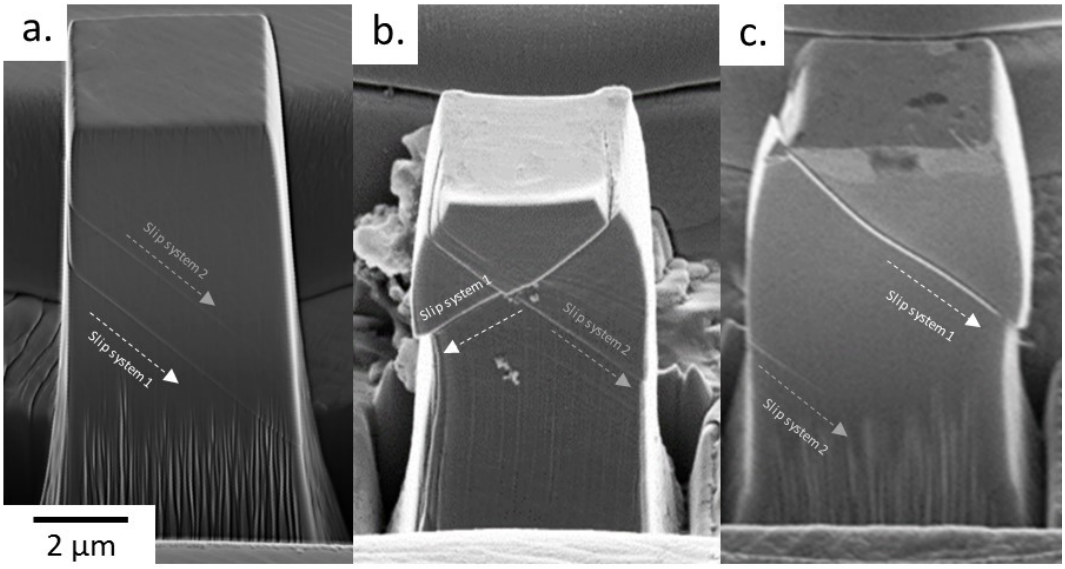


Figure 188: Deformed micropillars in the (a) <001> orientation, deformed to ~8% strain (b) <011> orientation, deformed to ~12% strain (c) <111> orientation, deformed to ~12% strain with accompanied slip traces highlighted.

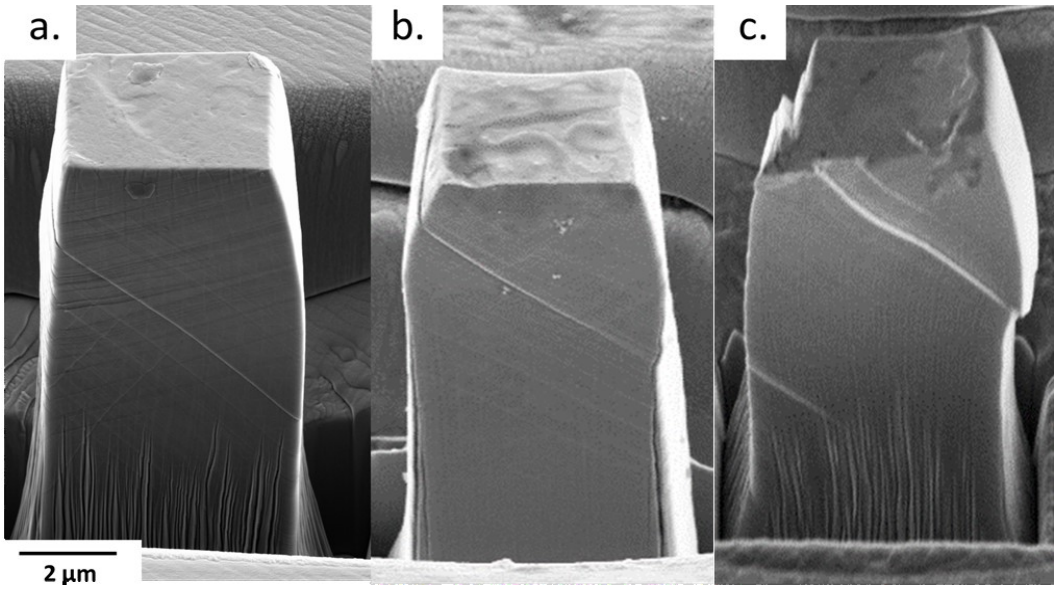


Figure 189: Deformed micropillars in the (a) <001> orientation, deformed to ~15% strain (b) <011> orientation, deformed to ~6% strain (c) <111> orientation, deformed to ~18% strain with accompanied slip traces highlighted.

Figure 30 a-c shows the <001>, <011> and <111> CMSX-4 pillars, that have been deformed to 8%, 12% and 12% respectively. The pillars in figure 188 were chosen to represent clear slip traces for slip traces analysis. Figure 31, shows the <001>, <011> and <111> pillars deformed to different strains, 15%, 6% and 18% respectively. Comparing the <001> orientated pillar in figure 188a and figure 189 a, the same $(111) < 0\bar{1}1 >$ slip trace can be seen clearly extending from the top left hand side of the pillar to the lower right. However at 18% strain, the competing slip systems can be seen being partially activated, due to the increase in deformation. The <001>, <011> and <111> orientations are analysed further in; figure 32 / figure 35, figure 33 / figure 36 and figure 34 / figure 37, respectively.

7.6.1.2. Slip traces and deformation CMSX-4

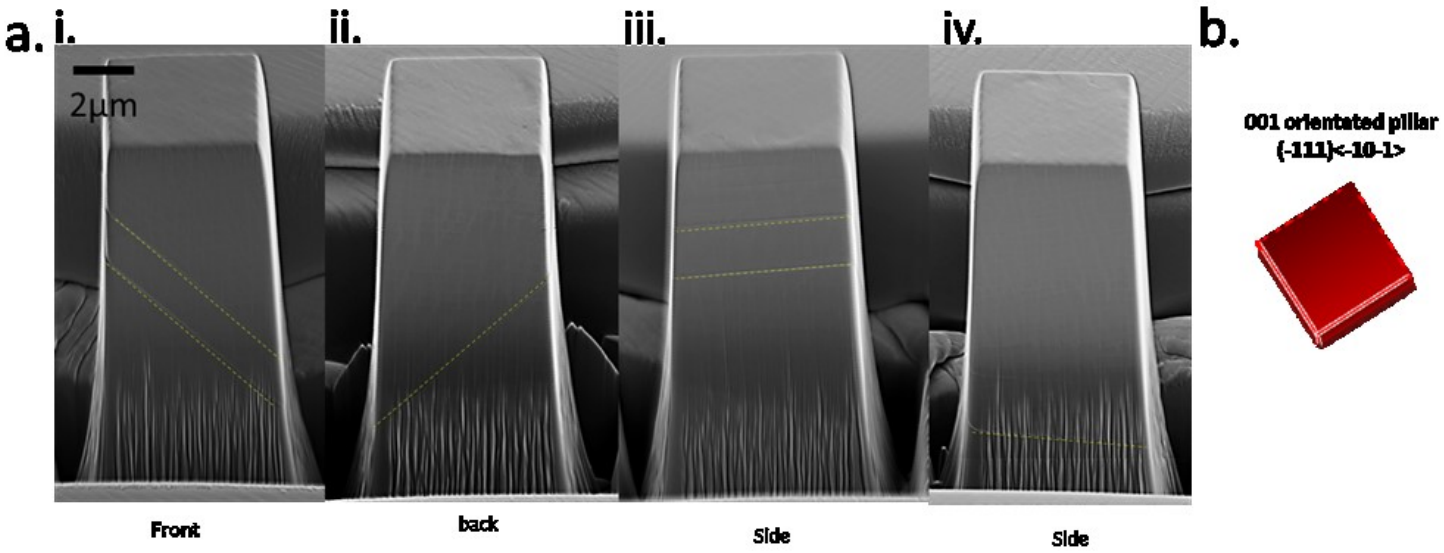


Figure 190: Slip trace analysis of <001> pillar orientated for localised shear slip (a) Four faces of the <001> micropillar compressed to 8% strain, with the crystal orientation adjusted for the viewing angle, as shown in Figure 190(d) i. front (north) ii. Back (south) iii. Side (east) iv. Side (west). (b) The crystal orientation (top down) aligned to the x,y axis of the micropillar and accompanying slip system, found from the value of the highest Schmid factor, Table 18. The slip traces have been highlighted in yellow.

Figure 190 shows the slip trace analysis for the single crystal CMSX-4 <001> orientated pillar. The dominant slip system is $(\bar{1}11) < \bar{1}0\bar{1} >$ and can be seen in figure 190 a. The secondary slip trace $(\bar{1}11) < \bar{1}0\bar{1} >$ as characterised by having the second highest Schmid factor, can be seen above the primary slip trace on the north and east faces. Only the primary slip trace can be seen on the back face of the pillar, suggesting that it has penetrated through the entire pillar creating a shear plane above and below it. The peak Schmid factor taken from the Esprit software, figure 190 c, is in agreement with the theoretical Schmid factor, table 18. The slip system with the second highest Schmid factor in the <001> orientated pillar is the same as the <011> pillar, however they appear different. This could be due to the competition of more slip systems in the <001> pillar as shown in figure 189 a. The competition of more slip systems on the micro scale can cause a deviation from Schmids law[180,15]

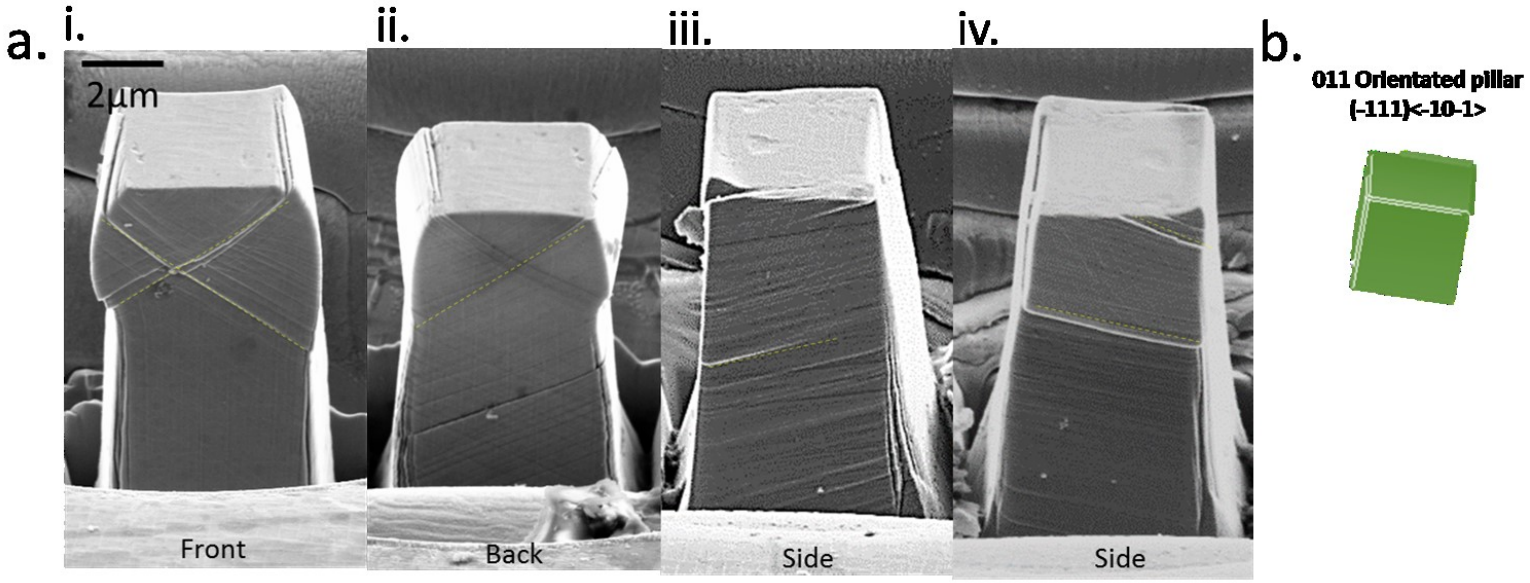


Figure 191: Slip trace analysis of <011> pillar orientated so that the in plane directions are aligned with the representative <011> directions (a) Four faces of the <011> micropillar compressed to 12% strain, with the crystal orientation adjusted for the viewing angle, as shown in Figure 191(d) i. front (north) ii. Back (south) iii. Side (east) iv. Side (west). (b) The crystal orientation (top down) aligned to the x,y axis of the micropillar and accompanying slip system, found from the value of the highest Schmid factor, Table 18. The slip traces have been highlighted in yellow.

Figure 191 shows the slip trace analysis for the single crystal CMSX-4 <011> orientated pillar. The dominant slip system is $(\bar{1}11) < \bar{1}0\bar{1} >$, this corresponds to the slip trace extending from the top left hand corner of the pillar down to the right side. Figure 191 a i, shows the south face of the pillar, the slip trace corresponding to the $(\bar{1}11) < \bar{1}0\bar{1} >$ slip system can also be seen extending from the opposite corner of the pillar. This slip trace can also be seen in a <011> pillar that has been deformed to a lower % strain, figure 189 b.

A secondary slip system has activated in the opposite direction to the primary, the secondary slip system is (111)<10-1>. The primary and secondary slip systems have different planes and directions, this can be seen in the two competing slip traces. The rotation of the pillar faces, north, west, south and east, Figure 191 a i-iv, shows a small change due to the shear faces sliding over each over and a small amount of rotation to accommodate this deformation. The peak Schmid factor taken from the Esprit software, figure 191 c, is in agreement with the calculated Schmid factor shown in table 18.

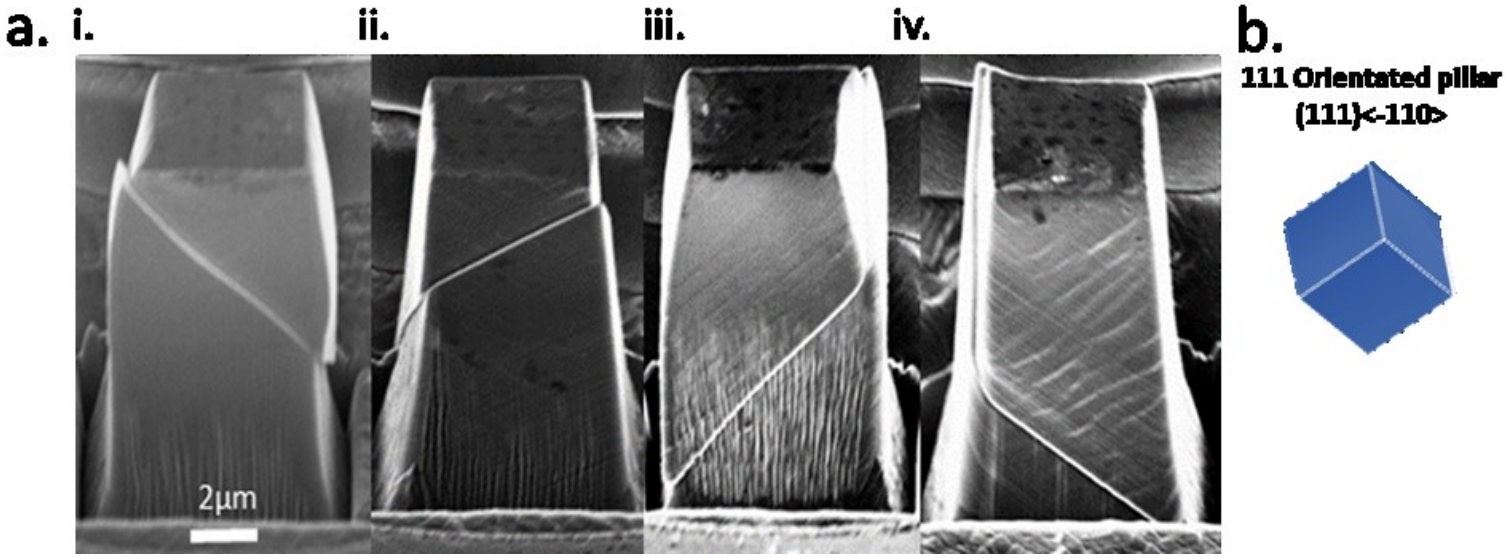


Figure 192: Slip trace analysis of <111> pillar orientated so that the in plane directions are aligned with the representative <111> directions (a) Four faces of the <111> micropillar compressed to 12% strain, with the crystal orientation adjusted for the viewing angle, as shown in figure 17(d)i-iv i. front (north) ii. Back (south) iii. Side (east) iv. Side (west). (b) The crystal orientation (top down) aligned to the x,y axis of the micropillar and accompanying slip system, found from the value of the highest Schmid factor, table 15. The slip traces have been highlighted in yellow.

Figure 192, shows the slip trace analysis for the single crystal CMSX-4 <111> orientation. The dominant slip system is the (111)<-110>. This slip system can be seen clearly in Figure 192 a, on all four faces of the pillar. The <111> orientated pillar in the CMSX-4 alloy has slightly wavy slip. The wavy slip characteristic can also be seen in figure 189 c. The pillar in figure 189 c has been deformed to 18% strain and the wavy slip trace is more prominent. The peak Schmid factor taken from the Esprit software, Figure 34 c, is in agreement with the theoretical Schmid factor, table 18.

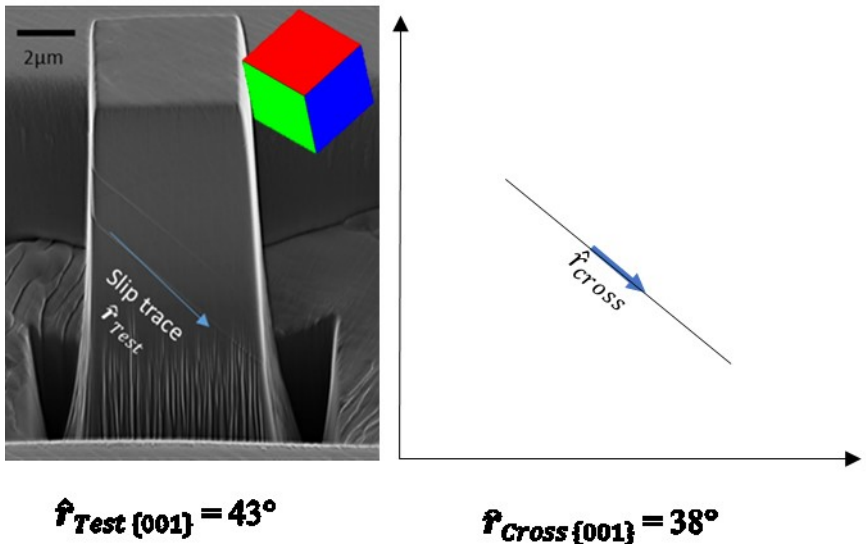


Figure 193: <001> orientated pillar, deformed to 8% strain with accompanying slip trace $\hat{r}$ test (34°) found from experiments, using the tan method and $\hat{r}$ cross (38°) found via , $\hat{n}$ x $\hat{p}$ as shown in figure 100.

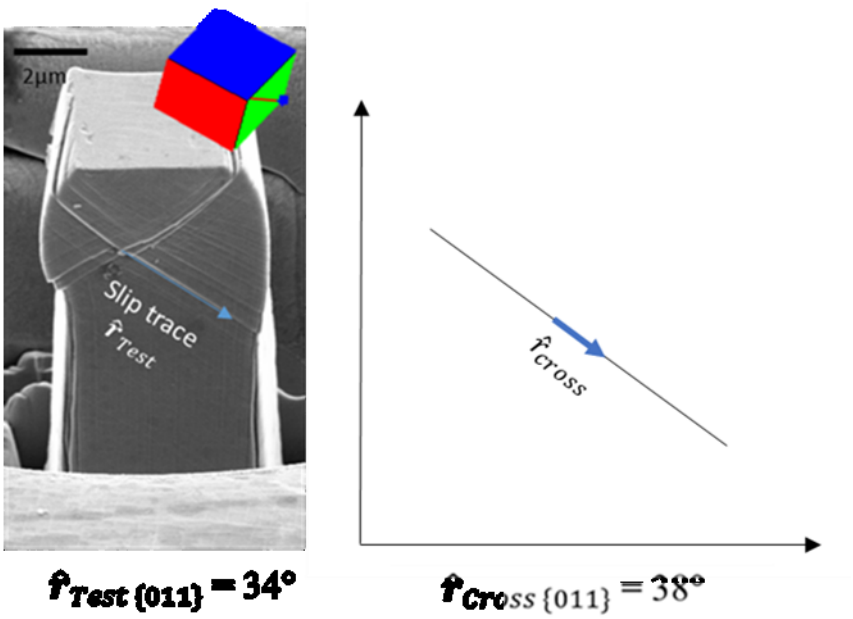


Figure 194: <011> orientated pillar, deformed to 12% strain with accompanying slip trace $\hat{r}$ test (34°) found from experiments, using the tan method and $\hat{r}$ cross (38°) found via , $\hat{n} \times \hat{p}$ as shown in figure 100.

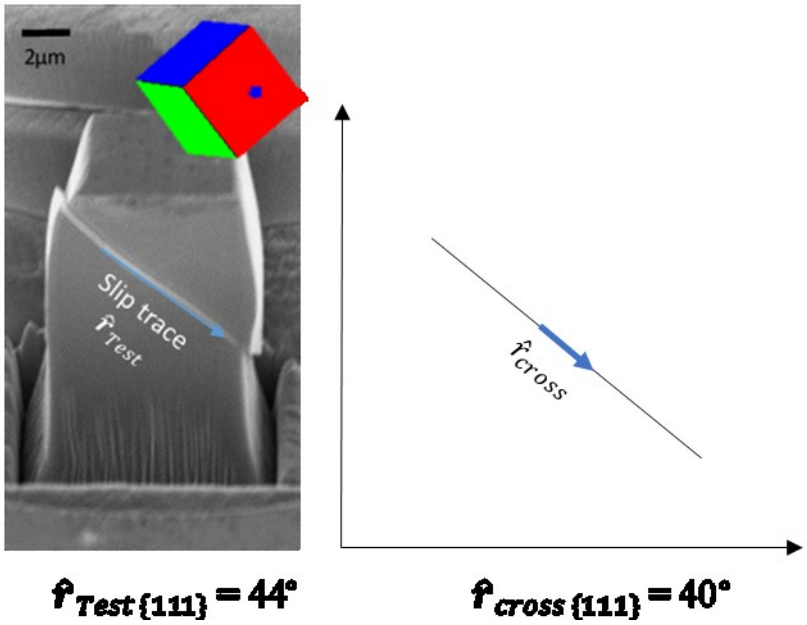


Figure 195: <111> orientated pillar, deformed to 12% strain with accompanying slip trace $\hat{r}$ test (34°) found from experiments, using the tan method and $\hat{r}$ cross (38°) found via , $\hat{n} \times \hat{p}$ as shown in figure 100.

Figure 193-39 show the comparison between the slip trace from the post deformation image, calculated via the Tan method and the slip trace determined from the cross product method. In general the angles agree, however due to the angle the pillars are subtended to during imaging and the displacement of the shear plane, a small margin of error is expected.

The <011> pillar has been slightly displaced along the slip direction through the shear plane, therefore the angle of the slip trace can be slightly off. The compounded stress strain traces for the single crystal CMSX-4 alloy in the <001>, <011> and <111> orientations can be seen below in figure 196.

7.6.1.3. Mechanical properties CMSX-4

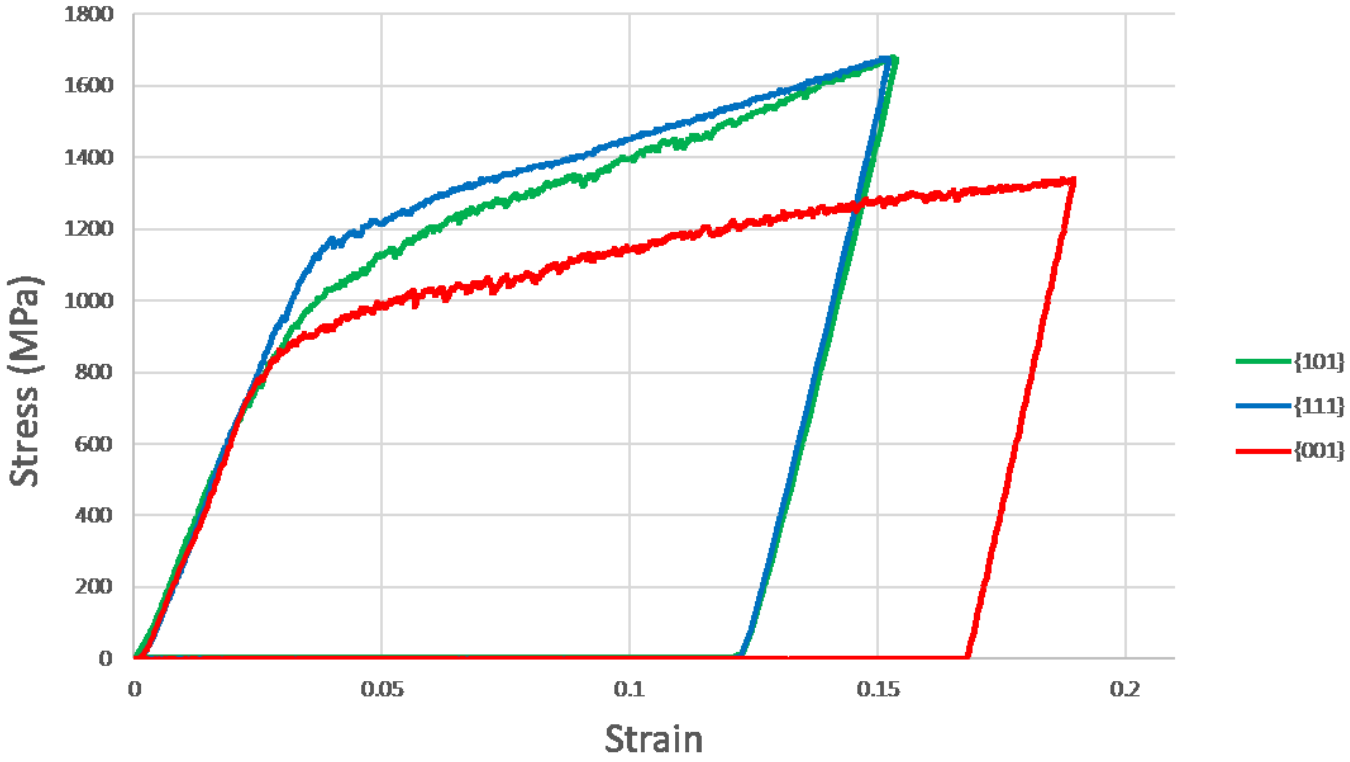


Figure 196: Compounded stress strain traces from the <001> <011> <111> goniometer cut samples. The <111> has the highest yield point, followed by <011> and <001> is the last. The <001> orientation is the least stiff, followed by the <011> the <111> is last.

The <111> orientation has the highest τ_{crss} / modulus and a median hardening rate, the values are; 464 MPa, 66 MPa and 4658 respectively. The <011> orientation has the highest hardening rate, and median modulus / τ_{crss}, the values are; 5238 MPa, 61 MPa, 453 MPa. The <001> pillar, has the lowest $\tau_{crss,}$ the lowest modulus and lowest hardening rate, the values are; 382 MPa, 60 GPa and 3048 MPa respectively. Table 19 lists the mechanical properties of the three orientations in the CMSX-4 single crystal testing.

Table 19: Mechanical properties of the CMSX-4 alloy in the <001>,<011>,<111> orientations. U_l – unloading modulus, Y_p – Yield point, H_r – Hardening rate, τ_{crss} – Critical resolved shear stress.

Orientation	U_l GPa	H_r MPa	Y_p MPa	τ_{crss} MPa
001_CMSX4	60	3048	806	382
011_CMSX4	61	5282	920	453
111_CMSX4	66	4658	1115	464

7.7. Comparison of FGH-96 and CMSX-4

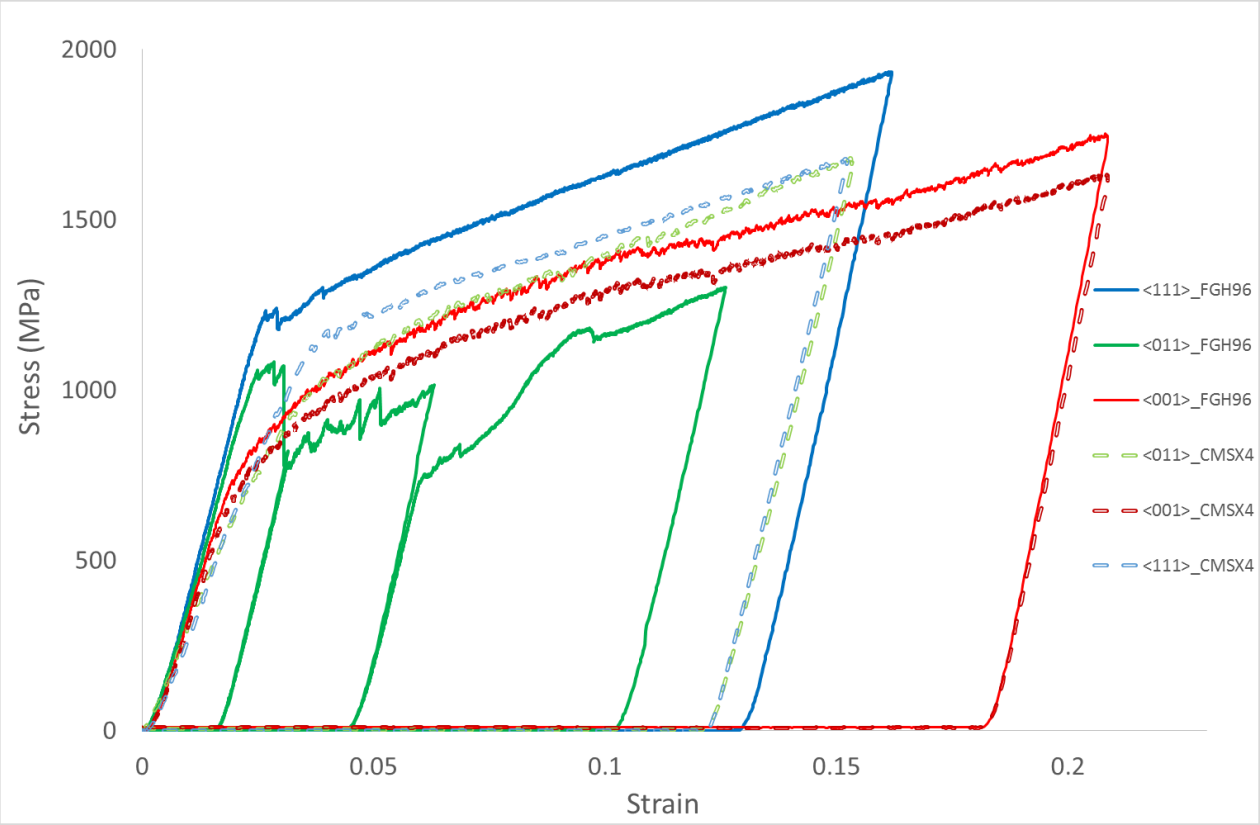


Figure 197: Compound stress strain traces for the FGH and CMSX-4 alloys in the <001>,<011>,<111> orientations. In both orientations the <001> orientation has the lowest τ_{crss} , followed by the <011> and the <111> has the highest. The modulus, U_l taken from the unloading region of the trace, follows the same trend. The hardening rate also follows the same trend apart from the <011> FGH pillar, as the flat punch was withdrawn and the pillar reloaded. The hardening was taken as an average of the three regimes seen in the <011> FGH trace.

Figure 197 shows the compound stress strain traces for the FGH and CMSX-4 <001>, <011> and <111> orientations. The mechanical trend for these three orientations tested at room temperature is an increase in yield point as we move upward from {001} to {111} with a similar response in stiffness also. The trends for the three orientations are in agreement with the theory and literature[76,188]. The values for yield point in these alloys are also consistent with other studies on orientation[188,189]. The modulus values are however not in agreement when compared to theoretical calculations[76] and experimental analysis[190] despite the trend of <111> being the stiffest and <001> the least stiff. Due to the test set up of micropillar compression, there is a substrate effect from the attachment of the sample surface to the stub and the Alemnis frame that causes a compliance issue[176] that alters the modulus values.

Table 20: Mechanical properties of the CMSX-4 alloy in the <001>,<011>,<111> orientations. U_l – unloading modulus, Y_p – Yield point, H_r – Hardening rate, τ_{crss} – Critical resolved shear stress.

Orientation	U_l GPa	H_r MPa	Y_p MPa	τ_{crss} MPa
001_CMSX4	60	3048	806	382
011_CMSX4	61	5282	920	453
111_CMSX4	66	4658	1115	464
001_FGH96	60	3154	750	317
011_FGH96	62	4264	1050	517
111_FGH96	66	4959	1200	500

The orientation of the pillars were taken from their respective top surfaces and measured through EBSD, their respective crystal orientations can be viewed below in figure 198 and figure 199.

Table 21: Euler angles for the <001>,<011>,<111> orientations in the FGH96 and CMSX4 alloys

Alloy	Euler angles		
	Φ_1	Φ	Φ_2
FGH-96$_{<001>}$	336.5	24.3	25
FGH-96$_{<011>}$	179.8	39.7	145.9
FGH-96$_{<111>}$	227.3	42.3	93.8
CMSX-4$_{<001>}$	313.3	11.8	4.4
CMSX-4$_{<011>}$	177.6	28.7	176.5
CMSX-4$_{<111>}$	51.9	53.5	332.8

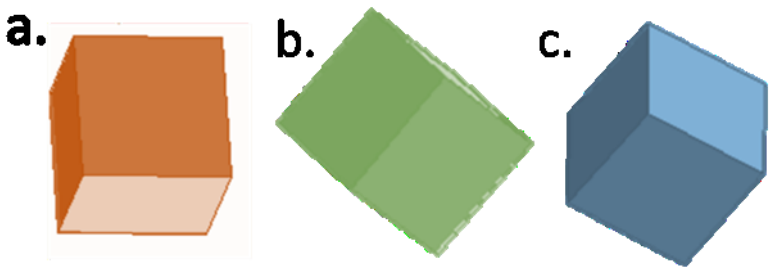


Figure 198: Crystal orientations of the (a) <001>, (b) <011>, (c) <111> micropillars in the polycrystalline FGH96 alloy.

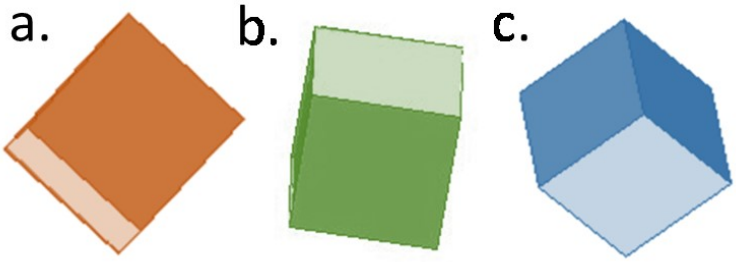


Figure 199: Crystal orientations of the (a) <001>, (b) <011>, (c) <111> micropillars in the single crystal CMSX4 alloy.

The orientations were within 10° of the specified orientation in the z direction, in accordance with the industrial standard for the orientation[181]. All orientations were as received, with the exception of the <001> CMSX-4 orientation. The <001> CMSX4 orientation was tailored to initiate shear localized slip, the <001> grain in the FGH96 alloy was chosen to deform with a "crumple" like deformation, in that the x,y,z axis were aligned orthogonal to the [001] directions by changing the in plane rotation. This is outlined in section (insert cross reference link). The alloying elements used for single crystal and polycrystalline alloys are different, these difference in chemistry can affect the mechanical properties. Table 22 shows the chemical compositions of the two alloys.

Table 22: Chemical composition wt% of the polycrystalline FGH96 vs the single crystal CMSX-4 alloy

	Ni	C	Co	Ta	W	Cr	Al	Re	Hf	Ti	Mo
CMSX-4	55.03	4.29	8.28	7.95	6.15	6.17	4.29	4.38	1.31	1.10	0.40
FGH96	54.32	-	12.92	-	2.03	19.63	1.41	-	-	5.39	4.3

Table 22, shows the chemical composition in wt% of the polycrystalline FGH96 vs the single crystal CMSX-4 alloy. The EDX scans on polycrystalline FGH96 and single crystal CMSX4, reveals that the elemental concentrations of the alloys agrees with the literature[191,192,122,193]. The main difference between the FGH96 and CMSX-4 is the presence of Ta in CMSX-4 which is a ϒ' stabiliser and the presence of Mo and larger concentrations of Co and Cr in FGH96 which are ϒ stabilisers[11].

7.8. Summary – Results chapter 2

The three principal axis of the fcc system; <001>, <011> and <111> were studied. The study of orientation in Ni superalloys is crucial in helping alleviate fatigue crack failure[5].

Mechanical testing on the microscale acts on the same length scale as the deformation processes themselves. This can provide deeper insight into deformation mechanisms to inform the designer, how to better tailor the next generation of alloys and prevent failures.

The crystal orientations of the tested pillars were measured through EBSD analysis, in which the pillars were aligned accordingly with respect to a fiducial marker. Pillars were fabricated on both the single crystal CMSX-4 and FGH96 polycrystalline alloy.

The pillars on both samples were tested and the deformation modes and mechanical variables measured. The in plane rotation of the grains in the FGH96 alloy cannot be changed, and as a consequence, from an orientation point of view, the mechanical variables; The yield point, hardening rate and unloading modulus deviated slightly from the goniometer cut samples.

As the micropillar is deformed in compression, the fcc crystal rotates clockwise towards the loading direction. The pillars in this study were deformed to high strains in excess of 10% and so the rotation of the pillar body was taken into account during post deformation analysis.

With regards to the CMSX-4 alloy, the <001> pillars were orientated for shear localised slip, in which the in plane axis are rotated 45° from the <100> and <010> respectively. Both the <011> and the <111> pillars were aligned so that the x,y,z axes are aligned orthogonal to the <011> and <111> respectively.

Dominant slip systems can be defined as slip systems that are within 20% of the highest Schmid factor of the given orientation. This is important to note, as the competition of slip systems with similar Schmid factors can alter the deformation mechanics of the system[15]. An orientation that has a large difference between the highest Schmid factor and the average of that orientation, will deform in a more predictable manner, and the slip trace should correspond to the slip system calculated from theory. In a system where the difference between the average Schmid factor and the highest Schmid factor is small the deformation will be less localised.

Control of the α and β orientations has the potential to dramatically improve the components resistance to fatigue crack growth, with no addition of weight or cost[5,14].

The β orientation corresponds to the in plane rotation and has been found that influencing the β orientations can minimise the onset of fracture[5] and thus improve the lifetime of the part. The α orientation of the pillars were within 10° of each other. The β orientations however varied. The testing supported that a change in β orientation can drastically change the deformation modes.

In the FGH 96 alloy The 011 grains were the predominant orientation. The 011 grains deformed in the most stable fashion and had good mechanical properties. In the CMSX4 alloy, the <001> orientation deformed in the most stable fashion. The trends in the mechanical values supported the literature[181] and the values of τ_{crss} agree with other experimental studies.

8. Results - Carburised Ni-based superalloy: CMSX-4

8.2. Objectives

The objectives in this chapter are to examine the presence of carbide type phase in the alloy whilst also characterising the carbide type phase. The characterisation will involve determining the chemical composition of the alloy and carbide type phase as a function of distance from the edge of the sample. Once the characterisation is complete the alloy will be tested mechanically as a function of distance from the edge using micropillars. The micropillar tests will then be validated with local micro indentation tests. Lastly the carbide type phases will be examined via TEM

8.3. Motivation

Carbides are precipitates derived from C that can alter the mechanical and chemical properties of the alloy. The carbides in CMSX-4 inhabit an area, up to 120 µm from the edge of the sample. The carbides vary in shape, size and orientation. The shape of the carbide type phase vary in shape from lenticular, to circular. The size, crystallography and position of the carbide type phase within the ϒ/ϒ' matrix will have an effect on the mechanical properties of the alloy; a consequence of a change in chemistry caused by the removal of alloying elements used to homogenise the ϒ/ϒ' microstructure.

As dislocations travel through the ϒ/ϒ' matrix and interact with carbides, they can operate a number of mechanisms such as Orowan bowing[24] to minimise energy and overcome the obstacle barrier[125]. This chapter will examine the characteristics of the carbide type phases and how their influence in the alloy effects mechanical properties, alloy chemistry and microstructure.

Studying variations in alloy chemistry and mechanical properties, requires accurate placement and testing area geometry. EDS, micropillars, micro indents and TEM techniques were used to do this.

8.4. Introduction

The carbide type phases exist within the ϒ, ϒ/ϒ' junctions and in the ϒ' precipitates. The sizes vary from 60 nm to 2 µm. The carbide type phases found in the Ni-based superalloys are distinct in character and can be separated into three microzones which vary in morphology as a function of distance from the edge of the sample.

The longer more elongated carbide type phase are believed to be of the TCP phase[194] and the more regular circular type carbide type phase are of the fcc crystal structure[5,195]. TCP phases have been found to have a negative effect on the microstructure and mechanical properties of Ni superalloys[196].

It was found that both carbide type phases, fcc and TCP alter the local mechanical properties in the alloy. Both the yield point and ductility decrease in the presence carbide type phase. In the presence of TCP phases the mechanical properties were reduced further.

The aluminizing process that has formed the carbide type phase, in this study is diffusion controlled[29]. The chemical composition of the carbide rich area, indicated that, Ti, Ta, Hf and Mo are carbide type phase stabilisers whereas Ni, Cr, Co are non-carbide type phase stabilisers, this was supported by both SEM and TEM based EDX and is consistent with literature[21]. The chemical composition as a function of zone, distance and carbide type phase was also analysed.

Micropillar experiments show that the size and shape of the carbide type phase, has an effect on mechanical properties with larger more irregular carbide type phase, contributing to greater shear stresses and phenomena such as strain bursts, whereas smaller carbide type phases contribute more to the activation of different slip systems.

CMSX-4 is a second-generation Ni superalloy composed of more than eight alloying elements. The alloying elements are homogenised to provide the alloy with a stable ϒ/ϒ' microstructure enabling strengthening properties suitable for high and low temperature applications[193]. Ni, Co, Fe and Mo stabilise the soft dis-ordered fcc ϒ phase. Al, Ti and Ta stabilise the stronger intermetallic Li_2 ordered ϒ' phase.

Single crystal Ni superalloys undergo a costly and time expensive heat treatment to promote the formation of the stable and evenly distributed ϒ/ϒ' microstructure[16]. It is common for single crystal alloys to undergo a 3-stage homogenization process with controlled rapid cooling[16], followed by a 2-stage aging treatment providing a fine dispersion of secondary and tertiary precipitates[17].

The precipitates in the carburised alloy under investigation are the by-product of pack aluminzation. Aluminization is used to grow an intermetallic gradient layer[197,21]. The intermetallic gradient layer is used to connect a ceramic thermal barrier coating (TBC) to the Ni superalloy substrate layer.

TBC's are made of ceramic materials and so an intermetallic gradient layer is grown to accommodate for the thermal mismatch between the Ni-based superalloy substrate and ceramic TBC[18]. The TBC is an important feature of the turbine blades in an aeroengine, The TBC prevents the degradation of the Ni superalloy and increases its in service lifetime[18].

For this study nanoindentatrion was used in collaboration with micropillar testing. The Berkovich indenter was chosen, the Berkovich indenter is favoured for small-scale indentation studies as it has the advantage that the edges of the pyramid are constructed to meet more conveniently at a single point[187],

figure 200. This is useful when local mechanical testing is needed, as in the case of the carbide type phases, which can be segmented into micro zones.

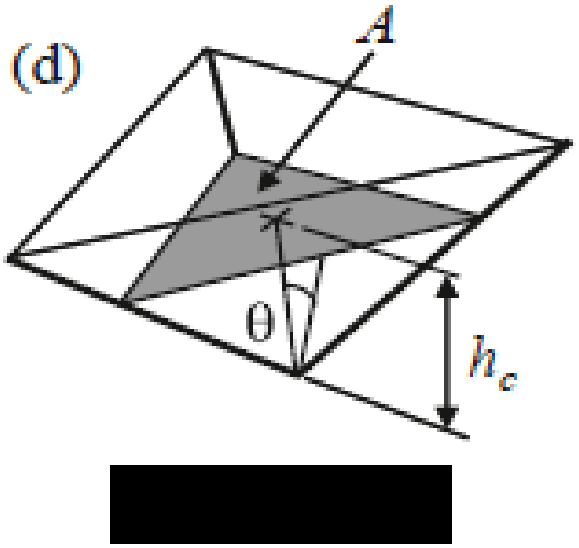


Figure 200 Indentation parameters for a Berkovich indenter (not to scale)[191]

Figure 200, shows a schematic representation of a Berkovich indenter. The size of the contact area of the indenter, is estimated from the depth of penetration with the known geometry of the indenter[198].

The mean contact pressure, of the indenter with the alloy is defined as the indentation hardness (H). The indentation hardness (H) is calculated from the indentation load (P) divided by the projected contact area (A), where:

$$H = \frac{P}{A}$$

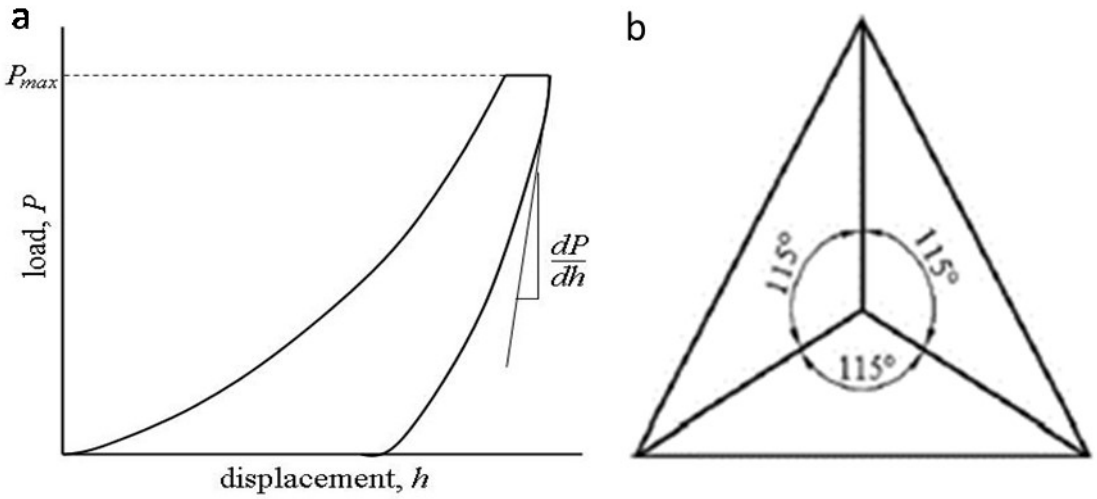


Figure 201: Results from a nanoindentation test (a) Compliance curves for loading and unloading, from a nanoindentation experiment with a maximum load (P_{max}) (a) schematic Berkovich plastic impression.

Figure 201, shows an exemplar load, displacement curve for a microindentation test and a schematic plastic impression left by a nanoindent. In this set of experiments we assume a non-ideal geometry and will therefore measure the area directly from the indentation impression using high res SEM imaging.

Thus the hardness can be evaluated as

$$H = \frac{P}{A_{exp}}$$

A sequential line array of microindents will be placed along the microstructure in CMSX-4 to ensure a large enough data set to account for statistical variations.

8.5. Characterisation of carburised CMSX-4

The CMSX-4 microstructure is comprised of a series of carbide type phases extending from the perimeter edge to 120 µm. The carbide type phases, vary in shape and size according to distance from the edge and can be separated into zones.

8.5.1. Energy Dispersive X-ray Spectroscopy (EDS) – Bulk carbide rich region

EDS provides a resolution of up to 1 µm[23] and is useful for identifying elements local to the carburised CMSX-4 microstructure.

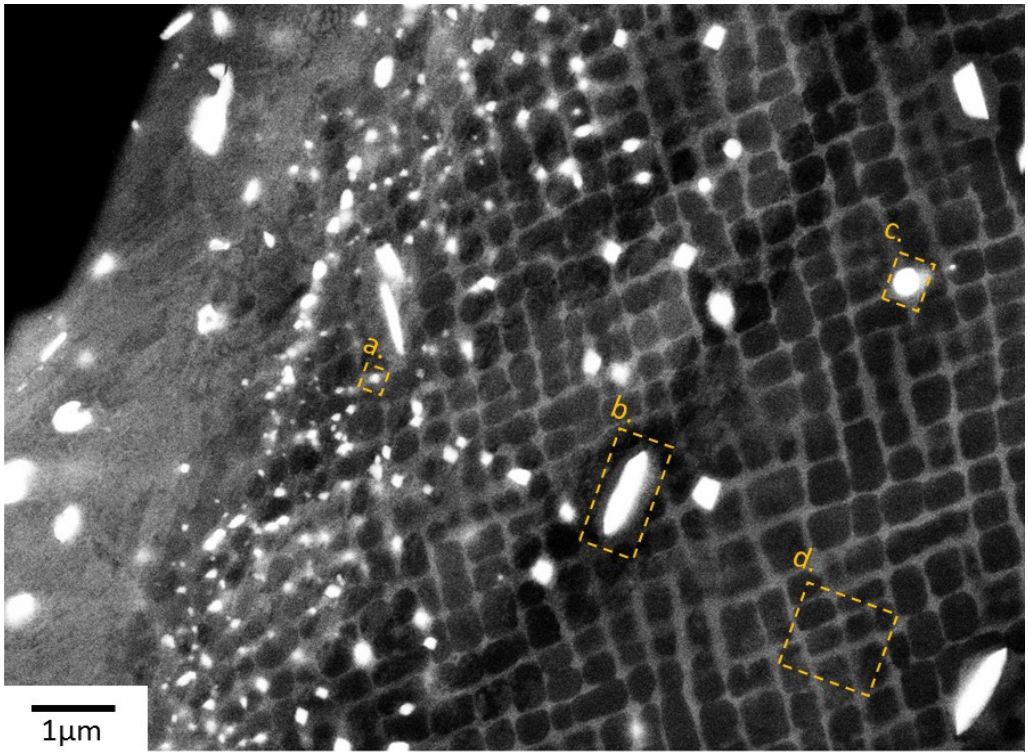


Figure 202: BSD image of <001> orientated carburised CMSX-4 0-40 µm from the perimeter edge illustrating different distributions of carbide type phases (a) faceted carbide type phase inhabiting a ϒ channel (b) a larger TCP phase across a ϒ/ϒ' junction (c) a faceted carbide type phase with a 400 nm diameter (d) bulk microstructure

Figure 202 shows a BSD image of the carburised ϒ/ϒ' microstructure in CMSX-4. An operating voltage of 20 kV, with a working distance of 8 mm combined with a low scanning speed was sufficient to image the carbide type phase, as seen in figure 202. Figure 202, shows; (a) a faceted carbide type phase, inhabiting a ϒ channel, (b) a larger TCP phase across a ϒ/ϒ' junction, (c) a faceted carbide type phase with a 400 nm diameter and (d) the bulk microstructure.

For EDS analysis a 10 mm working distance with a beam energy of 20 kV was sufficient to get a strong clear peaks of elements present in each scanning region, as evidenced by literature[16]. Initial EDS experiments indicated that elements such as Ta, Ti, Cr, Co, W, Hf, Cr and Ni change, as a function of distance, as the scan moves from a carbide type phase to bulk microstructure, as seen below in figure 203.

0

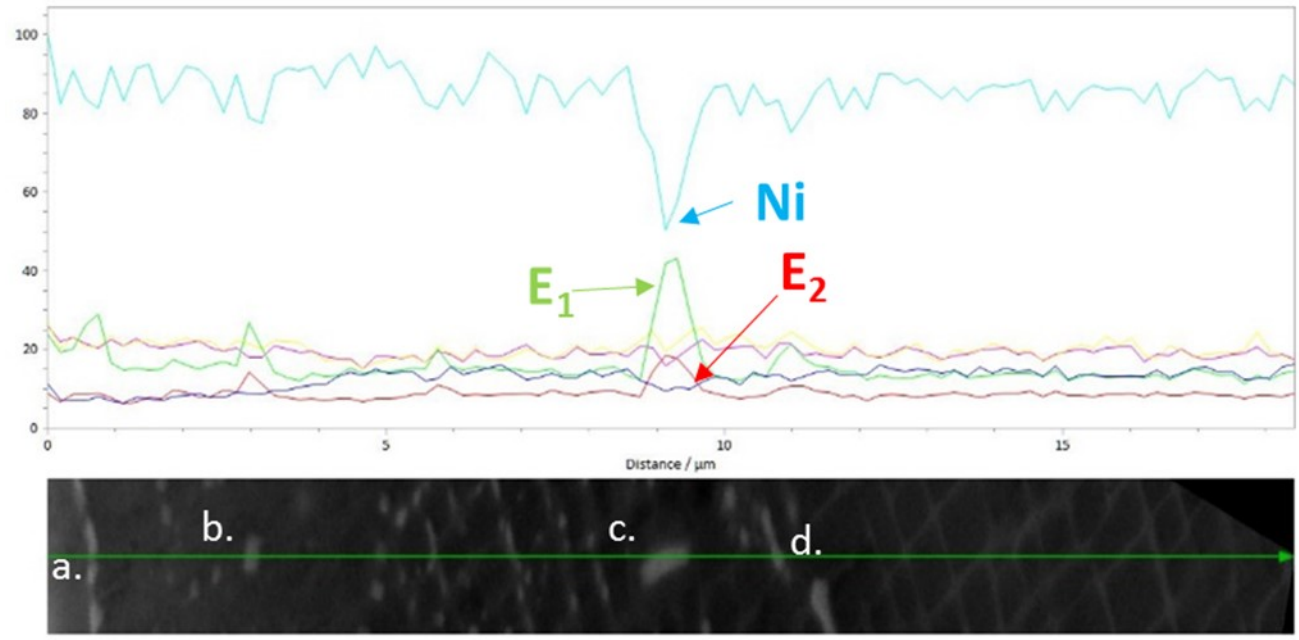


Figure 203: Line scan across carbide type phase, rich area in the CMSX-4 alloy from perimeter edge at 0 µm to 40 µm, as shown in figure 202.

Point's a-d in figure 203, show carbide type phases which intersect with the line scan. Point c, in figure 203, shows a point at which the line scan intersects a large carbide type phase, this point provides the clearest indication of the trend that occurs in the presence of a carbide type phase. Initial scans indicated that E_1 and E_2 constitute to transition metal elements, figure 205.

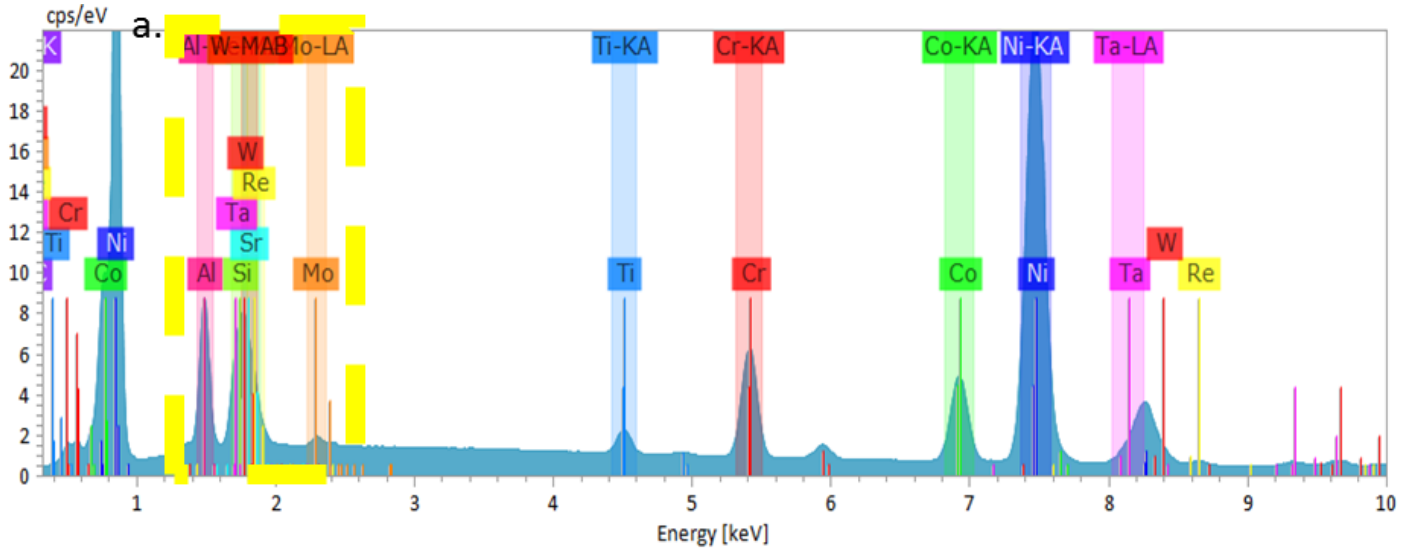


Figure 204: Native spectrum across carbide type phases (a) series of peaks with similar eV's including, W,Re,Ta,Si and Sr. Si and Sr, are not elements noted in the CMSX-4 alloy literature[16].

Figure 204 shows a spectrum over a carbide type phase, rich region in CMSX4. Elements native to CMSX-4, Ni, Ta, Al, Cr, W, Re, appear in the scan, as well as foreign elements, Si and Sr (highlighted in yellow) that appear with strong peaks. This can also be seen in the map scan results, figure 205.

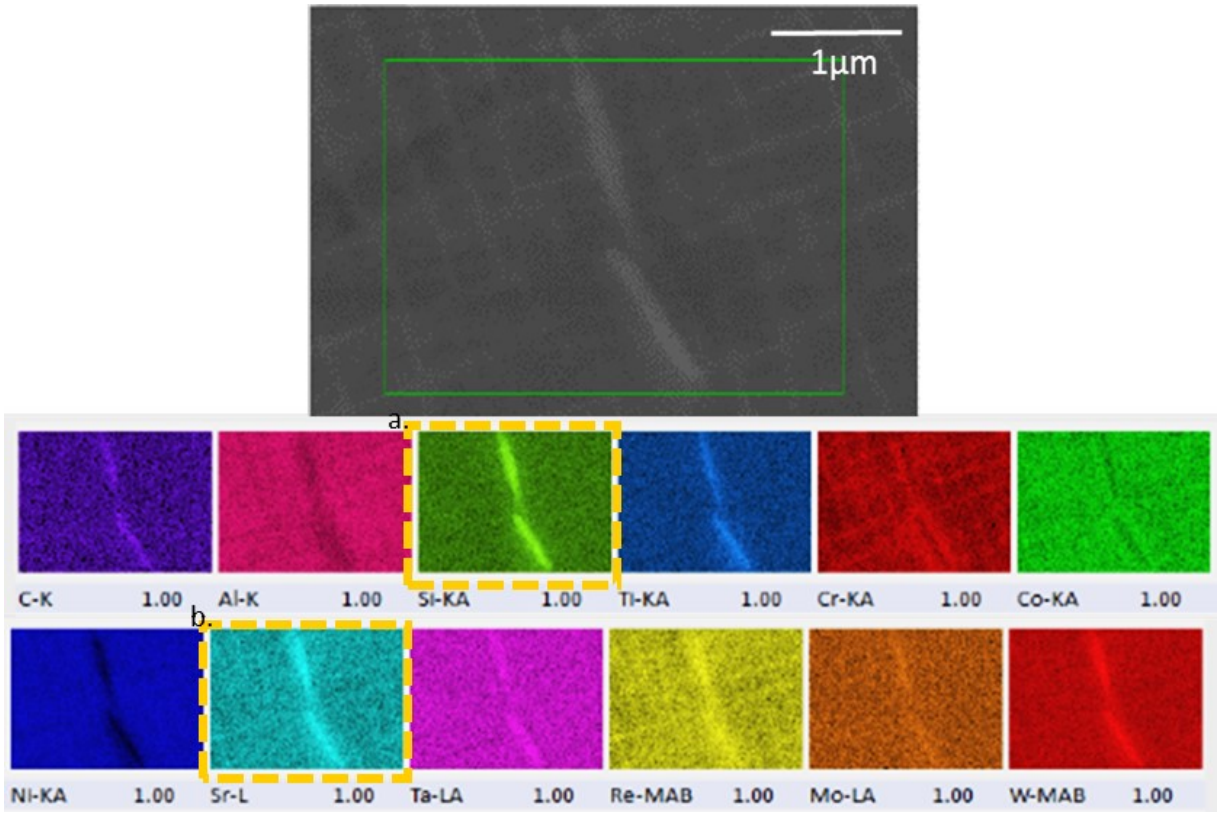


Figure 205: Map scan over large TCP phase (a-b) illustrating the strong presence of Si and Sr, two elements that are not local to CMSX-4

As there is no evidence to support either Si or Sr being present in this alloy, the elements Si and Sr have been removed from all further scans and not added to the custom quantification scripted to each scan on this alloy.

The alloying elements common to Ni superalloys are Ni, Co, Fe, Mo, Al, Ti, Ta with refectory elements such as Hf, W, Re added to later generation of alloys such as CMSX-4 to improve the mechanical properties[199]. Figure 205, illustrates the same trend as figure 203, in that as the line scan, which is comprised of a series of point scans, moves through the microstructure onto a carbide type phase; a clear drop in Ni is accompanied by an increase in other elements.

The difference in trends could be a consequence of the elements partial to ϒ or ϒ' but could also be due to the elemental leeching by different carbide type phases. The elemental leeching could explain a change in mechanical properties within carbide type phase, regions and some areas outside of the visible surface carbide type phase, area.

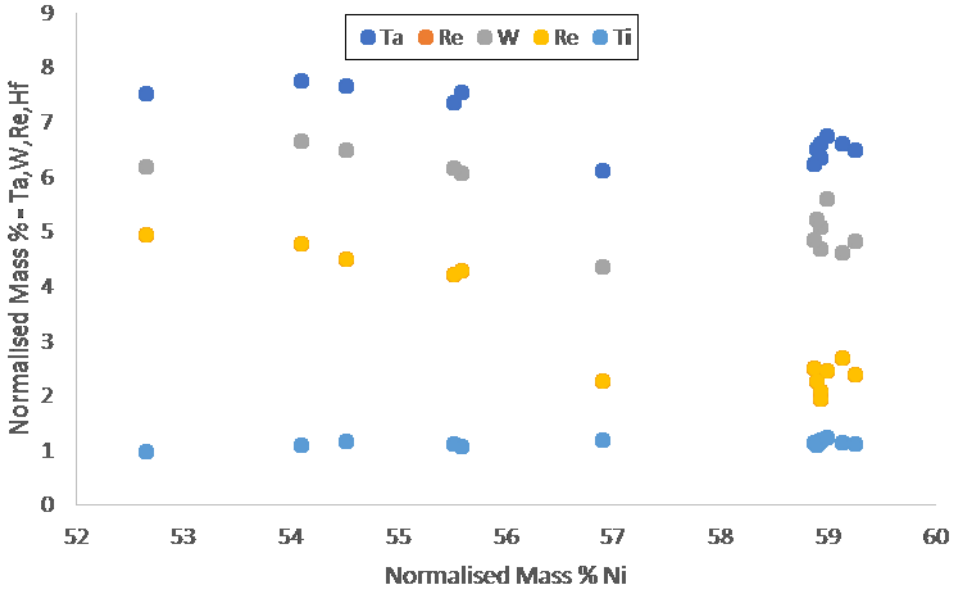


Figure 206: Normalised mass % of Ni vs carbide type phase stabilising alloying elements (Ta, W, Re, Ti)

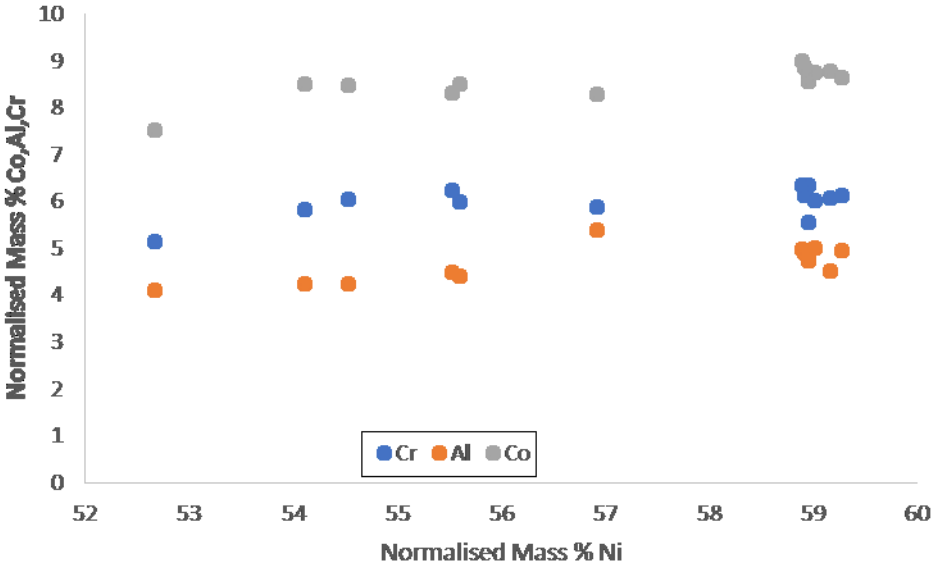


Figure 207: Normalised mass % of Ni vs non carbide type phase stabilisers (Cr, Al, Co)

Figure 206 and figure 207, illustrate the trends observed across the CMSX-4 alloying elements, in the vicinity of a carbide type phase, with respect to the normalised mass percent of Ni. The concentration of the carbide type phase stabilisers, Ta, W, Re and Ti, are inversely proportional to the concentration of the Ni. The concentration of the non-carbide type phase stabilisers are proportional to concentration of Ni. Hf was also found to be a carbide type phase stabiliser, however the changes in concentration are very small compared to Ta, W, Re, Ti.

There must be an appreciation of the correct measurement to take when establishing the elemental concentrations local to a specific region. Line scans are useful in telling the initial story, however area maps build a much better narrative. Figure 208 and figure 209 show the spectrum from an EDS map scan of a 15 μm^2 area, at distances 5 and 50 µm from the perimeter edge respectively.

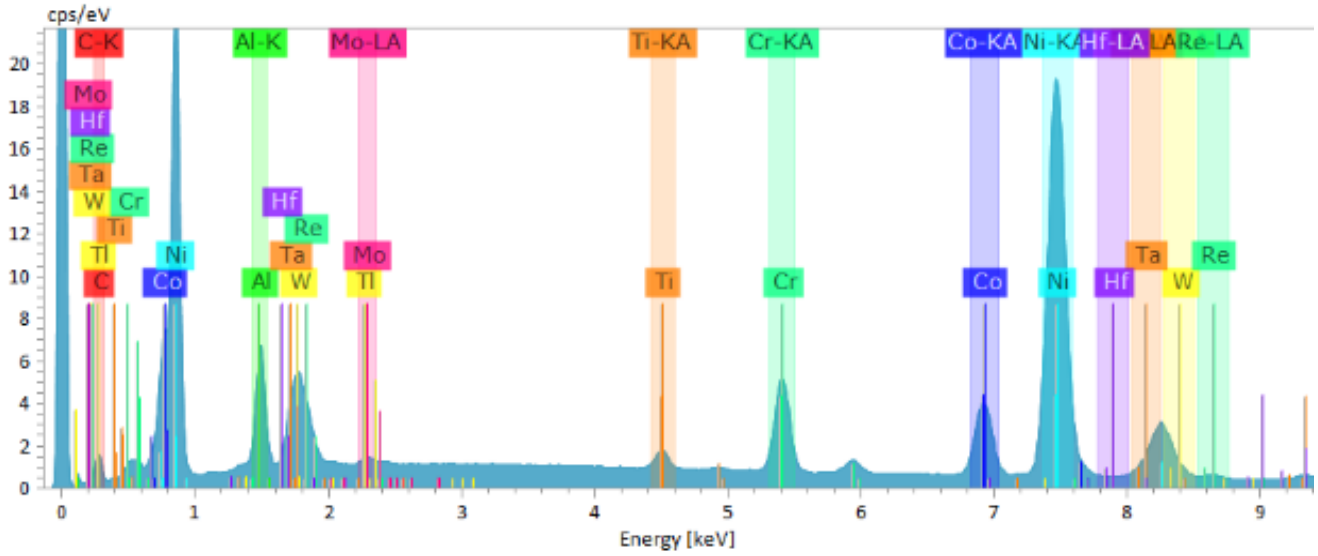


Figure 208: EDS scan in a 15 µm² region within the carbide type phase rich region 5 µm from the perimeter edge

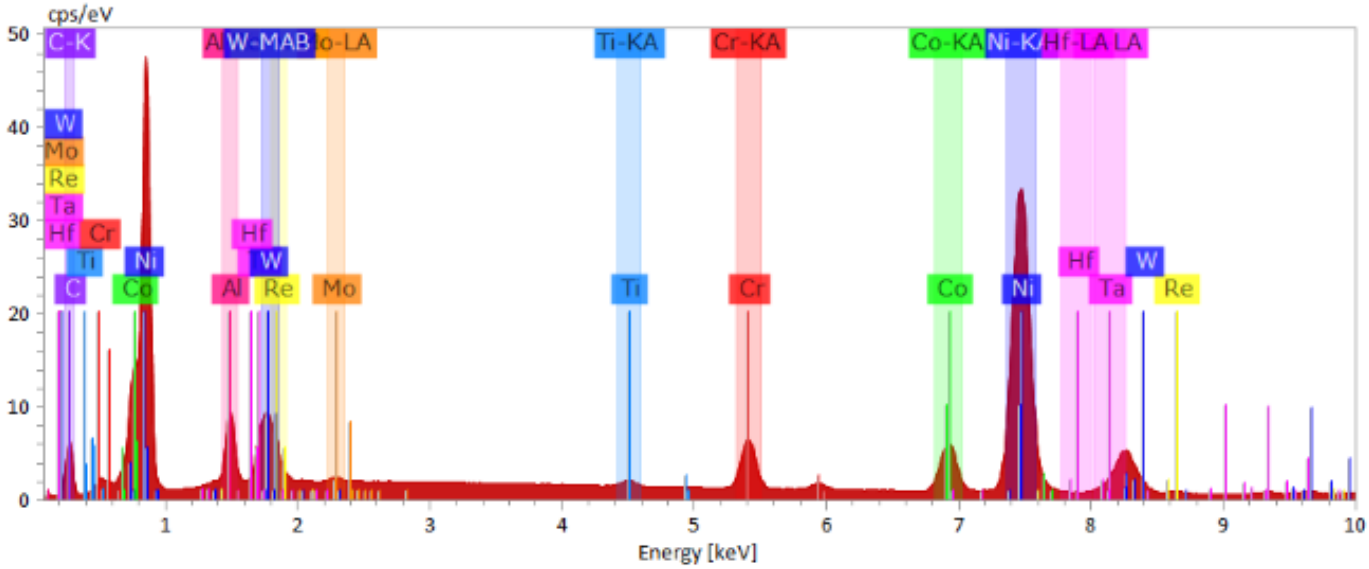


Figure 209: EDS scan in a 15 µm² region within the carbide type phase rich region 50 µm from the perimeter edge

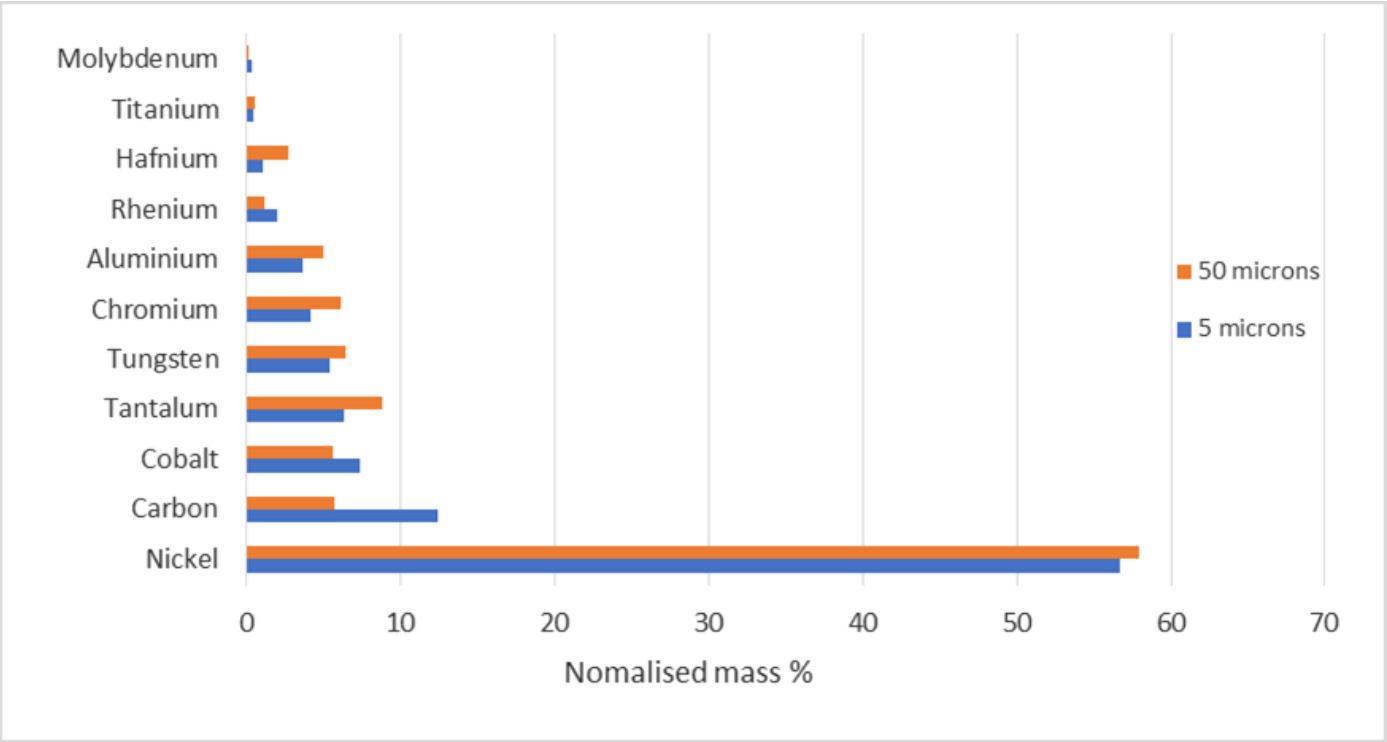


Figure 210: EDS map scan comparison of the normalised mass % of alloying elements in CMSX-4 between 5 µm and 50 µm distances from the perimeter edge of CMSX-4, as shown in figure 202.

To characterise the chemistry of the alloy, the microstructure as a function of carbide type phase and distance from the edge of the sample through the carbide type phase, rich region, into the bulk material, must first be understood. Figure 210 indicates that the elemental concentrations differ as a function of distance and thus localising the test region with respect to distance, is important to the study. In this case, the carbide type phase, rich region has been segmented into zones and will examined below in Section*8.5.2*.

In conclusion; to identify what elements are present within local regions in the carbide type phase, rich region, a comprehensive study local to an area and carbide type phase must be undertaken to understand which elements segregate where. This will hopefully begin to answer questions as to what elements constitute specific carbide type phases and how the changes in elemental concentrations can affect the mechanical behaviour of the alloy.

8.5.2. Microstructure

The carbide type phase, rich region in CMSX-4 extends from the perimeter edge at 0 µm to 120 µm, and the microstructure can be segmented into zones, based on distance from the perimeter edge, as shown in figure 211.

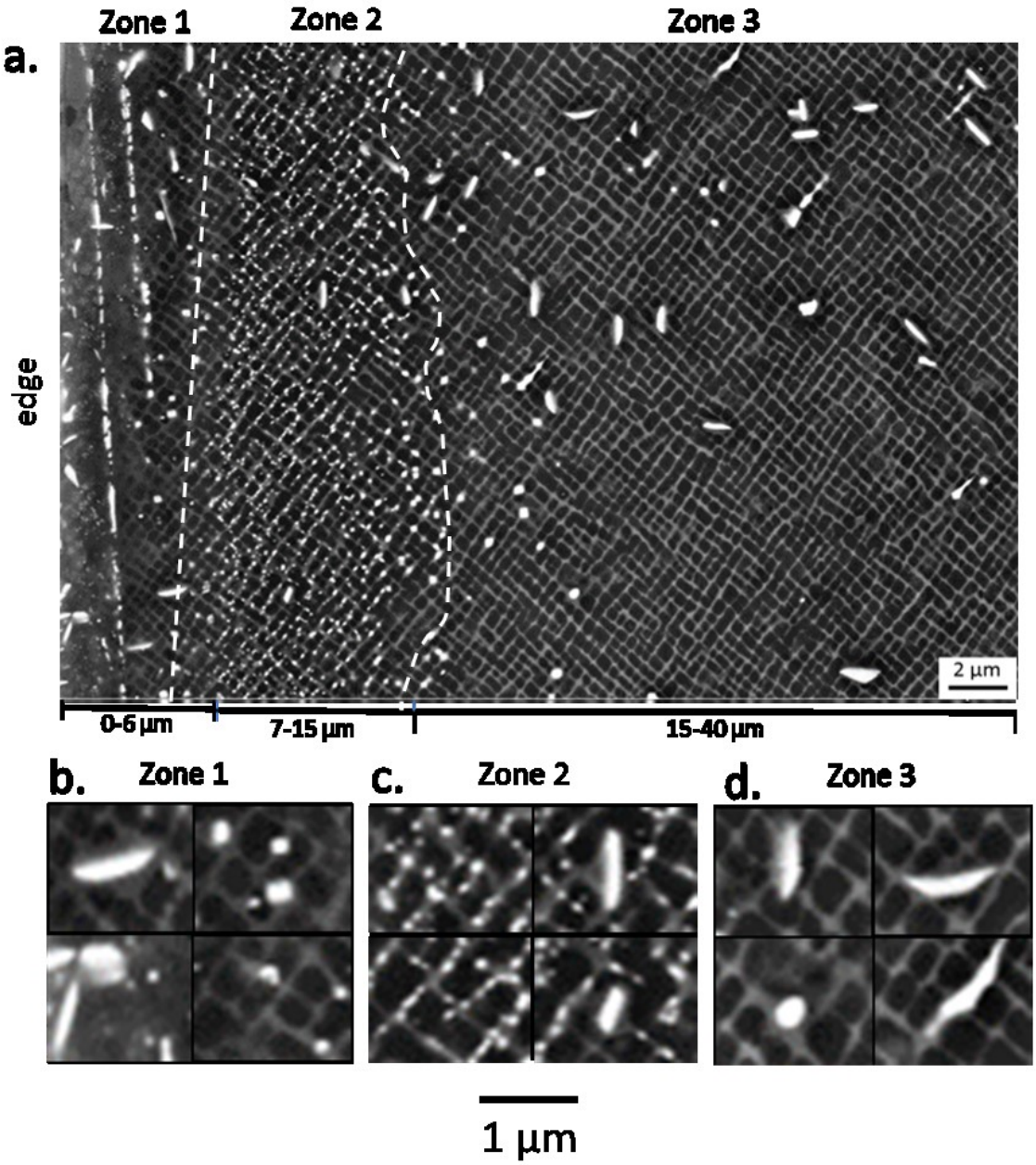


Figure 211: BSD micrograph taken 0-120 µm from the perimeter edge of the sample (a) Micrograph illustrating the three zones in the CMSX-4 carbide type phase microstructure. (b) Zone 1 (0-6 µm) dispersion of majority Chinese script type carbide type phase with some more regular spherical shaped type. (b) Zone 2 (7-15 µm) dispersion of small spherical shaped carbide type phase, mainly local to ϒ junctions with a high local number density per unit area (c) Zone 3 (15-40 µm) sporadic dispersion of majority TCP phase

The microstructure of carburised CMSX-4 can be segmented into zones which vary according to distance from the perimeter edge of the sample, figure 211. The carbide type phase, rich rim extends ~120 µm from the outer perimeter edge of the sample into the bulk.

As illustrated in figure 211; Zone 1 is located ~0-6 µm from the edge of the sample and contains both small round ϒ/ϒ' carbide type phase, as well as long needle like carbide type phase.

Zone 2 is located 6-15 µm from the edge, contains mainly smaller more circular carbide type phase, located within ϒ/ϒ' channels.

Zone 3 predominantly contains needle like carbide type phase, orientated randomly spanning the largest distance from 15 µm extending about 100 µm into the bulk material. The orientation and distribution of zone 3 carbide type phase, can change drastically depending on location.

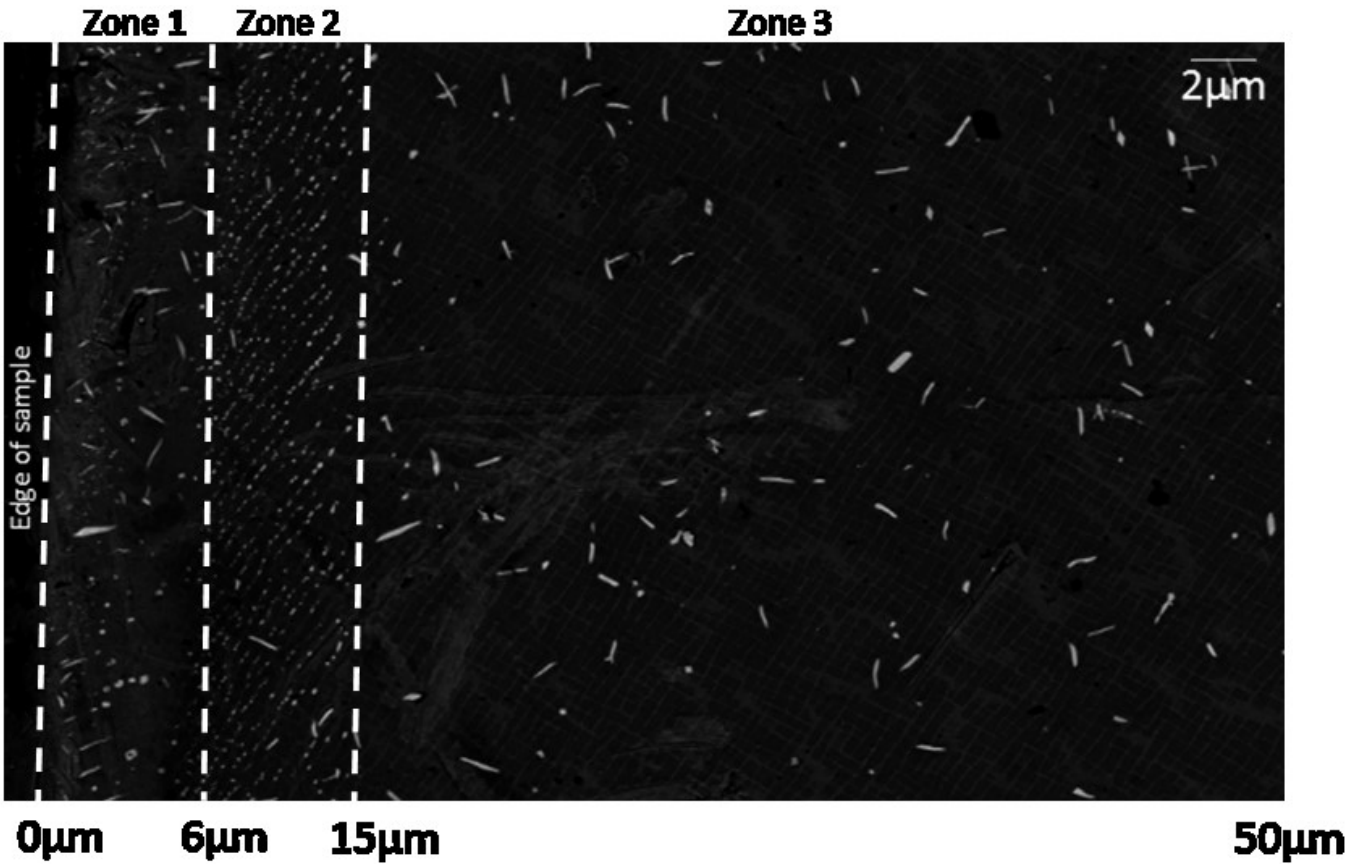


Figure 212: BSD Image of carbide type phase zones, from the perimeter edge of the sample through to 50 µm. BSD image was taken in a different region than that in figure 211. The trends throughout the zones remains consistent.

Figure 212, is a BSD scan of the carbide type phase, rich region of CMSX-4, segmented into zones, as shown in figure 211, however the image was taken in a different region than that in figure 211. The trends across the three zones remain consistent in both regions shown in figure 211 and figure 212.

8.5.3. Carbide zones

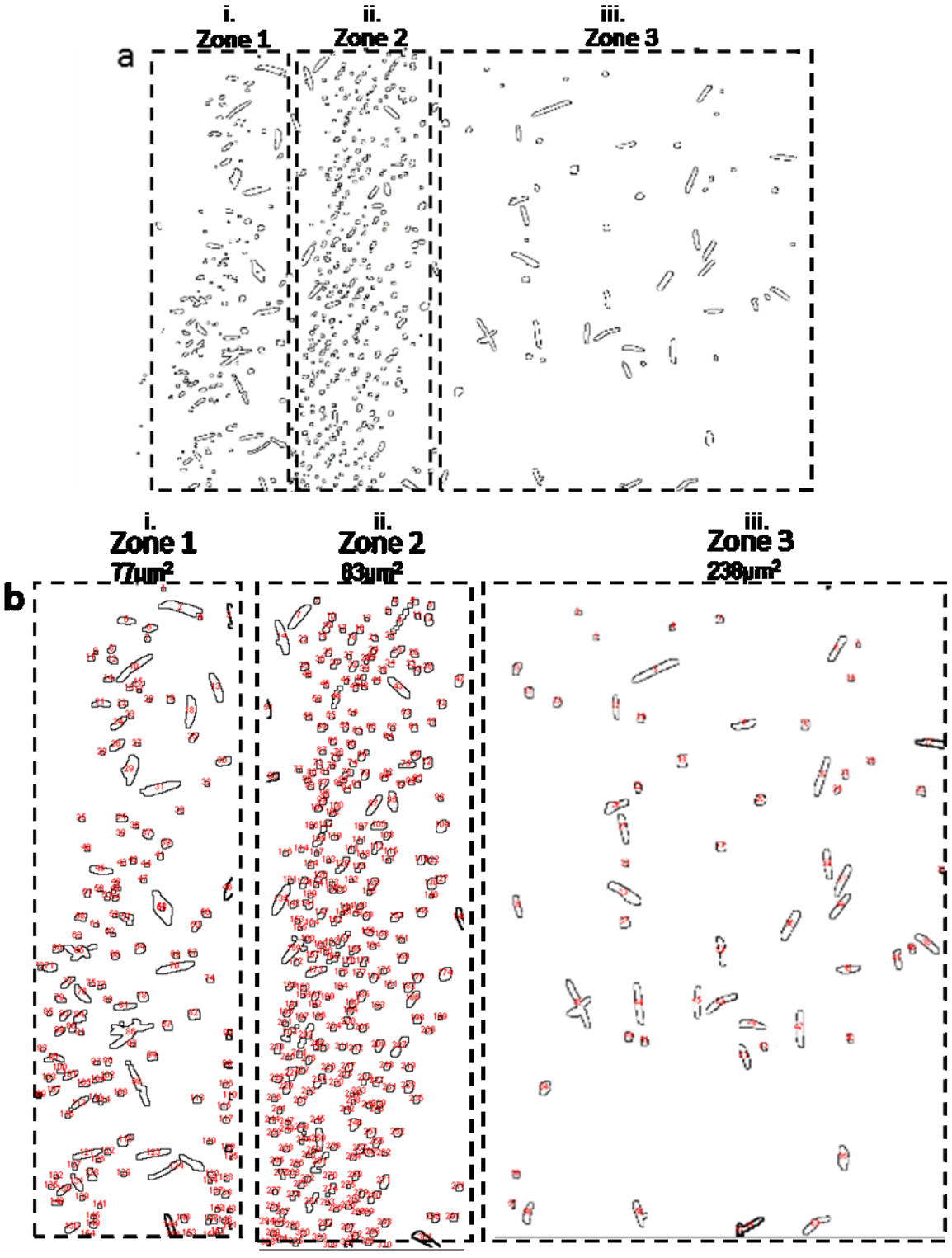


Figure 213: Image J micrographs a. Carbide type phase, represented as solid individual particles b. Carbide type phase, analysed

1.4.3.1. Zone 1

Zone 1 is the closest to the perimeter edge of the sample and has the most random configuration of carbide type phases. The average area of carbide type phase in zone 1 is 0.023 µm^2, circularity is 0.494, aspect ratio, 1.71, roundness 0.693, solidity 0.535 and the number of identified particles in the 77 µm^2

area, shown in figure 213 b i is 156. When comparing shape descriptors to the area of the carbide type phase, there is a trend which indicates, that there is a proportional relationship between carbide phase area and aspect ratio, however for the other shape descriptors there is an inversely proportional relationship, with a plateau that begins between 0.03 and 0.04 μm^2,figure 216. figure 214 to show the distribution of carbide type phases local to zone 1.

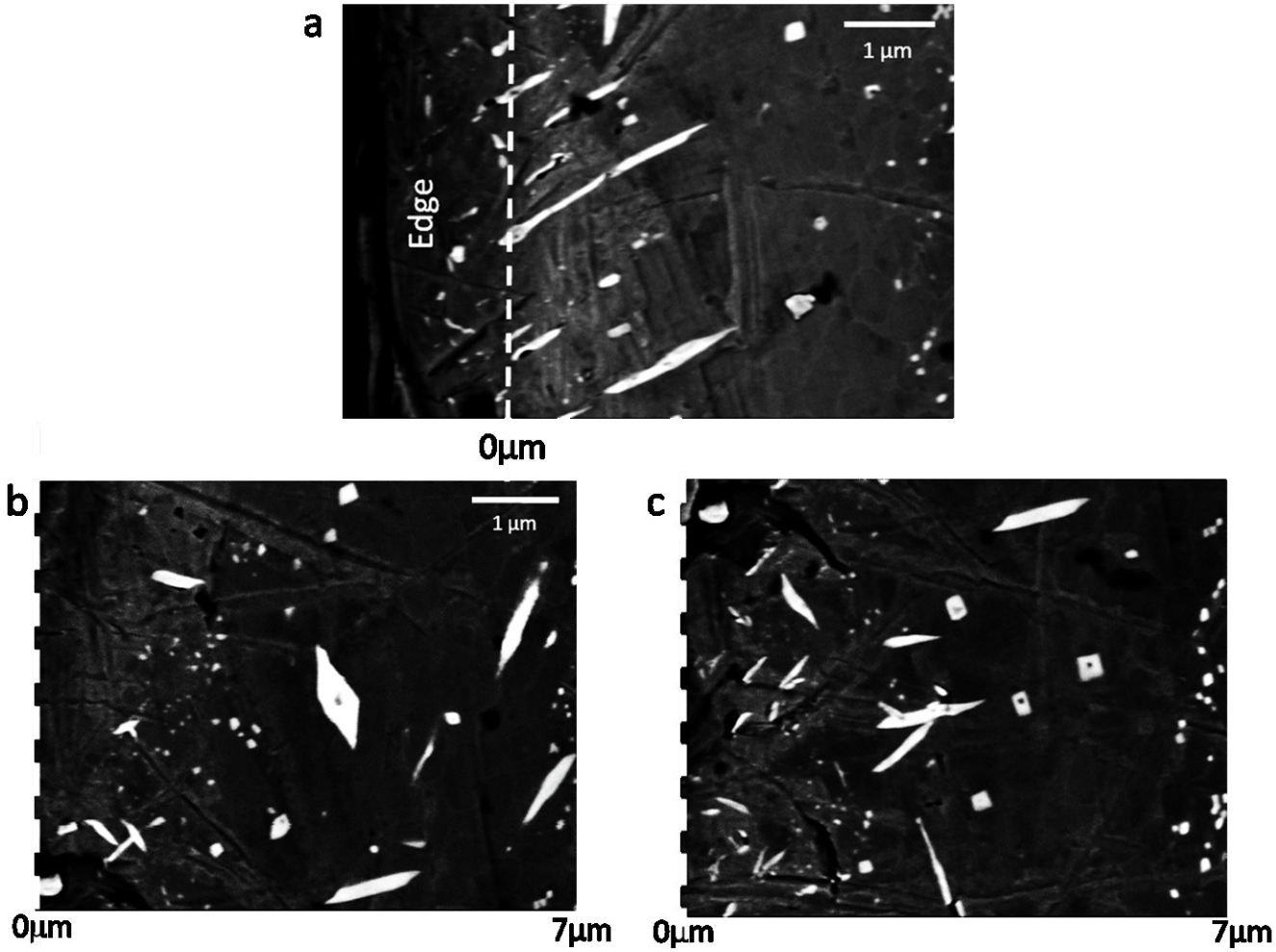


Figure 214: 45 μm^2 area maps of different regions in zone 1 (a) an area near the perimeter edge of the sample, showing long elongated carbide type phases and small carbide type phase freckles (b-c) 0-7 µm showing a spectrum of carbide phase shapes

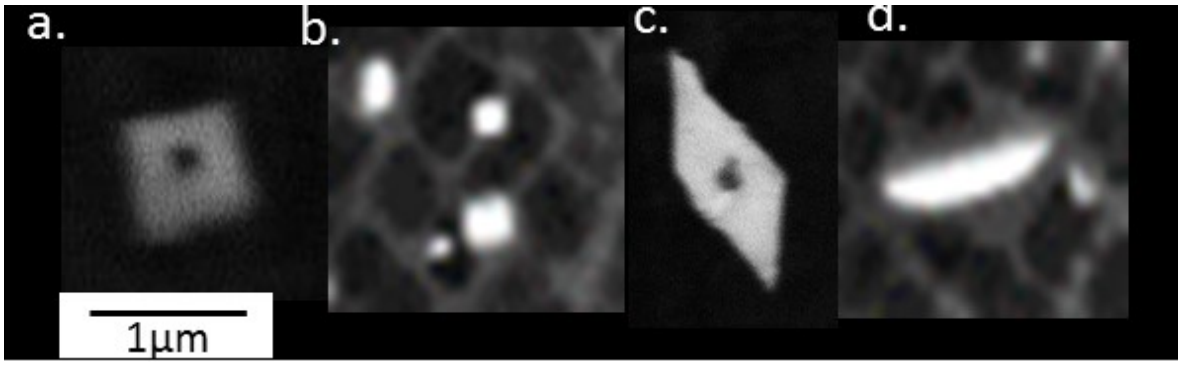


Figure 215. Carbide type phases local to zone 1

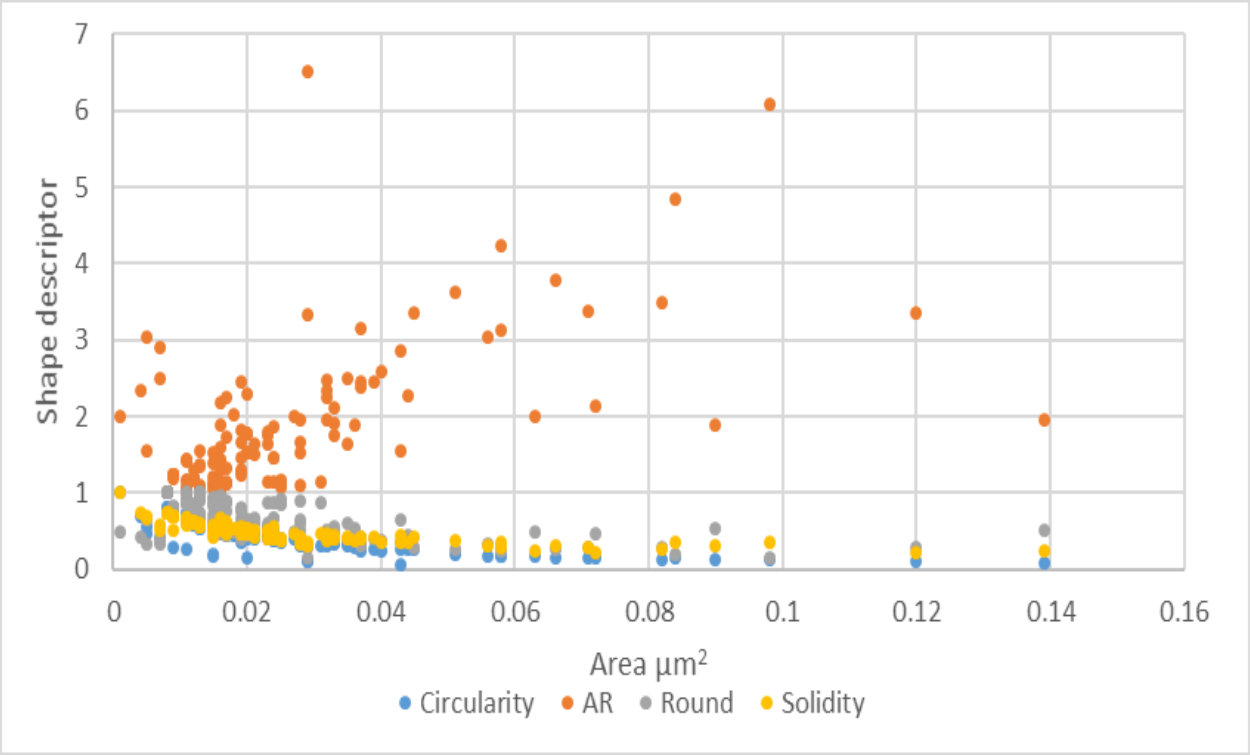


Figure 216: Shape descriptors vs area of identified carbide type phases in zone 1

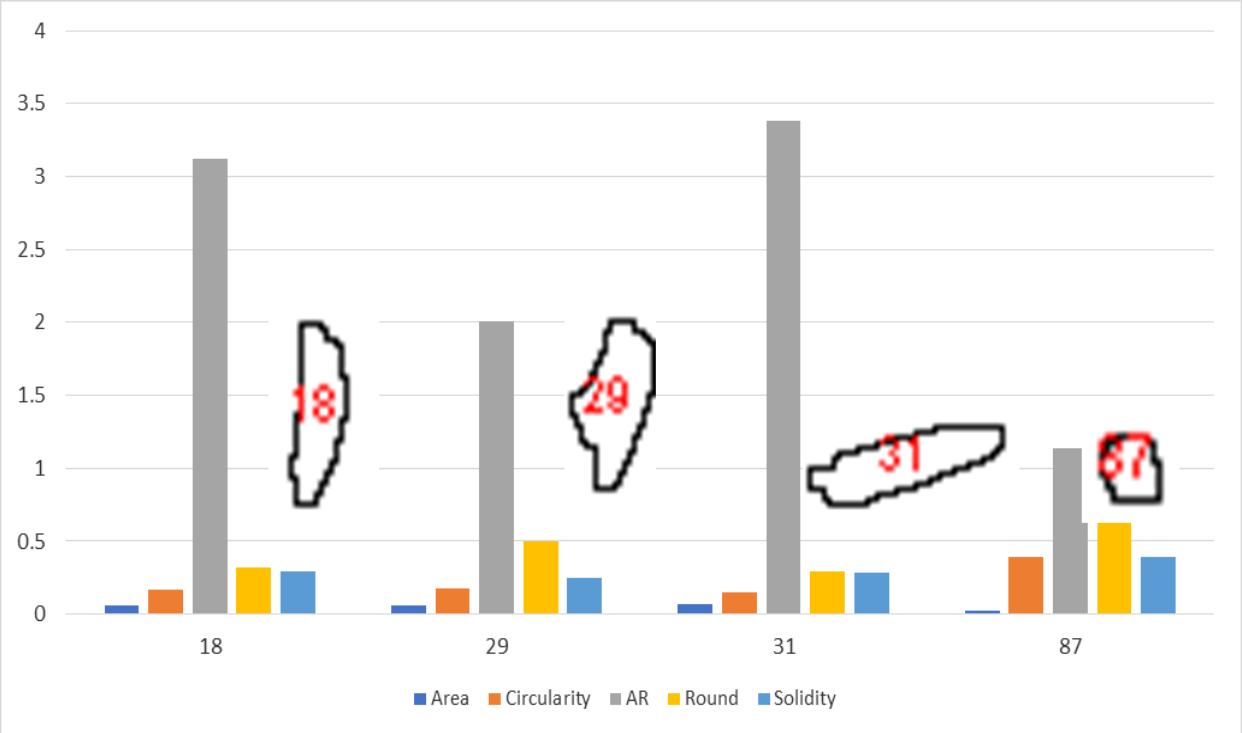


Figure 217: Four carbide type phases unique to zone 2

1.4.1.2. Zone 2

Zone 2 is a small region roughly 10 µm wide and has the most stable and consistent configuration of carbide type phases, which are predominantly located within ϒ channels. With some larger carbide type phases, occupying both ϒ/ϒ' networks. The average area of carbide type phases, in zone 2 is 0.018 µm^{2,} the circularity 0.531, aspect ratio 1.47, roundness 0.76, solidity 0.55 and the number of particles in the 83 µm^2, shown in figure 213 b ii area is 322. Figure 218- Figure 221 show the distribution of carbide types phases local to zone 2.

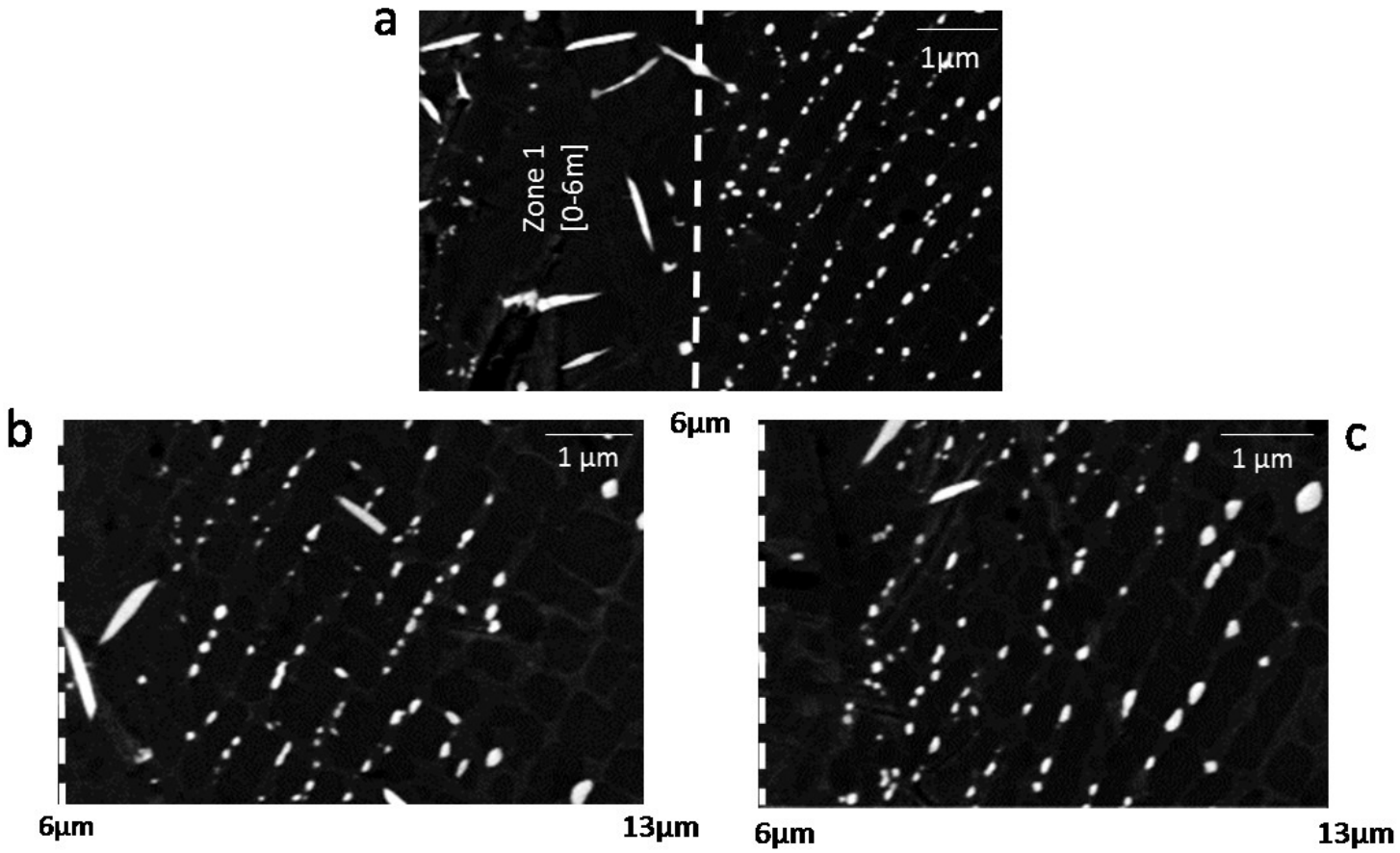


Figure 218: 45µm^2 area maps of regions in zone 2

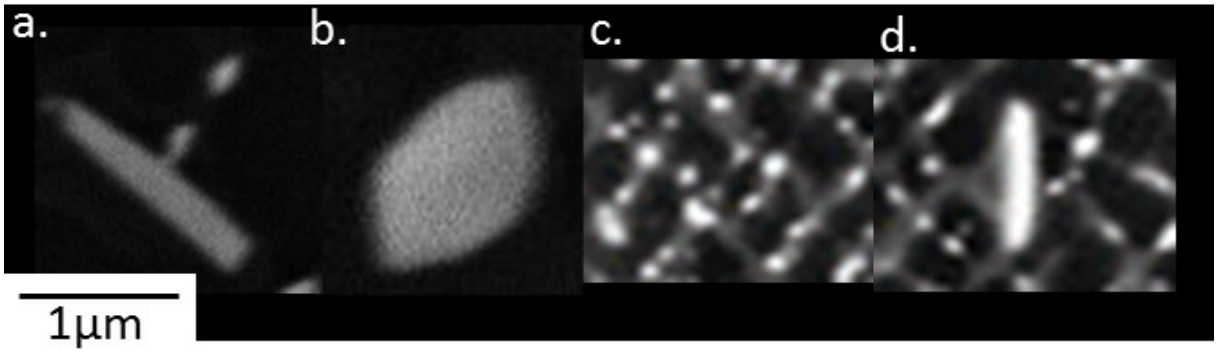


Figure 219: Carbide type phases local to zone 2

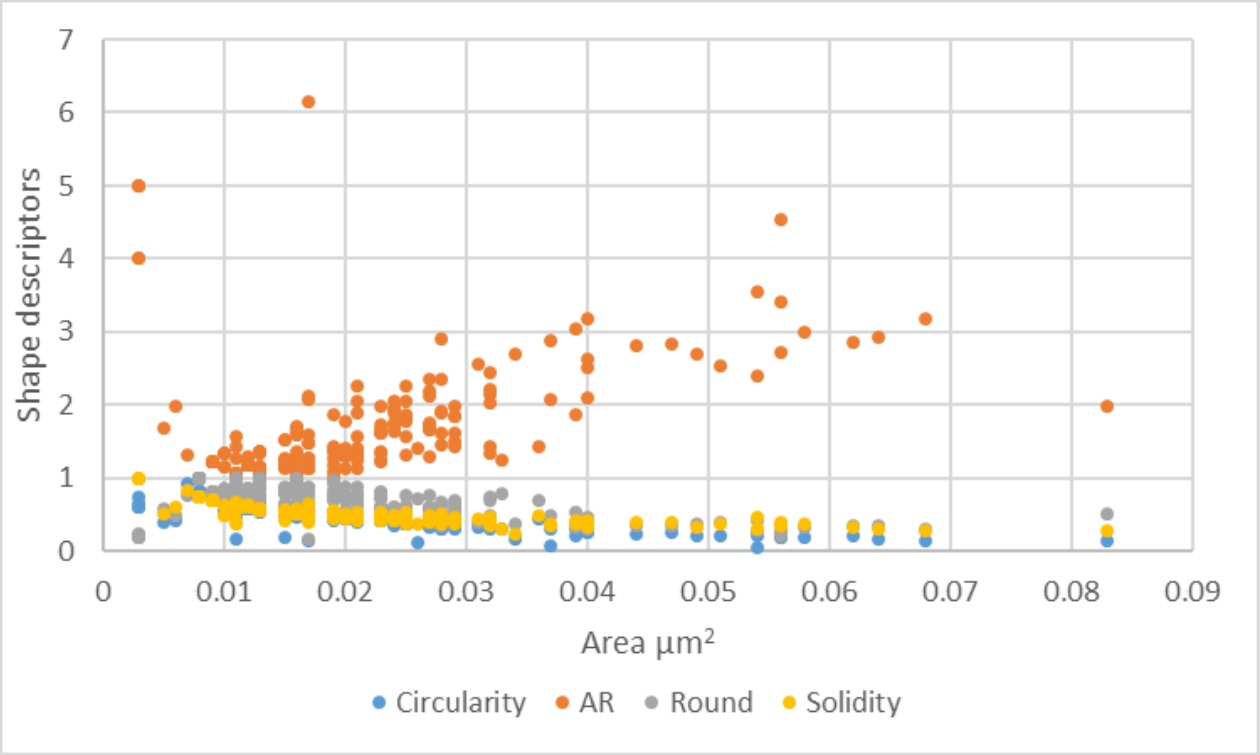


Figure 220: Shape descriptors vs Area of identified carbide type phases in zone 2

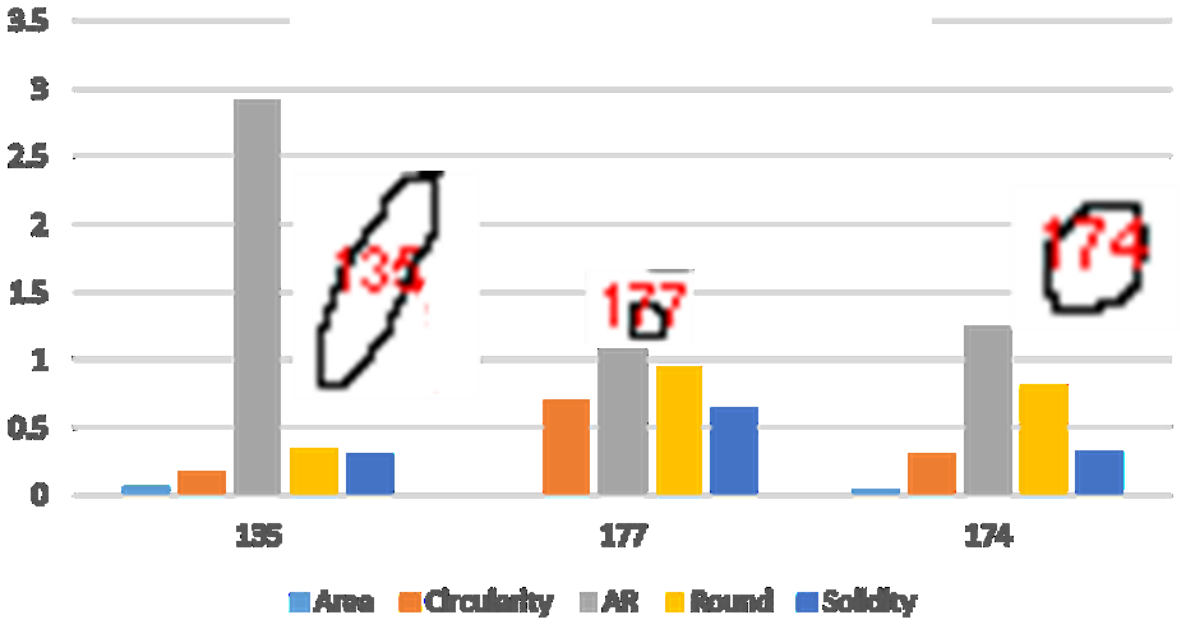


Figure 221: Three carbide type phases unique to zone 2

1.4.1.3. Zone 3

Zone 3 is the largest of all the zones with the carbide type phases spanning 100 µm with different orientations and sizes. Most of the carbide type phases in zone 3 are needle shaped, in literature these are referred to as "Chinese script"[30]. The average area of carbide type phases in zone 3 is 0.018, circularity 0.531, aspect ratio 1.47, roundness 0.76, solidity 0.55 and the number of particles in the 238 µm^2 area is 62. Figure 222 - Figure 225 show the distrubution of carbide type phases local to zone 3.

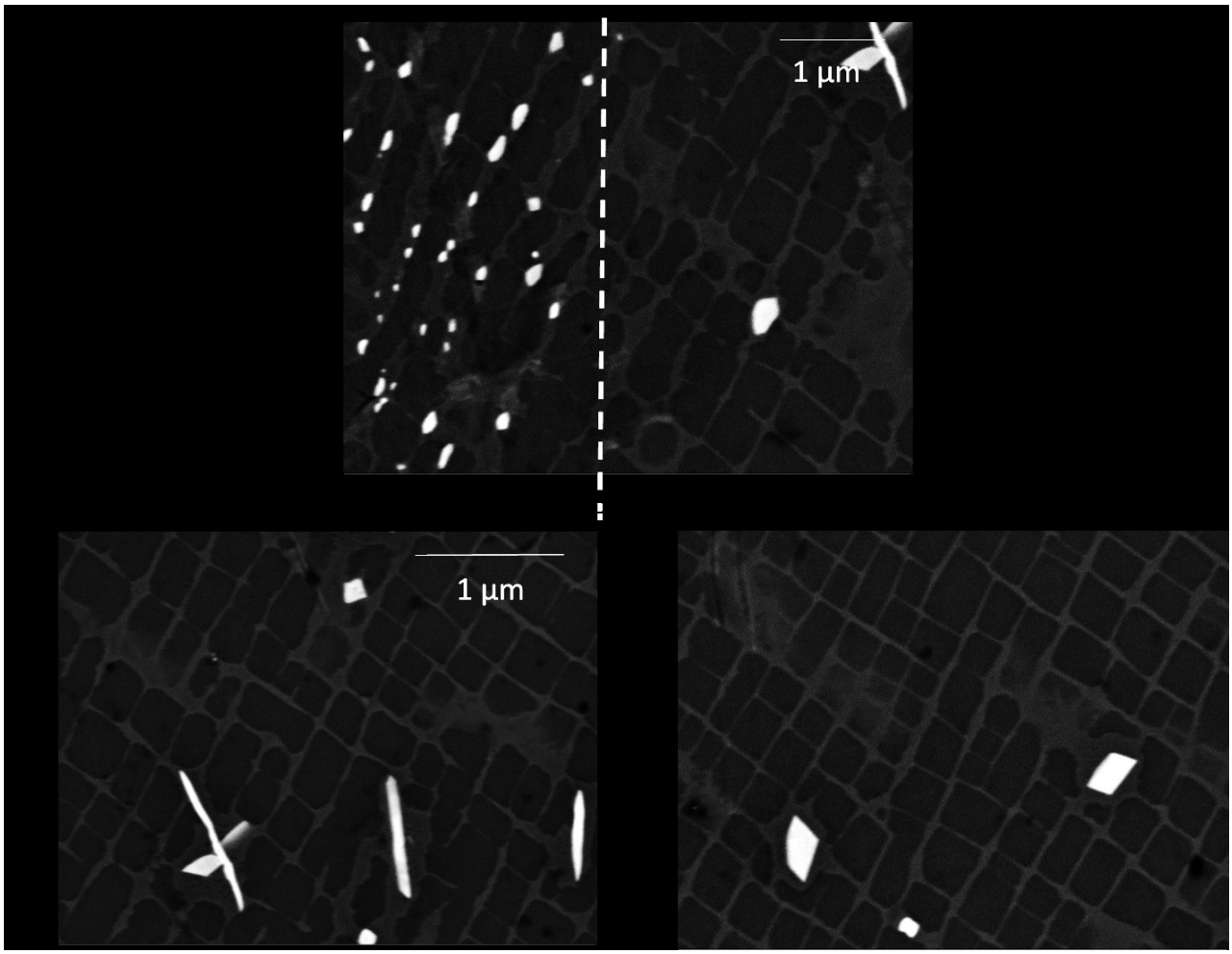


Figure 222. 45µm^2 area maps of regions in zone 3

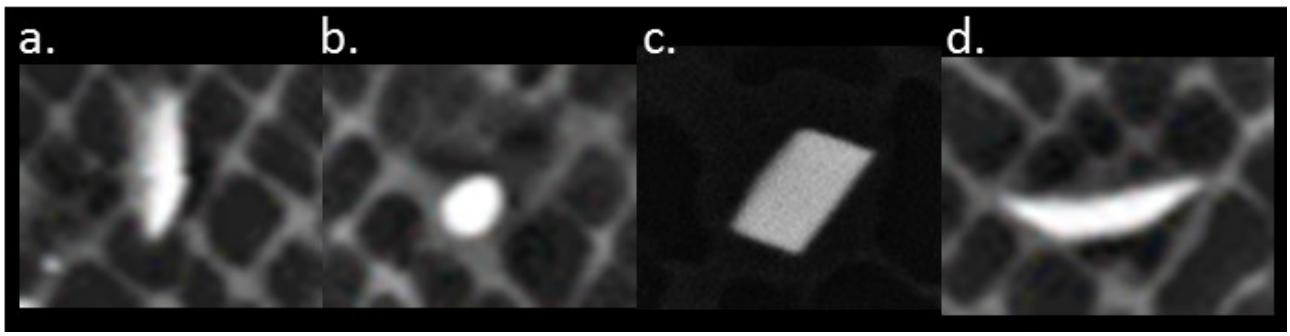


Figure 223. Carbide type phases local to zone 3

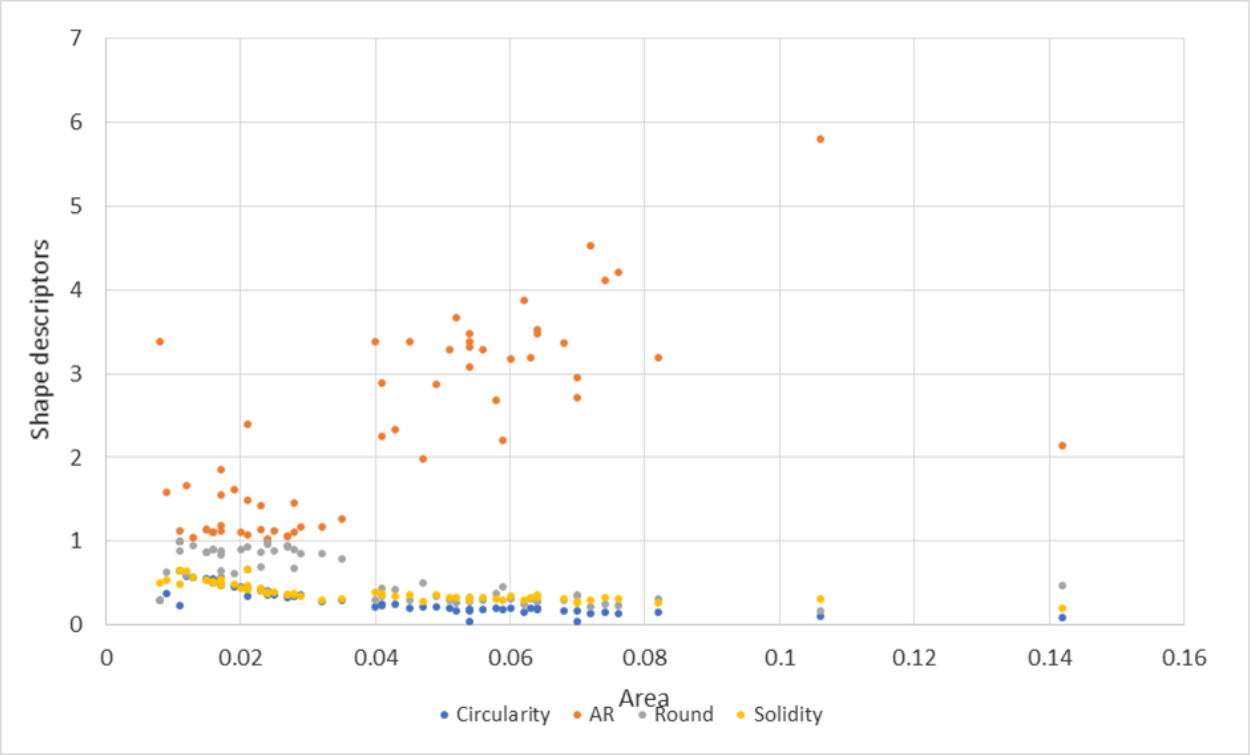


Figure 224: Shape descriptors vs Area of identified carbide type phases in zone 3

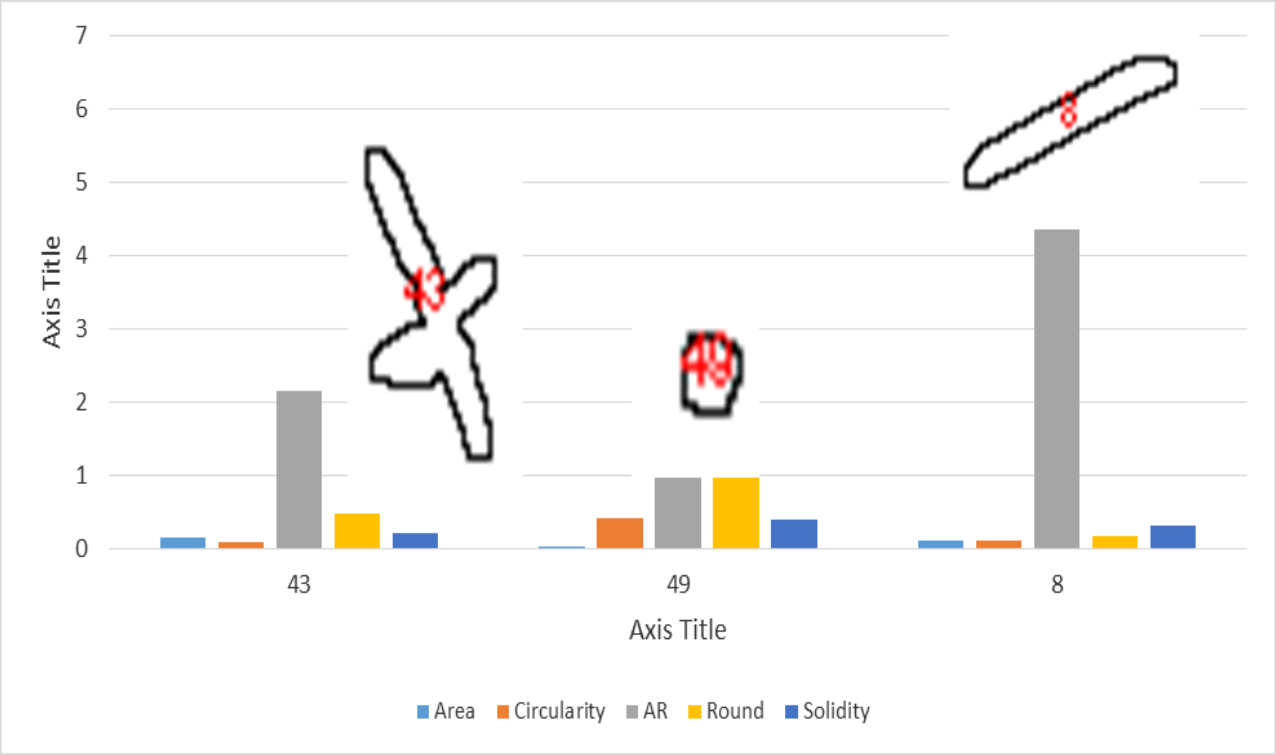


Figure 225. 4 Carbide type phases unique to zone 3

1.4.1.3. Carbide area fraction / number density

The area fraction of the carbide type phases and associated error margins, as a function of the distance from the perimeter edge, are a useful metric. The form of the carbide type phases can change,

depending on the area within the carbide type phase, rich region of the sample, therefore an average model of carbide type phase, population can be built based on several areas throughout the outer rim of the sample. The number density / area fraction per unit area can also be characterised in the carbide type phase, rich area, through its segmentation into zones. This is shown below in Figure 234.

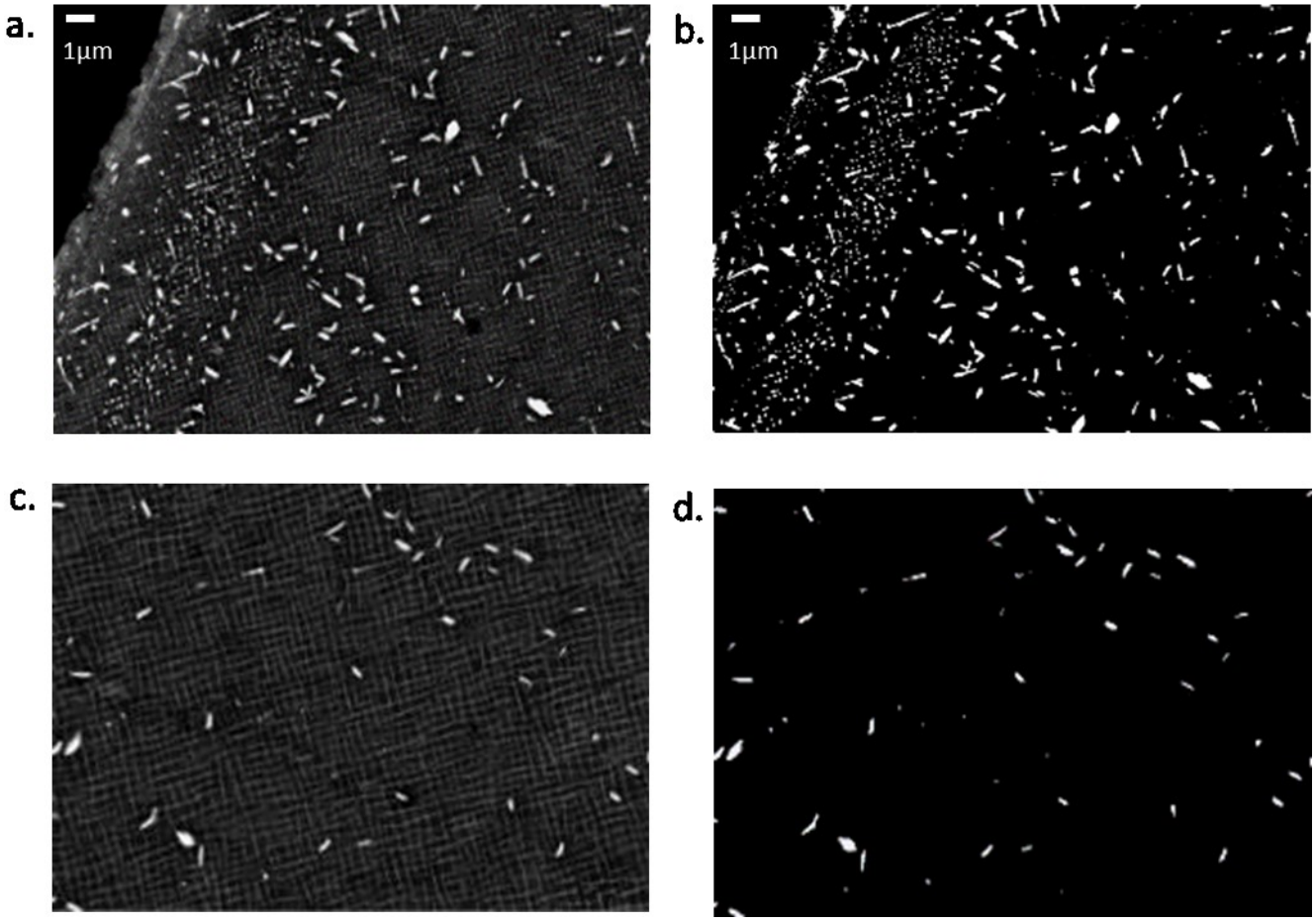


Figure 226: Micrographs of carbide type phase distributions in CMSX-4. The sample edge represents 0 (a) BSD image of carburised CMSX-4 0-40 µm (b) Black & White threshold version of micrograph (a) for image analysis of carbide type phase area fraction (c) BSD image of carbide type phase distribution 40-80 µm (d) Black & White threshold version of micrograph

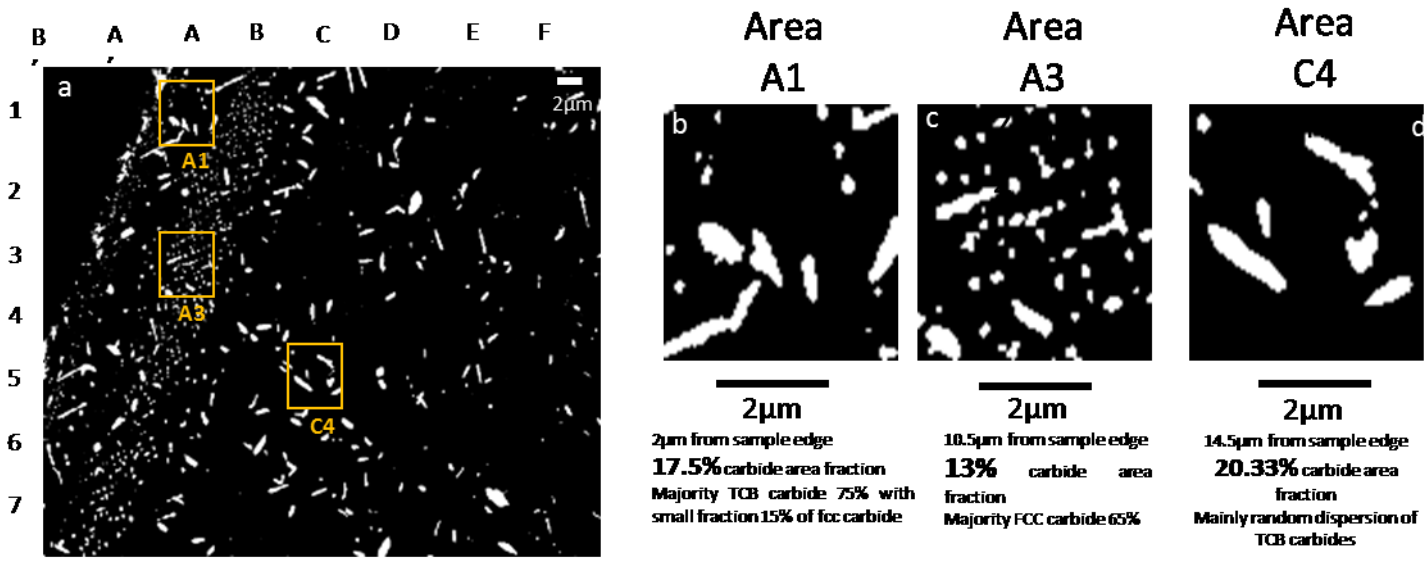


Figure 227: Black (bulk) & White (carbide type phase) threshold of CMSX-4 0-40 µm segmented into sections. Figures (b-d) represent 16 µm² areas within a specific region (b) 17.5% carbide type phase, area fraction in in zone 1 (c) 13% carbide type phase area fraction in zone 2 (d) 20.33% carbide type phase area fraction in zone 3.

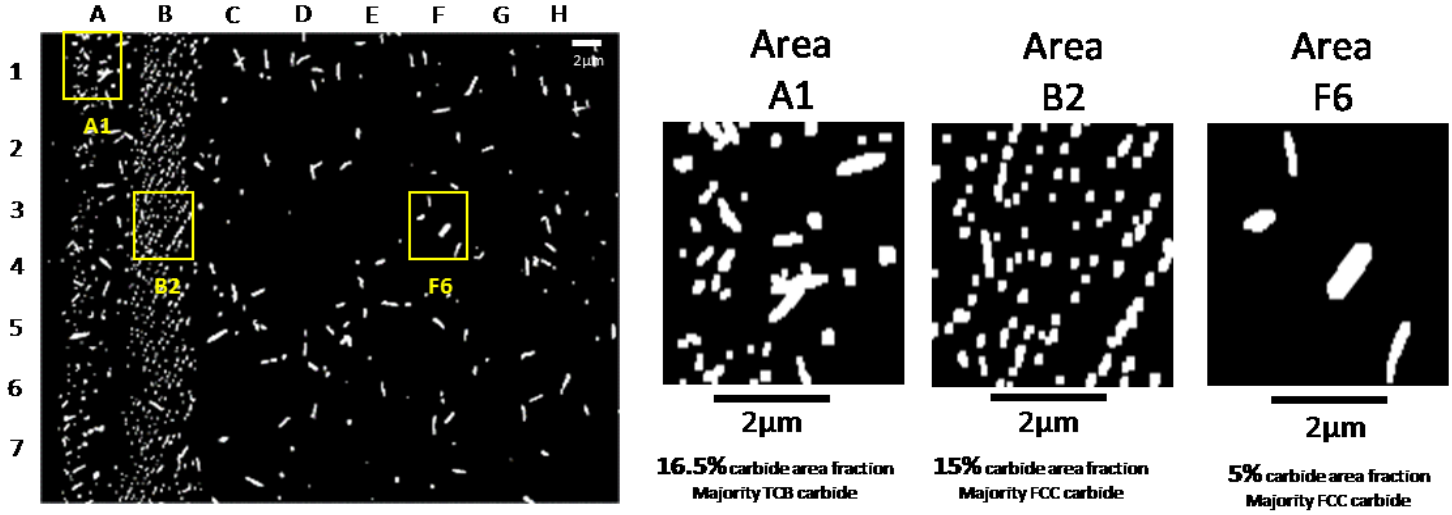


Figure 228. Black (bulk) & White (carbide type phase) threshold of CMSX-4 0-50 µm segmented into sections. Figures (b-d) represent 16 µm² areas within a specific region (b) 16.5% carbide type phase area fraction in in zone 1 (c) 15% carbide type phase area fraction in zone 2 (d) 5% carbide type phase area fraction in zone 3

Analysing different areas of the carbide type phase, rich perimeter is useful to build up error statistics for the microstructure as the structure and layout of the carbide type phase, changes depending on area, within the carbide type phase, rich region. This is particularly important for zone 3 which extends ~100 µm. The area in zone 3 is 9 times bigger than zones 1 & 2 combined.

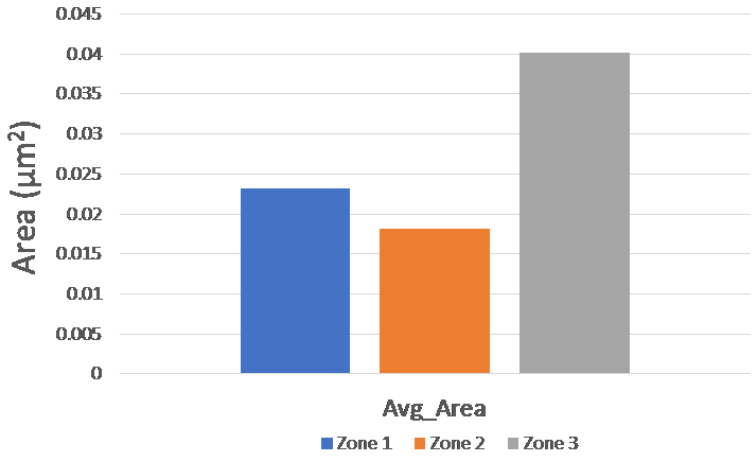


Figure 229: Average area of carbide type phase, in zones 1-3

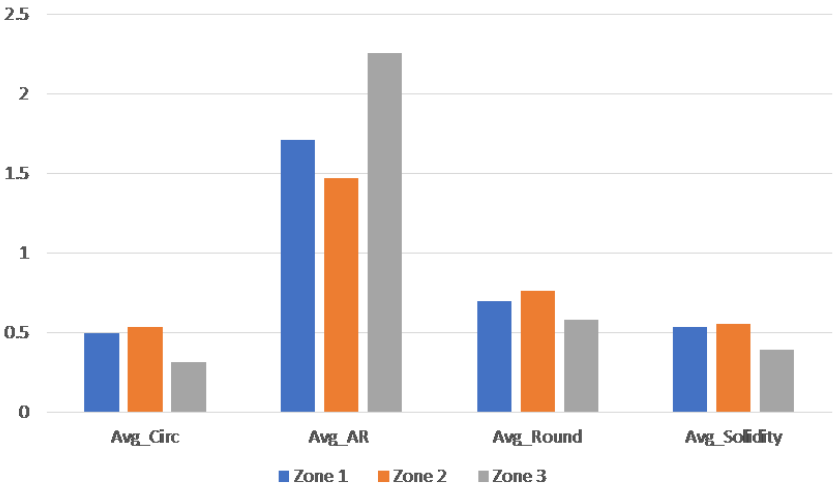


Figure 230. Average shape descriptors across zones 1-3 with respect to section, Shape descriptors paGE120

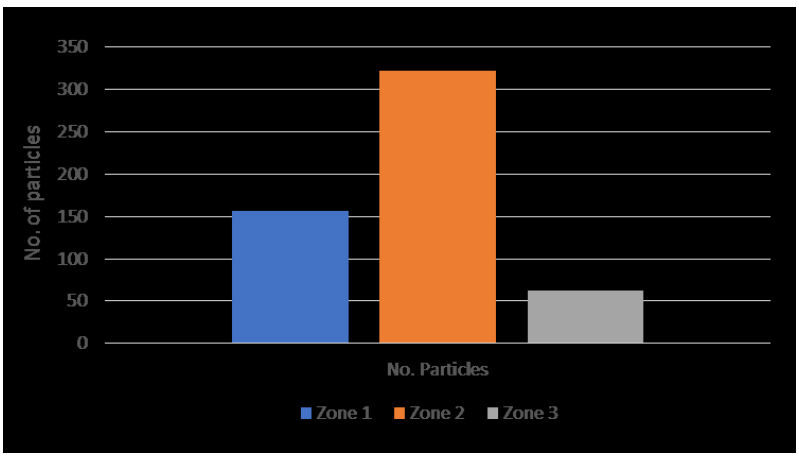


Figure 231: No. of particles in representative areas zones 1-3

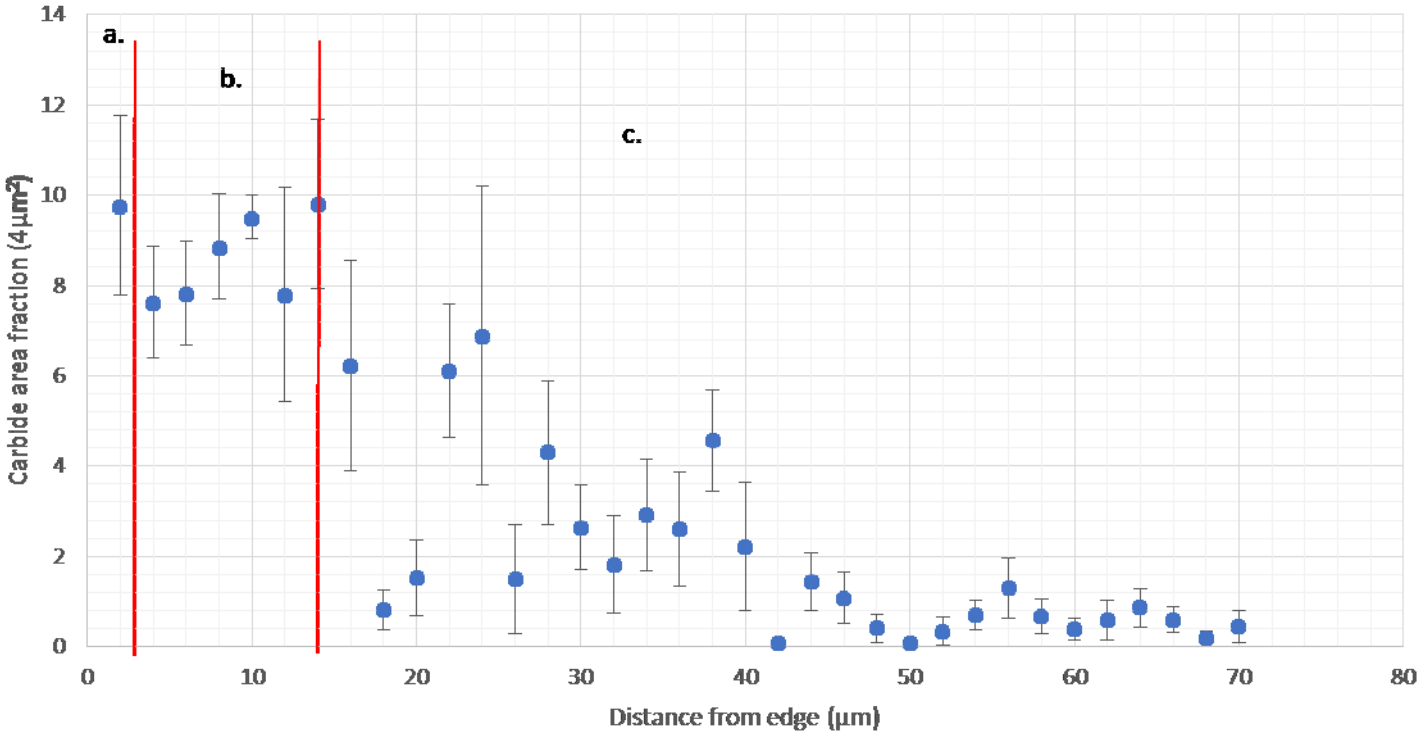


Figure 232: Carbide type phase, area fraction vs distance from the edge carburised CMSX-4 (a-c) represents zones (1-3) respectively

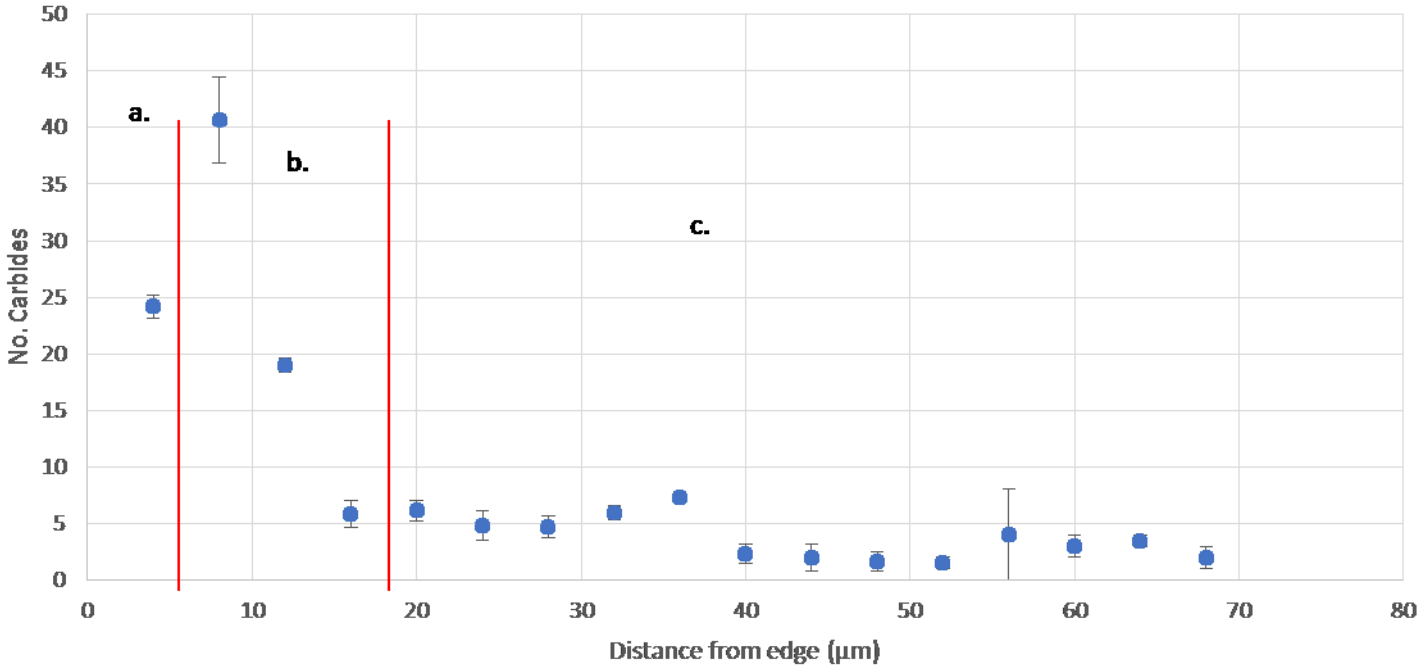


Figure 233: Carbide type phase, number density vs distance from the edge carburised CMSX-4 (a-c) represents zones (1-3) respectively

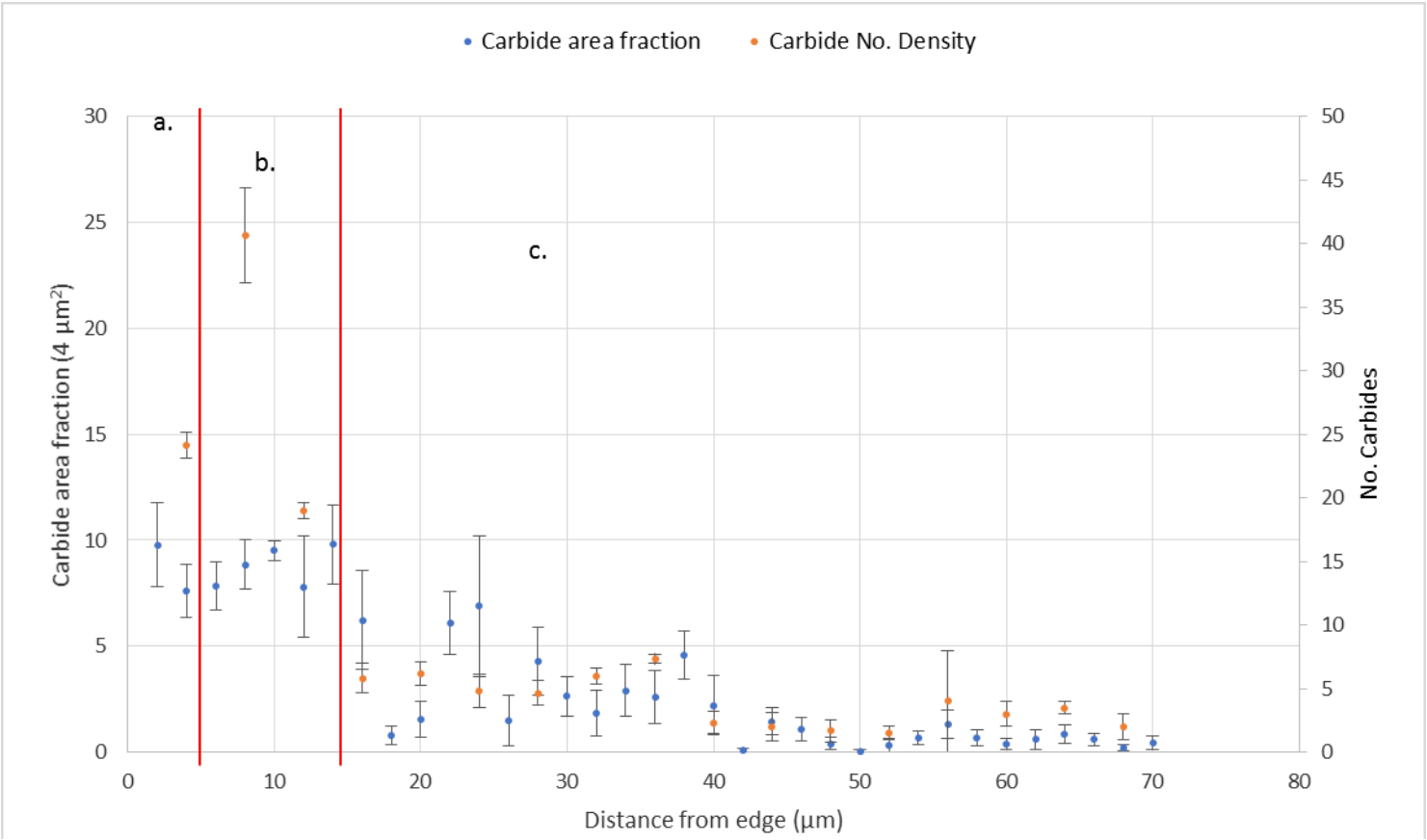


Figure 234. Carbide type phase, area fraction / no. density vs distance from edge

8.5.4. Summary – Characterisation of carbides

The carbide type phase, rich region in CMSX-4 can be segmented into three micro zones based on the character of the carbide type phases and distance from the perimeter edge. Zone 3 has the highest average area of carbide type phase, zone 2 the smallest. The same trend occurs with the average aspect ratio of the carbide type phases, with zone 3 having the highest aspect ratio and zone 2, the smallest. Zone 2 has the highest number density of carbide type phases and zone 3 the lowest. It can be concluded that zone 3 has majority TCP phase and the character of the carbide type phase, changes as a function of distance. Figure 235 below, shows a compounded graph illustrating carbide type phases unique to each zone, carbide type phase area fraction / no. density vs distance from the edge of the CMSX-4 sample.

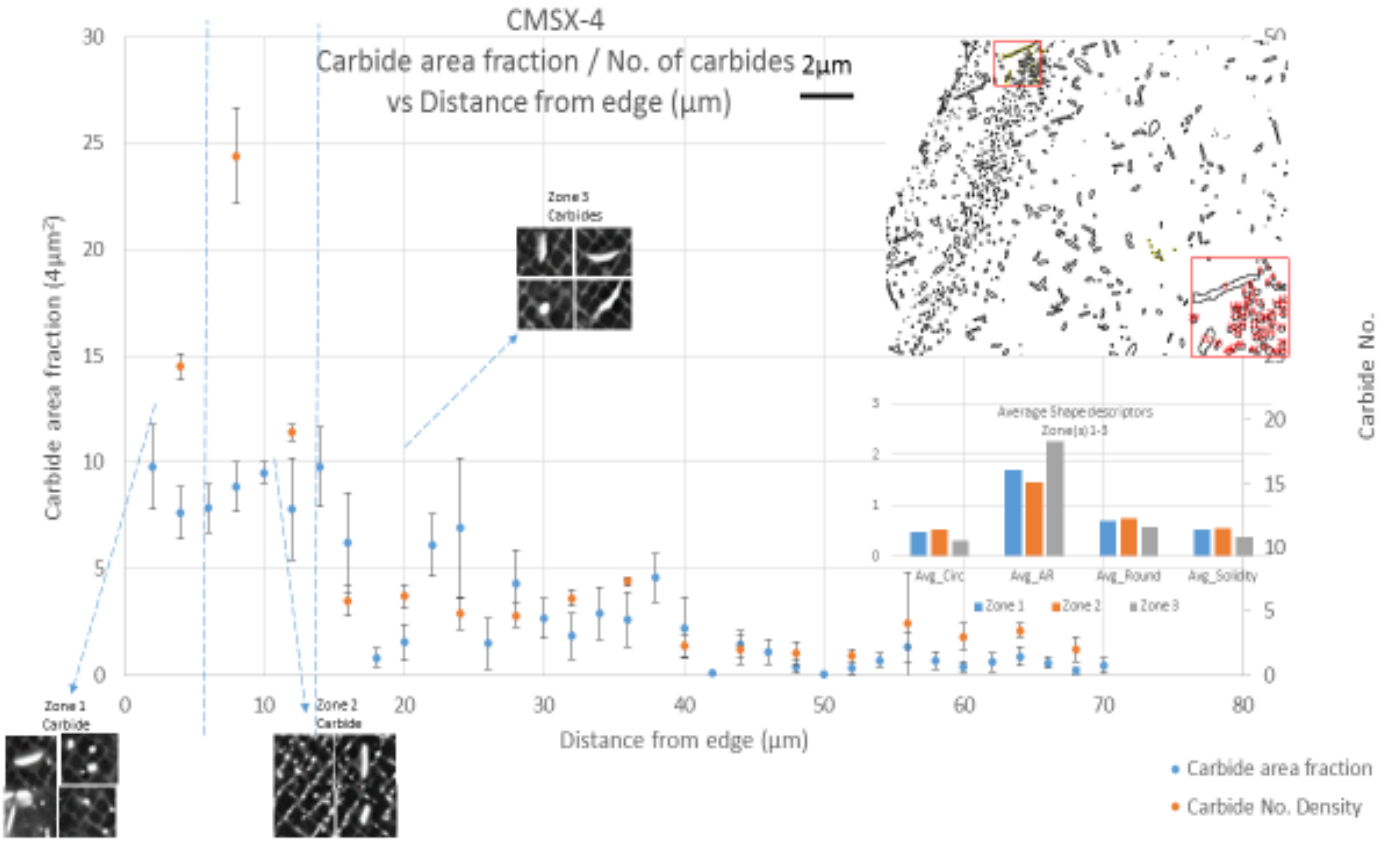


Figure 235: graph illustrating carbide type phases unique to each zone, carbide type phase area fraction / no. density vs distance from edge

8.6. Carbide zones & energy dispersive spectroscopy

Section 8.5, Characterisation of carburised CMSX-4, covered the microstructure of the carburised CMSX-4 alloy, segmented into zones and examined the carbide phase type, number density and area fraction. This section will examine the elemental concentrations of the alloy as a function of distance, zone and carbide type phase, through EDS.

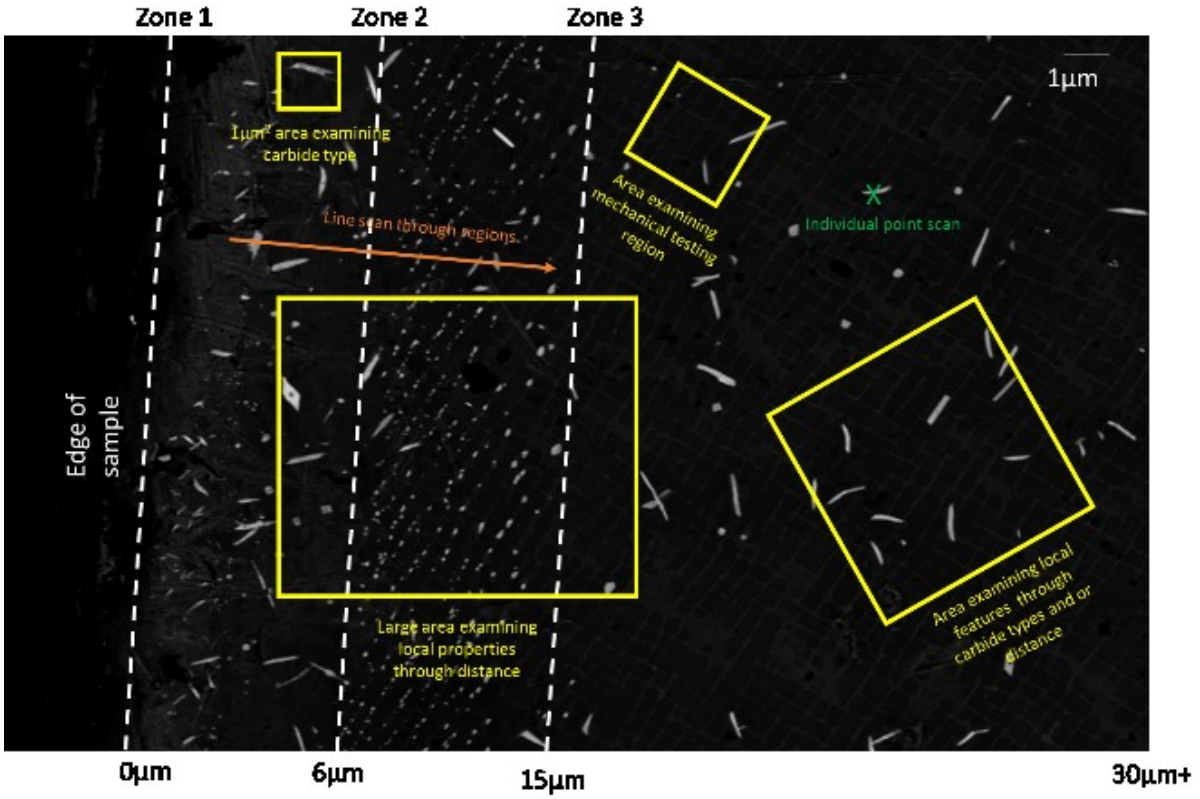


Figure 236: Micrograph of carburised CMSX-4 in the carburised rich region, illustrating the different EDS measurements used to establish the constituent elements local to each, area, point, or line segment.

Figure 236, illustrates the different EDS scanning methods that can be used to establish elements local to each region. For example, a line scan can be used to measure the drop or increase in concentrations through zones 1 to 3, as shown in figure 203. An area map, can be used to identify large areas, figure 239, individual carbide type phase, figure 237 or regions used for micropillar / micro indentation experiments.

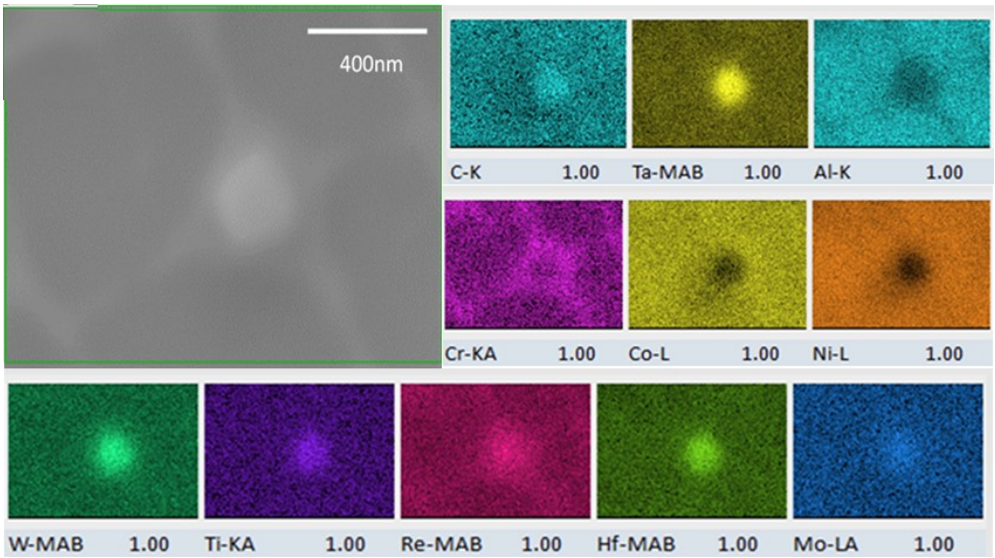


Figure 237: EDS Map scan of a Zone 3, faceted carbide type phase, in a γ channel, indicating that W,Ti,Re,C,Ta,Mo and Hf are carbide type phase stabilisers. Co, Ni and Al are non-carbide type phase stabilisers.

8.6.1. Carbide rich region

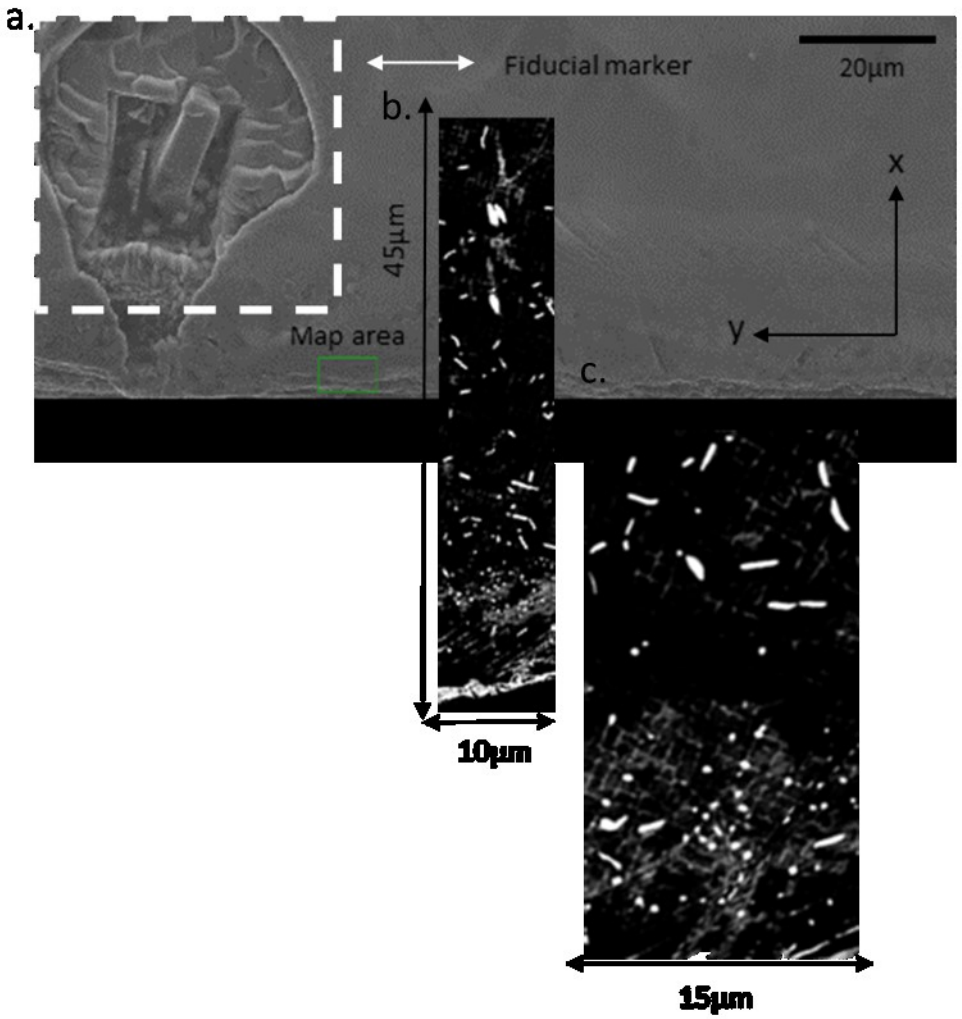


Figure 238: EDS map scan area, showing both x and y distances in BSD (a) Fiducial marker used to identify the scanning area (b) a BSD image of a 10 x 45 µm² area, illustrating the different clusters of carbide type phases (c) a 15 x 30 µm area

An experiment using 455 µm² area map scans taken along the x direction, as shown in figure 238, measured clusters of carbide type phases local to an area. The trends as shown in figure 239, exhibit a decrease in Ni, Co, Cr and an increase in Ta, Hf, Ti, W. There is also a sharp drop in Ni which starts around the 18 µm mark and is initially picked up by C, Al and Ti. Then as Ni begins to drop further, there is a strong increase in C, W and Ta, a smaller increase in Hf and Al, followed by a strong drop in Ti and Cr. All elements begin to flatten out around the 50 µm mark. This is shown graphically in figure 239 and figure 240.

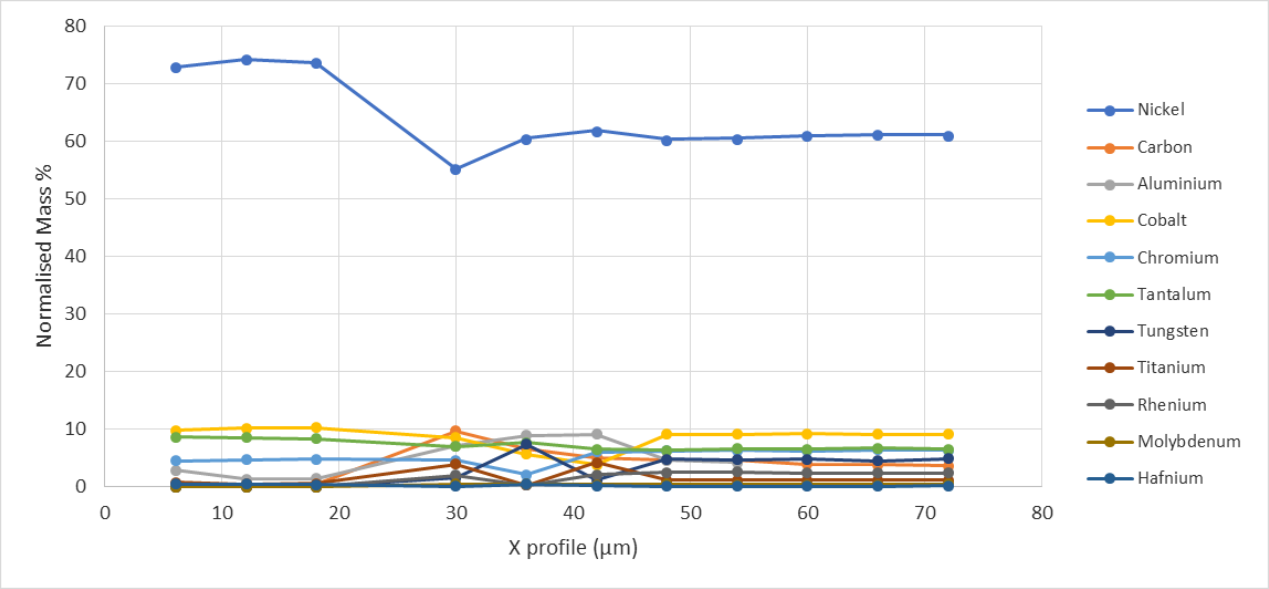


Figure 239: EDS maps taken across x profile from 5 µm to 70 µm indicating drops and peaks in alloying elements

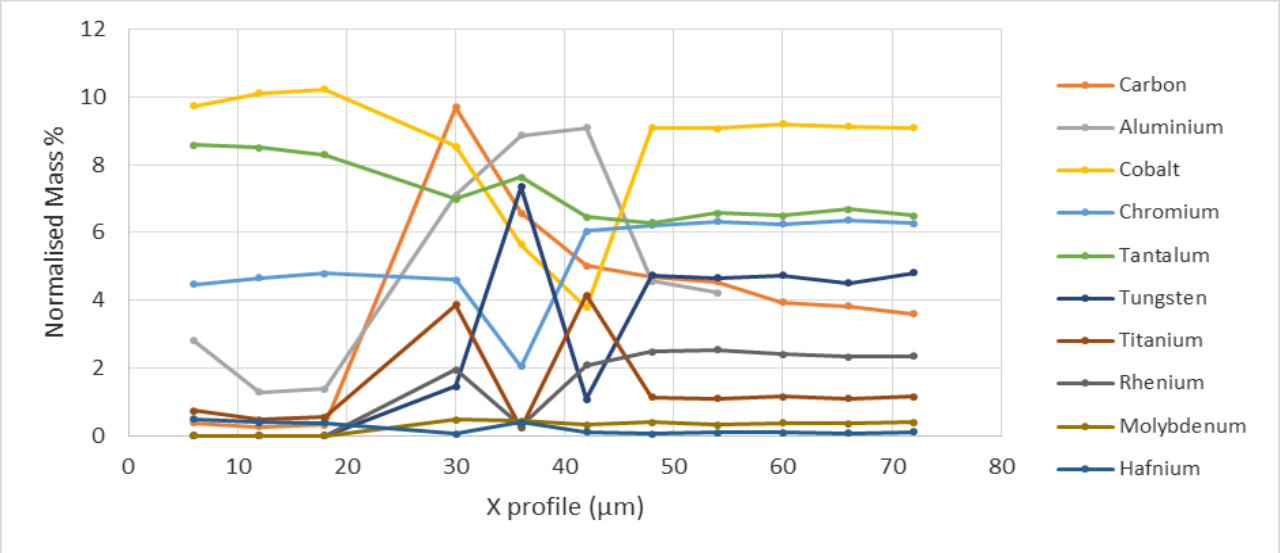


Figure 240: EDS maps taken across x profile from 5 µm to 70 µm indicating drops and peaks in alloying elements, neglecting Ni which represents the majority of the normalised mass %.

The mapping area distance profile, as shown in figure 239 and figure 240 validate, that the normalised mass % of certain elements increases in response to a drop-in Ni through long range (bulk) distances, as shown in figure 203. As the maps are quite large and include clusters of carbide type phases and bulk microstructure, a more local scan specific to each region and carbide type phase is needed to establish how the elements segregate, figure 237 .

8.6.2. Segregates zones 1-3, within the carbide rich region

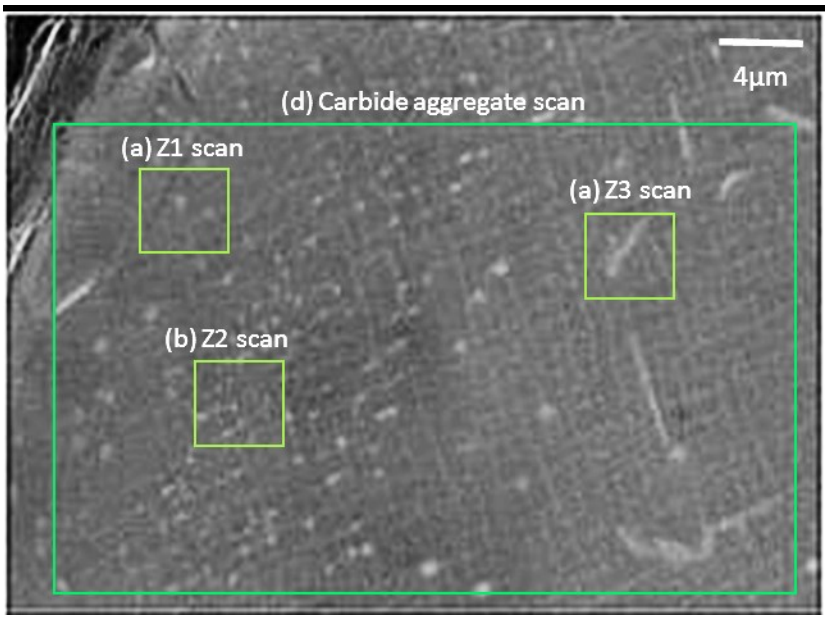


Figure 241: 850 µm² map area covering zones 1-3

The results in figure 239 and figure 240 when combined with earlier results in figure 203-7, indicate that Ti, Hf, W, Ta, C constitute the bulk of the carbide type phases and Al, Cr, Ni are depleted in response. The question that arises from this conclusion, is; what carbide zones / carbide type phases contribute to which elements. To do this, an area map of each zone and carbide type phase was taken. Figure 241, shows the area taken from a map scan of the area corresponding to the results in table 23.

Table 23: Area of testing region and respective elemental concentrations, from the aggregate carbide region, zone 1, zone 2 and zone 3 as shown in figure 241

Area	Normalised mass %										
	Ni	Co	Ta	C	W	Cr	Al	Re	Hf	Ti	Mo
Carbide_Agg	55.7	8.38	7.19	7.13	6.25	5.47	4.84	2.35	1.16	1.06	0.48
Z3_Bulk	56.43	9.07	6.93	6.38	6.11	5.14	4.48	2.63	1.13	1.08	0.51
Z2 Bulk	52.07	12.02	8.21	6.43	5.93	5.44	4.83	2.34	1.24	1.02	0.49
Z1 Bulk	56.74	12.47	7.37	6.33	5.37	4.19	3.63	2.00	1.03	0.48	0.38

Table 23 shows the elemental concentrations in the aggregate carbide type phase region, zone 1, zone 2 and zone 3, as shown in figure 241. Zone 2 has the lowest normalised mass % of Ni and highest Hf, which could link to the large number density of carbide type phases in zone 2. Zone 2 could be a direct consequence of a higher average Hf content compared to the other two zones whereby the fine precipitates in zone two are indicative of high surface energy structures formed via a high rate as supported by literature. Zone 3 has the highest amount of Ti, supporting the needle like carbide type phase forming TCP crystallography[17].

8.6.3. Carbide type

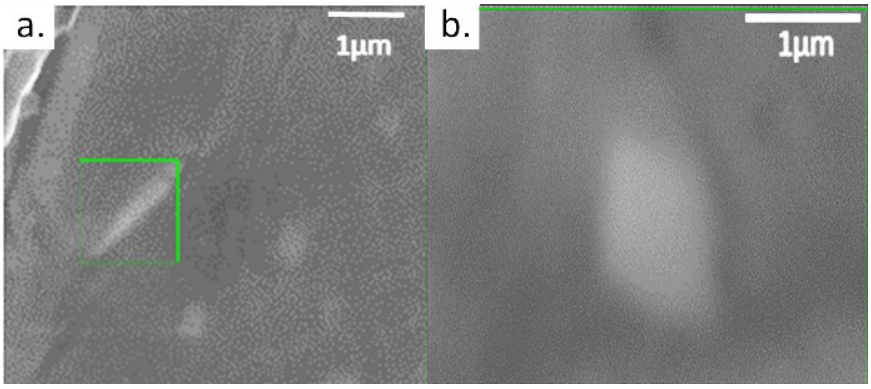


Figure 242: Zone 1 carbide type phase (a) lenticular carbide type phase (b) Circular / faceted carbide type phase

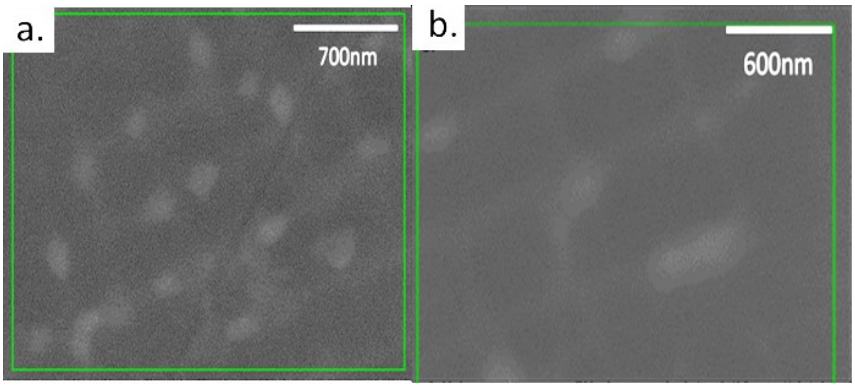


Figure 243: Zone 2 circular carbide type phase , inhabiting the ϒ and ϒ' (a) 35k magnification (b) 40k magnification

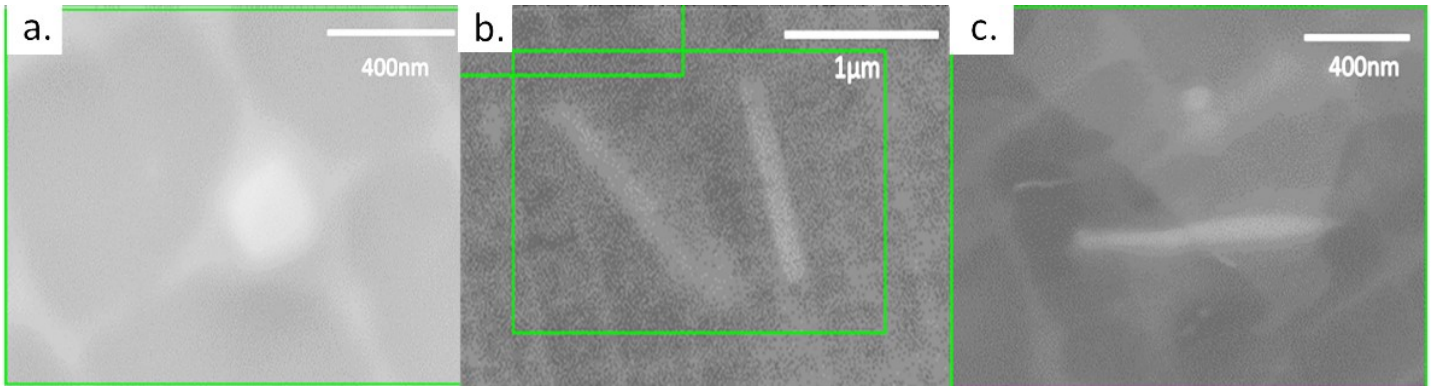


Figure 244: Zone 3 carbide type phase (a) Circular / faceted carbide type phase inhabiting a ϒ channel

The carbide type phase in the CMSX-4 alloy appear as either circular or lenticular, needle like shaped carbide type phase. Figure 242, figure 243 and figure 244 show the SEM images prior to map scans over the different carbide type phases both local to zones 1-3 respectively.

Table 24: Carbide type phase local to Zone 1-3 respectively and resultant elemental concentrations in wt%

Carbide type phase	C	Al	Ti	Cr	Co	Ni	Mo	Hf	Ta	W	Re
Z1 Lenticular	5.23	4.33	2.17	7.57	5.88	52.58	0.70	0.00	9.79	8.56	3.19
Z1 Circular	11.87	2.04	2.32	4.81	7.46	53.10	0.66	0.05	10.82	4.51	2.36
Z2 Small circular	8.67	5.05	1.16	5.8	7.24	55.82	0.52	1.14	6.35	5.82	2.42
Z3 Lenticular	6.52	4.39	1.26	6.35	8.25	53.43	0.47	1.33	7.65	6.2	4.16
Z3 Circular	5.4	4.99	1.26	6.11	8.75	55.37	0.64	1.12	7.56	6.39	2.41

Starting with the Zone 1 carbide type phase, it becomes clear that the lenticular carbide type phase have a preference for different elements when compared to the smaller spherical carbide type phase. Similar trends occur for both scans in Zone 2, suggesting that lenticular carbide type phase contain more Hf and Ti. This was validated by the results from zone 3 carbide type phase.

8.6.4. Summary – Carbide zones & chemical analysis

To summarise, smaller spherical carbide type phase believed to be fcc structure and thus coherent with the ϒ/ϒ' microstructure contain more Mo. Long thin carbide type phase believed to be the embrittling intermetallic TCP phase, comprised of one main metal cation occupying the Kasper polyhedral contain more Ti, Hf and Re. Hf has been found to increase the carbide forming temperature in Ni alloys[107]. Hf can change the morphology of the carbide type phase from fine and regular shaped to more nodular indicative of group 3 carbide type phase.

8.7. Mechanical properties of carburised CMSX-4

It is well documented in literature[200,75,201] that the strengthening mechanisms at high[48] and low temperatures[202] in the ϒ/ϒ' Ni superalloy microstructure are derived from the ϒ' precipitates. The ϒ' precipitates derive from Ni, Al and Ti additions which form the $L1_2$ type structure[72] with an $Ni_3(Al,Ti)$ composition [11]. Carburised CMSX-4 contains additional precipitates in the form of carbide type phase as seen in, figure 238, the carbide type phases contain Ti, Ta, W, Hf and Re. EDX analysis reveals that the carbide type phase incorporate these elements by extracting from the bulk microstructure. This extraction can be deleterious to mechanical properties and will be tested below.

The precipitate rich region in CMSX-4 extends 120 μm from the perimeter edge of the sample and the elemental concentration as a function of distance varies as we move from the perimeter edge into the bulk material, figure 239 and figure 240. The mechanical behaviour of the carburised CMSX-4 microstructure and precipitates can be tested on the microscale via micropillars and validated by microindents. The comparison between EDS and mechanical properties will be examined in the discussion section.

8.7.1. Micropillar testing

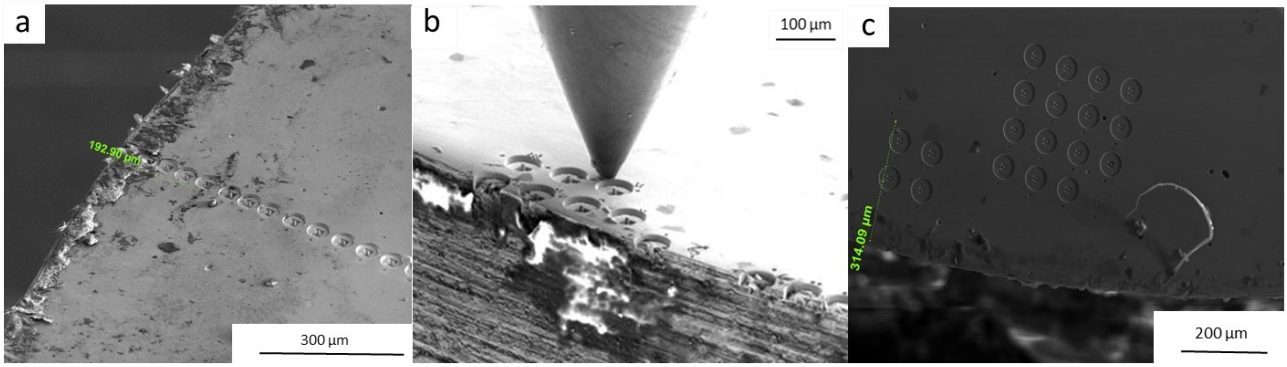


Figure 245: Micropillar testing areas on CMSX-4 through different data sets(a) Pillars running from the perimeter edge through to the bulk (b) Micropillars in the same orientation within the carbide type phase rich region exclusively (c) Micropillars at distances exceeding 120 µm I.e. away from the carbide type phase rich region.

The first set of mechanical tests performed on carburised CMSX-4 were micropillar experiments. Pillars in the same orientation were compressed, in several data sets at different regions as shown in figure 245, and the yield point was measured as a function of distance from the perimeter edge, figure 246 and figure 247. The results indicate that mechanical properties in the carbide type phase rich area are different from the bulk. The relationship between mechanical properties, zones and carbide type phase characteristics are examined below .

8.7.1.1. Distance x profile

Micropillars with areas ranging from 20-25 μm^2 were placed at regions extending from the outer edge of the sample well into the bulk. The pillars in data sets 1-4 were aligned to have the same orientation. The pillars were compressed in load control at a constant strain rate and the mechanical data measured.

Table 25: Yield point (Y_p), hardening rate (H_r), and unloading modulus vs distance for the different data sets testing the mechanical response as a function of distance through the carbide type phase rich (0-120 µm) zone in CMSX-4

Dataset	Pillar	Distance (µm)	Yp (MPa)	Hr (MPa)	Modulus (MPa)
1 450–550 µm	1	450	1144	4639	45699
	2	500	1053	3564	46530
	3	550	986	3494	46421
2 90-750 µm	4	89	1151	2793	30143
	5	152	1036	3313	27517
	6	215	1000	2802	28021
	7	633	970	4233	33499
	8	685	940	4526	34317
	9	748	945	3340	29788
3 17–96 µm	10	17	983	2630	36097
	11	25	850	4140	43895
	12	44	940	2863	32861
	13	70	870	3447	32068
	14	85	986	2604	33353
	15	96	960	3620	32536
4 200–450 µm	16	200	955	3096	28622
	17	250	970	3100	32122
	18	300	960	3166	34261
	19	350	950	3217	36824
	20	400	985	3299	38542
	21	450	1100	3328	39874

Table 25, shows the mechanical properties extracted from micro pillars extending 17 – 750 µm from the perimeter edge of the CMSX-4 sample. It was found that the mechanical properties change as a function of distance and begin to stabilise at some distance outside of the carbide type phase rich region. Pillars containing carbide type phase had noticeable differences in yield point, hardening and modulus when compared to pillars with no observable carbide type phase on the top section of the pillar. Pillars

11-13 were carbide type phase containing pillars and the BSD scans of the carbide type phases can be seen in figure 249.

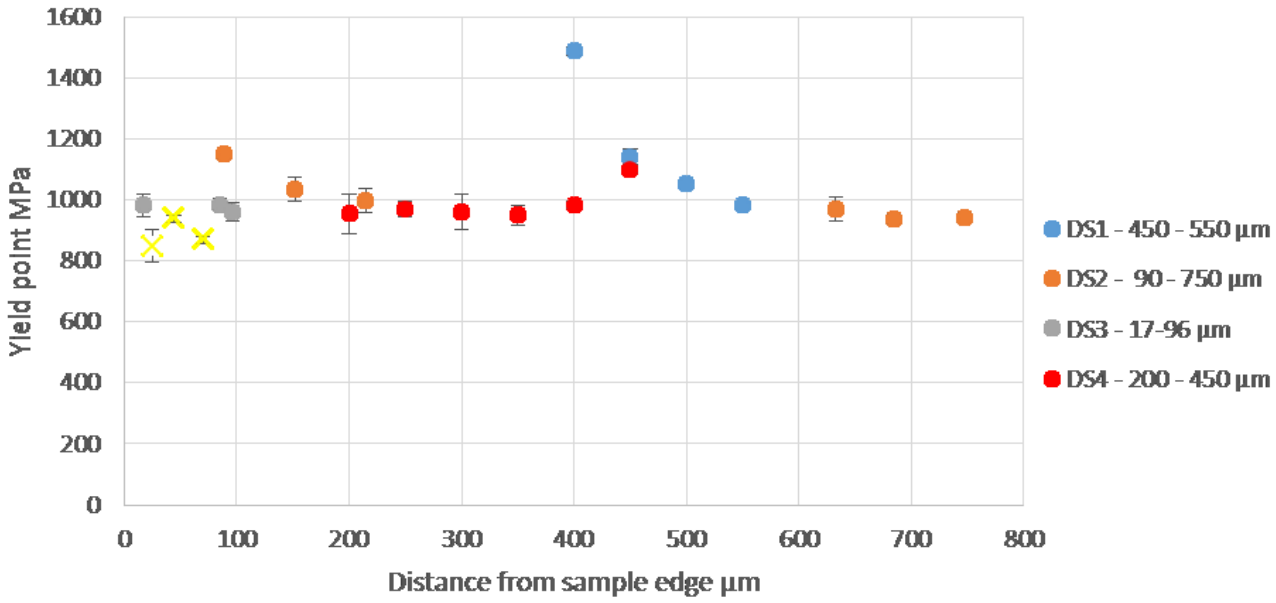


Figure 246: Yield point vs distance from the perimeter edge of the CMSX-4 sample, the yellow points in dataset 3 correspond to pillars with isolated carbide type phase, figure 249.

Figure 246 shows the yield point vs distance from the perimeter edge, ranging from 17 µm – 750 µm, in the CMSX-4 sample. The pillars, located in the diffusion zone had lower yield points, which were on average 20% lower than pillars not found in this region. Pillars placed around 400 µm appeared to have the highest strength and elastic modulus. The elastic modulus of the pillars ranged from 2.7 GPa to 4.7 GPa. The average strain modulus was 2 GPa with a 4.1 GPa maximum (The pillar with the lowest yield point) and a 2.6 GPa minimum (The pillar with the second highest yield point, located the closest to the edge of the sample.

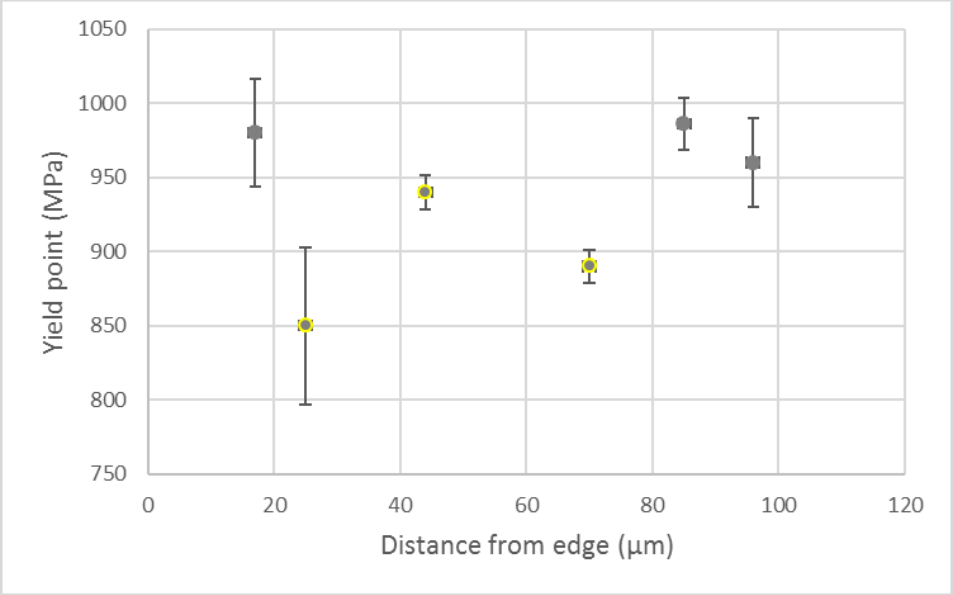


Figure 247: Results from micro pillars located within the carbide rich zone – yield point vs distance from the edge

Micro pillar testing indicated that pillars fabricated within the carbide type phase region had lower elasticity, higher hardening, and a lower yield point than pillars fabricated in the bulk material.

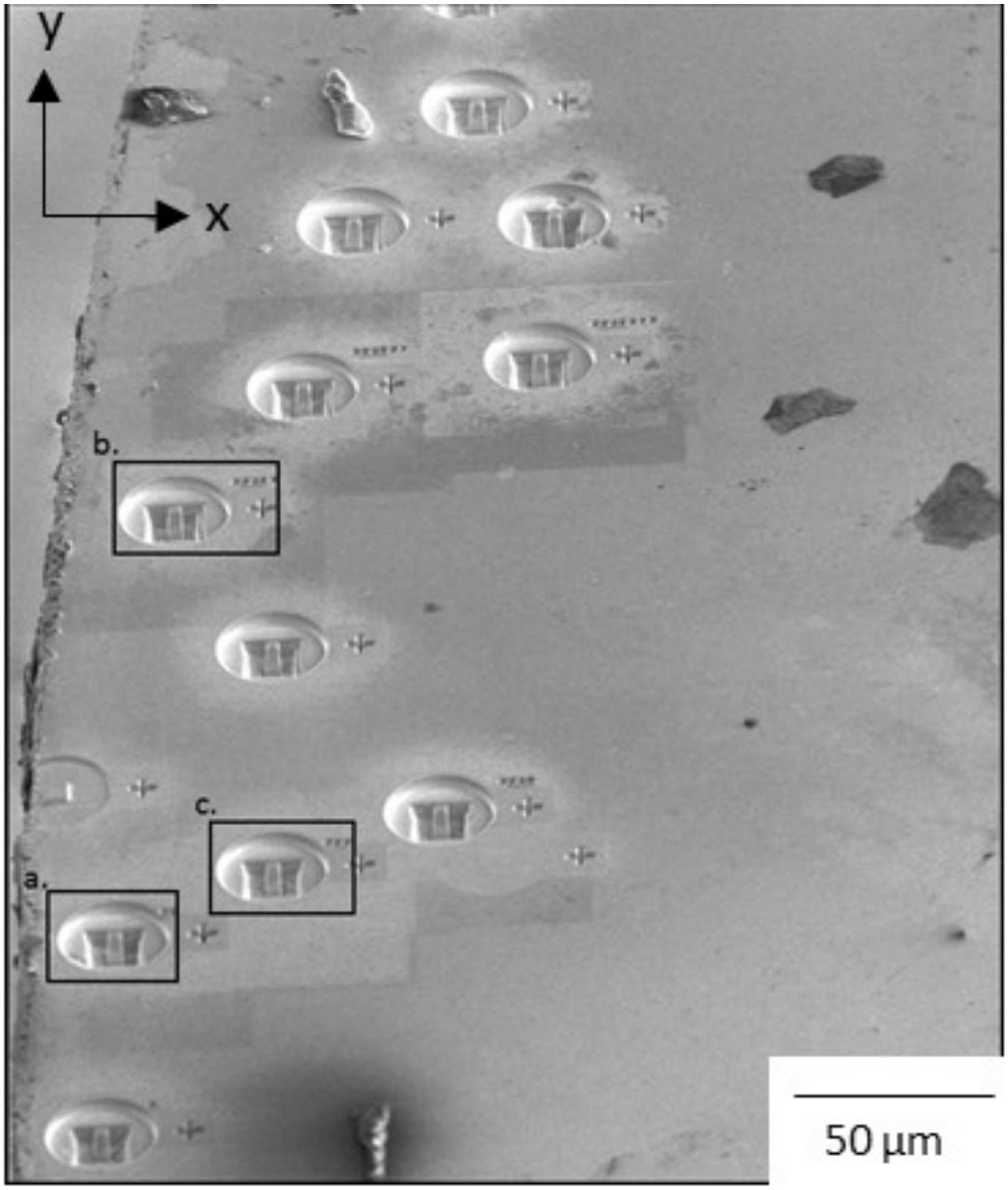


Figure 248: SEM image of pillars tilted to 52° in the carbide type phase rich region in CMSX-4, with carbide type phases isolated pillars, 11,12,13, heighted in a,b,c respectively.

Capturing carbide type phases within pillars is not an exact science and requires a clear set of fiducial markers and BSD images. Figure 248 shows an SEM image of pillars fabricated in the carbide type phase rich region of CMSX-4, tilted to 52°, all the pillars are aligned with the same crystal orientation and have varying distances from the perimeter edge. The pillars highlighted a-c, correspond to the carbide type phases isolated pillars 11-13 as shown in figure 249.

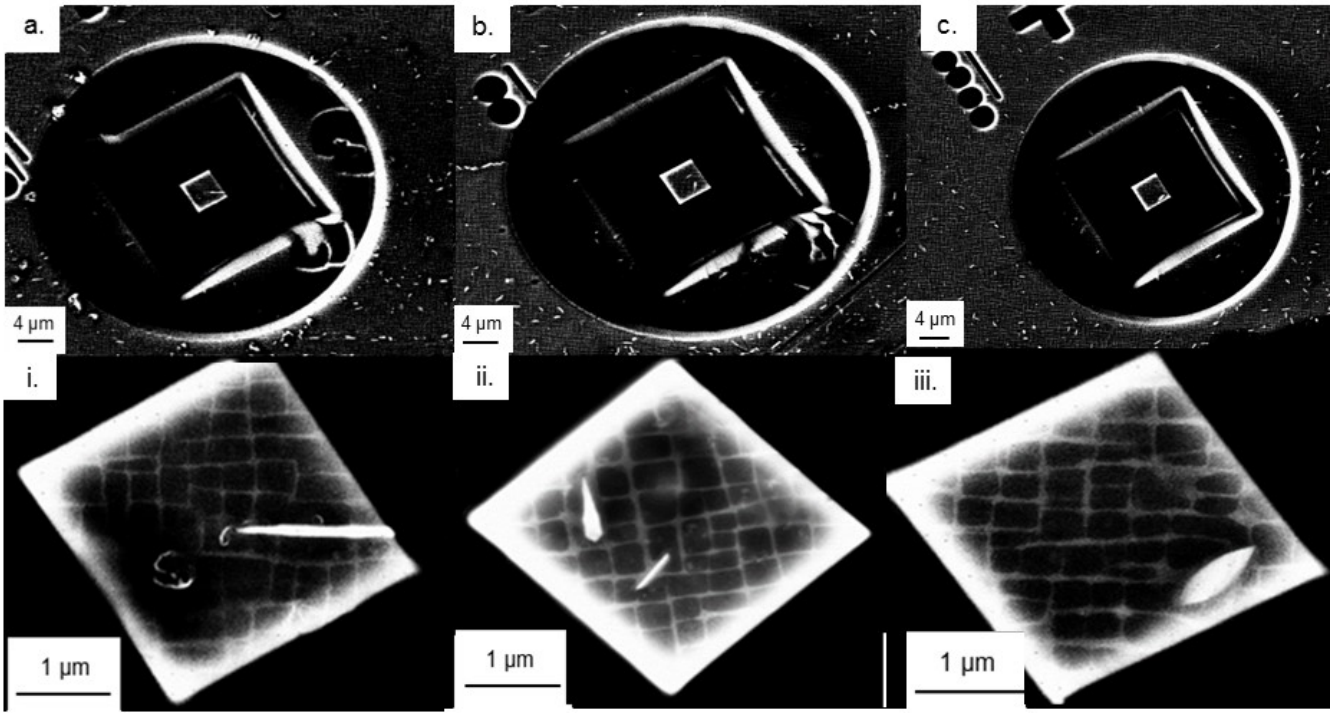


Figure 249: Carbide type phase isolated pillars 11, 12, 13, shown in figures a-c respectively. a-c show birdseye view of the top surface of the carbide type phase isolated pillar and surrounding area. i-iii show the birdseye view of the top surface of the pillar, illustrating the captured carbide type phase.

Figure 249 shows a bird's eye view, BSD image of the carbide type phase isolated pillars 11-13, table 25. When comparing the three carbide type phase isolated pillars; Pillar 11, shown in figure 249 a-i, has a needle like carbide type phase (indicative of TCP phase) that extends through several arrays of ϒ/ϒ'. Pillar 11 has the lowest yield point of the three carbide type phase isolated pillars. Pillar 12, figure 249 b-ii contains two carbide type phases and gave rise to a large stress drop post yield, the other pillars did not experience such an effect. Pillar 12 had the highest hardening rate (4.1 GPa) and also the highest modulus (43 GPa). Pillar 13 contained one large elliptical carbide type phase located at the corner, this pillar experienced the most deformation and had the lowest modulus and a median hardening rate.

The above analysis did not take into account the location of the pillars with respect to carbide type phase zones and carbide type phase characteristics as introduced in section 7.4 (Characterisation of carburised CMSX-4). Pillars 11-13 contained carbide type phases are in zones 2, 3 and 3 respectively. I.e. the data set was not representative of all three zones, figure 250 shows three carbide type phase captured pillars local to zone 1,2 and 3.

8.7.1.2. Shape descriptors and zones

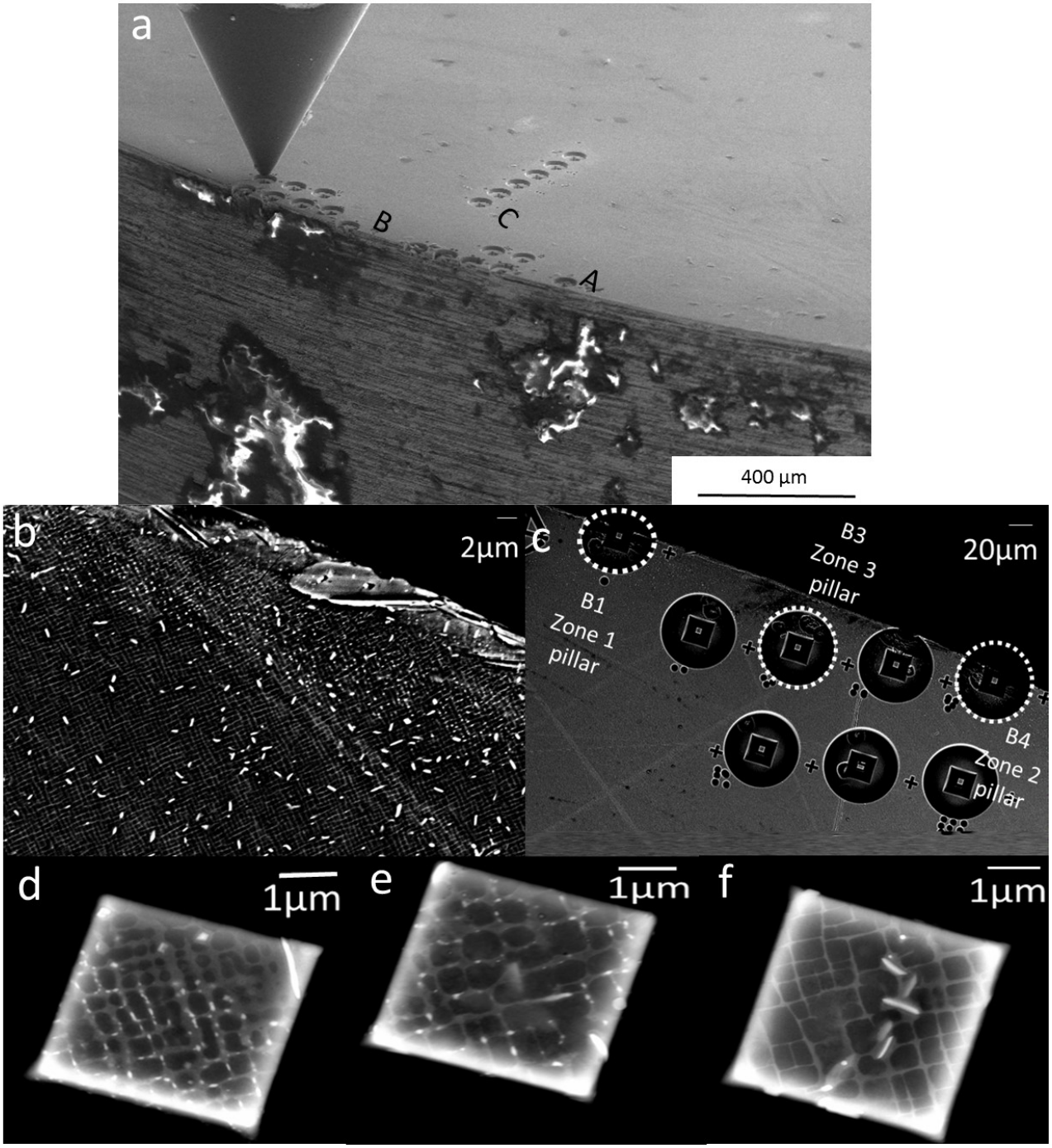


Figure 250: CMSX-4 perimeter edge through to bulk (a) SEM micrograph of perimeter edge through to bulk showing different data sets A,B,C, and flat punch.(b) BSD image of carbide type phase area before pillar fabrication (c) SEM birdsye view of pillars fabricated in the area in b, with pillars B1,B3 and B4 representing carbide type phase isolated pillars fabricated in zones 1-3 respectively. (d-f) BSD bird's eye images of carbide type phase isolated micro pillars in zones 1-3 respectively.

Figure 250, shows fabricated micropillars fabricated in three datasets, illustrating a group of carbide type phase isolated pillars that are local to zones 1-3. The characteristics of the carbide type phases that have been isolated on the top surface of the pillars have been analysed and the results can be seen in figure 251 and table 26.

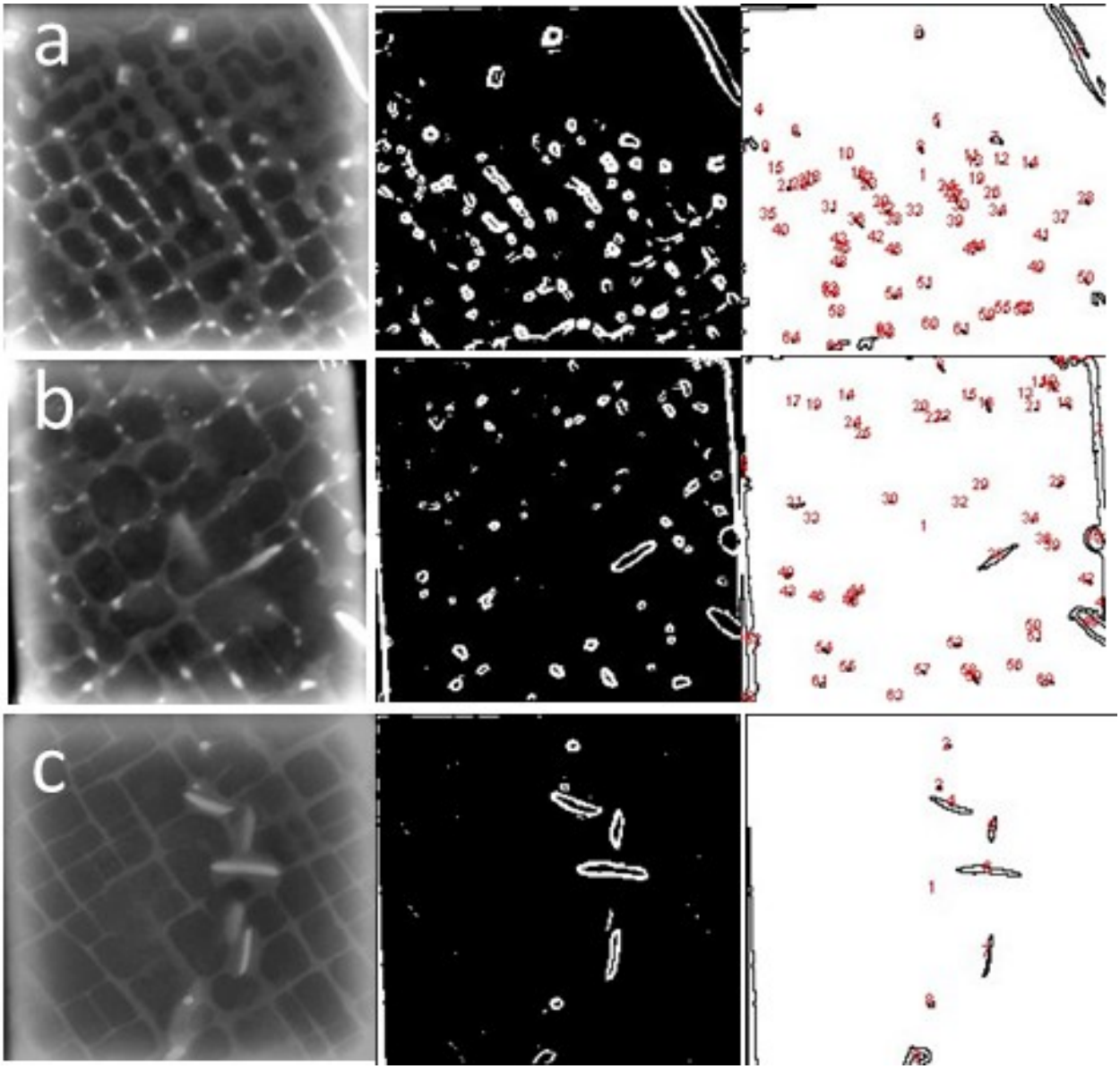


Figure 251: Carbide type phase isolated pillars a-c from zones 1-3 respectively, altered for image analysis highlighting the carbide type phase as individual particles, as described by table 26

Figure 251 shows the three carbide type phase isolated pillars located in zones 1-3, and respective alterations for image analysis allowing the identification and measurement of the carbide type phase particle characteristics, table 26. The trends show that the τ_{crss} decreases from zone 1-3 and the there is a proportional relationship between carbide type phase area fraction and τ_{crss}, figure 252.

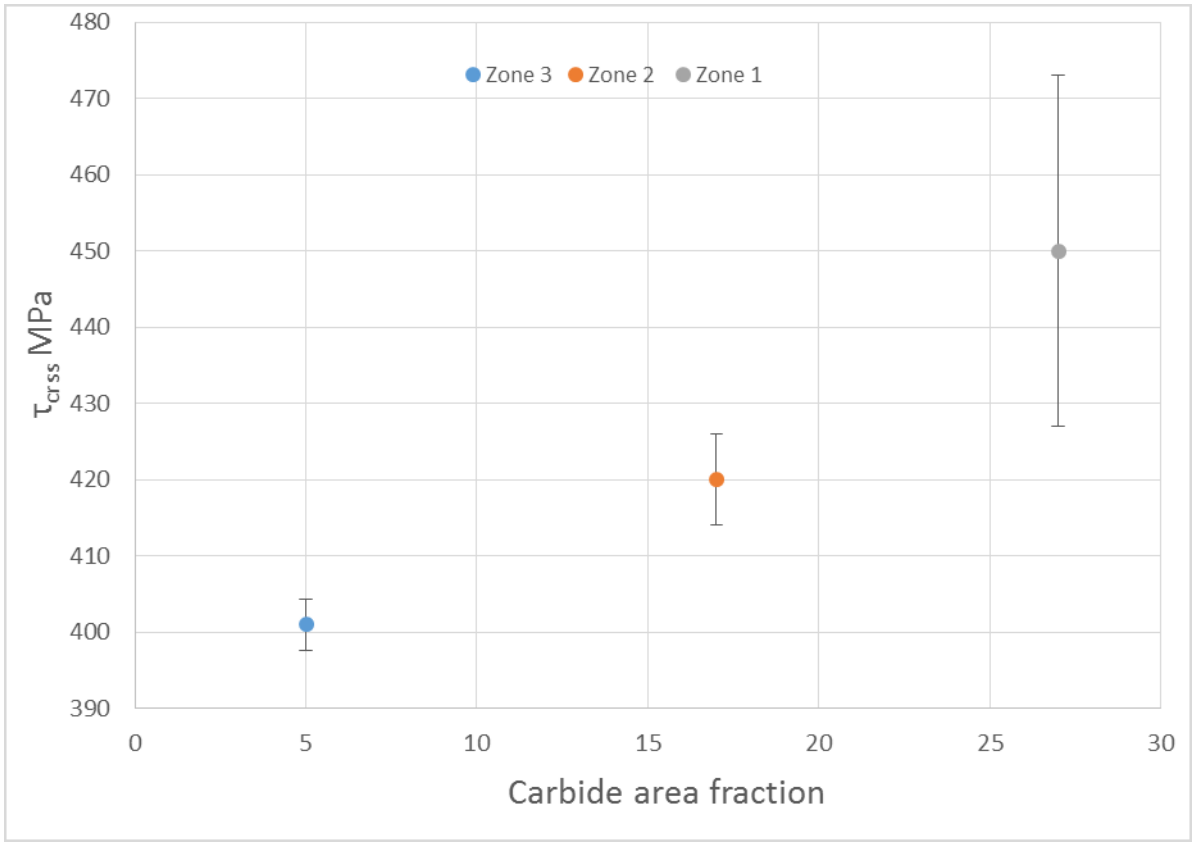


Figure 252: τ_{crss} vs Carbide type phase area fraction, for zones 1-3 in CMSX-4 as described by table 26

Figure 252 shows τ_{crss} vs the carbide type phase area fraction indicating the trend that the τ_{crss} is proportional to the carbide type phase area fraction and that the longer more elongated carbides indicative of the TCP phase when captured on the top surface of the pillar, weakens the material the most.

Table 26: No of carbides, carbide area fraction, average carbide area, aspect ratio and vs carbide zone.

Zone	No. Carbides	Carbide Area fraction (%)	Average Carbide Area (μm^2)	Aspect ratio
1	60	27	0.0096	1.66
2	65	17	0.042	2.6
3	8	5	0.063	5.2

8.7.2. Microindentation testing

The first set of mechanical tests performed on carburised CMSX-4 were micropillar experiments formed from several data sets. Pillars were compressed at different regions and the yield point was plotted as a function of distance from the edge. The results indicate that mechanical properties in the carbide phase, rich area are different from the bulk. An interesting question that arose from the micropillar testing, was; where do the mechanical properties homogenise and where does the bulk start? Microindent experiments were performed to validate the results found from micropillar experiments.

Initially a large array of pillars were fabricated from the same script. In a sequential line from the perimeter edge of the sample through to the bulk (Data set 2) table 24, the pillars began to break down in both the carbide type phase, rich region and 250-550 µm whereas the pillars in other regions maintained their shape.

This suggested that there is change in composition / mechanical properties within these region and hence pillars were fabricated separately in different data sets, with care taken to align them in the same orientation. It was found that there was a deviation in mechanical properties and thus micro indents were used to validate this finding.

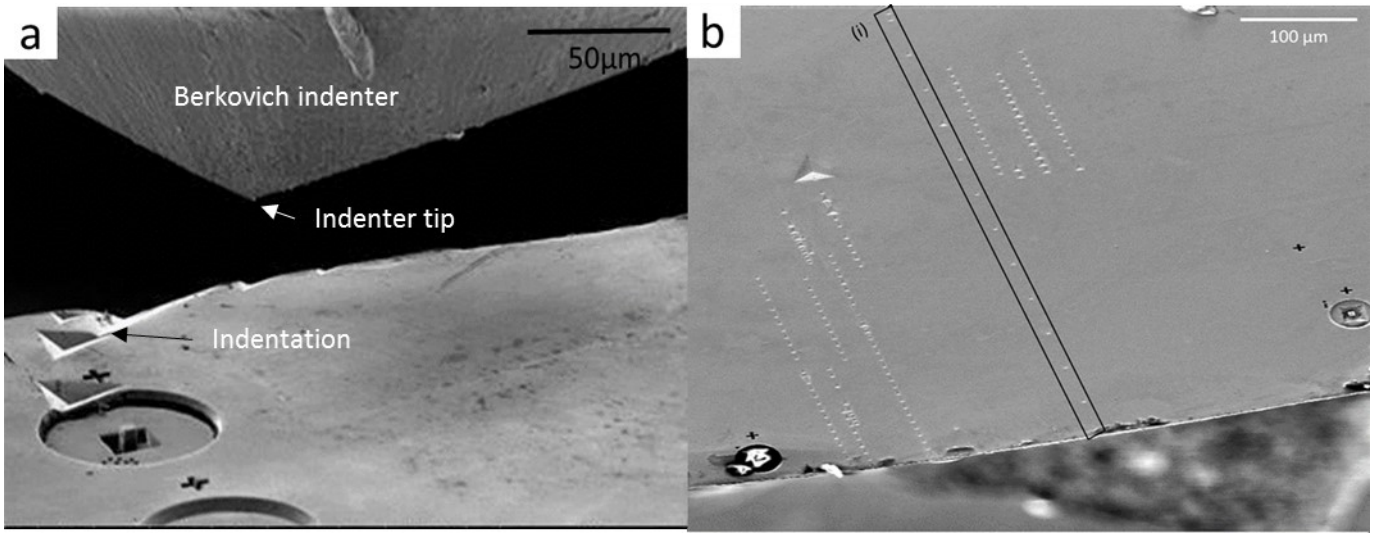


Figure 253: SEM microindentation images (a) 52 tilt showing the tip and small indents near the perimeter of the sample (b) Birdseye view of a series of indent tests.

Figure 253 shows the SEM microindentation images from experiments. Micro indent experiments were performed using the same Alemnis set up as micropillar experiments. A loading rate of 5-10 nm/s was applied, keeping in line with micropillar experiments. The peak load was measured from the peak of the load – displacement graph. A Quanta environmental SEM was used to perform the *in-situ* experiments at room temperature. The tip was changed to a Berkovich indenter and the machine was operated in displacement control.

For a constant loading rate, decreasing increments of indentation depths indicate that the deformation resistance increases during penetration, which can be applied to strain hardening mechanisms [198].

This experiment hopes to link these mechanisms to elemental segregation caused by the precipitation of the carbide type phase[20] and this will be explored in the discussion section.

The set displacement corresponded to the depth of the indent and thus the width. The lower operational limit of the machine, 50 nm displacement, gives 600 nm-1 µm width indents, whereas at

higher more stable displacements of 1 µm the indents were 5 µm. 5 µm indents are too large to accurately take the mechanical response of zones in carbide phase rich areas and were thus attributed to bulk testing.

8.7.2.1. 5 µm indents

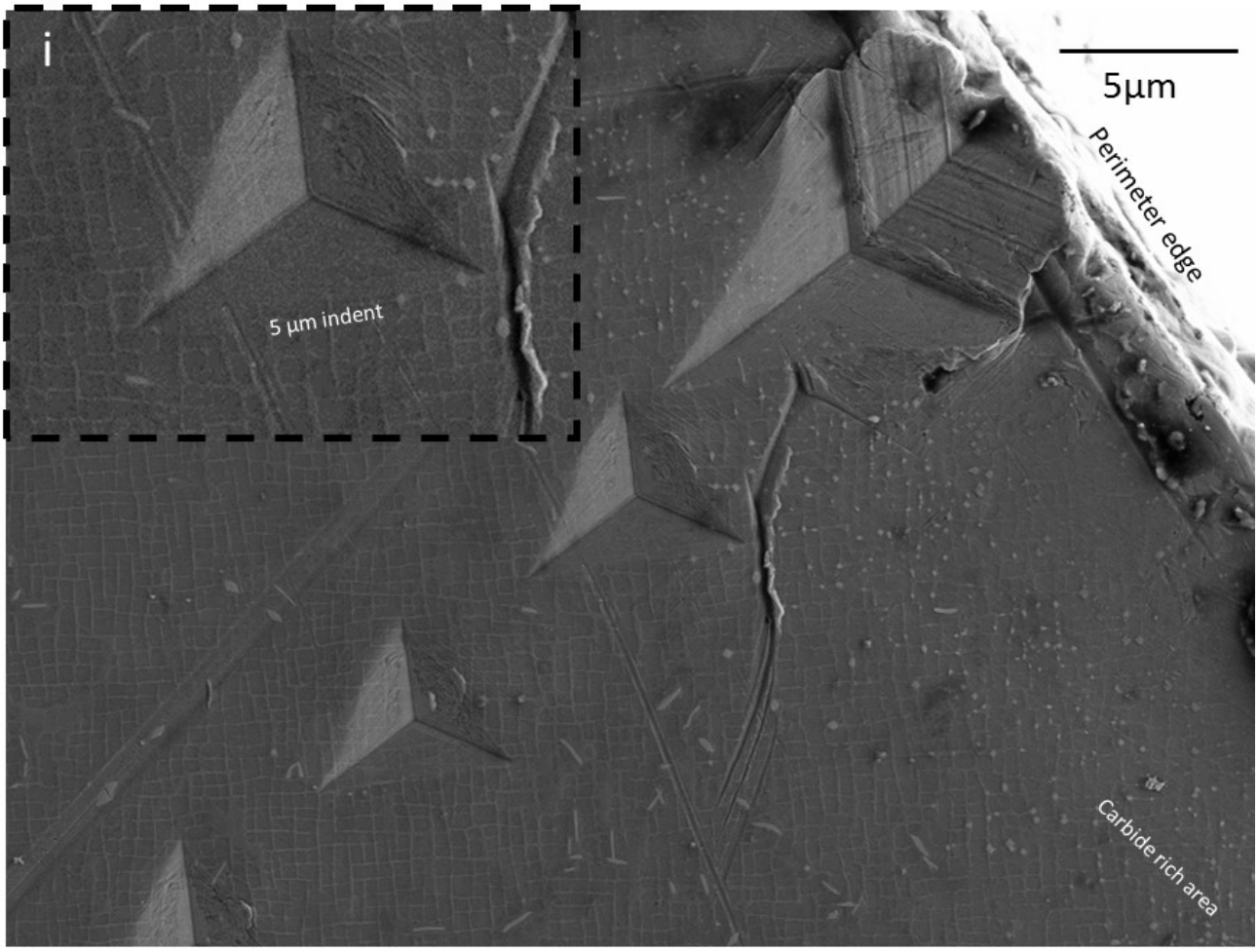


Figure 254: SEM image 5 µm indentation from the perimeter edge through the carbide type phase rich area, through to the bulk material in CMSX-4.

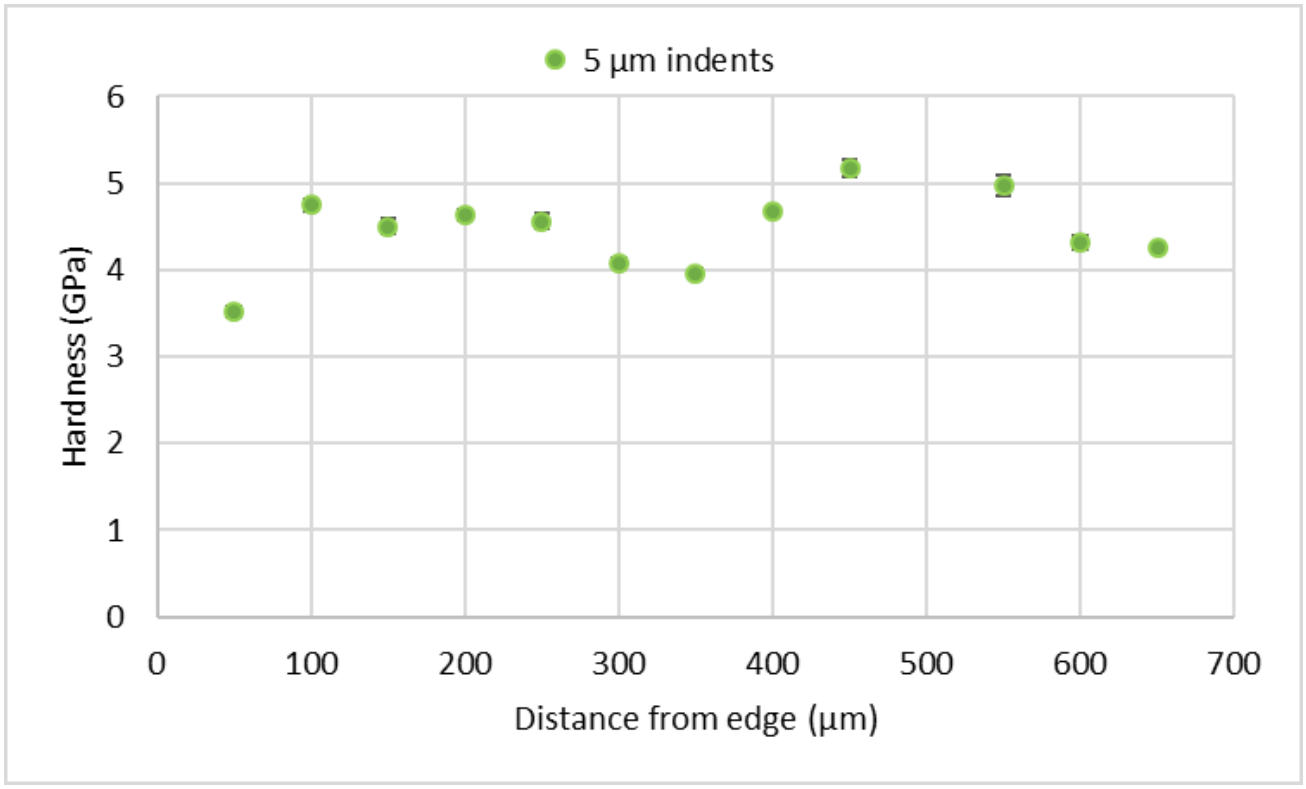


Figure 255: 5 µm indent hardness values (GPa) vs distance from the edge in CMSX-4

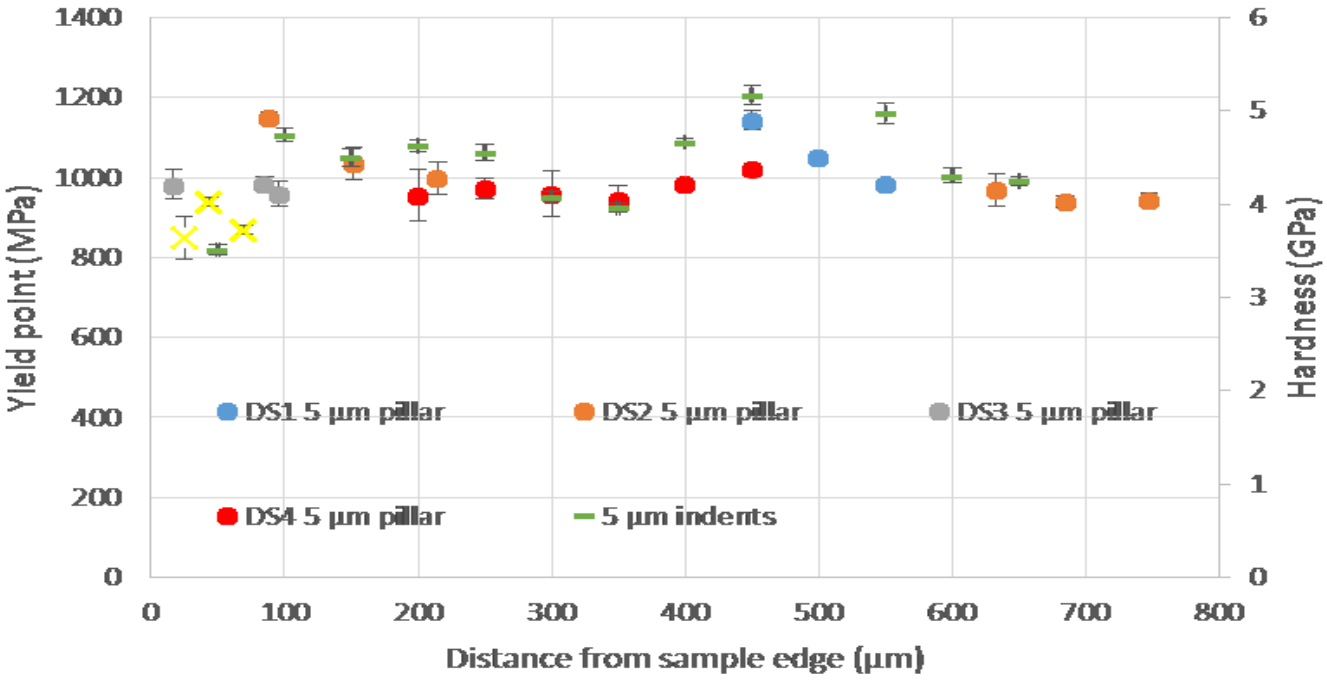


Figure 256: Comparison between 5 µm indents and 5 µm pillars, hardness vs GPa across 0-800 µm distance from the perimeter edge of the sample

Figure 255 shows the hardness values vs distance for the 5 µm indents between 15 and 650 µm. The results match those found from 5 µm pillar experiments and the comparison between the two results is shown in figure 256.

Placing a 5 µm indent near the edge of the sample is not possible, figure 254 and the mechanical properties cannot be trusted. The size of zones 1-3 collectively is 15 µm and the space between each indent should be at least twice the distance of the width, tests local to the carbide type phase, regions were therefore performed with displacements of 50nm (~1µm indents).

8.7.2.2. 1 µm indents

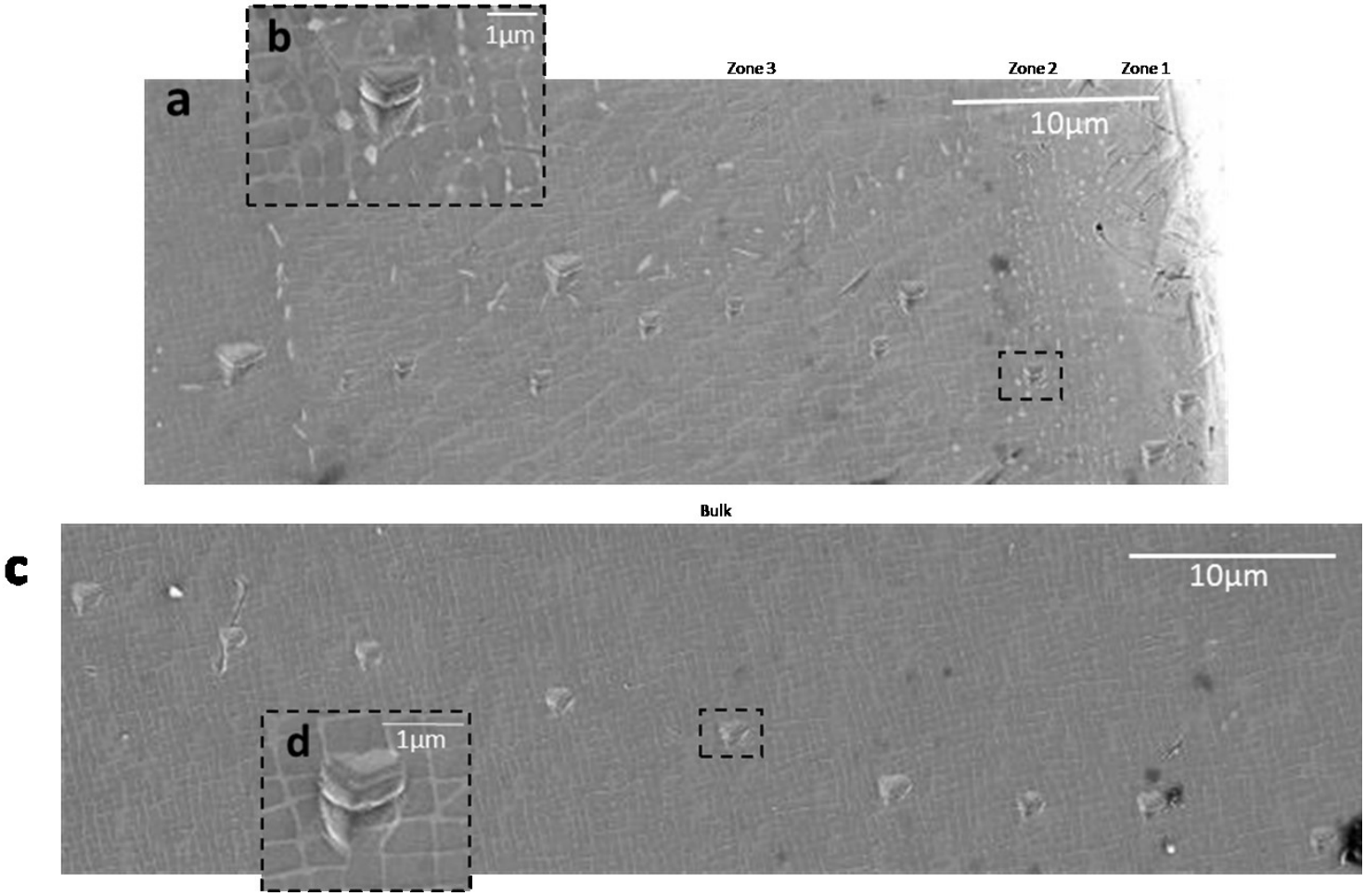


Figure 257: SEM image of 1 µm indents from the perimeter edge of the sample through to the bulk (a) 1 µm indents at 50 nm displacement testing local properties of carbide type phase, zones 1-3 (b) 1 µm indent with a carbide type phase, rich area (c) 1 µm indents at 50 nm displacement testing the bulk microstructure.

Figure 257, shows an SEM image of 1 µm indents spanning from the perimeter edge of the sample, through the carbide type phase, rich zones to 120 µm. The distance between the indents varied between 5 -10 µm and the tests were performed in several datasets. The trend shows several maxima and minima with peak value 4.2 GPa at 106 µm from the edge and minimum value of 1.1 GPa at 20 µm.

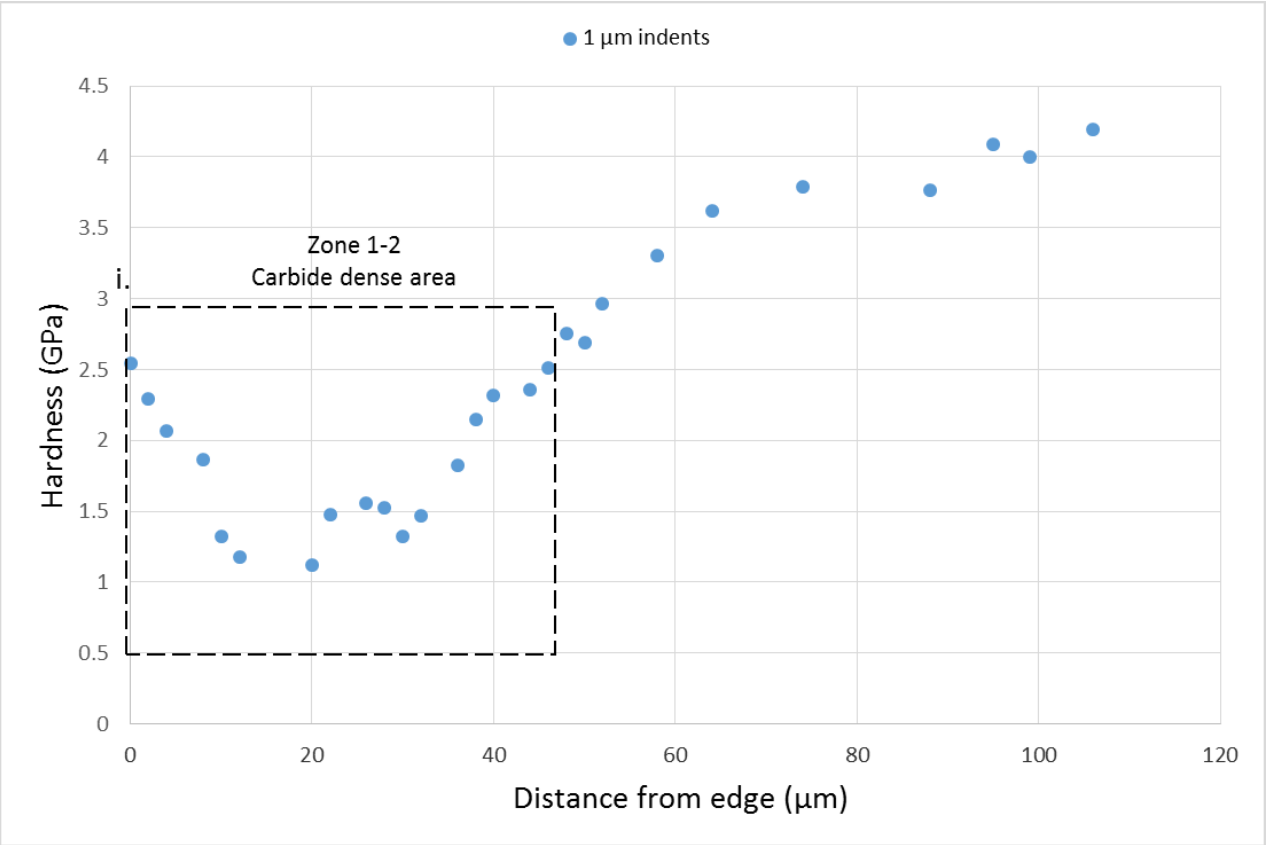


Figure 258: 1 µm hardness values vs distance 0-120 µm (i) 0- 50 µm as shown in figure 259, where the carbide type phase, density is the highest

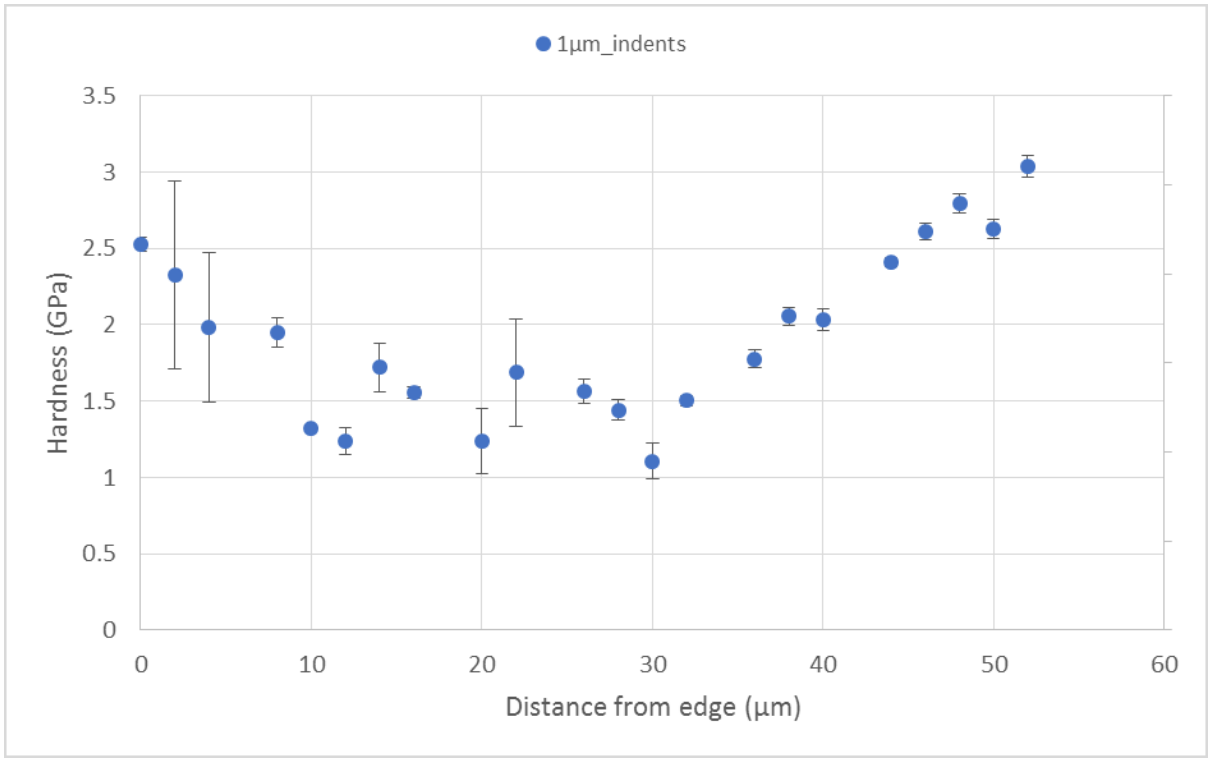


Figure 259: 1 µm hardness values vs distance 0-50 µm, showing the drop in hardness values between 10 – 30 µm

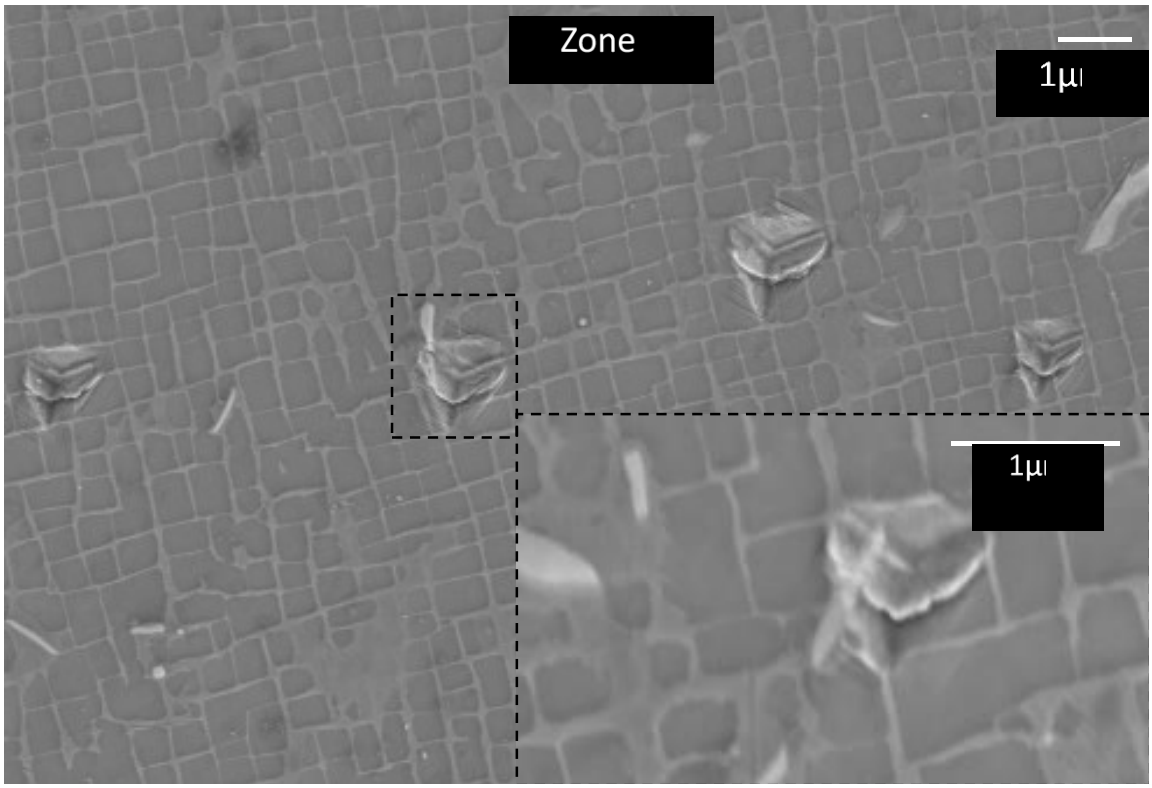


Figure 260: Array of 1 µm indents local to zone 3 (i) an indent piercing a zone 3 carbide type phase.

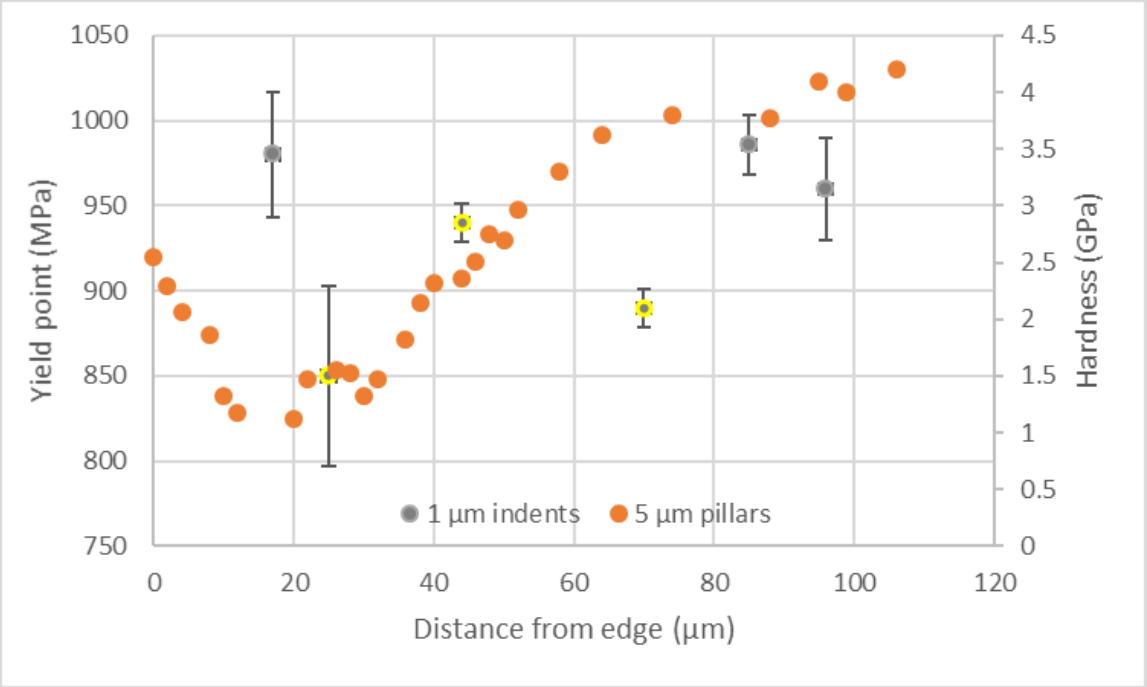


Figure 261: 1 µm indents vs 5 µm pillars, yield and hardness vs distance in the carbide type phase, rich area of CMSX-4. The yellow highlighted data points correspond to pillars with isolated carbide type phase..

Error! Reference source not found. shows an array of 1 µm indents local to zone 3 with an indent p iercing a zone 3 carbide type phase, the results of which can be seen above in **Error! Reference source not found.**.The 1 µm indent curves had more scatter when compared to the 5 µm indents, however as the 5 µm indents cannot test local to the carbide type phase, rich region these were used to test local properties. The peak load from 1 µm was still clear.

The micro indent experiments validated the findings found in the micropillar experiments. Indents placed closer to edge had a lower hardness than those heading towards the bulk. The average bulk hardness at 800 µm tested via 5 µm indent was 4.2 GPa. The micro indents flatten out to roughly 4-5 GPa. The 5 µm indents indicate that there is some stochastic behaviour at some region outside of the carbide, type phase, rich area. The 1 µm indents vary from 2.3 GPa to 4.3 GPa with a dip observed at regions corresponding to changes in chemistry.

8.7.3. Summary – Mechanical properties

Micropillars with a top width of ~5 µm were fabricated on the CMSX-4 alloy, with the aim of testing the mechanical response at various regions (diffusion zones, matrix and different carbide type phases).It was found that the yield point of the alloy changes as a function of distance and the carbide type phase, cause a decrease in yield point but increase in hardening. It was found that the highest the carbide type phase, area fraction, located on the top surface of the pillar is proportional to the τ_{crss}.

The micro indent experiments did not focus on how each carbide type phase, behaved independently but on the global behaviour of the carbide type phase, regions. It was found the micro indent experiments validated the micropillar experiments.

Indents placed closer to edge and in carbide type phase, heavy regions had a lower hardness than those heading towards the bulk. The average bulk hardness at 800 µm tested via a 50 µm indent was 4.2 Gpa. The micro indents flatten out to roughly 4-5 GPa. The larger 5µm indents indicate that there is some stochastic behaviour at some region outside of the carbide type phase, rich area. More analysis is necessary. The 1µm indents vary from 2.3 GPa to 4.3 GPa with a dip observed at regions corresponding to changes in chemistry.

At lower displacements the indents can reflect the extent of hardening the carbide type phase can impose on the ϒ/ϒ' matrix, however the clarity of the result suffers due to effects such as thermal drift and alignment.

8.8. Tranmission electron microscopy of carbides

A 10 x 10 µm section extracted from the carbide type phase, rich region of the CMSX-4 alloy, was examined via TEM. The TEM analysis was used to determine what elements were present in carbide type phase rich / bulk regions and how the dislocations interact with carbide type phase. The slice was extracted from a region that was within a 30 µm distance of a large indent, as seen in figure 262.

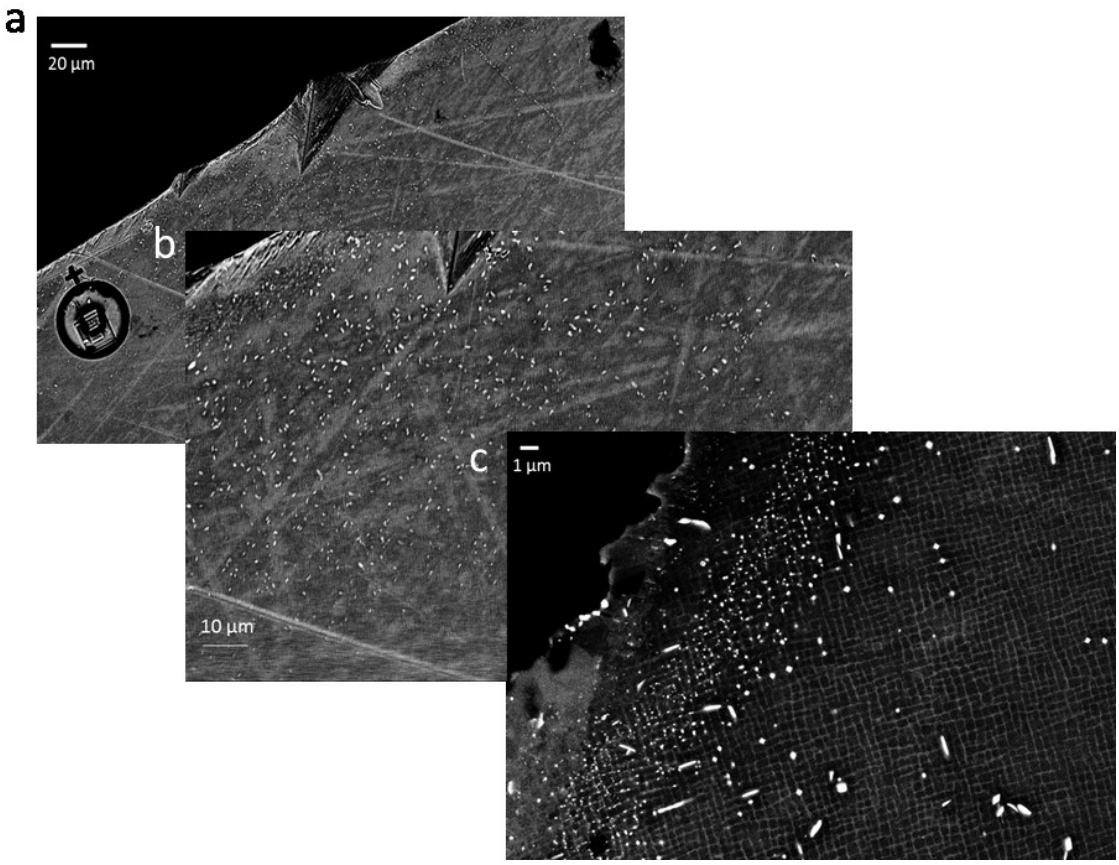


Figure 262: Region of CMSX-4 the TEM slice was extracted from, the indent was used as a fiducial marker, but due to its size resulted in some residual strain within the sample slice

Figure 262, shows the carbide type phase rich region that the TEM slice was extracted from. The slice was taken from zones 2-3. The TEM slice, indicates that the carbide type phase exist below the visible surface plane. Faceted regular carbide type phase can be seen running all the way down the vertical length (10 µm) of the slice, and two large TCP phase be seen at a depth of 7 µm, figure 263. The area had been slightly deformed with an indent and the effect of dislocations interacting with the carbides can be seen, in figure 264 d and figure 266 b.

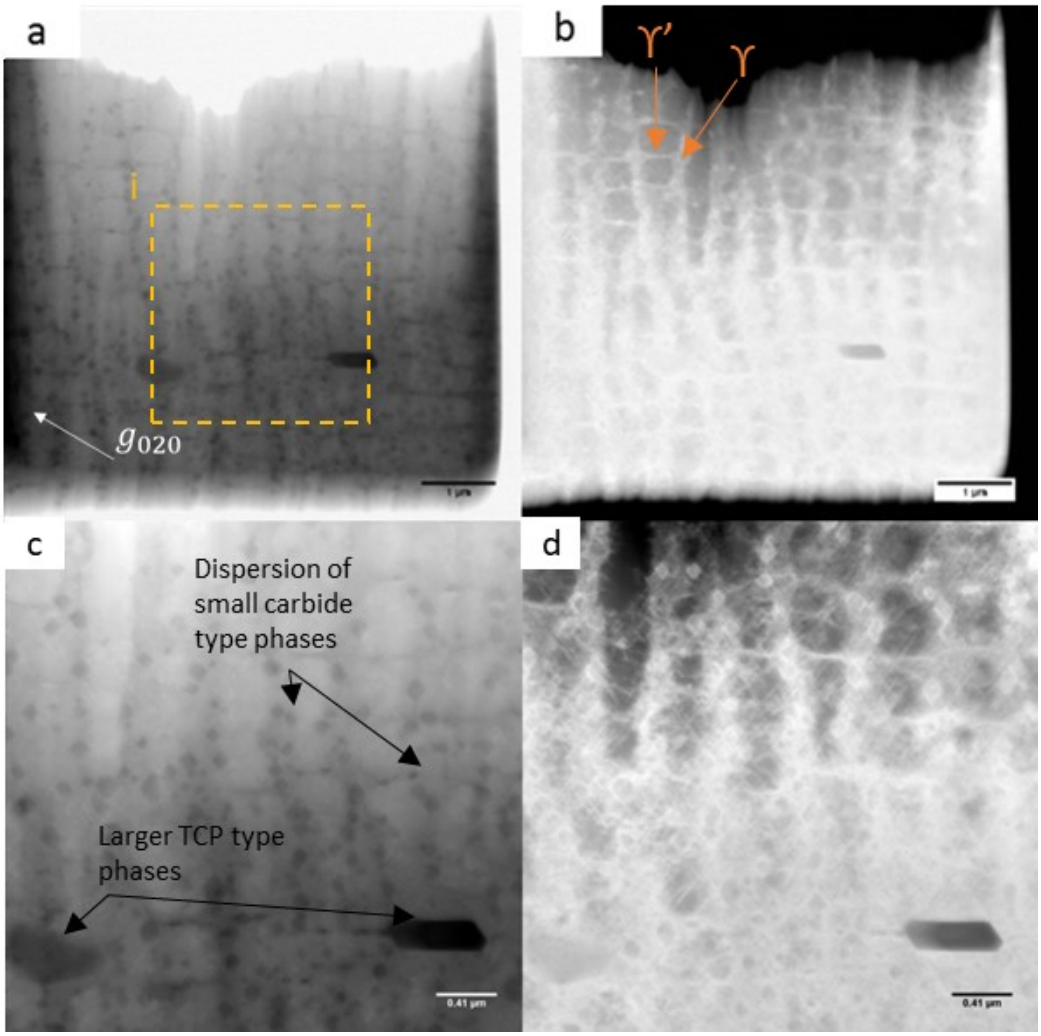


Figure 263: TEM 20-40k mag of extracted CMSX-4 slice, showing two large TCP type carbides and a dispersion of smaller more regular carbide type phase, mainly located in the γ and γ/γ' junctions (a) Bright field 20k (b) Dark field 20k (c) Bright field 40k, close up of region i (d) Dark field 40k, close up of region i.

Figure 263, shows the TEM slice illustrating the depth profile of the TCP and regular faceted carbide type phase. The objective lens had not been placed and so the interaction of the dislocations with the carbide type phase, at this magnification was not observable.

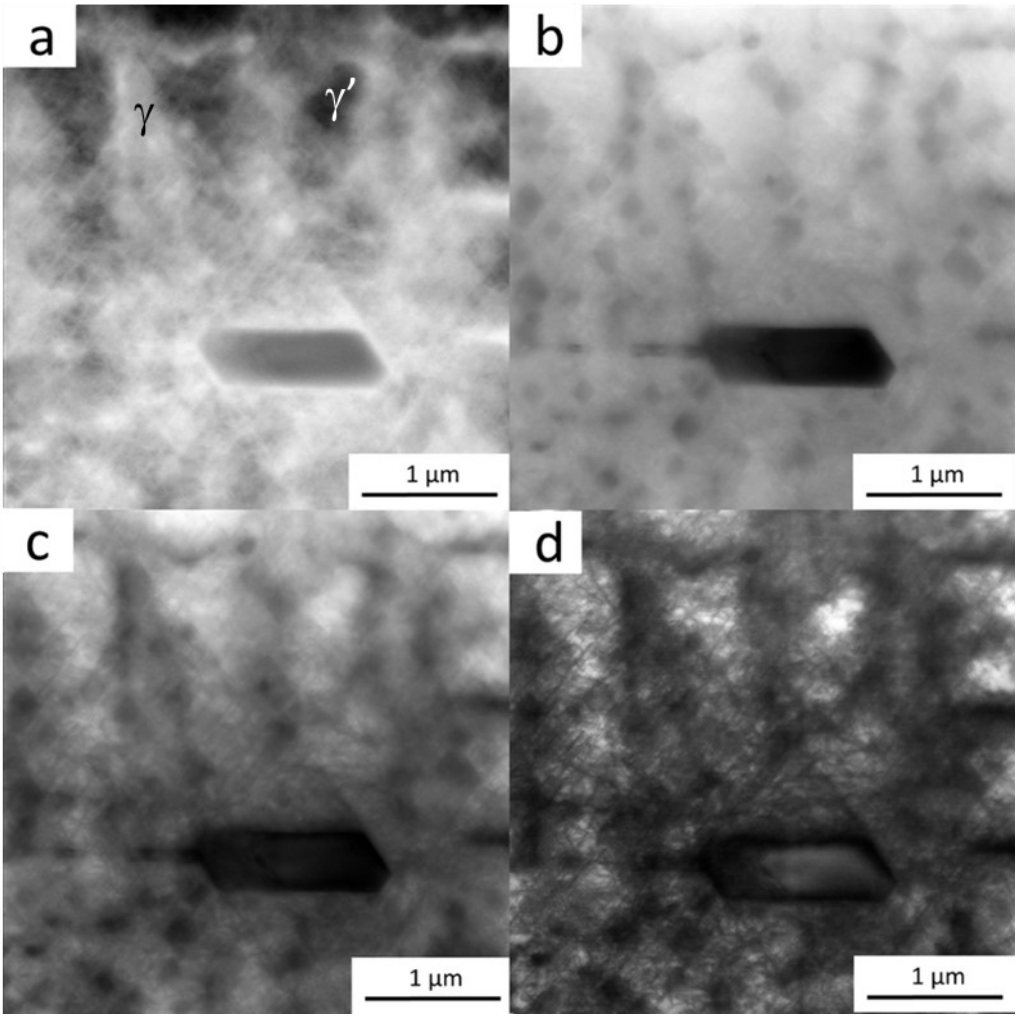


Figure 264: TEM 80k mag of TCP phase (a) Dark field (b) Bright field (c) Bright field (d) Bright field giving greater clarity to the dislocation networks surrounding the TCP phase.

Figure 264, shows the bright and dark field TEM scans around a TCP phase at 80k, straight extended dislocations can be seen interacting with the carbide type phase, however the carbide type phase is deep and so the level of deformation is expected to be low.

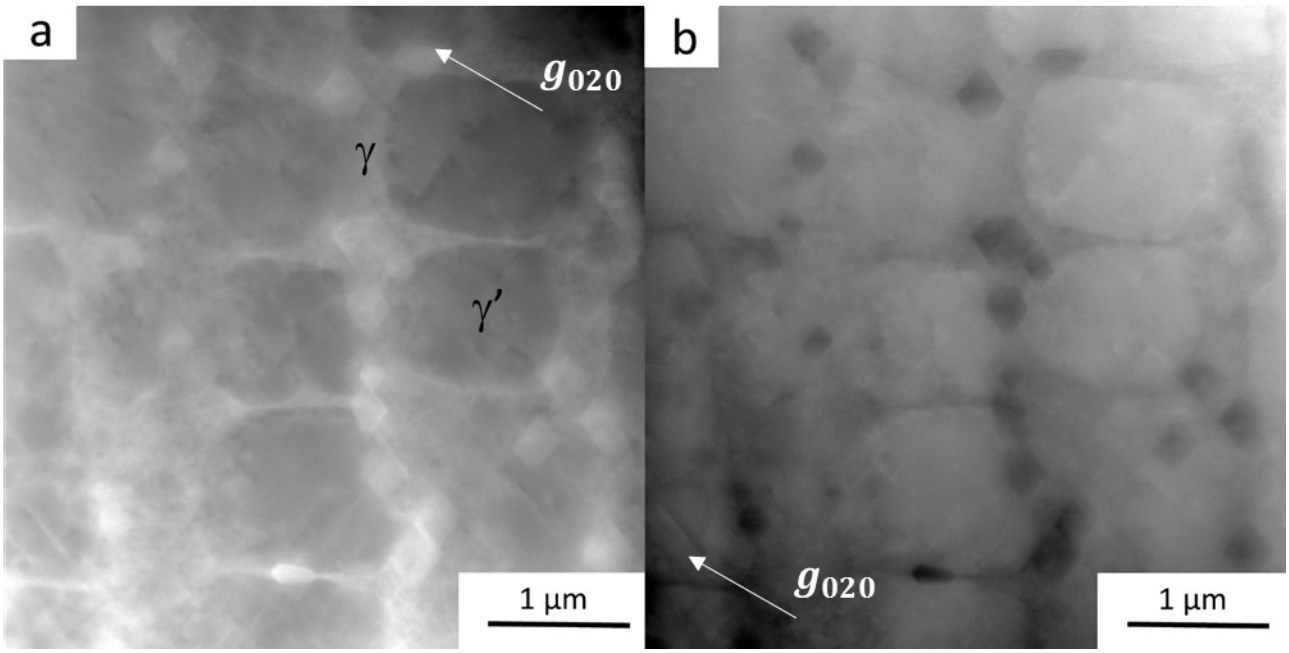


Figure 265: TEM 80k image of smaller spherical carbide type phase generally found to be local to zone 2 (a) Dark field (b) Bright field

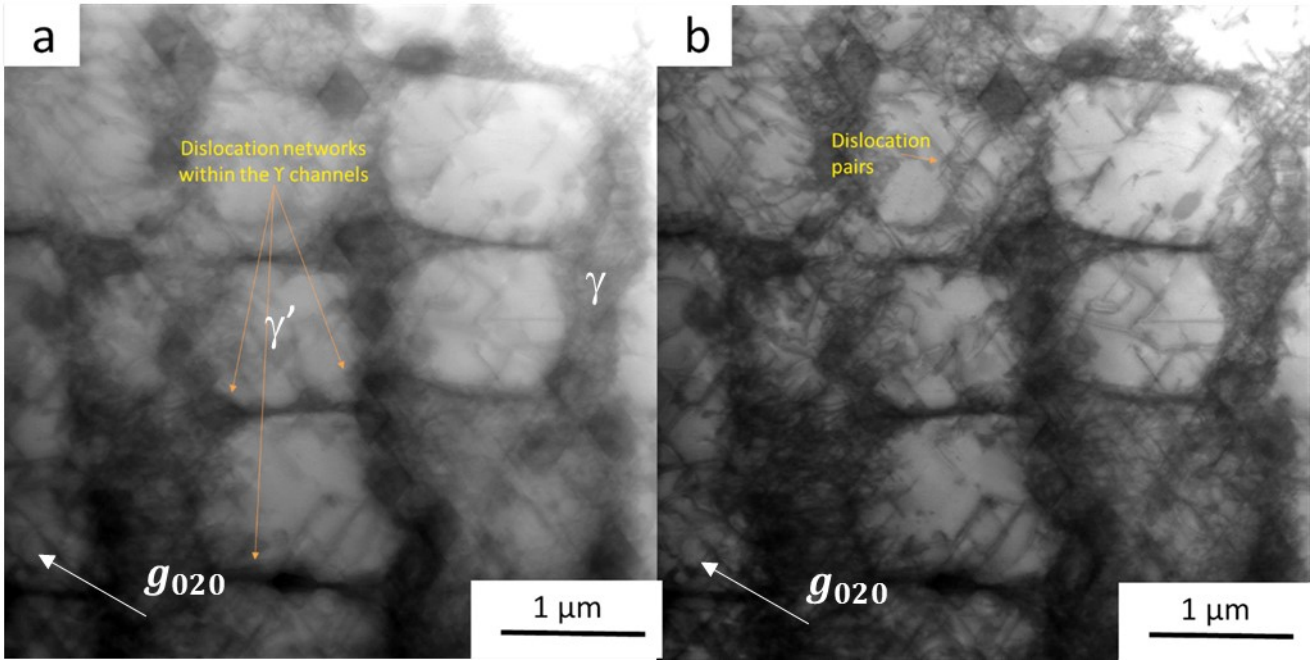


Figure 266: TEM 80k image of smaller spherical carbide type phase , from figure 265, showing dislocation networks, dislocation pairs and dislocation partials.

Figure 265 shows Bright and Dark field TEM images at 80k of the small faced carbide type phase within the Ɣ channels. Figure 266, shows the bright and dark field images of the faceted spherical carbide type phase at 80k clearly illustrating the effect of dislocations interacting with the carbide type phase within channels and precipitates, pairs and partials can be seen and what appear to a loop can also be observed.

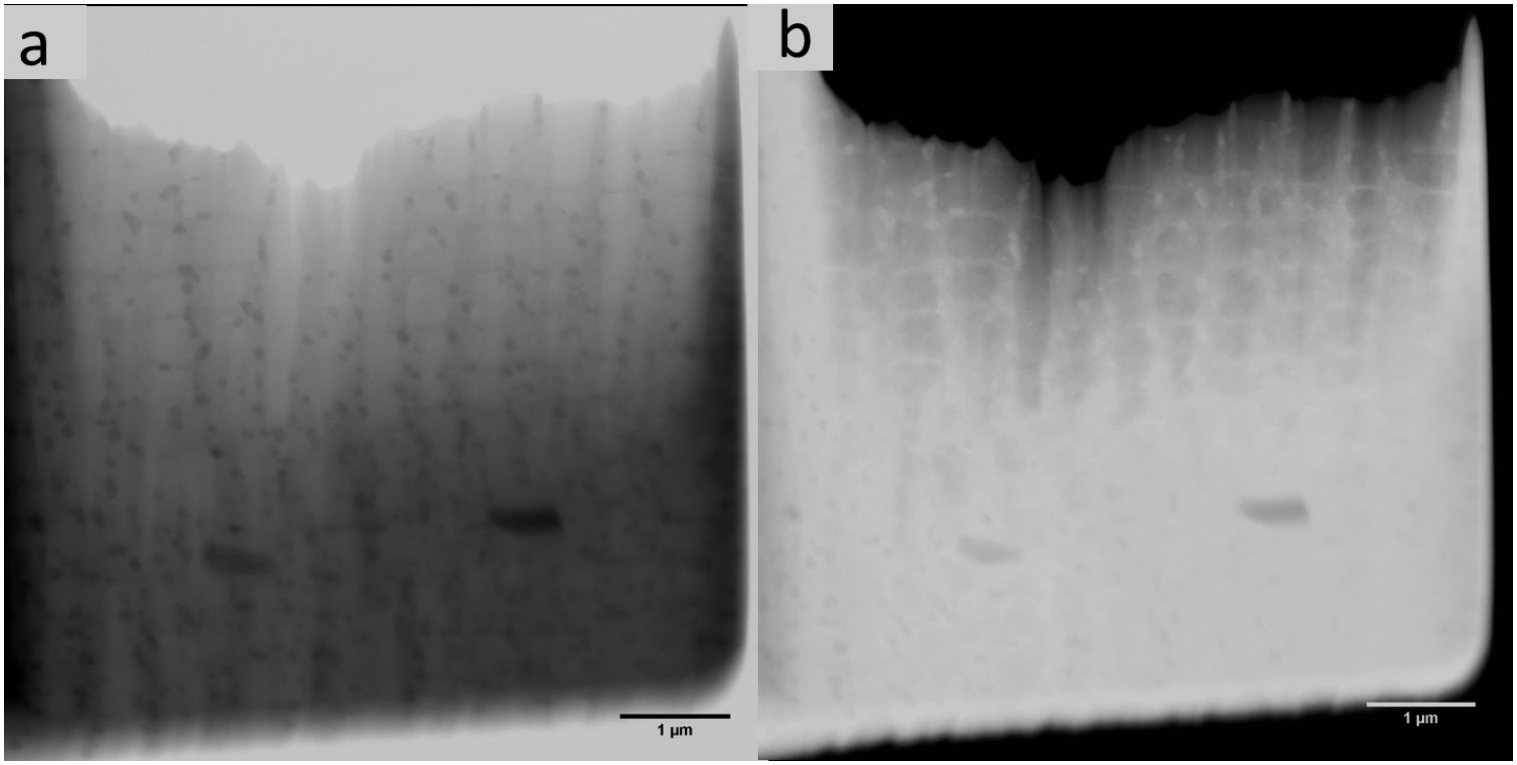


Figure 267: TEM of samples tilted for EDX, as shown in Figure 268, showing clearly the dispersion of small spherical carbide type phase and two larger TCP phase. (a) Bright field (b) Dark field

The sample was tilted for EDX analysis and Figure 267 shows the TEM bright and dark field scans of the slice tilted to this angle. The surface plane was removed during the preparation of the TEM foil.

Table 27: Compound table of TEM information from figures 263-267. Listing the foil normal, G vector, image mode and pager number, taken from carburised CMSX-4.

Fig No.	Foil norm	G vector	Image mode	Page no.
263(a&c)	1	020	BF	268
263(b&d)	001	020	DF	268
264(a)	001	020	DF	269
264(b-d)	001	na	BF	269
265(a)	001	020	DF	270
265(b)	001	020	BF	270
266(a-b)	001	020	BF	270
267(a)	001	020	BF	271
267(b)	001	020	DF	271

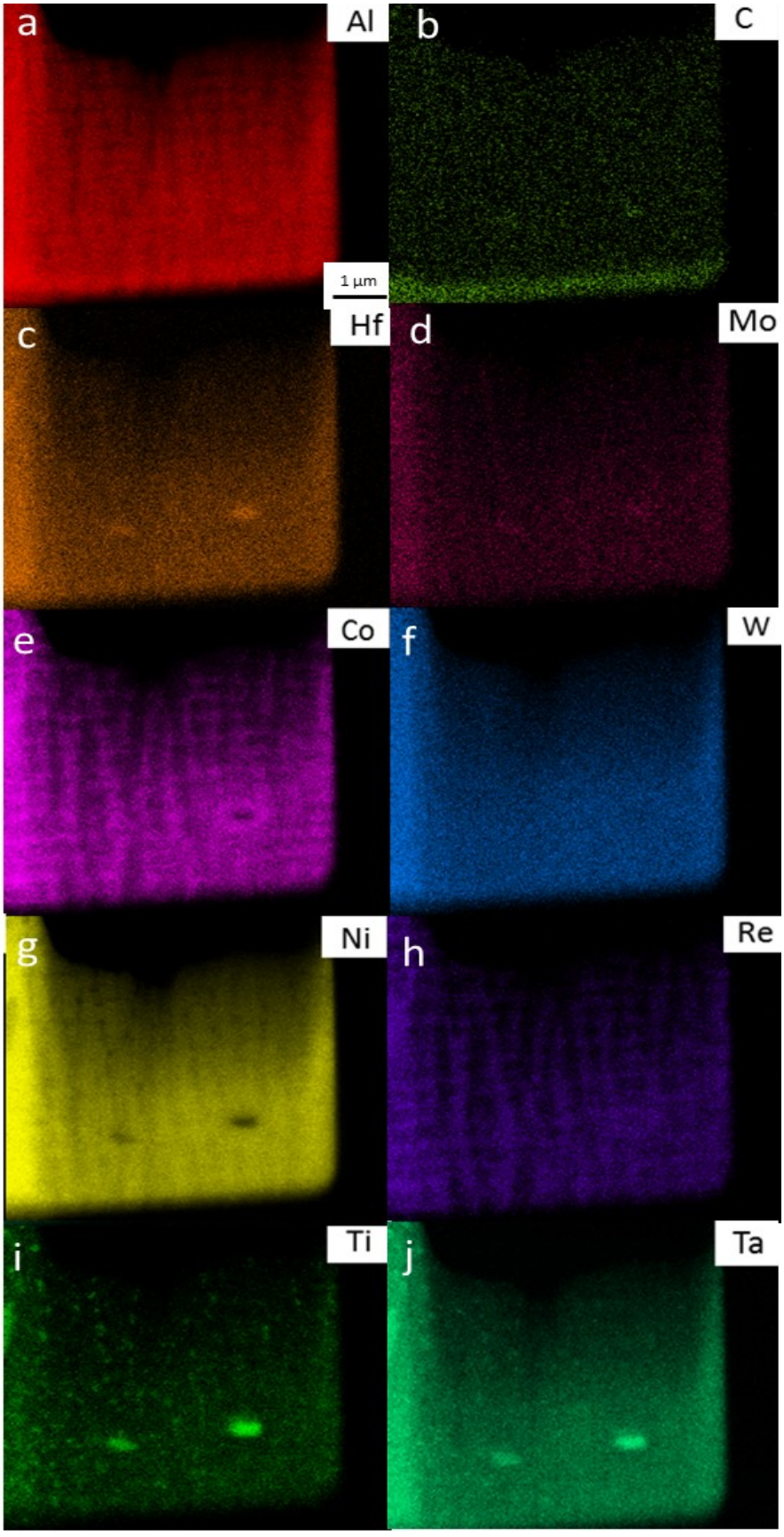


Figure 268: EDX results from TEM analysis on carburised CMSX4 slice. 1-j representative of Al, C, Hf, Mo, Co,W,Ni,Re,Ti and Ta respectively

Ti, Ta, Hf, trace Mo and C are carbide type phase stabilisers, Ni, Co depleted. The TEM EDX results validate the SEM results. Hf can be clearly seen to compromise the larger TCP phases but not the smaller more faceted carbide type phase. Both Ti and Ta are strong carbide type phase stabilisers across both types.

The change in refractory elements in the presence of carbide type phases could be a consequence of the elements partial to ϒ or ϒ' but could also be another effect which could explain the change in mechanical properties within carbide type phase regions and some areas outside of the visible surface carbide type phase area.

8.9. Summary – Results chapter 3

The defining feature of this alloy are the carbide type phase visible on the top surface. The carbide type phase orientate themselves into microzones. The zones contain carbide type phase of different sizes, from 60 nm to 2 µm. The carbide type phase, vary in shape and location. The shapes vary from spherical to elliptical and the locations vary between, ϒ/ϒ' junctions, ϒ channels and ϒ' cuboids.

The carbide type phase structures formed as a by-product of pack aluminsation and result in carbide type phase containing different element concentrations, having different character and orientation.

The exact extent of area densities of the carbide type phase in the carbide type phase rich rim changes per position on the sample however the trend of the shape descriptors characteristic to each zone remains the same regardless of position on the sample.

EDX experiments have been used to identify how the chemistry changes as a function of microstructure, precipitate, and distance.

EDX analysis indicates that the carbide type phase are C rich with traces of Ti,Ta,W,Hf and Re. As the line scan moves towards the carbide type phase, the concentration of Ni, Cr an Al drop.
Each carbide type phase, has its own preference for elemental segregation, which is why when scanning large clusters of carbide type phase, the elemental increases and drops can vary, when compared to more local tests (tests with smaller mapping areas).

Three clear morphologies and carbide phase, locations can be observed. Thin "needles" aligned in ϒ channels. Longer / fatter carbide type phase, randomly orientated near ϒ and inter penetrating ϒ and ϒ'. Small circular / faceted carbide type phase, are located sporadically occupying ϒ/ϒ' junctions, ϒ channels and ϒ' cuboids. TEM analysis shows the carbide type phase, penetrate to depths upto 10 µm beneath the surface.

The elemental constituents of each type of carbide type phase are different. The larger the difference in shape descriptor the larger the difference in chemistry between carbide phase, and mechanical properties. Theory would dictate that the longer more elongated precipitate phases are TCP and the more regular circular type carbide phase, are fcc crystal structure. They behave differently as evidenced by micropillar experiments.

Micropillar experiments show that the size and shape of the carbide type phase, has an effect on mechanical properties with larger more irregular carbide type phase, contributing to greater shear stresses and phenomena such as strain bursts, whereas smaller carbide type phases contribute more to the activation of different slip systems.

The deleterious carbide type phase, in CMSX-4 are needle shaped and coincide with TCP phases formed during the pack aluminization process which occurs at ~700-800 C. These phases were found to inhibit the strength of the pillars.

The pillar having the most needle like phases (indicative of TCP) that extends through several arrays of ϒ/ϒ’ having the lowest yield point at 850 MPa.

There appears to be some mechanical phenomena in regions where there are no visible surface carbide type phase.

The addition of refractory elements plays a pivotal role in the formation of precipitates such as carbides and leads to differences in morphology and crystal structure. Elements therefore need to be carefully selected during processing and tailored accordingly when creating multi-layered alloys containing bond coats and thermal barrier coatings.

9. Results - Carburised Ni superalloy: CMSX-10

9.2. Objectives

1. Analyse the carbide type phase, in the CMSX-10 alloy, through SEM/BSD and image analysis.
2. Asses the mechanical behaviour in the carbide phase rich and bulk microstructure of the CMSX-10 alloy

9.3. Motivation

The carbide type phase in CMSX-10 are different that those in CMSX-4, the shape of the carbide type phase, are more consistent and the extent of the carbide phase rich area is smaller. In regards to the formation of carbide type phases, the addition of refractory elements plays a pivotal role in their formation. The addition of these refractory elements can lead to differences in the morphology and crystal structure of the carbide type phase. This chapter will briefly study the carbide type phase character in CMSX-10 and the resultant effect on mechanical properties in the alloy via micropillar based testing.

9.4. Introduction

Two Ni superalloy samples containing a colony of carbide type phase located local to the perimeter of the edge of the sample have been examined. This chapter focuses on the third generation CMSX-10 alloy. In regards to alloying elements, compared to CMSX-4, CMSX-10 contains significantly less Cr, less Co, less Mo, less W slightly more Ta, significantly less Ti and 2-3x more Re than CMSX-4. As a consequence, the distribution and size of the carbide type phase varies between the two samples, CMSX-4 and CMSX-10. On average, CMSX-10 contains a larger volume fraction per unit area of carbide type phase, when compared to CMSX-4, however the carbide type phase area in CMSX-4 is 4x as large. The carbide type phase in CMSX-10 are in the form of regular fcc type and are not as deleterious to the mechanical properties as those in CMSX-4. This is believed to be due to the heat treatment and homogenisation of the CMSX-10 alloy. CMSX-4 contains more Ti which creates a larger solutioning window giving the deleterious carbide type phase more time to form and leech alloying elements from the microstructure. The leeching of alloying elements, weakens the strengthening ϒ' phase and destroys the alloy homogenisation. The carbide type phase in CMSX-10 contain high levels of Ta, whereas the carbide type phase in CMSX-4 favour Ti.

CMSX-10 and CMSX-4 are both single crystal Ni superalloys used as turbine blades in the hot section of an aero engine[203]. Successful Ni alloys generally contain a high volume fraction of refractory elements whilst maintaining a moderate Al & Ti content. With the exception of a few alloying elements, which include, Ti, Ta, Re and Cr, the chemistry of CMSX-10 can be considered close to CMSX-4[122]. CMSX-10 is a third generation alloy, which provides an approximate 30° C improved creep strength when compared to second generation alloys such as CMSX-4[204]. A key factor in determining the performance of carbide type phase within Ni superalloys arises from the heat treatability of the alloy[21]. The key difference in terms of heat treatability and alloying elements when comparing CMSX-10 to the second generation CMSX-4 is the smaller solutioning window in CMSX-10 and 30°C improvement in strength[205], both factors act to retard the formation of the deleterious TCP phase. The heat treatment window allows for a dispersion of fine precipitates to grow with a regular alignment.

The carbide type phase in CMSX-10 vary in nature when compared to those in CMSX-4. The carbide type phase in CMSX-4 extend 3-4 x the distance than those in CMSX-10 and vary in shape and size from small and circular to large and bulky / needle like in shape.

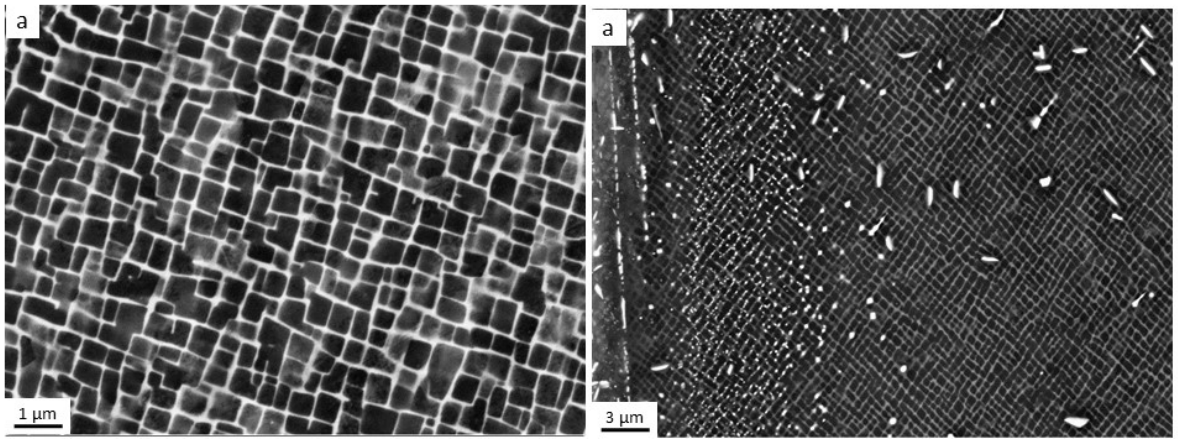


Figure 269: BSD images of carburised CMSX-4 microstructure (a) Ɣ/Ɣ' microstructure (b) Carbide type phase evolution through distance showing faceted and TCP phase.

Figure 269 and Figure 270 show BSD images of the carburised CMSX-4 microstructure. The needle like carbide type phase, in CMSX-4 appear to be TCP in nature as supported by the literature[194]. CMSX-4 has a higher Cr content that CMSX-10, Cr has been noted to aid in the formation of TCP type phases. TCP phases can take many phases and crystal structures based on the formation temperature and the size of atoms that sit on the Kasper polyhedral and have been found to be deleterious to the mechanical properties[122].

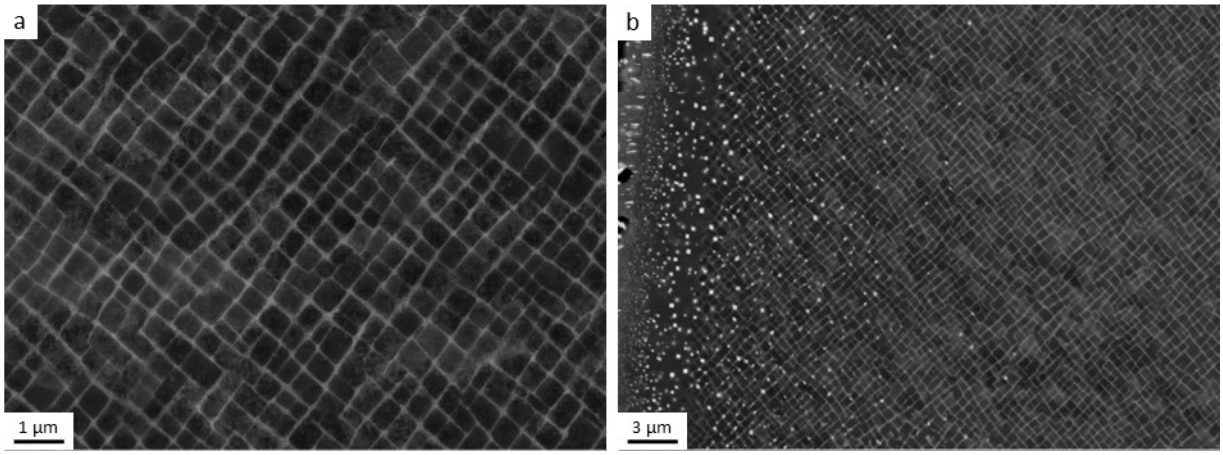


Figure 270: BSE images of carburised CMSX-10 microstructure (a) Ɣ/Ɣ' microstructure (b) Carbide type phase evolution through distance showing the smaller carbide type phase diffusion area and regular faceted carbides.

More regular shaped carbide type phase, as seen in CMSX-10 are of the form MC or $M_{23}C_6$. The MC carbides are generally found to be more circular whereas the $M_{23}C_6$ carbides more modular. This is unlike the long nodular Chinese script type M_6C type carbide type phase found in CMSX4.

9.5. Characterisation of Carburised CMSX-10

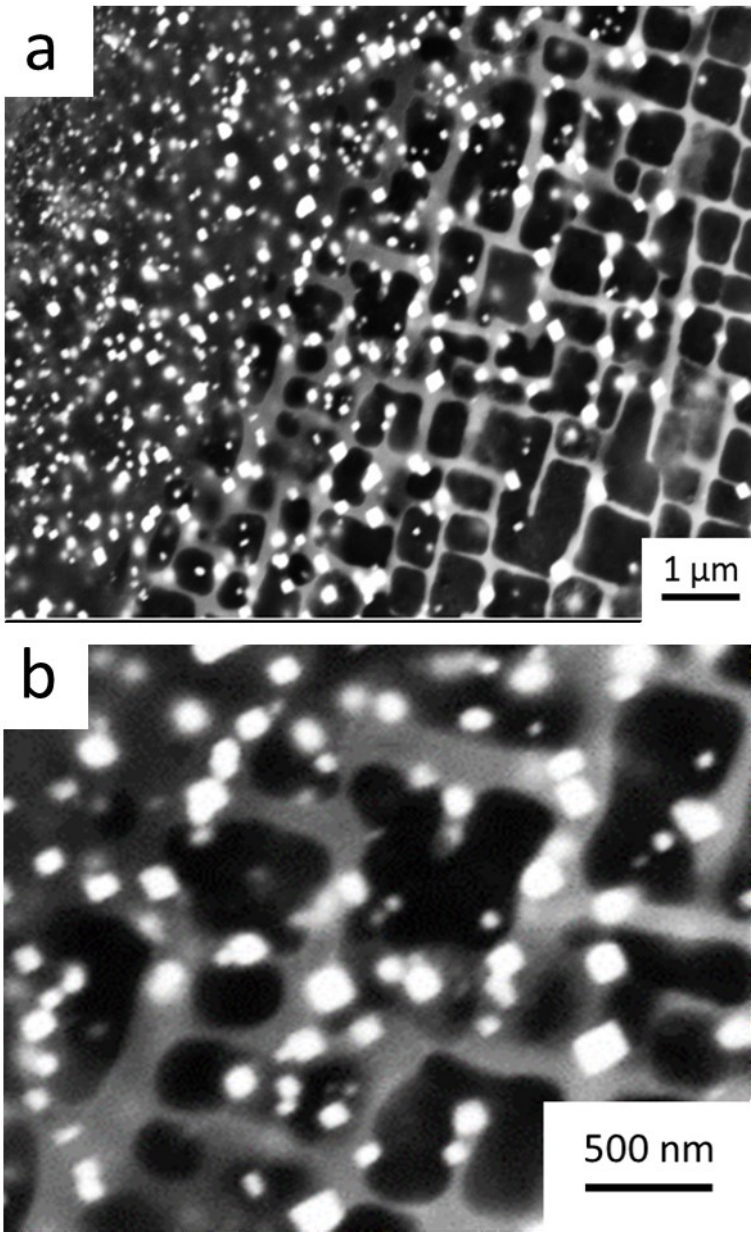


Figure 271: BSD micrograph of CMSX-10 (a) illustrating the carbide type phase rich region (b) Close up of the carbide type phase morphology of third generation CMSX-10 extending ~10 µm from outer rim of sample.

The carbide type phase in CMSX-10 are small and faceted in shape. They occur within the ϒ' channels and are more commonly found to be round and or faceted rather than needle like in character, figure 271b. With literature dictating that cuboidal / round carbide type phase generally favour the fcc crystal structure[122] whereas needle like carbide type phases are often found to be TCP in nature[120].

The shape of the carbide type phase in CMSX-10 remain consistent, with the average circularity and roundness in a 0.028 µm^2 area, extending 0-20 µm from the perimeter edge being as follows; 0.81 and 0.82 respectively. The carbide type phase in CMSX-10 penetrate ~ 40 µm into the bulk material, from the perimeter edge of the sample. The EDX analysis illustrates that similar to CMSX-4, Ni drops in a

response to an increase in several alloying elements. In CMSX-10, Ni drops and Ta increases, this is shown as a line scan passes from the perimeter edge of the sample through the carbide type phase rich area into the bulk. In regards to microstructure and carbide type phase orientation, three diffusion / boundary layers can be observed whereby the carbides orientate themselves differently, figure 273.

9.5.1. EDS

The initial EDS analysis indicates that the carbide type phases are Ta rich with traces of Ti.

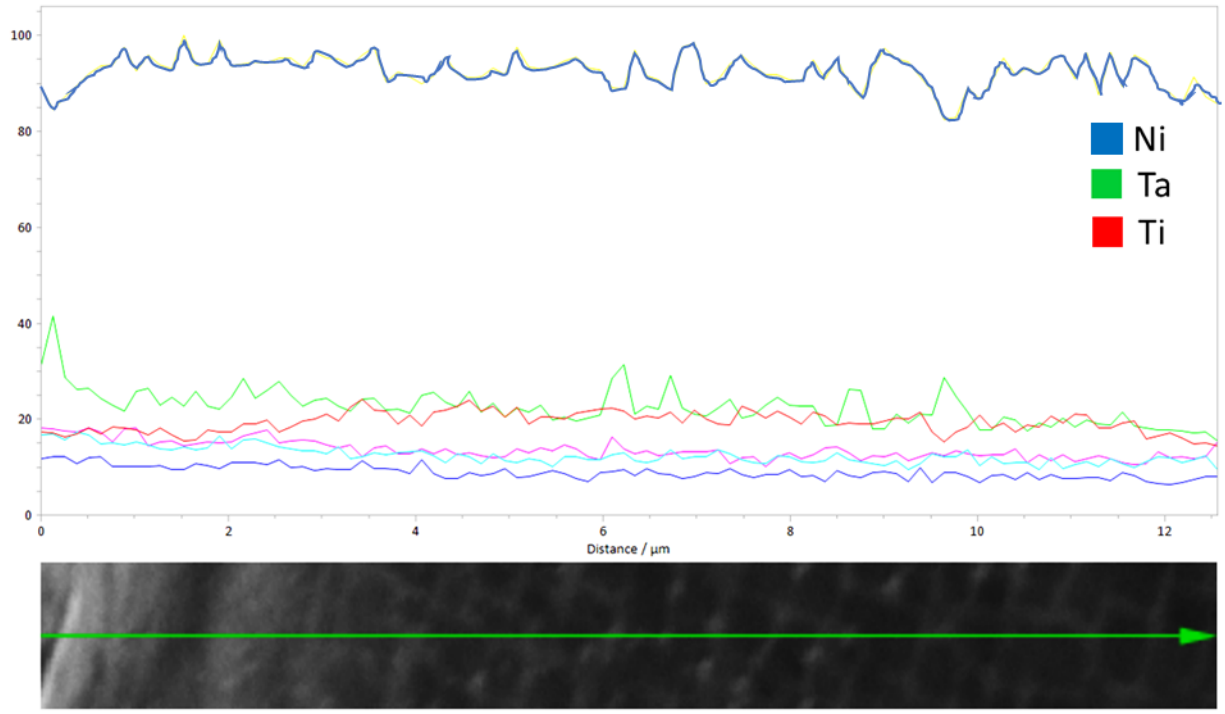


Figure 272: Line scan from the perimeter edge of CMSX-10 through the carbide type phase in the carbide phase rich area, through to the bulk microstructure.

Figure 272, shows a line scan from the perimeter edge of the sample through the carbide type phase towards the bulk microstructure. As the line scan moves towards the carbide type phase, the concentration of Ni drops and those of Ta and Ti increase. The other constituent elements present in this sample are Al, Co, Cr, Mo, Re, Hf.

The high Re content in CMSX-10 requires refractory hardeners such as W, Ta, and Mo[122]. Mo and Ta are added to CMSX-10 alloys to compensate for the low levels of Cr which is crucial for hot corrosion resistance. Ta has a higher atomic diameter than Mo and is a more efficient hardener, it also reduces freckle formation and is good for castability[21]. For these reasons it is clear why Ta is a preferential alloying element when compared to Mo for the third generation CMSX-10.

Alloys designed for high temperature operation generally contain a high Al & Ti content, however it has become better known that Ti alloying makes the attainment of an adequate solution heat treatment

window more difficult[122], newer generation alloys employ less Ti and more Al or alternative elements. One would then assume based on literature and the results from EDX that CMSX-10 has a much smaller solution heat treatment window than CMSX-4 and the ability to form more stable precipitates, hence the more uniform carbide type phase dispersion.

9.5.2. Carbide character

A BSD image of the carbide type phase-rich region in CMSX-10, as seen in figure 273, was analysed using imaging software as outlined in the previous chapter. It was found that; the average diameter of the carbide type phase was ~150 nm. With the spread of diameters varying from ~5-10 nm to ~600 nm. However it should be noted that the larger carbide type phase constitute ~5-10 % of the total population of carbide type phase in a 20 µm radius from the outer edge of the sample, figure 273.

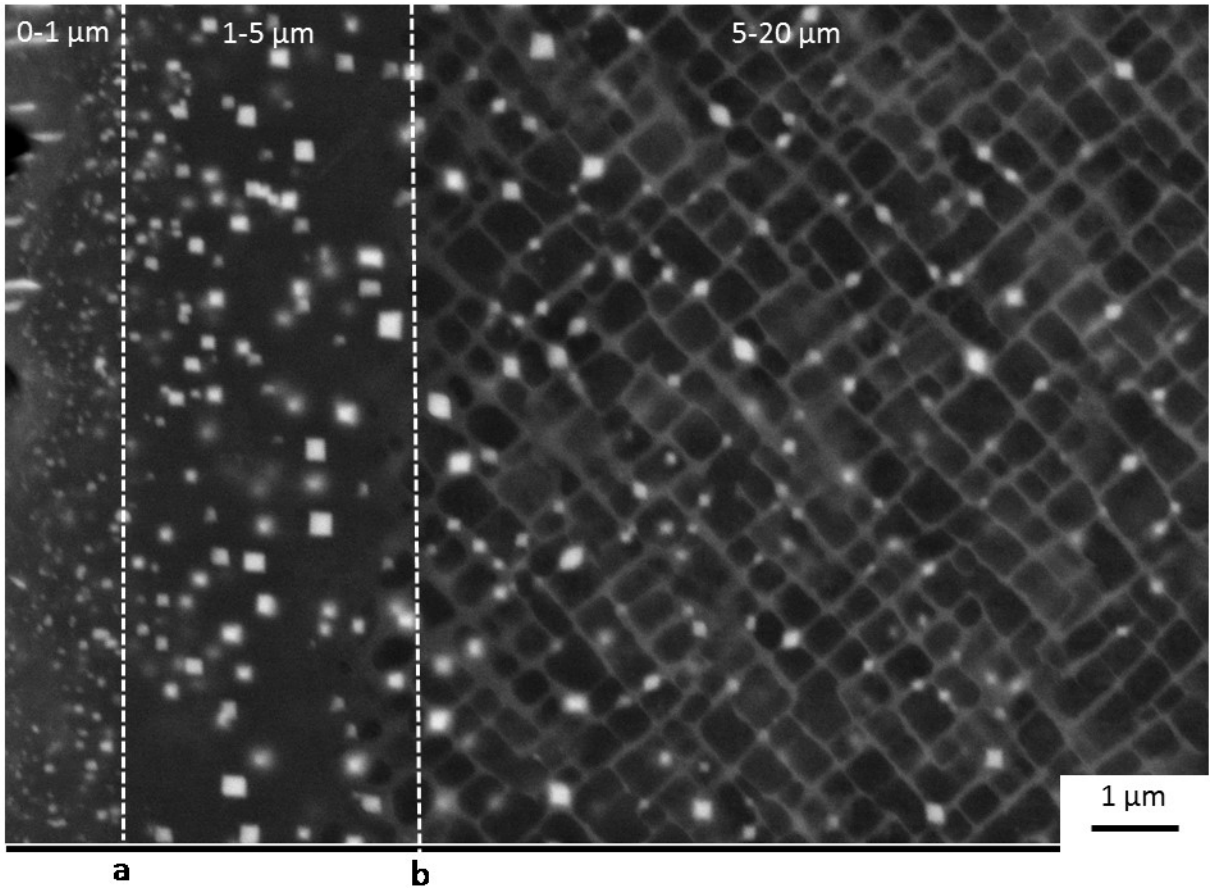


Figure 273: BSD micrograph of CMSX-10 illustrating different zones / morphologies of carbide type phase that can be isolated

Figure 273 shows a BSD micrograph of a characteristic carbide type phase rich area in CMSX-10 extending 20 µm into the sample from the perimeter edge. The carbide type phase could be found to arrange themselves into 3 diffusion regions, from 0-1 µm, 1-5 µm and 5-20 µm. The carbide type phase characteristics from the total area from 0-20 µm and the three smaller areas that make up the total area can be seen in table 1.

Table 28: Characteristics of the carbide type phase in CMSX-10

Distance (µm)	No.	Area (µm^2)	Circ	AR	Round	Solidity
0 -20	310	0.0282	0.8103	1.2895	0.8207	0.8077
0 -1	74	0.0155	0.8675	1.6834	0.7614	0.8941
1 -5	92	0.3110	0.0880	13.1160	0.0760	0.5070
5 -20	155	0.0281	0.7890	1.7938	0.8067	0.7920

Table 28 shows the carbide type phase characteristics of the carbide type phase in CMSX-10, the circularity and roundness values are very close to 1, indicating that the carbide type phase are indeed inherently regular and are indicative of the more stable fcc phase that should result in different mechanical characteristics when compared to the more irregular carbide type phase in CMSX-4. It was found that the orientation zones, as seen in figure 273, do not play a major role in the response of the mechanical properties.

9.6. Mechanical properties of CMSX-10

Table 29: Yield point (Y_p), Hardening rate (H_r), and Unloading Modulus vs distance for the different data sets testing the mechanical response as a function of distance through the carbide type phase rich (0-40 µm) zone in CMSX-10

Dataset	Pillar	Distance (µm)	Y_p (MPa)	Yield SD	H_r (MPa)	Modulus (MPa)
1	1	519	1000	44	4665	49211
252 – 541 µm	2	427	1050	37	4647	46672
Bulk	3	341	1043	12	5165	44463
	4	433	1030	25	4362	48060
	5	530	1050	12	4632	43204
	6	252	1050	26	4862	38664
	7	353	1040	28	4452	42544
	8	541	1000	41	4678	48521
2	9	19	700	9	6524	38140
8 - 45 µm	10	14	839	31	6786	38706
Carbide rich	11	11	684	12	5088	31653
	12	8	750	32	5220	33709
	13	45	860	25	5992	40177
	14	40	660	35	3113	32374
	15	36	700	11	3106	32431
	16	28	663	17	6372	30921
3	17	30	888	18	3201	39122
Carbide + Bulk	18	107	1000	40	4824	39541

Micropillars with areas ranging from 21-26 µm^2 were fabricated at regions within the CMSX-10 microstructure. The micropillars extended from the outer edge of the sample well into the bulk material

(~500 µm) in three different data sets, as shown in figure 274. The mechanical results are summarised in table 29.

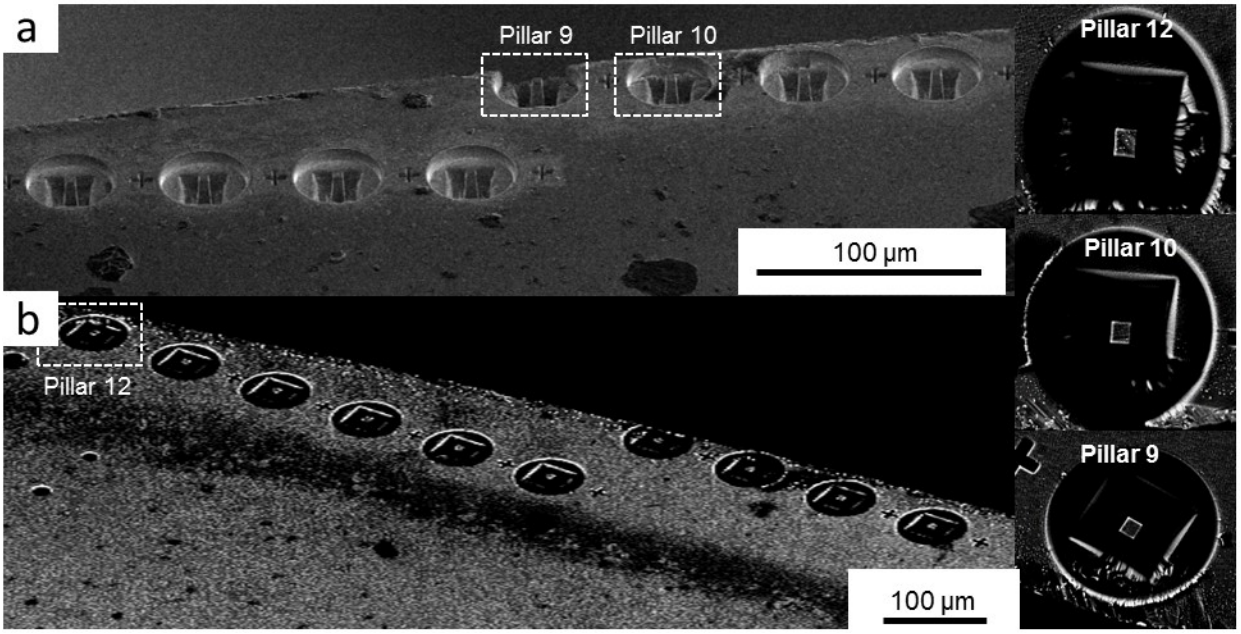


Figure 274: Pillars fabricated within the carbide type phase rich region of CMSX-10 , 0-40 µm from the perimeter edge, as shown in data set 2, pillars 9,10&12 are carbide type phase isolated pillars with carbide type phase area fractions respectively 3.2, 8.9 4.6 respectively, figure 281

Figure 274 shows micropillars fabricated on the CMSX-10 alloy within the carbide type phase, rich zone and some distance towards the bulk. The mechanical results of all the tested micropillars can be seen in figure 275. The diffusion zone in CMSX-10 is much less (4x less) than that of CMSX-4 and thus the variation in mechanical properties stabilises much quicker with respect to distance than CMSX-4,figure 275.

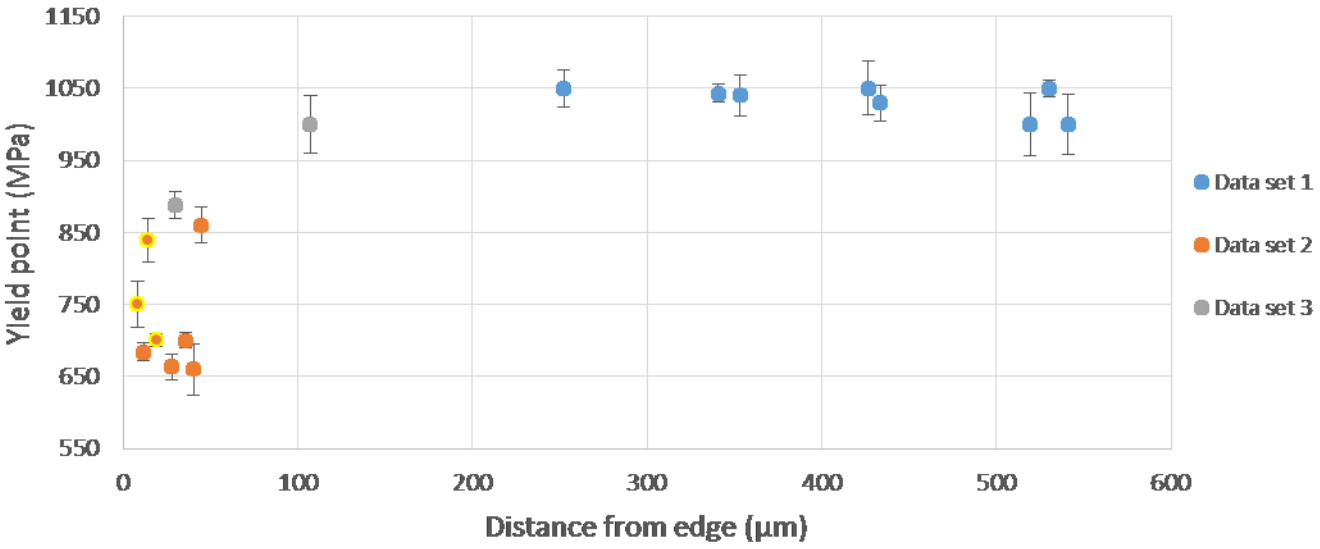


Figure 275: Yield point vs distance from the perimeter edge of the CMSX-10 sample, the yellow points in dataset 2 correspond to pillars with isolated carbide type phase,

Figure 275 shows the yield point vs distance for the micropillars in CMSX-10. The pillars in data set 2 were all located within the carbide type phase rich region, the points highlighted in yellow were the carbide isolated pillars as shown in, figure 274. The pillars tested within the carbide type phase, rich region (data set 2) have lower yield points than those outside of this region. This can be attributed to the disruption of the microstructure and leeching of alloying elements caused by the precipitation of the carbide type phase.

It can be seen that the minimum yield point occurs at 660 MPa (data set 2). The minimum yield point corresponds to a pillar containing no visible carbide type phase, located ~28 µm from the outer rim of the sample. The maximum yield point occurs at 1050 MPa (data set 1). It corresponds to a pillar containing no carbide type phase located ~430 µm from the perimeter edge. The elastic / strain moduli for the pillar with the minimum and maxiumum yield point were; 47 GPa / 3 GPa and 31 GPa / 6 GPa respectively.

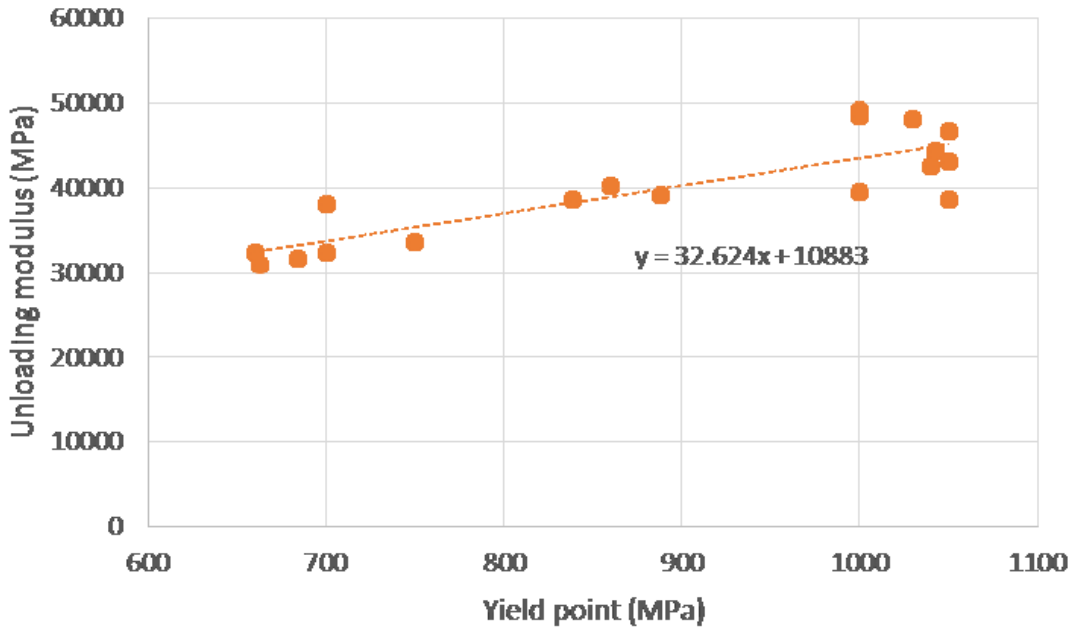


Figure 276: Yield point vs Hardening of pillars fabricated in cmsx-10 from the perimeter edge 0 - bulk microstructure 550 µm.

Figure 276 shows the elastic modulus vs the yield point for all the 18 pillars tested. It can be seen that there is a proportional relationship between the elastic modulus taken from the unloading region of the stress strain curve and the yield point.

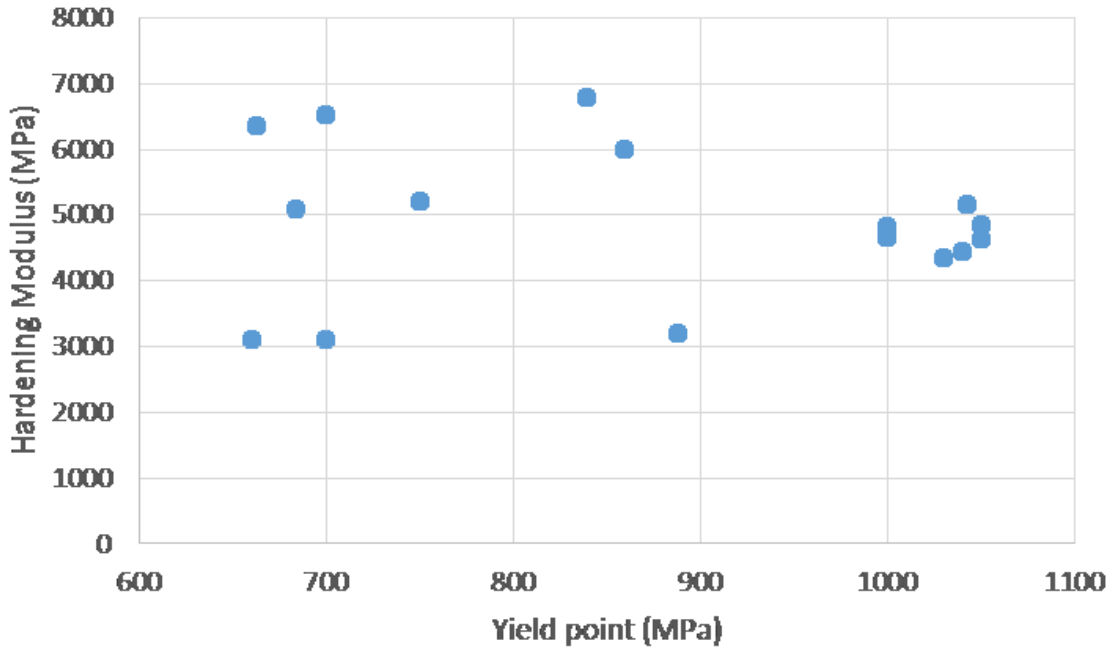


Figure 277: Yield point vs Unloading modulus of pillars fabricated in cmsx-10 from the perimeter edge 0 - bulk microstructure 550 µm.

Figure 277 shows yield point vs the hardening modulus for the tested pillars. The relationship between the hardening modulus and yield point is less clear. The TEM examination of the carbide type phase, rich area in CMSX-4 indicated that carbides exist below the surface plane, and so the carbide type phase, could also exist within the pillars and thus effect the hardening of the pillars as a consequence, causing the large degree of scatter.

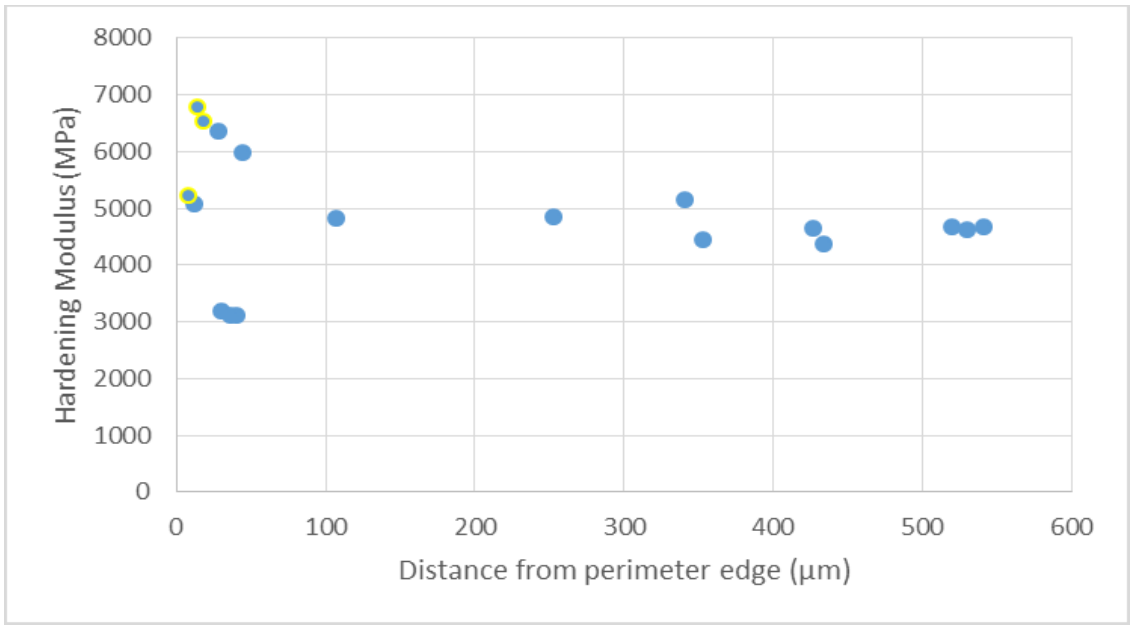


Figure 278: Hardening modulus vs Distance from the perimeter edge (µm), with the carbide type phase pillars highlighted in yellow

Figure 278 shows the hardening modulus vs distance from the perimeter edge for all the 18 pillars tested. It indicates that the majority of the scatter in the data comes from the carbide type phase rich region and the rest of the hardening values remain fairly constant. The scatter of data in the carbide rich area is to be expected.

Pillars located within the carbide type phase rich region (1-40 µm) in CMSX-10 had an average hardening moduli of ~6 GPa, pillars tested outside this region 40 µm+ has hardening moduli ~4 GPa.

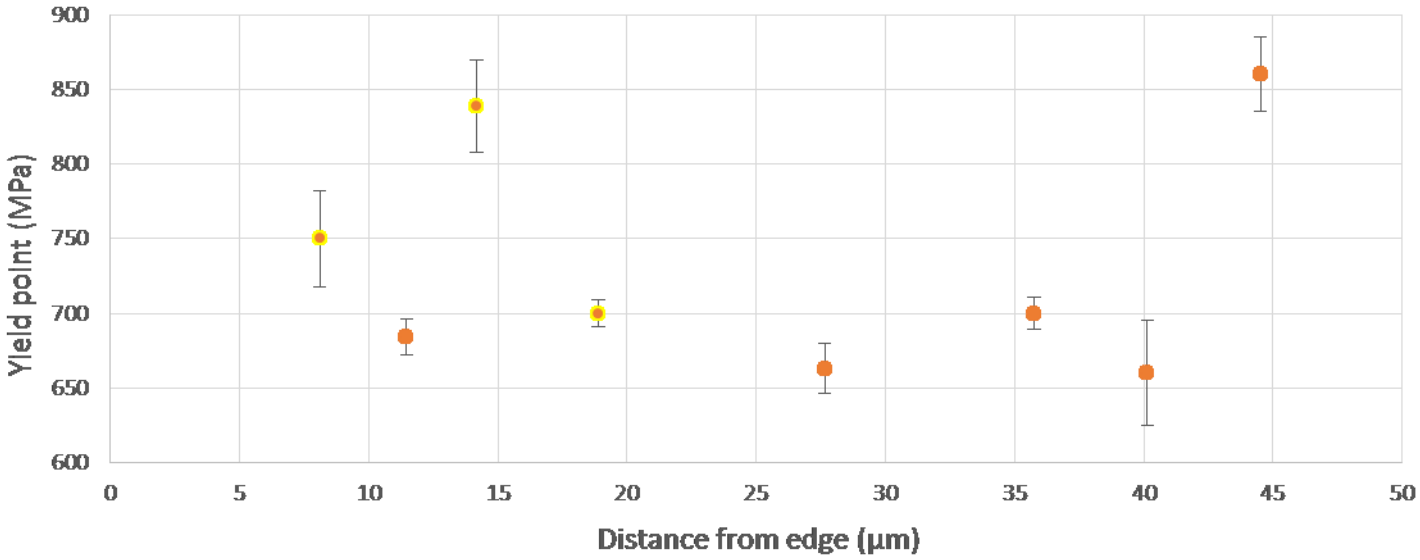


Figure 279: Results from micro pillars located within the carbide type phase rich zone – Yield point vs distance from the edge

Figure 279 shows the yield point vs distance for pillars located within the carbide type phase, rich region of CMSX-10, from 0-40 µm, where carbide type phases are clearly visible on the {001} surface plane of the sample. Of the 8 pillars fabricated in this region, 3 contained carbide type phases visible on the top section of the pillars, figure 281. It was found that pillars with isolated carbide type phases in CMSX-10 increase the local yield point of the pillars in this region by ~10%.

The strengthening ability of the carbide type phase in CMSX-10 indicates that the carbide type phase, have a degree of coherency with the ϒ/ϒ' matrix[122] and do not cause high levels of disruption to the flow of dislocations[206]. This is illustrated by the carbide type phase isolated pillars, highlighted in yellow in figure 279. The carbide type phase, isolated pillars, highlighted in yellow, do not correspond to a decrease in yield point and the moduli of these pillars remains fairly consistent to the average moduli in this region (35 GPa).

The average yield point of pillars in the carbide type phase, rich area is 732 MPa with the most noticeable deviations in yield point arising from carbide type phase, isolated pillars and a pillar 45 µm from the

perimeter edge. The pillar 45 µm from the perimeter edge is just outside of the area where the carbide type phases are clearly visible on the {001} surface plane.

The extent and average size of carbide type phase in CMSX-10 is much smaller than in CMSX-4 with an average size of 60 nm. With respect to the carbide type phase isolated pillars, pillar 9 was 19 µm from edge, pillar 10, 14 µm and pillar 12, 8 µm, figure 281.

Pillar 2 had the highest yield point 839 MPa, this could be due to the fact the carbide type phase are small in nature and orientated to lie within the ϒ' channels increasing the ϒ' strengthening effect. Pillar 10 also had the highest hardening moduli - 6.8 GPa and an elastic moduli of 39 GPa.

Pillar 12, which was 4 µm ahead of pillar 10, had a similar hardening / elastic moduli – 6.5 GPa / 38 GPa, but a much lower yield point, 700 MPa. This again suggests that the orientation / morphology of the carbide type phase plays a role in the strengthening effect[17].

Pillar 4, contained the lowest volume fraction of carbide type phase and had a yield point of 750 MPa and hardening / elastic moduli of 5.2 GPa and 34 GPa respectively, it was located 8 µm from the perimeter edge. In the case of CMSX-10 it appears that the distance from the perimeter edge does not play a major role of the mechanical properties in the carbide type phase rich region.

The stress strain response from data set 2, figure 279 shows good consistency (low level of deviations from the average) with the largest discrepancies arising from carbide type phase, isolated pillars. This again is to be expected and can be ascribed to the carbide type phase shape / distribution.

As explained above the formation of carbide type phase disrupts the heat treatment of the alloy and its ability to form stable precipitates which accommodate the heat / aging treatments used to produce a fine cuboidal dispersion of ϒ/ϒ'.

Table 30: Carbide type phase isolated pillars 9,10,12, associated carbide type phase area fraction and mechanical properties

Pillar no.	Carbide % Area	Y_p (MPa)	H_r (MPa)	E_i (MPa)
9	3.2	700	6524	38140
10	8.946	839	6786	38706
12	4.6	750	5220	33709

Out of the 18 pillars tested, three of the pillars (9,10 and 12) had carbide type phase isolated on the top surface. It was found that the yield point increased proportionally with the % carbide type phase area fraction, figure 280 and figure 281.

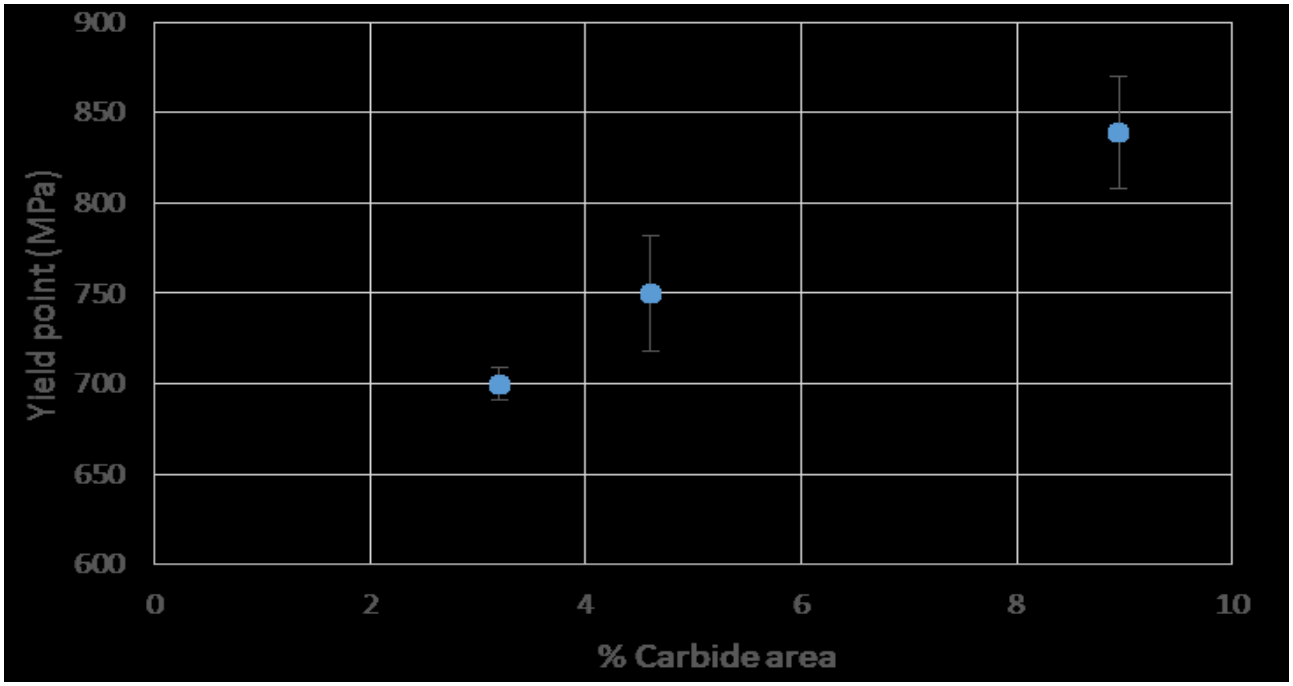


Figure 280: Yield point vs Carbide type phase area fraction for the three carbide type phase isolated pillars, 9, 10 and 12.

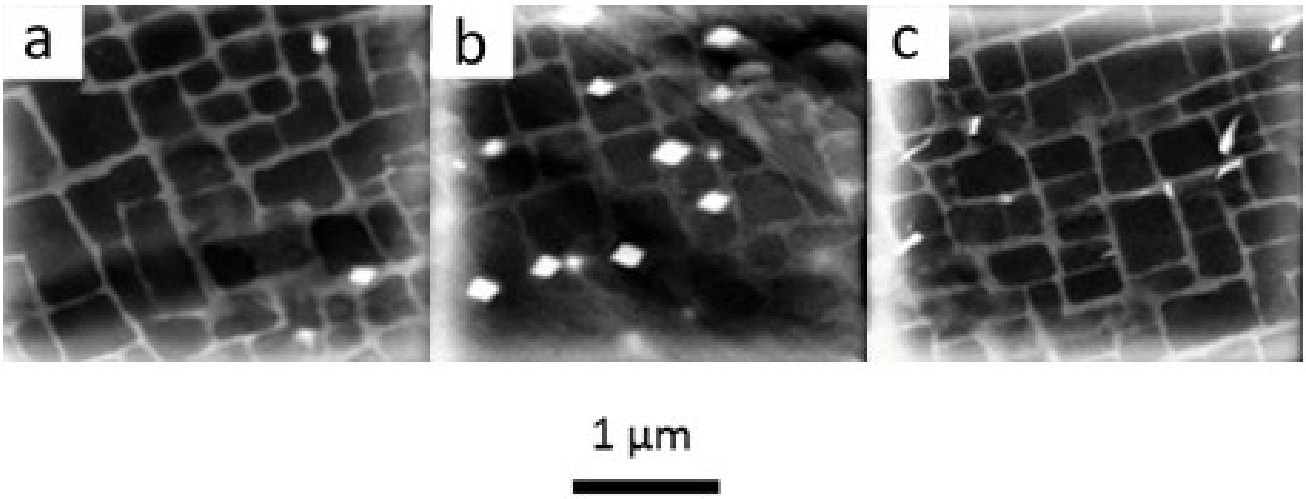


Figure 281: BSD image of three carbide type phase isolated pillars (a) Pillar 12 – 4.6 % carbide type phase area fraction. (b) pillar 10 – 8.9 % carbide type phase area fraction (c) pillar 9 – 3.2 % carbide type phase area fraction

9.7. Summary – Results chapter 4

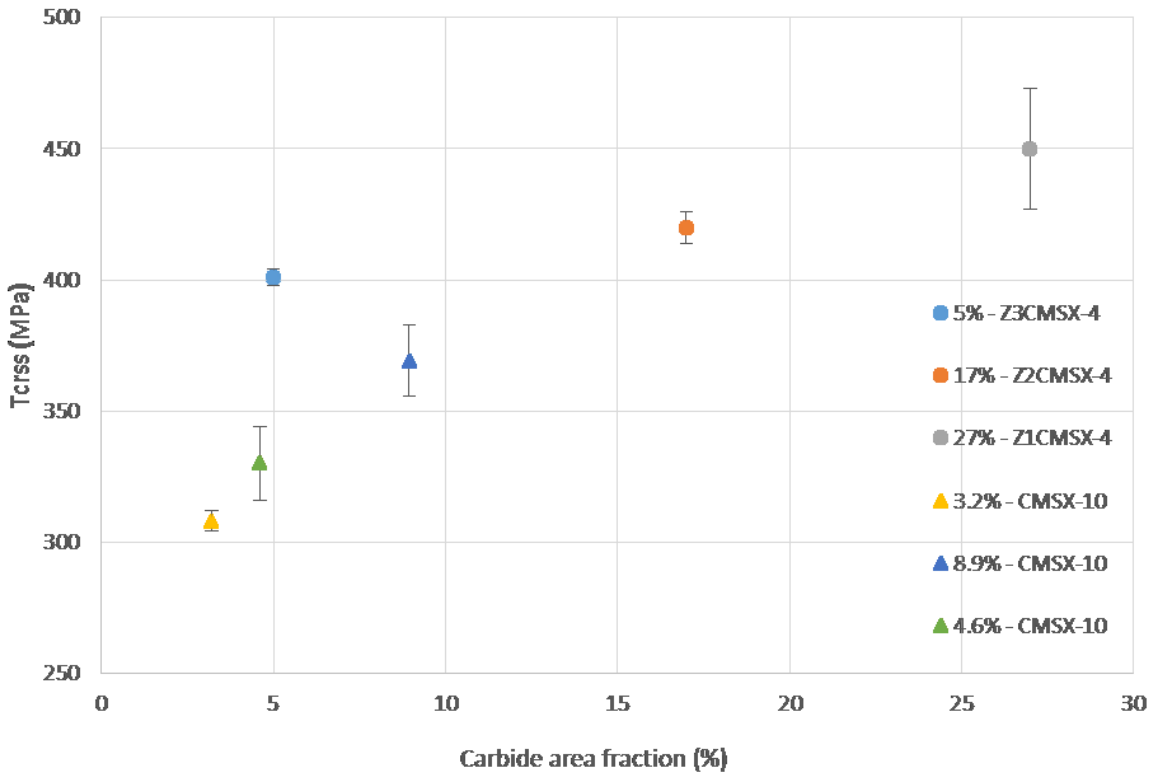


Figure 282: Carbide type phase area fraction vs Tcrss for carbide type phase isolated pillars in CMSX-4 and CMSX-10

The results from the carbide type phase isolated micropillar compression tests on CMSX-10 mirror those done on second generation CMSX-4. The carbide type phase area type phase fraction is calculated from the top surface of the pillar, and the assumption is made that the carbide type phase shape is regular and continues downwards in the z axis. It was found that the carbide type phase area fraction, is proportional to the τ_{Crss}, calculated through the orientation of the pillars. The data as shown in, figure 282 illustrates the proportional trend, there is however, one spurious result in the CMSX-4 data point at 5%. The micropillar corresponding to this point, contained large TCP phase that intersected through several Ɣ/Ɣ' junctions and cuboids, resulting in a catastrophic strain burst at the onset of yield and more brittle response when compared to the other pillars.

The response of the proportionality between the τ_{crss} and the carbide type phase area fraction, could be a consequence of the carbide type phase, acting as stress concentrators, thus increasing the overall strength of the pillar but subsequently decreasing the modulus. When comparing the elastic modulus to the carbide type phase area fraction, across both alloys, there appears to be no clear trend as other factors including distance and carbide type phase, must be taken in to consideration.

10. Discussion

10.1. Introduction

Ni based super alloys are used in the hot section of an aeroengine and they are one of the heaviest components. Improving the strength of the alloys means that less material can be used per unit area, thereby reducing the overall weight of the engine, improving fuel economy. Increasing the lifetime of these alloys requires an understanding of the deformation process. The advantage of the micro scale is that the deformation systems activate near these length scales (nm-µm) and the performance of individual and structural units can be extracted. Deformation behaviour, characterised by stress strain traces, mechanical variables and slip behaviour can be observed *in-situ* and analysed. Individual features such as grains, microstructural zones and precipitates which are of the length scale of micrometres can also be isolated and tested to determine characteristic behaviour.

The main features of this thesis have centred around micromechanical tests, examining the performance of Ni-based superalloy microstructures across second / third generation single and polycrystalline superalloys. The mechanical performance of these alloys are based on the relationship between the dual phase ϒ/ϒ' structure. The ϒ/ϒ' structure is created through a series of specialised heat treatments and homogenisation steps[207]. Dislocations travel through the ϒ/ϒ' structure at the onset of yield, characterised by an inflection and change in gradient of the corresponding stress strain curve. The stress strain curves in this thesis are derived from load displacement curves extracted from *in-situ* micromechanical testing. Micromechanical testing enables *in-situ* experiments to be performed, in which the deformation of the alloys can be viewed, as a specified displacement is placed on the test sample. The slip traces which occur as a consequence of deformation can subsequently be traced back to individual points on the stress strain curve and examined further. The influence of orientation and carbide precipitation have been examined and analysed. The testing on Ni-based superalloys includes experiments on carburised and an un carburised alloy in three orientations {001} {011} {111}, tested through micro pillar compression and Berkovich indentation. The tests highlight the differences in mechanical properties, in which characteristic slip behaviour is activated via a stress tensor which is different in each orientation / microstructure. This chapter will discuss the salient points from the combined testing on all alloys. Focusing in on chemistry effects on local mechanical properties of an alloy with a spectrum of carbide type phases inhabiting the ϒ/ϒ' microstructure. figure 283 to figure 286 show a compounded stress vs strain graph, pillar deformation images from three orientations and EDX map over carbide type phases respectively.

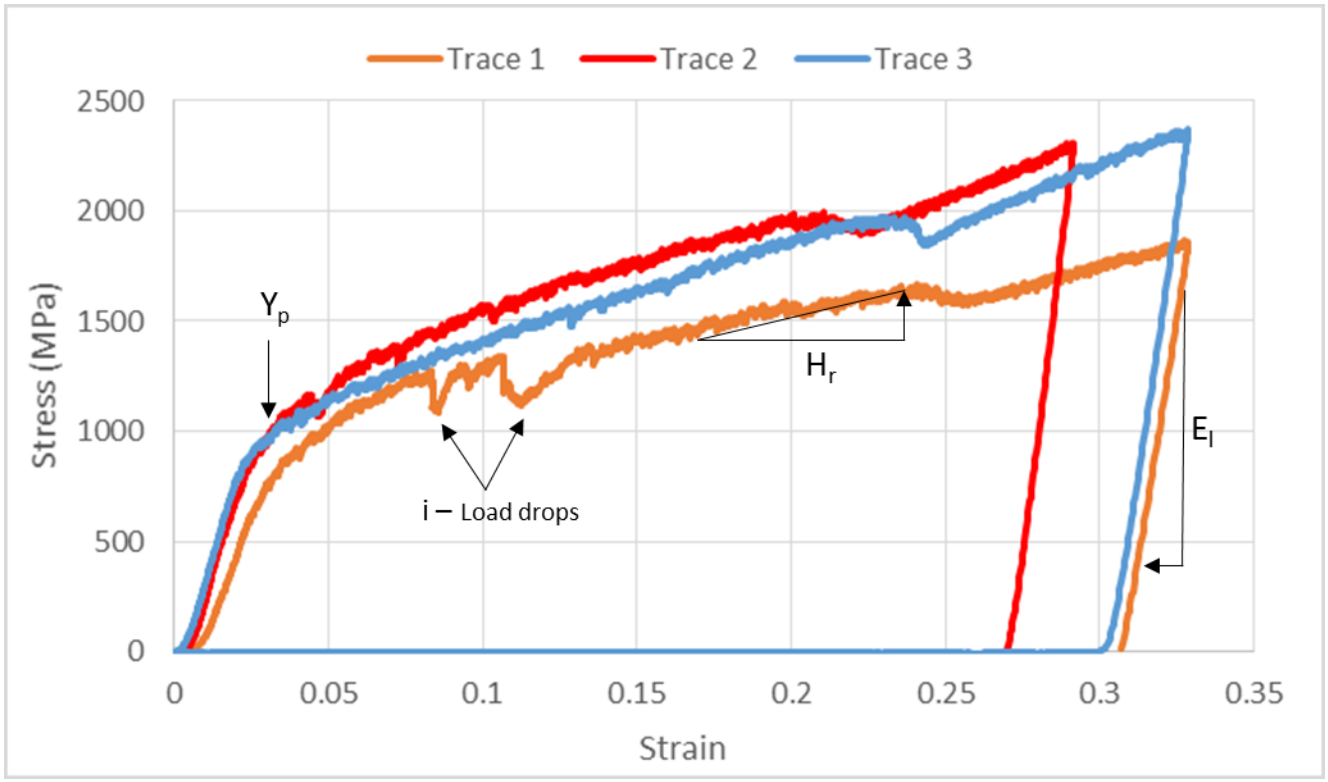


Figure 283: Stress strain trace from three deformed CMSX-4 micropillars, translated from load displacement data recorded during in-situ micromechanical testing. Examination of the traces informs of the yield point, Y_p, Hardening H_r and elastic modulus El of the alloy. The hardening trace is the most prominent of the three and can inform of strain phenomena shown an I, which can occur in unstable orientations / carbide type phase, rich alloys. Pillars compressed in the same orientation, with the same size and shape should produce repeatable traces that match each other. Trace 1 has a different Y_p,H_r and E_I than traces 2 and 3 as this is a pillar from a different alloy, the strain phenomena in this case is due to an unstable orientation. Traces 2 and 3 are from the same alloy, in the same orientation but slightly different sizes, in general the Y_p, E_I and H_r agree.

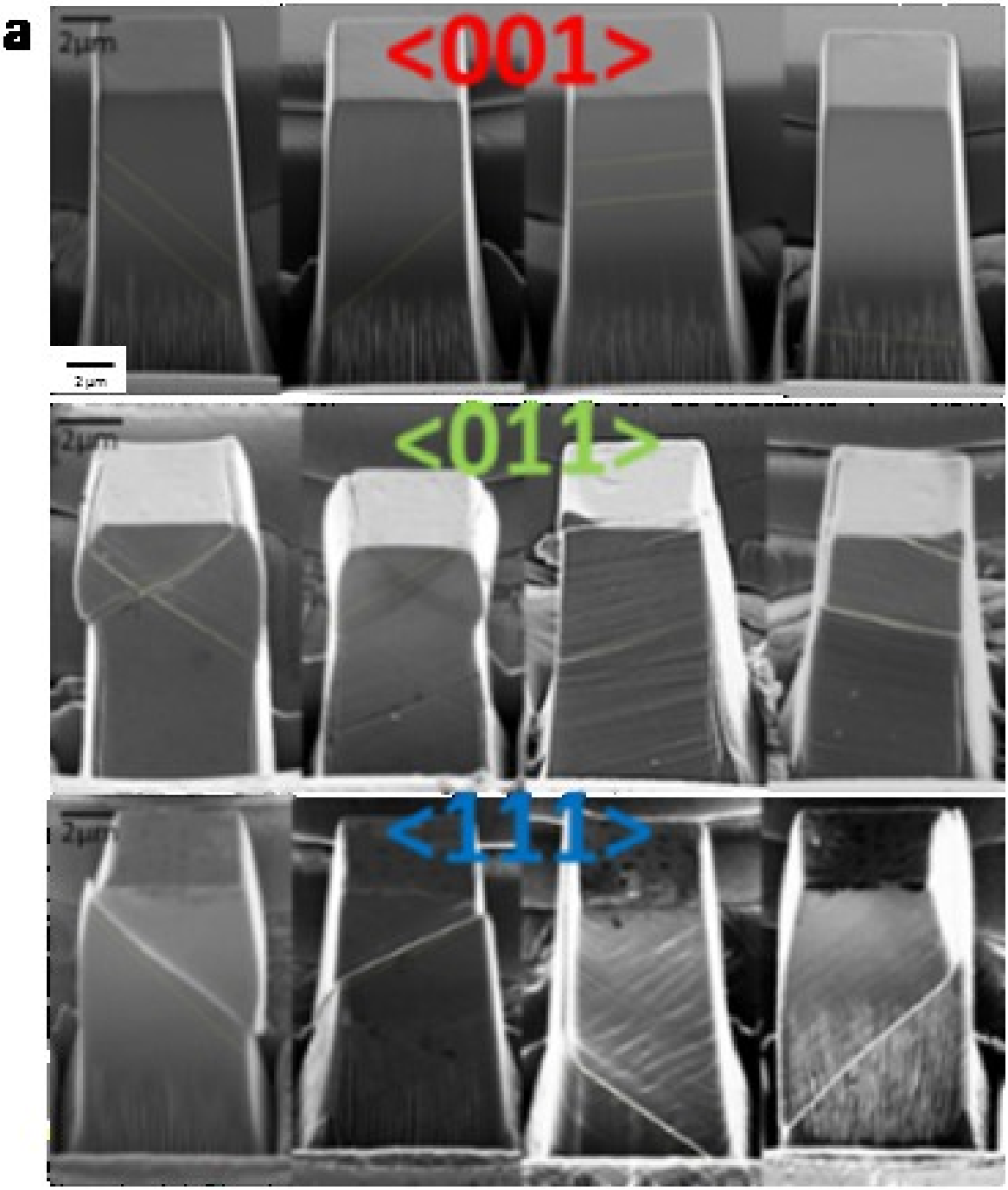


Figure 284: Compressed CMSX-4 micropillars (a) deformed pillars through orientations {001},{011},{111},top to bottom prepared via a goniometer stage, in which differing slip traces can be observed.

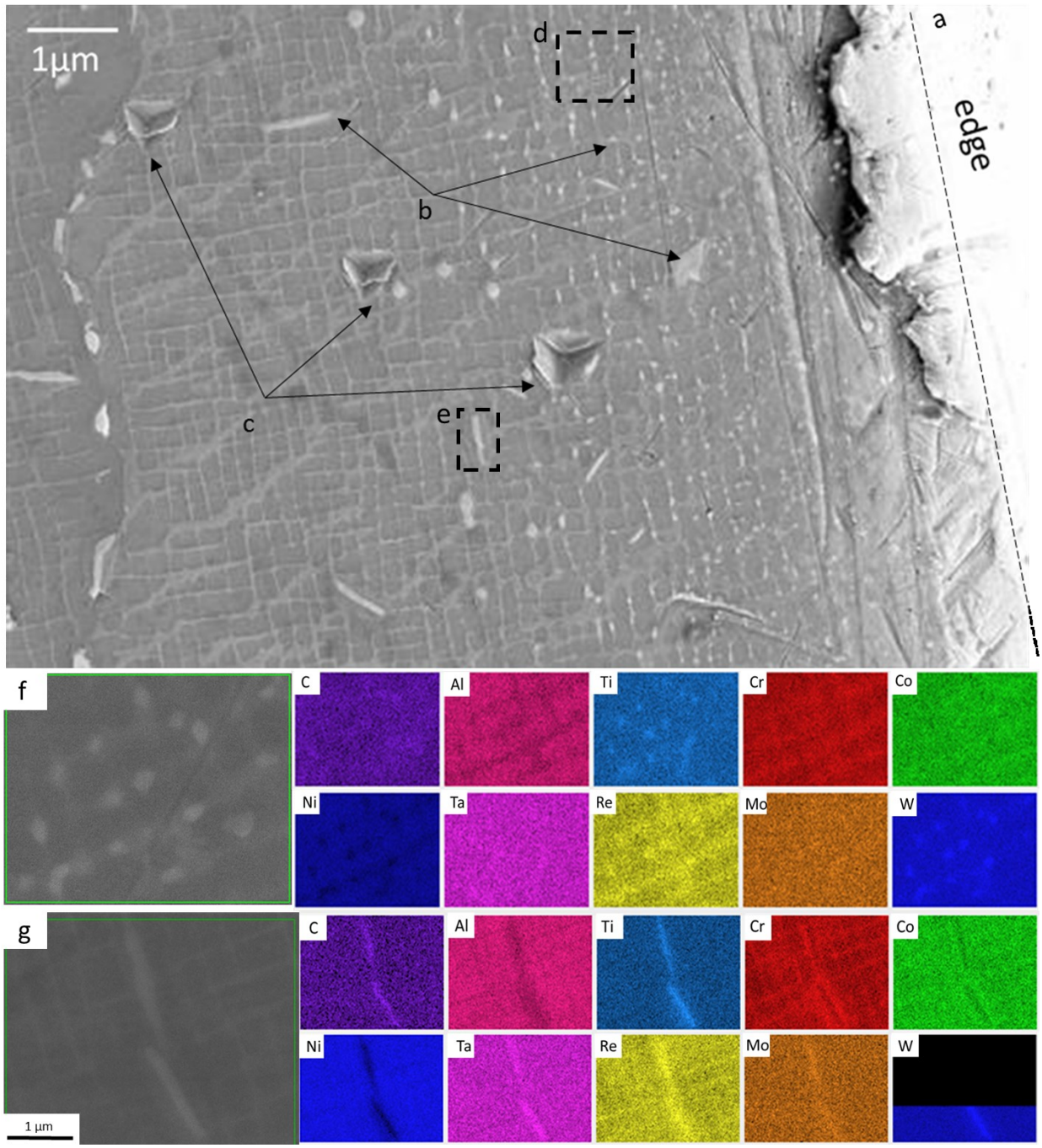


Figure 285: Carbide type phase, rich area in CMSX-4 (a) Perimeter edge of sample taken as 0 µm (b) several types of carbide type phase visible on the top surface of the alloy (c) A small array of micro indents (d) A representative EDX map scan area of fcc type carbide phases as shown in f. A representative EDX map scan area of TCP phase as shown in g. (f) An EDX map scan over small fcc type carbide phases inhabiting the ϒ and ϒ /ϒ' junctions, showing a strong presence of Ti and W and a strong depletion of Ni in the presence of a carbide type phase. (g) An EDX map scan over two large TCP phase intersecting several ϒ' cuboids and ϒ /ϒ' junctions, showing a strong presence of C,Ti,Ta,Re,Mo and W and a strong depletion of Ni,Al,Cr and Co in the presence of a carbide type phase.

10.2. Discussion overview

Micropillars were fabricated via joint FIB / SEM patterning. The micropillars were approximately 5 µm in width and 13 µm in height, these measurements were used as this was found to be the most stable configuration, as found via a size effect study. Pillar experiments enable the analysis of deformation at characteristic strain(s). Where roughly nominal 3.5% strain equates to the yield point, ≤ 3% strain is the elastic regime ≥ 3% plastic regime. This enables pillars to be loaded to specific strains taking a "snapshot in time" of the deformation mechanics within the microstructure of interest, ranging from single, polycrystalline and carbide phase microstructures.

The critical resolved shear stress of pillars fabricated in {001} {011} {111} on single crystal CMSX-4 varied by 380 ± 10 MPa, 420 ± 15 MPa, 460 ± 16 MPa respectively, the resolved shear stress of pillars fabricated on individual grains on a polycrystalline sample, with nearly identical areas in the same orientation varied by less than 5%. The critical resolved shear stress varies due to the activation of differing stress tensors[146] activated due to the change in crystal orientation and be characterised through slip traces, EBSD and the analysis of the yield point.

The critical resolved shear stress of pillars fabricated on single crystal CMSX-4, with carbide type phases captured on the top surface of the pillar varied by 400 ± 3.4 MPa, 420 ± 6 MPa 450 ± 23 MPa, despite being the same crystal orientation and in similar locations ± 20 µm. The variation was a consequence of changes in ϒ/ϒ' morphology carbide type phase area fraction and shapes, the area fraction of the pillars mentioned above were; 5% 17% and 27% respectively.

In the carburised study pillars were placed as a function of distance and microstructure. It was found that the carbide type phases leech alloying elements disrupting the homogenisation of the microstructure, thus disrupting the mechanical properties, leading to a weaker more brittle material. In the CMSX-4 alloy, which had a large carbide type phase rich region, the mechanical properties varied as a function of distance and continued to vary in regions outside of the carbide type phase region, upto approximately 400 µm. The slip characteristics in this region 200 – 450 µm is examined in this section. The greatest variation in mechanical properties in the CMSX-4 alloy, arose from pillars in the carbide type phase rich area and with carbide type phases isolated on the top surface of the pillar.

The same trend was found in a third generation CMSX-10 alloy. The carbide type phase, rich region in the CMSX-10 alloy was 4x less than in CMSX-4. It was found that in CMSX-10 the mechanical properties did not vary as a function of distance and were mainly influenced as a consequence of proximity to the carbide type phases which leech elements and act as a stress concentrator.

The first round of mechanical examination on the carburised CMSX-4 was done using micropillar experiments. Micro indents were placed on the CMSX-4 alloy to validate the findings of the micropillar

experiments, which were found to be consistent. EDX map scans were placed over 1 µm indent impressions and the elemental concentrations, as a function of distance and concentration were mapped.

10.3. Characterisation

10.3.1. ϒ/ ϒ’ structure

To ensure a fair analysis when testing individual alloys, the orientation and ϒ/ϒ’ volume fraction were kept as consistent as possible. The orientation can be checked via EBSD and ϒ/ϒ’ volume fraction was found using BSD and image analysis. It was found that the ϒ/ϒ’ volume fraction remains constant ± 3% across alloys assuming a constant pillar width of 4.5-5 µm.

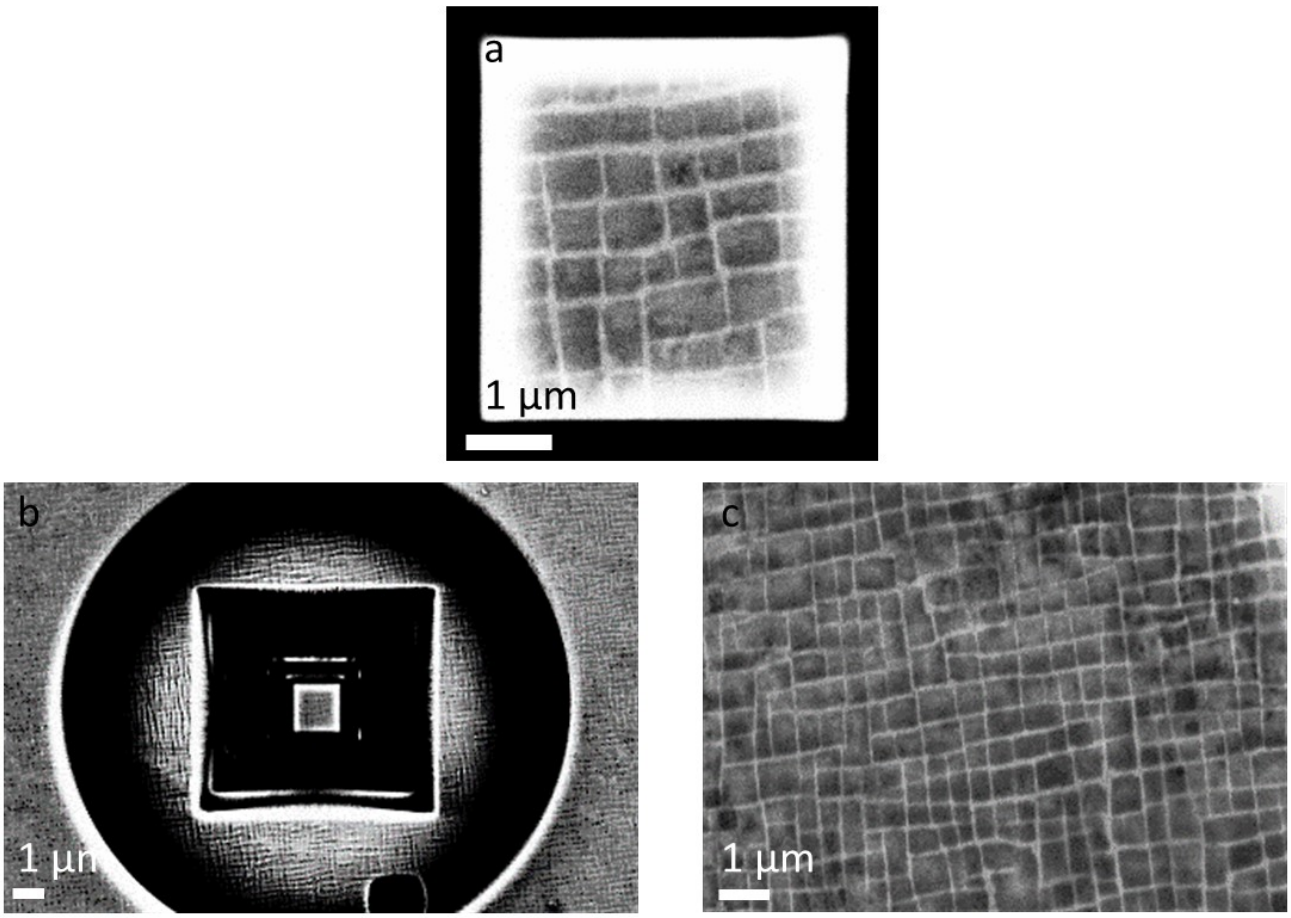


Figure 286: BSD images highlighting the ϒ/ϒ’ distributions on different features of micropillar (a) Top of micropillar (b) Surrounding area of a micropillar (c) pure ϒ/ϒ’ matrix of area surrounding pillar – 30 µm.

Figure 286, shows the ϒ/ϒ’ distributions in the top surface, surrounding area and bulk areas of a fabricated micropillar. The white contrast that can be seen on the trenches and top surface of the pillar represent ion damage from FIB milling, which was minimised as much as possible. As the interplay between the ϒ/ϒ’ gives rise to the bulk of the mechanical properties in Ni-based superalloys, the volume fraction of ϒ/ϒ’ across different alloys was checked using BSD and image J and it was found that the ϒ’ volume fraction remained consistent ± 3%.

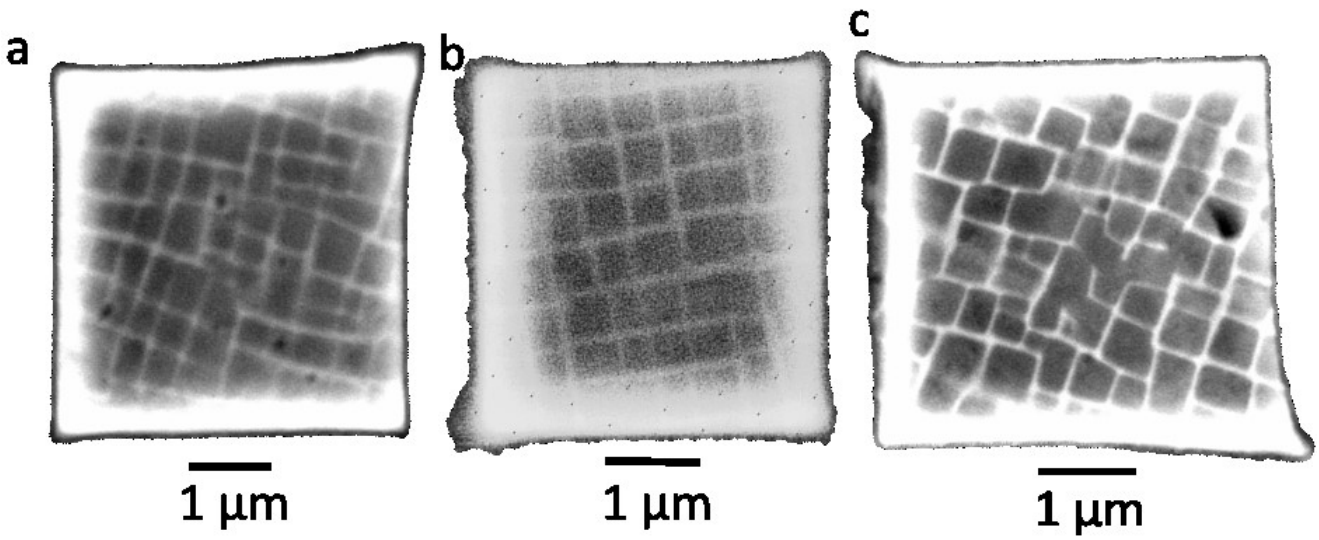


Figure 287: BSD images of (a) CMSX-10 (b) CMSX-4 (c) Carburised CMSX4

Figure 287, shows the top surface of three micropillars, fabricated on CMSX-10, CMSX-4 and carburised CMSX-4 respectively. The average ϒ' volume fraction / ϒ' width in each alloy respectively was 74% / 455 nm, 73% / 532 nm, 74% / 562 nm. The ϒ/ϒ' microstructure can be viewed by one of three methods, chemical etching, TEM, BSD. Chemical etching provides the highest resolution followed by TEM then BSD. BSD is however the most accessible and requires the lowest time to prepare and examine, this is shown in figure 288.

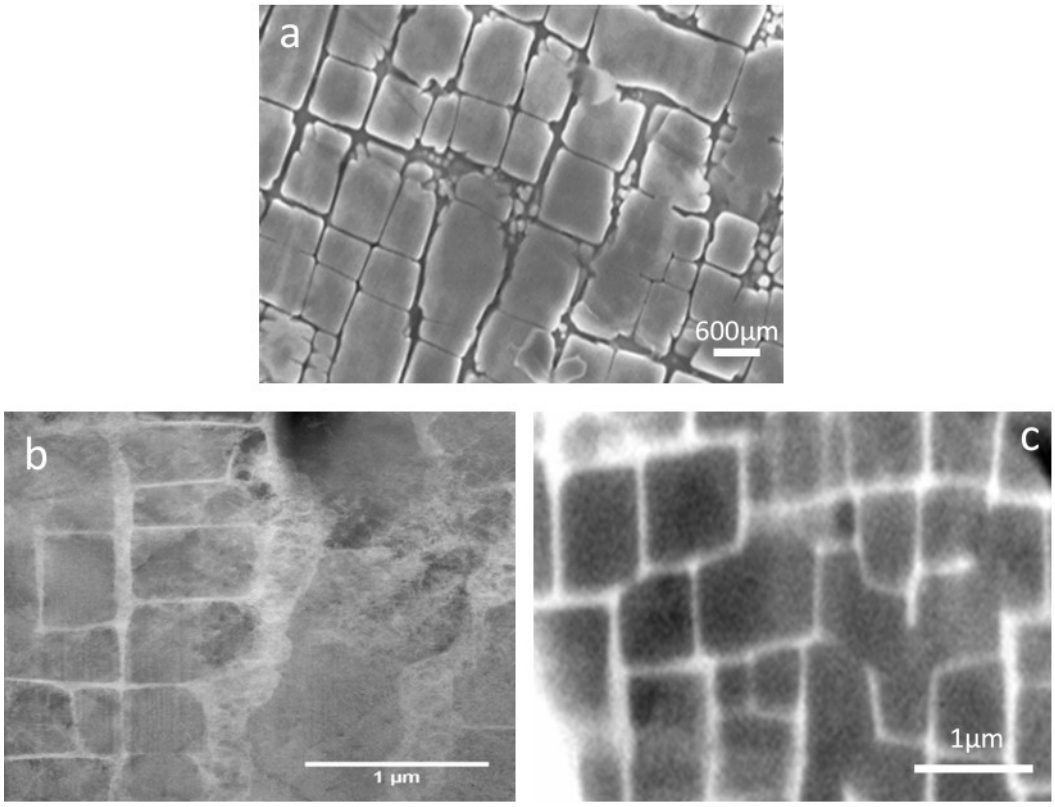


Figure 288: ϒ/ϒ' distributions in (a) electro etched (b) TEM (c) BSD

10.3.2. Chemical analysis

The Ni-superalloys are comprised of 10+ alloying elements with careful considerations made to each alloy type and generation of alloy to enable features such as, grain boundary strength in polycrystalline alloys, to higher creep strength in single crystal, to a lower solutioning window to prevent the formation of TCP phase in third generation alloys. Despite differing elemental concentrations across alloys, the predominant ϒ and ϒ' stabilisers still remain present. The ϒ and ϒ' stabilisers with their associated atomic radii are shown below in figure 289.

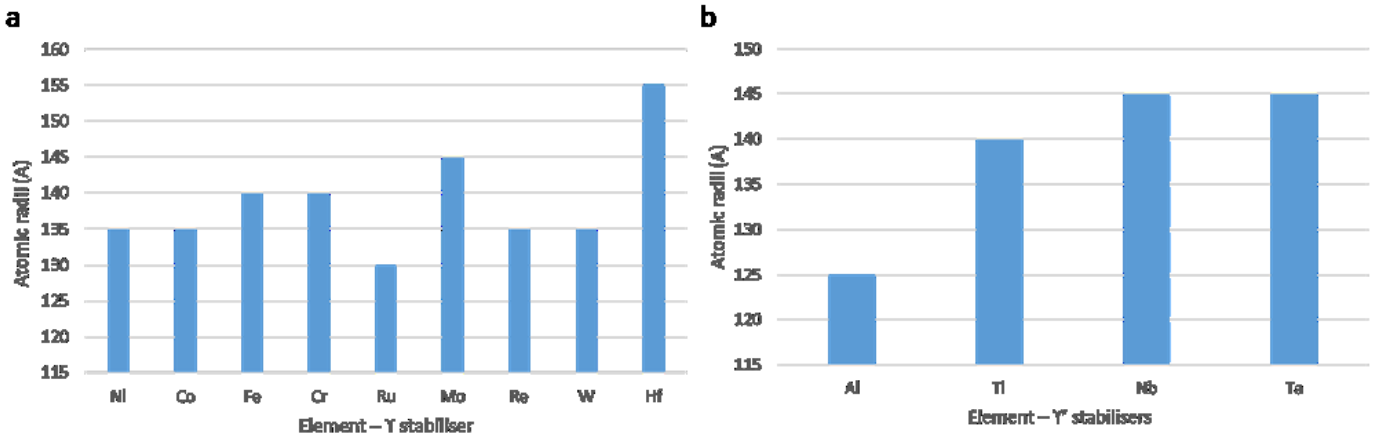


Figure 289: Atomic radii vs element of stabilisers

When considering carbide type phases, it was found that they were formed as a by-product of the pack aluminzation process, in which a gradient layer is grown from the Ni substrate to the Al_2O_3 top coat[96]. The carbide type phases form differently when comparing the CMSX-4 alloy to the CMSX-10 alloy, this is due to differences in alloy concentration and solutioning window. The main carbide type phase stabilisers were Ta, Ti and Mo, specifically for the formation of the deleterious TCP phase. Figure 289, shows the atomic radii vs the associated element, it can be seen that the carbide type phase stabilisers generally favour elements with atomic radiis of 140 A or higher. This could be a consequence of the formation of the stability of the kasper polyhedral[119], which gives the carbide type phase, its structure and orientation with the ϒ/ϒ' matrix.

Table 31: EDX results, listing the elements and normalised mass % across the virgin CMSX-4, polycrystalline FGH96 and carburised CMSX-4 & CMSX-10

	Al	Ti	Cr	Co	Ni	Mo	Hf	Ta	W	Re	C	Total
CMSX-4	4.29 ±0.2	1.1 ± 0.1	6.17 ± 0.1	8.28 ± 0.2	55.03 ± 1.1	0.4 + 0	1.31 + 0	7.95 ± 0.2	6.15 ± 0.1	4.38 ± 0.1	4.29 ± 0.8	99.35
FGH-96	1.41 ± 0.03	5.39 ± 0.03	19.63 ± 0.12	12.92 ± 0.12	54.32 ± 0.17	4.3 ± 0.15	-	-	2.03 ± 0.06	-	-	100
C_CMSX-4	5.24 ± 0.21	1.70 ± 0.05	5.94 ± 0.15	8.55 ± 0.19	61.70 ± 1.14	0.27 ± 0.04	0.017 ± 0.0	7.59 ± 0.16	1.37 ± 0.12	1.37 ± 0.08	5.9 ± 0.80	99.6464
C-CMSX-10	1.72 ± 0.12	1.31 ± 0.08	8.63 ± 0.21	11.12 ± 0.17	64.13 ± 0.8	0.45 ± 0.06	0.00	6.36 ± 0.14	2.27 ± 0.11	0.59 ± 0.01	3.4 ± 0.07	100

Table 31, shows the elemental concentrations taken across the virgin CMSX-4, FGH-96 and carburised; CMSX-4, CMSX-10. All of the compositions recorded via EDX agree with compositions found in literature[205,16,208]. The elemental compositions across the single crystal alloys CMSX-4, CMSX-10 and carburised CMSX-4 are in agreement, including the slight differences in alloy composition across the second and third generation alloys. Notably the carburised CMSX-4 contains more C than the virgin CMSX-4. FGH96 is a polycrystalline alloy and so the composition is different from the single crystal alloys. When comparing polycrystalline alloys to single crystal the polycrystalline alloys contain less C[21].Figure 290 shows the EDX results, listing the elements and normalised mass % across the virgin CMSX-4, polycrystalline FGH96 and carburised CMSX-4 & CMSX-10.

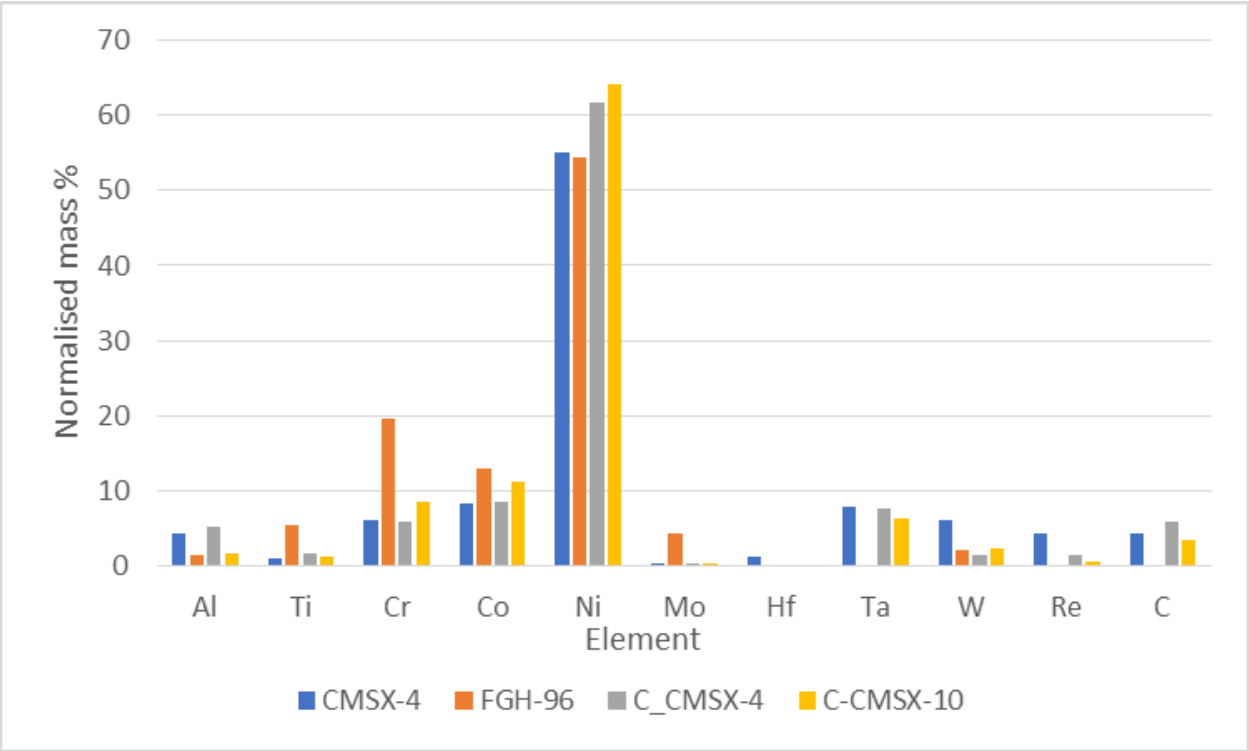


Figure 290: EDX results, listing the elements and normalised mass % across the virgin CMSX-4, polycrystalline FGH96 and carburised CMSX-4 & CMSX-10

10.4. Mechanical behaviour

10.4.1. Overview

Mechanical tests were performed across four alloys via micropillar compression tests, in which load displacement data was translated to stress vs strain data utilising the corrected measurements of the pillar area and length. In the case of the carburised CMSX-4 alloy, microindents were used to validate the micropillar experiments. The section below will analyse the stress strain behaviour across the alloys.

10.4.2. Stress strain analysis / phenomena

Table 32: Y_p, H_r and Elastic modulus of the four alloys, Carburised CMSX-4 and CMSX-10, polycrystalline FGH96, and virgin CMSX-4 all orientated near the <001> direction, as shown in figure 291.

Alloy	Y_p (MPa)	H_r (MPa)	Modulus (GPa)
C_CMSX-4	986 ± 34	2604 ± 40	48.78 ± 0.44
C_CMSX-10	860 ± 32	5992 ± 68	40.18 ± 0.38
FGH	750 ± 34	3154 ± 32	70.98 ± 0.61
V_CMSX-4	880 ± 38	3311 ± 31	43.33 ± 0.33

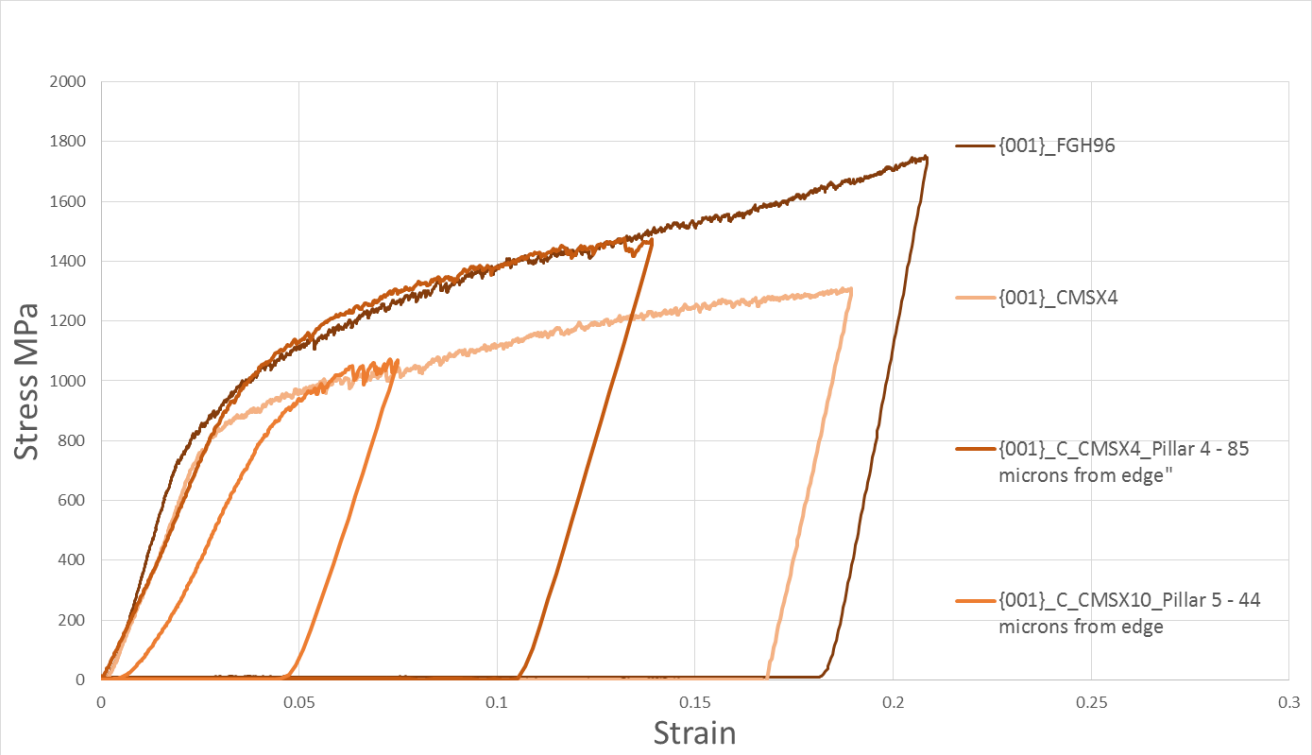


Figure 291: Stress strain traces of carburised CMSX-4 / CMSX-10, virgin CMSX-4 and polycrystalline FGH – all orientated near the <001> direction.

Table 32 shows the yield point, hardening rate and elastic modulus across the four alloys and figure 291 shows the representative stress strain traces, from which these values were taken. Carburised CMSX-4 had the highest yield point followed by carburised CMSX-10 and virgin CMSX-4 with FGH-96 having the lowest yield point. Carburised CMSX-10 had the highest hardening rate, followed by virgin CMSX-4, FGH-96 and carburised CMSX-4. Consequently FGH-96 had the highest elastic modulus, followed by virgin CMSX-4, carburised CMSX-10 and CMSX-4.

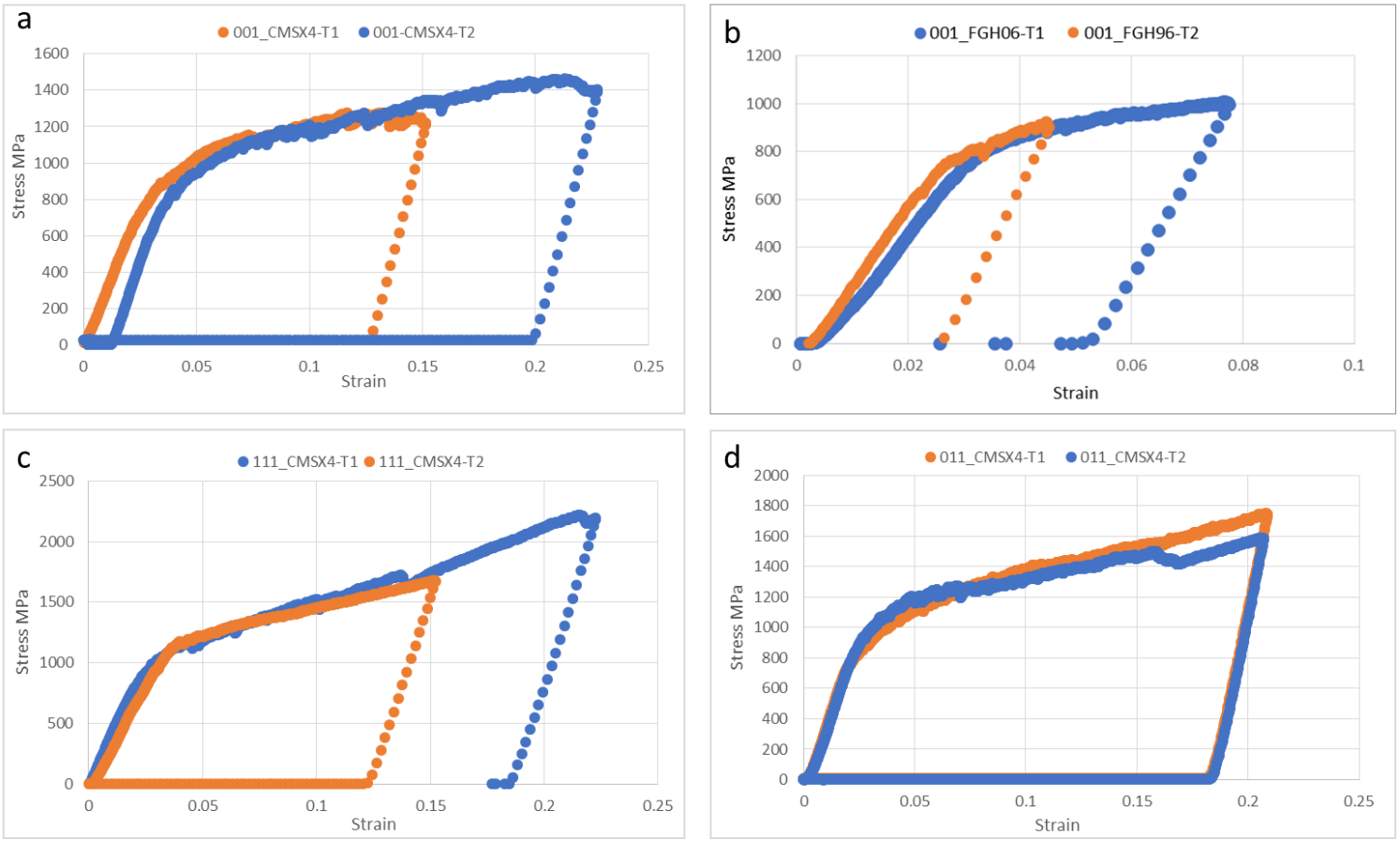


Figure 292: Stress strain traces across different orientations and alloys, illustrating the repeatability of the micropillar experiments (a) CMSX-4 alloy in the <001> direction (b) FGH96 alloy isolated <001> grain (c) CMSX-4 alloy in the <111> direction (d) CMSX-4 alloy in the <011> direction.

Figure 292, shows representative stress strain curves across non carburised alloys and orientations, showing the repeatability of the micropillar experiments. The repeatability is important as it validates the testing criteria. Every test was repeated to check the testing criteria and it was found that the repeatability remained consistent across all tests on all alloys and orientations.

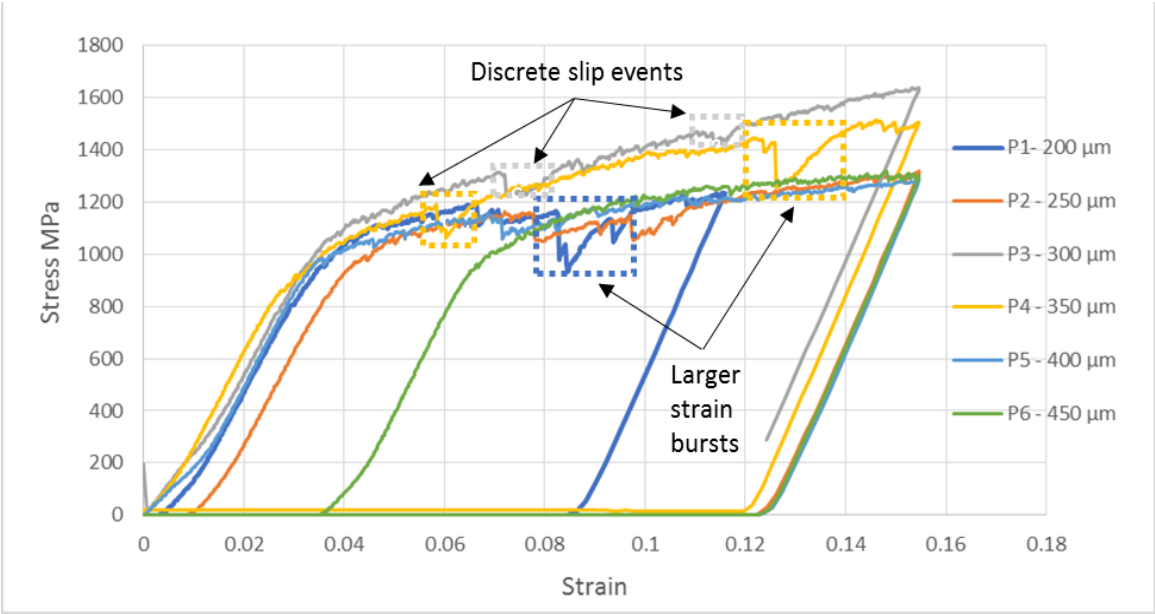


Figure 293: Stress strain traces from carburised CMSX-4 of pillars fabricated in the same orientation, outside of the carbide type phase rich region (200-450 µm). Illustrating the difference in mechanical properties, particular the hardening regime.

Figure 293 shows stress strain traces from six micropillars, located outside of the carbide type phase rich region in carburised CMSX-4, as shown in figure 298 and figure 300. The interesting thing is that even though these pillars are all in the same orientation and similar location the mechanical variables, most notably the hardening and moduli differ. Figure 293 also illustrates the occurrence of discrete slip events (strain bursts).

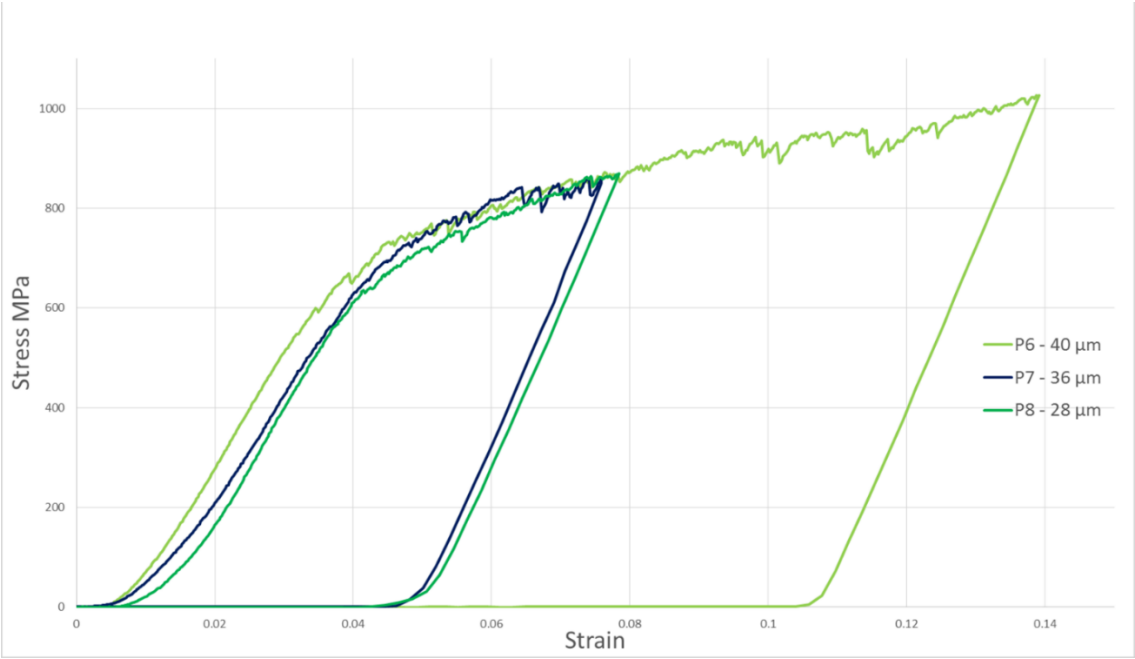


Figure 294: Stress strain traces from carburised CMSX-10 of pillars fabricated in the same orientation, outside of the carbide type phase rich region (28-40 µm). Illustrating the minimal difference in mechanical properties, with differences in the hardening regime being the most prominent.

The micropillars tested in CMSX-10 outside of the carbide type phase rich region are more in agreement with each other when compared to CMSX-4. This is shown in figure 294, in that the stress strain traces are semi repeatable. The mechanical results in carburised CMSX-4 show more variation and slip phenomena such as strain bursts, when compared to CMSX-10. The extent of the carbide type phase isolated pillars across both carburised alloys is examined below in figure 295 and figure 296.

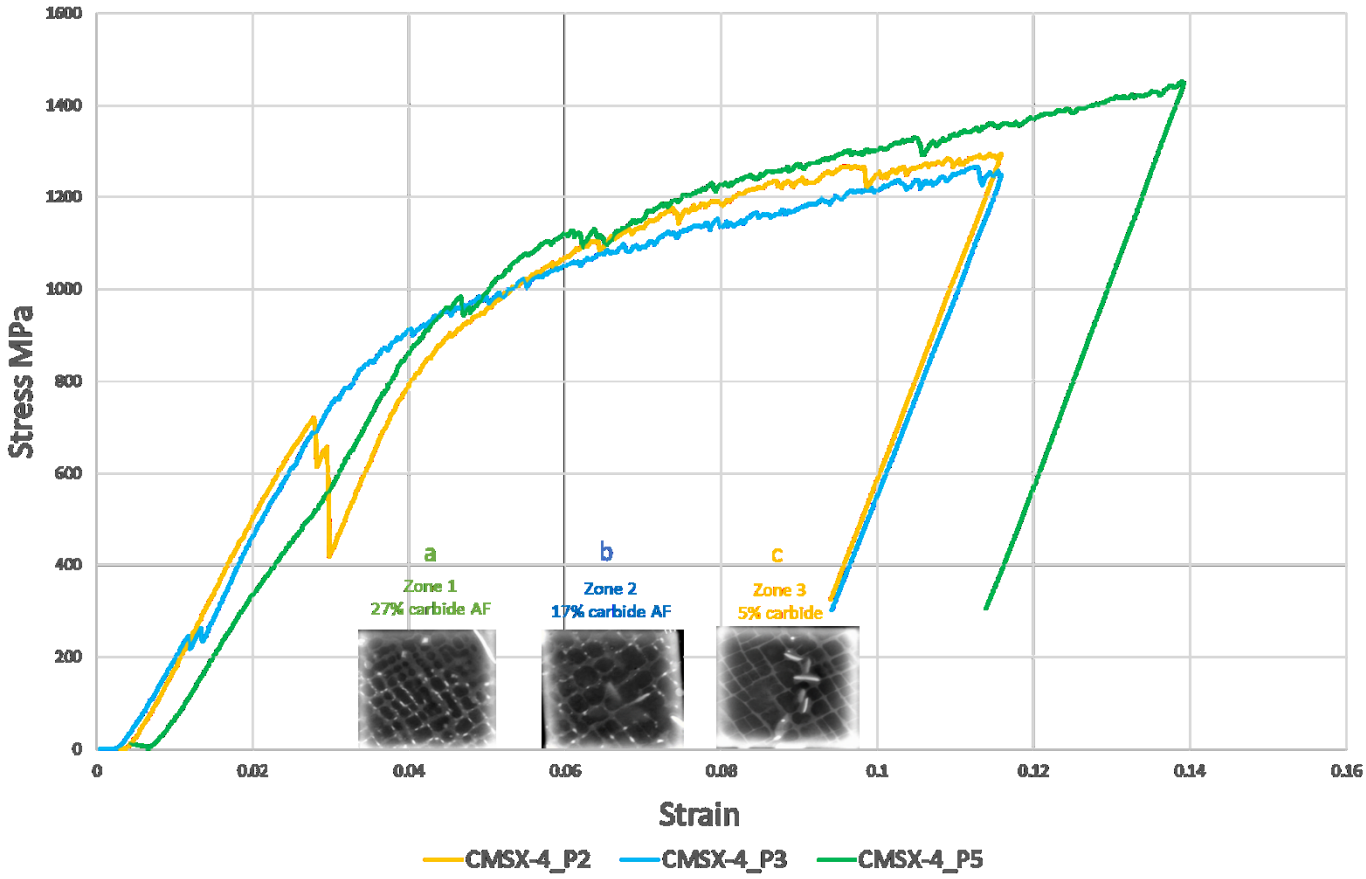


Figure 295: Stress strain traces from three carbide type phase isolated pillars in CMSX-4, as shown in table 33. Illustrating the influence of carbide type phases on the stress strain curves. It can be seen that the large TCP phase result in a large stress drop near yield.

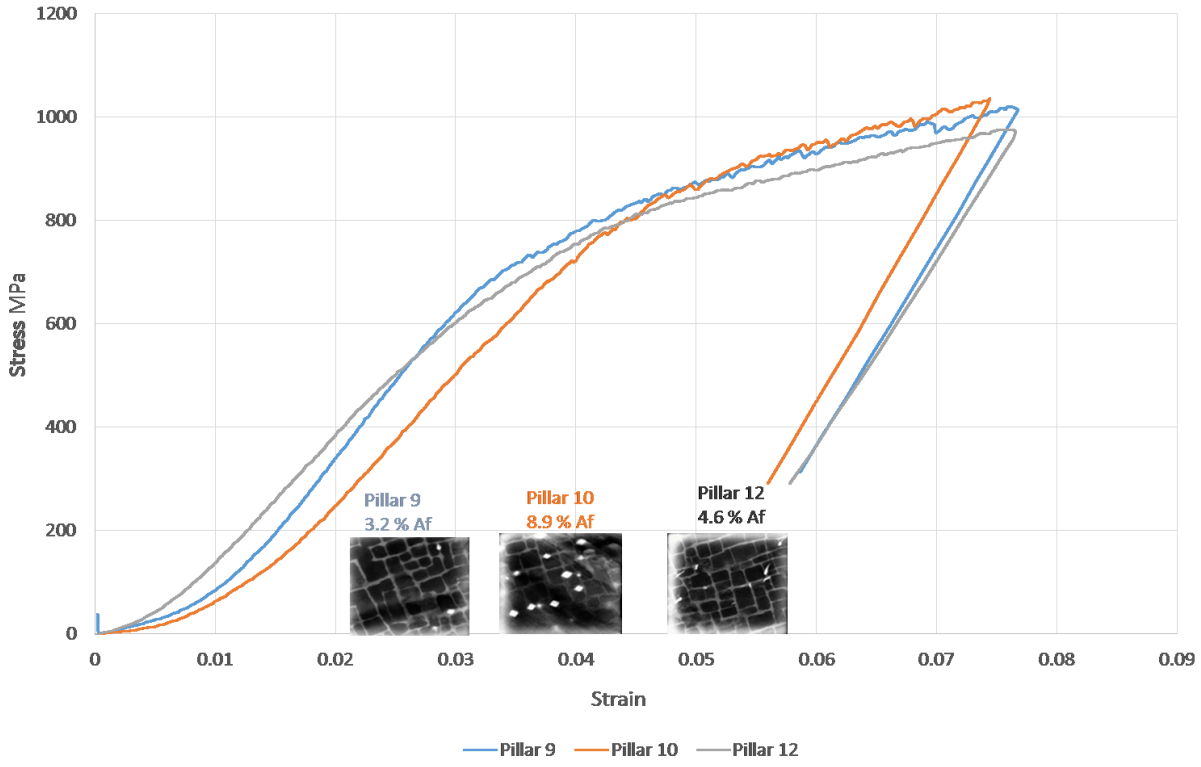


Figure 296: Stress strain traces from three carbide type phase isolated pillars in CMSX-10, as shown in table 33. Illustrating the influence of carbide type phases on the stress strain curves. It can be seen the traces are similar and there are no significant strain bursts.

Figure 295 shows the stress strain traces from three carbide type phase isolated pillars in carburised CMSX-4, with area fractions 27%,17% and 5% respectively. The carbide type phase isolated pillar with a large TCP phase located at the ϒ/ϒ' junctions resulted in a catastrophic strain burst just at the onset of yield. The other pillars experience much smaller sequential strain bursts throughout the hardening regime. The influence and relationship between the strain bursts in the stress strain traces and resultant slip traces on the micropillars can be seen in figure 299. Figure 296 shows the stress strain traces from the carbide type phase isolated pillars in the carburised CMSX-10 alloy, just like the non carbide type phase, isolated micropillars the stress strain curves agree more than those from the CMSX-4 alloy. Table 33, gives the mechanical variables, carbide type phase, area fraction and distance from the edge of the carbide type phase isolated pillars shown in figure 295 and figure 296. Figure 297 shows the compounded stress strain traces from the carburised CMSX-4 and CMSX-10 alloys, illustrating the lower yield point and elastic modulus of the CMSX-10 pillars.

Table 33: Carbide type phase isolated pillars and respective mechanical properties, across the CMSX-4 and CMSX-10 alloy, as shown in figure 295 and figure 296

Alloy	Pillar	Carbide Area fraction (%)	Distance (µm)	Yp (MPa)	Hr (MPa)	E_I (MPa)
CMSX-4	11	27	25	850 ± 39	4140 ± 68	43895 ± 190
	12	17	44	940 ± 41	2863 ± 23	32861 ± 59
	13	5	70	870 ± 32	3447 ± 41	32068 ± 104
CMSX-10	9	3.2	19	700 ± 21	6524 ± 42	38140 ± 87
	10	8.9	14	839 ± 23	6786 ± 56	38706 ± 96
	12	4.6	8	750 ± 28	5220 ± 44	33709 ± 84

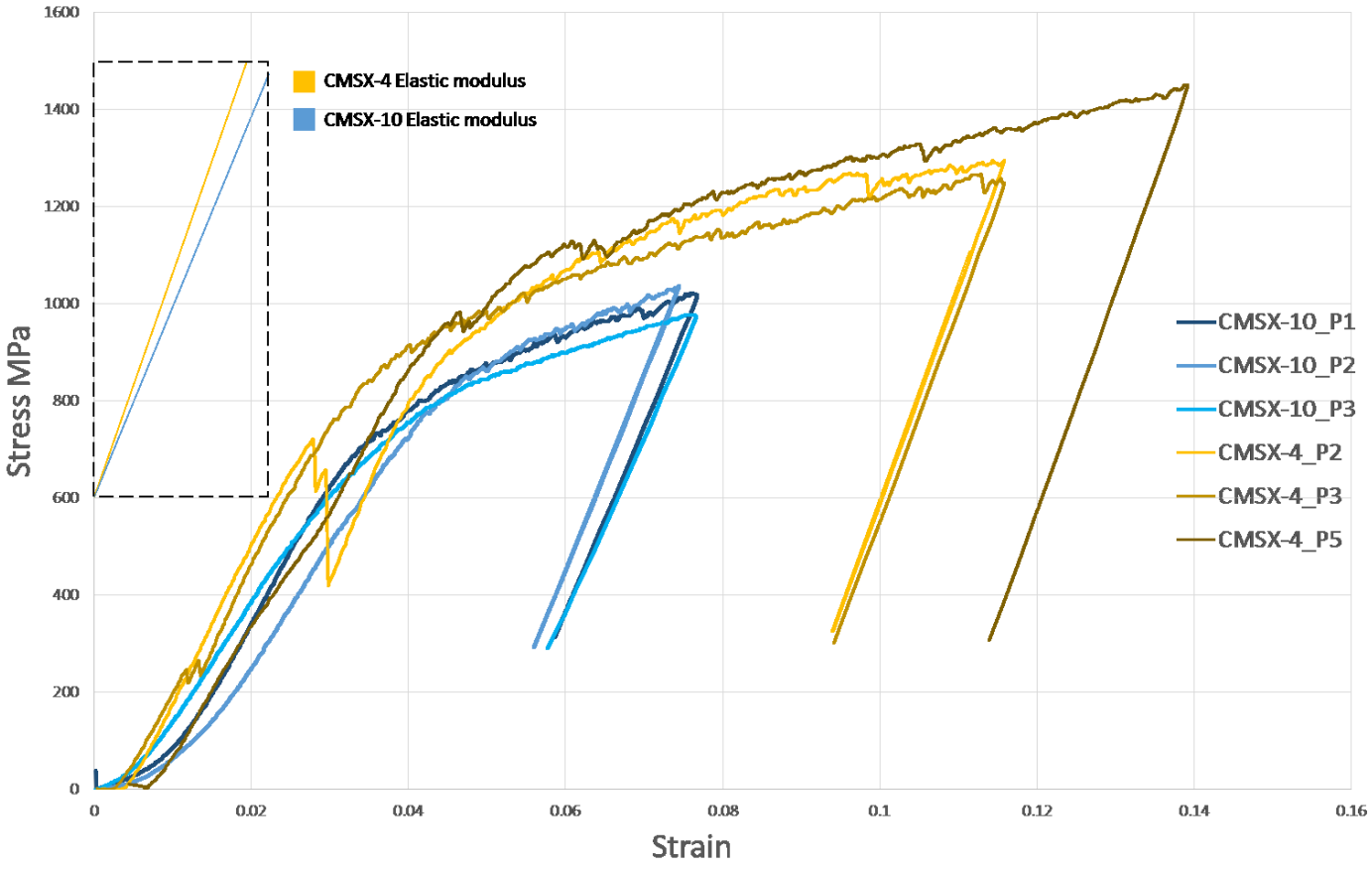


Figure 297: Compounded stress strain traces for the carbide type phase isolated pillars in CMSX-4 and CMSX-10. The carbide type phase isolated pillars in CMSX-4 are stiffer and have a higher yield than those in CMSX-10.

10.4.3. Orientation / slip trace phenomena

The plastic deformation behaviour within an alloy can be examined through analysis of slip bands. EBSD orientation studies involving the translation of crystal orientation to the sample frame and the rotation of the fcc {111} slip plane through viewing angles enables the slip systems to be evaluated and predicted pre deformation. In the case of carburised CMSX-4 the slip behaviour and hardening response is heavily influenced by carbide phase type and density and will be examined below, following on from the findings shown in figure 293.

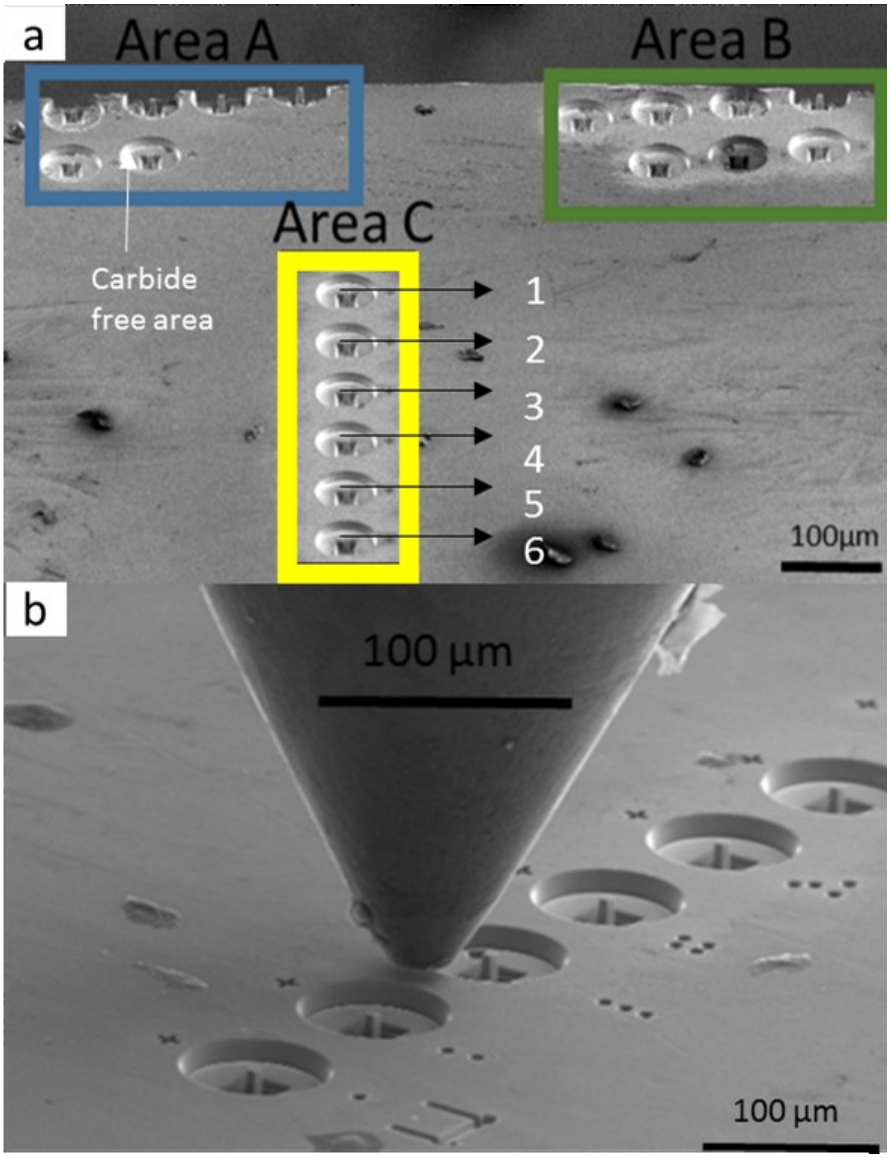


Figure 298: SEM image pf surface plane of CMSX-4 illustrating pillars fabricated in the carbide type phase rich areas, (Area A & B) and carbide type phase, free area, Area C. The carbide type phase, rich area is highlighted as the area in front of the white line (a) Area A-C (b) Area C, pillars 1-6 from 200 µm to 450 µm.

The pillars giving rise to the stress strain traces shown in figure 293 are all located in the same area with the same orientation, the SEM image of which is shown in figure 298 (area C). Area C contains pillars that have the same area and are in the same orientation, but give rise to different slip traces. Areas A and B contained carbide type phase, isolated pillars, the slip traces of three of these pillars as shown in figure 295 are shown below in figure 299.

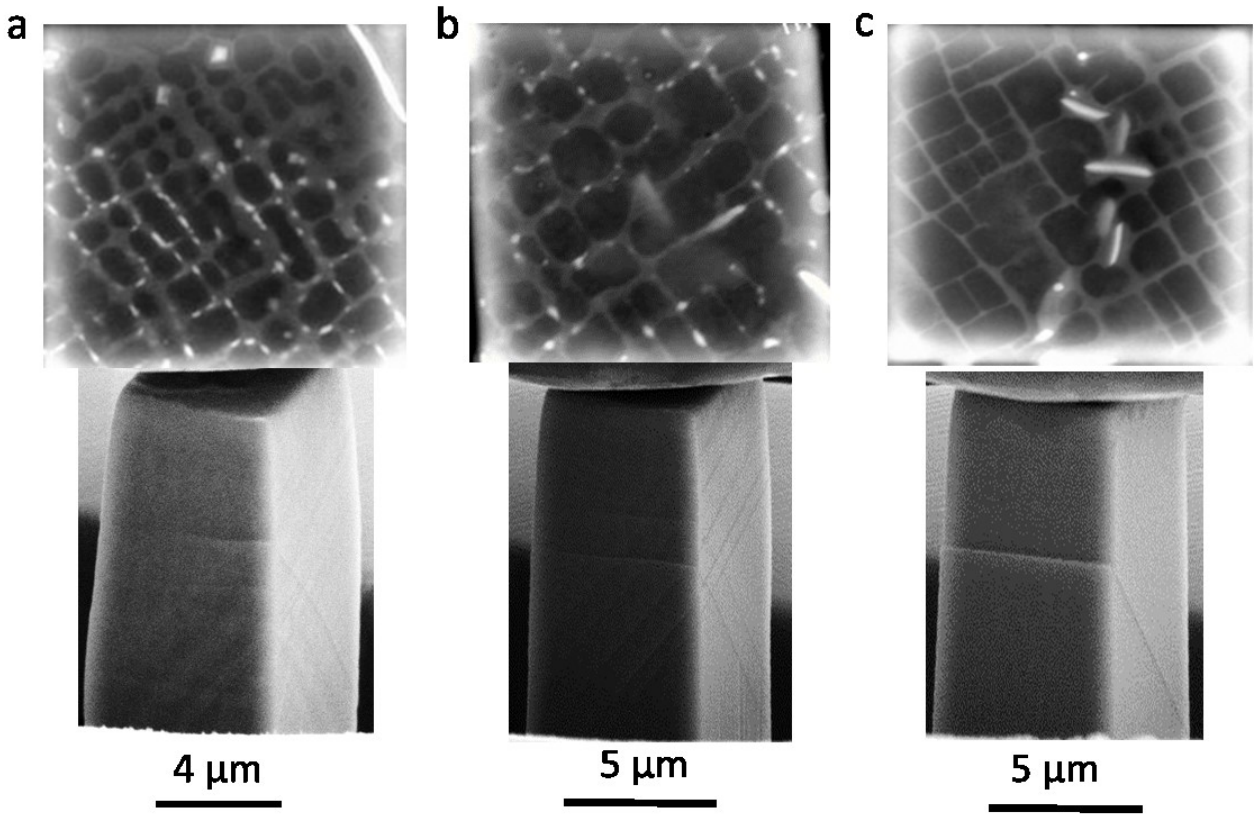


Figure 299: Three carbide type phase isolated pillars in CMSX-4 from areas A and B with, No of particles and average aspect ratio respectively *(a) Zone 1: 60, 1.66 (b) Zone 2: 65, 2.6 (c) Zone 3: 8, 5, 5.2.*

Figure 299 shows the *in-situ* pillar images of three carbide type phase isolated pillars post deformation. The effect of the carbide type phases can be seen to trace almost identically onto the side face of the pillar, with the exception of the pillar shown in figure 299c, that resulted in a catastrophic strain burst yield, shown by the sharp shear localised shear band, which differs from the more discrete multiple shear bands, in the other two pillars. A consistent shear band can be seen to have emerged in all three pillars. This shear band is dictated by the identical orientation, but is most predominant in the carbide type phase isolated pillar with TCP phase. As the pillar images were taken *in-situ* and not on a flat face a comparison of the theoretical slip trace with the experimental one was not done in this case.

The slip characteristics of micropillars can be considered in 4 planes of view, as shown in figure 284. The following two figures, consider the front face of the micopillars in area C, as the distance is moved move from 200 - 500 µm in CMSX-4. Where the 400 – 500 µm is considered the region where bulk properties start. Considering the front face of 6 pillars ranging from 200-400 µm, we can begin to see distinct slip characteristics native to this region.

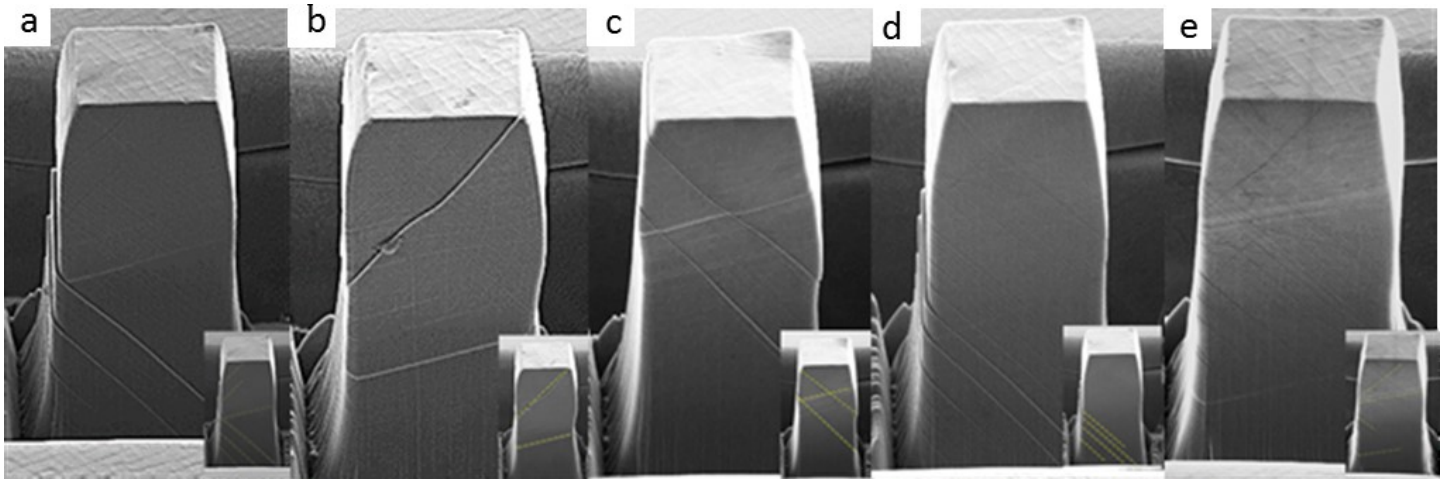


Figure 300: Pillars 1-6 from Area C, outside of the carbide type phase rich region in CMSX-4 at distances 200-450 µm, illustrating the different slip traces.

Figure 300 shows pillars 1-6 in area C, an area outside of the carbide type phase rich area at a distance of 200-450 µm from the perimeter edge. Although the pillars are in the same orientation and in a close vicinity on the same alloy, the slip traces are not the same, this is shown by the different stress strain traces observed in figure 293. The slip traces of pillar 1 and 4 both show large strain bursts, this is represented by the multiple localised slip bands observed in the lower part of the pillar figure 300 a and d respectively, and slip system 4 in figure 301. The theoretical slip trace is shown below in figure 301 and schematic comparison of slip traces in shown in figure 301.

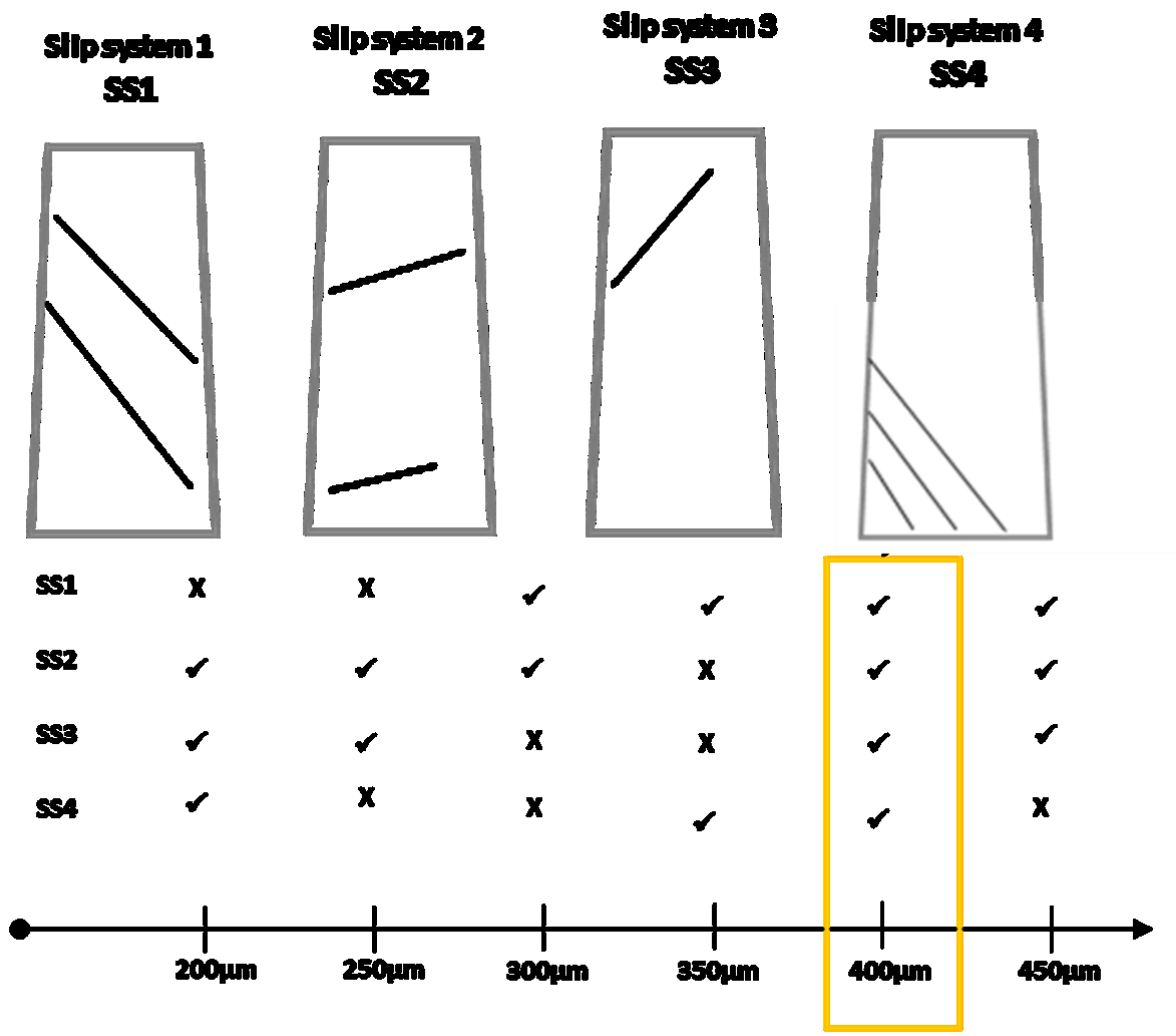


Figure 301: Local region close to the perimeter edge and carbide type phase rich region in CMSX4 with three areas, Area A and B have pillars fabricated with carbide type phases highlighted in (a) Area A,B,C (b) Area C

Figure 301 shows a schematic of slip traces observed on the front faces of the six pillars in area C. The slip systems can be categorised into four systems, a comparison of which slip system is active vs the distance of the micropillar is shown above in figure 301 . It was found that only one pillar showed all four slip systems. Comparing with the mechanical properties this represents an inflection point in the yield point vs distance graph. The evidence would suggest that the cause of this could be sub surface carbide type phases or a homogenisation of the alloy composition that occurs around this point and that the end of the visible surface carbide type phases is not indicative of a complete homogenisation back to equilibrium alloy composition.

10.4.4. EDS + Mechanical properties

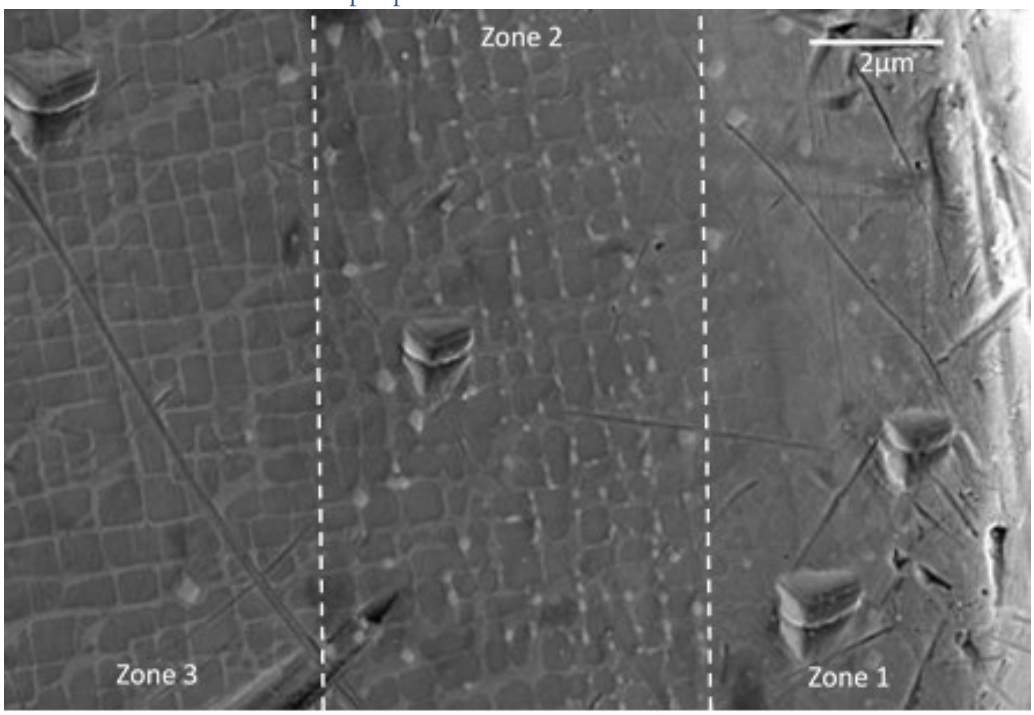


Figure 302: 1 µm micro indents in CMSX-4 in the carbide type phase rich region segmented into zones 1-3

Microindents were used to validate the small deviations in mechanical properties as a function of distance, found in the micropillar experiments. 5 µm and 1 µm indents were used. 5 µm indents were to large to use local to the carbide type phase rich region in CMSX-4, which extends 0-120 µm from the perimeter edge of the sample. 1 µm indents were thus used in this region, as shown in figure 302. Both the 1 µm and 5 µm indents validated the results found in the micropillar experiments. The findings indicated that the mechanical properties change as a function of distance, most notably in the carbide type phase, rich region. The mechanical properties continue to deviate further outside of this region and begin to homogenise post the 450 µm region. This finding can be married to the results seen in the slip trace examination and comparison of micropillars in an area 200 – 450 µm from the perimeter edge, as seen in figure 300 and figure 301. The change in mechanical properties is theorized to be linked to the disruption of the equilibrium alloy composition caused by the leeching of elements by the carbide type phases. Following on from this theory and analysis of the micropillar experiments, EDX scans were placed over the 1 µm indents from 0-70 µm from the perimeter edge of the sample, to map any changes in chemical composition and match them to the hardness indentation results.

10.4.5. Microindents

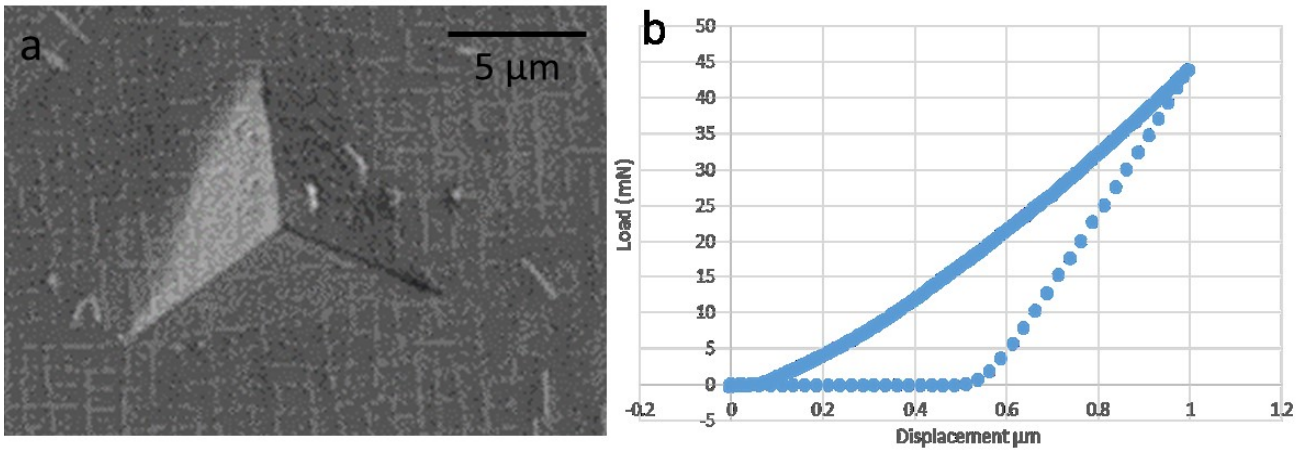


Figure 303: 5 µm indent and load displacement plot (a) SEM image of 5 µm indent in carbide type phase rich area (b) resultant load – displacement trace, showing a smooth curve with a max displacement / peak load of 1 µm / 50kN respectively.

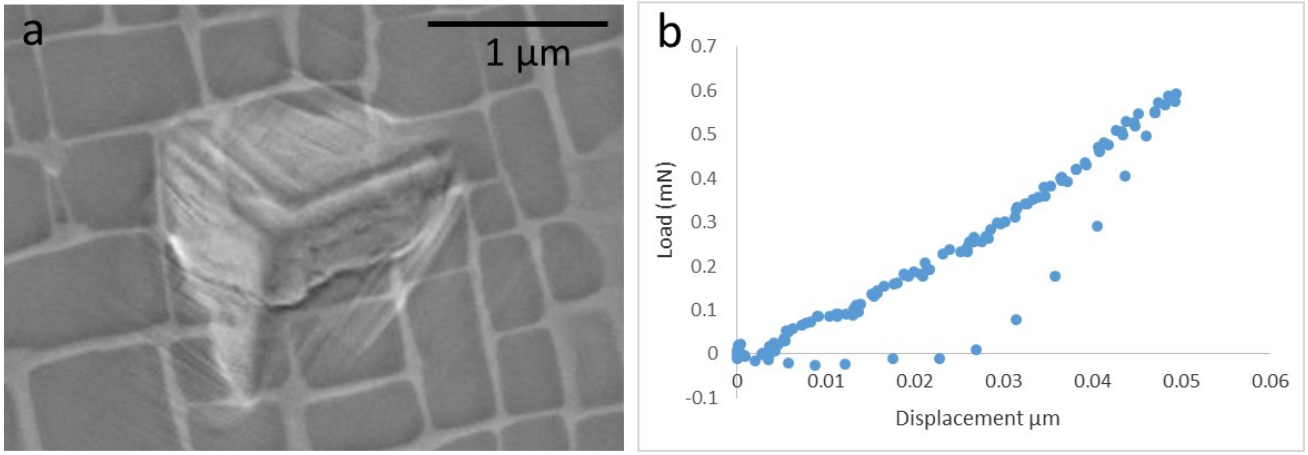


Figure 304: 1 µm indent and load displacement plot (a) SEM image of 1 µm indent in carbide type phase rich area, intersecting several Ɣ/Ɣ' junctions (b) resultant load – displacement trace, showing a smooth curve with a max displacement / peak load of 0.05 µm / 0.6 kN respectively.

Figure 302, figure 303 and figure 304 , show the indent imprint and load displacement traces for a 5 µm and 1 µm indent respectively. The 1 µm indents were used to test local properties in the carbide rich region and extend to `120 µm from the perimeter edge and 70 µm when incorporating the EDX map scans. The 5 µm indents were used to test bulk properties up to 700 µm from the perimeter edge and any deviations found outside the carbide type phase rich region as found in micropillar experiments, which tested up to 800 µm, figure 298. When comparing the resultant load – displacement traces between the 5 µm and 1 µm indents, the 1 µm trace is much nosier than the 5 µm. This is however to be expected, due to the substantially lower displacement, resulting in more susceptibility to thermal drift and noise. The peak displacement however remains un altered and the tests / traces for both the 5 µm and 1 µm indents were repeatable, as outlined in figure 292.

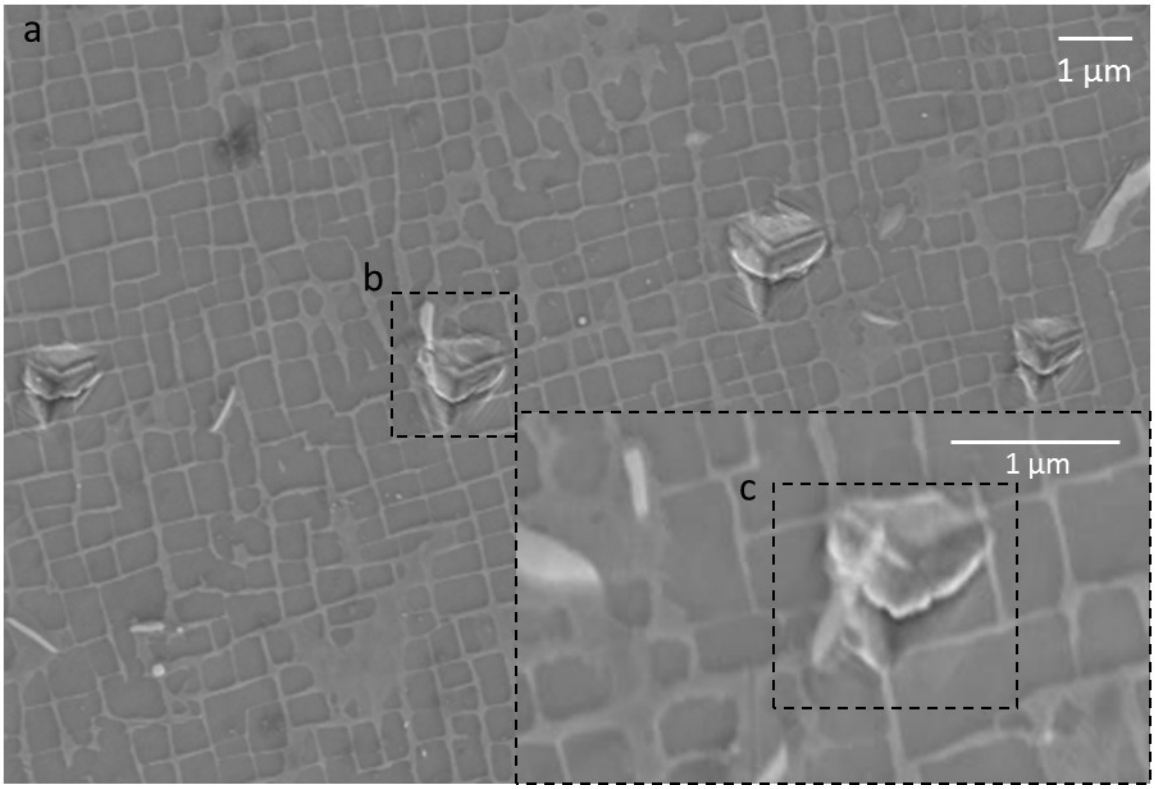


Figure 305: Local carbide type phase rich region zone 3, with 1 m indents, intercepting a carbide type phase, with insert taken from EDX chemical analysis. (b) 1 µm + carbide type phase (c) Scanned region used for EDX, figure 306.

EDX scans were done over microindents. The Micro indentation experiments validated micropillar experiments and enables local testing of microstructure, in which EDS map scans across 1µm indents map the changes in elemental concentrations as elements are depleted as a function of distance and carbide phase type. The mechanical properties vary as a function of distance, dictated by both the mechanics of dislocations as they interact with carbide type phases and the elemental depletion from the ϒ/ϒ' matrix. TEM can further validates these findings. The solid solution ϒ phase is depleted of W, Co, Cr, Mo In the presence of carbide type phases. The strengthening ϒ' phase is depleted of Ti and Ta, In the presence of carbide type phases. The smaller more circular carbide type phases with lower aspect ratios and higher roundness' favoured, Hf, Re, Mo, Ta. The longer more irregular TCP phase that have high aspect ratios and low roundness' favoured Ti and Ta.

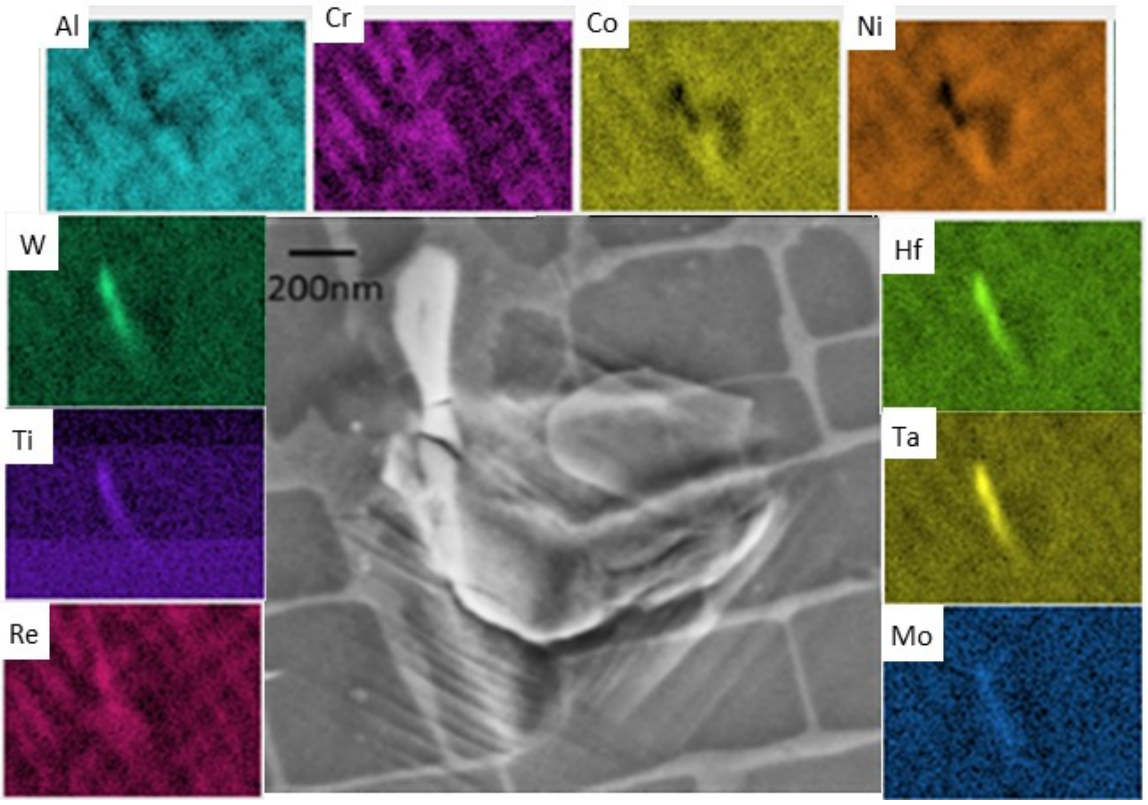


Figure 306: show a microindent imprint over a TCP phase in zone 3 in the carburised CMSX-4 alloy, with EDX results showing, {111} slip planes and the presence of Ta,W,Ti as carbide type phase stabilisers and Al, Cr, Co, Ni as non carbide type phase stabilisers.

Figure 305 and figure 306 show a micro indent imprint over a TCP phase in zone 3, EDX scans were done over several indent imprints from 0-70 µm (a region local to the carbide type phase rich area). The results of which can be seen in later figure 307, the figures show the compound chemical composition vs Vickers hardness as a function of distance for C, Ni, Al, Ti, Ta, Mo respectively. The trace for C, figure 307b shows a decrease in C from 0-10 µm, which corresponds to the initial dip in hardness, from 2-5-1.2GPa, with C decreasing from 8.7% to 5.8%. A small increase in hardness from 1-1.5 GPa corresponds to a small increase in C concentration from 5.5% to 7%. It can be concluded that a depletion in C links to a decrease in mechanical properties within the carbide type phase, rich region. Figure 307c shows the compound Ti trace, the relationship between and hardness is a little less clear as the line is generally flat, albeit a few small deviations. The concentration of Ti is seen to increase from the perimeter edge by a small amount. It can also be seen that the small dips in the concentration of Ti, corresponds to a small dip in the hardness, for example a 0.2% drop at 20 µm and a similar effect can be seen at 50 µm. The opposite effect happens at ~35 µm with a slight increase in hardness. The spurious point at 55 µm is also noted, but can be disregarded as a spurious result. figure 307c, shows the compounded Mo trace, it appears that Mo seems to be directly proportional to the hardness value. The concentration of Mo drops at ~2 µm by 0.3% in line with a drop in hardness from 2 to 1 GPa, this is quite significant and a similar trend follows as a hardness value increases and decreases accordingly, for example at 32 µm and

42 µm. Figure 308b shows the compounded Ni trace, this trace seems to be inversely proportional to the hardness. The concentration of Ni initially picks up quite dramatically as the scan moves from the perimeter edge at 0 µm. It appears that as the hardness decreases so does the normalised mass % of Ni, this trend is notable at 14 µm, 28 µm, 38 µm and 50 µm. figure 308c, shows the compounded Co trace, again the trace is less clear and appears quite flat. The concentration of Co begins to pick up slightly, similar to Ni and again appears to be inversely proportional to the hardness, this is notable at 10 µm, 40 µm and 50 µm. It can be concluded that non carbide type phase stabilisers as seen in figure 306, are inversely proportionally to the hardness, whereas the normalised mass % of carbide type phase stabilisers, such as Mo, Ti, Ta are proportional to the hardness in the carbide type phase, rich region. Indicating that the leeching of these elements indeed links to a loss in mechanical properties.

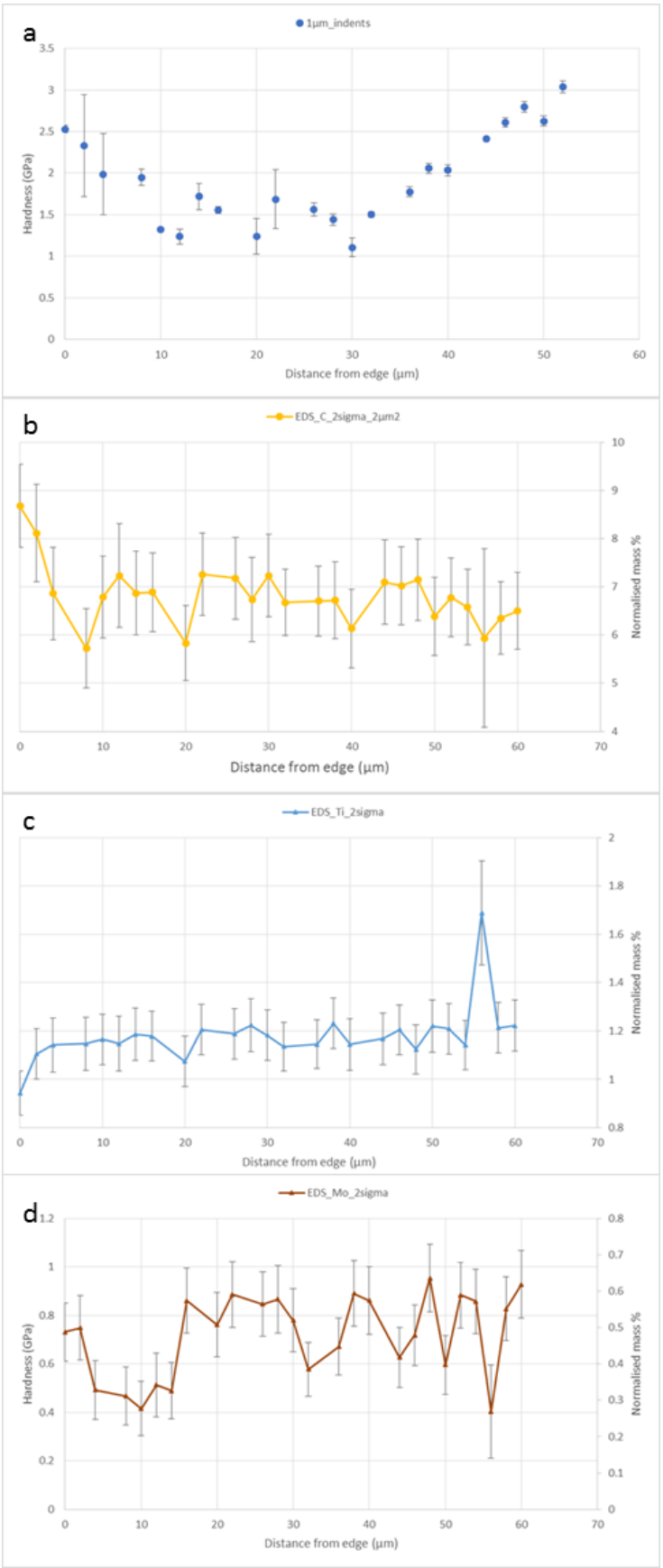


Figure 307: Hardness of 1 µm indents through carbide type phase, rich region & normalised mass % of carbide type phase, stabiliser, C Vs distance from the edge

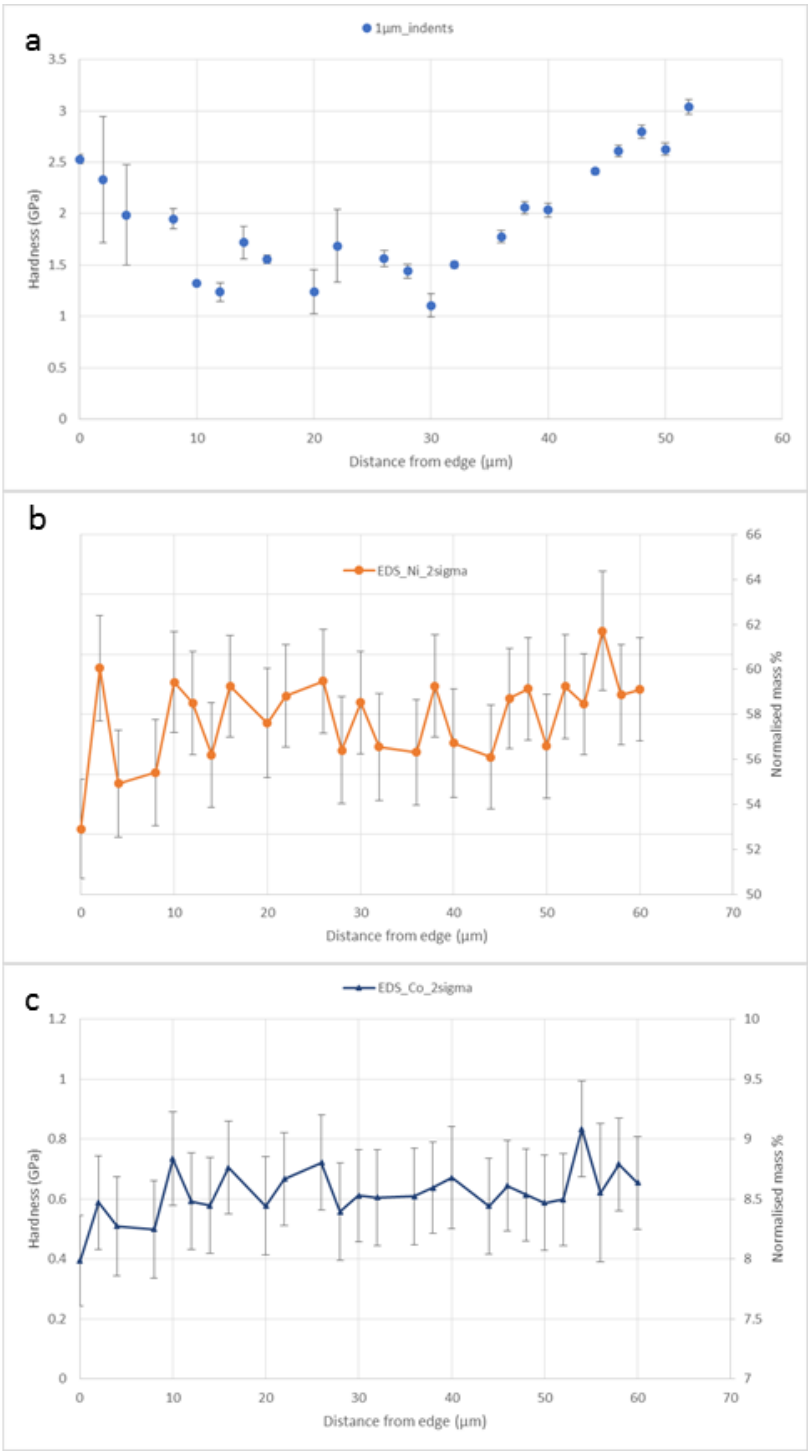


Figure 308: Hardness of 1 µm indents through carbide type phase rich region & normalised mass % of carbide type phase stabiliser, C Vs distance from the edge

Elements are leeched from both the ϒ and ϒ' stabilisers, it is therefore useful to understand which elements and at what concentrations are leeched from ϒ and ϒ' respectively and how this links to the mechanical properties as a function of distance as measured by hardness indents.

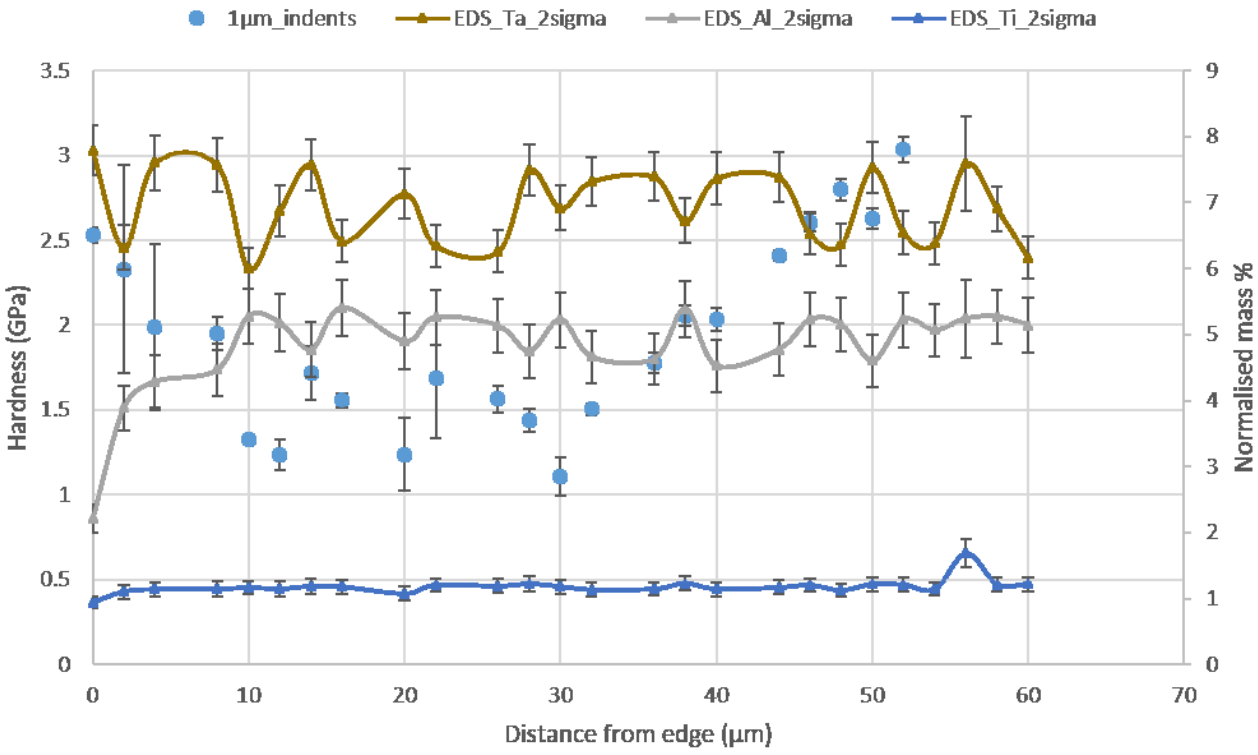


Figure 309: Normalised mass % of ϒ' stabilisers and Vickers hardness vs distance from the perimeter edge of carburised CMSX-4

Figure 309 shows the hardness as a function of distance in the carburised CMSX-4 alloy vs normalised mass % of the ϒ' stabilisers. Ta and Ti are carbide type phase stabilisers whereas Al is a non-carbide type phase stabiliser, comparing the Ta and Al traces it can be seen they mirror each other. Ta, which is a carbide type phase stabiliser, is inversely proportional to the hardness in the material, whereas Al is proportional. Ti is a carbide type phase, stabiliser and thus the normalised mass % is inversely proportional to the hardness in the material, but much less responsive than Ta as noted above

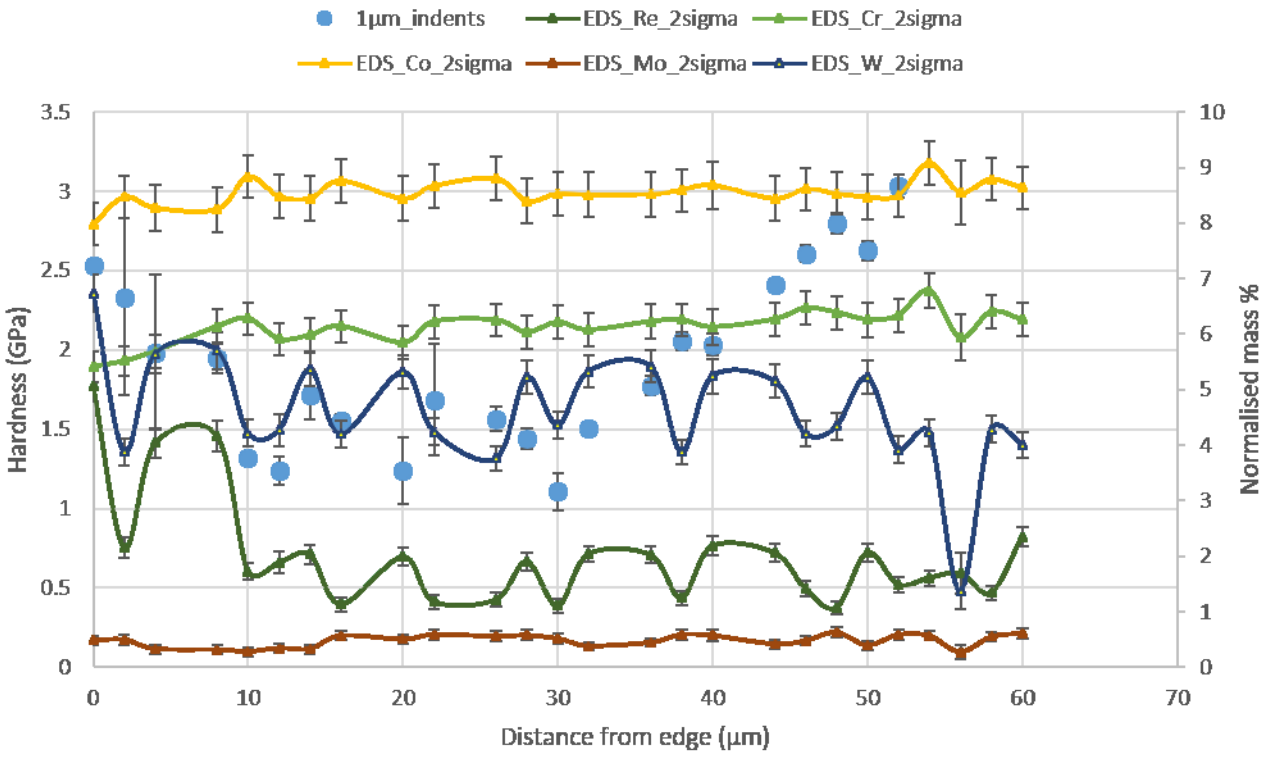


Figure 310: Normalised mass % of ϒ stabilisers (coloured points and guide lines) and Vickers hardness (blue points) vs distance from the perimeter edge of carburised CMSX-4

Figure 310 shows the hardness as a function of distance in the carburised CMSX-4 alloy vs normalised mass % of the ϒ stabilisers. Whereby W, Re and Mo correspond to carbide type phase stabilisers and the traces of these elements can be seen to be inversely proportional to the hardness across the alloy as a function of distance, with the trend most clearly observed in W - for example at 20 and 50 µm. Cr and Co are non-carbide type phase stabilisers, the response of the traces are proportional to the hardness and are nearly identical to each other.

The EDX map scans were done on areas within the carbide type phase, rich area on different areas other than the imprints / areas bigger than those on the imprints. This was done do check how reliable the elemental information is when comparing to the mechanical properties. Below are two examples done on Non carbide type phase stabiliser Ni and non-carbide type phase, stabiliser C, figure 311 and figure 312 respectively.

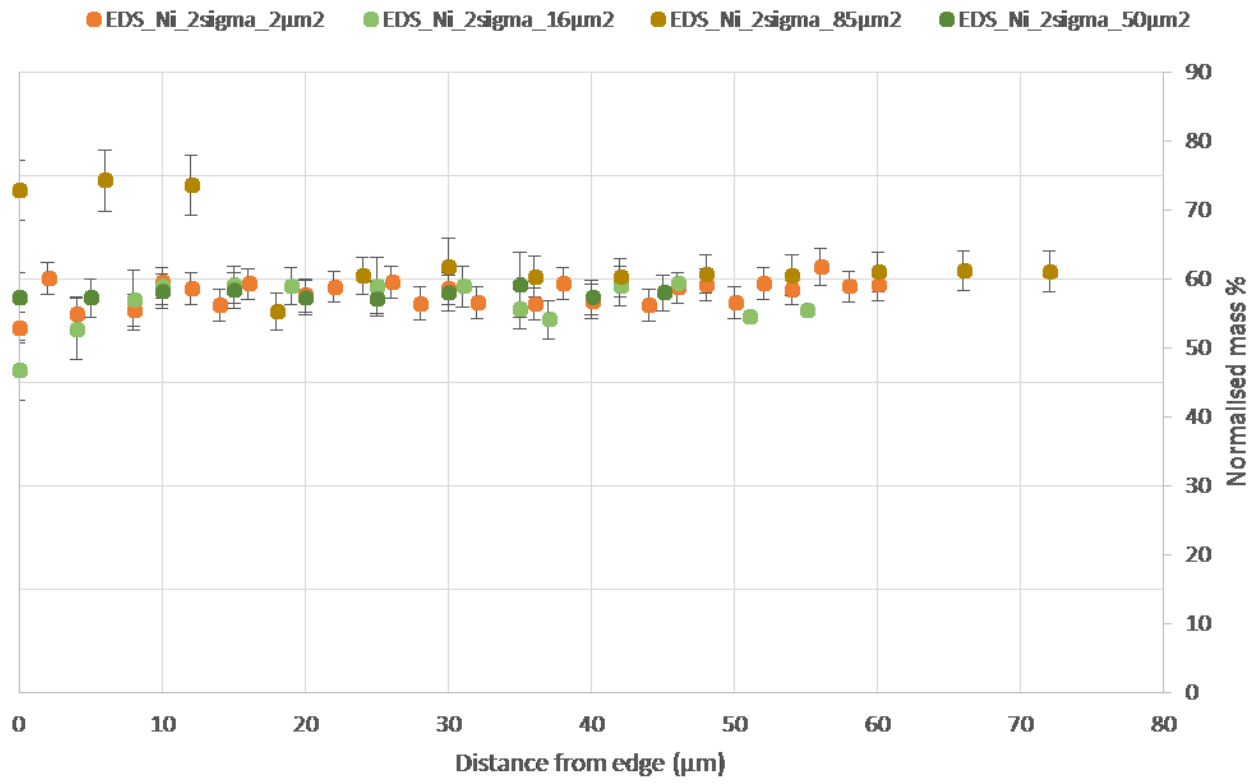


Figure 311: Normalised mass % of Ni, with map sizes of 2, 16, 50 and 85 µm² vs distance from the perimeter edge

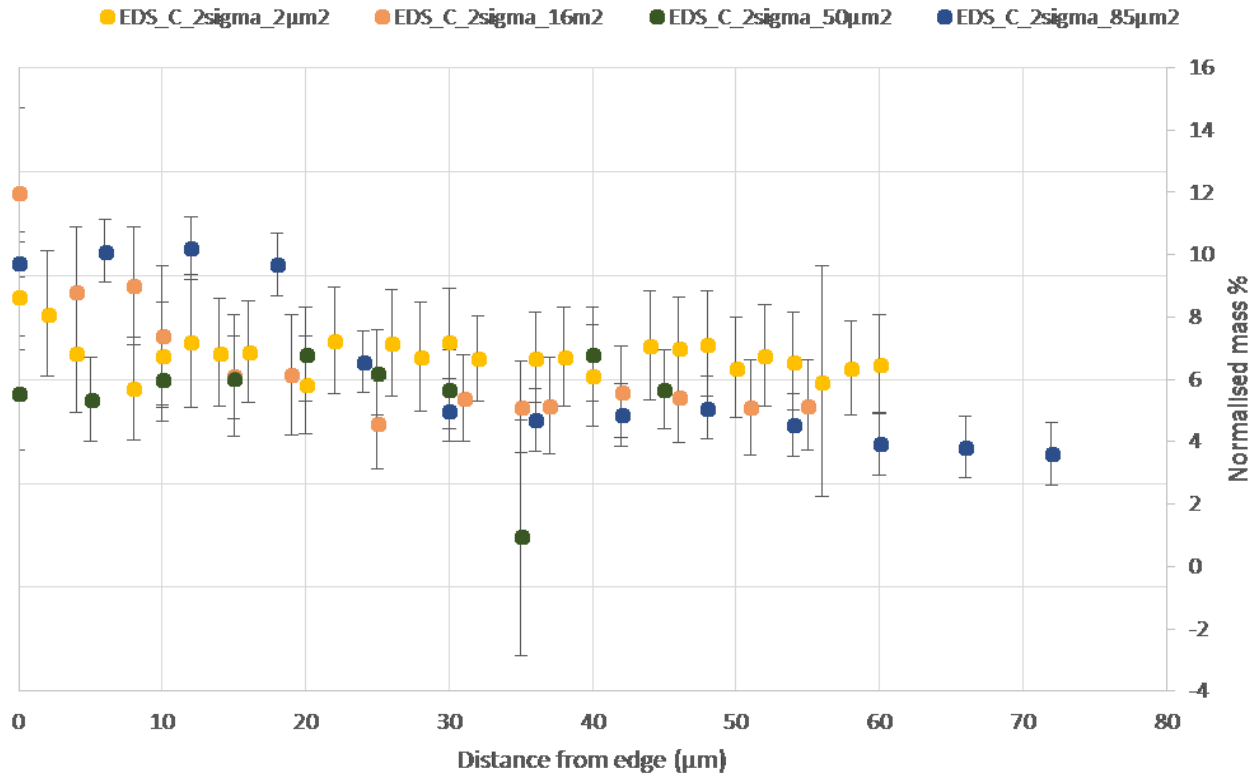


Figure 312: Normalised mass % of Ci, with map sizes of 2, 16, 50 and 85 µm² vs distance from the perimeter edge

Figure 311 and figure 312, shows the normalised mass % of Ni and C respectively, with EDX map scans of 2, 16, 50, 85 μm^2 vs distance from the perimeter edge of carburised CMSX-4. The figures show that despite the different scanning sizes the trend remains fairly consistent. There are some discrepancies expected as larger sizes take into large carbide type phase clusters.

II. Problems and advantages of methodology

11.1. The elastic modulus

The mechanical responses from the *in-situ* micropillar compression used in this study were derived from the remote measurement of a load cell and the displacement of the applied actuation of a flat punch within the loading frame[44,182].

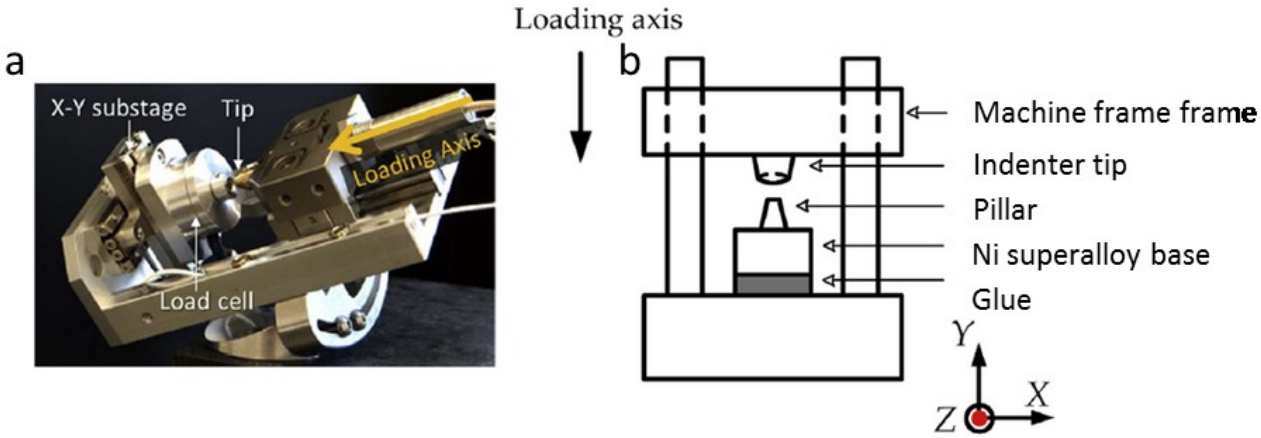


Figure 313: Micro-pillar compression testing setup used in the SEM chamber (b) simplified schematic diagram showing pillar, Ni superalloy base, cyanoacrylate-based glue substrate and machine frame[7].

Figure 313, shows the *in-situ* setup used to compress the micopillars in this study, figure 313b illustrates a two dimensional schematic, containing the individual components that make up the total compliance of the system.

The elastic modulus values found when 5 µm CMSX-4 pillars orientated in the <001> direction were compressed, differed greatly from those found in macro experiments[209,11]. The macro modulus values were ~130 GPa[210,209,11] which is much higher than those found in this study from micromechanical testing ~50 GPa. The average modulus taken from the compression of <011> and <111> micropillars were 61 and 66 GPa, which again differ greatly when compared to the macro values of 220 / 294 Gpa[210,209,11] respectively.

The low modulus values found in the micro compression experiments can essentially be attributed to the compliance of the cyanoacrylate-based glue substrate used to mount the sample[7] and to a lesser extent, substrate effects[182] combined with the compliance of the loading frame[7].

The modulus values extracted on the microscale need a correction applied to them, whereby the stiffness of the entire *in-situ* system, used to load the micopillars in compression, as seen above in figure 313, should be taken into consideration[182,38,211,2].

The stiffness values should include the substrate underneath the micropillar, the adhesive used to mount the sample and load test frame used for the *in-situ* experiment[7] as the micropillar is loaded in series; so each load bearing member carries the same force. This is what causes the large difference in elastic modulus values when compared to the macro values[7,175]. The result of this, is that the mechanical response comprises the deformation of the pillar, combined with the displacement of the substrate, and glue with a contribution from the load frame compliance.

A paper published in 2016 in which Zhen Zhang et al[7] used an identical setup to the one used in this study, coupled micropillar experiments with crystal plasticity modelling and it was found that the modulus range for a cyanoacrylate based adhesive as published by the manufacturer is 3-15 GPa and thus the effective stiffness is dominated by this value[7].

The consequence of the inaccurate modulus values to this study are not paramount; as the modulus value was used as a comparative tool to compare different alloy types and was effective in doing so. The proportional method was used to determine the yield point of the alloys as outlined in section 5, page 73, see figure 109-figure 111 . The proportional method was also used to compensate for the inaccurate modulus values (when compared to macro tests), the 0.2% offset method would have taken in the error associated with the incorrect elastic modulus and translated in to the hardening modulus from which the yield point is extracted using the 0.2% method, figure 111. A better correction, that incorporates the entire system as a set of different components acting in series would need to be applied to future work, particularly if the modulus values are to be used to aid in the development of future alloys. The focal mechanical variable of this study was the yield point.

11.2. Yield Point evaluation

The strength in Ni-based superalloys can be attributed to two main factors; coherency and ordering hardening[212,11,88]. Coherency hardening is due to the lattice mismatch between the γ and γ' phases[75] and order hardening is due to the structure of the ordered L_{12} γ' phase[134], in which an APB is created and the energy associated to create the APB opposes the passage of dislocations, thus strengthening the alloy[67].

When comparing the micro and macro CMSX-4 yield point values (800 ± 65 / 850[213,63,11] MPa respectively), in the <001> these values agree with each other. It was found that the values in the <011> and <111> directions also agreed with literature[11,145]. This was also the case when examining individual grains on polycrystalline FHG96 ± 40 MPa, and thus validates the accurate description of yield point

values extracted from micropillar compression tests, at suitable geometries, as outlined in section6, page 124.

The estimation of the yield point is outlined in the methodology section and was found to be useful in this study. The technique used in this thesis used the proportional limit in favour of the 0.2% offset method. This helped improve accuracy specifically when examining unstable orientations / carbide type phase alloys in which stress drops occur frequently, especially near the yield point.

In most cases however the yield point was distinct and the gradient change from elastic to plastic was sharp. The yield point values found in this study were useful when comparing different alloy types and changes in microstructure, as in the case of the carbide type phase alloys, CMXS-4 and CMSX-10.

When testing single crystal pillars the yield point values had the least scatter and the carbide type phase alloys had the most variation. The variation was due to the leeching of alloying elements that disrupted the propagation of dislocations through the γ/γ' structure. This is discussed in more detail later.

In the majority of the micropillars deformed past the yield point, slip traces can be seen to extend from one pillar edge to another as seen in figure 315, indicating that both the γ and γ' are sheared during loading and thus the strengthening mechanisms in both phases must be examined to provide a understanding of the role of strengthening mechanisms in these alloys[11,212,214] .

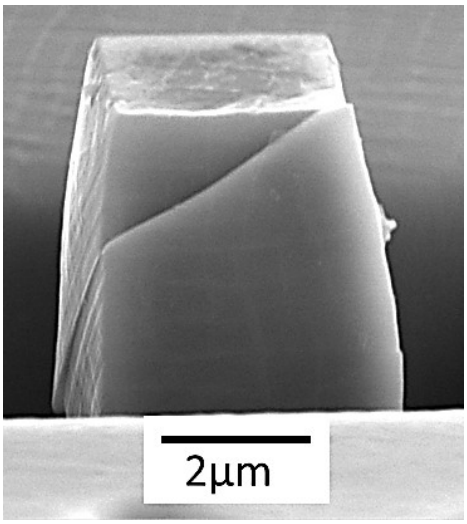


Figure 314: Compressed CMSX-4 micropillar, illustrating the shear line extending from one side of the pillar to the other

11.3. The effect of carbides on the yield point

The carbide type phase in the CMSX-4 and CMSX-10 alloys varied in size and character, most notably in CMSX-4, a full description is given in section 8.6, page 243. The carbide type phase are precipitates that orientate within the γ/γ' microstructure and act as points which interfere with the activation and flow

of dislocations, by providing sites in which the dislocations pin themselves, loop and shear. The method by which the dislocations interact with the carbide type phase is dependent on several factors such as; the size, no density / area fraction per unit area, type of carbide type phase and orientation with the microstructure. The carbide type phases in this study were orientated into three distinct zones within the CMSX-4 alloy and classified as regular fcc and TCP type. Using figure 315 as reference, the larger carbide type phases local to zone 3 were categorised as TCP and the smaller more faceted carbide type phases, fcc type.

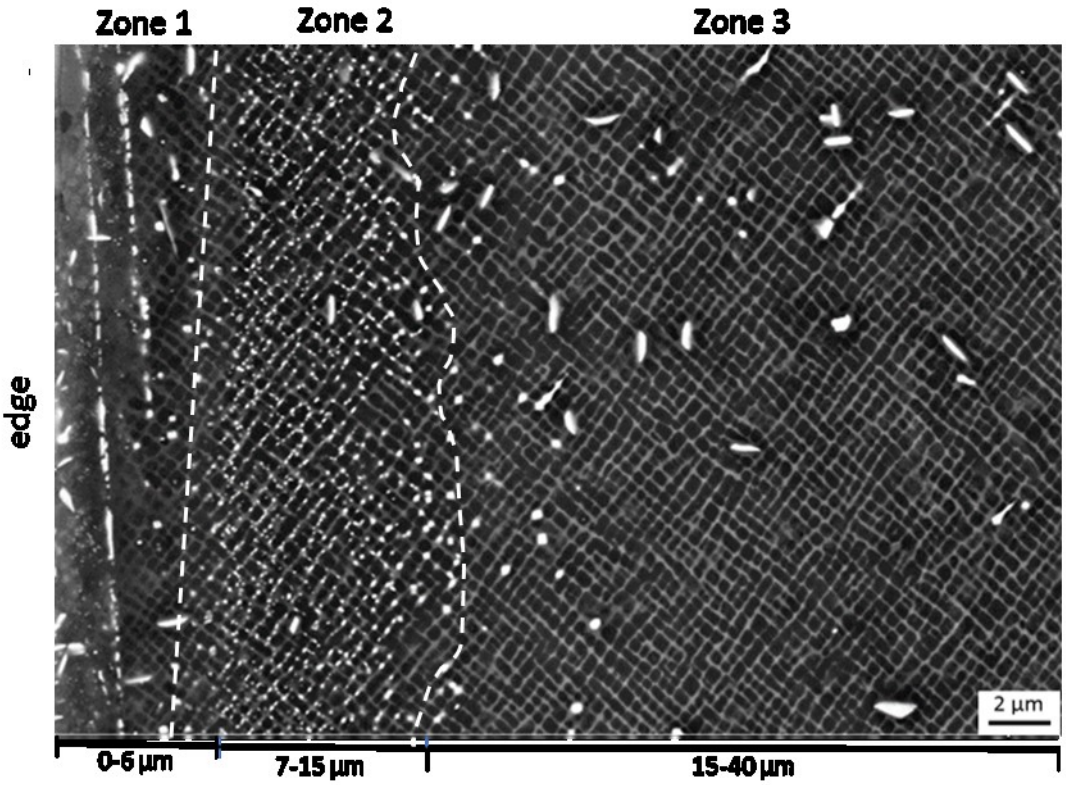


Figure 315: Carburised CMSX-4 microstructure illustrating the different carbide type phases and orientation within the γ/γ' microstructure

Table 2, shows the common carbide type phases found in an Ni superalloy, it show the lattice parameter orientation angle and constituent elements that are leeched to form the carbide type phase. The carbide type phases can act to leech elements from both the γ and γ' phases. Dislocations first start to form in the softer γ phase and pass through this phase in partials causing a stacking fault. The stacking fault energy SFE can be defined as the additional energy required to form a stacking fault of unit area[11] and it was found that a decrease in SFE acts to strengthen the alloy due to the increased repulsion between partial dislocations in the fcc phase[57].

As dislocations pass through the disordered γ channels and ordered γ' cuboids they dissociated in to partials. The segregation of the dislocation is different in each phase and it was found both in this study

and in literature[57,118] that carbide type phases tend to form at γ/γ' junctions, due to the low solubility of elements at these points[57] making it easier for the elements to be leeched from the microstructure[116,20]. The leeching of the alloying elements is undesirable and causes intrinsic flaws to the carefully tailored microstructure that is optimised for high performance at low and high temperatures[11,57].

The solubility of both the solid solution and precipitation elements within the γ/γ' matrix plays a major role in how effective they are[114] and this can be characterised by the Hume-Rothery rule that states that a high solubility can be achieved when the deviation of atomic diameters is less than 15%[120]. This fact is interesting when examining the γ / γ' junctions, which is an area in which the carbide type phases tend to precipitate as shown in figure 316 and has been reported in literature[215].

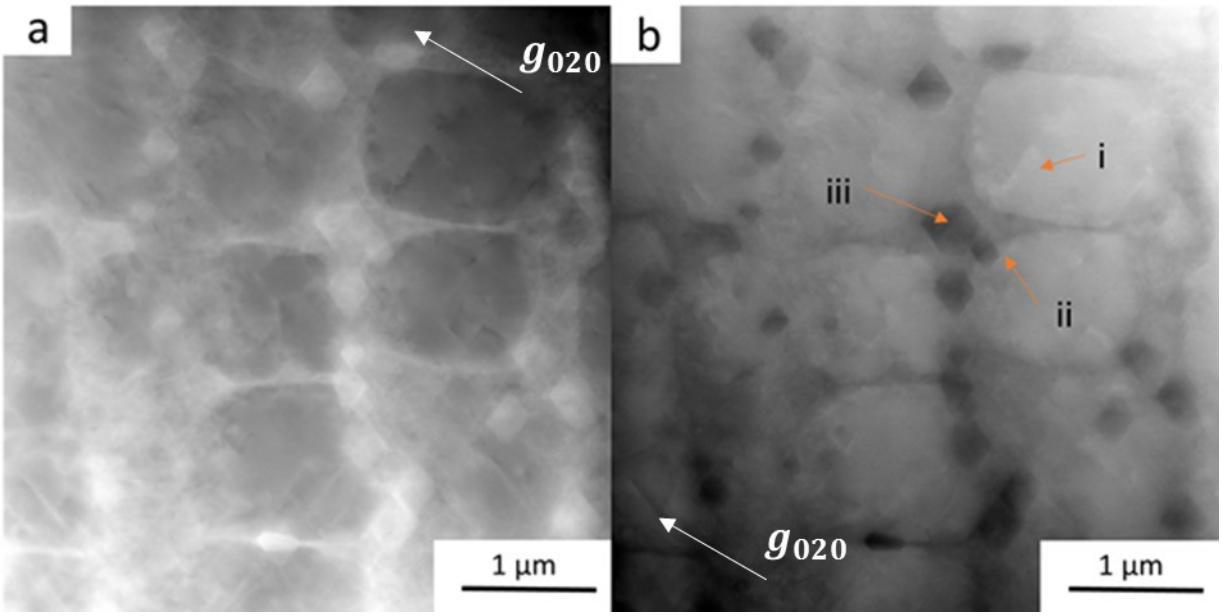


Figure 316: TEM image of carbide type phases inhabiting the γ/γ' microstructure in the CMSX-4 alloy (a) Dark field (b) Bright field, (I) γ' cuboid (ii) γ/ γ' junction (iii) cube type carbide type phase

Figure 316 shows TEM images of regular type carbide type phases in habiting the γ/γ' junctions in a CMSX-4 alloy. The reason for the precipitation of the carbide type phases at the γ/γ' junctions, being attributed to the low solubility of elements such as Mo, Re and Mo, which are slow to dissipate and enables the precipitation of the carbide type phases[57].

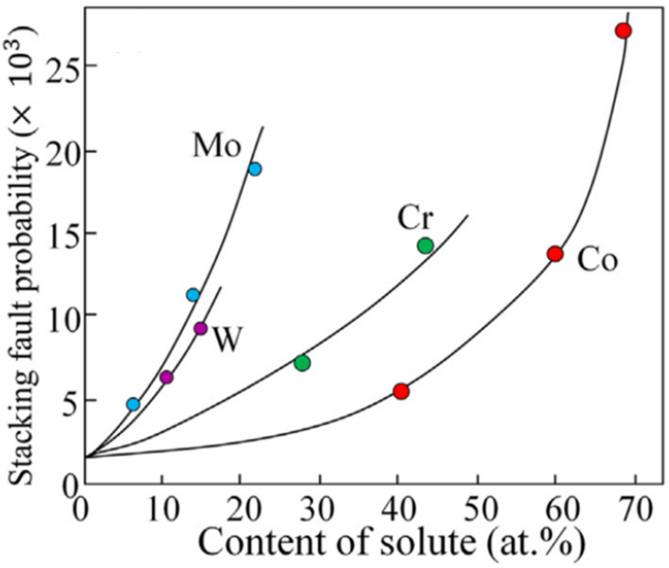


Figure 317: The role of alloying elements, Mo, W, Cr, Co on the occurrence of stacking faults in Ni-based superalloys[216,217]

Figure 317, shows the role of alloying elements, Mo, W, Cr, Co on the effect on the SFE via their respective influence on the stacking fault probability. Mo and W, as seen in this study and in literature[116,30,21] are both depleted in the presence of carbide type phases, thus lowering the strength of the alloy.

The ordered L_{12} γ' structure has a higher selectivity for alloying elements than the disordered γ[57]. The Burgers vector of a full dislocation in the disordered L_{12} structure, $b = a\langle 110 \rangle$ is twice that of the γ phase and as a consequence the dislocations in a γ' particle have a much higher lattice distortion energy[11], making the propagation of dislocations in a γ' particle more difficult and give rise to an APB when the full dislocation disassociates.

An APB occurs as a consequence of the lattice distortion, created when the Ni-Al bonds in the γ' are turned to Ni-Ni and Al-Al bonds. The distortion is characterised by the dissociation of the full dislocation, separating into two partials, as the partials slip across the (111) plane, with a Burgers vector equal to a full dislocation in the disordered γ.

In general, the net system increase caused by the breaking of bonds in the Ni-Al system is equivalent to ~150mj/m^2[2,11] and an increase in APB energy signifies an increase in resistance to dislocation motion[57].

As the γ and γ' volume fraction changes caused by the carbide type phase and TCP precipitates this is changes the local chemistry, which in turn changes the local lattice spacing and bond energy. Ultimately these changes alter activation of dislocation sources and propagation of dislocations.

Table 34: Common TCP phases in Ni single crystal alloys[119]

Type	Crystal structure	Space group	Atoms per Unite Cell	Lattice parameter (Å)	α
σ	Tetragonal	P42/mnm	30	a = b = 8.78; c = 4.54	90.0°
μ	Rhombohedra	R-3m	13	a = b = c = 9.04	30.5°
	Hexagonal		39	a = b = 4.75; c = 25.83	120.0°
P	Orthorhombic	Pnma	56	a = 16.98; b = 4.75; c = 9.07	90.0°
R	Rhombohedra	R-3m	159	a = b = 10.93; c = 19.34	120.0°

Carbide type phases, in particular TCP phases, table 34 act to lower the APB energy through the disruption of equilibrium elemental concentrations[57]. For example Ta, which is a strong carbide type phase stabilising element, is added to Ni super alloys to increase the APB energy[57].

A high Ti/Al ratio also acts to increase the APB energy as seen in figure 318 and it can be seen in fig that Ti is also a carbide stabiliser and thus the Ti/Al ratio would be decreased in the presence of a carbide type phase, further lowering the APB energy, the optimum Ti ratio was found to be 1.22[57].

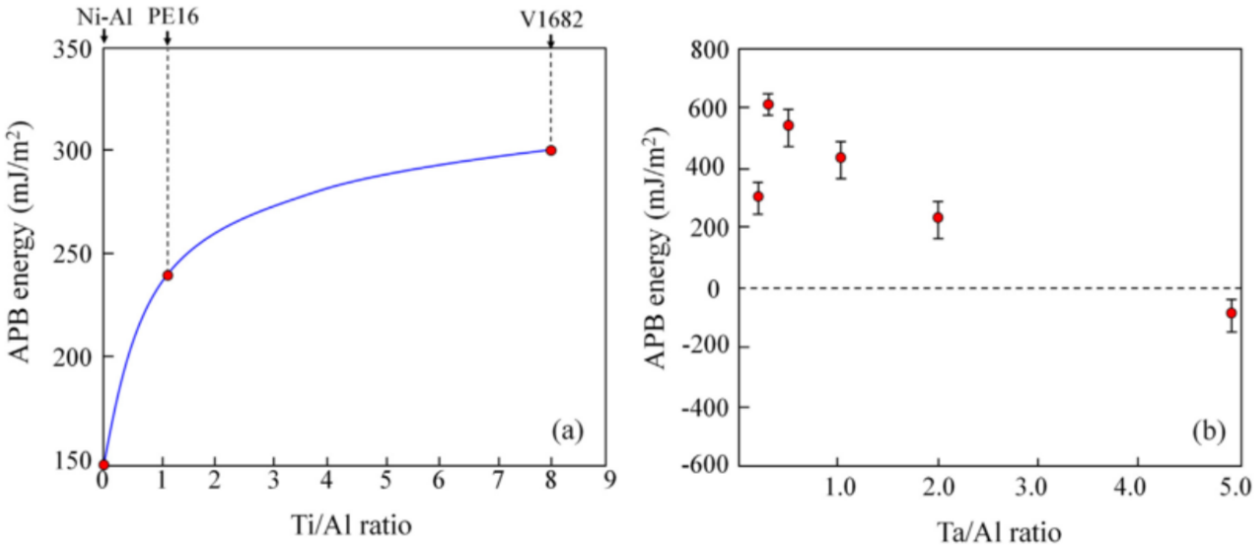


Figure 318: Effects of Ta/Ti on the anti-phase boundary (APB) energy of Ni-based alloys when compared to Al (a) Dependency of APB energy on Ti/Al ratio (b) Dependency of Ta/Al ratio on the APB energy[57]

Figure 318 shows how the Ti/Al and Ta/Al ratio affect the APB energy in a Ni superalloy. High dislocation networks that can exist around carbide type phases can promote the coarsening of the γ' cuboids, disrupting misfit causing problems at high and low temps[212,77]. If the carefully designed solid solution equilibrium is broken it can lead to precipitation of the TCP phase[57], which can significantly reduce the mechanical performance of the alloy[120,30].

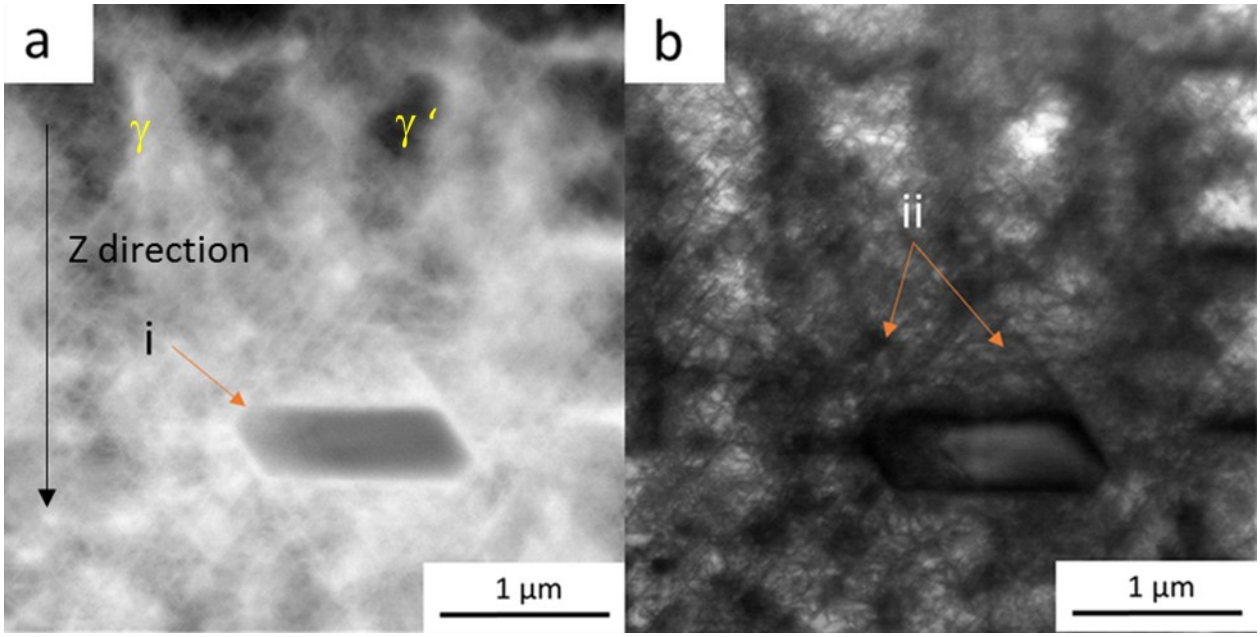


Figure 319: TEM image of a TCP phase the microstructure (a) Dark field (b) Bright field (i) TCP phase inhabiting a junction (ii) Dislocations surrounding the TCP phase.

TCP precipitates are considered deleterious for several reasons[120,194]; they consume strengthening elements, as shown in figs and in literature[120,194], there is a large lattice misfit between the TCP and γ' phase[75,212], this high degree of misfit creates internal stresses at the interface and can be a preferred region for crack nucleation[77,57]. The TCP phases are also intrinsically brittle and are easy to fracture under external load[57] and this is shown in fig indicated by the large stress drop and significant diagonal shear line observed in the compressed micropillar, figure 299c (page 306).

One of the largest areas of scatter, found in this study occurred as a consequence of the carbide type phases and can be attributed to the effects explained above. It can also be assumed that the carbide type phases are 3d in nature and the profile of the carbide type phase's shape continues in the z direction. Examination of a TEM foil which contains carbide type phases from this alloy shows that this is the case, figure 319. It can also be seen / theorised[212] that the leeching of elements can cause an increased γ channel width with can act to weaken the material[75].

Figure 319 also shows the dislocations accumulating around the carbide type phase, which is located at a γ/γ' junction and can be seen to arise sub surface and not in the visible plane. This is also shown in the case of more regular carbide type phases, shown below in figure 320. The sample was tilted to a different condition in which the dislocations can be seen more clearly and several exist within the γ / γ' junctions.

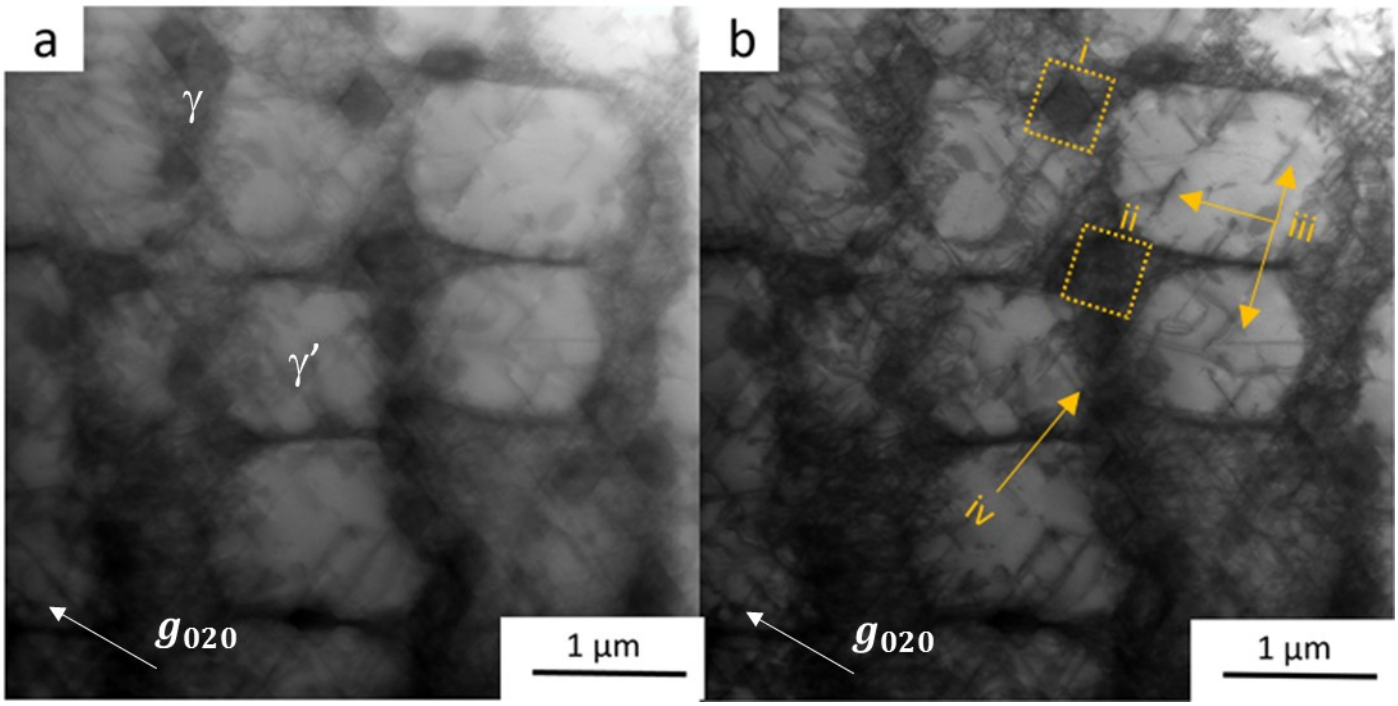


Figure 320:Bright field TEM images in a condition off the zone axis (a) Condition 1 showing cuboidal carbide type phases in γ/γ' junctions and dislocations surrounding them, with the γ channels flush with dislocations (b) Condition 2 clearer view of dislocations inhabiting γ' cuboids, surrounding γ channels and inflating the γ /γ' junctions (i) cuboidal carbide (iii) Partial dislocations in cuboids (iv) and junctions flush with dislocations

Figure 320, shows TEM foils of a slightly deformed section within the carbide type phase rich in CMSX-4. The figure shows the γ channels flush with dislocations and a multitude of partial dislocations that have entered the γ' cuboids. The carbide type phases acted to make the material weaker and more brittle and the effect was more predominant in TCP phase. The effects of carbide type phases interacting with dislocations is discussed in greater detail in section 9.5.5 (page 330).

Table 35: Compound table of TEM information from figures 316-320. Listing the foil normal, G vector, image mode and pager number, taken from carburised CMSX-4

Fig No.	Foil normal	G vector	Image mode	Page no.
316(a)	001	020	DF	322
316(b)	001	020	BF	322
319 (b)	001	020	BF	325
320(a-b)	001	020	BF	326

11.4. Plasticity and hardening

The Ni superalloys are fcc materials and thus are expected to have a high strain hardening component[209]. The hardening modulus values in this study were always taken from the same two points, as outlined in the methodology section and the values changed according to orientation and alloy type but generally remained consistent, when comparing similar alloy types and orientations, this can be seen in sections; 6.4.4, page 133, 7.7 page 215 and 8.7, page 249.

The plasticity of Ni alloys are linked to the travel of dislocations flowing through the γ/γ' matrix[19]. As the γ' constitiutes70+% of the alloy microstructure and is the strengthening phase, it is assumed the hardening is primarily due to the γ'. Studies have shown that varying the size of the micropillars can alter the dislocation source mechanisms and change the forest hardening via exhaustion[2] and truncation[128]. For this reason the pillar top width and area was kept constant ±3%.

When comparing slip traces on the respective faces of the micropillars at different strains, keeping the geometry and areas of the pillars consistent made the analysis more accurate.

It was found in the size effect study that the smaller the top width / area of the micropillar, the higher the hardening modulus was. In short the hardening modulus was inversely proportional to the top width of the pillar (maintaining an aspect ratio of approximately 1:3, width to height). The reason for the inverse relationship is linked to the dislocations acting in small / confined volumes[128],[218] and the effect of dislocation activation[219], dislocation motion[4] and the image forces[149] on the dislocations in these small volumes; these gave rise to phenomena such as the inverse hardening relation and stress drops[2] making the hardening regime more unstable at smaller pillar areas[139],[156].

In the case of carbide type phase isolated pillars and pillars within the carbide type phase rich region, the hardening values varied the most. The pillars with large TCP phase experienced large stress drops in the hardening regime as a consequence of a large build-up of stress and subsequent relaxation, as the dislocations need to accumulate enough energy to either shear or loop past the carbide type phase [63,89]. It can be assumed that the energy required to do this is proportional to the size and irregularity (which can be defined as a large aspect ratio) of the carbide type phase. It was also found that the yield point was inversely proportional to the carbide type phase area fraction, the trend deviated slightly when TCP phase were involved. The reasoning most likely linked to the increase leeching of alloying elements with increasing carbide type phase, area fraction, which alters the spacing of the partials in the γ/γ and thus the SFE and APB energies.

The carbide type phases can also act to alter the lattice misfit between the γ and γ' phases[212], the misfit has a strong influence on the density and evolution rate of dislocation networks[11,57]. This is particularly apparent in the plastic regime of the stress strain curves as shown, figure 109, page 131, whereby the dislocation forests are altered by the presence of carbide type phases and disruption to the equilibrium microstructure.

The lattice misfit in Ni superalloys can be adjusted by altering the segregation of alloying elements in the γ and γ' phases[59,58]. An alloy with a negative misfit will tend to form spherical γ' particles and one

with a positive misfit will form cuboidal γ' particles[57,212]. The atomic diameters of the alloying elements in an Ni superalloy are as follows: Ni<Co<Cr<Ru<Mo<W<Al<Ta<Ti.

W, Al, Ti and Ta are the elements most significantly affected by the carbide type phases, and thus it can be concluded that the carbide type phases alter the misfit significantly and would act to alter the low surface energy structures the γ' particles have formed as a consequence of minimising the elastic strain energy associated with the lattice distortion between the phases[57,212].

Dislocations are attracted to γ/γ' junctions as seen in figure 316, to relax the associated misfit that carbide type phases tend to form at these interfaces[21257], so it can be concluded that dislocations would tend to accumulate around the carbide type phases leading to large stress drops and areas of unstable, non-uniform hardening.

11.5. The effect of carbides on dislocations

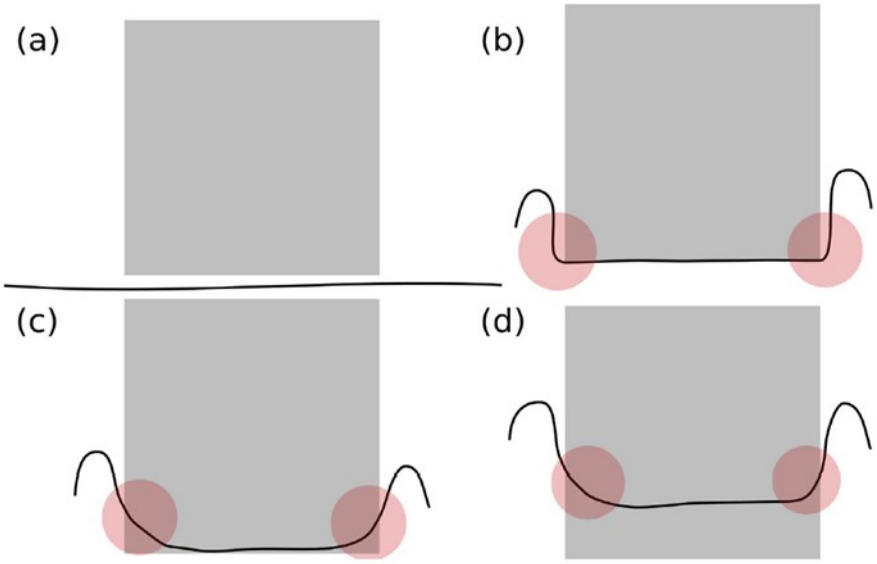


Figure 321: Schematic of the bowing assisted precipitate shearing: (a) a dislocation (black) approaches a precipitate and gets trapped at the γ/γ'interface; (b) the dislocation bows into the channels surrounding the precipitate creating high local self-stresses in the regions indicated by the red circles due to the high curvature of the dislocation in that region; (c) the high attractive self-stress pulls the dislocation into the precipitate and (d) the dislocation continues shearing the precipitate following the same mechanism as long as the shear stress is higher than the APB forces on the dislocation[220]

Figure 321 shows a schematic of the bowing assisted precipitate shearing. The energy of the dislocation line that propagates with applied shear stress post yield, is altered by the presence of carbide type phases. This is due to the disruption of interatomic bonds in the γ/γ' structure. The effect of which is shown in figure 11 and expounded upon on page 16.

When dislocations meet an obstacle they pile up at the obstacle, as seen in figure 19 and **Error! R eference source not found.**, pages 34-35, thus magnifying and concentrating the shear stress at this point. Depending on the size of the obstacle and the spaces between multiple obstacles (for example

small carbide type phases in CMSX-10), the dislocation can bow or shear through the obstacle. The carbide type phases in CMSX-4 acted to decrease the yield point, whereas the carbide type phases in CMSX-10 acted to increase the yield point within the carbide type phase, rich region.

The bowing of the dislocation into a loop can form more dislocations, via the Frank Read source mechanism. The presence of carbide type phases would thus act to interfere with the bowing process and create more dislocations at these points, thus interfering with the dislocation forests, affecting both yield and hardening. The effect of altering the yield point and hardening modulus can be observed in the stress strain response, resulting in stress drops such as those observed in figure 293. The larger the carbide type phase, the larger the loop radius, making the attractive ends of the dislocation weaker and the dislocation line less able to shear the carbide type phase, as explained in section 4.3.2, page 21 . This effect combined with the larger degree of element leeching in CMSX-4, can be used to explain why the yield point of carbide type phase, isolated pillars increases in CMSX-10 but decreases in CMSX-4.

Carbide type phases, can act as pinning sites for dislocations resulting in the activation of multiple slip systems and this can happen almost simultaneously. The activation of multiple slip systems can be altered both by the number density of the carbide type phases and the size and type as shown in, figure 299, page 306. It has been theorised that the main reason for the change in mechanical properties within the CMSX-4 alloy was again linked to the disruption of alloying elements, this was validated as explained in section 10.4.3. In section 5, page 101. It was concluded that the orientations with more active slip systems had a higher hardening modulus and it was found that pillars within the carbide type phase alloy that gave rise to multiple slip systems as observed on the front face of the pillars, figure 299-figure 303 also obeyed this phenomena.

The global trends of carbide type phases within CMSX-4 and CMSX-10 indicate that in both alloys the carbide type phase, rich regions act to alter the mechanical properties of the alloy when compared to the bulk material. The precise influence of carbide type phases on the dislocations in these alloys is stochastic and varies according to carbide type phase, area fraction and number density.

To summarise, as carbide type phases occur at the γ/γ' junctions, as shown in figure 316, the dislocation line can perform several operations in order to accommodate the plastic strain and travel through the microstructure. The type of operation such as shearing or looping / multiplication is dependent on the carbide type phase. The role of dislocations and carbide type phases, is dependent on multiple factors as outlined above and this thesis has introduced these factors, whereby the key tool in analysing these parameters lies in the use of TEM based analysis to characterise the orientations and dislocation propagations at characteristic strains within the elastic, near yield and plastic regimes.

12. Conclusion

This project examines the micromechanical testing of Ni-based superalloys at room temperature to create a robust and thorough testing regime that can be used to accurately measure the mechanical responses of novel alloy types on the same length scales as the deformation processes on which they operate. The micromechanical tests, used in this study were paired with characterisation techniques, such as SEM, EBSD, BSD, EDS and TEM to give a full description of the alloy behaviour, pre, post and during deformation. The advanced characterisation of deformation mechanisms with dislocation contrast based TEM was used in this thesis to evaluate the propagation of dislocations at representative strains, such as the elastic region <3% near the yield ~3% and the hardening >3%. The TEM technique was also used to characterise carbide type phases and dislocation types within the γ/γ' microstructure.

For this study rectangular shaped pillars were used, manufactured via the lathe method[142]. Rectangular pillars were used over circular pillars, as it makes the analysis of the slip behaviour in cubic fcc structure of Ni alloys more favourable. Circular pillars are generally used more on ceramic materials as the corners of rectangular pillars can act as stress concentrators and result in catastrophic brittle failures. Orientation changes, through microstructure can also lead to unstable and non-symmetric compression which will result in shape instability of the pillars[214]. These factors are taken into consideration when designing pillars as they can complicate analyses of the relationship between the load-displacement responses and slip activity within the tested volume.

The thesis has four results chapters and one discussion section and the salient points from each chapter are presented below.

- For comparative pillar studies, the areas and geometry of the micro pillar should be kept consistent.
- In this study the proportional limit is best used to assess the yield point, as it limits the error associated with strain bursts and the underestimation of the elastic modulus when compared to macro data.
- Pillars with a top width of 4-5 µm and an aspect ratio of 1:3 were found to be the most stable and have a reasonable milling time.
- The crystal orientation can be changed to give rise to different deformation modes, this is a consequence of ease of activating multiple slip systems.
- The activation of secondary slip systems leads to strong barriers to plastic flow accompanied with dislocation pile ups that can be quantified as strain bursts seen in the hardening regime in a stress v strain trace.

- It was found that pillars with different orientations that had multiple active slip systems had the highest hardening modulus. This fact was explored in more detail in results chapter 2.
- Shear localisation results in large dense regions of dislocations inhabiting both the ϒ and ϒ'.
- At areas less heavily influenced by strain the dislocations interact heavily in the ϒ before separating into partials, kinks and super kinks as they travel through the ϒ'.

- The micropillar technique can be used to isolate orientations on individual grains in polycrystalline materials.
- The closer the resolved shear stress of other slip systems the more unstable the deformation of the alloy, due to the interactions of dislocations on the intersecting slip planes.
- The slip trace produced on the face of a rectangular micropillar can be predicted, based on the orientation of the top surface.
- This was validated by micropillar experiments and this can be used to inform the alloy designer of the deformation character of bespoke alloy components, designed in specific orientations.

- The addition of refractory elements plays a significant role in the formation of carbides and carbide type phases and leads to differences in morphology and crystal structure.
- The carburised alloys under investigation in this study are the by-product of pack aluminzation, which is used to grow the gradient layer180,24.
- Elements therefore need to be carefully selected during processing and tailored accordingly when creating multi-layered alloys containing bond coats and thermal barrier coatings.
- Studying chemistry effects through length profiles requires accurate placement and testing area geometry, micropillars were placed as a function of distance from the perimeter edge of the sample and it was found that the carbide type phases in CMSX-4 acted to decrease the strength of the alloy.

- The carbide type phases in CMSX-10 are fcc type and extend 4x less than those in CMSX-4.
- The carbide type phases in CMSX-10 act to increase the strength of the alloy, this could be due to the lower solution treatment window of CMSX-10 which allows more stable precipitates to form.

- The micro yield point values found from micropillar compression experiments and macro yield point values194 were found to be in agreement with each other.
- The underestimation in elastic modulus found when comparing micro to macro values is due to the compliance of the in-situ system, which is comprised of several components being loaded in series. Where the elastic modulus of the cyanoacrylate based adhesive (3-15 GPa) was linked to the reduction in total stiffness8.
- Carbides and carbide type phases in Ni superalloys effect the propagation of the dislocation line with applied shear stress, post yield. In this study the strain rate was kept constant at 50 nm/s.
- The effect of the carbides and type phases on mechanical properties in the alloy can be linked to a competition between dislocation mobility and the leeching of alloying elements, which disrupt the interatomic structure in the ϒ/ϒ' microstructure.
- The effect of leeching in the carburised CMSX-4 alloy, was found to outweigh the strengthening effects of the carbide type phases acting as foreign obstacles preventing dislocation motion.
- The size of the TCP phase within zone 3 in the CMSX-4 alloy, combined with the large distances between the carbide type phases in this zone, could enable them to be modelled as individual particles. This can be seen in the large dominant shear band that occurs on the front face of the micropillar in the presence of TCP phase.
- The carbide type phases in zones 1-2 in CMSX-4 were so close together that they would not be viewed as individual precipitates and this could be seen in the multiple slip traces seen on the surface of the micropillar in the presence of zone 1-2 carbide type phases and also in the TEM foil.
- The yield point of the micropillars were weaker in the presence of TCP phase.
- The carbide type phases in CMSX-10 are generally spaced close together 2-5 nm and so would not be viewed as individual particles.

- Micropillar compression combined with companion EBSD, EDX and indentation experiments are a useful tool to ascertain the mechanical behaviour of alloys focusing on orientations and microstructural units. Enabling the analyst to begin to predict in service behaviours.
- The elemental constituents of each type of carbide type phase is different. The larger the difference in shape descriptor (indicated by TCP phase or fcc type carbide phase) the larger the difference in chemistry between carbide type phases and mechanical properties.
- Carbide type phases can act as stress concentrators and cause changes in the local mechanical properties, fcc type carbide phases are less deleterious to the mechanical properties than TCP phase.

- EDX analysis which provides a resolution of up to 1 μm[23] indicates the carbide type phases are primarily derived from C with additional elements such as Ti, Ta, Re and W being present. Depending on the crystal structure and degree of misfit with the matrix we would expect the carbide type phases to impede dislocation motion.
- The disruption to the equilibrium alloy concentrations can occur even with no visible carbide type phases present.
- As dislocations travel through the bulk matrix and interact with carbide type phases, they can operate a number of mechanisms such as Orowan bowing[221]to minimise energy and overcome the obstacle barrier[32].
- The carbide type phase, isolated pillars in the CMSX-4 alloy, caused a decrease in the yield point of the alloy. This was linked to the elemental leeching from the equilibrium microstructure.
- The carbide type phase, isolated pillars in the CMSX-10 alloy, caused an increase in the yield point of the alloy. This was due to the small finely spaced fcc carbide type phases acting as pinning points, disrupting dislocation motion.
- It was found that the key factor linking to the change of mechanical properties within the vicinity of the carbide type phase, rich area was linked to a change in alloy chemistry with contributions from carbide type phase, size and orientation.

The use of micromechanical testing on engineering alloys, provides an opportunity to enhance the development of the next generation of alloys[222,14]. These alloys will be used in a host of engineering applications, including; aerospace, power and nuclear applications.

The micromechanical testing used in this thesis has enabled local testing of microstructures. In alloys containing carbide type phases, it was found that the local strength of the alloy is linked to a compromise between the elemental leeching of the ϒ' precipitates by carbide type phases and their resistance to dislocation motion. If the carbide type phases are stable within the microstructure and closely spaced then locally the strength of the alloy will increase. If the carbide type phases, are widely spaced and non-coherent with the matrix (for example TCP phase) then the effect of elemental leeching will override the strengthening effect.

The mechanical variable focused on, in this thesis, was primarily the yield point, followed by the hardening rate and elastic modulus. Creating alloys with higher strength will enable parts to be manufactured with less material, thus enabling better fuel economy and more efficient designs. Improving the hardening modulus of engineering alloys can improve the lifetime of components and prevent the formation of microcracks[26]. Altering the growth direction of engineering parts, and thus

changing the crystal orientation can be useful when designing mission critical parts that need to have high wear resistance in favour of ultimate tensile strength for example. Or designing polycrystalline parts with a preference for a particular texture that favours strength, such as the case of the <011> direction in the FGH96 alloy. Finally, the orientation of parts can be altered to thus enable a specific deformation angle in the case of failure.

Techniques such as the TEM post mortem examination of micro pillars and the effect of local chemistry changes with respect to nm-μm sample specimens, clarify the variation in mechanical properties with local micropillar loading.

In regards to micromechanical testing; first establishing a robust and scalable testing regime is important for reproducibility. Reproducibility is necessary when one begins to think about establishing macro models based on the micromechanical data.

As new manufacturing methods and more complicated designs are needed to satisfy both the commercial and private sectors, the influence of alloy orientations, precipitates and alloying elements are becoming more sensitive and mission crucial. To realise a change in alloy design, micromechanical testing can be employed to explore the local contribution of each microstructure feature.

The precipitation of carbide type phases and TCP phases grown from the PVA masking layer during the pack aluminzation process at 700°C disrupts the ϒ/ϒ’ microstructure, altering the volume fraction and morphology thus altering the mechanical properties. This typically leads to a decrease in yield strength, local stress concentrations, and ultimately is likely to cause surface embrittlement.

This is supported through analysis of the number density, area fraction and shapes of the carbides and TCP phases (from the BSD analysis) and combined with chemical analysis using EDX. There is a direct correlation of the presence of these phases and local disruption in the local chemistry and phase fraction of the γ and γ’. This changes the plastic flow. Specific observations include an observation that high aspect ratio carbide type phases / TCP type phase cause more significant changes in local mechanical properties.

13. References

1. Uchic MD, Shade P a., Dimiduk DM. Plasticity of Micrometer-Scale Single Crystals in Compression. *Annu Rev Mater Res*. 2009;39(1):361-386. doi:10.1146/annurev-matsci-082908-145422

2. Dimiduk DM, Uchic MD, Parthasarathy T a. Size-affected single-slip behavior of pure nickel microcrystals. *Acta Mater*. 2005;53:4065-4077. doi:10.1016/j.actamat.2005.05.023

3. Nagoshi T, Shibata A, Todaka Y, Sato T, Sone M. Mechanical behavior of a microsized pillar fabricated from ultrafine-grained ferrite evaluated by a microcompression test. *Acta Mater*. 2014;73:12-18. doi:10.1016/j.actamat.2014.03.048

4. Frick CP, Clark BG, Orso S, Schneider a. S, Arzt E. Size effect on strength and strain hardening of small-scale [111] nickel compression pillars. *Mater Sci Eng A*. 2008;489(1-2):319-329. doi:10.1016/j.msea.2007.12.038

5. Arakere NK, Swanson G. Effect of Crystal Orientation on Fatigue Failure of Single Crystal Nickel Base Turbine Blade Superalloys. *J Eng Gas Turbines Power*. 2000;124(1):161-176. doi:10.1115/1.1413767

6. Jun T-S, Zhang Z, Sernicola G, Dunne FPE, Britton TB. Local strain rate sensitivity of single α phase within a dual-phase Ti alloy. *Acta Mater*. 2016;107(April):298-309. doi:10.1016/j.actamat.2016.01.057

7. Zhang Z, Jun TS, Britton TB, Dunne FPE. Intrinsic anisotropy of strain rate sensitivity in single crystal alpha titanium. *Acta Mater*. 2016;118:317-330. doi:10.1016/j.actamat.2016.07.044

8. Reuber C, Eisenlohr P, Roters F, Raabe D. Dislocation density distribution around an indent in single-crystalline nickel: Comparing nonlocal crystal plasticity finite-element predictions with experiments. *Acta Mater*. 2014;71:333-348. doi:10.1016/j.actamat.2014.03.012

9. Gong J, Wilkinson AJ. Anisotropy in the plastic flow properties of single-crystal a titanium determined from micro-cantilever beams. *Acta Mater*. 2009;57(19):5693-5705. doi:10.1016/j.actamat.2009.07.064

10. Maaß R, Van Petegem S, Van Swygenhoven H, Derlet P, Volkert C, Grolimund D. Time-Resolved Laue Diffraction of Deforming Micropillars. *Phys Rev Lett*. 2007;99(14):145505. doi:10.1103/PhysRevLett.99.145505

11. Reed RC. *The Superalloys, Fundamentals and Applications*.; 2006. doi:0521859042

12. Messe OMDM, Stekovic S, Hardy MC, Rae CMF. Characterization of Plastic Deformation Induced by Shot-Peening in a Ni-Base Superalloy. *Jom*. 2014;66(12):2502-2515. doi:10.1007/s11837-014-1184-8

13. Vattré A, Devincre B, Roos A. Orientation dependence of plastic deformation in nickel-based single crystal superalloys: Discrete-continuous model simulations. *Acta Mater*. 2010;58:1938-1951. doi:10.1016/j.actamat.2009.11.037

14. Steckmeyer a., Sauzay M, Weidner a., Hieckmann E. Micromechanical modelling of the cyclic

stress-strain behaviour of nickel polycrystals. *Int J Fatigue*. 2012;40:154-167. doi:10.1016/j.ijfatigue.2011.10.019

15. Raabe D, Ma D, Roters F. Effects of initial orientation, sample geometry and friction on anisotropy and crystallographic orientation changes in single crystal microcompression deformation: A crystal plasticity finite element study. *Acta Mater*. 2007;55(13):4567-4583. doi:10.1016/j.actamat.2007.04.023

16. Ramsperger M, Mujica Roncery L, Lopez-Galilea I, Singer RF, Theisen W, K??rner C. Solution Heat Treatment of the Single Crystal Nickel-Base Superalloy CMSX-4 Fabricated by Selective Electron Beam Melting. *Adv Eng Mater*. 2015;17(10):1486-1493. doi:10.1002/adem.201500037

17. Fuchs GE. Solution heat treatment response of a third generation single crystal Ni-base superalloy. *Mater Sci Eng A*. 2001;300(1-2):52-60. doi:10.1016/S0921-5093(00)01776-7

18. Karaoglanli AC, Ogawa K. Thermal Shock and Cycling Behavior of Thermal Barrier Coatings (TBCs) Used in Gas Turbines. 2014.

19. Nörtershäuser P, Frenzel J, Ludwig a., Neuking K, Eggeler G. The effect of cast microstructure and crystallography on rafting, dislocation plasticity and creep anisotropy of single crystal Ni-base superalloys. *Mater Sci Eng A*. 2015;626:305-312. doi:10.1016/j.msea.2014.12.030

20. Handa SS. Precipitation of Carbides in a Ni-based Superalloy. 2014:1-33.

21. Pillai R, Chyrkin A, Grüner D, et al. Carbides in an aluminised single crystal superalloy: Tracing the source of carbon. *Surf Coatings Technol*. 2016;288:15-24. doi:10.1016/j.surfcoat.2015.12.066

22. Kartal M, Uysal M, Gul H, Alp A, Akbulut H. Effect of surfactant concentration in the electrolyte on the tribological properties of nickel-tungsten carbide composite coatings produced by pulse electro co-deposition. *Appl Surf Sci*. 2015;354:328-336. doi:10.1016/J.APSUSC.2015.06.023

23. Chen YQ, Slater TJ a, Lewis E a, et al. Measurement of size-dependent composition variations for gamma prime (γ') precipitates in an advanced nickel-based superalloy. *Ultramicroscopy*. 2014;144:1-8. doi:10.1016/j.ultramic.2014.04.001

24. Nganbe M, Heilmaier M. Modelling of particle strengthening in the ϒ'and oxide dispersion strengthened nickel-base superalloy PM3030. *Mater Sci Eng A*. 2004;387-389(1-2 SPEC. ISS.):609-612. doi:10.1016/j.msea.2004.01.109

25. Howie a., Swann PR. Direct measurements of stacking-fault energies from observations of dislocation nodes. *Philos Mag*. 1961;6(March 2015):1215-1226. doi:10.1080/14786436108243372

26. Schwiedrzik J, Raghavan R, Bürki A, et al. In situ micropillar compression reveals superior strength and ductility but an absence of damage in lamellar bone. *Nat Mater*. 2014;(June):1-8. doi:10.1038/nmat3959

27. Zhang J, Jin T, Xu Y, Hu Z. Antiphase Boundary Strengthening in a Single Crystal Nickel-base Superalloy. *J Mater Sci Technol*. 2002;18:159-162.

28. Crudden DJ, Mottura a., Warnken N, Raeisinia B, Reed RC. Modelling of the influence of alloy composition on flow stress in high-strength nickel-based superalloys. *Acta Mater*. 2014;75:356-370. doi:10.1016/j.actamat.2014.04.075

29. Chen Y, Zhao X, Bai M, Chandio a., Wu R, Xiao P. Effect of platinum addition on oxidation behaviour of γ/γ′ nickel aluminide. *Acta Mater*. 2015;86:319-330. doi:10.1016/j.actamat.2014.12.023

30. Yu ZH, Liu L, Zhang J. Effect of carbon addition on carbide morphology of single crystal Ni-based superalloy. *Trans Nonferrous Met Soc China (English Ed*. 2014;24(2):339-345. doi:10.1016/S1003-6326(14)63066-1

31. Hull D and DJB. *Introduction to Dislocations (Fith Edition)*.; 2011.

32. Morris JW. Dislocation Plasticity : Overview. 1934;i:1-36.

33. Wen S, Zeng X, Kang Z, Yue Z. Investigation the effect of crystal orientation of nickel-based single crystal superalloys on bending creep tests. *Materwiss Werksttech*. 2014;45(3):200-206. doi:10.1002/mawe.201400195

34. Dimiduk DM, Woodward C, Lesar R, Uchic MD. Scale-free intermittent flow in crystal plasticity. *Science*. 2006;312(5777):1188-1190. doi:10.1126/science.1123889

35. Maaß R, Uchic MD. In-situ characterization of the dislocation-structure evolution in Ni micro-pillars. *Acta Mater*. 2012;60:1027-1037. doi:10.1016/j.actamat.2011.11.007

36. Lloyd JT, McDowell DL. Implications of limited slip in crystal plasticity. *Mech Eng*. 2010;Woodruff S.

37. Shade P a., Uchic MD, Dimiduk DM, Viswanathan GB, Wheeler R, Fraser HL. Size-affected single-slip behavior of Ren?? N5 microcrystals. *Mater Sci Eng A*. 2012;535:53-61. doi:10.1016/j.msea.2011.12.041

38. Lilleodden E. Microcompression study of Mg (0001) single crystal. *Scr Mater*. 2010;62(8):532-535. doi:10.1016/j.scriptamat.2009.12.048

39. Uenishi A, Sugiura N, Sugiyama M, Isogai E. Crystal Plasticity Analysis of Work Hardening Behavior at Large Strains in Ferritic Single Crystal. 2013;(102):57-62.

40. Cailletaud G, Diard O, Feyel F, Forest S. Computational Crystal Plasticity : From Single Crystal to Homogenized Polycrystals. *Tech Mech Uni Magdebg*. 2003:130-145.

41. Dimiduk DM, Uchic MD, Parthasarathy T a. Size-affected single-slip behavior of pure nickel microcrystals. *Acta Mater*. 2005;53(15):4065-4077. doi:10.1016/j.actamat.2005.05.023

42. Maeder X, Mook WM, Niederberger C, Michler J. Quantitative stress/strain mapping during micropillar compression. *Philos Mag*. 2011;91(7-9):1097-1107. doi:10.1080/14786435.2010.505178

43. Rao SI, Dimiduk DM, El-Awady J a., Parthasarathy T a., Uchic MD, Woodward C. Activated states for cross-slip at screw dislocation intersections in face-centered cubic nickel and copper via atomistic simulation. *Acta Mater*. 2010;58(17):5547-5557. doi:10.1016/j.actamat.2010.06.005

44. Sevillano JG. Intrinsic and Extrinsic Size Effects in Plasticity by Dislocation Glide. *MRS Proc*. 2000;653:393-405. doi:10.1557/PROC-653-Z8.5.1

45. Roters F, Eisenlohr P, Hantcherli L, Tjahjanto DD, Bieler TR, Raabe D. Overview of constitutive

laws, kinematics, homogenization and multiscale methods in crystal plasticity finite-element modeling: Theory, experiments, applications. *Acta Mater*. 2010;58(4):1152-1211. doi:10.1016/j.actamat.2009.10.058

46. Kiener D, Guruprasad PJ, Keralavarma SM, Dehm G, Benzerga a. a. Work hardening in micropillar compression: In situ experiments and modeling. *Acta Mater*. 2011;59(10):3825-3840. doi:10.1016/j.actamat.2011.03.003

47. Hussein AM, Rao SI, Uchic MD, Dimiduk M, El-awady JA. ScienceDirect Microstructurally based cross-slip mechanisms and their effects on dislocation microstructure evolution in fcc crystals. 2015;85:180-190.

48. Zitara M, Cetel A, Czyrska-Filemonowicz A. Microstructure Stability of 4th Generation Single Crystal Superalloy, PWA 1497, during High Temperature Creep Deformation. *Mater Trans*. 2011;52(3):336-339. doi:10.2320/matertrans.MB201003

49. Schneider R, Heine B, Grant RJ. Mechanical Behaviour of Commercial Aluminium Wrought Alloys at Low Temperatures. 2014.

50. Lomer-Cottrell-Versetzungen.

51. Kerans RJ, Hirth JP, Clark W a. T. Dislocation structures and the character of superdislocations in Ni3Al alloys. *Acta Metall Mater*. 1995;43(1):277-285. doi:10.1016/0956-7151(95)90283-X

52. Du B, Sheng L, Hu Z, Cui C, Yang J, Sun X. Investigation on the microstructure and tensile behavior of a Ni-based IN792 superalloy. *Adv Mech Eng*. 2018;10(2):168781401775216. doi:10.1177/1687814017752167

53. Field RD, Pollock TM, Murphy WH. *The Development of g / g' Interfacial Dislocation Networks During Creep in Ni-Base Superalloys*. https://www.tms.org/superalloys/10.7449/1992/Superalloys_1992_557_566.pdf. Accessed October 30, 2018.

54. Parthasarathy TA, Rao SI, Dimiduk DM. *A FAST SPREADSHEET MODEL FOR THE YIELD STRENGTH OF SUPERALLOYS*.; 2004. https://www.tms.org/Superalloys/10.7449/2004/Superalloys_2004_887_896.pdf. Accessed October 30, 2018.

55. Rao SI, Dimiduk DM, Parthasarathy T a., Uchic MD, Woodward C. Atomistic simulations of surface cross-slip nucleation in face-centered cubic nickel and copper. *Acta Mater*. 2013;61(7):2500-2508. doi:10.1016/j.actamat.2013.01.026

56. Niederberger C, Mook WM, Maeder X, Michler J. In situ electron backscatter diffraction (EBSD) during the compression of micropillars. *Mater Sci Eng A*. 2010;527(16-17):4306-4311. doi:10.1016/j.msea.2010.03.055

57. Long H, Mao S, Liu Y, Zhang Z, Han X. Microstructural and compositional design of Ni-based single crystalline superalloys — A review. *J Alloys Compd*. 2018;743:203-220. doi:10.1016/j.jallcom.2018.01.224

58. Nathal M V, Ebert LJ. The Influence of Cobalt, Tantalum, and Tungsten on the Elevated Temperature Mechanical Properties of Single Crystal Nickel-Base Superalloys. *Met Trans A*. 1985;16(10):1863-1870. doi:10.1007/BF02670373

59. Rao Y, Smith TM, Mills MJ, Ghazisaeidi M. Segregation of alloying elements to planar faults in γ'-Ni3Al. *Acta Mater*. 2018;148:173-184. doi:10.1016/j.actamat.2018.01.055

60. Wu XX, Wang CY. Influence of alloying elements upon the theoretical tensile strength of Ni-based model superalloy: ϒ-Ni/ϒ'-Ni3Al multilayer. *Comput Mater Sci*. 2016;119:120-129. doi:10.1016/j.commatsci.2016.04.001

61. Masoumi F, Shahriari D, Jahazi M, Cormier J, Devaux & A. Kinetics and Mechanisms of γ′ Reprecipitation in a Ni-based Superalloy OPEN. 2016. doi:10.1038/srep28650

62. Doi M, Miki D, Moritani T, Kozakai T. *GAMMA/GAMMA-PRIME MICROSTRUCTURE FORMED BY PHASE SEPARATION OF GAMMA-PRIME PRECIPITATES IN A Ni-Al-Ti ALLOY*.; 2004. https://www.tms.org/superalloys/10.7449/2004/Superalloys_2004_109_114.pdf. Accessed October 30, 2018.

63. Wang-Koh YM. Understanding the yield behaviour of L12-ordered alloys. *Mater Sci Technol (United Kingdom)*. 2017;33(8):934-943. doi:10.1080/02670836.2016.1215961

64. Ru Y, Li S, Zhou J, et al. Dislocation network with pair-coupling structure in {111} γ/γ′ interface of Ni-based single crystal superalloy. *Sci Rep*. 2016;6(1):29941. doi:10.1038/srep29941

65. Sheng L-Y, Yang F, Guo J-T, Xi T-F. Anomalous yield and intermediate temperature brittleness behaviors of directionally solidified nickel-based superalloy. *Trans Nonferrous Met Soc China*. 2014;24:673-681. doi:10.1016/S1003-6326(14)63110-1

66. Chandran M, Sondhi SK. First-principle calculation of APB energy in Ni-based binary and ternary alloys. *Model Simul Mater Sci Eng*. 2011;19(2):025008. doi:10.1088/0965-0393/19/2/025008

67. Horton J a., Liu CT. Anisotropic antiphase boundaries in rapidly solidified Ni3Al. *Acta Metall*. 1985;33(12):2191-2198. doi:10.1016/0001-6160(85)90180-4

68. Tichy G, Vitek V, Pope DP. , Alloys With Unstable Antiphase Boundaries on {111} Planes. *Philos Mag A*. 1986;53(April 2015):467-484. doi:10.1080/01418618608242846

69. Ardell a. J, Huang JC. Antiphase boundary energies and the transition from shearing to looping in alloys strengthened by ordered precipitates. *Philos Mag Lett*. 1988;58:189-197. doi:10.1080/09500838808214752

70. Caillard D, Molénat G, Paidar V. On the role of incomplete Kear-Wilsdorf locks in the yield stress anomaly of Ni3Al. *Mater Sci Eng A*. 1997;234-236(97):695-698. doi:10.1016/S0921-5093(97)00278-5

71. Nembach E, Schänzer S, Trinckauf K. The antiphase boundary energy of γ precipitates in nickel-based superalloys. *Philos Mag A*. 1992;66(April 2015):729-738. doi:10.1080/01418619208201587

72. Saada G, Veyssière P. The peak of flow stress in the L12 structure and the elimination of Kear-Wilsdorf locks. *Mater Sci Eng A*. 1993;164:281-285. doi:10.1016/0921-5093(93)90678-8

73. Glazer J, Morris JW. The effect of the precipitate size distribution on the aging curve of order hardening alloys. *Acta Metall*. 1988;36(4):907-915. doi:10.1016/0001-6160(88)90145-9

74. Brunetti G, Settefrati a., Hazotte a., et al. Determination of γ-γ' lattice misfit in a single-crystal

nickel-based superalloy using convergent beam electron diffraction aided by finite element calculations. *Micron*. 2012;43(2-3):396-406. doi:10.1016/j.micron.2011.10.009

75. Tiley J, Viswanathan GB, Hwang JY, Shiveley a., Banerjee R. Evaluation of gamma prime volume fractions and lattice misfits in a nickel base superalloy using the external standard X-ray diffraction method. *Mater Sci Eng A*. 2010;528(1):32-36. doi:10.1016/j.msea.2010.07.036

76. [Roger_C._Reed]_The_Superalloys_Fundamentals_and_(BookFi.org).pdf.

77. Pyczak F, Devirent B, Mughrabi H. The Effects of Different Alloying Elements on the Thermal Expansion Coefficients, Lattice Constants and Misfit of Nickel-Based Superalloys Investigated by X-Ray Diffraction. *Superalloys 2004*. 2004:827-836. doi:\url{10.7449/2004/Superalloys{\textunderscore }2004{\textunderscore }827{\textunderscore }836}

78. Smith SA, West GD, Chi K, Gamble W, Thomson RC. *Microstructural Evolution in Nimonic 263 for High Temperature Power Plant*. https://dspace.lboro.ac.uk/. Accessed October 30, 2018.

79. Kracke A. *Superalloys, the Most Successful Alloy System of Modern Times-Past, Present, and Future*. https://www.tms.org/superalloys/10.7449/2010/Superalloys_2010_13_50.pdf. Accessed October 30, 2018.

80. Yeh AC, Tin S. Effects of Ru and Re additions on the high temperature flow stresses of Ni-base single crystal superalloys. *Scr Mater*. 2005;52(6):519-524. doi:10.1016/J.SCRIPTAMAT.2004.10.039

81. Zhou X, Xu Z, Mu R, He L, Huang G, Cao X. Thermal barrier coatings with a double-layer bond coat on Ni3Al based single-crystal superalloy. *J Alloys Compd*. 2014;591:41-51. doi:10.1016/j.jallcom.2013.12.040

82. Gumbsch P, Schroll R. Atomistic aspects of the deformation of NiAl. 1999;7(July 1998):447-454.

83. Jiang C, Chen LQ, Liu ZK. First-principles study of constitutional point defects in B2 NiAl using special quasirandom structures. *Acta Mater*. 2005;53:2643-2652. doi:10.1016/j.actamat.2005.02.026

84. Alam MZ, Kamat S V., Jayaram V, Das DK. Micromechanisms of fracture and strengthening in free-standing Pt-aluminide bond coats under tensile loading. *Acta Mater*. 2014;67:278-296. doi:10.1016/j.actamat.2013.12.033

85. Van Sluytman JS, Moceri CJ, Pollock TM. A Pt-modified NI-base superalloy with High temperature precipitate stability. *Mater Sci Eng A*. 2015. doi:10.1016/j.msea.2015.05.023

86. Zhang Y, Ballard D a., Stacy JP, Pint B a., Haynes J a. Synthesis and oxidation behavior of platinum-enriched ϒ + ϒ' bond coatings on Ni-based superalloys. *Surf Coatings Technol*. 2006;201:3857-3861. doi:10.1016/j.surfcoat.2006.07.245

87. Das DK. Microstructure and high temperature oxidation behavior of Pt-modified aluminide bond coats on Ni-base superalloys. *Prog Mater Sci*. 2013;58(2):151-182. doi:10.1016/j.pmatsci.2012.08.002

88. Alam MZ, Kamat S V., Jayaram V, Das DK. Tensile behavior of a free-standing Pt-aluminide (PtAl) bond coat. *Acta Mater*. 2013;61(4):1093-1105. doi:10.1016/j.actamat.2012.10.012

89. Pope DP, Ezz SS. Mechanical properties of Ni 3 AI and nickel-base alloys with high volume fraction of. 1984;29(3).

90. Mollard M, Pedraza F, Bouchaud B, Montero X, Galetz MC, Schütze M. Influence of the superalloy substrate in the synthesis of the Pt-modified aluminide bond coat made by slurry. *Surf Coatings Technol*. 2015;270:102-108. doi:10.1016/j.surfcoat.2015.03.015

91. Zhao X, Cernik B, Tang CC, Thompson SP, Xiao P. Stress evolution in a Pt-diffused γ/γ' bond coat after oxidation. *Surf Coatings Technol*. 2014;247:48-54. doi:10.1016/j.surfcoat.2014.02.065

92. Danielewski M, Grzesik Z, Mrowec S. On the oxidation mechanism of Ni-Pt alloys at high temperatures. *Corros Sci*. 2011;53(9):2785-2792. doi:10.1016/j.corsci.2011.05.015

93. Bensch M, Sato a., Warnken N, Affeldt E, Reed RC, Glatzel U. Modelling of high temperature oxidation of alumina-forming single-crystal nickel-base superalloys. *Acta Mater*. 2012;60(15):5468-5480. doi:10.1016/j.actamat.2012.06.036

94. Sato a., Chiu YL, Reed RC. Oxidation of nickel-based single-crystal superalloys for industrial gas turbine applications. *Acta Mater*. 2011;59(1):225-240. doi:10.1016/j.actamat.2010.09.027

95. Jang C, Kim D, Kim D, Sah I, Ryu WS, Yoo YS. Oxidation behaviors of wrought nickel-based superalloys in various high temperature environments. *Trans Nonferrous Met Soc China (English Ed*. 2011;21(7):1524-1531. doi:10.1016/S1003-6326(11)60891-1

96. Perusin S, Viguier B, Salabura JC, Oquab D, Andrieu E. Behaviour of the oxide scale during SEM in situ plastic deformation of pure nickel foil. *Mater Sci Eng A*. 2004;387-389:763-767. doi:10.1016/j.msea.2004.01.103

97. Garruchet S, Politano O, Arnoux P, Vignal V. Diffusion of oxygen in nickel: A variable charge molecular dynamics study. *Solid State Commun*. 2010;150(9-10):439-442. doi:10.1016/j.ssc.2009.12.012

98. A.U Seybolt, Westbrook JH. Oxygen-induced grain boundary hardening in NiGa. *Acta Metall*. 1964;12(5):449-460.

99. Konrad CH, Glatzel U. Determination of oxygen diffusion along nickel/ zirconia phase boundaries by internal oxidation. *Oxid Met*. 2012;77:149-165. doi:10.1007/s11085-011-9278-y

100. Foss BJ, Hardy MC, Child DJ, McPhail DS, Shollock B a. Oxidation of a Commercial Nickel-Based Superalloy under Static Loading. *Jom*. 2014;66(12):2516-2524. doi:10.1007/s11837-014-1196-4

101. Zou C, Shin YK, van Duin ACT, Fang H, Liu Z-K. Molecular dynamics simulations of the effects of vacancies on nickel self-diffusion, oxygen diffusion and oxidation initiation in nickel, using the ReaxFF reactive force field. *Acta Mater*. 2015;83:102-112. doi:10.1016/j.actamat.2014.09.047

102. Nam HO, Hwang IS, Lee KH, Kim JH. A first-principles study of the diffusion of atomic oxygen in nickel. *Corros Sci*. 2013;75:248-255. doi:10.1016/j.corsci.2013.06.006

103. Jin Kim J, Hun Shin S, Ang Jung J, Joon Choi K, Hyun Kim J. First-principles study of interstitial diffusion of oxygen in nickel chromium binary alloy. *Appl Phys Lett*. 2012;100(2012). doi:10.1063/1.3696079

104. Wert C a. Diffusion coefficient of C in α-iron. *Phys Rev*. 1950;79(4):601-605.

doi:10.1103/PhysRev.79.601

105. Wert C, Zener C. Interstitial atomic diffusion coefficients. *Phys Rev*. 1949;76(8):1169-1175. doi:10.1103/PhysRev.76.1169

106. Young G, Wilkening W, Morton D, et al. LM-05K045 The Mechanism and Modeling of Intergranular Stress Corrosion Cracking of Nickel-Chromium- Iron Alloys Exposed to High Purity Water. 2005.

107. Zhang Y, Pint B a., Haynes J a., Wright IG. A platinum-enriched ϒ+ϒ two-phase bond coat on Ni-based superalloys. *Surf Coatings Technol*. 2005;200:1259-1263. doi:10.1016/j.surfcoat.2005.07.086

108. Haynes J a., Pint B a., Zhang Y, Wright IG. The effect of Pt content on ϒ-ϒ' NiPtAl coatings. *Surf Coatings Technol*. 2008;203(5-7):413-416. doi:10.1016/j.surfcoat.2008.08.063

109. Jiang C. Site preference of transition-metal elements in B2 NiAl: A comprehensive study. *Acta Mater*. 2007;55:4799-4806. doi:10.1016/j.actamat.2007.04.049

110. Haynes J a., Pint B a., Zhang Y, Wright IG. Comparison of the cyclic oxidation behavior of β-NiAl, β-NiPtAl and ϒ-ϒ' NiPtAl coatings on various superalloys. *Surf Coatings Technol*. 2007;202:730-734. doi:10.1016/j.surfcoat.2007.06.039

111. Grushko B, Kapush D. A refinement of the Al-Ni-Pt phase diagram. *J Alloys Compd*. 2014;594:127-132. doi:10.1016/j.jallcom.2014.01.114

112. Zhu J, Zhang C, Ballard D, et al. Study of the Ni-rich multi-phase equilibria in Ni-Al-Pt alloys using the cluster/site approximation for the face-centered cubic phases. *Acta Mater*. 2010;58(1):180-188. doi:10.1016/j.actamat.2009.08.068

113. Cutler ER, Wasson AJ, Fuchs GE. Effect of minor alloying additions on the solidification of single-crystal Ni-base superalloys. *J Cryst Growth*. 2009;311(14):3753-3760. doi:10.1016/j.jcrysgro.2009.05.002

114. Jena AK, Chaturvedi MC. The role of alloying elements in the design of nickel-base superalloys. *J Mater Sci*. 1984;19(10):3121-3139. doi:10.1007/BF00549796

115. Li Q, Tian S, Yu H, Tian N, Su Y, Li Y. Effects of carbides and its evolution on creep properties of a directionally solidified nickel-based superalloy. *Mater Sci Eng A*. 2015;633:20-27. doi:10.1016/j.msea.2015.02.056

116. Wang L, Xie G, Zhang J, Lou LH. On the role of carbides during the recrystallization of a directionally solidified nickel-base superalloy. *Scr Mater*. 2006;55(5):457-460. doi:10.1016/j.scriptamat.2006.05.013

117. Basak A, Das S. Carbide Formation in Nickel-Base Superalloy MAR-M247 Processed through Scanning Laser Epitaxy (SLE). *Solid Free Fabr Symp – An Addit Manuf Conf Rev Pap*. 2016:460-468.

118. Sundararaman M, Mukhopadhyay P, Banerjee S. Carbide precipitation in nickel base superalloys 718 and 625 and their effect on mechanical properties. *TMS Superalloys 718*. 1997:625-706. doi:10.7449/1997/Superalloys_1997_367_378

119. Rae CMF, Karunaratne MS a., Small CJ, Broomfield RW, Jones CN, Reed RC. Topologically close packed phases in an experimental rhenium-containing single crystal superalloy. *Superalloys 2000 (Ninth Int Symp*. 2000:767-776. doi:10.7449/2000/Superalloys_2000_767_776

120. Seiser B, Drautz R, Pettifor DG. TCP phase predictions in Ni-based superalloys: Structure maps revisited. *Acta Mater*. 2011;59(2):749-763. doi:10.1016/j.actamat.2010.10.013

121. Widom M, Huhn WP. Prediction of orientational phase transition in boron carbide. *Solid State Sci*. 2012;14(11-12):1648-1652. doi:10.1016/j.solidstatesciences.2012.05.010

122. Erickson GL. The Development and Application of CMSX®-10. *Superalloys 2006*. 1996:035-044. doi:10.7449/1996/Superalloys_1996_35_44

123. Deshpande VS, Needleman a., Van Der Giessen E. Plasticity size effects in tension and compression of single crystals. *J Mech Phys Solids*. 2005;53:2661-2691. doi:10.1016/j.jmps.2005.07.005

124. Keller C, Hug E, Habraken AM, Duchêne L. Effect of stress path on the miniaturization size effect for nickel polycrystals. 2015;64:26-39.

125. El-Awady J a., Rao SI, Woodward C, Dimiduk DM, Uchic MD. Trapping and escape of dislocations in micro-crystals with external and internal barriers. *Int J Plast*. 2011;27(3):372-387. doi:10.1016/j.ijplas.2010.06.006

126. Uchic MD, Dimiduk DM, Florando JN, Nix WD. Sample dimensions influence strength and crystal plasticity. *Science*. 2004;305:986-989. doi:10.1126/science.1098993

127. Demir E, Raabe D, Zaafarani N, Zaefferer S. Investigation of the indentation size effect through the measurement of the geometrically necessary dislocations beneath small indents of different depths using EBSD tomography. *Acta Mater*. 2009;57(2):559-569. doi:10.1016/j.actamat.2008.09.039

128. Parthasarathy T a., Rao SI, Dimiduk DM, Uchic MD, Trinkle DR. Contribution to size effect of yield strength from the stochastics of dislocation source lengths in finite samples. *Scr Mater*. 2007;56:313-316. doi:10.1016/j.scriptamat.2006.09.016

129. Norfleet DM, Dimiduk DM, Polasik SJ, Uchic MD, Mills MJ. Dislocation structures and their relationship to strength in deformed nickel microcrystals. *Acta Mater*. 2008;56(13):2988-3001. doi:10.1016/j.actamat.2008.02.046

130. Ng KS, Ngan a. HW. Effects of trapping dislocations within small crystals on their deformation behavior. *Acta Mater*. 2009;57(16):4902-4910. doi:10.1016/j.actamat.2009.06.053

131. Uchic MD, Dimiduk DM, Wheeler R, Shade P a., Fraser HL. Application of micro-sample testing to study fundamental aspects of plastic flow. *Scr Mater*. 2006;54(5):759-764. doi:10.1016/j.scriptamat.2005.11.016

132. Shade P a., Uchic MD, Dimiduk DM, Viswanathan GB, Wheeler R, Fraser HL. Size-affected single-slip behavior of René N5 microcrystals. *Mater Sci Eng A*. 2012;535:53-61. doi:10.1016/j.msea.2011.12.041

133. El-Awady J a., Uchic MD, Shade P a., et al. Pre-straining effects on the power-law scaling of size-dependent strengthening in Ni single crystals. *Scr Mater*. 2013;68:207-210.

doi:10.1016/j.scriptamat.2012.10.035

134. Norfleet DM, Dimiduk DM, Polasik SJ, Uchic MD, Mills MJ. Dislocation structures and their relationship to strength in deformed nickel microcrystals. *Acta Mater*. 2008;56:2988-3001. doi:10.1016/j.actamat.2008.02.046

135. Ozdemir N, Karaman I, Mara N a., Chumlyakov YI, Karaca HE. Size effects in the superelastic response of Ni54Fe19Ga27 shape memory alloy pillars with a two stage martensitic transformation. *Acta Mater*. 2012;60(16):5670-5685. doi:10.1016/j.actamat.2012.06.035

136. Benzerga a a, Chet YB, Needleman a, Giessen E Van Der. Incorporating three-dimensional mechanisms into two-dimensional dislocation dynamics. *Model Simul Mater Sci Eng*. 2004;12:557-559. doi:10.1088/0965-0393/12/3/C01

137. Weygand D, Poignant M, Gumbsch P, Kraft O. Three-dimensional dislocation dynamics simulation of the influence of sample size on the stress–strain behavior of fcc single-crystalline pillars. *Mater Sci Eng A*. 2008;483-484:188-190. doi:10.1016/j.msea.2006.09.183

138. Kheradmand N, Vehoff H, Barnoush A. An insight into the role of the grain boundary in plastic deformation by means of a bicrystalline pillar compression test and atomistic simulation. *Acta Mater*. 2013;61(19):7454-7465. doi:10.1016/j.actamat.2013.08.056

139. Senger J, Weygand D, Gumbsch P, Kraft O. Discrete dislocation simulations of the plasticity of micro-pillars under uniaxial loading. *Scr Mater*. 2008;58(7):587-590. doi:10.1016/j.scriptamat.2007.11.031

140. Benzerga a. a., Shaver NF. Scale dependence of mechanical properties of single crystals under uniform deformation. *Scr Mater*. 2006;54:1937-1941. doi:10.1016/j.scriptamat.2006.02.003

141. Lee S-W, Nix WD. Geometrical analysis of 3D dislocation dynamics simulations of FCC micro-pillar plasticity. *Mater Sci Eng A*. 2010;527(7-8):1903-1910. doi:10.1016/j.msea.2009.11.020

142. Rao SI, Dimiduk DM, Tang M, Uchic MD, Woodward C. SINGLE-ENDED DISLOCATION SOURCES IN MICROMETER-SIZED SINGLE CRYSTALS. 2007.

143. Uchic MD, Dimiduk DM, Florando JN, Nix WD. Sample dimensions influence strength and crystal plasticity. *Science*. 2004;305(5686):986-989. doi:10.1126/science.1098993

144. El-Awady J a., Uchic MD, Shade P a., et al. Pre-straining effects on the power-law scaling of size-dependent strengthening in Ni single crystals. *Scr Mater*. 2013;68(3-4):207-210. doi:10.1016/j.scriptamat.2012.10.035

145. Schneider a. S, Clark BG, Frick CP, Gruber P a., Arzt E. Effect of orientation and loading rate on compression behavior of small-scale Mo pillars. *Mater Sci Eng A*. 2009;508(1-2):241-246. doi:10.1016/j.msea.2009.01.011

146. Parthasarathy T a., Rao SI, Dimiduk DM, Uchic MD, Trinkle DR. Contribution to size effect of yield strength from the stochastics of dislocation source lengths in finite samples. *Scr Mater*. 2007;56(4):313-316. doi:10.1016/j.scriptamat.2006.09.016

147. Dou R, Derby B. A universal scaling law for the strength of metal micropillars and nanowires. *Scr Mater*. 2009;61(5):524-527. doi:10.1016/j.scriptamat.2009.05.012

148. Konstantinidis A a., Aifantis KE, De Hosson JTM. Capturing the stochastic mechanical behavior of micro and nanopillars. *Mater Sci Eng A*. 2014;597:89-94. doi:10.1016/j.msea.2013.12.053

149. Volkert C a., Lilleodden ET. Size effects in the deformation of sub-micron Au columns. *Philos Mag*. 2006;86(June 2015):5567-5579. doi:10.1080/14786430600567739

150. Greer JR, Oliver WC, Nix WD. Size dependence of mechanical properties of gold at the micron scale in the absence of strain gradients. *Acta Mater*. 2005;53:1821-1830. doi:10.1016/j.actamat.2004.12.031

151. Brinckmann S, Kim JY, Greer JR. Fundamental differences in mechanical behavior between two types of crystals at the nanoscale. *Phys Rev Lett*. 2008;100(APRIL):1-4. doi:10.1103/PhysRevLett.100.155502

152. Greer JR, Weinberger CR, Cai W. Comparing the strength of f.c.c. and b.c.c. sub-micrometer pillars: Compression experiments and dislocation dynamics simulations. *Mater Sci Eng A*. 2008;493(1-2):21-25. doi:10.1016/j.msea.2007.08.093

153. Maaß R, Van Petegem S, Grolimund D, Van Swygenhoven H, Kiener D, Dehm G. Crystal rotation in Cu single crystal micropillars: In situ Laue and electron backscatter diffraction. *Appl Phys Lett*. 2008;92(7):071905. doi:10.1063/1.2884688

154. Maaβ R, Grolimund D, Van Petegem S, et al. Defect structure in micropillars using x-ray microdiffraction. *Appl Phys Lett*. 2006;89(15):151905. doi:10.1063/1.2358204

155. Puri S, Roy A, Acharya A, Dimiduk D. Modeling dislocation sources and size effects at initial yield in continuum plasticity. *J Mech Mater Struct*. 2010;4(9):1603-1618. doi:10.2140/jomms.2009.4.1603

156. Motz C, Weygand D, Senger J, Gumbsch P. Initial dislocation structures in 3-D discrete dislocation dynamics and their influence on microscale plasticity. *Acta Mater*. 2009;57(6):1744-1754. doi:10.1016/j.actamat.2008.12.020

157. Rao SI, Dimiduk DM, Parthasarathy T a., Uchic MD, Tang M, Woodward C. Athermal mechanisms of size-dependent crystal flow gleaned from three-dimensional discrete dislocation simulations. *Acta Mater*. 2008;56:3245-3259. doi:10.1016/j.actamat.2008.03.011

158. Gong J, Wilkinson AJ. A microcantilever investigation of size effect , solid-solution strengthening and second-phase strengthening for h a i prism slip in alpha-Ti. *Acta Mater*. 2011;59(15):5970-5981. doi:10.1016/j.actamat.2011.06.005

159. Motz C, Scho T, Pippan R. Mechanical properties of micro-sized copper bending beams machined by the focused ion beam technique. 2005;53:4269-4279. doi:10.1016/j.actamat.2005.05.036

160. Shim S, Bei H, Miller MK, Pharr GM, George EP. Effects of focused ion beam milling on the compressive behavior of directionally solidified micropillars and the nanoindentation response of an electropolished surface. *Acta Mater*. 2009;57(2):503-510. doi:10.1016/j.actamat.2008.09.033

161. Hütsch J, Lilleodden ET. The influence of focused-ion beam preparation technique on microcompression investigations: Lathe vs. annular milling. *Scr Mater*. 2014;77:49-51. doi:10.1016/j.scriptamat.2014.01.016

162. Jun TS, Sernicola G, Dunne FPE, Britton TB. Local deformation mechanisms of two-phase Ti alloy. *Mater Sci Eng A*. 2016;649:39-47. doi:10.1016/j.msea.2015.09.016

163. Bhowmik A, Dolbnya IP, Britton T Ben, et al. Using coupled micropillar compression and micro-Laue diffraction to investigate deformation mechanisms in a complex metallic alloy Al13Co4. *Appl Phys Lett*. 2016;108(11). doi:10.1063/1.4944486

164. Ouyang C, Li Z, Huang M, Hu L, Hou C. Combined influences of micro-pillar geometry and substrate constraint on microplastic behavior of compressed single-crystal micro-pillar: Two-dimensional discrete dislocation dynamics modeling. *Mater Sci Eng A*. 2009;526(1-2):235-243. doi:10.1016/j.msea.2009.07.037

165. Kiener D, Motz C, Dehm G. Micro-compression testing: A critical discussion of experimental constraints. *Mater Sci Eng A*. 2009;505(1-2):79-87. doi:10.1016/j.msea.2009.01.005

166. Takagi H, Fujiwara M, Kakehi K. Measuring Young's modulus of Ni-based superalloy single crystals at elevated temperatures through microindentation. *Mater Sci Eng A*. 2004;387-389(1-2 SPEC. ISS.):348-351. doi:10.1016/j.msea.2004.01.061

167. Zimmermann J, Van Petegem S, Bei H, Grolimund D, George EP, Van Swygenhoven H. Effects of focused ion beam milling and pre-straining on the microstructure of directionally solidified molybdenum pillars: A Laue diffraction analysis. *Scr Mater*. 2010;62(10):746-749. doi:10.1016/j.scriptamat.2010.02.013

168. Uchic MD, Dimiduk DM. A methodology to investigate size scale effects in crystalline plasticity using uniaxial compression testing. *Mater Sci Eng A*. 2005;400-401:268-278. doi:10.1016/j.msea.2005.03.082

169. Aitken ZH, Fan H, El-awady JA, Greer JR. Journal of the Mechanics and Physics of Solids The effect of size, orientation and alloying on the deformation of AZ31 nanopillars. 2015;76:208-223.

170. Kashihara K. The Relationship between Crystal Rotation Axis Orientation and Active Slip System in Pure Aluminum Tricrystal Deformed in Compression. *Mater Trans*. 2008;49(3):419-423. doi:10.2320/matertrans.MBW200704

171. Uchic MD, Dimiduk DM, Florando JN, Nix WD. Exploring specimen size effects in plastic deformation of Ni3(Al, Ta). *MRS Proc*. 2002;753:1-6. doi:10.1557/PROC-753-BB1.4

172. Keller C, Hug E, Retoux R, Feaugas X. TEM study of dislocation patterns in near-surface and core regions of deformed nickel polycrystals with few grains across the cross section. *Mech Mater*. 2010;42(1):44-54. doi:10.1016/j.mechmat.2009.09.002

173. Wilkinson AJ, Britton T Ben. Strains, planes, and EBSD in materials science. *Mater Today*. 2012;15(9):366-376. doi:10.1016/S1369-7021(12)70163-3

174. fei-helios-nanolabtm-600-dualbeam-fibsem @ cemas.osu.edu.

175. Yang Y, Ye JC, Lu J, Liu FX, Liaw PK. Effects of specimen geometry and base material on the mechanical behavior of focused-ion-beam-fabricated metallic-glass micropillars. *Acta Mater*. 2009;57(5):1613-1623. doi:10.1016/j.actamat.2008.11.043

176. Fei H, Abraham A, Chawla N, Jiang H. Evaluation of Micro-Pillar Compression Tests for Accurate Determination of Elastic-Plastic Constitutive Relations. *J Appl Mech*. 2012;79(6):061011.

doi:10.1115/1.4006767

177. Olaf Engler VR. *Introduction to Texture Analysis: Macrotexture, Microtexture, and Orientation Mapping, Second Edition*.; 2008. doi:interface shear stre

178. Lu X, Du J, Deng Q, Zhuang J. Stress rupture properties of GH4169 superalloy. *J Mater Res Technol*. 2014;3(2):107-113. doi:10.1016/j.jmrt.2014.03.003

179. Jozwik P, Jezierska E, Bojar Z. TEM investigations of Ni3Al-based intermetallic polycrystals. *Mater Chem Phys*. 2003;81(2-3):448-451. doi:10.1016/S0254-0584(03)00044-0

180. Ng KS, Ngan a. HW. Breakdown of Schmid's law in micropillars. *Scr Mater*. 2008;59(7):796-799. doi:10.1016/j.scriptamat.2008.06.019

181. Swanson R. Effect of Crystal Orientation on Fatigue Failure of Single Crystal Nickel Base Turbine Blade Superalloys.

182. Fei H, Abraham A, Chawla N, Jiang H. Evaluation of Micro-Pillar Compression Tests for Accurate Determination of Elastic-Plastic Constitutive Relations. *J Appl Mech*. 2012;79:061011. doi:10.1115/1.4006767

183. Parsa A, Ramsperger M, Kostka A, Somsen C, Körner C, Eggeler G. Transmission Electron Microscopy of a CMSX-4 Ni-Base Superalloy Produced by Selective Electron Beam Melting. *Metals (Basel)*. 2016;6(12):258. doi:10.3390/met6110258

184. TAN Y, ZANG C, ZHOU B, WANG X, PETROV EP. Identification of crystal orientation for turbine blades with anisotropy materials. *Chinese J Aeronaut*. 2018;31(2):412-419. doi:10.1016/j.cja.2017.12.001

185. Arakere NK, Swanson G. Fretting Stresses in Single Crystal Superalloy Turbine Blade Attachments. *J Tribol*. 2001;123(April):413. doi:10.1115/1.1308032

186. Swanson GR. *Effect of Crystal Orientation on Analysis of Single-Crystal , Nickel-Based Turbine Blade Superalloys*.; 2000.

187. Zhang M, Li F, Yuan Z, Li J, Wang S. Effect of heat treatment on the micro-indentation behavior of powder metallurgy nickel based superalloy FGH96. *Mater Des*. 2013;49(August):705-715. doi:10.1016/j.matdes.2013.02.024

188. Leidermark D, Moverare JJ, Simonsson K, Sjöström S, Johansson S. Room temperature yield behaviour of a single-crystal nickel-base superalloy with tension/compression asymmetry. *Comput Mater Sci*. 2009;47(2):366-372. doi:10.1016/j.commatsci.2009.08.012

189. Segersäll M, Moverare JJ. Crystallographic orientation influence on the serrated yielding behavior of a single-crystal superalloy. *Materials (Basel)*. 2013;6(2):437-444. doi:10.3390/ma6020437

190. Dye D, Coakley J, Vorontsov VA, Stone HJ, Rogge RB. Elastic moduli and load partitioning in a single-crystal nickel superalloy. *Scr Mater*. 2009;61(2):109-112. doi:10.1016/j.scriptamat.2009.03.008

191. Zhang M, Li F, Yuan Z, Li J, Wang S. Effect of heat treatment on the micro-indentation behavior of powder metallurgy nickel based superalloy FGH96. *Mater Des*. 2013;49:705-715.

doi:10.1016/j.matdes.2013.02.024

192. Zhang M, Li F, Wang L, Wang S. Investigations of inhomogeneous mechanical properties and plastic deformations in HIPed P/M nickel-base superalloy FGH96 by using micro-indentation methods. *Mater Sci Eng A*. 2012;556:233-245. doi:10.1016/j.msea.2012.06.081

193. Boota M, Gäbler J, Schäfer L, Keunecke M. Investigations of suitable hard coatings on nickel-based single-crystal superalloy (CMSX-4). *Surf Coatings Technol*. 2012;207:300-304. doi:10.1016/j.surfcoat.2012.07.003

194. Pigrova GD. TCP-phases in nickel-base alloys with elevated chromium content. *Met Sci Heat Treat*. 2005;47(11-12):544-551. doi:10.1007/s11041-006-0029-7

195. Dreshfiezd RL. Estimation of gamma phase composition in nickel-base superalloys (based on geometric analysis of a four-component phase diagram.

196. CHOI BG, JO CY, HONG HU, KIM IS, SEO SM, KIM HM. Effect of pre-strain on microstructural evolution during thermal exposure of single crystal superalloy CMSX-4. *Trans Nonferrous Met Soc China*. 2011;21(6):1291-1296. doi:10.1016/S1003-6326(11)60855-8

197. Yang YF, Jiang CY, Bao ZB, Zhu SL, Wang FH. Effect of aluminisation characteristics on the microstructure of single phase - (Ni , Pt) Al coating and the isothermal oxidation behaviour. *Eval Program Plann*. 2016;106:43-54. doi:10.1016/j.corsci.2016.01.024

198. Roa JJ, Jiménez-Piqué E, Tarragó JM, Zivcec M, Broeckmann C, Llanes L. Berkovich nanoindentation and deformation mechanisms in a hardmetal binder-like cobalt alloy. *Mater Sci Eng A*. 2015;621:128-132. doi:10.1016/j.msea.2014.10.064

199. Zhang JX, Murakumo T, Harada H, Koizumi Y, Kobayashi T. Creep deformation mechanisms in some modern single-crystal superalloys. *Superalloy 2004*. 2004:189-195. doi:10.7449/2004/Superalloys_2004_189_195

200. Tang S, Zheng Z, Ning LK. Gamma prime coarsening in a nickel base single crystal superalloy. *Mater Lett*. 2014;128:388-391. doi:10.1016/j.matlet.2014.04.185

201. Harris K, Erickson GL, Schwer RE. MAR M 247 Derivations - CM 247 LC DC alloy CMSX Single crystal alloys Properties & Performance. *Superalloys 1984*. 1984:221-230. doi:10.1353/shb.0.0105

202. Xiang S, Mao S, Wei H, et al. Selective evolution of secondary γ′ precipitation in a Ni-based single crystal superalloy both in the γ matrix and at the dislocation nodes. *Acta Mater*. 2016;116:343-353. doi:10.1016/j.actamat.2016.06.055

203. MacLachlan DW, Wright LW, Gunturi SSK, Knowles DM. Modelling the Anisotropic and Biaxial Creep Behaviour of Ni-Base Single Crystal Superalloys CMSX-4 and SRR99 at 1223K. *Superalloys 2000*. 2000:357-366. doi:\url{10.7449/2000/Superalloys{\textunderscore }2000{\textunderscore }357{\textunderscore }366}

204. Wang F, Ma D, Bogner S, Bührig-Polaczek A. Comparative Investigation of the Downward and Upward Directionally Solidified Single-Crystal Blades of Superalloy CMSX-4. *Metall Mater Trans A*. 2016;47(5):2376-2386. doi:10.1007/s11661-016-3415-9

205. Terner M, Yoon HY, Hong HU, Seo SM, Gu JH, Lee JH. Clear path to the directional solidification

of Ni-based superalloy CMSX-10: A peritectic reaction. *Mater Charact*. 2015;105:56-63. doi:10.1016/j.matchar.2015.04.018

206. Raabe D. On the contribution of screw dislocations to internal stress fields associated with dislocation cell structures. *Philos Mag A*. 1996;73(5):1363-1383. doi:10.1080/01418619608245139

207. Warnken N, Ma D, Drevermann A, Reed RC, Fries SG, Steinbach I. Phase-field modelling of as-cast microstructure evolution in nickel-based superalloys. *Acta Mater*. 2009;57(19):5862-5875. doi:10.1016/j.actamat.2009.08.013

208. Zhang M, Li F, Chen B, Wang S. Investigation of micro-indentation characteristics of P/M nickel-base superalloy FGH96 using dislocation-power theory. *Mater Sci Eng A*. 2012;535:170-181. doi:10.1016/j.msea.2011.12.060

209. Sengupta A, Putatunda SK, Bartosiewicz L, et al. Tensile behavior of a new single-crystal nickel-based superalloy (CMSX-4) at room and elevated temperatures. *J Mater Eng Perform*. 1994;3(1):73-81. doi:10.1007/BF02654502

210. Huang M, Li Z, Tong J. The influence of dislocation climb on the mechanical behavior of polycrystals and grain size effect at elevated temperature. *Int J Plast*. 2014;61:112-127. doi:10.1016/j.ijplas.2014.06.002

211. Choi YS, Uchic MD, Parthasarathy T a., Dimiduk DM. Numerical study on microcompression tests of anisotropic single crystals. *Scr Mater*. 2007;57(9):849-852. doi:10.1016/j.scriptamat.2007.06.057

212. Arora K, Kishida K, Tanaka K, Inui H. Effects of lattice misfit on plastic deformation behavior of single-crystalline micropillars of Ni-based superalloys. *Acta Mater*. 2017;138:119-130. doi:10.1016/j.actamat.2017.07.044

213. Segersäll M. *Nickel-Based Single-Crystal Superalloys Temperature Properties*.; 2013.

214. Deformation E, Strength Y, Limit P, et al. Interpretation of Stress-Strain Curves and Mechanical Properties of Materials. (4):1-6.

215. Long H, Wei H, Liu Y, et al. Effect of lattice misfit on the evolution of the dislocation structure in Ni-based single crystal superalloys during thermal exposure. *Acta Mater*. 2016;120:95-107. doi:10.1016/j.actamat.2016.08.035

216. Deléhouzée L, Deruyttere A. The stacking fault density in solid solutions based on copper, silver, nickel, aluminium and lead. *Acta Metall*. 1967;15(5):727-734. doi:10.1016/0001-6160(67)90353-7

217. Gallagher PCJ. The influence of alloying, temperature, and related effects on the stacking fault energy. *Metall Trans*. 1970;1(9):2429-2461. doi:10.1007/BF03038370

218. Guruprasad PJ, Benzerga a. a. Size effects under homogeneous deformation of single crystals: A discrete dislocation analysis. *J Mech Phys Solids*. 2008;56:132-156. doi:10.1016/j.jmps.2007.03.009

219. Zhu Y, Xiang Y. A continuum model for dislocation dynamics in three dimensions using the dislocation density potential functions and its application in understanding the micro-pillar size

effect. *J Mech Phys Solids*. 2015;84:230-253. doi:10.1016/j.jmps.2015.07.015

220. Hussein AM, Rao SI, Uchic MD, Parthasarathay TA, El-Awady JA. The strength and dislocation microstructure evolution in superalloy microcrystals. *J Mech Phys Solids*. 2017;99(October 2016):146-162. doi:10.1016/j.jmps.2016.11.014

221. Pollock TM, Argon a. S. Creep resistance of CMSX-3 nickel base superalloy single crystals. *Acta Metall Mater*. 1992;40(95):1-30. doi:10.1016/0956-7151(92)90195-K

222. Sweeney C a, O'Brien B, Dunne FPE, McHugh PE, Leen SB. Micro-scale testing and micromechanical modelling for high cycle fatigue of CoCr stent material. *J Mech Behav Biomed Mater*. 2015;46:244-260. doi:10.1016/j.jmbbm.2015.02.011